FROM THE SATELLITE TO THE EARTH'S SURFACE: STUDIES RELEVANT TO NASA'S PLANKTON, AEROSOL, CLOUD, OCEAN ECOSYSTEMS (PACE) MISSION

EDITED BY: David Antoine and Oleg Dubovik

PUBLISHED IN: Frontiers in Earth Science and Frontiers in Environmental Science

frontiers Research Topics

ISSN 1664-8714
ISBN 978-2-88963-500-9
DOI 10.3389/978-2-88963-500-9

About Frontiers

Frontiers is more than just an open-access publisher of scholarly articles: it is a pioneering approach to the world of academia, radically improving the way scholarly research is managed. The grand vision of Frontiers is a world where all people have an equal opportunity to seek, share and generate knowledge. Frontiers provides immediate and permanent online open access to all its publications, but this alone is not enough to realize our grand goals.

Frontiers Journal Series

The Frontiers Journal Series is a multi-tier and interdisciplinary set of open-access, online journals, promising a paradigm shift from the current review, selection and dissemination processes in academic publishing. All Frontiers journals are driven by researchers for researchers; therefore, they constitute a service to the scholarly community. At the same time, the Frontiers Journal Series operates on a revolutionary invention, the tiered publishing system, initially addressing specific communities of scholars, and gradually climbing up to broader public understanding, thus serving the interests of the lay society, too.

Dedication to Quality

Each Frontiers article is a landmark of the highest quality, thanks to genuinely collaborative interactions between authors and review editors, who include some of the world's best academicians. Research must be certified by peers before entering a stream of knowledge that may eventually reach the public - and shape society; therefore, Frontiers only applies the most rigorous and unbiased reviews.
Frontiers revolutionizes research publishing by freely delivering the most outstanding research, evaluated with no bias from both the academic and social point of view. By applying the most advanced information technologies, Frontiers is catapulting scholarly publishing into a new generation.

What are Frontiers Research Topics?

Frontiers Research Topics are very popular trademarks of the Frontiers Journals Series: they are collections of at least ten articles, all centered on a particular subject. With their unique mix of varied contributions from Original Research to Review Articles, Frontiers Research Topics unify the most influential researchers, the latest key findings and historical advances in a hot research area! Find out more on how to host your own Frontiers Research Topic or contribute to one as an author by contacting the Frontiers Editorial Office: researchtopics@frontiersin.org

FROM THE SATELLITE TO THE EARTH'S SURFACE: STUDIES RELEVANT TO NASA'S PLANKTON, AEROSOL, CLOUD, OCEAN ECOSYSTEMS (PACE) MISSION

Topic Editors:
David Antoine, Curtin University, Australia
Oleg Dubovik, UMR8518 Laboratoire d'optique atmosphèrique (LOA), France

Earth's atmosphere and oceans play individual and interconnected roles in regulating climate and the hydrological system, supporting organisms and ecosystems, and contributing to the well-being of human communities and economies. Recognizing the importance of these two geophysical fluids, NASA designed the Plankton, Aerosol, Cloud and ocean Ecosystems (PACE) mission to bring cutting edge technology to space borne measurements of the atmosphere and ocean. PACE will carry the Ocean Color Instrument (OCI), a radiometer with hyperspectral capability from the ultraviolet through the near-infrared, plus eight discreet shortwave infrared bands. Thus, OCI will measure the broadest solar spectrum of any NASA instrument, to date. PACE's second instrument will be a Multi-Angle Polarimeter (MAP). MAP will be NASA's first imaging polarimeter on board a comprehensive Earth science mission.

These instruments bring new capability to the science community, but also new challenges. Fundamentals, such as basic radiative transfer models, require review, enhancements and benchmarking in order to meet the needs of the atmosphere-ocean communities in the PACE era. Both OCI and MAP will bring opportunities to continue heritage climate data records of aerosols and clouds and to advance characterization of these atmospheric constituents with new macrophysical and microphysical parameters. The ability to better characterize atmospheric constituents is a necessity to better separate ocean and atmosphere signals in order to fully realize the potential of PACE measurements for oceanic observations. Atmospheric correction in the PACE era must address the expanded wavelength range and resolution of OCI images, requiring new approaches that go beyond heritage algorithms.

This Research Topic encompasses fundamental radiative transfer studies, with application to the atmosphere, ocean or coupled atmosphere-ocean system. It includes remote sensing of aerosols, clouds and trace gases, over ocean or over land, but with particular focus on algorithms that take advantage of OCI's new capabilities or multi-angle polarimetry. The Research Topic embraces studies of atmospheric correction over ocean including addressing issues of aerosols, cloud masking, foam, bubbles, ice etc., as well as ocean bio-optics and biogeochemical studies taking advantage of the PACE and polarization spectral capabilities.

Citation: Antoine, D., Dubovik, O., eds. (2020). From the Satellite to the Earth's Surface: Studies Relevant to NASA's Plankton, Aerosol, Cloud, Ocean Ecosystems (PACE) Mission. Lausanne: Frontiers Media SA. doi: 10.3389/978-2-88963-500-9

Table of Contents

frontiers
in Earth Science

ORIGINAL RESEARCH
published: 26 February 2019
doi: 10.3389/feart.2019.00014

Hyperspectral Measurements, Parameterizations, and Atmospheric Correction of Whitecaps and Foam From Visible to Shortwave Infrared for Ocean Color Remote Sensing

*Heidi M. Dierssen**

Department of Marine Sciences, University of Connecticut, Groton, CT, United States

Breaking waves are highly reflective features on the sea surface that change the spectral properties of the ocean surface in both magnitude and spectral shape. Here, hyperspectral reflectance measurements of whitecaps from 400 to 2,500 nm were taken in Long Island Sound, USA of natural and manufactured breaking waves to explore new methods to estimate whitecap contributions to ocean color imagery. Whitecap reflectance was on average ∼40% in visible wavelengths and decreased significantly into the near infrared and shortwave infrared following published trends. The spectral shape was well-characterized by a third order polynomial function of liquid water absorption that can be incorporated into coupled ocean-atmospheric models and spectral optimization routines. Localized troughs in whitecap reflectance correspond to peaks in liquid water absorption and depths of the troughs are correlated to the amount and intensity of the breaking waves. Specifically, baseline-corrected band depths at 980 and 1,200 nm explained 77 and 90% of the whitecap-enhanced reflectance on a logarithmic scale, respectively. Including these wavebands into future ocean color sensors could potentially provide new tools to estimate whitecap contributions to reflectance more accurately than with wind speed. An effective whitecap factor was defined as the optical enhancements within a pixel due to whitecaps and foam independent of spatial scale. A simple mixed-pixel model of whitecap and background reflectance explained as much of the variability in measured reflectance as more complex models incorporating semi-transparent layers of foam. Using an example atmosphere, enhanced radiance from whitecaps was detectable at the top of the atmosphere and a multiple regression of at-sensor radiance at 880, 1,038, 1,250, and 1,615 nm explained 99% of the variability in whitecap factor. A proposed model of whitecap-free reflectance includes contributions from water-leaving radiance, glint, and diffuse reflected skylight. The epsilon ratio at 753 and 869 nm commonly used for aerosol model selection is nearly invariant with whitecap factor compared to the ratio at shortwave infrared bands. While more validation data is needed, this research suggests several promising avenues to retrieve estimates of the whitecap reflectance and to use ocean color to further elucidate the physics of wave breaking and gas exchange.

Keywords: whitecap, hyperspectral, foam, reflectance, ocean color, sea surface, atmospheric correction

Edited by:
David Antoine,
Curtin University, Australia

Reviewed by:
Martin Hieronymi,
Helmholtz Centre for Materials and Coastal Research (HZG), Germany
Alexander Kokhanovsky,
Vitrociset, Germany

***Correspondence:**
Heidi M. Dierssen
heidi.dierssen@uconn.edu

Specialty section:
This article was submitted to Atmospheric Science, a section of the journal Frontiers in Earth Science

Received: *01 December 2018*
Accepted: *28 January 2019*
Published: *26 February 2019*

Citation:
Dierssen HM (2019) Hyperspectral Measurements, Parameterizations, and Atmospheric Correction of Whitecaps and Foam From Visible to Shortwave Infrared for Ocean Color Remote Sensing. Front. Earth Sci. 7:14. doi: 10.3389/feart.2019.00014

INTRODUCTION

Breaking wind-waves or whitecaps are highly reflective features on the sea surface that change the spectral properties of the ocean surface in both magnitude and spectral shape. Whitecaps are weakly absorbing, highly light-scattering media (Kokhanovsky, 2004). At wind speeds of around 3 m s^{-1} and higher, waves can break and entrain air in the water which subsequently breaks up into bubbles which rise to the surface (Thorpe, 1982; Monahan and O'Muircheartaigh, 1986). The presence of breaking waves or whitecaps serves to significantly enhance the reflectance of the sea surface measured by aircraft or satellites. Since the seminal work by Gordon and Wang (1994), atmospheric correction approaches for ocean color imagery have included models to account for elevated reflectance of whitecaps. This study builds off of the research from the last few decades to provide new insights into hyperspectral approaches for estimating whitecap contributions for satellites of varying spatial resolutions.

The amount of whitecaps on the sea surface is commonly characterized as a fractional coverage of the sea with actively breaking waves. The fractional whitecap coverage is relatively small across the global ocean (<1%), but can be up to 10% in very active seas (Zhao and Toba, 2001; Brumer et al., 2017). This fractional component includes Stage A whitecap representing the actively breaking wave or bright white portion of the wave (Monahan, 1993). Elevated reflectance also occurs due to the residual plume of foam and subsurface bubbles that is referred to as a Stage B whitecap. Differentiating between these two stages is challenging and it is unclear as to how much of the Stage B plume is included in different methods of estimating whitecap fraction. With image analysis methods, the foam portion of Stage B is generally included in the estimate of whitecap fraction, but elevated reflectance from the submerged bubble plume is not often visible in photography (Brumer et al., 2017). A recent study taken in high wind conditions of the Southern Ocean suggests fractional whitecap coverage retrievals from a radiometer were consistently higher than estimates from high-resolution digital photographs due to the enhanced sensitivity of the radiometer and the ability to detect more of the decaying bubble plume area (Randolph et al., 2017).

The use of a whitecap fraction is appropriate for sensors with a 1-km pixel, which is the footprint of most ocean color missions like the proposed hyperspectral mission PACE. However, higher spatial resolution satellites have smaller pixels ranging from 30 m down to 1 m that can resolve individual whitecap features. For example, the proposed hyperspectral missions Enmap and HyspIRI aim to have 30-m pixel resolution (Guanter et al., 2015; Lee et al., 2015). Hence, the fraction of whitecaps within a pixel can be much higher than the average fractional whitecap coverage and can vary from 0 to 1 within a given scene. For example, a pan-sharpened Landsat-8 image (15-m pixels) off the coast of Normandy where winds were 12.5 m s^{-1} illustrates how ocean swell and the contribution of breaking waves can vary on a pixel-by-pixel basis (**Figure 1A**). The imagery also highlights how the impact of a ship wake, observed as the larger "white" feature centered in the image, can also impact the observed ocean color in high resolution imagery (Vanhellemont and Ruddick, 2014).

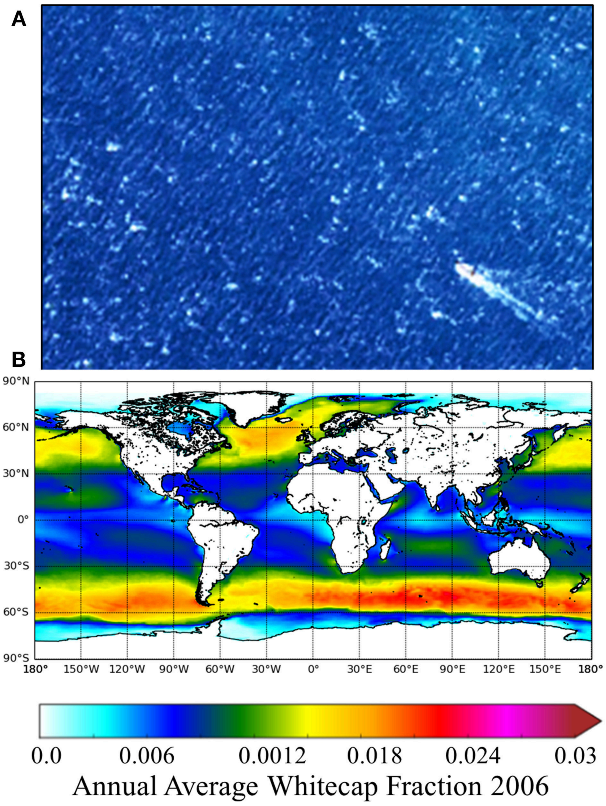

FIGURE 1 | (A) Pseudo-true color image from a 15-m pan sharpened Landsat-8 OLI image from the coast of Normandy with winds estimated at 12.5 m s^{-1} illustrating whitecap features and a boat wake. **(B)** Estimate of the average whitecap fraction for 2006 calculated from a parameterization of wind speed and satellite-derived whitecap fraction from microwave brightness temperature. Modified from Albert et al. (2016) with permission from M. Anguelova.

Some of the first measurements of whitecap reflectance were made in the 1980's (Whitlock et al., 1982; Koepke, 1984). While most optical studies dealing with whitecaps and bubbles focus on the visible and near infrared (NIR) wavelengths, limited studies suggest that whitecaps can reflect significantly in the short wave infrared (SWIR) and would interfere with atmospheric correction routines that use SWIR bands (e.g., 1,240 and 1,640 nm) (Whitlock et al., 1982; Frouin et al., 1996; Wright et al., 2012). The reflectance of whitecaps has been modeled using parameterizations of the absorption coefficient of water (Whitlock et al., 1982; Kokhanovsky, 2004). However, as discussed further in this contribution, there were errors in the Whitlock et al. (1982) study, including the water absorption values used in visible wavelengths and the reflectance standard, that make these values inaccurate.

Although technically not a constituent of the atmosphere, corrections for whitecaps, foam, and bubbles are included in the current atmospheric correction routines. Whitecap reflectance is often modeled using an empirical cubic relationship to wind speed and an approximate reflectance value for an individual whitecap (Gordon and Wang, 1994; Ahn et al., 2012). However, such models are overly simplistic and presume that whitecap coverage at an individual daily pixel can be estimated as a simple function of wind speed throughout the world ocean. As shown in many different studies (Anguelova and Webster, 2006; Brumer et al., 2017), instantaneous whitecap coverage can vary by several orders of magnitude at the same wind speed. The fraction of whitecaps can be influenced by the fetch and duration and the wind, water temperature, air temperature and stability of the lower atmosphere defined by the air/water temperature differential, salinity, current shear, and long wave interaction, wave age, and the presence of surfactants such as organic films (reviewed in Scanlon and Ward, 2016). "At different locations in the world ocean, various environmental and meteorological factors act in concert but with different strengths and form a composite effect that either enhances or suppresses the effect of wind alone" (Anguelova and Webster, 2006). Hence, any wind speed parameterization of whitecaps is meant to be climatological rather than instantaneous.

Whitecaps on the sea surface are relevant to air-sea gas exchange, generation of sea spray aerosols and the climate cycle (Blanchard, 1985; Asher and Wanninkhof, 1998; Monahan, 2008). They are especially critical in retrieving accurate ocean color in regions like the Southern Ocean which are characterized by persistent high winds and breaking waves (**Figure 1B**). Here, new measurements are presented of natural and manufactured whitecaps and foam from the ultraviolet through the shortwave infrared. These data are used to address whether whitecaps can be well-approximated in shape and magnitude by an average whitecap reflectance, what parameterizations can be used to model mixed pixels of varying fractions of whitecaps, and whether more accurate algorithms can be developed to approximate whitecap reflectance for hyperspectral remote sensing applications based on the measured spectrum itself rather than ancillary wind speed.

METHODS

The experiments were conducted in Long Island Sound in surface waters near the University of Connecticut Avery Point campus, U.S.A. Sampling included the region known as the Race which spans 5.6 km between Fishers Island and Little Gull Island and serves as the main entrance into Long Island Sound (41°14′36.6″N 72°2′49.2″W). This region is known for a large rip line and large waves due to the depth range from 15 to 75 m coupled with the massive water exchange in and out of Long Island Sound. The water color in this region is peaked in green wavelengths and there are higher amounts of suspended material causing higher backscattered light compared to many other regions of the world ocean (Aurin et al., 2010; Aurin and Dierssen, 2012). However, the waters are not considered turbid (total suspended matter $<2\,\mathrm{g\,m^{-3}}$) and water-leaving reflectance is negligible in NIR and SWIR wavelengths.

Data Collection

Whitecap reflectance was measured using a PANalytical Boulder ASD FieldSpec 4 spectroradiometer with a wavelength range from 350 to 2,500 nm interpolated to a 1 nm resolution under ambient sunlight during clear sky conditions. The sensor was equipped with an 8.5° fore-optic and was optimized for the light field with dark current. The sensor was pointed to a 99% white Spectralon plaque held horizontally to the sea surface at a distance of ~2 cm from the plaque. The plaque was held in a relative azimuth orientation toward the sun to avoid user shading on the measurement. The plaque measurement provided an estimate of downwelling irradiance during the experiment and was taken periodically to normalize the measurement as described further below. After the measurement was taken over Spectralon, the sensor was extended over the target at ~0.5–1.5 m above the sea surface depending on the size of the swell and motion of the boat at an azimuth angle of ~145° from the sun to minimize sun glint. This translates to a field of view covering a 7.5–22-cm diameter circle on the sea surface.

For the natural breaking waves, measurements were made from the side of the *R/V Lowell Weicker* on 19 January 2016 pointing with a heading into the wind in order to maintain position with the wave field. On this day, wind speed varied from 10 to 12 $\mathrm{m\,s^{-1}}$ measured at 3 m height at the Eastern Sound Buoy in Long Island Sound (41○ 15.48′N, 72° 04.00′W) and significant wave heights estimated to be 1.5–2 m using measurements from the Central Sound Buoy (lisicos.uconn.edu). The background reflectance followed standard NASA protocols where 5-replicates were taken of a sequence of measurements from a 12% spectralon reference panel, water, and sky while maintaining a 45° zenith angle of the sensor. The sensor was positioned at an azimuth angle of ~145° from the sun to minimize sun glint. Whitecap measurements were taken in a time-series mode at 8 ms over a 20-min interval with the radiometer pointing down at a nadir angle at the sea surface for roughly 75,000 samples. Measurements were taken of the 99% spectralon reference panel at the beginning and end of sampling and after every whitecap event in an azimuthal angle facing the sun with the sensor at a nadir angle to the plaque. The time series of measurements taken over rolling breakers were considered to be spectral mixtures of whitecap, foam and undisturbed water. Four different breaking events were measured with varying intensities and contributions of breaking waves.

Measurements were also taken over manufactured breaking waves and foam from various sources including boat wakes and an outflow pipe. During these experiments, the field of view of the sensors was focused on the breaking feature and these measurements are considered to be spectral endmembers of breaking waves/foam without undisturbed water. Forward motion of the 23-m long *R/V Connecticut* produced a boat wake with a large breaking wave on the side of the ship on 29 June 2017 16:01–16:15 UTC at Race Point Long Island Sound (41° 14.62′N, 72° 02.52′W) with clear skies and a 20° solar zenith angle. In addition, measurements were taken of the boat wake and multiple layers of foam produced by circular motion of a small Carolina Skiff on 25 June 2015. Measurements were also taken of layers of foam produced on the sea surface by an outflow pipe from the high-flow pressurized seawater distribution system at the Rankin Seawater Laboratory, University of Connecticut 27 January 2015.

Data Analysis

Lambertian-equivalent reflectance of the sea surface was calculated as ratio of the measurement obtained of a breaking wave and measurement of the lambertian Spectralon plaque. Normalization was conducted using a recent calibration of the white plaque which varied from 97% in ultraviolet, 99% in visible, and 93% reflective in SWIR wavelengths out to 2,500 nm. No corrections were conducted for reflection of glint or skylight from the sea surface when estimating the reflectance from background water or water enhanced by foam and whitecaps. From a satellite perspective, the removal of sun/sky glint is a separate step from removing whitecap reflectance. Hence, the methods developed here included the sun/sky glint in the background reflectance in order to differentiate the contribution from the whitecap signal from the remaining signal.

Reflectance from breaking waves, foam, and bubbles is treated with different methods in the literature and these different methods are considered in the results section. Because whitecaps are so bright, the signal is commonly thought to dwarf the contributions from water-leaving radiance and reflected skylight or glint and is treated as a "white" patch on the sea surface. For atmospheric correction approaches, the estimated whitecap reflectance is generally considered invariant of the water-leaving signal, sky conditions, and wind speed (Gordon and Wang, 1994). Whitecaps, and particularly bubble plumes, can also be treated as an augmentation above a background reflectance (Moore et al., 2000). The total reflectance (R_t) is considered to be the background water-leaving reflectance (R_b) plus some additional amount due to whitecaps (R_{aug}), such that:

$$R_{aug} = R_t - R_b \tag{1}$$

A recent study defined an "augmented reflectance ratio" as the fractional augmentation of a whitecap above a background reflectance (Xu et al., 2015). This definition is not used in this manuscript because it is felt that an augmentation ratio does not properly reflect the physics of the system. A more nuanced approach is to treat whitecaps as a two-layered system where a semi-transparent layer of foam and bubbles overlays a background water reflectance (Frouin et al., 1996), as described further in the results. Radiative transfer modeling based on the theoretical work of Kokhanovsky (2004) and Zege et al. (2006) is presented in the Results. Radiative modeling of whitecaps bridges the measured reflectance to the optical properties of foam.

Whitecap measurements were compared to the absorption coefficient of seawater, a_w. The a_w (m^{-1}) used in this analysis were calculated for standard ranges of salinity (30–34 ppt) and temperature (0–20°C) encountered in the world ocean using the Water Optical Properties Processor (Rottgers et al., 2011). Differences in a_w with temperature and salinity are insignificant to the results presented here out to 2,500 nm, but water properties of 20°C 34 ppt are used for analyses.

Propagation of Sea Spectral Reflectance to the Top of the Atmosphere

Sea surface reflectance is converted to radiance and propagated through the atmosphere to estimate the radiance due to mixed pixels of whitecaps and background at the satellite. First, the reflectance is converted from water-leaving reflectance ($R_w = E_u(0^+)/E_d(0^+)$) to an estimate of the upwelling radiance leaving the sea surface in the nadir direction, L_w (note that this definition includes mixed pixels of radiance from foam and bubbles, as well as water-leaving radiance and sea surface reflected diffuse and direct irradiance). This conversion is conducted assuming the sea surface reflectance is lambertian and the downwelling irradiance reaching the sea surface can be approximated by the solar constant, F_o, adjusted by the cosine of the solar zenith angle (θ_s), the transmission of diffuse irradiance between the sun and earth, t_{ds}, and the mean distance between the Sun and Earth, f_s, such that for each wavelength:

$$E_u\left(0^+\right) = L_w\,\pi \tag{2}$$

$$E_d\left(0^+\right) = F_0\,\cos\left(\theta_s\right) t_{ds} f_s \tag{3}$$

$$L_w = R_w\,F_0\,\cos\left(\theta_s\right) t_{ds} f_s/\pi \tag{4}$$

Finally, this estimate of radiance at the sea surface is attenuated by the intervening atmosphere according to the diffuse transmission factor in the direction of the satellite, t_{dv}. For purposes of this investigation, an experimental atmosphere was used to investigate whether the water impacted by different amounts of foam and whitecap could be detected with an intervening atmosphere containing water vapor and other constituents that could obscure the signal. Hence, experimental values of at-sensor radiance due to Rayleigh scattering (L_r) and aerosols (L_a) were added to the spectra to create a typical top of the atmosphere radiance spectrum (L_{TOA}). An atmosphere typical to the MOBY buoy (157°11′36″W, 20°49′07″N) was used with a solar zenith angle of 42°, humidity of 72.8%, water vapor of 1.737 g cm^{-2}, and pressure of 1,015.19 mb. No sun glint contribution is considered at TOA because the direct and diffuse reflected skylight was included in the field measurements of water reflectance and propagated through the atmosphere with L_w. This approach neglects any atmospheric effects that may occur due to enhanced reflectance of the sea surface from whitecaps and aerosol-molecular coupling.

The observed epsilon, ε^{obs}, is used to assess spectral dependence of aerosols from the TOA radiance and is estimated here for water surfaces with different levels of foam. The observed aerosol reflectance for a given wavelength $R_a^{obs}(\lambda)$ was estimated as the difference between the total and Rayleigh radiance components adjusted by an estimate of downwelling irradiance using $F_o(\lambda)$, such that:

$$R_a{}^{obs} = \frac{\left(L_{TOA} - L_r\right)\pi}{F_o \cos(\theta_s)} \tag{5}$$

The ratio of this parameter with different combinations of wavebands provides the ε^{obs} as:

$$\varepsilon^{obs} = \frac{R_a{}^{obs}(\lambda_1)}{R_a{}^{obs}(\lambda_2)} \tag{6}$$

The Lw contribution is presumed to be 0 in NIR and SWIR wavelengths rather than running a bio-optical model to estimate the contribution of $L_w(NIR)$ (Bailey et al., 2010). The addition of whitecaps, however, could impact the radiance at 670 nm and implementation of the bio-optical model. The wavelengths used to estimate this parameter are typically from the MODIS Ocean Color Sensor 748, 869, 1,240, 1,640, and 2,130 nm (Wang and Shi, 2007). Here the analysis was conducted with 753, 869, 1,253, 1,617, and 2,132 nm, similar to the bands proposed for the PACE mission.

Statistical Analyses

Arithmetic means were calculated and shown with plus or minus the standard deviation. The average spectral whitecap model was developed using a dataset of measured bright white foam data. This average spectrum was used to model the fractional whitecap coverage from a different dataset of field measurements of mixed pixels of whitecap, foam, and background.

Performance of various models to retrieve the whitecap fraction of mixed pixels were considered using mean average error (MAE), mean average percent error (MAPE), coefficient of variation, bias, and R^2 and slope (Seegers et al., 2018). These metrics were done in logarithmic space and are reported transformed back from logarithmic space, since whitecap fraction followed a lognormal distribution. Bootstrapping was not conducted for the proposed algorithms using the mixed pixel dataset, as the data was collected over similar water types and the number of data points was considered too limited to divide into algorithm development and validation subsets.

The whitecap reflectance spectrum was fit to water absorption with nonlinear regression using least squares. A $p < 0.05$ is considered to be statistically significant. For the radiative transfer and fractional whitecap estimates, model parameters were fit to the data with a non-linear regression function using least squares estimation. Spectral weights were not applied, but the spectrum was constrained between 400 and 1,800 nm. For some of the spectral matching modeling, the parameter fits were constrained within a range of realistic values (e.g., 0–1 for whitecap factor). Reflectance of mixed pixels measured from 1800 to 2,500 nm had low signal to noise and were excluded in the spectral fitting analysis.

RESULTS AND DISCUSSION

The results and discussion are divided into a section presenting the new whitecap measurements and comparisons to historic data followed by sections focused on different parameterizations and algorithms to estimate whitecap fraction using spectral reflectance.

Natural Breaking Waves

Whitecap reflectance varies depending on the layers of foam on the sea surface and the amount of submerged bubbles. Examples of reflectance measured with different manifestations of whitecap, foam and bubbles from Long Island Sound are shown in **Figure 2A**. These examples and their corresponding pictures illustrate how the highest reflectance across the spectrum occurs with multiple layers of foam at the sea surface from a wave breaking (**Figure 2A**, magenta). The color in visible wavelengths can be nearly spectrally flat or "white" with high reflectance ~0.50 for Stage A whitecaps with many layers of foam, and is considerably higher than background (black line). The spectrum decreases into the NIR and SWIR wavelengths with several apparent peaks and troughs. Gaps in the spectrum centered at 1.5 and 1.9 μm occur in regions where the atmosphere is highly absorbing and downwelling irradiance is too low for a measurable signal in the field.

High reflectance can also occur when considerable amounts of bubbles are produced at depth (**Figure 2A**, green lines). In comparison to breaking waves, however, the spectral shape in visible wavelengths is different likely due to multiple scattering within the water. The waters of Long Island Sound have considerable blue-absorbing colored dissolved organic matter and detritus causing waters with submerged bubbles to be less "white" in visible wavelengths and have a more green-peaked reflectance spectrum (**Figure 2A**, green lines). The spectra appear as amplifications of the background water reflectance (Stramski and Tegowski, 2001). However, these spectra from deep bubbles produced from a submerged engine are not necessarily representative of normal surface wave breaking and are not considered further in this analysis.

Reflectance of thin layers of foam and residual bubble plumes diminish with similar spectral shapes to the breaking waves (blue lines, **Figure 2A**). Of note, our field measurements of thin foam produced by whitecaps had ~18% reflectance in the visible wavelengths was nearly equivalent to 22% in visible wavelengths used as an average whitecap reflectance in current atmospheric correction algorithms. This value was estimated by Koepke (1984) who showed that reflectance varied from 20 to 55% upon initial wave breaking to 3–10% after 10 s and an time-averaged effective reflectance of whitecaps of 22% was derived. However, there is considerable uncertainty in those values because a radiometer was not used to measure reflectance but rather a measure of film density was used assuming that the maximum reflectance was 55% (Whitlock et al., 1982) and presuming background water reflectance was equal to Fresnel reflectance of sun glint. Moreover, simply averaging the reflectance over the time-course of a breaking wave may not accurately reflect the physics of wave breaking. The spectral shape of the wave can change as the wave transitions to Stage B with more bubble plumes and more of the underlying water color contributes to the color (Moore et al., 2000).

Our measurements of both natural and manufactured foam are compared to other published measurements of spectral reflectance. Past studies reveal considerable variability in whitecap reflectance varying from 75 to 40% in the visible wavelengths (**Figure 2B**). Many of the past measurements were conducted with multi-spectral instruments that covered discreet bands within the visible and near-infrared (NIR). Frouin et al. (1996) studied the visible and NIR of sea foam found in the turbulent surf zone. As shown in **Figure 2B**, sea foam reflectance was found to monotonically decrease into the near infrared wavelengths due to enhanced water absorption in these wavelengths decreasing by 40% at 850 nm, 50% at 1020 nm, and 85% at 1650 nm (Frouin et al., 1996). Measurements by Moore et al. (1998) of foam produced by the bow of a large ship have

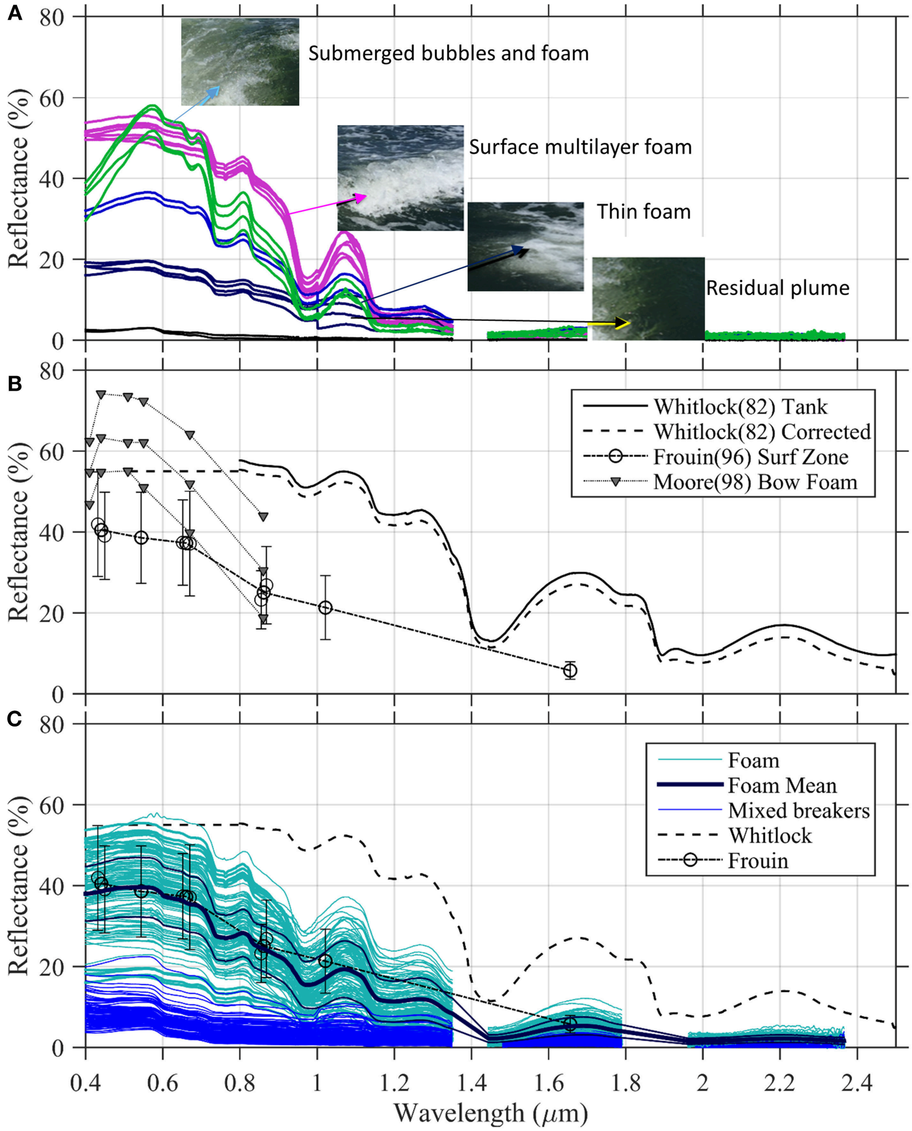

FIGURE 2 | (A) Select examples of manufactured whitecap reflectance and the associated pictures of the sea surface. **(B)** Historic whitecap reflectance measured over the last 25 years from an indoor tank (Whitlock et al., 1982), bow wake from a research vessel (Moore et al., 2000) and natural breaking in the surf zone (Frouin et al., 1996). The Whitlock et al. (1982) spectrum was modeled using the published relationship to absorption by waters spectrum for wavelengths >800 nm (black line) and corrected for the reflectivity of the barium sulfate standard (dashed black line). **(C)** Reflectance measured in Long Island Sound, USA of intense wave breaking from a ship bow (cyan) and mixed pixels of natural waves breaking (blue) in relationship to published studies. Average whitecap reflectance is shown as the thick black line overlying the cyan measurements with ±1 standard deviation.

higher reflectance values (50–75%) and a more green-peaked spectrum in visible wavelengths. However, a similar decay in reflectance out to 860 nm near infrared wavelengths was found by Moore et al. (1998), as well as a decrease at 670 nm compared to blue-green wavelengths. These peaked spectra are closer to the ones produced by deep submerged bubbles in **Figure 2A** and this may be a result of the type of foam and deeper bubbles produced by the wake of a large ship.

Whitlock et al. (1982) was the first to measure the full spectral reflectance of different layers of foam from 350 to 2700 nm. The reflectance profiles are generally spectrally flat in visible wavelengths with a maximum of 60% and higher reflectance into the NIR and SWIR than observed in other studies (Whitlock et al., 1982). Reflectance from 500 to 800 nm shown in **Figure 2B** (black line) are from Whitlock et al. (1982 **Figure 2A**) and derived from the polynomial fit with absorption by water at wavelengths >800 nm (Whitlock et al., 1982, Equation 1). Whitlock et al. (1982) also found a strong relationship between the absorption by pure water at >800 nm and the measured whitecap spectrum and noted reflectance minima at 1,500 and 1,900 nm that correspond to absorption peaks of clean water. A fourth order polynomial model was developed to model the whitecap reflectance from absorption by water. A similar approach was used in this study, as developed below.

While the work was seminal, several problems are evident in the Whitlock et al. (1982) study. First, the values of water absorption from 400 to 800 nm, shown in **Figure 2B** of Whitlock et al. (1982), are roughly an order of magnitude higher than the cited values (Smith and Baker, 1981). This could explain why the polynomial model of Whitlock does not extend into visible wavelengths. Secondly, the values are quite high in NIR and SWIR compared to other datasets. A reference standard of barium sulfate (EASTMAN 6080 paint) reference surface was used and reported to have 94–99% reflectivity out to 2,000 nm with no correction. While this non-luminescent coating yields reflectance values of 95–98% over the wavelength region from 300 to 1,200 nm, it is spectrally varying from 60 to 80% out to 2,500 nm. Hence, the Whitlock et al. (1982) values are too high and these were "corrected" based on the estimated spectral reflectance of this coating (**Figures 2B,C** dotted line), although the amount and condition of the coating are not known. However, even with this correction, the Whitlock values are much higher in the NIR and SWIR compared to field measurements made in natural seawater, which could also be due to artifacts in the tank setup that lead to further uncertainty in the NIR and SWIR values of Whitlock et al. (1982).

Two different datasets are provided in **Figure 2C** and compared to the Whitlock and Frouin measurements. The blue lines in **Figure 2C** represent measurements of mixed pixels of naturally produced foam, bubbles and background water from rolling breakers obtained close to the water surface from a small boat. The cyan lines represent a compilation of measurements made over bright thick foam at the sea surface mostly generated from a boat wake produced by the shallow-draft 11-m long *R/V Lowell Weicker*. These waves have considerably larger reflectance than the 22% average used in the standard algorithm for average open ocean waves and average reflectance of ∼40% in visible wavelengths. Reflectance dips are prominent particularly at 750, 980, and 1,150 nm which have enhanced liquid water absorption, a result of multiple scattering in and around the bubbles and foam. The cyan lines tend to follow the range measured by Frouin et al. (1996) despite the fact that the measurements were taken over very different types of water and generated foam (i.e., Long Island Sound vs. San Diego surf zone). A mean from our spectrum is highlighted in the thick blue line (**Figure 2C**) and reveals a similar decay in NIR wavelengths to Frouin et al. (1996) but with more spectral features in the NIR and SWIR.

Model of Average Whitecap Reflectance From Water Absorption

Similar to the approach followed by Whitlock et al. (1982), we modeled the average whitecap spectrum (**Figure 2C** thick black line) using a polynomial fit to water absorption. The relationship between liquid water absorption and whitecap reflectance is predicted from visible to SWIR wavelengths. The high reflectance corresponds to low water absorption primarily in visible wavelengths and the low reflectance corresponds to high water absorption in NIR and SWIR. A second order polynomial fit to the data explains much of the inverse relationship (**Figure 3A**, $R^2 = 0.975$), but misses the complexity of the shape. A simple third order polynomial on the log-transformed water absorption is a near match to the average whitecap reflectance spectrum across the visible to SWIR wavelengths (**Figure 3B**):

$$R_f = 0.47x^3 - 1.62x^2 + 8.66x + 31.81 \quad (7)$$
$$\text{where: } x = \log(a_w)$$

For wavelengths <400 nm, there is a slightly lower reflectance spectrum than that predicted by water absorption (**Figure 3B**). This is likely due to absorbing constituents within the water like colored dissolved organic matter and more investigation is needed to accurately explore whitecap reflectance in the ultraviolet wavelengths.

The whitecap reflectance reveals troughs that occur in local liquid absorption maxima evident in the water absorption spectrum (**Figure 4**). These troughs are centered around 600, 756, 970, 1,198, 1,448, and 1,932 nm and are specific to water in the liquid form, as the maxima shift when water is in solid or vapor form. For example, the snow community uses the shift from 1,030 nm of the imaginary index of refraction (i.e., absorption) of pure ice to 970 nm for liquid water in algorithms to estimate the liquid water content of melting snow (Green et al., 2002). This same absorption feature is shifted to 940 nm for water vapor and is often a channel used for estimating perceptible water vapor and other atmospheric remote sensing applications (Ningombam et al., 2016; Ibrahim et al., 2018). Hence, the liquid absorption features detectable in the whitecap reflectance measured at the sea surface may wholly or in part be obscured by water found in various forms in the atmosphere due to the close and overlapping absorption bands of water in its various forms (see analysis in Section Whitecap Modeling for the PACE sensor below).

Radiative Transfer Modeling of Whitecaps

The close relationship between whitecaps and liquid water absorption implies that these can be tied within the theoretical framework of radiative transfer modeling. Indeed whitecaps belong to a broad class of strongly multiple-scattering media where the volumetric concentration of bubbles is >70% (Kokhanovsky, 2004). Radiative transfer modeling typically applies to media with a low concentration of scatterers (<1% by volume), but progress has been made in the development of the phenomenological optics of whitecaps (Kokhanovsky, 2004; Ma et al., 2015). Zege et al. (1991) provide a radiative transfer model of closely packed optical foam. Kokhanovsky (2004) furthered this work to provide a simple model semi-infinite foam, but notes this can extend to the case of finite foamed media having a large optical thickness (which is similar to a whitecap). Whitecap reflectance has been related to the liquid bulk water absorption (a_w), the reflectance function for a single scattering albedo of 1 (i.e., a non-absorbing media) (R_o), and a spectrally neutral

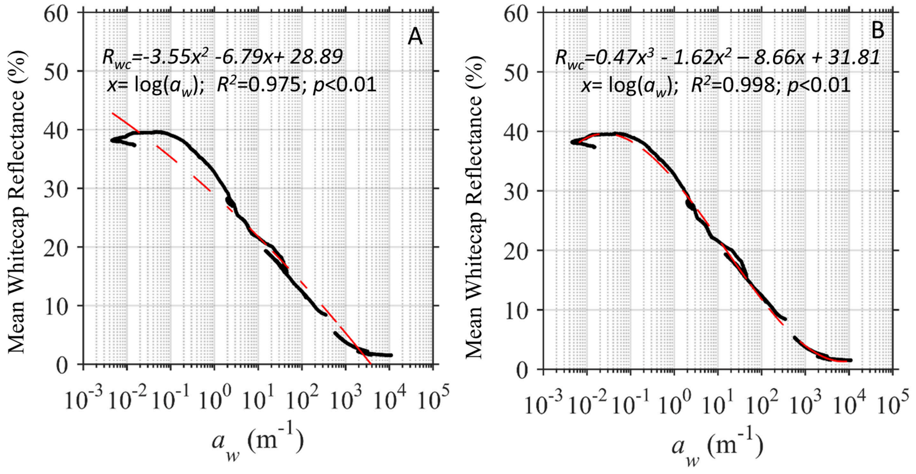

FIGURE 3 | Relationship between absorption by seawater on a logarithmic scale (Rottgers et al., 2011) and the average whitecap reflectance measured here fit with a **(A)** second order and **(B)** third order polynomial.

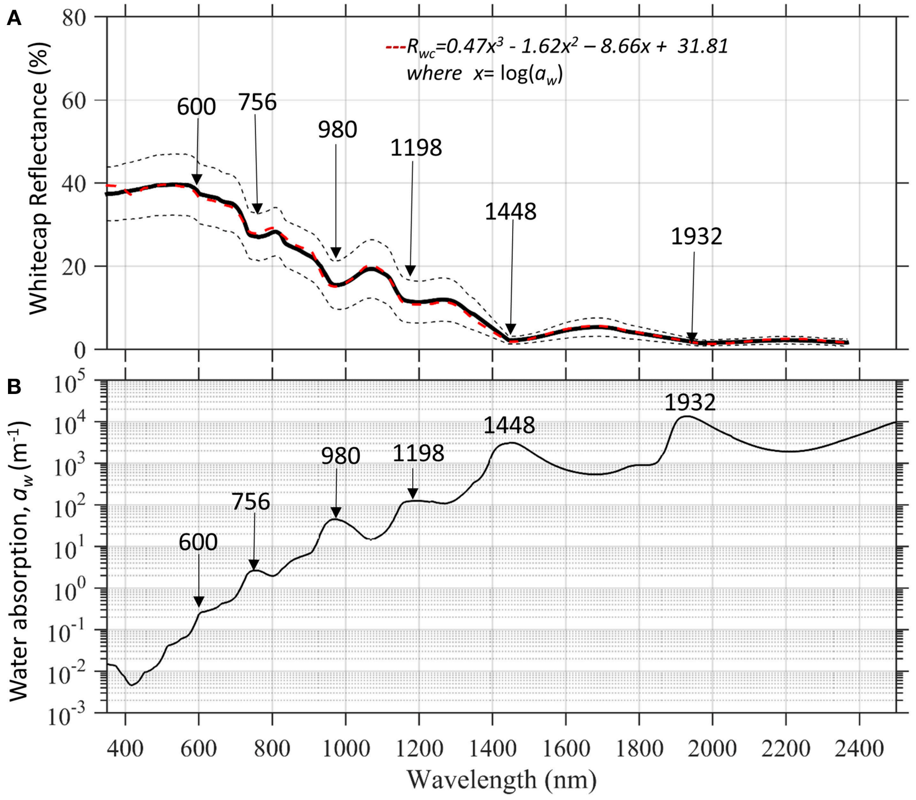

FIGURE 4 | (A) Average whitecap reflectance measured for intense breaking waves with ± 1 standard deviation reveals local reflectance troughs corresponding to **(B)** Local maxima in liquid water absorption (Rottgers et al., 2011).

constant (h) through the following relationship valid for a semi-infinite foam layer (Kokhanovsky, 2004):

$$R = R_o \exp\left(-\sqrt{a_w h}\right) \tag{8}$$

$$h = Q^2 B^2 d\sqrt{l} \tag{9}$$

The values for b and Ro can be fit to experimental data or solved based on the physics using the liquid fraction (l), the average diameter of the bubbles (d), the constant B related to the real part of the index of refraction of liquid water, and Q related to the illumination conditions and observation geometry.

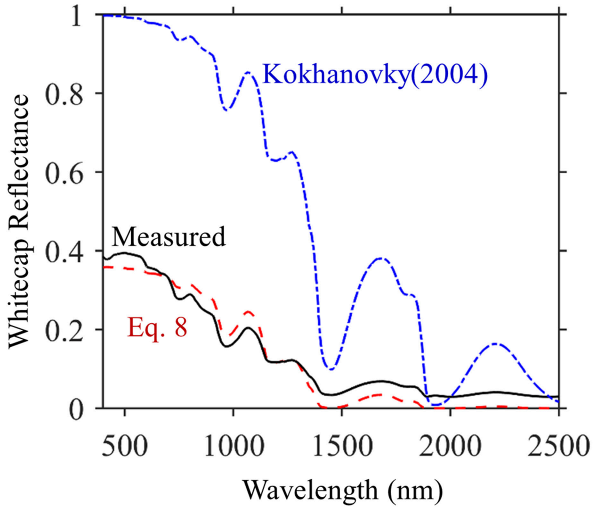

FIGURE 5 | Radiative transfer theory of whitecaps (Kokhanovsky, 2004) was modified from the high published values (blue line) to fit the average whitecap reflectance (black line) by tuning the parameters in Equation 8. The best fit (dotted red line) had an R_O=0.36 with a spectrally neutral constant *b* of 10.3 mm that translates to an equivalent water thickness of ∼0.01 mm and a mean bubble size range from 0.16 to 1 mm.

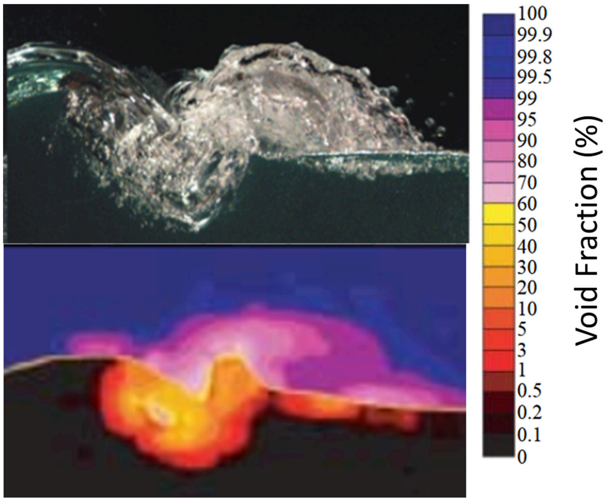

FIGURE 6 | High resolution cross-section of a breaking wave in a laboratory setting and the corresponding void fraction measured using an optical fiber detection probe (Blenkinsopp and Chaplin, 2007). As it is difficult to define the free surface in a turbulent aerated flow, the 50% void fraction contour is used to approximate the position of the free surface. Published with permission from C. Blenkinsopp.

However, more research is needed to fully interpret these parameters in the scope of breaking waves and foam on the sea surface. Kokhanovsky (2004) was able to match the Whitlock et al. (1982) spectrum at wavelengths >800 nm only by adding a component to water absorption equivalent to 0.000270 μm^{-1}, three orders of magnitude higher than values found in the ocean (e.g., ∼0.270 m^{-1}). If typical values of water absorption are used in Equation (8), then the modeled spectrum is much higher in magnitude and the water absorption features are much more dramatic than that of a typical whitecap (**Figure 5**, blue line). To achieve the appropriate magnitude of whitecap reflectance, the R_o parameter can also be tuned to <1.0, which may account for some loss of energy as light passes through the air-water interface (Kokhanovsky pers. comm.). If we fit our whitecap spectrum (**Figure 5** black line) with Equation (8) using non-linear least squares, we arrive at R_o= 0.36 and b = 10.3 mm (**Figure 5** red dotted line, R^2= 0.97, RMSE = 0.0311).

This h can be deconstructed to estimate the amount of liquid water and size of bubbles using (Equation 9) above. The parameter B was assumed to ∼2.3 for media similar to whitecaps following from Kokhanovsky (2004). The parameter Q can be calculated as follows (Zege et al., 1991):

$$Q = q(\theta)\, q(\theta_o) / R_o \tag{10}$$

$$q(\theta) = 3(1 + 2cos(\theta))/7 \tag{11}$$

Given an incidence angle of 20° equivalent to the solar zenith angle and a nadir observation angle and presuming R_o is 0.36 (modeled), Q is 4.40 for our measurement. With these assumptions, we can solve for the equivalent water thickness $\left(d\sqrt{l}\right)$ of 0.099 mm for our average whitecap reflectance. The question arises whether this parameter can be further decomposed into realistic liquid water content and bubble size distributions of a breaking wave.

Bubble clouds near the surface may be crudely separated into short-lived high void-fraction plumes of large bubbles close to the surface embedded in a more slowly varying low-void fraction background field of smaller bubbles extending to greater depths (Melville, 1996). Technology has allowed for better visualizations of breaking wave processes at small scales within the surface ocean (Blenkinsopp and Chaplin, 2007, 2011). As highlighted in **Figure 6**, modified from Blenkinsopp and Chaplin (2007, 2011), the fraction of air or "void fraction" is much larger in the above water whitecap compared to the underlying submerged bubble plumes. If we infer that the reflectance of the whitecap is largely from the above-water portion of bubbles, the void fractions range from 60 to 99%. The liquid water fraction is the non-air fraction and would then range from ∼1 to 40% (Melville, 1996; Blenkinsopp and Chaplin, 2007). Using this range for l in Equation (9), the average bubble diameter, d, contributing to the measured whitecap reflectance would range from 0.16 to 1 mm.

Bubble size distributions are generally measured on the submerged plume within the water column. They generally follow a power law distribution (Blenkinsopp and Chaplin, 2010; Randolph et al., 2014; Deane et al., 2016). However, determining an average bubble diameter is dependent on the size range of bubbles under consideration and the technology used to assess their sizes. For example, acoustics tend to measure a larger size range than afforded by optical methods (Randolph et al., 2014). Most of these approaches are designed to measure bubbles plumes within the water and not surface expressions of foam. However, the larger range of diameter (1 mm) found here is consistent with measurements of bubbles sizes in plumes of breaking waves (e.g., Deane et al., 2016). More experimental research is needed to further constrain the radiative transfer model and underlying assumptions. The ultimate objective would be to use optical measurements of whitecaps from satellites to further elucidate the physics of wave breaking and gas exchange under different environmental conditions across the world ocean.

Estimation of Whitecap Coverage With Known Background Reflectance

Various components of breaking waves can contribute to the reflectance (Frouin et al., 1996). The simplest formulation and the one currently employed by ocean color correction algorithms is to treat the ocean as a mixed pixel where the whitecap component has a constant reflectance, R_f, and covers a fraction of the sea surface, A, and the remaining fraction of sea surface is comprised of a constant background water-leaving reflectance, R_w, such that:

$$R_t = AR_f + (1 - A)\,R_w \tag{12}$$

Even though area-weighted averages should be used for the whitecap and white-cap free areas in atmospheric correction routines (Gordon, 1997), the *(1-A)* term is not explicitly incorporated in retrievals of water-leaving reflectance. Presumably this introduces little error under most wind regimes where whitecap fraction, *A,* is very low and when considering standard 1-km ocean color pixels that average over a large ocean footprint. However, as satellite spatial resolution becomes smaller, the fraction of whitecap within a pixel can become higher and this error would need to be rectified. The fractional whitecap coverage in pan-sharpened Landsat or Sentinel 2 images (e.g., **Figure 1A**) can vary from 0 to nearly 1 within a given scene. For this modeling, *A* is derived as a "whitecap factor" rather than a whitecap fraction since it can be applied to an individual pixel and has no spatial dependence.

A whitecap can also be treated as semi-transparent where there is a contribution from the water layer below. Such a two-layer system can be modeled by the following equation which considers reflectance from the foam layer and an approximation of the water layer which has been attenuated by the overlying foam layer. The optical properties of diffusing materials (Duntley, 1942) can be used to consider a layered whitecap system water the water-leaving reflectance is attenuated by the overlying foam layer (Frouin et al., 1996), such that:

$$R_t = A\left(R_f + R_W\left(1 - R_f\right)^2 / \left(1 - R_W R_f\right)\right) + (1 - A)\,R_w \tag{13}$$

However, it should be noted that the contribution of the water-leaving radiance is negligible when overlain by a thick surface foam, as measured here. The utility of this formulation would only be significant when there is a thin foam and the presumed R_f is low.

Hence, another way to consider the problem is to specify separate contributions from thick foam, as well as a semitransparent thin foam/bubble layer overlying the background water, which can also contain submerged bubbles, and potentially submerged bubbles without surface foam (Zege et al., 2006; Randolph et al., 2014). This would imply a fraction covered by the opaque whitecaps (A_1) and another fraction that may be covered by semitransparent layer (A_2). If we presume that the thinner foam has the same spectral shape but reduced magnitude when compared to thick foam (e.g., **Figure 2A**), then the thin foam could be written as a fraction, *F*, of R_f and the formulation would look like:

$$\begin{aligned} R_t = {} & A_1 R_f + A_2\left(FR_f + R_W\left(1 - FR_f\right)^2 / \left(1 - R_W FR_f\right)\right) \\ & + (1 - A_1 - A_2)\,R_W \end{aligned} \tag{14}$$

These 3 different models (Equations 10–12) were tested using a time series of reflectance measurements made over natural mixed pixels of background, bubbles, and whitecaps (e.g., rolling breakers) (blue lines in **Figure 2C**). Model parameters were fit to 88 different spectra using non-linear least squares to the total reflectance measured between 400 and 1,800 nm presuming a known background reflectance of water, R_w, and the average whitecap reflectance from Equation (7) (**Figure 4A**). The simplest model was able to capture the spectral shape from mixed pixels with lots of foam to those just above the background, as illustrated by a range of selected spectra shown in **Figure 7A**. The modeled retrieval of total reflectance showed good correspondence across all wavelengths (**Figure 7B**) with and R^2 of 0.96 and a slope of 0.98. The MAPE estimate for each wavelength (**Figure 7C**) shows that the model achieves an average of 18.5% across the spectrum and 9.0% in visible wavelengths (400–700 nm). Application of the second model (Equation 13) which includes a term for semi-transparent whitecap provided little improvement in fit with an average MAPE of 18.69% and 8.27% in visible wavelengths. As mentioned earlier, this is likely because the whitecap reflectance is high and the contribution of the water-leaving radiance is negligible when overlain by a thick surface foam. The third model (Equation 14) allows for a thinner foam layer, but has more free parameters to fit (*F*, A_1, and A_2) and unique solutions were difficult to constrain. The model seemed to overfit either *A1* or *A2* with either fractions of 0 or 1.0. Additionally, the complexity of this model did not significantly improve the fit to the measured spectra and the MAPE was 18.20 and 8.85% in visible wavelengths. Hence, the simplest model (Equation 13) captured the large range in reflectance from mixed pixels, particularly at higher whitecap factors. This provides further evidence that the mixed pixel behaves in a linear manner and the retrieved effective whitecap factor is able to account for different thicknesses of foam on the sea surface.

Estimating Whitecap Coverage With Unknown Background Reflectance

The above exercise illustrates that a simple model is capable of reproducing the total reflectance from a mixed pixel of foam and background reflectance using the average whitecap reflectance spectrum (Equation 7). The retrieved whitecap factor is an "effective" whitecap coverage that incorporates different levels of foam and bubbles within the pixel varying from 0.01 to 1. With this parameter, the contribution of whitecaps can be removed from the mixed pixel in order to retrieve an estimate

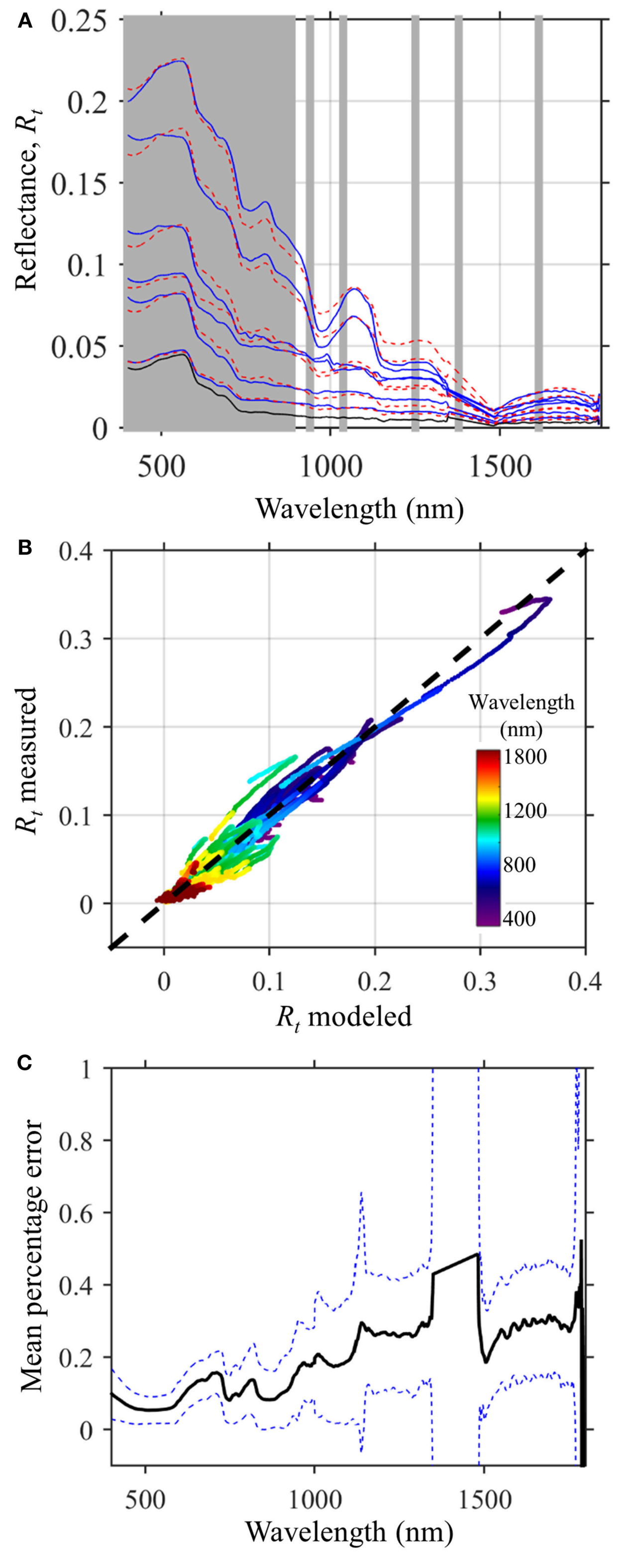

FIGURE 7 | **(A)** Reflectance measurements of selected mixed pixels (blue lines) of whitecaps and background reflectance (black line) measured in Long Island Sound, USA and a modeled fit using the average whitecap reflectance *(Continued)*

FIGURE 7 | (Equation 7) and a simple mixed pixel model (Equation 12). The gray regions highlight spectral bands proposed for the PACE mission. **(B)** spectral fit of the mixed pixel model (Equation 12) showing measured and observed reflectance colored by wavelength for 88 spectra. **(C)** mean percentage error and ± 1 standard deviation by wavelength varied from 8% in visible wavelengths to 20% in shortwave infrared wavelengths.

of the background water-leaving reflectance that is needed for implementation of ocean color products. In this section, we consider different algorithms that could be used to retrieve to the effective whitecap factor assuming that the background reflectance is not known.

Following from the previous section, an iterative procedure could be implemented to retrieve both the fractional whitecap coverage and the background reflectance with a constant whitecap reflectance by adjusting the shape of background reflectance and fractional whitecap coverage with an optimization routine. Constraints could be applied such that background reflectance is retrieved within the scope of known water-leaving reflectance shapes. Such an optimization, however, may be sensitive to other components of atmospheric correction, such as the choice of aerosol models and removal of diffuse and direct sea surface reflected solar radiance. Hence, the average whitecap reflectance (Equation 7) could be straightforwardly incorporated into existing models that solve both the water and atmospheric components simultaneously (Stamnes, 2003; Fan et al., 2017) or atmospheric correction schemes that rely on spectral matching and optimization (Steinmetz et al., 2011).

Other atmospheric correction algorithms from ocean color satellites are stepwise and incorporate an independent determination of the contribution of whitecaps to the total radiance at the top of the atmosphere (Gordon, 1997; Bailey et al., 2010; Ibrahim et al., 2018). To assess the parts of the spectrum most useful for discrimination of whitecap factor, a correlation matrix was constructed to assess how combinations of different wavelengths could be used to predict whitecap factor, *A*. A Normalized Difference Index (NDI) was used which is the difference between two wavelengths normalized by the sum of the wavelengths (**Figure 8**; Dierssen et al., 2015). The normalization constrains the index to values between −1 and 1 with 0 indicating no difference and can be used to isolate narrowband features within a hyperspectral signal. Using this index, regions of highest correlation are localized in discrete wavebands and primarily include water absorption bands at 750 nm, 900–980 nm, and 1,100–1,300 nm. Specifically, a higher effective whitecap factor resulting either from more whitecaps in a pixel or more intense breaking waves are expressed as greater reflectance troughs in the liquid water absorption bands highlighted in **Figure 4** (600, 756, 980, 1,198, 1,448 nm).

The initial correlation was done on a linear scale, but a logarithmic scale is more appropriate given the distribution of whitecap factor and the radiance values (**Figure 9**). Areal-averaged whitecap factors can range over three orders of magnitude roughly from 0.001 to 0.1 (Brumer et al., 2017). Using a logarithmic distribution in the correlation analysis

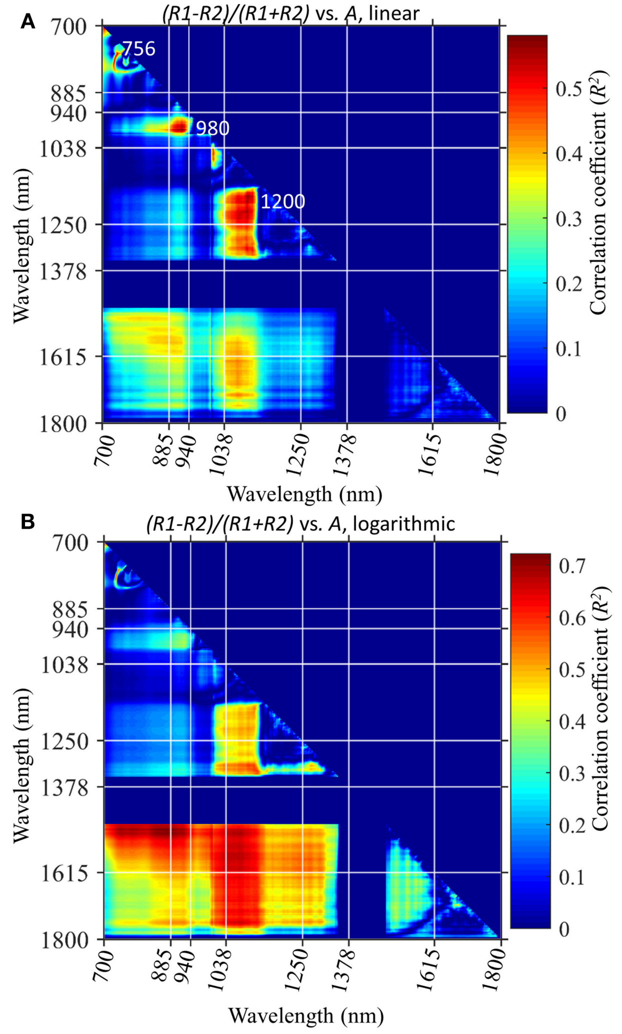

FIGURE 8 | Correlation matrix of normalized difference index calculated using pairs of wavelengths from near infrared through the shortwave infrared in relationship to the derived effective whitecap factor (*A*) from Equation 12. The colors represent the correlation coefficients derived on a **(A)** linear scale with *NDI* vs. *A*; **(B)** logarithmic scale with *log(NDI)* vs. *log(A)*. Selected wavelengths proposed for the PACE mission are highlighted in white.

(**Figure 8B**), the correlation coefficients are higher and the SWIR features are more prominent compared to the linear fit. The amount of reflectance in SWIR bands (1500–1800 nm) is found to be highly correlated to the whitecap factor with $R^2 > 0.90$ for some combinations of wavebands (**Figure 8B**). While these SWIR bands are not specific liquid water absorption features, the enhanced reflectance in SWIR wavelengths can be important predictors of whitecap contribution and can potentially interfere with aerosol and glint atmospheric correction methods (see Section Whitecap Modeling for the PACE sensor below).

Whitecap Modeling for the PACE Sensor

This analysis focuses on the proposed bands for incorporation in the PACE OLI sensor which include hyperspectral bands from 350 to 890 nm in 5 nm increments with additional largely heritage NIR/SWIR bands at 940, 1,038, 1,250, 1,378, 1,615, 2,130, 2,260 nm. The 1,378 nm channel is not included further in this analysis, because the atmosphere highly attenuates radiance in this band and reflectance at the sea surface is not measurable under most conditions. The PACE OLI sensors misses many of the NIR/SWIR bands related to liquid water absorption such as features around 980 and 1,200 nm. However, PACE is poised to be hyperspectral into the NIR and this analysis shows narrowband information in the 730–800 nm region that are related to the liquid water absorption features at 756 nm. In addition, the 1,038 nm band also may provide information on whitecap, although this region is likely also used for aerosols and sun glint extrapolations.

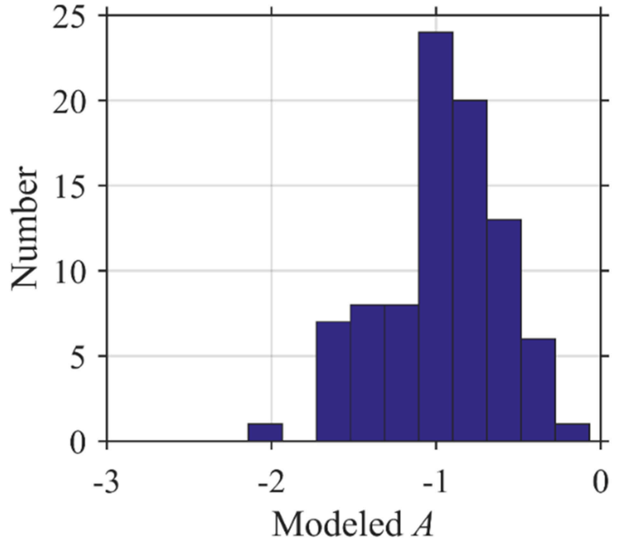

FIGURE 9 | Histogram of the derived effective whitecap factor (*A*) from mixed pixels of natural breaking waves using Equation 12 reveals the logarithmic distribution of *A* ranging from −2 to 0 in logarithmic space or 0.01 to 1.

If we presume that the sea surface is a mixture of pure whitecap with whitecap-free background reflectance, then a simple linear mixing model could be developed to quantify the depth of the reflectance trough for different liquid water absorption bands. For the data collected here, the depth of the trough related to liquid water absorption is related to the derived whitecap factor for the 980 and 1,200 nm features. A baseline subtraction approach (also referred to as continuum removed) has proven to be robust for many environmental remote sensing applications (Clark, 1999; Dierssen et al., 2015; Khan et al., 2017; Garaba and Dierssen, 2018) and is explored here (**Figure 10**). The water absorption features at $\sim$750 nm is not a robust indicator when the whitecap factor is low. However, the absorption features at 980 nm and 1,200 nm are well-correlated to whitecap factor across several orders of magnitude (0.02–1) and have little bias and fairly low error (**Figure 10**). Similar results are found for a simple band difference algorithm (**Table 1**). The NDI does not perform as well in predicting whitecap factor

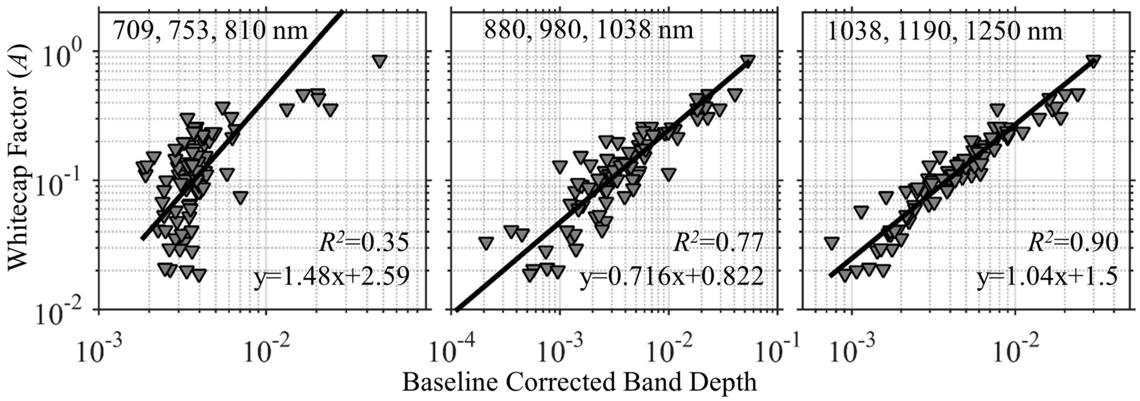

FIGURE 10 | Various models to derive effective whitecap factor (*A*) from baseline corrected band-depths calculated using different combinations of 3 wavelengths (see **Table 1** for additional statistics). Band depths at the liquid water absorption features centered at 980 and 1,200 nm are highly correlated to the whitecap factor on a logarithmic scale. These bands are not proposed to be part of the PACE mission.

TABLE 1 | Statistical results from various algorithms to estimate the whitecap factor, *A*, from spectral reflectance at the sea surface and at sensor radiance.

Algorithm	a_0	a_1	*n*	Bias	MAE	MAPE	r^2
Baseline subtraction			$log(A) = a_0 + a_1\ log(bd),\ bd = (\lambda_2 - \lambda_1)*(R3 - R1)/(\lambda_3 - \lambda_1) + R1 - R2$				
709, 750, 810	2.59	1.48	87	0.058	0.134	0.891	0.35
880, 980, 1038	0.822	0.716	86	0.0020	0.034	0.225	0.77
1038, 1190, 1250	1.50	1.04	87	0.0046	0.027	0.179	0.90
Band difference			$log(A) = a_0 + a_1\ log(bd)\ ,\ bd = R1 - R2$				
756, 800	2.01	0.861	68[1]	−0.0031	0.060	0.523	0.13
880, 980	1.18	0.934	87	0.0120	0.059	0.395	0.80
1038, 1190	0.884	1.04	87	0.0022	0.028	0.184	0.87
Multiple regression PACE R_T			$A = -0.0237 + 4.003\ R(880) + 1.6657\ R(1038) - 3.750\ R(1250) + 3.424\ R(1615)$				
880, 1038, 1250, 1615			87	<0.0001	0.0068	0.0068	0.99
Multiple regression PACE L_{TOA}			$A = -\ 0.443 + 0.183\ L(879) + 0.111\ L(1038) - 0.366L(1253) + 0.600L(1617)$				
879, 1038, 1253, 1617			87	<0.0001	0.0067	0.0443	0.99

[1] *Lower number of samples due to negative band depths.*

for any of these spectral regions because the normalization to the sum of the reflectance values tends to obscure the relative differences (**Table 1**).

While these liquid water absorption bands are not currently part of the PACE mission, this analysis suggests their addition, particularly 980 and 1,200 nm, could be valuable for predicting whitecap factor and other sea surface applications. High correlations can also be found with a multiple linear regression for select bands in the far NIR/SWIR including 880, 1,038, 1,250, and 1,615 nm (**Table 1**). As discussed earlier, whitecaps elevate the reflectance in the NIR/SWIR above background and the amount of signal within these bands is a good predictor of the fractional whitecap coverage. The 940 nm band was excluded from the regression analysis because this band varies with atmospheric water vapor absorption. The generality and applicability of these algorithms broadly across different oceanic regimes and atmospheric conditions remains to be tested.

Many of the features unique to whitecaps may be part or wholly obscured by the intervening atmosphere. Hence, a simple transformation was conducted to determine whether the signal observed at the sea surface could "potentially" be observed at the Top of the Atmosphere (TOA). This transformation is for a single atmospheric condition with a realistic set of aerosols and atmospheric gases and does not consider the impact of highly scattering waters on atmospheric processes (e.g., multiple scattering). It provides a glimpse of what a satellite might observe over whitecap-enhanced waters in the bands expected on PACE. The TOA radiance is nearly an order of magnitude higher in visible wavelengths, but the two datasets become closer in magnitude into the NIR and SWIR wavelengths (**Figure 11A**). The separate contribution of Rayleigh (L_r) and aerosols (L_a) are shown in comparison to a whitecap pixel (Lw maximum) and an unimpacted background pixel (L_w minimum) (**Figure 11B**). Pixels completely covered by whitecaps ($A = 1$) contribute more radiance than aerosols at the TOA from visible to 1,615 nm.

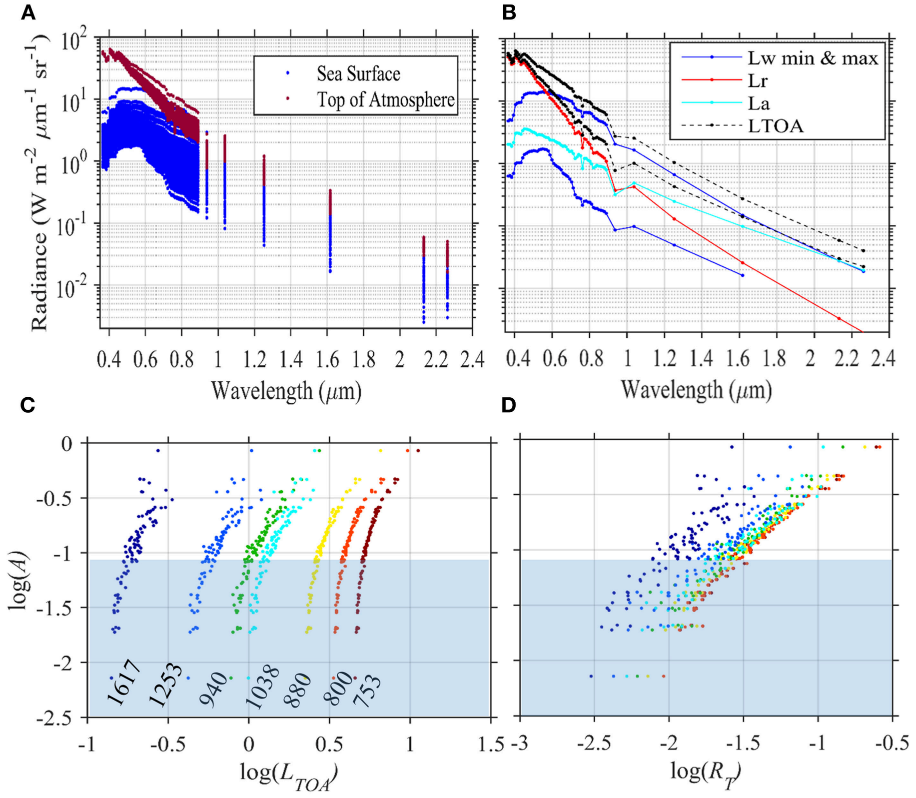

FIGURE 11 | (A) An example of radiance (W m-2 µm^{-1} sr^{-1}) at the sea surface and the top of the atmosphere in bands similar to those proposed to be on the PACE mission estimated from 88 spectra measured over different mixtures of whitecap and background including direct and diffuse reflected skylight for a single marine atmosphere. **(B)** Individual contributions to the top of the atmosphere radiance (L_{TOA}) from Rayleigh (L_r), aerosol (L_a), and the water signal (L_w) over background (min) and whitecap-covered (max) sea surfaces. **(C)** Relationship between the logarithm of L_{TOA} (from Panel A) and the effective whitecap reflectance for the near infrared (NIR) and shortwave infrared (SWIR) bands. **(D)** Same analysis as in **(C)** But for total reflectance measured at the sea surface.

This would not be observed on PACE, however, given the large spatial footprint of 1 km and typical values of $A < 0.1$. Another feature of note is that the changes in radiance are less sensitive to whitecap factor at the top of the atmosphere having steeper slopes (**Figure 11C**) compared to reflectance at the sea surface (**Figure 11D**). This could impact the ability to retrieve low whitecap factors common to open ocean conditions from TOA radiance. The impact of different atmospheric conditions will also need to be explored.

Gordon (1997) writes that "area-weighted averages" of the whitecap-covered and whitecap-free areas of the surface should be considered in the formulation for atmospheric correction (Gordon, 1997). However, current correction routines do not incorporate the (1-A) fraction for the remaining signal emanating from the sea. This may not introduce much error in the current implementation of the whitecap correction routine, which only considers low fractions of whitecaps ($A < 0.02$). The formulation by Gordon (1997) also presumes that reflection of the direct and diffuse skylight would be the same over whitecap-covered and background waters; however, seas with breaking waves and foam do not reflect light in the same way as flat or wind-ruffled seas. Hence, the area-weighted average of whitecap-free sea surface should potentially include the direct beam (sun glint, L_g) and diffuse skylight (L_d) in addition to the water-leaving component. A modification of the traditional algorithm for conducting atmospheric correction (Gordon, 1997) is proposed that explicitly incorporates the fraction of whitecap-covered and whitecap-free areas following:

$$L_t = L_{r-d} + L_{a+ra} + AtL_f + (1-A)(tL_w + TL_g + tL_d) \quad (15)$$

where t is the diffuse and T is the direct transmittance of the atmosphere. This equation separates the component of the diffuse reflected skylight, L_d, from the computed Rayleigh radiance and includes it as part of the water signal. This allows for true validation of the atmospheric correction approach, whereby values of L_g, L_d, L_w, and L_f can be individually measured and compared to those derived from the atmospheric correction algorithm.

The ε^{obs} used to estimate the aerosol model for atmospheric correction purposes was evaluated at different combinations of NIR and SWIR wavelengths (**Figure 12**). As shown in **Figure 12A**, ε^{obs} is quite insensitive to whitecap factor using the NIR wavebands of 753 and 869 nm. The liquid water absorption feature at 753 nm compensates for the enhanced reflectance due to the whitecaps. However, the SWIR wavelengths

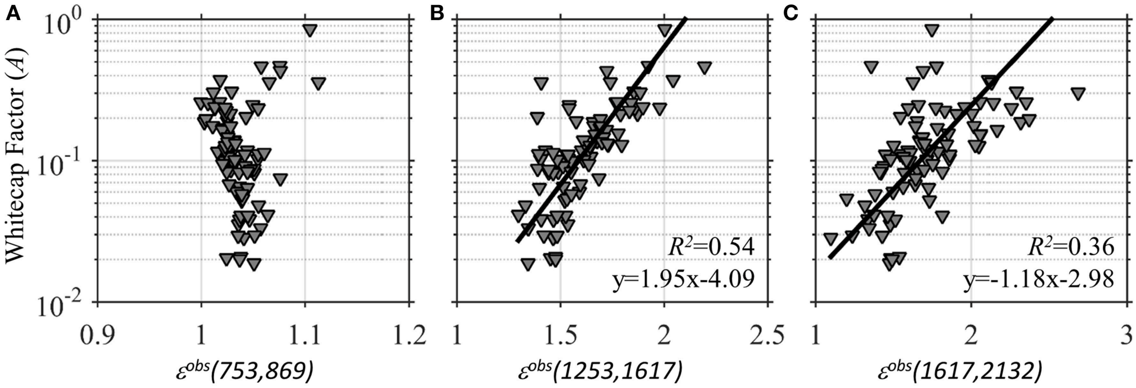

FIGURE 12 | Estimates of the observed epsilon ε^{obs} for the two specified wavelengths (Equation 5,6) used in the selection of aerosol models is shown in relationship to the logarithm of effective whitecap factors. The ε^{obs} calculated using the near infrared (753 and 869 nm) is nearly invariant of whitecap factor **(A)** compared to the ratios calculated with shortwave infrared wavelengths (1,253, 1,617, and 2,132 nm) **(B,C)**.

at 1,253, 1,617, and 2,132 nm do not incorporate the liquid water features and ε^{obs} is dependent on the whitecap factor with different combinations of SWIR bands. No correlation is found between whitecap factor and $\varepsilon^{obs}(753,869)$, while the correlation coefficients are 0.54 and 0.36 for $\varepsilon^{obs}(1,253,1,617)$ and $\varepsilon^{obs}(1,617,2,132)$, respectively. The range in ε^{obs} is large for **Figures 12B,C** and would result in different aerosol spectral models and variable amounts removed from visible wavelengths, even though the atmospheric properties and water-leaving reflectance were the same.

CONCLUSIONS AND OUTLOOK

Field measurements of the spectral reflectance of whitecaps are challenging to collect due to the many types and stages of whitecaps, the rapid time scale on the order of seconds, the changing contributions of foam and still water, and potential contamination from reflectance of sun and skylight. Reflectance of whitecaps also varies with the type of breaking wave (e.g., rolling breakers and plunging breakers) and the layers of foam and bubbles produced (Frouin et al., 1996; Moore et al., 2000). This was evident in the early measurements of Koepke (1984) who demonstrated the time dependent-variability of the reflectance of breaking waves averaging around 22%. However, that study was limited to simple photography and the spectral shape was presumed to be flat, with later studies highlighting the reduction in reflectance in the NIR (Frouin et al., 1996). Few studies have evaluated whitecap reflectance into the SWIR and at the spectral resolution necessary for atmospheric correction of hyperspectral sensors (e.g., the proposed PACE).

This study builds upon past research to present new whitecap measurements from 350 to 2,500 nm that are useful not only for atmospheric correction, but for sensor design in terms of waveband selection in NIR and SWIR wavelengths. Our measurements in visible and NIR wavelengths are consistent in magnitude with several of the past multi-spectral measurements of whitecaps from vastly different water conditions (Frouin et al., 1996). This consistency in measurements may be a further indication of a phenomena called "turbulence saturation," whereby the time- and space-averaged fluid turbulence in actively breaking wave crests is proposed to remain approximately constant (Deane et al., 2016). As highlighted in the radiative transfer section above, bridging the physics of wave breaking and radiative transfer (Kokhanovsky, 2004; Ma et al., 2015) is a subject requiring more intensive research and could lead to new predictive capabilities from ocean color data that include estimates of whitecap factor and the intensity of breaking wave features on the sea surface.

Similar to the pioneering work of Whitlock et al. (1982), the average whitecap spectrum is empirically related to the liquid water absorption coefficient from visible to SWIR using a third order polynomial (Equation 7). However, the new hyperspectral parameterization is proposed to be more accurate for natural breaking waves across all wavelengths compared to the laboratory study of Whitlock et al. (1982) and is now consistent from 400 to 2,500 nm. This whitecap parameterization can be easily input into radiative transfer models and various atmospheric correction schemes for ocean color imagery. In particular, the new whitecap parameterization could be input as a spectral shape in spectral matching and optimization algorithms (Steinmetz et al., 2011), which could result in improved atmospheric correction over whitecap-prone seas like the Southern Ocean. Prominent reflectance troughs in the whitecap spectrum correspond to liquid water absorption features at ∼750, 980, and 1,200 nm. These absorption features are related to the intensity of breaking wave features whereby more intense foam production leads to enhanced multiple scattering by the medium (Zege et al., 1991; Kokhanovsky, 2004) and enhanced absorption in these localized bands. As shown here, the depths of the reflectance trough at 980 and 1,200 nm are highly related to the effective whitecap factor from 0.01 to 1 and could provide new means to estimate this parameter from the ocean color image.

The liquid water absorption features highlighted here are not unique to reflectance features of whitecaps and can occur from other types of floating or suspended constituents at the sea surface. For example, various types of floating vegetation including the macroalgae *Sargassum* sp. and floating leaf debris of seagrass (i.e., seagrass wrack) can contain these same water features out to nearly 2,500 nm (Dierssen et al., 2015; Hu et al., 2015). For example, the liquid water absorption feature at ∼980 nm has been used for terrestrial applications to map drought within plant communities (Peñuelas et al., 1997; Roberts et al., 2016). Dierssen et al. (2015) related the dip in reflectance at 980 nm to the age of floating seagrass wrack advected from coastal seagrass beds to the oligotrophic ocean. Highly turbid sediment plumes also have similar dips in reflectance at these same liquid water absorption bands up until 1,150 nm (Knaeps et al., 2015). Differentiating highly scattering media at the sea surface, such as sediments, floating vegetation and whitecaps, is possible using spectral characteristics that are unique to each constituent (e.g., red edge of vegetation) (Dierssen et al., 2006) and will be considered in future research.

The "effective" whitecap factor, *A*, derived here is based on optical reflectance rather than the traditional interpretation of whitecap fraction as an aerial average of bright features observed over a large area of the sea surface. In photographic methods commonly used to estimate whitecap fraction, the threshold of what is considered a "bright feature" is not easy to standardize and large uncertainty exists in derivation of whitecap fractions (Brumer et al., 2017). The "effective" whitecap factor (Equation 12) is the fraction of a standard whitecap reflectance (e.g., Equation 7) that accounts for enhancements in spectral reflectance of the sea surface above the background reflectance. Since *A* is optically derived, it is better suited for atmospheric correction techniques because it specifically incorporates different levels of foam and bubbles associated with breaking waves and can incorporate small enhancements in reflectance that may not be observable with the eye or photographic systems (Randolph et al., 2017). Moreover, unlike the whitecap fraction parameterized with wind speed measurements, no spatial extent is implicit to *A* and "effective" whitecap factor can apply to reflectance measurements at any spatial scale on the sea surface. For a large pixel, *A* can be related directly to the whitecap fraction on the sea surface. For a small pixel, *A* can be higher than 1.0, if reflectance is greater than the average whitecap reflectance used in the model, and *A* can be lower than the limit used here of 0.01.

The simple whitecap model (Equation 12) is consistent with the standard model used in most atmospheric correction routines where the sea is treated as a mixed pixel comprising both whitecap and background reflectance (Gordon and Wang, 1994). Gordon (1997) specifically states that "area-weighted averages" of the whitecap-covered and whitecap-free areas of the surface should be considered, but the terms describing the area-weighted averages, specifically *A* and (*1-A*), are missing from the standard equation (Gordon, 1997, Equation 5). Without explicitly including these terms, the standard model is commonly misinterpreted as enhancements or augmentations in reflectance above a background reflectance (Equation 1). To clarify this misconception, these terms are explicitly added to the atmospheric correction equation in Equation (15). Incorporating these terms is especially important for satellites with smaller footprints and when considering an "effective" whitecap factor as described above (Thompson et al., 2015; Bender et al., 2018). In addition, the new formulation considers the reflectance from whitecap-free areas of the sea surface to include all contributions of sea spectral reflectance, including sun glint, and diffuse reflected skylight. Current models include a wind-roughened estimate of the diffuse reflected skylight in the Rayleigh component of atmospheric correction (Gordon, 1997; Ibrahim et al., 2018), which is challenging to validate. Enhanced surface roughness, which is directly linked to the generation of whitecaps and air bubble entrainment and to the formation of sea spray as significant aerosol contribution in the lower atmospheric layer, will challenge the atmospheric correction performance and in turn will affect the estimates of whitecap factor (Hieronymi, 2016).

Errors in treating whitecap reflectance for atmospheric correction of satellite imagery, particularly at high winds, are generally accounted for in the aerosol model. Specifically, any enhancement that is not removed as a whitecap is added to the aerosol reflectance in the NIR/SWIR and can impact the retrieved spectral dependence of the selected aerosol model. Even though the selected aerosol concentration and type may be inaccurate, the amount of reflectance that is subtracted may still be approximately correct to retrieve accurate water-leaving reflectance across the visible. If the PACE mission aims to improve retrievals of both aerosols and water-leaving reflectance, however, then better treatment of whitecaps is needed to ensure that errors are not propagated into the retrieved aerosol or water-leaving reflectance values. Here, the ε^{obs} used for aerosol model selection was calculated using NIR wavelengths of 753 and 869 nm and found to be quite invariant to changes in the effective whitecap factor. In contrast, ε^{obs} calculated for SWIR wavebands (i.e., 1,253, 1,617, and 2,132 nm) was highly variable with whitecap factor. A more thorough analysis of how whitecaps impact top of the atmosphere radiance and aerosol modeling under a variety of environmental conditions will be important for estimating uncertainties of parameters derived from future satellite missions, particularly in whitecap-prone regions like the Southern Ocean. Alternative methods for estimating whitecaps may also be feasible such as using depolarization characteristics of whitecaps or the use of space-based lidars (Hu et al., 2008; Hieronymi, 2016)

Rather than considering whitecaps a contamination to ocean color imagery, these results point the way forward to new avenues of research and ocean color products that could have important implications to physical oceanographers, atmospheric scientists, and climate modelers. Wave breaking leads to enhanced air-sea transfer of gases through additional turbulence and bubble-mediated transfer (Asher and Wanninkhof, 1998). Bursting of surface bubbles injects sea spray aerosols into the atmosphere and the aerosol production flux is thought to be directly proportional to the whitecap coverage. Sea salt aerosols play an important role in the earth's radiation budget through scattering of and serve as cloud condensation nuclei influencing the microphysical and radiative properties of clouds. They are also direct scatterers of solar radiation (Andreae and Rosenfeld, 2008). Including new wavebands specific to liquid water absorption features could open the door for new applications to sea surface processes with potential ecological and climatological applications.

AUTHOR CONTRIBUTIONS

The author confirms being the sole contributor of this work and has approved it for publication.

FUNDING

Funding was provided by NASA Ocean Biology and Biogeochemistry through the PACE project (NNX15AC32G).

ACKNOWLEDGMENTS

The following individuals are gratefully acknowledged for assisting in data collection: Kaylan Randolph, Shungudzemwoyo Garaba, Alexandre Castagna, Timothy Bateman and Brandon Russell. Turner Cabaniss and vessel operations at the University of Connecticut Marine Sciences are also acknowledged for providing field operations in rough seas. Amir Ibrahim and Bryan Franz provided data and methods to extrapolate reflectance values to the top of atmosphere. Thanks are extended to Alexandre Castagna, Bo-Cai Gao, Robert Frouin, Kaylan Randolph and Alexander Kokhanovsky and Martin Hieronymi for insightful conversations regarding this work. I also acknowledge Norman Kurig for providing the Landsat 8 image, Monique Albert and Magdalena Anguelova for the image of whitecap fractions and C.E. Blenkinsopp and J.R. Chaplin for the measurements of void fraction.

REFERENCES

Ahn, J.-H., Park, Y.-J., Ryu, J.-H., and Lee, B. (2012). Development of atmospheric correction algorithm for geostationary ocean color imager (GOCI). *Ocean Sci. J.* 47, 247–259. doi: 10.1007/s12601-012-0026-2

Albert, M. F., Anguelova, M. D., Manders, A. M., Schaap, M., and De Leeuw, G. (2016). Parameterization of oceanic whitecap fraction based on satellite observations. *Atmos. Chem. Phys.* 16, 13725–13751. doi: 10.5194/acp-16-13725-2016

Andreae, M. O., and Rosenfeld, D. (2008). Aerosol–cloud–precipitation interactions. Part 1. The nature and sources of cloud-active aerosols. *Earth Sci. Rev.* 89, 13–41. doi: 10.1016/j.earscirev.2008.03.001

Anguelova, M. D., and Webster, F. (2006). Whitecap coverage from satellite measurements: a first step toward modeling the variability of oceanic whitecaps. *J. Geophys. Res.* 111:C03017. doi: 10.1029/2005JC003158

Asher, W. E., and Wanninkhof, R. (1998). The effect of bubble-mediated gas transfer on purposeful dual-gaseous tracer experiments. *J. Geophys. Res.* 103, 10555–10560. doi: 10.1029/98JC00245

Aurin, D. A., and Dierssen, H. M. (2012). Advantages and limitations of ocean color remote sensing in CDOM-dominated, mineral-rich coastal and estuarine waters. *Remote Sens. Environ.* 125, 181–197. doi: 10.1016/j.rse.2012.07.001

Aurin, D. A., Dierssen, H. M., Twardowski, M. S., and Roesler, C. S. (2010). Optical complexity in Long Island sound and implications for coastal ocean color remote sensing. *J. Geophys. Res.* 115, 1–11. doi: 10.1029/2009JC005837

Bailey, S. W., Franz, B. A., and Werdell, P. J. (2010). Estimation of near-infrared water-leaving reflectance for satellite ocean color data processing. *Optics Express* 18, 7521–7527. doi: 10.1364/OE.18.007521

Bender, H. A., Mouroulis, P., Dierssen, H. M., Painter, T. H., Thompson, D. R., Smith, C. D., et al. (2018). Snow and water imaging spectrometer: mission and instrument concepts for earth-orbiting cubesats. 12, 044001. doi: 10.1117/1.JRS.12.044001

Blanchard, D. C. (1985). The oceanic production of atmospheric sea salt. *J. Geophys. Res.* 90, 961–963. doi: 10.1029/JC090iC01p00961

Blenkinsopp, C. E., and Chaplin, J. R. (2007). Void fraction measurements in breaking waves. *Proc. R. Soc. A* 463, 3151–3170. doi: 10.1098/rspa.2007.1901

Blenkinsopp, C. E., and Chaplin, J. R. (2010). Bubble size measurements in breaking waves using optical fiber phase detection probes. *IEEE J. Oceanic Eng.* 35, 388–401. doi: 10.1109/JOE.2010.2044940

Blenkinsopp, C. E., and Chaplin, J. R. (2011). Void fraction measurements and scale effects in breaking waves in freshwater and seawater. *Coastal Eng.* 58, 417–428. doi: 10.1016/j.coastaleng.2010.12.006

Brumer, S. E., Zappa, C. J., Brooks, I. M., Tamura, H., Brown, S. M., Blomquist, B. W., et al. (2017). Whitecap coverage dependence on wind and wave statistics as observed during SO GasEx and HiWinGS. *J. Phys. Oceanogra.* 47, 2211–2235. doi: 10.1175/JPO-D-17-0005.1

Clark, R. N. (1999). "Chapter 1: Spectroscopy of rocks and minerals, and principles of spectroscopy," in *Manual of Remote Sensing, Vol. 3, Remote Sensing for the Earth Sciences*, ed A. N. Rencz (New York, NY: John Wiley and Sons), 3–58.

Deane, G. B., Stokes, M. D., and Callaghan, A. H. (2016). The saturation of fluid turbulence in breaking laboratory waves and implications for whitecaps. *J. Phys. Oceanogra.* 46, 975–992. doi: 10.1175/JPO-D-14-0187.1

Dierssen, H. M., Chlus, A., and Russell, B. (2015). Hyperspectral discrimination of floating mats of seagrass wrack and the macroalgae Sargassum in coastal waters of Greater Florida Bay using airborne remote sensing. *Remote Sens. Environ.* 167, 247–258. doi: 10.1016/j.rse.2015.01.027

Dierssen, H. M., Kudela, R. M., Ryan, J. P., and Zimmerman, R. C. (2006). Red and black tides: quantitative analysis of water-leaving radiance and perceived color for phytoplankton, colored dissolved organic matter, and suspended sediments. *Limnol. Oceanogr.* 51, 2646–2659. doi: 10.4319/lo.2006.51.6.2646

Duntley, S. Q. (1942). The optical properties of diffusing materials. *JOSA* 32, 61–70. doi: 10.1364/JOSA.32.000061

Fan, Y., Li, W., Gatebe, C. K., Jamet, C., Zibordi, G., Schroeder, T., et al. (2017). Atmospheric correction over coastal waters using multilayer neural networks. *Remote Sens. Environ.* 199, 218–240. doi: 10.1016/j.rse.2017.07.016

Frouin, R., Schwindling, M., and Deschamps, P.-Y. (1996). Spectral reflectance of sea foam in the visible and near-infrared: *in situ* measurements and remote sensing implications. *J. Geophys. Res.* 101, 14361–14371.

Garaba, S. P., and Dierssen, H. M. (2018). An airborne remote sensing case study of synthetic hydrocarbon detection using short wave infrared absorption features identified from marine-harvested macro-and microplastics. *Remote Sens. Environ.* 205, 224–235. doi: 10.1016/j.rse.2017.11.023

Gordon, H. R. (1997). Atmospheric correction of ocean color imagery in the Earth Observing System era. *J. Geophys. Res.* 102, 17081–17106. doi: 10.1029/96JD02443

Gordon, H. R., and Wang, M. (1994). Influence of oceanic whitecaps on atmospheric correction of ocean-color sensors. *Appl. Optics* 33, 7754–7763. doi: 10.1364/AO.33.007754

Green, R. O., Dozier, J., Roberts, D., and Painter, T. (2002). Spectral snow-reflectance models for grain-size and liquid-water fraction in melting snow for the solar-reflected spectrum. *Ann. Glaciol.* 34, 71–73. doi: 10.3189/172756402781817987

Guanter, L., Kaufmann, H., Segl, K., Foerster, S., Rogass, C., Chabrillat, S., et al. (2015). The EnMAP spaceborne imaging spectroscopy mission for earth observation. *Remote Sens.* 7, 8830–8857. doi: 10.3390/rs70708830

Hieronymi, M. (2016). Polarized reflectance and transmittance distribution functions of the ocean surface. *Optics Express* 24, A1045–A1068. doi: 10.1364/OE.24.0A1045

Hu, C., Feng, L., Hardy, R. F., and Hochberg, E. J. (2015). Spectral and spatial requirements of remote measurements of pelagic Sargassum macroalgae. *Remote Sens. Environ.* 167, 229–246. doi: 10.1016/j.rse.2015.05.022

Hu, Y., Stamnes, K., Vaughan, M., Pelon, J., Weimer, C., Wu, D., et al. (2008). Sea surface wind speed estimation from space-based lidar measurements. *Atmos. Chem. Phys.* 9, 3593–3601. doi: 10.5194/acp-8-3593-2008

Ibrahim, A., Franz, B., Ahmad, Z., Healy, R., Knobelspiesse, K., Gao, B.-C., et al. (2018). Atmospheric correction for hyperspectral ocean color retrieval with application to the Hyperspectral Imager for the Coastal Ocean (HICO). *Remote Sens. Environ.* 204, 60–75. doi: 10.1016/j.rse.2017.10.041

Khan, A. L., Dierssen, H., Schwarz, J. P., Schmitt, C., Chlus, A., Hermanson, M., et al. (2017). Impacts of coal dust from an active mine on the spectral reflectance of Arctic surface snow in Svalbard, Norway. *J. Geophys. Res.* 122, 1767–1778. doi: 10.1002/2016JD025757

Knaeps, E., Ruddick, K. G., Doxaran, D., Dogliotti, A. I., Nechad, B., Raymaekers, D., et al. (2015). A SWIR based algorithm to retrieve total suspended matter in extremely turbid waters. *Remote Sens. Environ.* 168, 66–79. doi: 10.1016/j.rse.2015.06.022

Koepke, P. (1984). Effective reflectance of oceanic whitecaps. *Appl. Opt.* 23, 1816–1824. doi: 10.1364/AO.23.001816

Kokhanovsky, A. A. (2004). Spectral reflectance of whitecaps. *J. Geophys. Res.* 109:C05021. doi: 10.1029/2003JC002177

Lee, C. M., Cable, M. L., Hook, S. J., Green, R. O., Ustin, S. L., Mandl, D. J., et al. (2015). An introduction to the NASA Hyperspectral InfraRed Imager (HyspIRI) mission and preparatory activities. *Remote Sens. Environ.* 167, 6–19. doi: 10.1016/j.rse.2015.06.012

Ma, L. X., Wang, F. Q., Wang, C. A., Wang, C. C., and Tan, J. Y. (2015). Investigation of the spectral reflectance and bidirectional reflectance distribution function of sea foam layer by the Monte Carlo method. *Appl. Optics* 54, 9863–9874. doi: 10.1364/AO.54.009863

Melville, W. K. (1996). The role of surface-wave breaking in air-sea interaction. *Annu. Rev. Fluid Mech.* 28, 279–321. doi: 10.1146/annurev.fl.28.010196.001431

Monahan, E. C. (1993). "Occurrence and evolution of acoustically relevant sub-surface bubble plumes and their associated, remotely monitorable, surface whitecaps," in *Natural Physical Sources of Underwater Sound* (Springer), 503–517. Available online at: https://link.springer.com/chapter/10.1007/978-94-011-1626-8_37 (Accessed September 20, 2017).

Monahan, E. C. (2008). "Whitecaps and Foam," in *Encyclopedia of Ocean Sciences, 2nd Edn*, eds J. Steele, S. Thorpe, and K. Turekian (San Diego, CA: Elsevier; Academic), 3213–3219.

Monahan, E. C., and O'Muircheartaigh (1986). Whitecaps and the passive remote sensing of the ocean surface. *Int. J. Remote Sens.* 7, 627–642. doi: 10.1080/01431168608954716

Moore, K. D., Voss, K. J., and Gordon, H. R. (1998). Spectral reflectance of whitecaps: instrumentation, calibration, and performance in coastal waters. *J. Atmo. Oceanic Tech.* 15, 496–509.

Moore, K. D., Voss, K. J., and Gordon, H. R. (2000). Spectral reflectance of whitecaps: their contribution to water-leaving radiance. *J. Geophys. Res.* 105, 6493–6499. doi: 10.1029/1999JC900334

Ningombam, S. S., Jade, S., Shrungeshwara, T. S., and Song, H.-J. (2016). Validation of water vapor retrieval from moderate resolution imaging spectro-radiometer (MODIS) in near infrared channels using GPS data over IAO-Hanle, in the trans-Himalayan region. *J. Atmosphe. Solar-Terrestrial Phys.* 137, 76–85. doi: 10.1016/j.jastp.2015.11.019

Peñuelas, J., Pinol, J., Ogaya, R., and Filella, I. (1997). Estimation of plant water concentration by the reflectance water index WI (R900/R970). *Int. J. Remote Sens.* 18, 2869–2875. doi: 10.1080/014311697217396

Randolph, K., Dierssen, H. M., Cifuentes-Lorenzen, A., Balch, W. M., Monahan, E. C., Zappa, C. J., et al. (2017). Novel methods for optically measuring whitecaps under natural wave-breaking conditions in the Southern Ocean. *J. Atmosphe. Ocean. Technol.* 34, 533–554. doi: 10.1175/JTECH-D-16-0086.1

Randolph, K., Dierssen, H. M., Twardowski, M., Cifuentes-Lorenzen, A., and Zappa, C. J. (2014). Optical measurements of small deeply penetrating bubble populations generated by breaking waves in the Southern Ocean. *J. Geophys. Res.* 119, 757–776. doi: 10.1002/2013JC009227

Roberts, D. A., Roth, K. L., and Perroy, R. L. (2016). "Chapter 14: Hyperspectral vegetation indices," in *Hyperspectral Remote Sensing of Vegetation*, eds P. S. Thenkabail, J. G. Lyon, and A. Huete (Boca Raton, FL: CRC Press), 309–328.

Rottgers, R., Doerffer, R., McKee, D., and Schonfeld, W. (2011). *Algorithm Theoretical Basis Document: The Water Optical Properties Processor (WOPP).* Technical Report, Helmholtz-Zentrum Geesthacht, University of Strathclyde, Geesthacht.

Scanlon, B., and Ward, B. (2016). The influence of environmental parameters on active and maturing oceanic whitecaps. *J. Geophys. Res.* 121, 3325–3336. doi: 10.1002/2015JC011230

Seegers, B. N., Stumpf, R. P., Schaeffer, B. A., Loftin, K. A., and Werdell, P. J. (2018). Performance metrics for the assessment of satellite data products: an ocean color case study. *Optics Express* 26, 7404–7422. doi: 10.1364/OE.26.007404

Smith, R. C., and Baker, K. S. (1981). Optical properties of the clearest natural waters (200–800 nm). *Appl. Opt.* 20, 177–184. doi: 10.1364/AO.20.000177

Stamnes, K. (2003). Accurate and self-consistent ocean color algorithm: simultaneous retrieval of aerosol optical properties and chlorophyll concentrations. *Appl. Opt.* 42, 939–951. doi: 10.1364/AO.42.000939

Steinmetz, F., Deschamps, P.-Y., and Ramon, D. (2011). Atmospheric correction in presence of sun glint: application to MERIS. *Opt. Exp.* 19, 9783–9800. doi: 10.1364/OE.19.009783

Stramski, D., and Tegowski, J. (2001). Effects of intermittent entrainment of air bubbles by breaking wind waves on ocean reflectance and underwater light field. *J. Geophys. Res.* 106, 345–360. doi: 10.1029/2000JC000461

Thompson, D. R., Gao, B.-C., Green, R. O., Roberts, D. A., Dennison, P. E., and Lundeen, S. R. (2015). Atmospheric correction for global mapping spectroscopy: ATREM advances for the HyspIRI preparatory campaign. *Remote Sens. Environ.* 167, 64–77. doi: 10.1016/j.rse.2015.02.010

Thorpe, S. A. (1982). On the clouds of bubbles formed by breaking wind-waves in deep water, and their role in air-sea gas transfer. *Phil. Trans. R. Soc. Lond. A* 304, 155–210. doi: 10.1098/rsta.1982.0011

Vanhellemont, Q., and Ruddick, K. (2014). Turbid wakes associated with offshore wind turbines observed with Landsat 8. *Remote Sens. Environ.* 145, 105–115. doi: 10.1016/j.rse.2014.01.009

Wang, M., and Shi, W. (2007). The NIR-SWIR combined atmospheric correction approach for MODIS ocean color data processing. *Optics Express* 15, 15722–15733. doi: 10.1364/OE.15.015722

Whitlock, C. H., Bartlett, D. S., and Gurganus, E. A. (1982). Sea foam reflectance and influence on optimum wavelength for remote sensing of ocean aerosols. *Geophys. Res. Lett.* 9, 719–722. doi: 10.1029/GL009i006p00719

Wright, R., Deloatch, J., Osgood, S., and Yuan, J. (2012). "The spectral reflectance of ship wakes between 400 and 900 nanometers," in *Geoscience and Remote Sensing Symposium (IGARSS), 2012 IEEE International* (IEEE), 4186–4189. Available online at: http://ieeexplore.ieee.org/xpls/abs_all.jsp?arnumber=6351746 (Accessed March 31, 2014).

Xu, Z., Zhou, W., Sun, Z., Yang, Y., Lin, J., Wang, G., et al. (2015). Estimating the augmented reflectance ratio of the ocean surface when whitecaps appear. *Remote Sens.* 7, 13606–13625. doi: 10.3390/rs71013606

Zege, E. P., Katsev, I. L., and Kokhanovsky, A. A. (1991). Phenomenological model of optical properties of close-packed media and its application to the foam optics. *Opt. Spectrosc* 71, 486–489.

Zege, E. P., Katsev, I. L., Prikhach, A. S., Gilbert, G., and Witherspoon, N. (2006). Simple model of the optical characteristics of bubbles and sediments in seawater of the surf zone. *Appl. Opt.* 45, 6577–6585. doi: 10.1364/AO.45.006577

Zhao, D., and Toba, Y. (2001). Dependence of whitecap coverage on wind and wind-wave properties. *J. Oceanogr.* 57, 603–616. doi: 10.1023/A:1021215904955

Conflict of Interest Statement: The author declares that the research was conducted in the absence of any commercial or financial relationships that could be construed as a potential conflict of interest.

frontiers in Earth Science

ORIGINAL RESEARCH
published: 29 March 2019
doi: 10.3389/feart.2019.00054

Sensitivity of Inherent Optical Properties From Ocean Reflectance Inversion Models to Satellite Instrument Wavelength Suites

P. Jeremy Werdell[1]* *and Lachlan I. W. McKinna*[1,2]

[1] *Ocean Ecology Laboratory, NASA Goddard Space Flight Center, Greenbelt, MD, United States,* [2] *Go2Q Pty Ltd., Buderim, QLD, Australia*

The Earth science community seeks to develop climate data records (CDRs) from satellite measurements of ocean color, a continuous data record that now exceeds 20 years. Space agencies will launch additional instruments in the coming decade that will continue this data record, including the NASA PACE spectrometer. Inherent optical properties (IOPs) quantitatively describe the absorbing and scattering constituents of seawater and can be estimated from satellite-observed spectroradiometric data using semi-analytical algorithms (SAAs). SAAs exploit the contrasting optical signatures of constituent matter at spectral bands observed by satellite sensors. SAA performance, therefore, depends on the spectral resolution of the satellite spectroradiometer. A CDR spanning SeaWiFS, MODIS, OLCI, and PACE, for example, would include IOPs derived using varied wavelength suites if all available wavelengths were considered. Here, we explored differences in derived IOPs that stem simply from the use of (eight) different wavelength suites of input radiometric measurements. Using synthesized data and SeaWiFS Level-3 mission-long composites, we demonstrated equivalent SAA performance for all wavelength suites, but that IOP retrievals vary by several percent across wavelength suites and as a function of water type. The differences equate to roughly $\leq$ 6, 12, and 7% for $a_{dg}(443)$, $a_{ph}(443)$, and $b_{bp}(443)$, respectively, for waters with $C_a \leq 1\,\mathrm{mg\,m^{-3}}$. These values shrink for sensors with similar wavelength suites (e.g., SeaWiFS, MODIS, and MERIS) and rise to substantially larger values for higher C_a waters. Our results also indicate that including 400 nm (in the case of OLCI) influences the derived IOPs, using longer wavelengths (>600 nm) influences the derived IOPs when there is a red signal, and, including additional spectral information shows potential for improved IOP estimation, but not without revisiting SAA parameterizations and execution. While modest in scope, we believe this study contributes to the knowledge base for CDR development. The implication of ignoring such an analysis as CDRs continue to be developed is a prolonged inability to distinguish between algorithmic and environmental contributions to trends and anomalies in the IOP time-series.

Keywords: ocean color satellites, ocean remote sensing, bio-optics, semi-analytic inversion algorithms, inherent optical properties, remote-sensing reflectance

Edited by:
David Antoine,
Curtin University, Australia

Reviewed by:
Vittorio Ernesto Brando,
Istituto di Scienze Marine (ISMAR), Italy
Severine Alvain,
Centre National de la Recherche Scientifique (CNRS), France

***Correspondence:**
P. Jeremy Werdell
jeremy.werdell@nasa.gov

Specialty section:
This article was submitted to Atmospheric Science, a section of the journal Frontiers in Earth Science

Received: *02 November 2018*
Accepted: *06 March 2019*
Published: *29 March 2019*

Citation:
Werdell PJ and McKinna LIW (2019) Sensitivity of Inherent Optical Properties From Ocean Reflectance Inversion Models to Satellite Instrument Wavelength Suites. Front. Earth Sci. 7:54. doi: 10.3389/feart.2019.00054

INTRODUCTION

The oceanographic community seeks to develop biogeochemical climate data records (CDRs) from satellite measurements of ocean color (NRC, 2011). The U.S. National Research Council defines a CDR as "a time series of measurements of sufficient length, consistency, and continuity to determine climate variability and change" (NRC, 2004). The continuous global data record from ocean color satellites now exceeds 20 years, including (but not limited to) the following instruments: the NASA Sea-viewing Wide Field of View Sensor (SeaWiFS; 1997–2010), the NASA Moderate Resolution Imaging Spectroradiometers (MODIS; 1999-present onboard Terra and 2002-present onboard Aqua), the ESA Medium Resolution Imaging Spectrometer (MERIS; 2002–2012), the Visible Infrared Imaging Radiometer Suite (VIIRS; 2012-present onboard Suomi NPP and 2018-present onboard JPSS-1), the ESA Ocean and Land Color Instrument (OLCI; 2016-present onboard Sentinel-3A and 2018-present onboard Sentinel-3B), and the JAXA Second generation GLobal Imager (SGLI; 2017-present). NASA and several international space agencies plan to launch additional ocean color instruments in the coming decade, including the NASA Plankton, Aerosol, Cloud, ocean Ecosystem (PACE; 2022 launch) ocean color instrument. To facilitate CDR development, the community invests substantially into ensuring the characterization of the space-borne radiometric measurements (e.g., Meister et al., 2012; Zibordi et al., 2014; Meister and Franz, 2014) and the consistency of their derived data products (e.g., Franz et al., 2005; Werdell et al., 2009; Melin and Sclep, 2015; Barnes and Hu, 2016; Mélin et al., 2016). Sathyendranath et al. (2017) provides a useful exploration of desired characteristics of satellite-derived ocean color products for CDR development, including, and perhaps more importantly, analyses to support discussion of the implications potentially realized when these characteristics are not met.

Ocean color satellite instruments provide estimates of spectral remote-sensing reflectance [$R_{rs}(\lambda)$; sr^{-1}], the light exiting the water normalized to the hypothetical condition of a non-attenuating atmosphere with an overhead Sun, after atmospheric correction (Mobley et al., 2016). Bio-optical algorithms are applied to the $R_{rs}(\lambda)$ to produce estimates of geophysical and optical quantities, such as the near surface concentration of the phytoplankton pigment chlorophyll-a (C_a; mg m^{-3}) (O'Reilly et al., 1998) and spectral marine inherent optical properties (IOPs) (Werdell et al., 2018). Time-series of remotely-sensed IOPs provide valuable data records for studying long-term changes in ocean ecosystems. IOPs, the spectral absorption and scattering properties of seawater and its particulate and dissolved constituents, can be used to infer the contents of the upper ocean. This information is critical for advancing our understanding of biogeochemical oceanic processes such as carbon exchanges and fluxes, phytoplankton community dynamics, and ecosystem responses to disturbances (e.g., Behrenfeld et al., 2005; IOCCG, 2009, 2014, 2018; Siegel et al., 2014).

Semi-analytical algorithms (SAAs) provide one mechanism for estimating marine IOPs from $R_{rs}(\lambda)$ using a combination of empiricism and radiative transfer theory (Werdell et al., 2018). Most SAAs attempt to simultaneously estimate the magnitudes of spectral backscattering by particles [$b_{bp}(\lambda)$; m^{-1}], absorption by phytoplankton [$a_{ph}(\lambda)$; m^{-1}], and the combined absorption by non-algal particles and colored dissolved organic material [$a_{dg}(\lambda)$; m^{-1}]. This is typically accomplished by assigning constant spectral values for seawater absorption and backscattering, assuming spectral shape functions for the remaining constituent absorption and scattering components, and retrieving the magnitudes of each remaining constituent required to match the spectral distribution of $R_{rs}(\lambda)$. Such spectral-matching algorithms require contrasting optical signatures for $a_{dg}(\lambda)$, $a_{ph}(\lambda)$, and $b_{bp}(\lambda)$ within the spectral bands detected by the satellite. The performance of most SAAs therefore depends on the spectral resolution of $R_{rs}(\lambda)$ used as input to the algorithm, which is primarily driven by the spectral resolution of the satellite radiometer (Lee et al., 2007; Werdell et al., 2014; Wolanin et al., 2016; Vandermuelen et al., 2017). Conventional wisdom now supports the inclusion of additional ultraviolet-visible wavelengths into new satellite radiometers (relative to historical instruments such as SeaWiFS) to enable the improved discrimination of particulate and dissolved components within seawater and of absorbing and non-absorbing atmospheric aerosols (PACE Science Definition Team, 2018).

Semi-analytical algorithms continue to evolve rapidly, and substantial focus has been placed on intercomparisons (IOCCG, 2006; Brewin et al., 2015), reducing the number of required assumptions [e.g., Zheng and Stramski, 2013; and estimation of uncertainties (Werdell et al., 2018) and references therein]. Uncertainties in SAA-derived IOPs arise from multiple sources: uncertainties in input $R_{rs}(\lambda)$ (Maritorena et al., 2010), assumptions embedded into the adopted $R_{rs}(\lambda)$-to-IOPs relationship (Lee et al., 2004, 2011), the choice of spectral-matching method [see Appendix A of Werdell et al. (2013a)], accounting (or not accounting) for inelastic scattering (Lee et al., 1994; Westberry et al., 2013; McKinna et al., 2016; Loisel et al., 2018), the ancillary data sources used for various corrections (Werdell et al., 2013b), and the assignment of spectral shape functions for $a_{dg}(\lambda)$, $a_{ph}(\lambda)$, and $b_{bp}(\lambda)$ to name only a few. With regards to the latter, for example, any single spectrum cannot unequivocally represent all water masses at all times and Werdell et al. (2013a) demonstrated that selecting alternate spectral shapes can vary derived IOPs by up to ∼100%. Note also that most SAAs do not currently include account for the polarization of light (Ibrahim et al., 2012; Gilerson et al., 2014).

In concert with this ongoing refinement, time-series of data products from SAAs continue to be developed, with the larger goal of producing CDRs (Behrenfeld et al., 2005; Siegel et al., 2013). Some focus has been placed on merging satellite IOP data records (Maritorena et al., 2010), but fewer studies have explored differences in derived products that stem simply from the use of different suites of input $R_{rs}(\lambda)$. For example, SeaWiFS had a green wavelength centered on 510 nm, whereas the MODIS instruments' green wavelength is centered on 531 nm and VIIRS does not include a green wavelength. A CDR from these instruments spanning 1997 to present would therefore include IOPs derived using varied wavelength suites if all available wavelengths were considered. It remains conceivable that different combinations of input $R_{rs}(\lambda)$ yield differences in IOPs that exceed the magnitude of observable environmental change in a CDR. Albeit modest in scope, the goal of this paper is simply to use a controlled modeling environment to quantify the magnitude of change in derived IOPs associated with the use of different spectral suites of satellite $R_{rs}(\lambda)$. The implication of ignoring such an analysis as CDRs continue to be developed is a prolonged inability to distinguish between algorithmic and environmental contributions to trends and anomalies in the IOP time-series.

METHODS

Data Acquisition

For the sensitivity analyses, we generated a synthesized dataset of coincident $R_{rs}(\lambda)$, $a_{dg}(\lambda)$, $a_{ph}(\lambda)$, $b_{bp}(\lambda)$, and C_a that closely mimics the IOCCG Ocean Color Algorithms Working Group synthetic dataset (IOCCG, 2006), but with expanded and finer spectral resolution. Appendix A describes its development (see the online article page to access the **Appendix**). This dataset maintains a spectral resolution of 1 nm intervals from 350 to 800 nm. We targeted $R_{rs}(\lambda)$ and IOPs at the following center satellite wavelengths:

- SeaWiFS: 412, 443, 490, 510, 555, 670
- MODIS: 412, 443, 488, 531, 547, 667
- MERIS: 412, 443, 490, 510, 560, 620, 665
- VIIRS: 410, 443, 486, 551, 671
- OLCI: 400, 412, 443, 490, 510, 560, 620, 665
- PACE: 400, 412, 425, 443, 460, 475, 490, 510, 532, 555, 583, 617, 640, 655, 665
- 410–670 nm: 5 nm intervals from 410 to 670 nm
- 410–600 nm: 5 nm intervals from 410 to 600 nm

The latter three wavelength suites all represent possibilities for PACE, with the first of these three (15 wavelengths) indicating aggregated bands to be distributed by the mission (PACE Science Definition Team, 2018) and the second and third representing the full science resolution of the spectrometer (5 nm) spanning two ranges for inversion (410–600 nm vs. 410–670 nm). While it remains tempting to execute the inversion using the full spectrum of the synthesized dataset, we opted to limit our 5 nm examples to a SeaWiFS-like range to specifically compare differences in performance when using contiguous (so called hyperspectral) spectra vs. discrete heritage wavelengths. Furthermore, we feel the extension of SAA inversions into the ultraviolet remains sufficiently underdeveloped to warrant examination in separate works. We explored a more limited hyperspectral range—to only 600 nm in lieu of 670 nm—to evaluate the impact of very low red radiometric signals in the inversion. For comparative purposes with heritage instruments, we also estimated IOP retrievals for the two 5 nm cases (410–670 and 410–600 nm) at 443 nm using a cubic spline fit on the retrieved $a_{dg}(\lambda)$, $a_{ph}(\lambda)$, and $b_{bp}(\lambda)$.

The native synthesized dataset defines its IOPs using four orders of magnitude of C_a (20 values within the range 0.03 to 30 mg m^{-3}, $N = 500$) (IOCCG, 2006). In most cases (specifically noted), we limited our analyses to $0.03 \leq C_a \leq 5$ mg m^{-3}, as the SAA became sufficiently unstable from instrument-to-instrument above 5 mg m^{-3} such that low retrieval sample sizes confounded meaningful reporting of results ($N \cong 350$). We discuss the strengths and weaknesses of these synthesized data for our analyses in section Discussion. For the satellite comparisons, we acquired the mission-mean (1997–2010) SeaWiFS Level-3 $R_{rs}(\lambda)$ bin file at 9 km spatial resolution from the NASA Ocean Biology Processing Group (OBPG; https://oceancolor.gsfc.nasa.gov; reprocessing version 2018.0). For several analyses, we stratified the results into three C_a ranges—$C_a \leq 0.1$ mg m^{-3} (intended to represent oligotrophic water), $0.1 < C_a \leq 1$ mg m^{-3} (mesotrophic), and $C_a > 1$ mg m^{-3} (eutrophic)—to broadly evaluate performance differences as a function of water type. We note that shape and magnitude of synthesized $R_{rs}(\lambda)$ spectra shift from being blue-dominated to red-dominated as the water type transitions from oligotrophic to eutrophic as shown in **Figure 1**.

Regarding our use of single center wavelengths for this exercise, we acknowledge that different satellite instruments maintain inherently different radiometric bandpasses. Standard NASA processing applies an out-of-band correction using instrument-specific spectral response functions that adjusts the retrieved $R_{rs}(\lambda)$ to the nominal band centers after atmospheric correction (Wang et al., 2001; Patt et al., 2003). Given that this is done prior to execution of an SAA, our use of center wavelengths sufficiently mimics the satellite input $R_{rs}(\lambda)$—acknowledging, of course, that the out-of-band adjustment carries uncertainties that inevitably impact the final IOP retrievals.

Inversion Modeling

Our default SAA adopts the default generalized IOP (GIOP) form described in Werdell et al. (2013a). Briefly, $R_{rs}(\lambda)$ are first converted to their subsurface values following (Lee et al., 2002):

$$r_{rs}\left(\lambda, 0^{-}\right) = \frac{R_{rs}\left(\lambda\right)}{0.52 + 1.7\, R_{rs}\left(\lambda\right)}. \tag{1}$$

Subsurface remote-sensing reflectances relate to marine IOPs following (Gordon et al., 1988):

$$r_{rs}\left(\lambda, 0^{-}\right) = 0.0949\, u + 0.0794\, u^2, \tag{2a}$$

$$u(\lambda) = \frac{b_b\left(\lambda\right)}{a\left(\lambda\right) + b_b\left(\lambda\right)} \tag{2b}$$

where $b_b(\lambda)$ is the total backscattering coefficient (m^{-1}) and $a(\lambda)$ is the total absorption coefficient (m^{-1}). Total backscattering can be expanded as the sum of all backscattering components. Further, each component can be expressed as the product of its mass-specific backscattering spectrum (spectral shape; b^*) and its magnitude or concentration (M):

$$b_b\left(\lambda\right) = b_{bw}\left(\lambda\right) + M_{bp}\, b^*_{bp}(\lambda). \tag{3}$$

Similarly, total absorption can be expanded to:

$$a\left(\lambda\right) = a_w\left(\lambda\right) + M_{dg} a^*_{dg}\left(\lambda\right) + M_{ph} a^*_{ph}\left(\lambda\right). \tag{4}$$

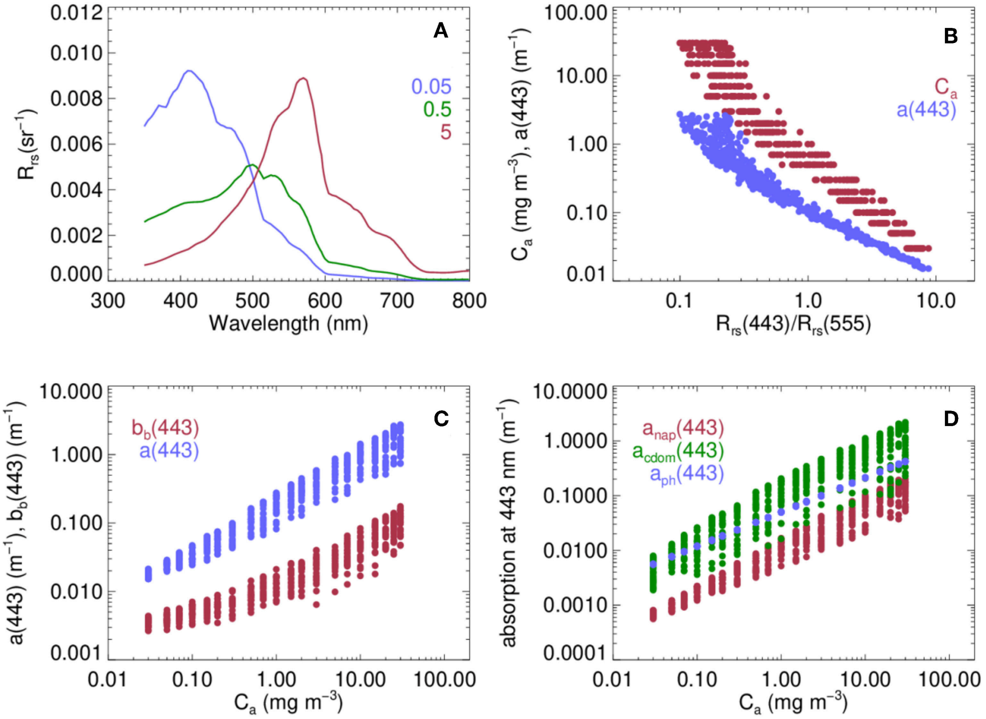

FIGURE 1 | Characteristics of the simulated AOP-IOP dataset: Three example $R_{rs}(\lambda)$ spectra selected from the synthesized AOP-IOP dataset for C_a of 0.05, 0.5, and 5 mg m^{-3} **(A)**; C_a and $a(443)$ as a function of the ratio of $R_{rs}(443)$:$R_{rs}(555)$ **(B)**; $b_{bp}(443)$ and $a(443)$ as a function of C_a **(C)**; and, $a_{nap}(443)$, $a_{cdom}(443)$, and $a_{ph}(443)$ as a function of C_a **(D)**.

where the subscript w indicates contributions by water. Both $b_{bw}(\lambda)$ and $a_w(\lambda)$ are known (Pope and Fry, 1997; Zhang et al., 2009). Werdell et al. (2013a) describes in the detail the rationale for the default choices of $b^*_{bp}(\lambda)$, $a^*_{dg}(\lambda)$, and $a^*_{ph}(\lambda)$. By default, we expressed $b^*_{bp}(\lambda)$ as λ^{Sbp}, where S_{bp} defines the steepness of the power law and typically varies between −2 and 0 in natural waters (Stramski et al., 2004). We dynamically assigned S_{bp} to each station/pixel using the $R_{rs}(\lambda)$ band-ratio method described in Lee et al. (2002). We expressed $a^*_{dg}(\lambda)$ as exp($-S_{dg}$ λ), where S_{dg} describes the rate of exponential decay and typically varies between 0.01 and 0.02 nm^{-1} (Roesler et al., 1989), and adopted a fixed S_{dg} of 0.018 nm^{-1}. Finally, we expressed $a^*_{ph}(\lambda)$ as the C_a-specific absorption spectrum of Bricaud et al. (1998) seeded using each station/pixel-specific C_a and normalized to 0.055 m^2 mg^{-1} at 443 nm. Broadly speaking, many alternatives for such parameterizations exist (as explored in Werdell et al., 2013a), but our choices in parameterization remain of secondary importance for this paper given that we apply them consistently across analyses.

Three unknowns remain in Equations (1–4) after assignment of the eigenvectors, namely M_{bp}, M_{dg}, and M_{ph}. Using $R_{rs}(\lambda)$ as input, the SAA estimates these eigenvalues via non-linear least squares (Levenberg-Marquardt) inversion of Equation (2) with minimization of a χ^2 cost function [see Equation (11) of Werdell et al., 2013a]. We retained only those solutions with viable estimates of M_{bp}, M_{dg}, and M_{ph} [for example, $-0.005 \leq a_{dg}(\lambda) \leq 5$ m^{-1}] that resulted in reconstructed $R_{rs}(\lambda)$ that differed from the input $R_{rs}(\lambda)$ by < 33% in the range 400 to 600 nm. We reconstructed $R_{rs}(\lambda)$ using the retrieved eigenvalues as input into Equations (1–4) and defined failure as non-convergence in the inversion. Werdell et al. (2013a) outlines exclusion criteria used to determine viable estimates, as well as the similarities in accuracy shared by this SAA configuration and other common approaches.

Analyses

We ran the inversion model using the synthesized $R_{rs}(\lambda)$ for every satellite input wavelength suite listed in section Data Acquisition. We then statistically compared the model-derived IOPs (hereafter referred to by satellite to identify the input wavelength suite) with the source synthesized IOPs. Our reported statistics include the sample size (N), the Type I linear regression slope, the median absolute error (MAE), and the bias. We calculated MAE as:

$$MAE = 10^\wedge \left(\frac{\sum_{i=1}^{N} \left| \log_{10}\left(satellite_i\right) - \log_{10}\left(synthesized_i\right) \right|}{N} \right) \quad (5)$$

and bias as:

$$bias = 10^\wedge \left(\frac{\sum_{i=1}^{N} \log_{10}\left(satellite_i\right) - \log_{10}\left(synthesized_i\right)}{N} \right). \quad (6)$$

TABLE 1 | Statistics for SAA-derived vs. synthesized IOPs at 443 nm.

		Bias	MAE	Slope
SeaWiFS	a	1.08	1.10	1.07
$N = 356$	a_{dg}	0.93	1.27	1.03
	a_{ph}	1.24	1.50	1.05
	b_{bp}	1.10	1.15	1.01
MODIS	a	1.07	1.09	1.05
$N = 335$	a_{dg}	0.92	1.27	1.03
	a_{ph}	1.17	1.51	0.92
	b_{bp}	1.08	1.14	0.99
MERIS	a	1.04	1.06	1.02
$N = 354$	a_{dg}	0.91	1.26	1.01
	a_{ph}	1.14	1.47	0.92
	b_{bp}	1.05	1.12	0.96
VIIRS	a	1.07	1.10	1.06
$N = 345$	a_{dg}	0.91	1.27	1.03
	a_{ph}	1.24	1.52	0.99
	b_{bp}	1.09	1.16	0.99
OLCI	a	1.04	1.07	1.02
$N = 364$	a_{dg}	0.89	1.26	1.01
	a_{ph}	1.23	1.48	0.97
	b_{bp}	1.07	1.13	0.97
PACE	a	1.03	1.05	1.01
$N = 343$	a_{dg}	0.89	1.25	1.00
	a_{ph}	1.11	1.54	0.85
	b_{bp}	1.05	1.12	0.94
410–670 nm	a	0.98	1.05	1.00
$N = 332$	a_{dg}	0.85	1.27	1.00
	a_{ph}	1.00	1.53	0.84
	b_{bp}	1.01	1.10	0.94
410–600 nm	a	0.98	1.05	1.01
$N = 347$	a_{dg}	0.86	1.27	1.01
	a_{ph}	1.04	1.50	0.87
	b_{bp}	1.01	1.10	0.94

Note that observations are log-transformed such that MAE and bias present multiplicative metrics (that is, a MAE of 1.5 indicates that the satellite observations are 1.5 × (50% greater) on average than the synthesized observations and a bias less than unity indicates a negative bias). Note also that **Table 1** reports bias and MAE as calculated in Equations (5) and (6), but we discuss these performance metrics using their more intuitive percentage counterparts throughout the Results and Discussion sections.

Next, we compared derived IOPs from each satellite wavelength suite with those from every other satellite wavelength suite. This comparison included determination of unbiased percent differences (UPD). We calculated UPD for two satellites ($satellite_1$ and $satellite_2$) as:

$$UPD = 200\% \left(\frac{satellite_2 - satellite_1}{satellite_2 + satellite_1} \right) \tag{7}$$

and report the median UPD for the complete population of match-ups. A negative UPD indicates that the IOP from $satellite_2$ is biased low relative to $satellite_1$.

To evaluate if the results varied with the configuration of the inversion model (that is, if they varied with assignment of spectral shapes), we ran the inversion model for each satellite input $R_{rs}(\lambda)$ wavelength suite an additional seven times, sequentially re-assigning one variable per run as: (1) default S_{bp} from Lee et al. (2002) + 33%; (2) default S_{bp} from Lee et al. (2002)−33%; (3) default S_{dg} + 33% (= 0.024 nm^{-1}); (4) default S_{dg}−33% (= 0.012 nm^{-1}); (5) seed C_a to calculate $a^*_{ph}(\lambda)$ using Bricaud et al. (1998) + 50%; (6) seed C_a to calculate $a^*_{ph}(\lambda)$ using Bricaud et al. (1998)−50%; and, (7) replacing 0.0949 and 0.0794 in Equation (2a) with 0.0895 and 0.1247 as in Lee et al. (2002).

Finally, we twice ran the default inversion model (as defined in section Inversion Modeling) on the mission-long mean Level-3 SeaWiFS $R_{rs}(\lambda)$ to determine if results from our controlled modeling environment were generally representative of real satellite data. To do so, we used OBPG-supported satellite data processing software (l3 gen) to run the inversion model via the GIOP software framework, which allows assignment of wavelengths to be used in the inversion, on the Level-3 SeaWIFS $R_{rs}(\lambda)$. The NASA SeaWiFS Data Analysis Software (SeaDAS; https://seadas.gsfc.nasa.gov) package includes this software. The first run used all six SeaWiFS wavelengths. The second run served to mimic VIIRS and, as such, we only assigned the five common SeaWiFS-VIIRS wavelengths. Given the known differences between SeaWiFS and VIIRS $R_{rs}(\lambda)$ (Eplee et al., 2015; Barnes and Hu, 2016), using a narrower SeaWiFS band set as a surrogate for VIIRS provided a more suitable controlled environment to explore differences in band selection.

RESULTS

Data Product Validation

Broadly speaking, the satellite-to-synthesized IOP validation analyses demonstrated equivalent performance across all wavelength suites (**Figure 2**, **Table 1**), with performance metrics that mirror those from previous studies that used equivalent simulated datasets (e.g., IOCCG, 2006; Lee et al., 2010; Werdell et al., 2013a). All runs reported very similar MAE, ranging from 5 to 10% for $a(443)$ and 10 to 16% for $b_{bp}(443)$ and from 5 to 8% for $a(555)$ and 8 to 14% for $b_{bp}(555)$. In general, we achieved comparable results across blue-green wavelengths for all analyses and, thus, our tables and figures focus only on 443-nm for clarity in presentation of results. MAEs for the absorption subcomponents ranged from 25 to 27% for $a_{dg}(443)$ and 47 to 54% for $a_{ph}(443)$. Every wavelength suite carried its lowest MAEs for $a(443)$ and the highest MAE for $a_{ph}(443)$. The regression slopes behaved similarly. All runs reported very similar values for $a(\lambda)$, $a_{dg}(\lambda)$, and $b_{bp}(\lambda)$, ranging from 1.00 to 1.07 for $a(443)$, 1.03 to 1.06 for $a_{dg}(443)$ and 0.94 to 1.01 for $b_{bp}(443)$. Across IOPs for each wavelength suite, $a_{ph}(443)$ deviated most substantially from unity. It also exhibited the broadest range across wavelength suites, ranging from 0.72 to 1.05. Interestingly, the runs with the most

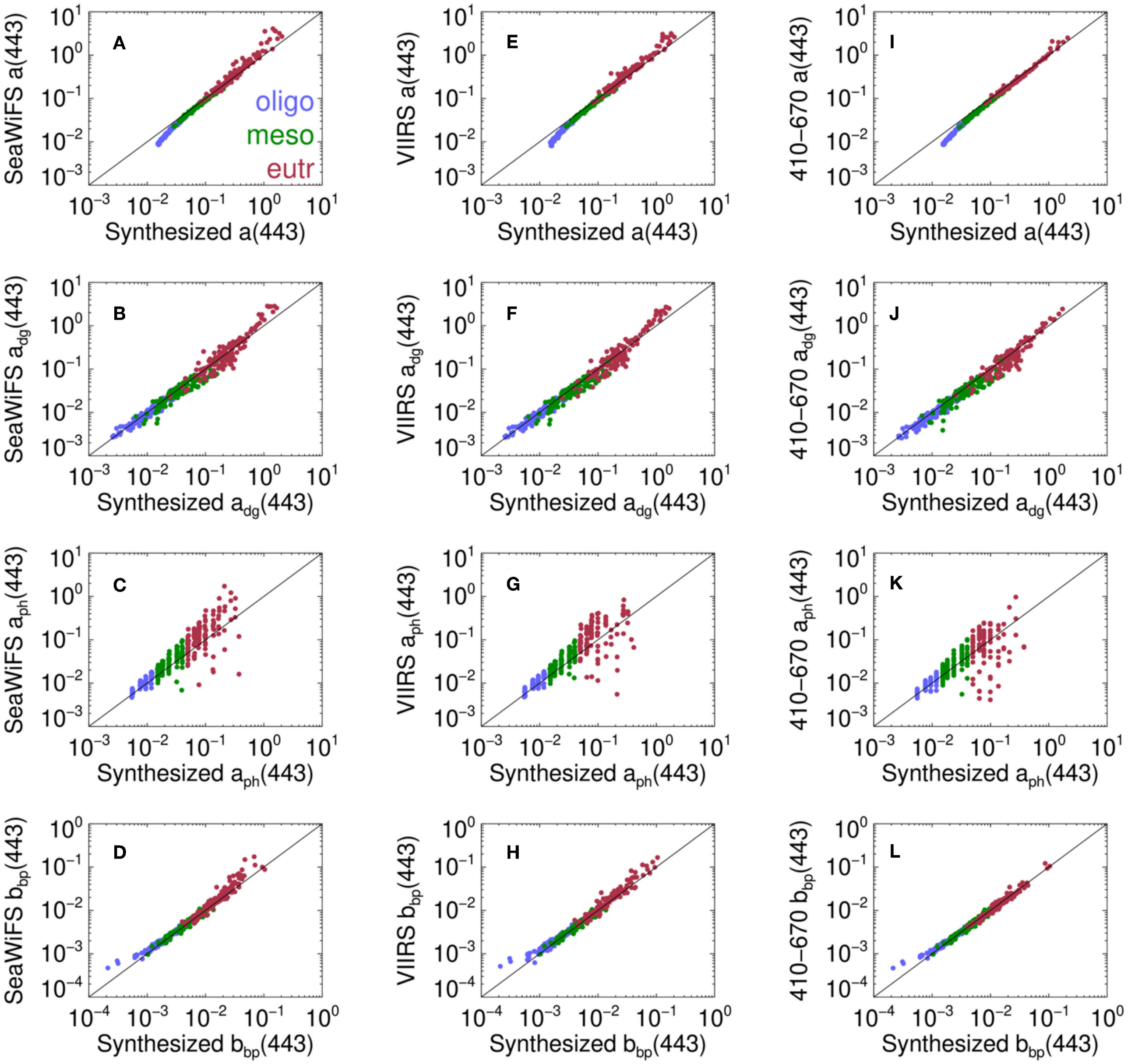

FIGURE 2 | Synthesized-vs.-satellite IOPs at 443 nm for SeaWiFS **(A–D)**, VIIRS **(E–H)**, and 410–670 nm **(I–L)**. IOPs include $a(443)$ **(A,E,I)**, $a_{dg}(443)$ **(B,F,J)**, $a_{ph}(443)$ **(C,G,K)**, and $b_{bp}(443)$ **(D,H,L)**. The solid line represents a 1:1 relationship. The colors indicate chlorophyll-a ranges, with the oligotrophic range presented in red ($C_a \leq$ 0.1 mg m^{-3}), the mesotrophic in green (0.1 $< C_a <$ 1 mg m^{-3}), and the eutrophic in red ($C_a \geq$ 1 mg m^{-3}).

wavelengths (PACE, 410–670 nm, and 410–600 nm) reported the $a_{ph}(443)$ regression slopes that deviated most from unity. The satellite-to-synthesized biases diverged more across runs than either MAE or regression slope. While $a(443)$ biases spanned across unity, all $a_{dg}(443)$ biases fell below unity (recall that a bias less than unity indicates a negative bias), ranging from 7% for SeaWiFS to 15% for the 410–670 nm run, and all $a_{ph}(443)$ biases fell either very close to unity or were positive, ranging from exactly unity for the 410–670 nm run to 24% for SeaWiFS and VIIRS. All $b_{bp}(443)$ biases exceeded unity (were positive), ranging from 1% for the two 5 nm runs to 10% for SeaWiFS.

These results predominantly encompass simulations with $C_a \leq 5$ mg m^{-3}, as 85% of SAA failures occurred for those simulations with higher C_a values (reducing the viable N to ≅350 as previously mentioned). Few failures resulted from non-convergence in the inversion. Rather, most occurred because of quality assurance metrics applied to the IOP retrievals, including requiring them to fall within predefined acceptable ranges (for example, $-0.005 \leq a_{dg}(\lambda) \leq 5$ m^{-1}) and requiring

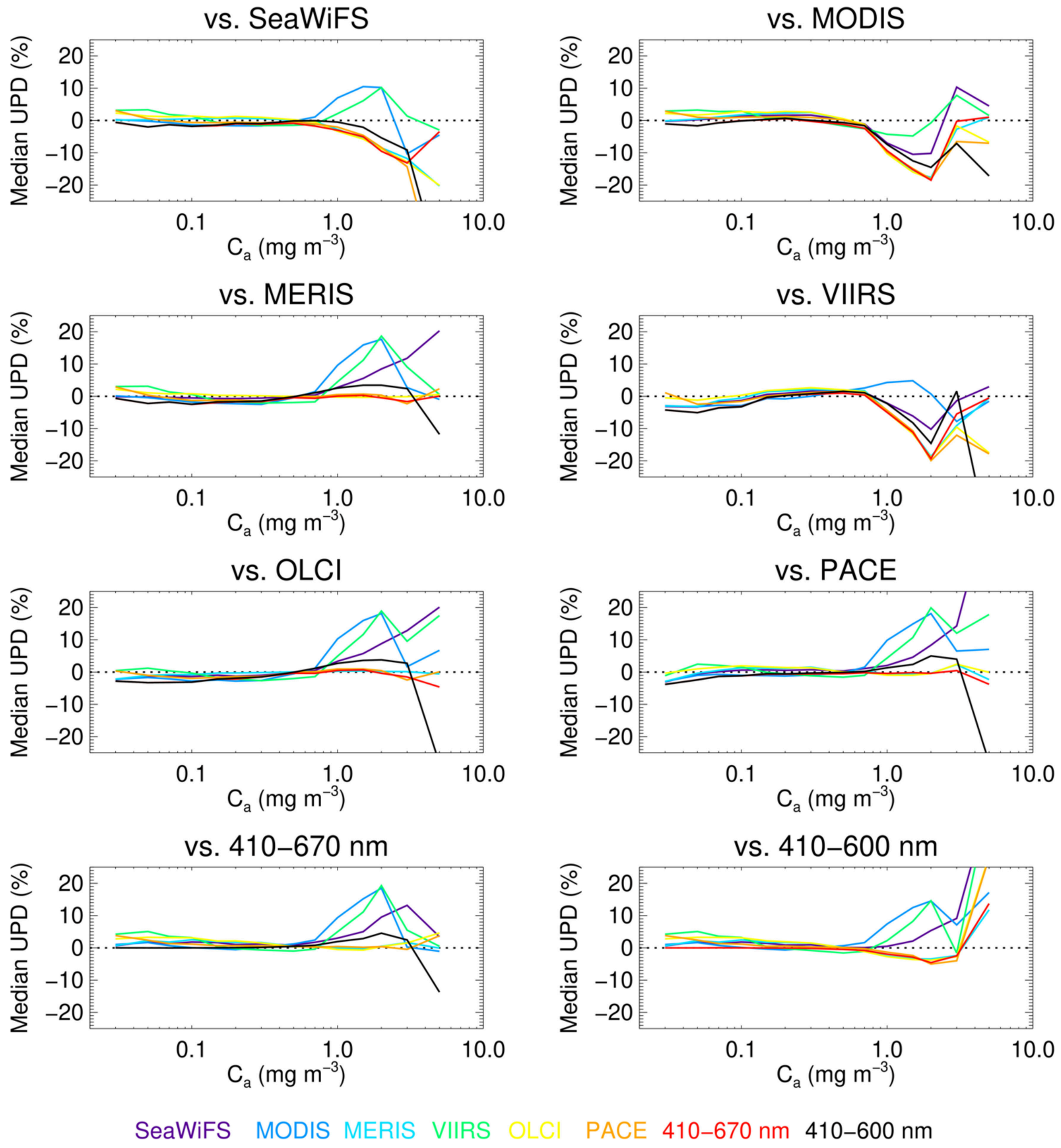

FIGURE 3 | Satellite-to-satellite median UPD for *a*(443) at each C_a interval. Each panel title refers to the reference satellite to which the others are compared (satellite$_1$ in Equation 7). Each comparative satellite (satellite$_2$ in Equation 7) maintains a unique color: SeaWiFS (violet), MODIS (blue), MERIS (cyan), VIIRS (green), OLCI (yellow), PACE (orange), 410-670 nm (red), and 410-600 nm (black).

that reconstructed $R_{rs}(\lambda)$ differ from input $R_{rs}(\lambda)$ by < 33% at every wavelength in the range 400 to 600 nm. While relaxing or modifying these quality assurance metrics would enable extending our analyses into more complex water, we opted to not do so to: (a) ensure that our results encompassed only the highest quality SAA retrievals; (b) limit the introduction of results biases that emerge from global SAA parameterizations that do not properly represent complex waters; and, (c) acknowledge that the simulated dataset itself may be the least representative of natural conditions in this C_a range. Moreover, as simulations with $C_a > 5$ mg m^{-3} realized so few results (low sample sizes), we opted to exclude them from subsequent analyses and data product intercomparisons. Follow-on analyses will benefit from additional attention to SAAs and datasets that better represent optically complex water.

Data Product Inter-comparisons

IOP retrievals for the synthetic dataset varied across wavelength suites and as a function of water type as defined by C_a (**Figures 3–6**, **Tables 2–4**). UPDs in $a(443)$, $a_{dg}(443)$, $a_{ph}(443)$,

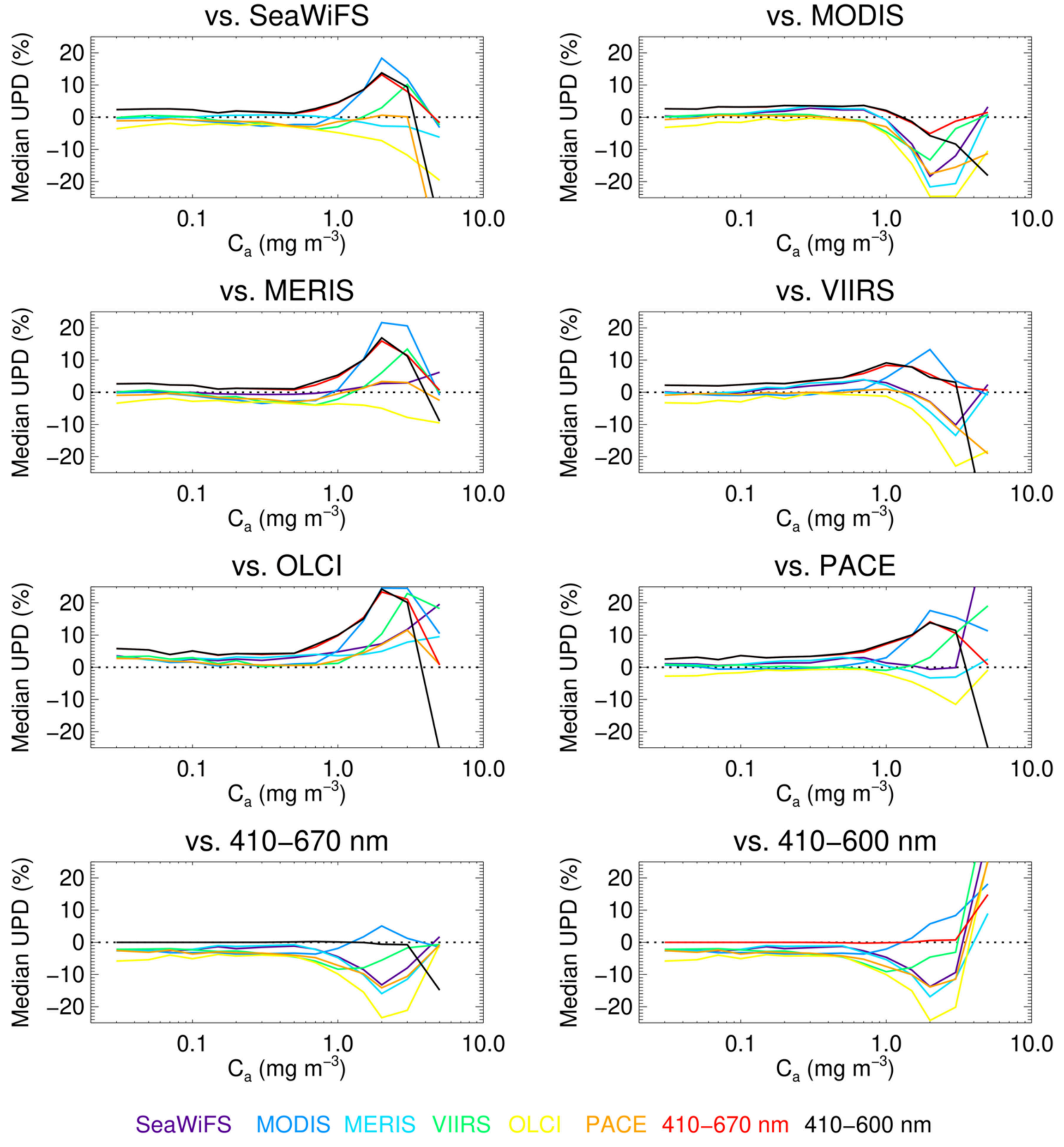

FIGURE 4 | As for **Figure 3**, but for $a_{dg}(443)$.

and $b_{bp}(443)$ across all wavelength suites ranged from −3.83 to 2.91%, −3.14 to 5.27%, −11.57 to 6.33%, and −6.09 to 4.74%, respectively, for the lowest C_a waters (**Table 2**). For comparison, UPDs in $a(555)$, $a_{dg}(555)$, $a_{ph}(555)$, and $b_{bp}(555)$ for SeaWiFS, PACE, and the two 5 nm wavelength suites (the only four suites with 555 nm) ranged from −0.51 to 0.35%, −0.74 to 3.13%, −6.65 to 1.47%, and −2.78 to 1.52%, respectively. Generally speaking, the differences between any two wavelength suites remained constant for all $C_a \leq 0.1$ mg m^{-3} (**Figures 3–6**). Retrievals for the wavelength suites we consider most similar, SeaWiFS, MODIS, and MERIS, generally differed the least—by ≤ 0.92, 0.40, 1.11, and 1.25% for $a(443)$, $a_{dg}(443)$, $a_{ph}(443)$, and $b_{bp}(443)$, respectively, in absolute terms. OLCI retrieved low $a_{dg}(443)$ and high $a_{ph}(443)$ relative to all other wavelength suites, perhaps due to the inclusion of a 400 nm band that altered the separation of the two absorption subcomponents. The two 5 nm wavelength suites retrieved high $a_{dg}(443)$, low $a_{ph}(443)$, and low $b_{bp}(443)$ relative to all other wavelength suites. With only several exceptions, they also realized the highest magnitude UPDs.

For the mesotrophic C_a range, UPDs in $a(443)$, $a_{dg}(443)$, $a_{ph}(443)$, and $b_{bp}(443)$ across all wavelength suites ranged from −1.66 to 1.80%, −3.18 to 4.79%, −10.46 to 4.50%, and −2.27

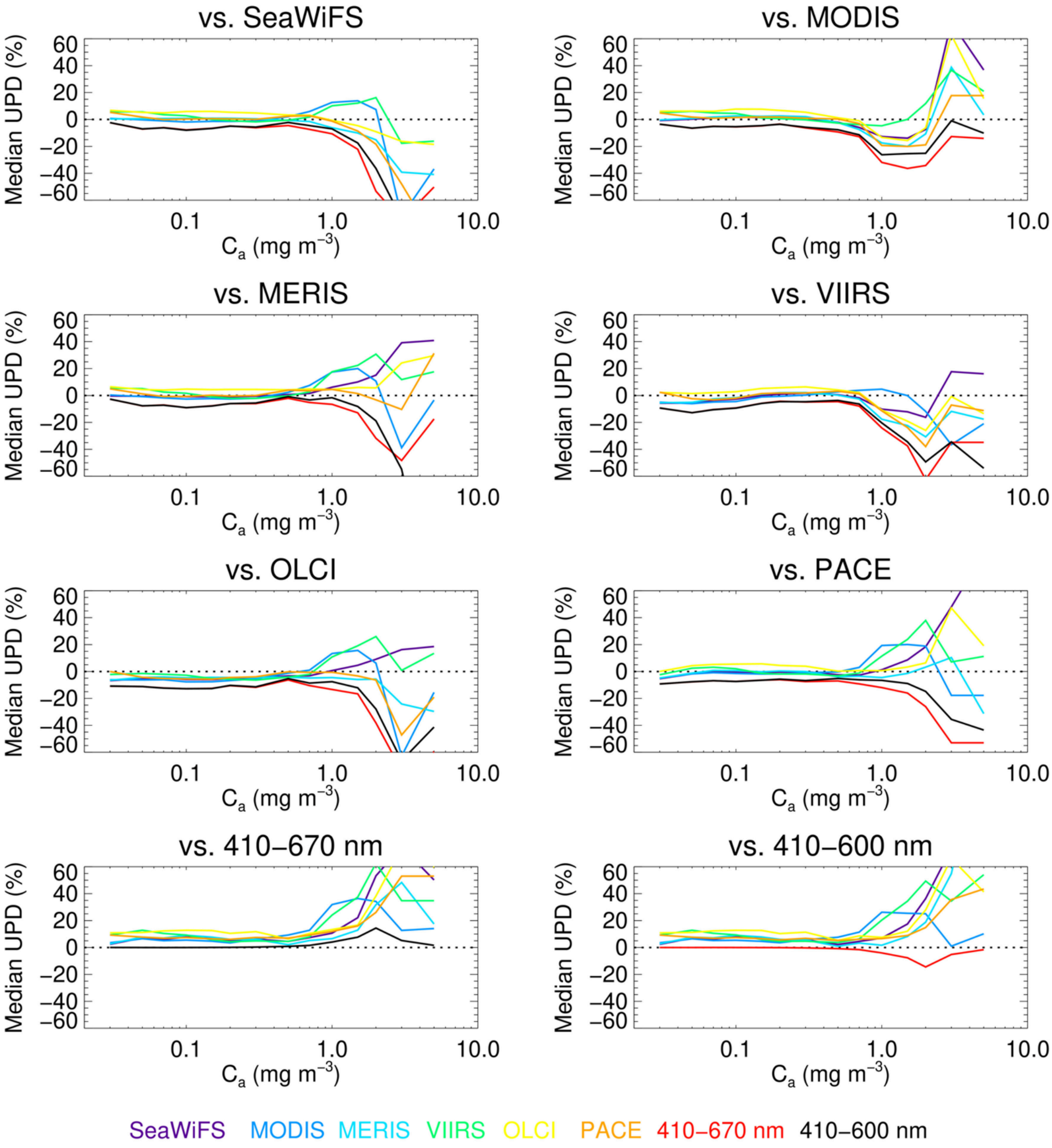

FIGURE 5 | As for **Figure 3**, but for $a_{ph}(443)$.

to 2.60%, respectively (**Table 3**). These ranges for $a_{dg}(443)$ and $a_{ph}(443)$ generally match those for the oligotrophic C_a range, whereas these ranges for $a(443)$ and $b_{bp}(443)$ compress closer to unity. For comparison, UPDs in $a(555)$, $a_{dg}(555)$, $a_{ph}(555)$, and $b_{bp}(555)$ for SeaWiFS, PACE, and the two 5 nm wavelength suites ranged from −1.50 to 0.21%, −1.74 to 3.99%, −7.47 to 1.34%, and −1.32 to 0.24%, respectively. Generally speaking, the differences between any two wavelength suites remained invariant for $0.1 \leq C_a \leq 0.5$ mg m^{-3}, above which they started to diverge (**Figures 3–6**). SeaWiFS, MODIS, and MERIS differed by ≤ 1.50, 2.32, 0.75, and 2.59% for $a(443)$, $a_{dg}(443)$, $a_{ph}(443)$, and $b_{bp}(443)$, respectively, in absolute terms. Like the oligotrophic subset, OLCI retrieved low $a_{dg}(443)$ relative to all other wavelength suites. Unlike that subset, however, its $a_{ph}(443)$ retrievals exceeded all other wavelength suites. As for the oligotrophic subset, the two 5 nm wavelength suites retrieved high $a_{dg}(443)$, low $a_{ph}(443)$, and low $b_{bp}(443)$ relative to all other wavelength suites. Their UPD magnitudes, however, fell more in line with the others.

The eutrophic C_a range (capped at 5 mg m^{-3}) realized the most diversity and highest magnitudes in UPDs across all wavelength suites [noting that: (a) SAA retrievals often realize

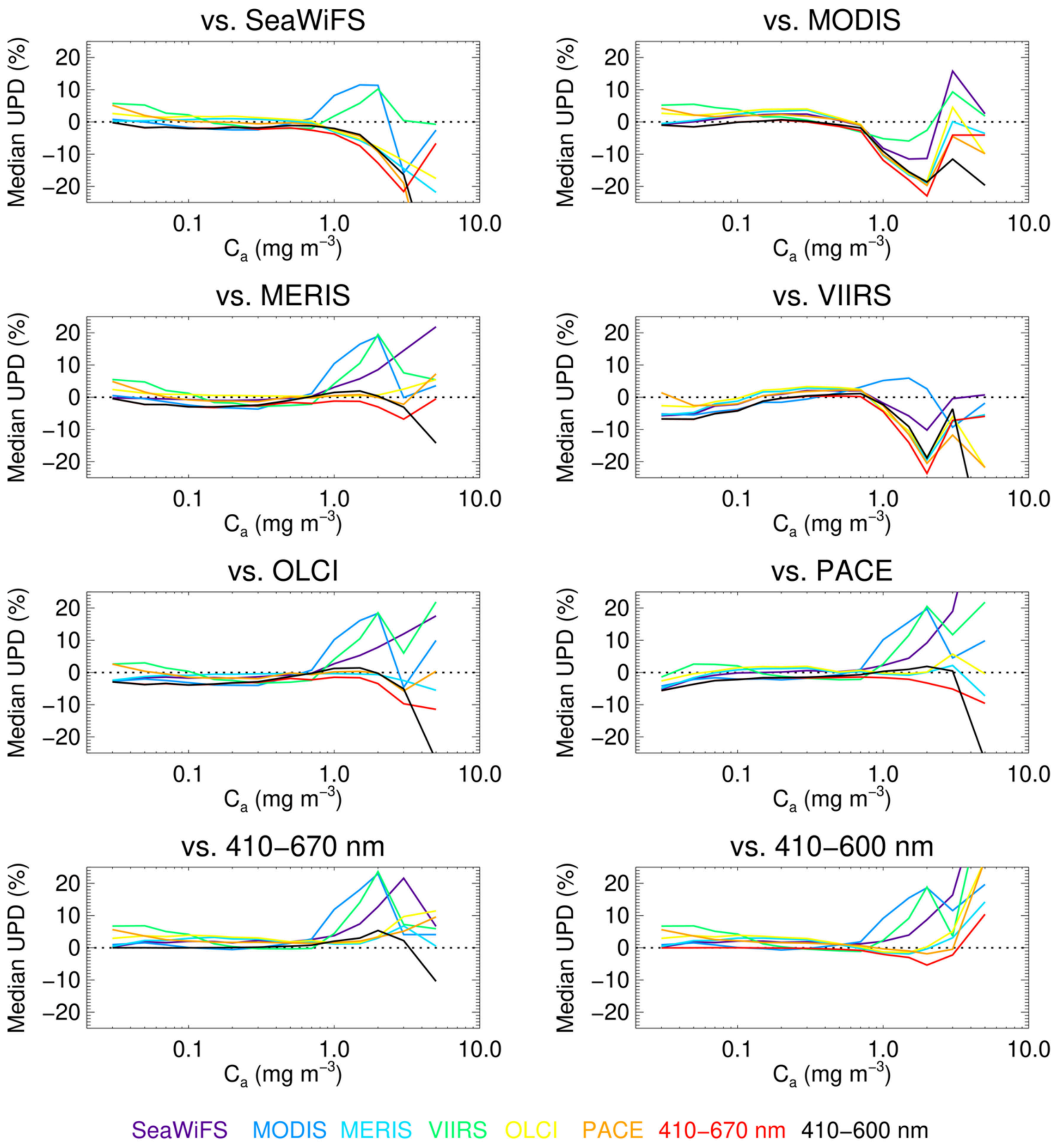

FIGURE 6 | As for **Figure 3**, but for $b_{bp}(443)$.

instabilities in such ranges (Werdell et al., 2009, 2018); and (b) the synthesized dataset represents the widest diversity in water in this range (IOCCG, 2006)]. UPDs in $a(443)$, $a_{dg}(443)$, $a_{ph}(443)$, and $b_{bp}(443)$ across all wavelength suites ranged from −16.07 to 12.70%, −19.69 to 17.67%, −53.92 to 12.01%, and −19.50 to 12.99%, respectively (**Table 4**). For comparison, UPDs in $a(555)$, $a_{dg}(555)$, $a_{ph}(555)$, and $b_{bp}(555)$ for SeaWiFS, PACE, and the two 5 nm wavelength suites ranged from −17.00 to 5.33%, −0.24 to 11.23%, −42.26 to 9.31%, and −10.60 to 3.54%, respectively. The differences between any two wavelength suites varied considerably for $C_a > 1$ mg m^{-3} (**Figures 3–6**). Even SeaWiFS, MODIS, and MERIS differed more substantially than in other C_a ranges—by ≤15.74, 15.03, 18.64, and 17.12% for $a(443)$, $a_{dg}(443)$, $a_{ph}(443)$, and $b_{bp}(443)$, respectively, in absolute terms. Like the oligotrophic subset, OLCI retrieved low $a_{dg}(443)$ and high $a_{ph}(443)$ relative to all other wavelength suites, with the exception of MERIS. As for the other two subsets, the two 5 nm wavelength suites retrieved high $a_{dg}(443)$, low $a_{ph}(443)$, and low $b_{bp}(443)$ relative to all other wavelength suites. Their UPDs for $a_{ph}(443)$ far exceeded those for the other suites.

Differences in IOPs from SeaWiFS and SeaWiFS-modified-to-look-like-VIIRS largely demonstrated similar patterns. For

TABLE 2 | Satellite-to-satellite median UPD for IOPs at 443 nm for oligotrophic water ($C_a \leq 0.1$ mg m^{-3}). Relative to Equation (7), columns represent satellite$_1$ and rows represent satellite$_2$ (e.g., MODIS *a*(443) is 0.49% lower (thus, negative) on average than that for SeaWIFS).

	SeaWiFS	MODIS	MERIS	VIIRS	OLCI	PACE	410–670 nm
***a*(443)**							
MODIS	−0.49						
MERIS	0.30	0.92					
VIIRS	2.30	2.91	2.08				
OLCI	1.41	2.13	1.05	−0.44			
PACE	0.56	1.10	0.35	−1.35	−0.71		
410–670 nm	−1.30	−0.84	−1.76	−3.78	−3.15	−1.97	
410–600 nm	−1.31	−0.88	−1.75	−3.83	−3.15	−1.95	0.00
a_{dg}(443)							
MODIS	−0.40						
MERIS	−0.13	0.28					
VIIRS	0.19	0.60	0.20				
OLCI	−2.61	−2.42	−2.67	−3.14			
PACE	−0.74	0.10	−0.75	−0.62	2.38		
410–670 nm	2.43	2.94	2.55	2.08	5.27	3.13	
410–600 nm	2.43	2.93	2.56	2.08	5.27	3.13	0.00
a_{ph}(443)							
MODIS	−0.42						
MERIS	0.64	1.11					
VIIRS	4.37	5.04	3.50				
OLCI	5.60	6.33	4.82	2.25			
PACE	1.47	2.11	0.89	−1.72	−3.22		
410–670 nm	−5.15	−5.03	−5.99	−9.85	−11.57	−7.46	
410–600 nm	−5.15	−5.14	−6.08	−9.79	−11.56	−7.59	0.01
b_{bp}(443)							
MODIS	−0.75						
MERIS	0.48	1.25					
VIIRS	4.13	4.74	3.55				
OLCI	1.70	2.50	1.15	−1.68			
PACE	1.52	2.21	1.00	−1.65	0.01		
410–670 nm	−1.22	−1.00	−1.64	−6.09	−3.63	−2.99	
410–600 nm	−1.18	−0.94	−1.65	−6.08	−3.61	−2.98	0.01

Sample sizes follow those presented in ***Table 1****.*

context, **Figure 7** shows SeaWiFS-derived C_a (Hu et al., 2012) and the spatial distribution of olig-, meso-, and eutrophic waters, and **Figure 8** shows the SeaWiFS-derived $a_{dg}(443)$, $a_{ph}(443)$, and $b_{bp}(443)$. Naturally, the cumulative distribution of observations falling into each of the trophic levels differs widely in comparison to the synthesized data set, which might be considered in the interpretation of these results. The median SeaWiFS-derived C_a for its olig-, meso-, and eutrophic regions were 0.066, 0.19, and 1.6 mg m^{-3}, respectively. The corresponding median UPDs for $a_{dg}(443)$ for these regions were 1.7, 1.8, and 4.2%, respectively, which approximately track the magnitude of the UPDs at these C_a values in **Figure 4** (upper left panel, green line). Note, however, that VIIRS $a_{dg}(443)$ falls below that for SeaWiFS by ∼2% on average across the synthesized mesotrophic subset. Note also that the mesotrophic subset dominates globally and represents a great diversity in water type (**Figure 7**). The median UPDs for $a_{ph}(443)$ for the three trophic regions were 9.8, 7.7, and −3.4%, respectively. These also roughly track the UPDs at the corresponding C_a shown in **Figure 5**, with the exception of the eutrophic subset, which also has a sign difference. Finally, the median UPDs for $b_{bp}(443)$ for these regions were 8.9, 8.0, and 2.3%, respectively. These UPDs match those shown in **Figure 6** for the oligo- and eutrophic subsets. Geographically, $a_{dg}(443)$ differ the least between SeaWiFS and surrogate VIIRS, with UPDs that hover around unity (**Figure 8B**). Both $a_{ph}(443)$ and $b_{bp}(443)$ show some latitudinal dependence in their UPDs and surrogate VIIRS-derived values almost unequivocally exceed those from SeaWiFS (**Figures 8D,F**).

As an additional thought experiment to loosely begin to tie our results to marine particle size distributions (PSDs) and, thus, phytoplankton functional types (PFTs), we applied the approach of Hirata et al. (2011) to locate pixels in this SeaWiFS imagery

TABLE 3 | As in **Table 2**, but for mesotrophic water ($0.1 < C_a \leq 1.0$ mg m^{-3}).

	SeaWiFS	MODIS	MERIS	VIIRS	OLCI	PACE	410-670 nm
a(443)							
MODIS	−0.97						
MERIS	0.44	1.50					
VIIRS	−1.09	−0.99	−1.66				
OLCI	0.53	1.37	0.05	1.80			
PACE	−0.69	0.57	−0.58	0.77	−0.67		
410–670 nm	−1.20	−0.36	−1.06	0.07	−1.00	−0.53	
410–600 nm	−0.71	−0.15	−0.57	0.56	−0.74	−0.29	0.22
a_{dg}(443)							
MODIS	−1.83						
MERIS	0.50	2.32					
VIIRS	−2.19	0.22	−2.39				
OLCI	−2.79	−1.08	−3.18	−0.94			
PACE	−1.74	0.08	−2.08	0.12	0.79		
410–670 nm	1.82	3.31	1.31	4.01	4.50	3.73	
410–600 nm	1.94	3.31	1.57	4.55	4.79	4.00	0.04
a_{ph}(443)							
MODIS	0.75						
MERIS	0.15	−0.50					
VIIRS	−0.25	−1.93	−0.67				
OLCI	4.31	3.11	4.50	4.46			
PACE	1.34	0.31	1.35	1.38	−2.55		
410–670 nm	−6.14	−6.84	−5.13	−6.29	−10.46	−7.37	
410–600 nm	−4.61	−6.50	−4.24	−5.81	−8.95	−6.26	0.45
b_{bp}(443)							
MODIS	−1.53						
MERIS	0.65	2.59					
VIIRS	−1.37	−1.08	−2.10				
OLCI	0.94	2.60	0.40	2.45			
PACE	−0.55	1.50	−0.78	1.29	−1.17		
410–670 nm	−2.27	−0.41	−2.18	−0.30	−2.71	−1.66	
410–600 nm	−1.64	−0.18	−1.74	0.00	−2.21	−1.22	0.24

dominated by pico-, nano-, and microplankton (with dominance defined as >50%). On average, SeaWiFS and surrogate VIIRS-derived $a_{dg}(443)$ differed by 1.7, 1.7, and 2.1% for these size classes, whereas $a_{ph}(443)$ and $b_{bp}(443)$ differed by 8.4, 7.6, and 7.8% and 8.0, 7.4, and 8.0%, respectively. These values do not differ substantially from those of the previous exercise as expected, given that Hirata et al. (2011) seeds with C_a, but they offer a modest confirmation of the spatial patterns realized in our analyses. While evaluating the impact of our findings on PSD and PFT retrievals extends beyond the scope of this paper, we feel it remains an obvious follow-on to this work. Many options for estimation of PSDs and PFTs exist and follow-on activities could: (a) build upon our brief example using model-derived distributions of phytoplankton (e.g., Dutkiewicz et al., 2009; Rousseaux and Gregg, 2015); (b) quantify the impacts of varied SAA retrievals within PSD and PFT algorithms that use IOPs as input (see, e.g., IOCCG, 2014; Bracher et al., 2017; Mouw et al., 2017); or; (c) explore in more detail how differences in SAA retrievals for multiple sensors compare to spectral changes in marine IOPs that occur across natural variations in phytoplankton community composition (Alvain et al., 2012).

Sensitivity of the SAA Parameterization

Our choice in SAA parameterization made little difference in results achieved from the synthesized dataset. **Figures 9–12** follow **Figures 3–6** with the exception that the reported UPDs represent the average for eight SAA parameterizations. At $C_a \leq 0.5$ mg m^{-3}, the patterns in satellite-to-satellite UPDs for the ensemble of runs almost exactly mimicked those for the default SAA runs. This C_a range represents roughly 86% of the retrieved ocean in **Figure 7**. The most obvious difference in UPD patterns emerge at $C_a > 2$ mg m^{-3}, which represents roughly 1.5% of the retrieved ocean. Interestingly, when C_a exceeded 2 mg m^{-3}, UPD values for $b_{bp}(443)$ remained reasonably steady (**Figure 12**) for wavelength suites that included one or more orange/red bands placed between 550 and 670 nm (e.g., 620 nm

TABLE 4 | As in **Table 2**, but for eutrophic water ($1.0 < C_a \leq 5.0$ mg m^{-3}).

	SeaWiFS	MODIS	MERIS	VIIRS	OLCI	PACE	410–670 nm
***a*(443)**							
MODIS	9.07						
MERIS	−8.60	−15.74					
VIIRS	6.58	−0.99	12.70				
OLCI	−9.15	−15.84	−0.18	−13.31			
PACE	−8.82	−16.05	−0.92	−13.91	−0.54		
410–670 nm	−8.24	−16.07	−0.36	−13.59	0.08	−0.17	
410–600 nm	−3.43	−12.72	3.12	−9.58	3.54	3.08	3.36
a_{dg}(443)							
MODIS	13.14						
MERIS	−2.56	−15.03					
VIIRS	2.79	−10.08	5.70				
OLCI	−8.78	−19.69	−5.85	−10.17			
PACE	−0.03	−13.52	2.04	−3.02	6.58		
410–670 nm	9.53	−2.89	12.17	5.85	17.67	11.65	
410–600 nm	9.62	−3.21	12.44	5.80	17.17	11.23	−0.24
a_{ph}(443)							
MODIS	5.88						
MERIS	−18.64	−10.67					
VIIRS	11.83	12.01	23.45				
OLCI	−8.67	−6.21	7.98	−19.08			
PACE	−21.02	−14.05	−3.60	−26.31	−12.40		
410–670 nm	−41.96	−32.87	−28.56	−53.92	−36.99	−25.70	
410–600 nm	−30.47	−22.87	−15.93	−41.08	−21.52	−15.05	9.31
b_{bp}(443)							
MODIS	9.33						
MERIS	−9.20	−17.12					
VIIRS	6.34	−2.68	12.99				
OLCI	−8.38	−16.15	0.69	−12.02			
PACE	−8.40	−16.89	−0.47	−13.85	−1.56		
410–670 nm	−10.83	−19.50	−2.85	−15.52	−3.59	−2.58	
410–600 nm	−6.13	−15.51	1.35	−11.57	0.30	1.44	3.54

on MERIS, OLCI, PACE, and the two 5 nm suites). This may be explained, in part, as due to eutrophic $R_{rs}(\lambda)$ spectral features being more distinct in the red and less so in the blue. While differences in SAA retrievals almost certainly increase when directly comparing two parameterizations (vs. comparing one SAA to an ensemble of SAAs), this analysis serves to confirm that our default parameterization sufficiently represents a global average to reinforce that, in general, our results apply universally and do not depend on our choice in SAA parameterization.

DISCUSSION

We set out to use a controlled modeling environment to reveal and quantify the magnitude of change in derived IOPs associated with the use of eight different suites of satellite $R_{rs}(\lambda)$. Ignoring such an analysis as CDRs continue to be developed will result in a prolonged inability to distinguish between algorithmic and environmental contributions to trends and anomalies in the IOP time-series. We believe we chose a sufficiently robust SAA (and parameterization) to execute this analysis, as we achieved respectable validation results across varied satellite wavelength suites and demonstrated that variations in algorithm parameterization do not affect the final results. Our results ultimately indicated, however, that different suites of satellite $R_{rs}(\lambda)$ do indeed result in divergent IOP retrievals and that these divergences vary with global geography and water type.

Knowledge of these divergences carries implications and provokes additional questions about remediation strategies and paths forward. A comprehensive evaluation of the implications of our results on trend analyses or CDR development exceeds the scope of this paper. Suffice it to say, however, several of the differences we report will exceed the IOP trends one might wish to reveal, even for sensors with near common wavelengths. These differences will potentially translate into differences in downstream data products (e.g., PSDs, PFTs, and carbon and

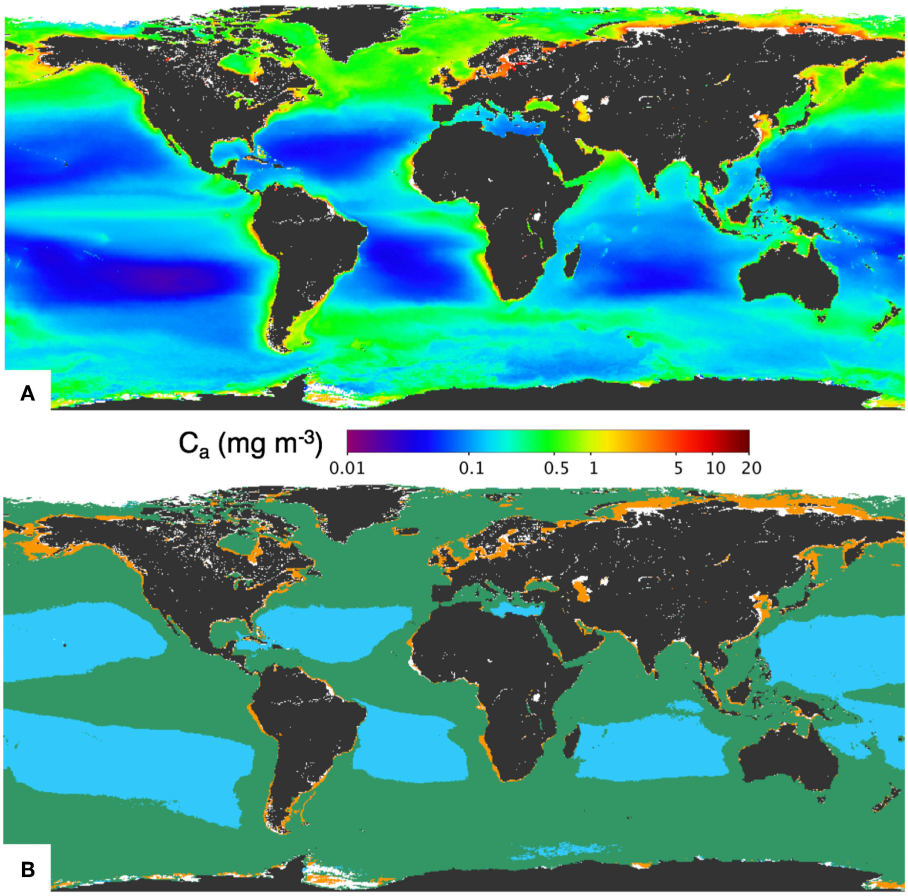

FIGURE 7 | SeaWiFS C_a calculated using mission-long $R_{rs}(\lambda)$ as input into the OCI algorithm (Hu et al., 2012) **(A)** and the global spatial distribution of oligotrophic (cyan), mesotrophic (green), and eutrophic (orange) waters **(B)**. Black and white indicate land and SAA algorithm failure, respectively.

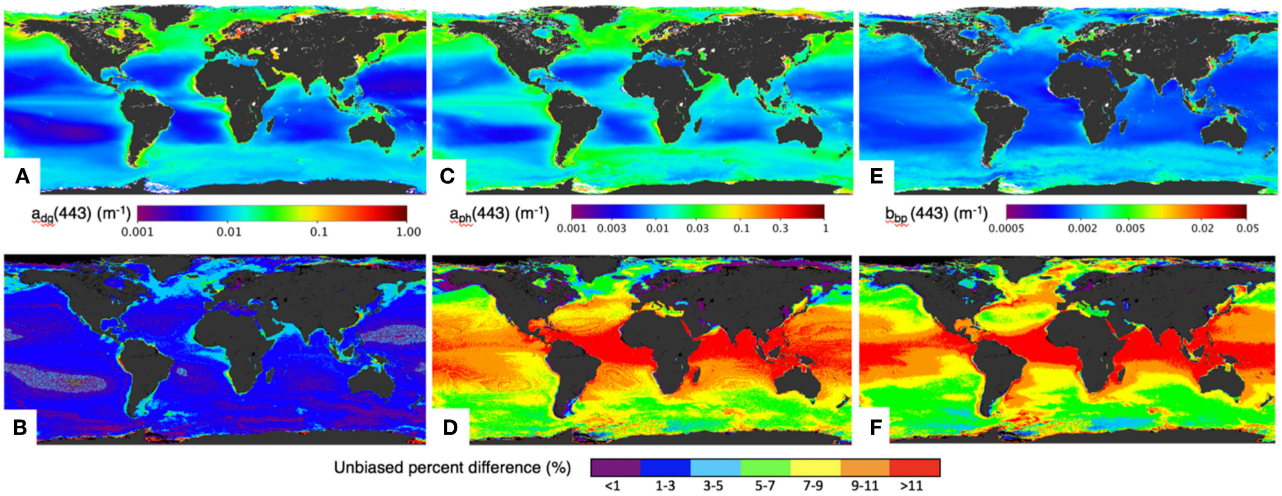

FIGURE 8 | Global IOPs calculated using SeaWiFS mission-long $R_{rs}(\lambda)$ and the UPD between IOP values calculated using SeaWiFS and VIIRS wavelength suites (SeaWIFS = satellite$_1$ and VIIRS = satellite$_2$ in Equation 7). Geophysical values and UPD for $a_{dg}(443)$ shown in **(A,B)**, for $a_{ph}(443)$ in **(C,D)**, and for $b_{bp}(443)$ in **(E,F)**.

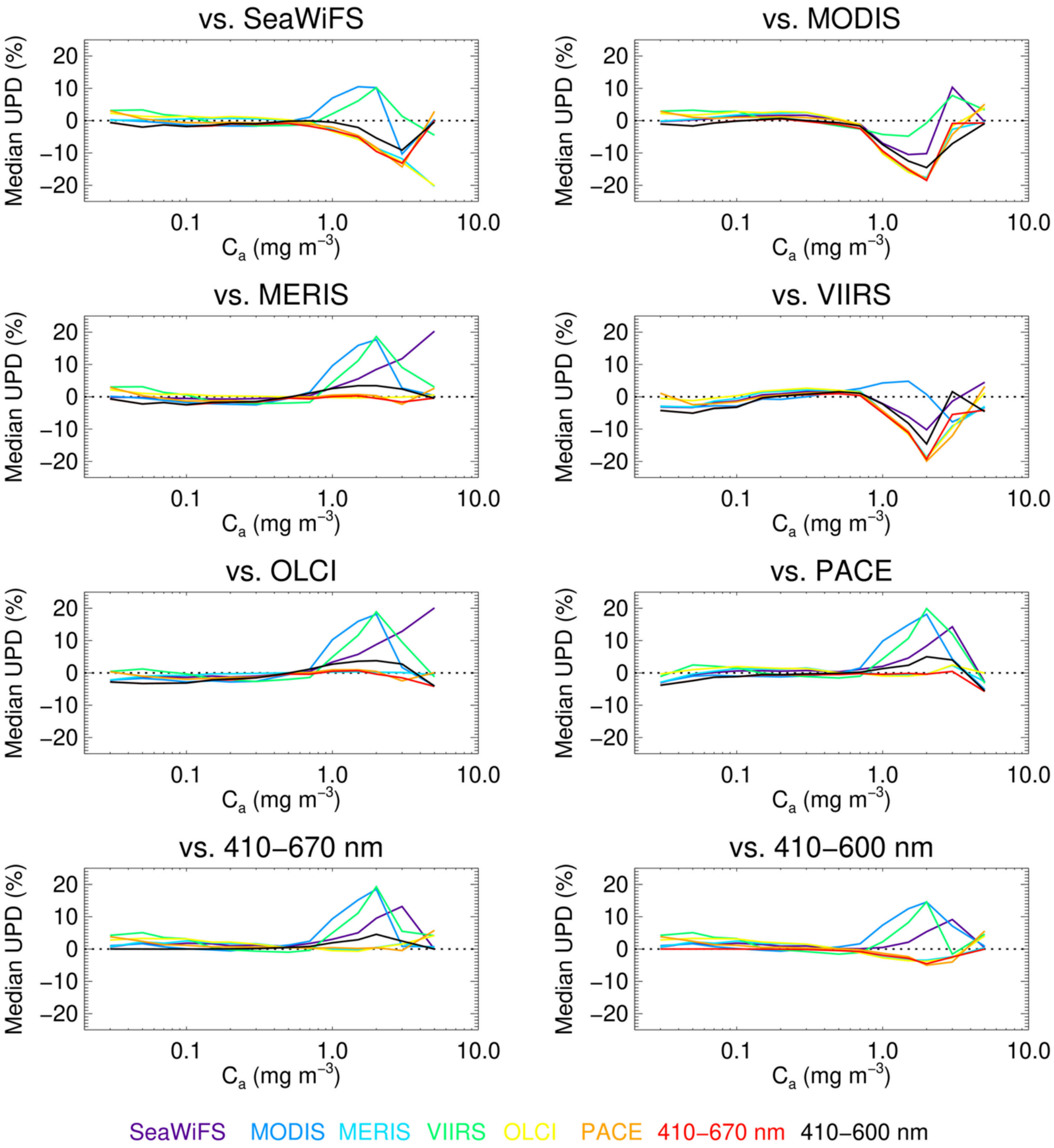

FIGURE 9 | Satellite-to-satellite median UPD for $a(443)$ at each C_a interval as for **Figure 3**, but cumulatively considering all eight SAA parameterizations introduced in section Analyses.

primary production data products) that use IOPs as inputs. We devote the remainder of this paper to brief discussions of what we learned, the limitations of our analyses, other confounding issues, and potential remediation strategies that might merit community attention in the future.

As previously stated, we revealed that differences in wavelengths in input $R_{rs}(\lambda)$ lead to several percent differences in derived IOPs when using SAAs (and spectral matching approaches). We contend that this is critical to understand when developing CDRs across satellite platforms. But, we also acknowledge that, while the realized differences occasionally exceeded several percent, the absolute differences may be small. For example, a 5% window around an absorption value of 0.1 m^{-1} corresponds to ±0.005 m^{-1}, which approaches the detection limit of *in situ* absorption meters. With this in mind, we offer that our results contribute to the knowledge base for CDR development, but should not necessarily be cause for enduring alarm. Perhaps more importantly—at least in the context of identifying needs for future studies—our results also suggest that: (a) validation exercises alone cannot unequivocally identify the differences that will be realized across varied satellite instrument wavelength suites; (b) including 400 nm (in the

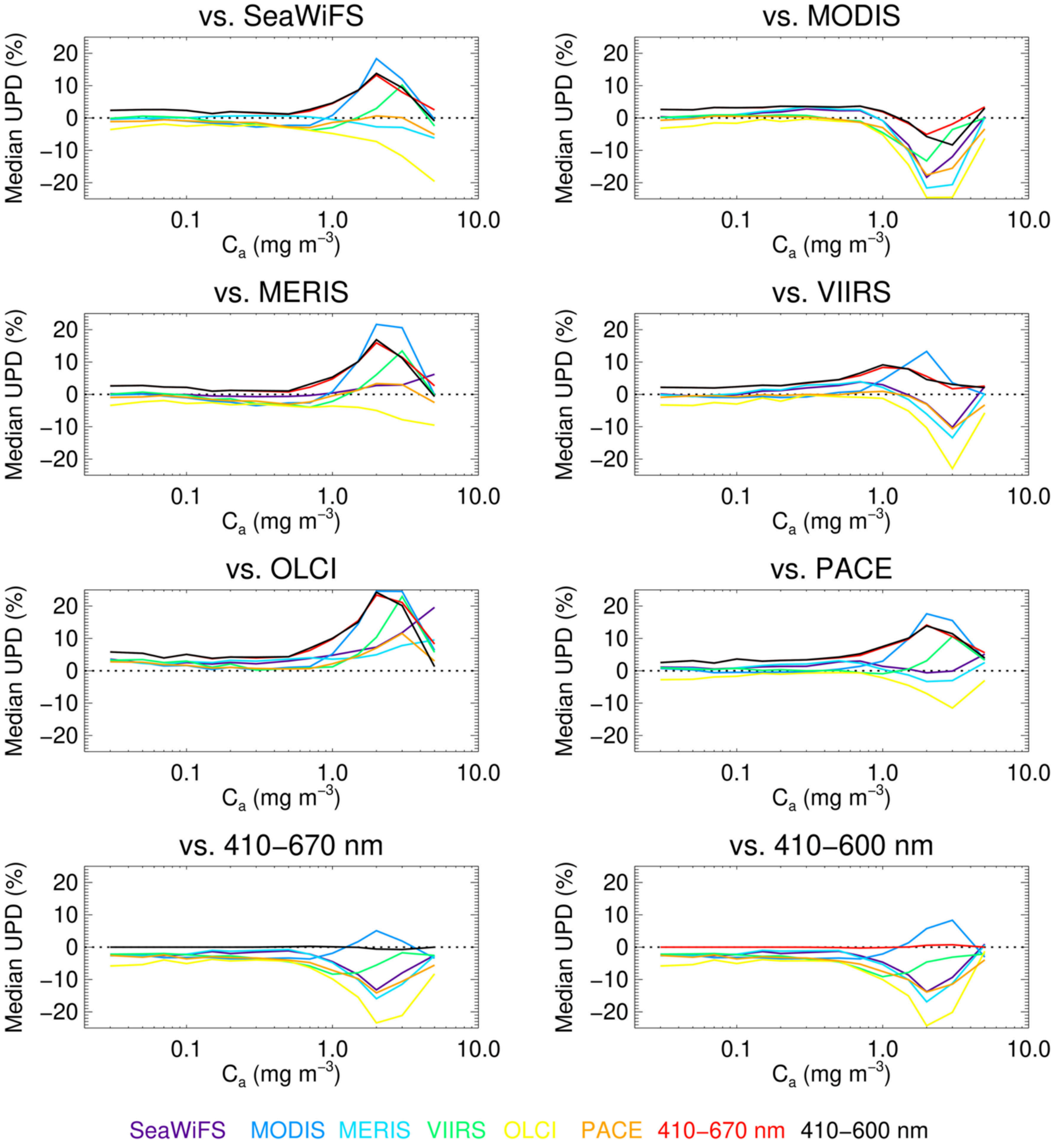

FIGURE 10 | As for **Figure 9**, but for $a_{dg}(443)$.

case of OLCI) influences the derived IOPs and UPDs relative to other wavelength suites; (c) using longer wavelengths (> 600 nm) influences the derived IOPs when there is a red signal (e.g., eutrophic conditions); and (d) including additional spectral information shows potential for improved IOP estimation [e.g., those suites with greater spectral resolution reported the lowest combined biases in derived $a_{ph}(443)$ and $b_{bp}(443)$], but not without revisiting SAA parameterizations and execution [e.g., they often also carried the highest biases in derived $a_{dg}(443)$].

What points (b)–(d) above really indicate is the need for additional consideration of SAA behavior as the community moves toward increased spectral information. This could involve revisiting the use of alternate S_{dg} parameterization when considering additional shorter wavelengths, improved consideration of band-to-band covariances within the inversion strategy, the use of alternate cost functions that exploit additional spectral information (e.g., through weighting or consideration of instrument noise and uncertainties), additional evaluation of the AOP-to-IOP relationship expressed in Equation (2), and the development of schemes that switch between parameterizations under different regions, trophic levels, or bio-optical, hydrological, or environmental conditions, to name

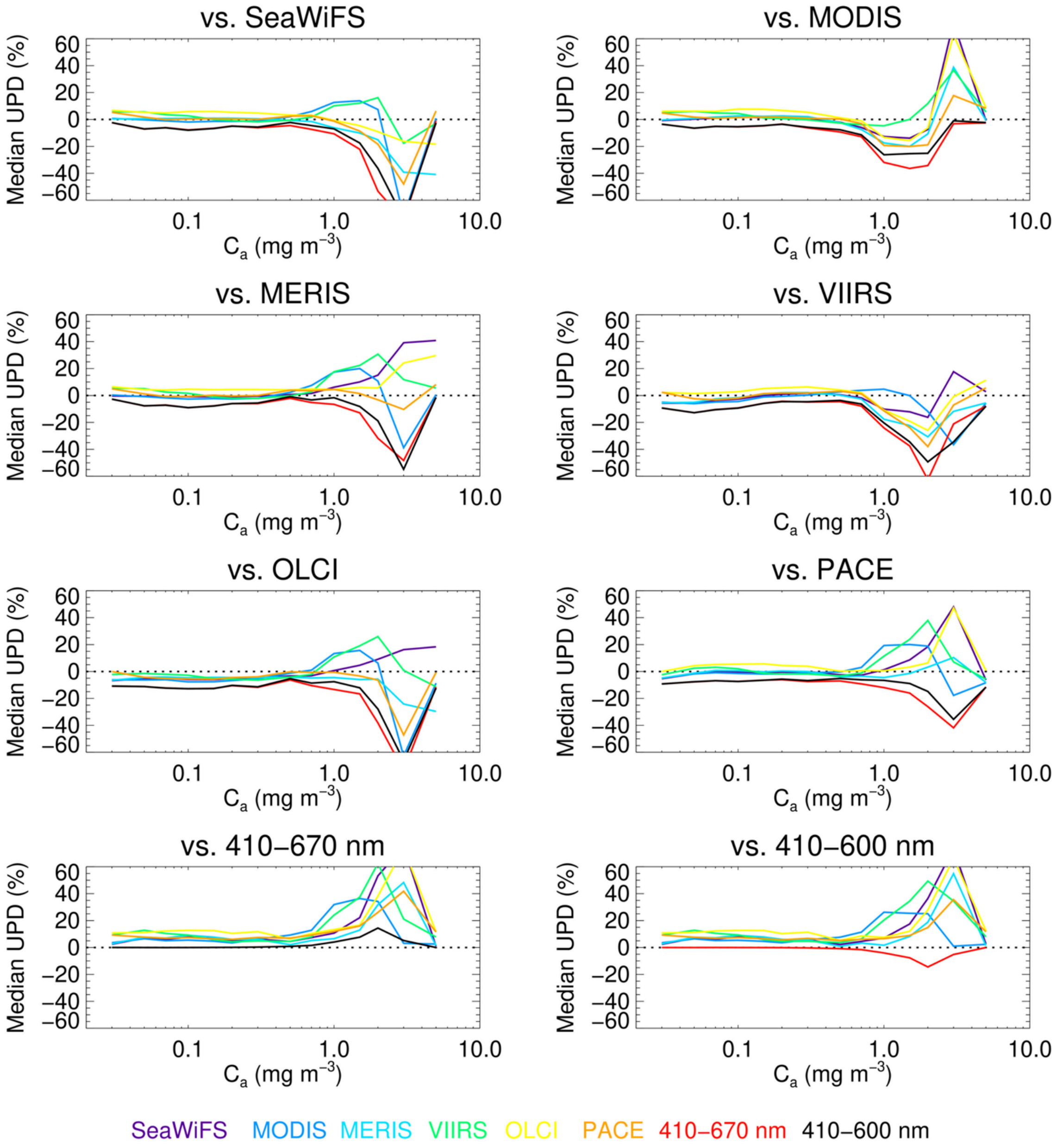

FIGURE 11 | As for **Figure 9**, but for $a_{ph}(443)$.

only a few (Werdell et al., 2018). Within the paradigm of CDR development, the need also exists for robust datasets to explore, train, and evaluate SAAs for application to varied satellite instruments.

We considered two independent datasets, but neither perfectly encapsulate or represent all marine conditions at all times. Despite not being perfectly aligned in composition, the two datasets revealed the existence of differences in derived IOPs that generally matched each other in direction and magnitude. Their differences in composition, however, should be considered while interpreting our results. While the synthesized dataset represents a wide dynamic range of water types, it only represents those conditions that follow its inherent bio-optical assumptions (and, recall, that all bio-optical relationships within this dataset begin with C_a). Note that bio-optical relationships within our SAA differ from those in the synthesized dataset. Furthermore, the cumulative distribution of stations within the synthesized dataset do not numerically represent natural global oligo-, meso-, and eutrophic distributions of seawater. While the mission-long Level-3 SeaWiFS data provided a representation of global distributions of data, they offered long-term averages without explicit consideration of seasonal and geographic variations that

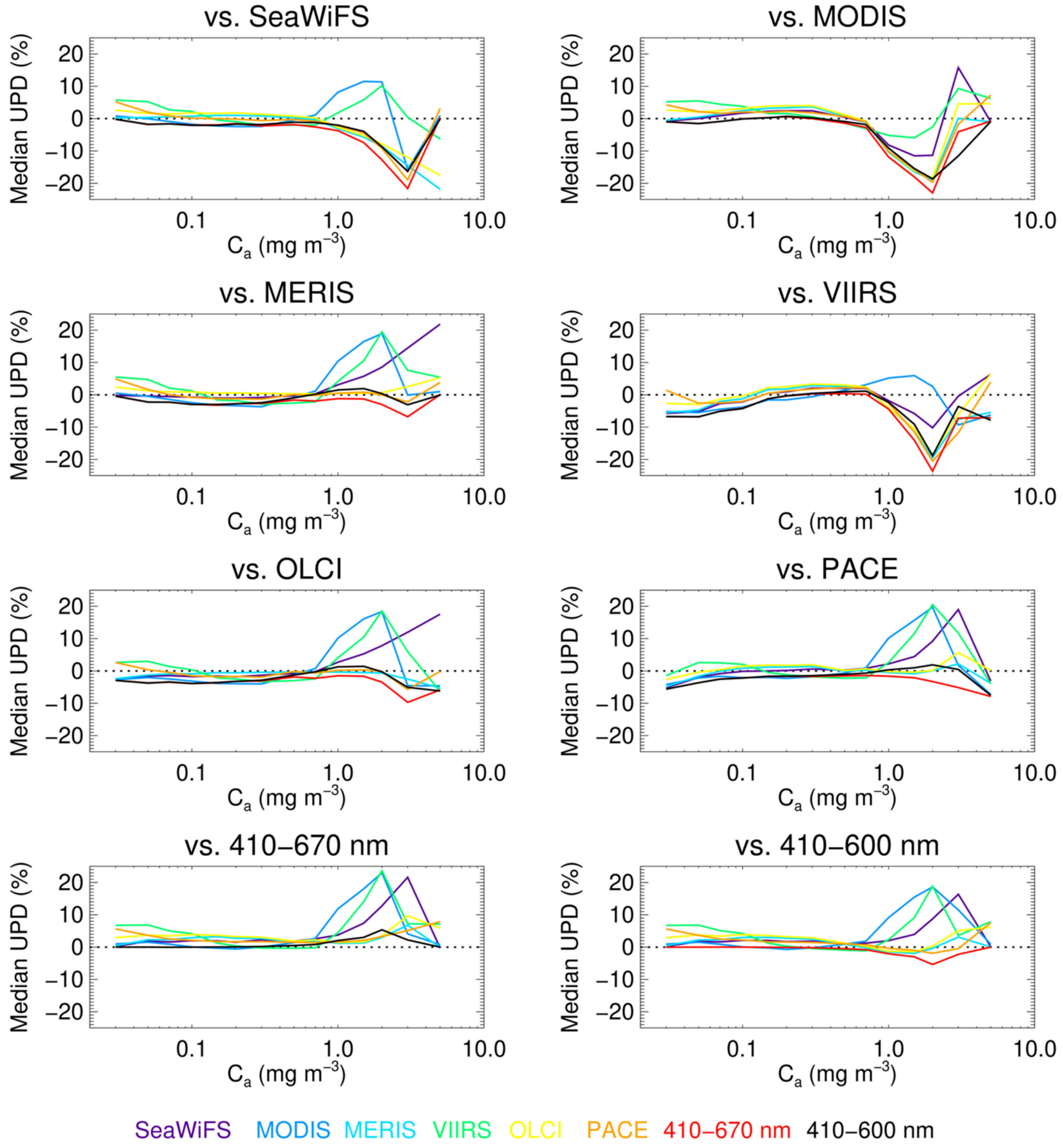

FIGURE 12 | As for **Figure 9**, but for $b_{bp}(443)$.

emerge in time-series analyses. All this said, we believe our two datasets adequately complemented each other and offered a broad dynamic range of conditions for this initial study. They successfully indicated similar differences in IOP retrievals, but future results will likely vary depending on the dataset under consideration.

Our analyses used common and consistent input $R_{rs}(\lambda)$ across all eight wavelength suites, which we well known does not represent real life in multi-mission CDR development (e.g., Franz et al., 2005, 2018). Space agencies invest substantial effort into absolute and temporal radiometric characterization of ocean color satellite instruments that minimizes cross-instrument biases in $R_{rs}(\lambda)$, but differences inevitably remain (Zibordi et al., 2014; Barnes and Hu, 2016; Mélin et al., 2016). Such differences will certainly further confound the compatibility of derived IOPs across satellite instruments, although whether they amplify or dampen our results will vary instrument-to-instrument based on the relative consistencies of the $R_{rs}(\lambda)$. Naturally, relative temporal stability across satellite instruments presents the greatest concern and challenge in long-term CDR development. Other confounding issues include variations in instrument design (e.g., pushbroom vs. whiskbroom and the resulting number of detectors providing science data), differences in pre-launch instrument characterization activities and methods, differences in protocols and data sources for on-orbit instrument calibration, and variations in algorithms applied prior to executing an SAA, all of which contribute in some way to varied instrument-to-instrument uncertainties in $R_{rs}(\lambda)$.

Once again ignoring the latter for the moment, several proposed strategies exist to mitigate the use of differing $R_{rs}(\lambda)$ as input into bio-optical algorithms. The first, and perhaps least satisfying, simply reduces the number of input wavelengths to the lowest common suite (e.g., limiting SAA execution to roughly 412, 443, 490, 547-555-560, and 667-670-665 nm for MODIS-SeaWiFS-MERIS/OLCI for comparison with VIIRS). Werdell et al. (2009) provides a relevant example of doing so in Chesapeake Bay to retrieve C_a using an SAA. Approaches to shift bands, say from $R_{rs}(547)$ to $R_{rs}(555)$, also exist. Several of the bio-optical algorithms under the OBPG purview, for example, require such adjustment (e.g., Stramski et al., 2008; Hu et al., 2012), which they perform using simple linear statistical relationships developed using *in situ* data (Werdell and Bailey, 2005). Melin and Sclep (2015) developed a more sophisticated band-shifting approach that employs bio-optical models to adjust band centers. Their approach uses preliminary estimates of IOPs such that its use within the context of this analyses would ultimately results in an iterative scheme.

Ultimately, none of these remediation strategies assist with moving from multispectral heritage instruments to future hyperspectral instruments (e.g., PACE). While degrading PACE's spectral resolution to mimic heritage instrumentation remains possible, doing so discards the advances of its instrumentation that we ultimately expect to improve SAA performance and IOP estimation in general, such as inclusion of ultraviolet bands. In the end, this may be unavoidable, with multi-decade IOP-based CDRs in the PACE era reduced to the best available approach across heritage instruments. While we expect novel approaches to emerge that include additional ancillary (environmental) information or spectral weighting/balancing that somewhat mitigate differences in input wavelength suites, the promise of the emerging era of satellite spectroscopy is that additional wavelengths will result in superior data products. Intuitively, we therefore expect two parallel paths forward in SAA development: one that continues to push the boundary of what is possible with heritage, existing, and planned multispectral instruments (e.g., VIIRS and OLCI) and one that exploits spectroscopy and contiguous spectral resolution. The challenge to the community will then become tracking and understanding differences between the two paths such that the presumably advanced approaches (through spectroscopy) can inform on the underlying limitations and additional uncertainties associated with the long-term (multispectral) data record.

DATA AVAILABILITY

The synthetic dataset generated for this study can be found on PANGAEA (https://doi.pangaea.de/10.1594/PANGAEA.899407). The satellite imagery can be found on the NASA OceanColor Web site (https://oceancolor.gsfc.nasa.gov).

AUTHOR CONTRIBUTIONS

PW: conceptualization, methodology, and data analysis. LM: synthetic dataset development. PW and LM: original draft, reviewing, editing, and revision.

FUNDING

This research was funded by the NASA Ocean Biology and Biogeochemistry Program via an award under the solicitation *The Science of Terra, Aqua, and Suomi NPP*.

ACKNOWLEDGMENTS

We thank the NASA Ocean Biology Processing Group staff for their advice during the preparation of this manuscript. We also thank our two reviewers for their highly constructive comments and recommendations.

SUPPLEMENTARY MATERIAL

The Supplementary Material for this article can be found online at: https://www.frontiersin.org/articles/10.3389/feart.2019.00054/full#supplementary-material

REFERENCES

Alvain, S., Loisel, H., and Dessailly, D. (2012). Theoretical analysis of ocean color radiances anomalies and implications for phytoplankton groups detection in case 1 waters. *Opt. Express* 20, 1070–1083. doi: 10.1364/OE.20.001070

Babin, M., Morel, A., Fournier-Sicre, V., Fell, F., and Stramski, D. (2003). Light scattering properties of marine particles in coastal and open ocean waters as related to the particle mass concentration. *Limnol. Oceanogr.* 48, 843–859. doi: 10.4319/lo.2003.48.2.0843

Barnes, B. B., and Hu, C. (2016). Dependence of satellite ocean color data products on vie wing angles: a comparison between SeaWiFS, MODIS, and VIIRS. *Remote Sens. Environ.* 175, 120–129. doi: 10.1016/j.rse.2015.12.048

Behrenfeld, M. J., Boss, E., Siegel, D. A., and Shea, D. M. (2005). Carbon-based ocean productivity and phytoplankton physiology from space. *Glob. Biogeochem. Cycles* 19:GB1006. doi: 10.1029/2004GB002299

Bracher, A., Bouman, H. A., Brewin, R. J. W., Bricaud, A., Brotas, V., Ciotti, A. M., et al. (2017). Obtaining phytoplankton diversity from ocean color: a scientific roadmap for future development. *Front. Mar. Sci.* 4:e00055. doi: 10.3389/fmars.2017.00055

Brewin, R. J. W., Sathyendranath, S., Muller, D., Brockmann, C., Deschamps, P.-Y., Devred, E., et al. (2015). The Ocean colour climate change initiative: III. A round-robin comparison on in-water bio-optical algorithms. *Remote Sens. Environ.* 162, 271–294. doi: 10.1016/j.rse.2013.09.016

Bricaud, A., Babin, M., Morel, A., and Claustre, H. (1995). Variability in the chlorophyll-specific absorption coefficients of natural phytoplankton: analysis and parameterization. *J. Geophys. Res.* 100, 13321–13332. doi: 10.1029/95JC00463

Bricaud, A., Morel, A., Babin, M., Allali, K., and Claustre, H. (1998). Variations of light absorption by suspended particles with chlorophyll a concentration in oceanic (case 1) waters: analysis and implications for bio-optical models. *J. Geophys. Res. Oceans* 103, 31033–31044. doi: 10.1029/98JC02712

Dutkiewicz, S., Follows, M. J., and Bragg, J. G. (2009). Modeling the coupling of ocean ecology and biogeochemistry. *Glob. Biogeochem. Cycles* 23:GB4017. doi: 10.1029/2008GB003405

Eplee, R. E., turpie, K. R., Meister, G., Patt, F. S., Franz, B. A., and Bailey, S.W. (2015). On-orbit calibration of the suomi national polar-orbiting parnership visible infrared imaging radiometer suite for ocean color applications. *Appl. Opt.* 54, 1984–2006. doi: 10.1364/AO.54.001984

Franz, B. A., Karakoylu, E. M., Siegel, D. A., and Westberry, T. K. (2018). Global ocean phytoplankton [in "State of the Climate 2017"]. *Bull. Am. Meteorol. Soc.* 99, S94–S96. doi: 10.1175/2018BAMSStateoftheClimate.1

Franz, B. A., Werdell, P. J., Meister, G., Kwiatkowska, E., Thomas, D., Werdell, J. P., et al. (2005). The continuity of ocean color measurements from SeaWiFS to MODIS. *Proc. SPIE* 58820W. doi: 10.1117/12.620069

Gilerson, A., Ibrahim, A., Foster, R., Carrizo, C., El-Habshi, A., and Ahmed, S. (2014). Retrieval of water optical properties using polarization of light underwater: case I and II waters, *Proc. SPIE* 92400R. doi: 10.1017/12.2067963

Gordon, H. R., Brown, O. B., Evans, R. H., Brown, J. W., Smith, R. C., Baker, K. S., et al. (1988). A Semianalytic Radiance Model of Ocean Color. *J. Geophys. Res.* 93, 10909–10924. doi: 10.1029/JD093iD09p10909

Hirata, T., Hardman-Mountford, N. J., Brewin, R. J. W., Aiken, J., Barlow, R., Suzuki, K., et al. (2011). Synoptic relationships between surface Chlorophyll-a and diagnostic pigments specific to phytoplankton functional types. *Biogeosciences* 8, 311–327. doi: 10.5194/bg-8-311-2011

Hu, C. M., Lee, Z., and Franz, B. (2012). Chlorophyll a algorithms for oligotrophic oceans: a novel approach based on three-band reflectance difference. *J. Geophys. Res. Oceans* 117:C01011. doi: 10.1029/2011jc007395

Ibrahim, A., Gilerson, A., Harmel, T., Tonizzo, A., Chowdhary, J., and Ahmed, S. (2012). The relationship between upwelling underwater polarization and attenuation/absorption ratio. *Opt. Express* 20, 25662–25680. doi: 10.1364/OE.20.025662

IOCCG (2006). *Remote Sensing of Inherent Optical Properties: Fundamentals, Tests of Algorithms, and Applications*. Dartmouth, NS: IOCCG.

IOCCG (2009). *Remote Sensing in Fisheries and Aquaculture*. Dartmouth, NS: IOCCG.

IOCCG (2014). *Phytoplankton Functional Types from Space*. Dartmouth, NS: IOCCG.

IOCCG (2018). *Earth Observations in Support of Global Water Quality Monitoring*. Dartmouth, NS: IOCCG.

Lee, Z. P., Arnone, R., Hu, C. M., Werdell, P. J., and Lubac, B. (2010). Uncertainties of optical parameters and their propagations in an analytical ocean color inversion algorithm. *Appl. Opt.* 49, 369–381. doi: 10.1364/AO.49.000369

Lee, Z. P., Carder, K., Arnone, R., and He, M. X. (2007). Determination of primary spectral bands for remote sensing of aquatic environments. *Sensors* 7, 3428–3441. doi: 10.3390/s7123428

Lee, Z. P., Carder, K. L., and Arnone, R. A. (2002). Deriving inherent optical properties from water color: a multiband quasi-analytical algorithm for optically deep waters. *Appl. Opt.* 41, 5755–5772. doi: 10.1364/AO.41.005755

Lee, Z. P., Carder, K. L., and Du, K. P. (2004). Effects of molecular and particle scatterings on the model parameter for remote-sensing reflectance. *Appl. Opt.* 43, 4957–4964. doi: 10.1364/AO.43.004957

Lee, Z. P., Carder, K. L., Hawes, S. K., Steward, R. G., Peacock, T. G., and Davis, C. O. (1994). Model for the interpretation of hyperspectral remote-sensing reflectance. *Appl. Opt.* 33, 5721–5732. doi: 10.1364/AO.33.005721

Lee, Z. P., Du, K. P., Voss, K. J., Zibordi, G., Lubac, B., Arnone, R., and Weidemann, A. (2011). An inherent-optical-property-centered approach to correct the angular effects in water-leaving radiance. *Appl. Opt.* 50, 3155–3167. doi: 10.1364/AO.50.003155

Loisel, H., Stramski, D., Dessailly, D., Jamet, C., Li, L., and Reynolds, R. A. (2018). An inverse model for estimating the optical absorption and backscattering coefficients of seawater from remote-sensing reflectance over a broad range of oceanic and coastal marine environments. *J. Geophys. Res.* 123, 2141–2171. doi: 10.1002/2017JC013632

Maritorena, S., d'Andon, O. H. F., Mangin, A., and Siegel, D. A. (2010). Merged satellite ocean color data products using a bio-optical model: characteristics, benefits and issues. *Remote Sens. Environ.* 114, 1791–1804. doi: 10.1016/j.rse.2010.04.002

McKinna, L. I. W., Werdell, P. J., and Proctor, C. W. (2016). Implementation of an analytical Raman scattering correction for satellite ocean-color processing. *Opt. Express* 24, A1123–1137. doi: 10.1364/OE.24.0A1123

Meister, G., and Franz, B. A. (2014). Corrections to the MODIS Aqua calibration derived from MODIS Aqua ocean color products. *IEEE Trans. Geosci. Remote Sens.* 52, 6534–6541. doi: 10.1109/TGRS.2013.2297233

Meister, G., Franz, B. A., Kwiatkowska, E. J., and McClain, C. R. (2012). Corrections to the calibration of MODIS Aqua Ocean color bands derived from SeaWiFS data. *IEEE Trans. Geosci. Remote Sens.* 50, 310–319. doi: 10.1109/TGRS.2011.2160552

Melin, F., and Sclep, G. (2015). Band shifting for ocean color multi-spectral reflectance data. *Opt. Express* 23, 2262–2279. doi: 10.1364/OE.23.002262

Mélin, F., Sclep, G., Jackson, T., and Sathyendranath, S. (2016). Uncertainty estimates of remote sensing reflectance derived from comparison of ocean color satellite data sets. *Remote Sens. Environ.* 177, 107–124. doi: 10.1016/j.rse.2016.02.014

Mobley, C. D., and Sundman, L. K. (2008). *Hydrolight 5 Ecolight 5*. Washington, DC: Sequoia Scientific Inc.

Mobley, C. D., Werdell, J., Franz, B., Ahmad, Z., and Bailey, S. (2016). *Atmospheric Correction for Satellite Ocean Color Radiometry*. NASA Technical Memorandum, NASA/TM-2016-217551, 85.

Mouw, C. B., Hardman-Mountford, N. J., Alvain, S., Bracher, A., Brewin, R. J. W., Bricaud, A., et al. (2017). A consumer's guide to satellite remote sensing of multiple phytoplankton groups in the global ocean. *Front. Mar. Sci.* 4:41. doi: 10.3389/fmars.2017.00041

NRC (2004). *Climate Data Records From Environmental Satellites: Interim Report*. Washington, DC: National Academies Press.

NRC (2011). *Assessing Requirements for Sustained Ocean Color Research and Operations*. Washington, DC: National Academies Press.

O'Reilly, J. E., Maritorena, S., Mitchell, B. G., Siegel, D. A., Carder, K. L., Garver, S. A., et al. (1998). Ocean color chlorophyll algorithms for SeaWiFS. *J. Geophys. Res.* 103, 24937–24953. doi: 10.1029/98JC02160

PACE Science Definition Team (2018). *Pre-Aerosols, Clouds, and Ocean Ecosystem (PACE) Mission Science Definition Team Report*. PACE Technical Report Series, NASA/TM-2018-219027/Vol. 2, 316.

Patt, F. S., Barnes, R. A., Eplee, R. E. Jr, Franz, B. A., Robinson, W. D., et al. (2003). "Algorithm updates for the fourth seawifs data reprocessing," in *Goddard Space Flight Center*, eds S. B. Hooker and E. R. Firestone (Greenbelt, MD: National Aeronautics and Space Administration), 74.

Pope, R. M., and Fry, E. S. (1997). Absorption spectrum (380-700 nm) of pure water. II. Integrating cavity measurements. *Appl. Opt.* 36, 8710–8723. doi: 10.1364/AO.36.008710

Roesler, C., Perry, M. J., and Carder, K. L. (1989). Modeling *In-situ* phytoplankton absorption from total absorption-spectra in productive inland marine waters. *Limnol. Oceanogr.* 34, 1510–1523. doi: 10.4319/lo.1989.34.8.1510

Rousseaux, C. S., and Gregg, W. W. (2015). Recent decadal trends in global phytoplankton composition. *Glob. Biogeochem. Cycles* 29, 1674–1688. doi: 10.1002/2015GB005139

Sathyendranath, S., Brewin, R. J. W., Jackson, T., Melin, F., and Platt, T. (2017). Ocean-colour products for climate-change studies: what are their ideal characteristics? *Remote Sens. Environ.* 203, 125–138. doi: 10.1016/j.rse.2017.04.017

Siegel, D. A., Behrenfeld, M., Maritorena, S., McClain, C. R., Antoine, D., Bailey, S. W., et al. (2013). Regional to global assessments of phytoplankton dynamics from the SeaWiFS mission. *Remote Sens. Environ.* 135, 77–91. doi: 10.1016/j.rse.2013.03.025

Siegel, D. A., Buesseler, K. O., Doney, S. C., Sailley, S. F., Behrenfeld, M. J., and Boyd, P. W. (2014). Global assessment of ocean carbon export by combining satellite observations and food-web models. *Glob. Biogeochem. Cycles* 28, 181–196. doi: 10.1002/2013GB004743

Stramski, D., Boss, E., Bogucki, D. J., and Voss, K. J. (2004). The role of seawater constituents in light backscattering in the ocean. *Progr. Oceanogr.* 61, 27–56. doi: 10.1016/j.pocean.2004.07.001

Stramski, D., Reynolds, R. A., Babin, M., Kaczmarek, S., Lewis, M. R., Rottgers, R., et al. (2008). Relationships between the surface concentration of particulate organic carbon and optical properties in the eastern South Pacific and eastern Atlantic Oceans. *Biogeosciences* 5, 171–201. doi: 10.5194/bg-5-171-2008

Twardowski, M. S., Boss, E., Sullivan, J. M., and Donaghay, P. L. (2004). Modeling the spectral shape of absorption by chromophoric dissolved organic matter. *Mar. Chem.* 89, 69–88. doi: 10.1016/j.marchem.2004.02.008

Vandermuelen, R. A., Mannino, A., Neeley, A. R., Werdell, P. J., and Arnone, R. (2017). Determining the optimal spectral sampling frequency and uncertainty thresholds for hyperspectral remote sensing of ocean color. *Opt. Express* 25, A785–A797. doi: 10.1364/OE.25.00A785

Wang, M., Franz, B. A., Barnes, R. A., and McClain, C. R. (2001). Effects of spectral bandpass on SeaWiFS-retrieved near-surface optical properties of the ocean. *Appl. Opt.* 40, 343–348. doi: 10.1364/AO.40.000343

Werdell, P. J., and Bailey, S. W. (2005). An improved *in-situ* bio-optical data set for ocean color algorithm development and satellite data product validation. *Remote Sens. Environ.* 98, 122–140. doi: 10.1016/j.rse.2005.07.001

Werdell, P. J., Bailey, S. W., Franz, B. A., Harding, L. W. Jr, Feldman, G. C., and McClain, C. R. (2009). Regional and seasonal variability of chlorophyll-a in Chesapeake Bay as observed by SeaWiFS and MODIS-Aqua. *Remote Sens. Environ.* 113, 1319–1330. doi: 10.1016/j.rse.2009.02.012

Werdell, P. J., Franz, B. A., Bailey, S. W., Feldman, G. C., Boss, E., Brando, V. E., et al. (2013a). Generalized ocean color inversion model for retrieving marine inherent optical properties. *Appl. Opt.* 52, 2019–2037. doi: 10.1364/AO.52.002019

Werdell, P. J., Franz, B. A., Lefler, J. T., Robinson, W. D., and Boss, E. (2013b). Retrieving marine inherent optical properties from satellites using temperature and salinity-dependent backscattering by seawater. *Opt. Express* 21, 32611–32622. doi: 10.1364/OE.21.032611

Werdell, P. J., McKinna, L. I. W., Boss, E., Ackleson, S. G., Craig, S. E., Gregg, W. W., et al. (2018). An overview of approaches and challenges for retrieving marine inherent optical properties from ocean color remote sensing. *Progr. Oceanogr.* 160, 186–212. doi: 10.1016/j.pocean.2018.01.001

Werdell, P. J., Roesler, C. S., and Goes, J. I. (2014). Discrimination of phytoplankton functional groups using an ocean reflectance inversion model. *Appl. Opt.* 53, 4833–4849. doi: 10.1364/AO.53.004833

Westberry, T. K., Boss, E., and Lee, Z. (2013). Influence of Raman scattering on ocean color inversion models. *Appl. Opt.* 52, 5552–5561. doi: 10.1364/AO.52.005552

Wolanin, A., Soppa, M. A., and Bracher, A. (2016). Investigation of spectral band requirements for improving retrievals of phytoplankton functional types. *Remote Sens.* 8:871. doi: 10.3390/rs8100871

Zhang, X. D., Hu, L. B., and He, M. X. (2009). Scattering by pure seawater: effect of salinity. *Opt. Express* 17, 5698–5710. doi: 10.1364/OE.17.005698

Zheng, G. M., and Stramski, D. (2013). A model based on stacked-constraints approach for partitioning the light absorption coefficient of seawater into phytoplankton and non-phytoplankton components. *J. Geophys. Res.* 118, 2155–2174. doi: 10.1002/jgrc.20115

Zibordi, G., Donlon, C., and Parr, A. (2014). *Optical Radiometry for Ocean Climate Measurements*. Academic Press.

Conflict of Interest Statement: LM was employed by company Go2Q Pty Ltd.

The remaining author declares that the research was conducted in the absence of any commercial or financial relationships that could be construed as a potential conflict of interest.

frontiers in Earth Science

ORIGINAL RESEARCH
published: 31 May 2019
doi: 10.3389/feart.2019.00116

Multiband Atmospheric Correction Algorithm for Ocean Color Retrievals

Amir Ibrahim[1,2]*, Bryan A. Franz[1], Ziauddin Ahmad[1,3] and Sean W. Bailey[1]

[1] Ocean Ecology Laboratory, Goddard Space Flight Center, National Aeronautics and Space Administration, Greenbelt, MD, United States, [2] Science Systems and Applications Inc., Lanham, MD, United States, [3] Science Application International Corp., McLean, VA, United States

National Aeronautics and Space Administration's (NASA's) current atmospheric correction (AC) algorithm for ocean color utilizes two bands and their ratio in the near infrared (NIR) to estimate aerosol reflectance and aerosol type. The algorithm then extrapolates the spectral dependence of aerosol reflectance to the visible wavelengths based on modeled spectral dependence of the identified aerosol type. Future advanced ocean color sensors, such as the Ocean Color Instrument (OCI) that will be carried on the Plankton, Aerosol, Cloud, and ocean Ecosystem (PACE) satellite, will be capable of measuring the hyperspectral radiance from 340 to 890 nm at 5-nm spectral resolution and at seven discrete short-wave infrared (SWIR) channels: 940, 1,038, 1,250, 1,378, 1,615, 2,130, and 2,260 nm. To optimally employ this unprecedented instrument capability, we propose an improved AC algorithm that utilizes all atmospheric-window channels in the NIR to SWIR spectral range to reduce the uncertainty in the AC process. A theoretical uncertainty analysis of this, namely, multiband AC (MBAC), indicates that the algorithm can reduce the uncertainty in remote sensing reflectance (R_{rs}) retrievals of the ocean caused by sensor random noise. Furthermore, in optically complex waters, where the NIR signal is affected by contributions from highly reflective turbid waters, the MBAC algorithm can be adaptively weighted to the strongly absorbing SWIR channels to enable improved ocean color retrievals in coastal waters. We provide here a description of the algorithm and demonstrate the improved performance in ocean color retrievals, relative to the current NASA standard AC algorithm, through comparison with field measurements and assessment of propagated uncertainties in applying the MBAC algorithm to MODIS and simulated PACE OCI data.

Keywords: ocean color, atmospheric correction, PACE, aerosol, turbid waters

Edited by:
David Antoine,
Curtin University, Australia

Reviewed by:
Quinten Vanhellemont,
Royal Belgian Institute of Natural Sciences, Belgium
Thomas Schroeder,
CSIRO Oceans and Atmosphere (O&A), Australia

***Correspondence:**
Amir Ibrahim
amir.ibrahim@nasa.gov

Specialty section:
This article was submitted to Atmospheric Science, a section of the journal Frontiers in Earth Science

Received: *05 December 2018*
Accepted: *06 May 2019*
Published: *31 May 2019*

Citation:
Ibrahim A, Franz BA, Ahmad Z and Bailey SW (2019) Multiband Atmospheric Correction Algorithm for Ocean Color Retrievals. Front. Earth Sci. 7:116. doi: 10.3389/feart.2019.00116

INTRODUCTION

Ocean color retrieval algorithms require an atmospheric correction (AC) process to separate the radiometric contribution of the atmosphere from the ocean, given the radiance measured at the top of atmosphere (TOA). The National Aeronautics and Space Administration (NASA) standard approach to the AC is a two-step process: the atmosphere and surface contributions are first removed using minimal assumptions about the water optical properties (Gordon and Wang, 1994; Franz et al., 2007; Ahmad et al., 2010; Bailey et al., 2010; Mobley et al., 2016), and the resulting spectral water-leaving radiances are then used to infer water column optical properties and constituent concentrations (e.g., Gordon et al., 1988; O'Reilly et al., 1998; Morel and Maritorena, 2001; Hu et al., 2012; Werdell et al., 2013). AC involves finding a solution to a set of deterministic models, enabling the removal of atmospheric path and surface effects from the TOA signal. The primary challenge is determining the contribution of aerosols (a primary source of uncertainty in the AC) to the atmospheric path radiance, which is highly variable and, thus, must be inferred from observation. This approach takes advantage of the strong absorption of water in the Near Infrared to Shortwave Infrared (NIR-SWIR) (longward of 700 nm) to separate the atmospheric and oceanic signals (Gordon and Wang, 1994; Wang et al., 2009; Ahmad et al., 2010). This AC process aims for retrievals that meet ocean color requirements (i.e., 5% uncertainty on water-leaving radiance at 443 nm) over the open ocean and in the absence of strongly absorbing aerosols (i.e., dust, organic, and black carbon) (Gordon and Wang, 1994; Mobley et al., 2016). In coastal and optically complex waters, the water-leaving radiance retrievals often fail in meeting that requirement due to non-negligible water-leaving radiance in the NIR bands used for the AC, with water-leaving radiance often underestimated or even negative in value. Iterative AC techniques have been developed to model the ocean reflectance in the NIR, which mitigate the problem effectively in moderately turbid and productive waters (Siegel et al., 2000; Bailey et al., 2010). Although this iterative approach has been used in the NASA standard processing (Bailey et al., 2010), it has been shown that such methods can fail in highly turbid waters (Wang et al., 2012; Goyens et al., 2013). Other methods, based on the SWIR bands, have been shown effective in separating the aerosol signal from the TOA signal over highly turbid waters, due to the increased water absorption at these longer wavelengths (Shi and Wang, 2007; Wang and Shi, 2007, 2012; Jiang and Wang, 2014; Vanhellemont and Ruddick, 2015; Pahlevan et al., 2017). The SWIR-based methods has limitations, however, for two reasons: (1) the signal-to-noise ratio (SNR) on SWIR bands is low for current ocean color sensors [i.e., MODIS (Moderate Resolution Imaging Spectroradiometer) and VIIRS (Visible Infrared Imaging Radiometer Suite)] and (2) the approach generally requires discrete switching from the NIR AC bands to SWIR bands over coastal waters, thus producing spatial inconsistency or artifacts in the retrievals. For example, Shi and Wang (2007) utilized 1,240 and 2,130 nm for MODIS to perform the AC using the 2-band Gordon and Wang (1994) AC approach. The algorithm switches from NIR to SWIR based on a turbidity index threshold (Shi and Wang, 2007; Wang and Shi, 2007; Wang et al., 2009). Werdell et al. (2010) have shown the effectiveness of the 2-band SWIR AC approach, but with increased uncertainties in the ocean color retrievals due to low SWIR SNR of MODIS-Aqua. Still, other studies have shown failure in the NIR-SWIR switching method due to the NIR sensor saturation at moderate to high turbidity (i.e., $>35\ \mathrm{g\ m^{-3}}$) where the NIR bands on MODIS-Aqua saturate at TOA radiances >2.8–$3.45\ \mathrm{mW\ cm^{-2}\ \mu m^{-1}\ sr^{-1}}$ for 748 nm and >1.9–$2.45\ \mathrm{mW\ cm^{-2}\ \mu m^{-1}\ sr^{-1}}$ for 869 nm and improper cloud masking (Aurin et al., 2013). A recent study by Liu et al. (2019) indicated that the turbidity index, responsible for the switching, varies with the aerosol size distribution, optical depth, and observing geometry, thus rendering the effectiveness of the NIR-SWIR switching questionable.

One way for reducing the uncertainty in ocean color retrievals using the SWIR bands is to use more spectral information to reduce sensor random noise impact produced by low SNR. Gao et al. (2000, 2007) used a spectral matching technique to fit the measured TOA signal with an aerosol lookup table (LUT) for bands >860 nm and demonstrated improved retrieval of ocean reflectance in turbid and shallow waters from MODIS-Aqua and Airborne Visible/Infrared Imaging Spectrometer (AVIRIS). They also showed a sensitivity study indicating that SWIR bands are sensitive to variations in aerosol size distributions including some fine-mode dominant types, although the sensitivity is weaker than that of the visible–NIR spectral regime. Other methods that utilize more spectral information for the AC, such as machine learning techniques (i.e., neural network) and coupled atmosphere–ocean simultaneous retrievals, have shown promising results (Gordon et al., 1997; Chomko and Gordon, 1998, 2001; Chomko et al., 2003; Stamnes et al., 2003; Jamet et al., 2005; Brajard et al., 2006; Schroeder et al., 2007; Spurr et al., 2007; Kuchinke et al., 2009; Steinmetz et al., 2011; He et al., 2012; Frouin and Gross-Colzy, 2016; Fan et al., 2017; Gossn et al., 2019). Some of these algorithms were more successful over the open ocean, while others were specifically tuned for coastal cases, and they often require the use of a bio-optical ocean model with inherent assumptions about the marine optical properties.

Cloud detection and masking in turbid waters can also be challenging. Extremely turbid waters are masked as clouds when a simple NIR threshold technique is used, as is the case for the standard NASA processing. Wang and Shi (2006) proposed an improved cloud masking in coastal regions using SWIR channels. Other cloud masking methods that utilize more spectral bands have shown improved discrimination between clouds and water in highly turbid conditions (Nordkvist et al., 2009).

NASA is planning to launch the Plankton, Aerosol, Cloud, and ocean Ecosystem (PACE) satellite in 2022. The PACE satellite will host a state-of-the-art hyperspectral ocean color sensor (the Ocean Color Instrument, OCI). OCI will measure the hyperspectral radiance at the TOA from 340 to 890 nm at 5-nm spectral resolution and at seven discrete channels in the SWIR: 940, 1,038, 1,250, 1,378, 1,615, 2,130, and 2,260 nm, of which two are water vapor bands (940 and 1,378 nm) and five are window bands (i.e., no major gas absorption features). In fact, OCI will host the first instrument with a set of SWIR bands primarily designed for the ocean AC. The SWIR bands will have sufficient radiometric performance (i.e., high SNR with low systematic bias) to enable their use for AC over open oceans as well as coastal water conditions (Ibrahim and McKinna, 2018). The analysis throughout the manuscript assumed the following SNRs for OCI (420 at 1,038 nm, 280 at 1,250 nm, 220 at 1,615 nm, and 76 at 2,260 nm, excluding 2,130 nm as cloud band), for the typical ocean scene, which are based on current best estimates since the design is currently subject to slight changes. The AC algorithm proposed here attempts to exploit the unprecedented capabilities of OCI to improve the quality of ocean color retrievals from the PACE mission.

MULTIBAND AC ALGORITHM

The heritage aerosol correction algorithm utilizes two bands either in the NIR or SWIR spectral range by calculating a band ratio of the Rayleigh (+ surface) and gas corrected reflectance, namely, epsilon, as follows:

$$\varepsilon = \frac{\rho_a(\lambda_s)}{\rho_a(\lambda_l)}, \tag{1}$$

where λ_s and λ_l correspond to the short and long wavelength either in the NIR or SWIR range (e.g., for MODIS, $\lambda_s = 748\ nm$ and $\lambda_l = 869\ nm$) and $\rho_a(\lambda)$ is the aerosol reflectance defined as:

$$\rho_a(\lambda) = \frac{\pi \times [L_a(\lambda) + L_{ra}(\lambda)]}{F_0 \times \mu_0}, \tag{2}$$

F_0 is the extraterrestrial solar irradiance and μ_0 is the cosine of the solar zenith angle. Since the aerosol radiance term is a strong function of the viewing/illumination geometry, the LUT is generated as a function of the solar and sensor zenith angle and relative azimuth angle. NASA's current approach to estimate the aerosol reflectance term is by finding the best match of the observed single scattering epsilon value to the model single scattering epsilon value. Since the LUT is calculated for a set of deterministic aerosol models based on Ahmad et al. (2010), the algorithm interpolates the single scattering aerosol reflectance from the LUT to match the observed reflectance. Accounting for multiple scattering interactions between the aerosol and molecules, is crucial when extrapolating the reflectance to shorter wavelengths. Given the aerosol type estimated from the single scattering epsilon in the longer wavelengths, the multiple scattered aerosol radiance is then estimated through a polynomial relationship derived through vector radiative transfer simulations (Gordon and Wang, 1994), and this multi-scattering estimate of aerosol path reflectance is then used in the aerosol correction.

The process of deriving single scattering epsilon and then converting it into multiple scattering radiance is unnecessary since currently computationally feasible multiple scattering tables can be easily generated and irreversible since there is no 1–1 relationship between multiple and single scattering when different aerosol types are mixed. Ahmad and Franz (2018) proposed an alternative approach, where the aerosol model and optical properties determination is done in multiple scattering space. It is based on the Ahmad et al. (2010) aerosol models, for which the TOA reflectance due to aerosols can be described by three parameters: relative humidity (RH), Angstrom exponent (α), or the analogous fine-mode fraction (f), and optical thickness of the aerosols (τ) in the model atmosphere. Briefly, for any relative humidity suite, the dependence of multiple-scattering epsilon $\varepsilon(\lambda) = \frac{\rho(\lambda)}{\rho(869)}$ on $\rho(869)$ would look like the x–y plot shown in **Figure 1**. Here, ρ refers to TOA aerosol reflectance and the subscript numbers refer to wavelength bands.

In **Figure 1**, the aerosol optical depth (τ) varies along the "horizontal" axis, and the Angstrom exponent (α) and extinction coefficients (ξ) vary along the "vertical" axis. This parametrization of the LUT allows one to readily calculate the aerosol reflectance at any grid point. One advantage of this approach over the current NASA standard algorithm is that it provides a mathematical framework for the aerosol reflectance determination that facilitates the application of standard error propagation techniques.

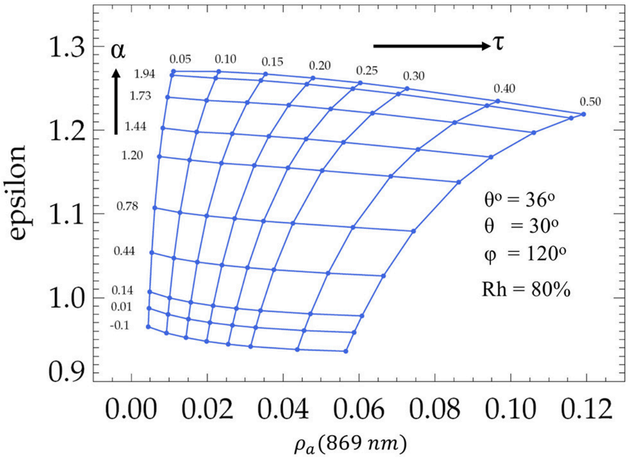

FIGURE 1 | A graph of multiple-scattering epsilon ($\varepsilon_{748} = \rho_{748}/\rho_{869}$) vs. ρ_{869} for solar zenith, $\theta_0 = 36°$, view zenith, $\theta = 30°$, relative azimuth angle, $\varphi = 120°$, and relative humidity (RH) = 80% from MODIS LUT (Ahmad and Franz, 2018).

The multiband AC (MBAC) algorithm is based on this multi-scattering epsilon approach by Ahmad and Franz (2018), but it utilizes all the spectral window channels (i.e., not affected by strongly absorbing gases such as water vapor, oxygen, and carbon dioxide) available at which the water absorption is high to separate the aerosol signal (i.e., black-pixel). MBAC determines the best aerosol model by fitting the magnitude and the spectrum of the aerosol reflectance at all window NIR to SWIR bands (e.g., excluding 940- and 1,378-nm channels for OCI). The aerosol reflectance at each wavelength is stored in a LUT as a polynomial function of the geometry (not shown in Equation 3 for simplicity), aerosol optical depth, relative humidity, and fine-mode fraction:

$$\rho_a(\lambda, \tau_a, RH, f) = a(\lambda, RH, f) + b(\lambda, RH, f) \times \tau_a + c(\lambda, RH, f) \times {\tau_a}^2, \tag{3}$$

where a, b, and c are the fitting coefficients stored in the aerosol LUT. For any spectral band in the NIR-SWIR range at which the water-leaving radiance can be assumed negligible, the atmospheric path radiance can be derived from the observed TOA radiance. Assuming a proper correction for absorbing gases (discussed in the section Correction for Absorbing Gases) and Rayleigh scattering has been done, aerosol reflectance can be determined and the aerosol optical depth can then be estimated by solving the quadratic equation, as

$$\tau_a\left(\lambda = 869\ nm,\ RH,\ f\right) = \frac{-b\left(\lambda_{869}, RH,f\right) + \sqrt{b\left(\lambda_{869}, RH,f\right)^2 - 4 \times c\left(\lambda_{869}, RH,f\right) \times \left(a\left(\lambda_{869}, RH,f\right) - \rho_a^{obs}(\lambda_{869})\right)}}{2 \times c\left(\lambda_{869}, RH,f\right)}, \quad (4)$$

For consistency with the system vicarious calibration procedure, which is performed relative to one wavelength in the NIR (e.g., 869 nm for MODIS), the optical depth is estimated at that wavelength.

For an observed aerosol reflectance, the optical depth can be calculated for each aerosol model set (RH,f) as shown in **Figure 2**.

The algorithm then calculates the aerosol optical depth and reflectance spectrally for all aerosol models as:

$$\tau_a\left(\lambda, RH,f\right) = \frac{\xi\left(\lambda, RH,f\right)}{\xi\left(\lambda_{869}, RH,f\right)} \times \tau_a\left(\lambda_{869}, RH,f\right), \quad (5)$$

where $\xi\left(\lambda, RH,f\right)$ is the aerosol extinction coefficient for each aerosol model. Then, the spectral aerosol reflectance for each aerosol model set (RH,f) is recalculated from the polynomial equation.

The MBAC algorithm fits the aerosol reflectance in the NIR and SWIR for all models calculated in the previous step. However, since multiple solutions can exist, especially at low optical depth over the open ocean, we constrain the model selection to consider only those models with the two relative humidities bracketing the observed RH (as obtained from ancillary meteorological data). The maximum likelihood method is used to find the closest solution by minimizing the cost function:

$$\chi^2\left(RH,f\right) = \frac{1}{DOF} \times \sum_{\lambda=\lambda_s}^{\lambda_l} \frac{\left[\rho_{obs}\left(\lambda\right) - \rho_a\left(\lambda, RH,f\right)\right]^2}{\sigma^2(\lambda)} \times SW(\lambda), \quad (6)$$

where $\rho_{obs}\left(\lambda\right)$ is the observed aerosol reflectance and $\rho_a\left(\lambda, RH,f\right)$ is the aerosol reflectance from the LUT for each relative humidity and fine-mode fraction. Note that the geometry is omitted from Equation 6 for simplicity; however, it depends on the solar and viewing zenith and relative azimuth angles. *DOF* is the degree of freedom of the observed signal. Assuming each band in the NIR and SWIR is an independent observations, *DOF* is the number of bands from the shortest band in the NIR, λ_s, to the longest band in the SWIR, λ_l. $\sigma^2(\lambda)$ is the squared measurement uncertainty (variance assuming gaussian random noise) of the sensor, as determined from the sensor-specific noise model for a given radiance level.

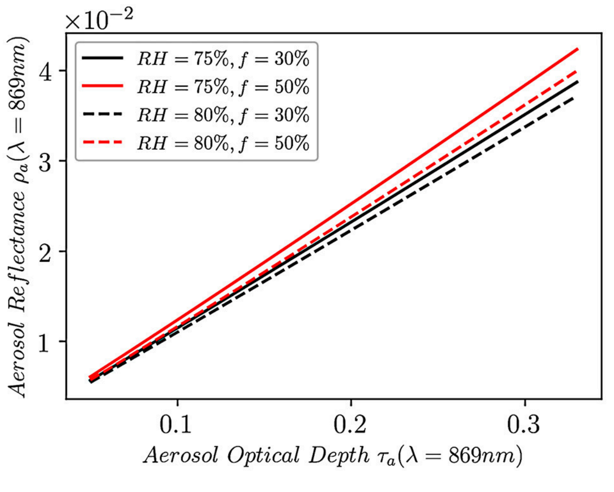

FIGURE 2 | The aerosol reflectance as a function of the aerosol optical depth at 869 nm for aerosol models with relative humidity RH = 75% and 80% and for fine-mode fraction *f* = 30% and 50%.

$SW(\lambda)$ is a spectral weight (SW) that is set to change the relative weighting in the cost function for the spectral bands in different environmental conditions. For example, setting $SW\left(\lambda\right)$ to 1 in all bands will minimize the cost function to fit the aerosol reflectance to all NIR/SWIR bands. The method will then be skewed to bands with better radiometric performance (i.e., the NIR). And when the weight is set 0 for NIR bands, the cost function will be skewed toward longer wavelengths in the SWIR, where the ocean signal is still negligible. In this implementation, we vary the SW, adaptively, as a function of the number of iterations in the iterative scheme of Bailey et al. (2010), which is currently used in the standard NASA AC algorithm to estimate any non-negligible water-leaving reflectance contribution in the NIR bands. The Bailey algorithm works by modeling the ocean reflectance in the NIR based on a bio-optical model for productive waters. The algorithm is initiated by a first guess of the NIR ocean reflectance [i.e., $R_{\mathrm{rs}}(\mathrm{NIR}) = 0$], where the AC is performed, and then the $R_{\mathrm{rs}}(\mathrm{NIR})$ is estimated based on a bio-optical model that is propagated to the TOA to perform another AC and this process is repeated until the changes in the retrieved ocean reflectance is <2%. Similarly, the MBAC algorithm performs the AC at every iteration while bio-optical model parameters and the SW are tuned until the convergence criterion of 2% change in ocean reflectance is met. Thus, more iterations indicate more difficulty in fitting the bio-optical model possibly due to a higher optical complexity in turbid waters. The SW is then calculated as $SW\left(\lambda\right) = \exp(-\tilde{\beta}\left(\lambda\right) \times \frac{[i-2]}{[i_{\max}-2]})$, where i is the number of iterations in the current step and $i_{\max}$ is the maximum number of iterations set in the Bailey algorithm (operationally $i_{\max} = 11$). Note that the actual number of iterations is reduced by 2 since the algorithm always performs at least two iterations in the AC: the first one with Rayleigh correction only (to estimate glint), and the second one for the aerosol correction. $\tilde{\beta}\left(\lambda\right)$ is an empirically estimated value that determines the slope of the exponential function for a given sensor by processing various scenes to inspect for image artifacts. We adopted an exponential function for the SW to ensure a quick transition toward the SWIR bands once non-negligible NIR ocean signal is detected since the SWIR bands will have an effect only when the weight on the NIR bands is largely reduced. This is because measurement uncertainty on the NIR is nearly an order of magnitude lower than the SWIR bands (at least for MODIS and VIIRS sensors). Higher value of the slope $\tilde{\beta}(\lambda) > 10$ leads to a quick switching to the SWIR bands in coastal waters, including for low/moderate turbidity, while smaller values <5 give more dependence on the NIR AC in the same water conditions. For MODISA, $\tilde{\beta}(\lambda) = 7$ for NIR bands and 0 for SWIR bands, as this provides for a smooth transition from open ocean AC, where we want an equal SW on all bands to a smaller weight on the NIR in more turbid waters. In the open ocean, NIR bands will dominate the cost function; thus, the AC will be similar to the standard approach, while in turbid waters, the AC will depend more on the SWIR bands. The slope $\tilde{\beta}(\lambda)$ will primarily impact the number of iterations required in the convergence; thus, it is not critically important to have an exact optimal value. What really matters is the bio-optical model used in the R_{rs} convergence in the first few iterations where the AC is affected by the modeled NIR reflectance. After three or four iterations, the bio-optical model becomes irrelevant since the cost function will be mostly skewed toward the SWIR bands. With every iteration, a new cost function will be calculated with new aerosol models, and the NIR-SWIR ocean radiance will be estimated until the convergence criteria in Bailey et al. (2010) is met. If the bio-optical model does not converge in sediment-dominant waters, the SW in those cases will skew all of the cost function toward the SWIR bands, thus improving the AC.

At each iteration of the AC, the following steps are performed.

Assuming a smooth unimodal shape to the cost function $\chi^2(RH, f)$, the minimum of the function at which the best solution exists can be calculated as:

$$\nabla \chi^2 (RH, f) = 0 \tag{7}$$

For the sake of simplicity in the operational code implementation, the 2-d partial derivate can be converted into 1-d minimization problem by finding the minimum of the cost function for a given RH set (i.e., RH_1) from National Centers for Environmental Prediction (NCEP). However, ideally, the cost function minimization could be done for optical depth, fine-mode fraction, and relative humidity [i.e., $\nabla \chi^2 (\tau, RH, f) = 0$]. The cost function will be minimized for a set of fine-mode fractions of aerosols. The smallest two χ^2 values in the set will be:

$$\chi^2{}_{\min 1}(f) = min : \{\chi^2 (f)\} \tag{8}$$

$$\chi^2{}_{\min 2}(f) = min : \{\chi^2 (f) \sim (\chi^2_{\min 1} \in \boldsymbol{\chi}^2)\} \tag{9}$$

The observed aerosol reflectance typically falls in-between the two closest aerosol reflectance, $\rho_a (\lambda, RH_1, f_{\min 1})$ and $\rho_a (\lambda, RH_1, f_{\min 2})$ from the model set, and are chosen based on the $\chi^2{}_{\min 1}(f)$ and $\chi^2{}_{\min 2}(f)$, similar to the current operational algorithm. Since the fine-mode fractions in the table are discrete values with a relatively coarse step, an interpolation or a smoothing scheme of the aerosol reflectance is necessary. One way of doing this is to weight all of the aerosol models within the set for all fine-mode fractions with the χ^2.

$$\rho_a (\lambda, RH_1, f_{mix}) = \frac{\sum_{n=1}^{\max} 1/\chi^2{}_n \times \rho_a (\lambda, RH_1, f_n)}{\sum_{n=1}^{\max} 1/\chi^2{}_n}, \tag{10}$$

where n is the number of models to be mixed such that n starts from minimum χ^2 and ends with the maximum χ^2. However, there is no strong justification to mix all models since a mixture of all the models is not what happens in the atmosphere. A more physical description is to find the most immediate models around the observations, of which $\chi^2{}_{\min 1}$ and $\chi^2{}_{\min 2}$ can be used as a weight to the aerosol reflectance, where n is 2.

This process is repeated for the second set of RH in the case that the ancillary RH falls between two values in the aerosol LUT to estimate $\rho_a (\lambda, RH_2, f_{mix})$. Finally, a linear interpolation of the two estimated aerosol reflectance is calculated as follows:

$$\begin{aligned} \rho_a (\lambda, RH_{obs}, f_{mix}) = {} & (1 - w_{RH}) \times \rho_a (\lambda, RH_1, f_{mix}) \\ & + w_{RH} \times \rho_a (\lambda, RH_2, f_{mix}) \end{aligned} \tag{11}$$

The final $\rho_a (\lambda, RH_{obs}, f_{mix})$ should fit through the observed aerosol reflectance in the NIR and SWIR channels, while the extrapolated reflectance to the visible channels based on the model mixtures are used for the aerosol correction.

To demonstrate how the fitting of the spectral information improves the determination of the aerosol spectral dependence, we show in **Figure 3** an example of two retrievals of the aerosol reflectance for a 50% fine-mode fraction case and coarse-mode dominant aerosol case, 10% fine-mode fraction, at 77.5% RH, using the 2-band and the 6-band MBAC algorithms. The analysis is done by propagating an assumed ocean reflectance for Chlor-a = 0.03 mg m^{-3}, from The International Ocean-Color Coordinating Group (IOCCG) report 10 for MODIS bands, to the TOA and adding the Rayleigh (+ glint) and the aerosol reflectance at one geometry (solar zenith $\theta_0 = 25^\circ$, view zenith, $\theta = 26^\circ$, relative azimuth angle, $\varphi = 90^\circ$) (IOCCG, 2010). We assume an optical depth of 0.2 at 869 nm for the two aerosol cases. The summation of all these signals at TOA is the total radiance (reflectance), of which we add sensor random + systematic noise (as described in the section Error Assessment). This would simulate the expected measurement uncertainty for these specific observations. The Rayleigh (+ glint) reflectance is then removed from the total signal, and the resultant signal is the noised observed TOA reflectance (blue curve), which is the summation of the water and aerosol reflectance at TOA needed for the aerosol correction algorithms. We also show the true (input) aerosol reflectance that we aim to retrieve, shown as the black curve. The red and green curves show the retrieved aerosol reflectance from the observed (noised) reflectance, for the 2-band standard AC and the 6-band MBAC algorithm, respectively.

Since the 2-band algorithm aims to match the spectral dependence of the aerosol as a two-band ratio in the NIR, extrapolating that information to the visible (and SWIR) will depend on the radiometric quality of these two NIR bands and the linear mixing of the aerosol types in the LUT necessary for the visible correction. As can be seen from **Figure 3**, the spectral dependence of the retrieved aerosol reflectance using the 2-band algorithm (red curve) is similar to the observed reflectance (blue curve) within the NIR range, which is expected. However, that does not necessarily retrieve the correct reflectance in the visible and SWIR, of which the retrieval departs from the input reference reflectance (black curve) in both fine-mode fraction cases. On the

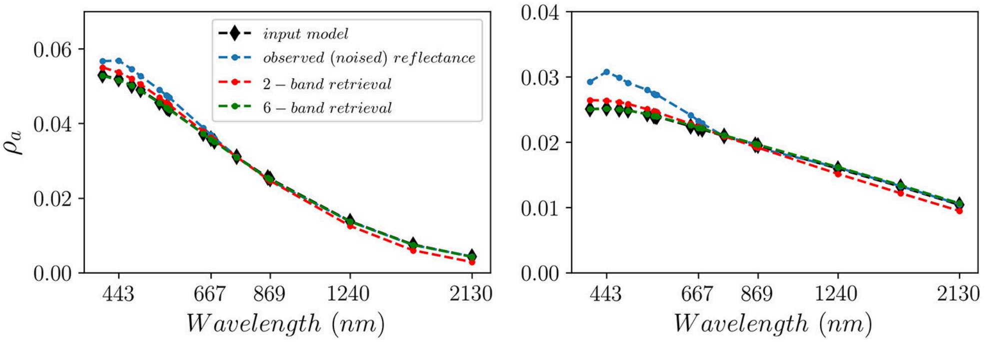

FIGURE 3 | Example to demonstrate the aerosol reflectance retrievals for MODISA using the 2-band (red curve) and 6-band (green curve) algorithms. The input model reflectance (black curve) is before adding noise; meanwhile, the observed reflectance (blue curve) is the noised reflectance after removing the Rayleigh + glint reflectance (i.e., the observed reflectance is the aerosol + water signal). The left panel is for aerosol with 50% fine-mode fraction and the right panel is for 10% fine-mode fraction, and in both cases for 0.2 optical depth at 869 nm. Solar zenith $\theta_0 = 25°$, view zenith, $\theta = 26°$, relative azimuth angle, $\varphi = 90°$.

other hand, the 6-band algorithm fits the spectral information for the whole NIR-SWIR range and thus is less affected by the sensor noise as more spectral information improves the chance to fit the right model. This is also demonstrated as the 6-band algorithm retrievals (green curve) overlap with the input reference model reflectance (black curve) throughout the whole spectrum. This demonstration, however, is qualitative; thus, a more thorough analysis is shown in the section Error Assessment, including the method to add noise to the reflectance.

CORRECTION FOR ABSORBING GASES

Ocean color bands are designed to avoid detection in spectral regions contaminated by strongly absorbing gases such as water vapor, oxygen, methane, and carbon dioxide. However, due to the imperfect spectral response of the detectors (i.e., broad bandwidth and out-of-band response), the measured TOA radiance is modulated by strongly absorbing gases. AC requires a correction for strongly absorbing gases as well as broadly absorbing gases, such as ozone and nitrogen dioxide that mostly absorb in the visible. The current NASA algorithm uses the method of Gordon (1995) that was implemented for SeaWiFS and then extended to all ocean color sensors. The method corrects for strongly absorbing gases, primarily for water vapor, by correcting the epsilon ratio using an empirical polynomial function for a given column gas (water vapor) concentration and air mass. To avoid this step in our proposed AC algorithm, we generate a LUT of transmittances of all strongly absorbing gases that include oxygen, water vapor, methane, and carbon dioxide using HITRAN 2012 LBL absorption database (Rothman et al., 2013; Ibrahim et al., 2018). The water vapor LUT is a function of column water vapor following the ATREM method of Gao et al. (2000). The other gases are corrected based on ancillary or climatology column concentrations, while the transmittance is adjusted for air mass per pixel. MODIS and VIIRS sensors have strong out-of-band effects from absorbing gases in the SWIR range; thus, the LUT correction method allows for a proper correction to utilize all window SWIR bands (i.e., excluding water vapor bands) in the MBAC algorithm.

ERROR ASSESSMENT

Algorithm

The aerosol LUT in the MBAC algorithm is pre-computed at discretized optical properties of the aerosols; thus, the interpolation step between different fine-mode fractions and relative humidity increases the uncertainty in the retrieval of the remote sensing reflectance. To assess the algorithm error, we introduce a set of aerosol optical properties that are not part of the discretized LUT. We do so by simulating the aerosol reflectance set for an RH of 77.5%, which falls between the 75% and 80% RH in the operational LUT. The aerosol properties and reflectance are then calculated using the model set of Ahmad et al. (2010) (i.e., 10 fine-mode fractions), but with an RH of 77.5%. To define the uncertainty in the AC, we estimate the root mean squared error (RMSE) in $\Delta\rho_w$ for the normalized water-leaving radiance. We do so by assuming a reference ocean reflectance from IOCCG report 10 for case I clear waters with chlorophyll concentration, Chlor-a, 0.03 mg m^{-3} (IOCCG, 2010). That reference reflectance is then propagated to the TOA assuming different aerosol types and optical thicknesses for different geometries to perform the uncertainty analysis. The aerosol models are based on Ahmad et al. (2010) operational LUTs. **Figure 4** shows the polar plot of $\Delta\rho_w$ at 443 nm for all view geometries in the LUT, where 0° relative azimuth is specular reflection plane, and for three solar angles, 10, 20, 30, and 60°.

The aerosol models encompass all aerosol types, as defined in Ahmad et al. (2010), from fine-mode to coarse-mode dominant cases with equal weights, and the aerosol reflectances were calculated for optical depth ranging from 0.05 to 0.35 at 869 nm. The uncertainty level in the retrievals is generally smaller than the scale midpoint at 0.0015 and increases with increasing solar angle from 10 to 60°. There are some hotspots in the geometry plot that indicated a higher uncertainty in the retrievals. These regions could be due to the decreased sensitivity of the aerosol models, where the algorithm finds it difficult to determine the type due to the ambiguity in the phase function of aerosols at certain scattering angles, or geometry midpoint interpolation errors, but further analysis is needed. The uncertainty in the aerosol reflectance at 443 nm,

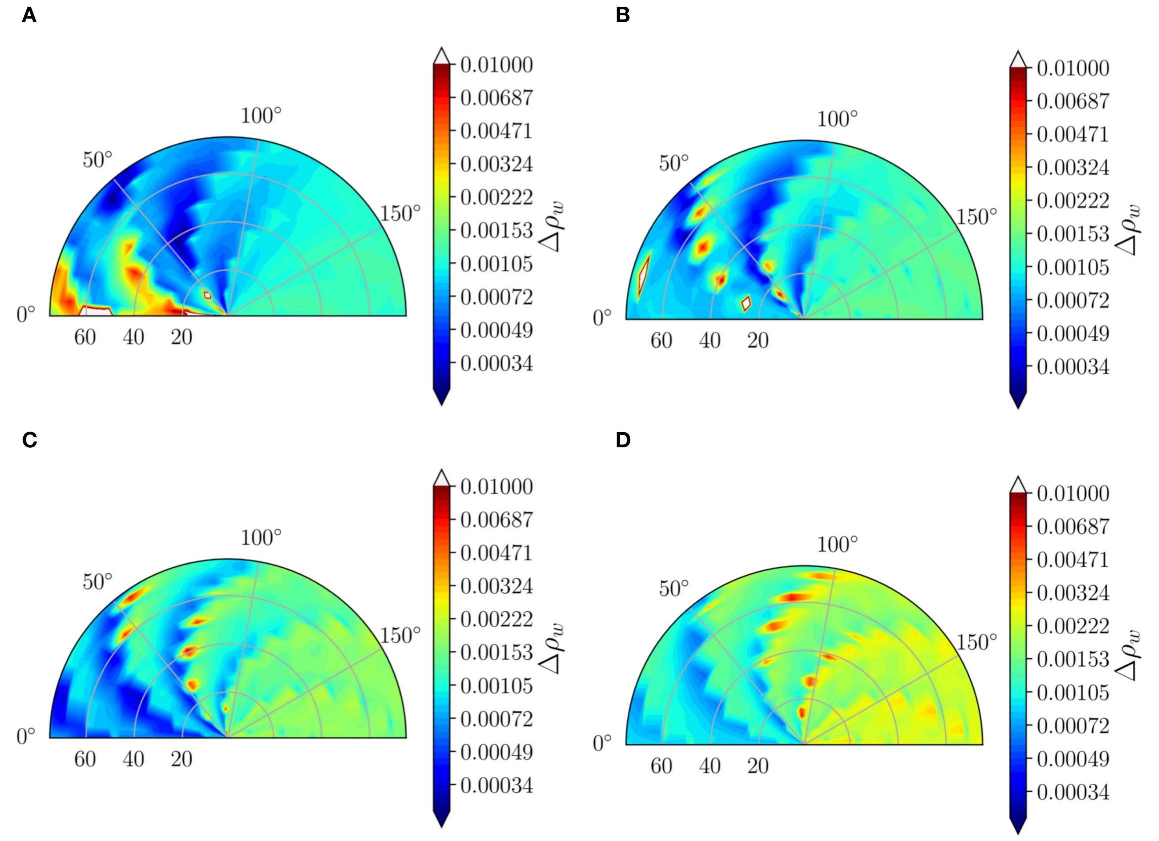

FIGURE 4 | (A–D) are the algorithm uncertainty in water reflectance, $\Delta\rho_{\mathbf{w}}$, at 443 nm as a function of the viewing geometry for solar zenith angles of 10, 20, 30, and 60°, respectively. The simulations are done for all aerosol models with relative humidity RH = 77.5% at optical depth at 869 nm from 0.05 to 0.35, and the retrieval is done using models with RH = 75% and 80%.

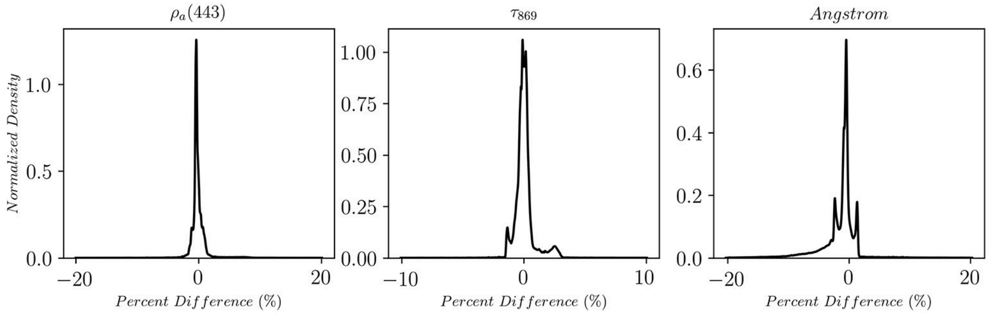

FIGURE 5 | The normalized density histogram of the percentage difference for the aerosol reflectance and optical depth retrievals at 443 and 869 nm, respectively, and the Angstrom coefficient for all cases of different aerosol types, optical depths, and geometries.

optical depth retrievals at 869 nm, and the Angstrom coefficient expressed as a percent difference are shown in **Figure 5** for all simulated cases of 1,037,400 (i.e., 12 solar angle × 35 sensor angle × 19 azimuth angle × 10 models × 13 optical depth).

The mean bias in the aerosol reflectance at 443 nm is −0.04% and the standard deviation is 3.5%, while optical depth retrieval is 0.05% with a standard deviation of 1.35%, and the Angstrom coefficient retrieval shows a mean bias of −1.9% with a standard deviation of 15%. The small bias and standard deviation indicate that the algorithm can well-retrieve the optical depth; however, there is a more significant uncertainty in the Angstrom coefficient retrievals with tendency to retrieve coarser aerosol types than the input data. This could be an inherent error due to the definition of the Angstrom coefficient that assumes a power law relationship of the aerosol spectral dependence from 443 to

869 nm. Since we are including all cases of aerosol types with equal representation, the uncertainty is overestimated. In the cases at the extreme ends of the aerosol's LUT, there could be large errors in the retrievals because of the necessity to extrapolate to models that are not in the table. However, these extreme ends of the LUT are intentionally added to reduce that necessity for the extrapolation since these aerosol conditions are rarely observed based on AERONET data (Ahmad et al., 2010). Finally, note that the uncertainty increases at the highest two values of fine-mode fractions (i.e., $f = 0.95$ and $f = 0.80$). Since most of the aerosol absorption is in the fine-mode aerosols, these two models are more absorbing than others; thus, the difference in the single scattering albedo is >0.05 in the blue wavelengths, which can induce more than 3% errors in the aerosol reflectance at TOA by linear mixing (Abdou et al., 1997; Ahmad et al., 2010). Additionally, NIR and SWIR bands used in the cost function are less sensitive to fine-mode aerosols; thus, fine-mode dominant cases will be erroneously observed as coarser aerosols, which is the case for the operational algorithm. The only method to reduce that uncertainty is by inferring the aerosol properties at shorter wavelengths while minimizing the impact of the marine reflectance. For example, observations in the UV could improve the MBAC algorithm when non-absorbing fine-mode aerosols are present over coastal (absorbing) waters where the UV signal is negligible. OCI will measure in the UV, which will be a subject of future work.

Random Noise

The uncertainty in the TOA radiance measurements due to sensor random noise will impact the retrieval uncertainty of the ocean reflectance through influence on the AC process. The uncertainty propagation of the sensor noise is simulated here using the Monte Carlo method, where the sensor noise at a given SNR value is generated for 300 iterations for all aerosol model sets mentioned above. We performed the sensitivity analysis using the NIR 2-band AC (standard approach) and a 6-band MBAC (i.e., for MODIS 748, 859, 869, 1,240, 1,640, and 2,130 nm). The theoretical analysis for MODIS-Aqua is done for the six bands; however, we drop 1,640 nm in our real retrievals because of defective detectors at that band. The noise model here is based on the MODIS model with the noise-equivalent radiance of:

$$NE\Delta L\left(\lambda\right) = \left[C_0\left(\lambda\right) + C_1\left(\lambda\right) \times L_t\left(\lambda\right)\right] \times S\left(\lambda\right), \quad (12)$$

where $C_0(\lambda)$ and $C_1(\lambda)$ are linear fit coefficients of the noise model from Xiong et al. (2010), and $S(\lambda)$ is the spectral-dependent spatial weight to bring all bands to a common spatial resolution since MODIS land bands have finer spatial resolution than ocean bands. We also performed an analysis at PACE-OCI radiometric performance levels, where the MODIS noise model was scaled to OCI noise levels such that the noise equivalent radiance, $NE\Delta L$, response to the dynamic range is consistent for both instruments.

The random noise for each iteration is generated as follows:

$$\sigma = \frac{NE\Delta L(\lambda)}{L_t(\lambda)}, \quad (13)$$

and the Gaussian random noise is generated as:

$$L_{noise} = \mathcal{N}\left(0, \sigma\right), \quad (14)$$

The result of the analysis shown in **Figures 6A,B** indicates that the geometrically averaged uncertainty in reflectance, $\Delta\rho_w$, is closer to 0.0016 levels for the 6-band MBAC algorithm, while it is slightly higher near 0.0021 levels for the 2-band AC for MODIS-Aqua noise levels. The improvement in the uncertainty between the two algorithms is shown in **Figure 6C** as the ratio of $\Delta\rho_w(6 - band)$ to the $\Delta\rho_w(2 - band)$ AC. The average reduction in uncertainty is nearly 24% using the 6-band MBAC for the MODIS-Aqua sensor; however, when the same analysis for the 6-band MBAC is done using the expected OCI performance, the average reduction in the uncertainty approaches 29% as shown in **Figure 6D**. The relatively modest improvement for MODIS-Aqua using the MBAC algorithm is attributed to the reduced performance of the SWIR radiometric detection. The high $NEL(\lambda)$ for MODIS SWIR channels reduces the weight in the cost function in determining the best aerosol models, relative to the higher radiometric quality of the NIR bands. The MBAC algorithm, however, shows more improvement for the OCI type of radiometric performance due to the increased SNR of the SWIR detectors relative to its NIR channels, although the visible performance is kept the same as MODIS for relative comparison. It is apparent that the merit of the MBAC algorithm will prevail when the estimated aerosol reflectance at the NIR bands is compromised. In fact, that is the case for nearly 10% of the global ocean, where the non-negligible reflectance from the turbid/coastal ocean leads to systematic underestimation and often negative reflectance retrievals due to overcorrection for aerosols. More details will be discussed in the section Application to Ocean Color Instrument.

Systematic Errors

To have a complete understanding of the potential sources of uncertainty for the MBAC algorithm, we also performed an analysis to understand the impact of systematic uncertainty on the retrievals. Systematic errors in measurements are very difficult to characterize post-launch due to the lack of an accurate absolute calibration apparatus on-orbit. Typically, a solar diffuser is used as a calibration reference; however, due to the immediate degradation of the diffuser, the absolute calibration with a high degree of certainty cannot generally be achieved. Thus, the ocean color community depends on a system vicarious calibration, which aims to remove any systematic bias due to the sensor or algorithm errors. For all ocean color sensors processed by NASA GSFC, we use the vicarious calibration method by Franz et al. (2007) using the MOBY *in situ* measurements as ground truth. The vicarious calibration procedure reduces the systematic uncertainty to 0.5% for all bands relative to the 869-nm band for MODIS sensors. However, the absolute calibration at 869 nm and SWIR bands is assumed to be 2%. Typically, systematic errors will depend on the environment and geometry at which the instrument is observing the Earth. Systematic bias can be influenced by various observing conditions and sensor characteristics, such as the operating temperature, instrument polarization sensitivity, stray light, and optical or electronic

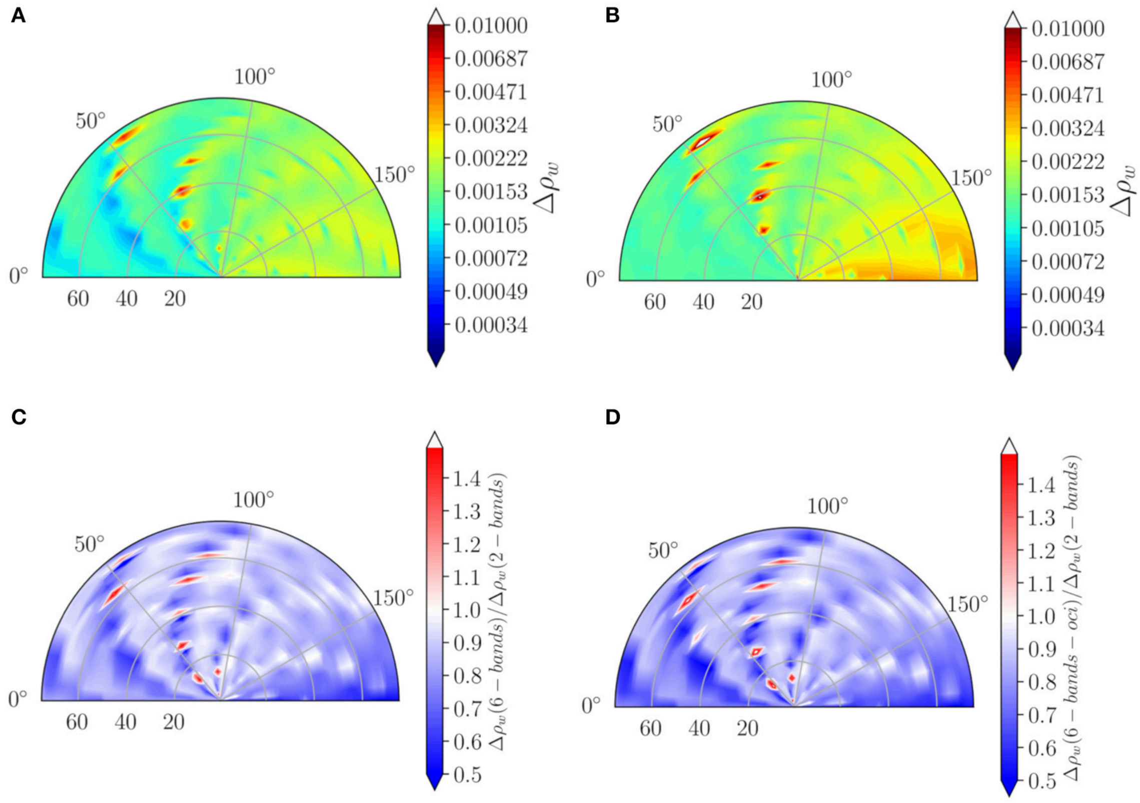

FIGURE 6 | (A,B) are the algorithm + random uncertainty in water reflectance, $\Delta\rho_\mathbf{w}$, at 443 nm as a function of the viewing geometry for solar zenith angles of 30°, using six bands MBAC and two NIR bands AC, respectively. **(C,D)** are the ratio between the reflectance uncertainty using six bands AC with MODIS-Aqua noise levels, and PACE OCI noise levels. The simulations are done for all aerosol models with relative humidity RH = 77.5% at optical depth at 869 nm from 0.05 to 0.35, and the retrieval is done using models with RH = 75 and 80%.

cross-talk. The behavior of the errors on a per-pixel basis cannot be easily predicted; thus, it remains unknown; however, the bias can be reduced through prelaunch characterization and derived correction algorithms (e.g., polarization correction of the instrument, correction for out-of-band response, estimation, and correction for straylight). The spectral correlation of systematic bias can play an important role in determining the uncertainty of the retrievals. For example, the spectral correlation of the two-band ratio algorithm will suffer when the systematic bias is random and independent at the two bands. Since such a spectral covariance in bias cannot be directly measured on-orbit, we assume a conservative scenario in our analysis by assuming a 10% correlation inter-bands, although the spectral correlation between bands could increase/decrease depending on the spectral distance. We ran the MC analysis assuming a random bias at the levels mentioned above for MODIS-Aqua observations. The covariance matrix, $\boldsymbol{Cov}(\lambda_n, \lambda_m)$, of the system errors is equal to 0.1 for off-diagonal elements and 1 for diagonal ones. The correlated random bias is then calculated as follows:

$$Bias\,(iterations, \lambda) = \mathcal{U}(-1,1)\cdot \boldsymbol{L}(\lambda_n, \lambda_m) \tag{15}$$

The bias is generated for the number of iterations in the MC analysis for each band. $\mathcal{U}(-1,1)$ is uniform distribution of random numbers from -1 to 1, while $\boldsymbol{L}(\lambda_n, \lambda_m)$ is Lower Cholesky factorization of the covariance matrix such that:

$$\boldsymbol{Cov}(\lambda_n, \lambda_m) = \boldsymbol{L}(\lambda_n, \lambda_m)\ \boldsymbol{D}(\lambda_n, \lambda_m)\ \boldsymbol{L}^*(\lambda_n, \lambda_m) \tag{16}$$

$\boldsymbol{L}^*(\lambda_n, \lambda_m)$ is the conjugate value of the matrix and $\mathbf{D}(\lambda_n, \lambda_m)$ is the diagonal matrix. The Cholesky matrix allows the generation of random errors with inter-bands correlation specified in the covariance matrix. The bias levels are then re-adjusted to match the level of the instrument.

In **Figures 7A,B**, the uncertainty, $\Delta\rho_w$, at 443 nm is due to algorithm + random + systematic errors for the 6-band MBAC and NIR 2-band AC, respectively. The average uncertainty for the 2-band AC is 0.0036, while for the 6-band MBAC algorithm, the average uncertainty is 0.0024, with an improvement of 33% over the 2-band standard algorithm as shown in **Figure 7C**. For the OCI configuration, at higher SNRs, the improvement is only slight at 37% relative to the MODIS-Aqua configuration in **Figure 7D**. This can be attributed to the dominant impact of systematic uncertainty over random noise; however, in practice, OCI is expected to have lower systematic errors at 1.6% levels,

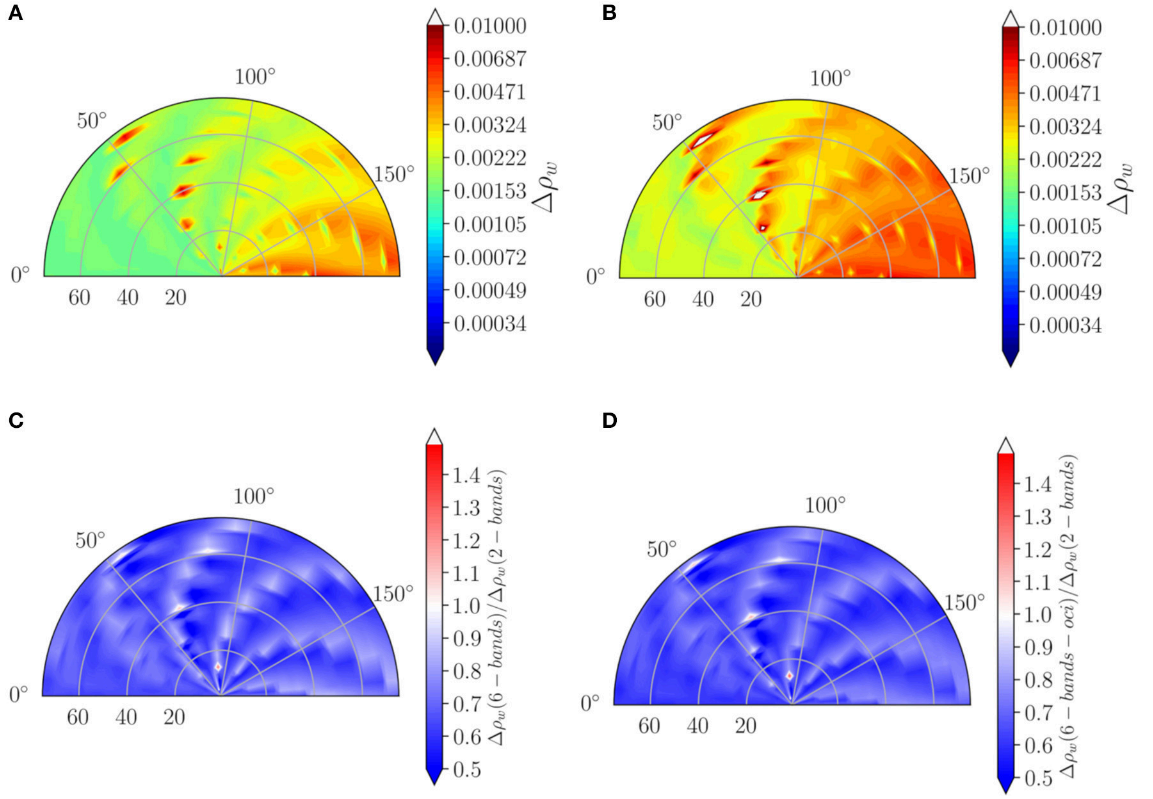

FIGURE 7 | (A,B) are the algorithm + random + systematic uncertainty in water reflectance, $\Delta\rho_\mathbf{w}$, at 443 nm as a function of the viewing geometry for solar zenith angles of 30°, using six bands MBAC and NIR two bands AC, respectively. **(C,D)** are the ratio between the reflectance uncertainty using 6-bands AC with MODIS-Aqua noise levels and PACE OCI noise levels. The simulations are done for all aerosol models with relative humidity RH = 77.5% at optical depth at 869 nm from 0.05 to 0.35, and the retrieval is done using models with RH = 75 and 80%.

which is not simulated here. Additionally, the high SNR on OCI's SWIR will have a more significant impact when retrieving in coastal waters, when the NIR signal is contaminated by non-negligible water-leaving radiance.

APPLICATION TO OCEAN COLOR INSTRUMENT

Unlike MODIS or VIIRS, the SWIR detection assembly on OCI will include channels specifically tuned for good radiometric performance over the relatively dark ocean. This significant advancement will provide an opportunity to improve ocean color observations in complex water environments (i.e., coastal ocean) due to the increased sensitivity to the aerosols and less to the water signal. With the MBAC algorithm, the combined utilization of all SWIR channels (excluding water vapor bands) and NIR channels will offer an improved AC over coastal waters and open ocean by utilizing more spectral bands to reduce the effect of sensor noise and with adaptive weighting toward the bands that are less influenced by non-negligible water-leaving radiance.

Figure 8 shows the spectral uncertainty, $\Delta\rho_w$, for proxy OCI wavelengths from the UV to red wavelengths for open ocean and coastal turbid waters (with high total suspended material, TSM). The open ocean reflectance was simulated with Hydrolight assuming Chlor-a = 0.03 mg/m^3 and TSM = 0 g m^{-3} while turbid waters assume TSM = 10 g m^{-3} that has been propagated to the TOA for each atmospheric composition and geometry [more details are in Ibrahim and McKinna (2018)]. The retrieval was done with the 2-band NIR-only algorithm and the SWIR-only MBAC algorithm. The uncertainty is calculated for the aerosol set as in the section Error Assessment except for one specific geometry in the operational LUTs (i.e., solar zenith, $\theta_0 = 25°$, view zenith, $\theta = 26°$, relative azimuth angle, $\varphi = 90°$). For an OCI-like instrument, the SWIR MBAC algorithm shows a slight reduction in the uncertainty as compared to the 2-band NIR AC over open ocean conditions. In contrast, over turbid waters, the non-negligible water-leaving radiance at the NIR bands shows a large uncertainty (systematic bias) in the reflectance retrievals from the 2-band NIR AC, which is substantially reduced using the SWIR MBAC algorithm. As previously discussed, the SW, $SW(\lambda)$, in the cost function is based on the NIR iteration scheme of Bailey et al. (2010) to reduce the impact of contaminated NIR bands in the AC over productive waters. The algorithm sequentially iterates over a bio-optical model until a convergence criterion is met. The SW is directly dependent on the convergence process such that the weight on

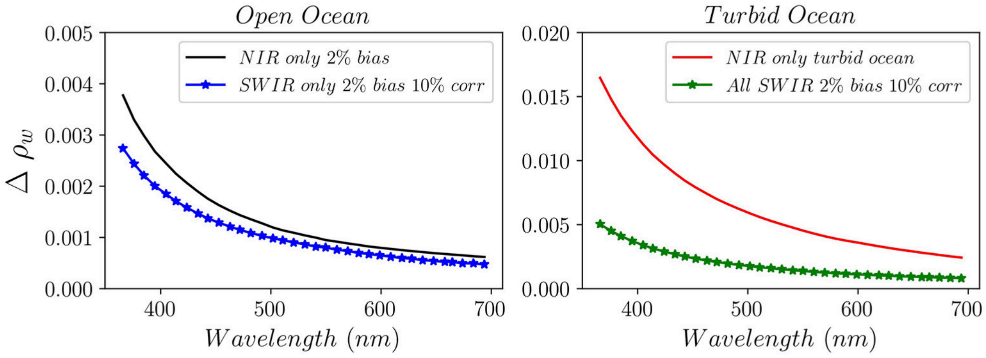

FIGURE 8 | The spectral uncertainty, $\Delta\rho_\mathbf{w}$, for a proxy OCI wavelengths from the UV to red wavelengths for open ocean and coastal turbid waters. The uncertainty is calculated at one specific geometry (i.e., solar zenith $\theta_0 = 25°$, view zenith, $\theta = 26°$, relative azimuth angle, $\varphi = 90°$). The analysis assumes a 2% systematic bias at NIR and SWIR bands.

the contaminated NIR bands is quickly (exponentially) reduced with increasing difficulty in the bio-optical model fit. The SW is proportional to the number of iterations; thus, it translates linearly. At the maximum of the iterations range, the SW is set to zero on the NIR bands; thus, the algorithm transitions into a full SWIR MBAC. This adaptive weight allows for a smooth transition in the processing between clear waters and productive waters; thus, it does not require switching between two or more algorithms. This allows for producing more consistent products, while maximizing the information content from all observations at all bands.

APPLICATION TO MODIS RETRIEVALS

The MBAC algorithm has been implemented into NASA's L2gen processing code. L2gen (Level-2 generator) within the SeaDAS software package is the multi-sensor Level-1 to Level-2 processing code developed and maintained by NASA's Ocean Biology Processing Group (OBPG) that is capable of retrieving ocean color products from TOA radiances for a host of sensors. L2gen supports multiple AC methods and variations that can be applied to a variety of ocean color sensors (Gordon and Wang, 1994; Ruddick et al., 2000; Wang et al., 2009; Ahmad et al., 2010; Bailey et al., 2010; Ibrahim et al., 2018).

Figure 9 shows the Chlor-a retrieval from MODISA observations for both the operational algorithm and the MBAC algorithm (748, 859, 869, 1,240, and 2,130 nm, excluding 1,640 nm for Aqua because of bad detectors), the average percent difference (APD), and the SW at NIR over the East Coast of the United States. Qualitatively, there is general agreement between the two algorithms for the Chlor-a product and through the APD histogram. This agreement confirms the feasibility of implementation in an operational environment. Differences are evident, however, in coastal waters such as the turbid Chesapeake Bay (39.5°-37° N, 75.5°-76° W) or the shallow Pamlico Sound (35° N, 76° W) as shown in the APD figure. There are some apparent artifacts in the upper part of the scene from the MBAC retrievals that could be due to strong NIR/SWIR calibration artifacts at the edge of the scan; however, a further assessment of SWIR calibration for MODIS is necessary for reliable retrievals. The SW map shows lower values (i.e., closer to 0) near the coast where the Bailey NIR iterative algorithm was triggered, thus relying more on the SWIR bands with each increased iteration. The SW is, however, higher over more clear water over the open Atlantic waters; thus, the algorithm relies on both the NIR and SWIR bands. We believe that the MBAC algorithm should be validated in the more common moderate turbid waters and highly productive waters. That scene includes regions with high turbidity such as the upper bay regions and inland rivers as well as shallow water regions such as Pamlico Sound, highly productive waters such as middle Chesapeake Bay region, highly absorbing waters such as Long Island Sound, and the less productive to more clear waters in the open Atlantic waters. Testing the MBAC algorithm over a large dynamic range of water conditions and more complex atmospheric conditions (i.e., including the large range of Angstrom coefficients from coarse to fine aerosols) provides more insight.

We also show in **Figure 10** the aerosol's Angstrom coefficient retrieval over these coastal regions for both the operational and the MBAC algorithm.

The operational algorithm shows an increased Angstrom over turbid or shallow regions near the coast that can be attributed to the failure in the NIR iterative algorithm to mitigate the non-negligible water-leaving radiance in the NIR bands. This artifact in the aerosol properties typically leads to the overcorrection of aerosol radiance and the potential retrieval of negative radiances. However, using the adaptive SW in the MBAC algorithm, it quickly damps that NIR contamination by decreasing the weight of the NIR bands in the cost function, and thus, the Angstrom coefficient is reduced to a range that agrees better with the surrounding pixels. Notice that the southwesternmost part of the scene shows an increase in the Angstrom coefficient with the MBAC algorithm, which could be a more realistic retrieval or an artifact due to a bias in the SWIR calibration. However, this could indicate that the MBAC algorithm is sensitive to fine-mode as much as coarse-mode aerosols. Better quantitative evidence is further discussed in the next section.

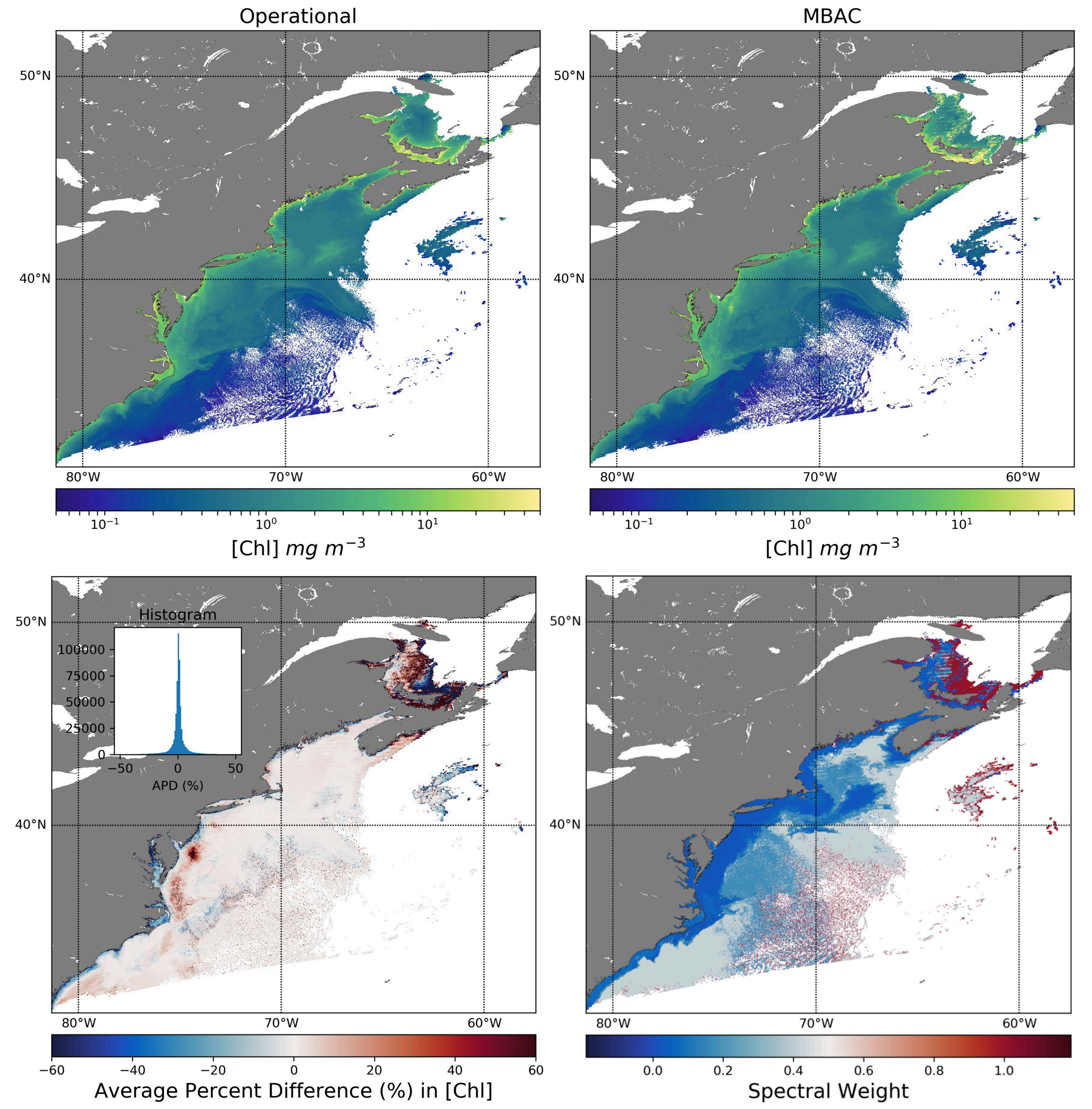

FIGURE 9 | MODISA chlor-a retrieval of a scene over the east coast of the US using the operational 2-bands and the MBAC algorithm, the average percent difference (APD), and the NIR Spectral Weight (SW) map used in the MBAC retrievals.

VALIDATION

Using NASA's SeaBASS dataset of *in situ* R_{rs} measurements, we performed match-up to MODIS retrievals at eight bands in the visible spectral range near 412, 443, 488, 531, 547, 555, 667, and 678 nm, using both the 2-band operation algorithm and the MBAC algorithm for MODIS-Aqua. Many of the SeaBASS data points are coastal, however less frequent than AERONET-OC data. **Table 1** below shows the spectral uncertainty, $\Delta R_{rs}(\lambda)$, R^2, and the mean bias in the retrievals compared to *in situ* observations for MODISA for both the operational and the MBAC algorithm. The retrieval uncertainty, $\Delta R_{rs}(\lambda)$, for the 6-band MBAC algorithm is reduced as compared to the operational algorithm, especially in the green wavelengths at 531, 547, and 555 nm, where the uncertainty is reduced by 52, 55, and 29%, respectively. There is a slight increase in uncertainty at 678 nm,

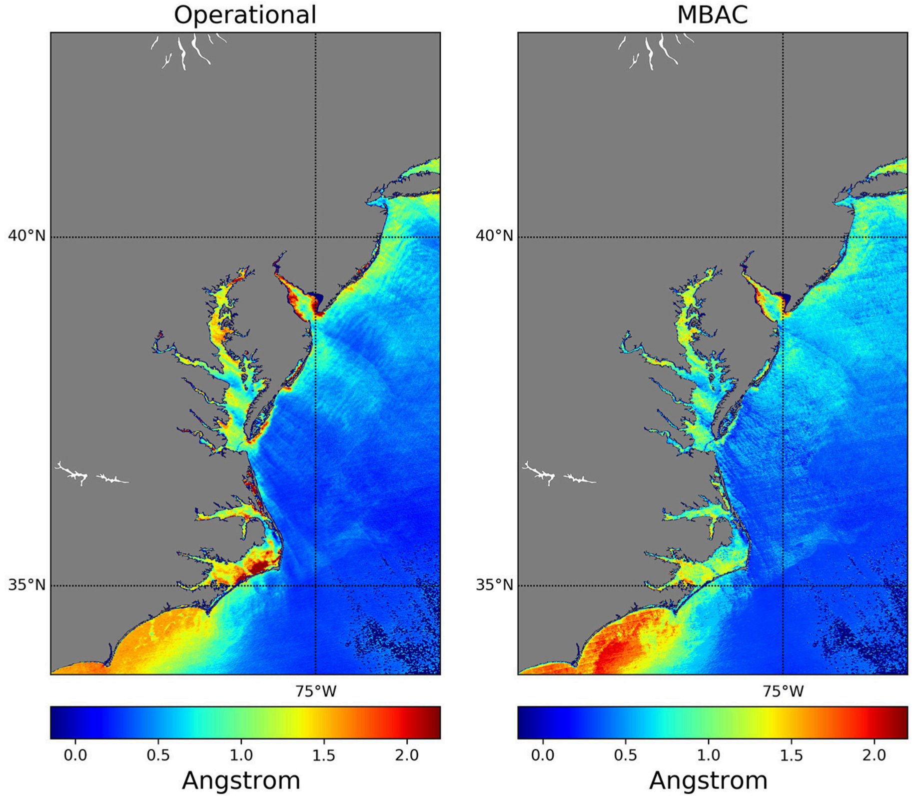

FIGURE 10 | MODISA retrieval of the aerosols' Angstrom coefficient of a scene over the east coast of the US using the operational 2-band and the MBAC algorithm.

TABLE 1 | A summary of statistical indicators to match-ups of MODISA retrievals with *in situ* R_{rs} from the SeaBASS dataset.

Wavelength (nm)	N	In situ R_{rs} range (sr^{-1})	Operational Algorithm			MBAC Algorithm		
			ΔR_{rs} (sr^{-1})	R^2	Mean Bias (sr^{-1})	ΔR_{rs} (sr^{-1})	R^2	Mean Bias (sr^{-1})
412	331	0.00078–0.01783	0.0020	0.74	−0.00089	0.0020	0.71	−0.000012
443	486	0.00126–0.02289	0.0014	0.73	−0.00044	0.0014	0.71	0.000029
488	506	0.00146–0.02587	0.0013	0.74	−0.00053	0.0011	0.76	−0.00017
531	95	0.00137–0.02759	0.0021	0.77	−0.00050	0.0011	0.91	−0.00013
547	51	0.00102–0.02799	0.0029	0.68	−0.00079	0.0013	0.90	−0.00018
555	353	0.00002–0.01196	0.0014	0.76	−0.00058	0.0010	0.83	−0.00040
667	380	0.00013–0.00286	0.0005	0.72	−0.00007	0.0003	0.85	−0.00008
678	12	0.00078–0.01783	0.0004	0.78	−0.00004	0.0005	0.69	−0.00006

which could be due to the lack of high-quality *in situ* observations at longer wavelengths. The coefficient of determination, however, is slightly lower for 412 and 443 for the MBAC algorithm relative to the operational one. There is a more significant correlation for the green channels, 531, 547, and 555, using the MBAC algorithm. Overall, the uncertainty is reduced using the MBAC algorithm due to the decreased mean bias in retrievals. Because of the extrapolation of the aerosol information from the NIR/SWIR to the visible, at shorter wavelengths, the retrievals uncertainty will increase specifically in coastal waters where the ocean blue reflectance is small. Thus, retrievals in the blue bands are slightly noisier due to the impact of low-SNR SWIR bands due to the spectral extrapolation of the selected aerosol models.

A further investigation into a proper estimation of systematic uncertainty and its spectral correlation is necessary to provide uncertainties that are similar to *in situ* validation. It is important to note that the validation analysis has been done with an initial SWIR vicarious calibration following Franz et al. (2007). The reduction of systematic bias is essential to provide reliable MBAC retrievals, which will require a thorough assessment of the SWIR calibration in a future study.

CONCLUSION

The MBAC algorithm shows several potential merits over NASA's current operational Gordon and Wang (1994) 2-band ratio aerosols correction algorithm. The utilization of multibands from the NIR to SWIR in the AC reduces the uncertainty in the retrieval of ocean color reflectance due to sensor random and systematic noise. The adaptive SW reduces the weight on the NIR bands over turbid or highly productive waters; thus, the contamination from bright ocean signal in the NIR is reduced. This algorithm enables the production of spatially consistent ocean color data in turbid and open ocean conditions. The limitations of the algorithm are mainly tied to the radiometric performance in the SWIR bands. A significantly decreased performance in the SWIR for some sensors leads to noisy retrievals in the coastal regions. For the OCI on PACE, the SWIR bands are expected to have a much higher SNR compared to MODISA within the radiance range observed over oceans; thus, a significant improvement using the MBAC algorithm is expected, especially in coastal regions. The sensitivity analysis shows an overall reduction in the reflectance uncertainty by 33% over open ocean conditions and over 300% over turbid water conditions in the blue spectral region. In addition, the SeaBASS *in situ* match-ups show an improvement in the retrievals using the MBAC algorithm relative to the 2-band algorithm, especially in the green spectral range where the reduction in the uncertainty is nearly 50% at 531 nm. An improvement in the system vicarious calibration of the SWIR bands for current ocean color sensors shall increase the value of the MBAC algorithm in producing more consistent products.

AUTHOR CONTRIBUTIONS

AI performed the analysis in the manuscript for the sections Error Assessment, Application to Ocean Color Instrument, Application to MODIS Retrievals, and Validation. BF contributed to editing and guiding the manuscript discussion. ZA provided **Figure 1** and the aerosol LUTs. SB provided the SWIR vicarious calibration gains necessary for the MBAC algorithm.

FUNDING

Support for this work was provided by a NASA Ocean Biology and Biogeochemistry PACE Science Team and Aqua, Terra, and Sumi-NPP Science Team award.

ACKNOWLEDGMENTS

We acknowledge the MOBY team of NOAA for providing the *in situ* MOBY radiometry, Chris Proctor for providing the SeaBASS dataset, and other OBPG team members for their valuable input.

REFERENCES

Abdou, W. A., Martonchik, J. V., Kahn, R. A., West, R. A., and Diner, D. J. (1997). A modified linear-mixing method for calculating atmospheric path radiances of aerosol mixtures. *J .Geophys. Res. Atmos.* 102, 16883–16888. doi: 10.1029/96JD03434

Ahmad, Z., and Franz, B. A. (2018). "Uncertainty in aerosol model characterization and its impact on ocean color retrievals," in *PACE Technical Report Series, Volume 6: Data Product Requirements and Error Budgets*, eds I. Cetinić, C. R. McClain, and P. J. Werdell (Greenbelt, MD: NASA Goddard Space Flight Space Center), 45–55.

Ahmad, Z., Franz, B. A., McClain, C. R., Kwiatkowska, E. J., Werdell, J., Shettle, E. P., et al. (2010). New aerosol models for the retrieval of aerosol optical thickness and normalized water-leaving radiances from the SeaWiFS and MODIS sensors over coastal regions and open oceans. *Appl. Opt.* 49:5545. doi: 10.1364/AO.49.005545

Aurin, D., Mannino, A., and Franz, B. (2013). Spatially resolving ocean color and sediment dispersion in river plumes, coastal systems, and continental shelf waters. *Remote Sens. Environ.* 137, 212–225. doi: 10.1016/j.rse.2013.06.018

Bailey, S. W., Franz, B. A., and Werdell, P. J. (2010). Estimation of near-infrared water-leaving reflectance for satellite ocean color data processing. *Opt. Express* 18, 7521. doi: 10.1364/OE.18.007521

Brajard, J., Jamet, C., Moulin, C., and Thiria, S. (2006). Use of a neuro-variational inversion for retrieving oceanic and atmospheric constituents from satellite ocean colour sensor: application to absorbing aerosols. *Neural Networks* 19, 178–185. doi: 10.1016/j.neunet.2006.01.015

Chomko, R. M., and Gordon, H. R. (1998). Atmospheric correction of ocean color imagery: use of the Junge power-law aerosol size distribution with variable refractive index to handle aerosol absorption. *Appl. Opt.* 37, 5560–5572. doi: 10.1364/AO.37.005560

Chomko, R. M., and Gordon, H. R. (2001). Atmospheric correction of ocean color imagery: test of the spectral optimization algorithm with the sea-viewing wide field-of-view sensor. *Appl. Opt.* 40, 2973–2984. doi: 10.1364/AO.40.002973

Chomko, R. M., Gordon, H. R., Maritorena, S., and Siegel, D. A. (2003). Simultaneous retrieval of oceanic and atmospheric parameters for ocean color imagery by spectral optimization: a validation. *Remote Sens. Environ.* 84, 208–220. doi: 10.1016/S0034-4257(02)00108-6

Fan, Y., Li, W., Gatebe, C. K., Jamet, C., Zibordi, G., Schroeder, T., et al. (2017). Atmospheric correction over coastal waters using multilayer neural networks. *Remote Sens. Environ.* 199, 218–240. doi: 10.1016/j.rse.2017.07.016

Franz, B. A., Bailey, S. W., Werdell, P. J., and McClain, C. R. (2007). Sensor-independent approach to the vicarious calibration of satellite ocean color radiometry. *Appl. Opt.* 46, 5068. doi: 10.1364/AO.46.005068

Frouin, R. J., and Gross-Colzy, L. S. (2016). *Contribution of Ultraviolet and Shortwave Infrared Observations to Atmospheric Correction of PACE Ocean-Color Imagery*. eds R. J. Frouin, S. C. Shenoi, K. H. Rao. New Delhi, SPIE.

Gao, B., Montes, M. J., Li, R., Dierssen, H. M., and Davis, C. O. (2007). An atmospheric correction algorithm for remote sensing of bright coastal waters using MODIS land and ocean channels in the solar spectral region. *IEEE Trans. Geosci. Remote Sens.* 45, 1835–1843. doi: 10.1109/TGRS.2007.895949

Gao, B.-C, Montes, M. J., Ahmad, Z., and Davis, C. O. (2000). Atmospheric correction algorithm for hyperspectral remote sensing of ocean color from space. *Appl. Opt.* 39, 887. doi: 10.1364/AO.39.000887

Gordon, H. R. (1995). Remote sensing of ocean color: a methodology for dealing with broad spectral bands and significant out-of-band response. *Appl. Opt.* 34, 8363–8374. doi: 10.1364/AO.34.008363

Gordon, H. R., Brown, O. B., Evans, R. H., Brown, J. W., Smith, R. C., Baker, K. S., et al. (1988). A semianalytic radiance model of ocean color. *J .Geophys. Res. Atmos.* 93, 10909–10924. doi: 10.1029/JD093iD09p10909

Gordon, H. R., Du, T., and Zhang, T. (1997). Remote sensing of ocean color and aerosol properties: resolving the issue of aerosol absorption. *Appl. Opt.* 36, 8670–8684. doi: 10.1364/AO.36.008670

Gordon, H. R., and Wang, M. (1994). Retrieval of water-leaving radiance and aerosol optical thickness over the oceans with SeaWiFS: a preliminary algorithm. *Appl. Opt.* 33, 443. doi: 10.1364/AO.33.000443

Gossn, J. I., Ruddick, K. G., and Dogliotti, A. I. (2019). Atmospheric correction of OLCI imagery over extremely turbid waters based on the red, NIR and 1016 nm bands and a new baseline residual technique. *Rem. Sensing*. 11:220. doi: 10.3390/rs11030220

Goyens, C., Jamet, C., and Schroeder, T. (2013). Evaluation of four atmospheric correction algorithms for MODIS-aqua images over contrasted coastal waters. *Remote Sens. Environ.* 131, 63–75. doi: 10.1016/j.rse.2012.12.006

He, X., Bai, Y., Pan, D., Tang, J., and Wang, D. (2012). Atmospheric correction of satellite ocean color imagery using the ultraviolet wavelength for highly turbid waters. *Opt. Express* 20, 20754–20770. doi: 10.1364/OE.20.020754

Hu, C., Lee, Z., and Franz, B. (2012). Chlorophyll A algorithms for oligotrophic oceans: a novel approach based on three-band reflectance difference. *J. Geophys. Res. Oceans* 117, C01011. doi: 10.1029/2011JC007395

Ibrahim, A., Franz, B., Ahmad, Z., Healy, R., Knobelspiesse, K., Gao, B., et al. (2018). Atmospheric correction for hyperspectral ocean color retrieval with application to the Hyperspectral Imager for the Coastal Ocean (HICO). *Remote Sens. Environ.* 204, 60–75. doi: 10.1016/j.rse.2017.10.041

Ibrahim, A., and McKinna, L. (2018). "Uncertainty in aerosol model characterization and its impact on ocean color retrievals," in *PACE Technical Report Series, Volume 6: Data Product Requirements and Error Budgets*, eds I. Cetinić, C. R. McClain, and P. J. Werdell (NASA Goddard Space Flight Space Center). Available online at: https://pace.oceansciences.org/docs/TM2018219027Vol.7.pdf (accessed November 2018).

IOCCG (2010). *Atmospheric Correction for Remotely-Sensed Ocean-Colour Products*. Dartmouth, NS: The International Ocean-Colour Coordinating Group.

Jamet, C., Thiria, S., Moulin, C., and Crepon, M. (2005). Use of a neurovariational inversion for retrieving oceanic and atmospheric constituents from ocean color imagery: a feasibility study. *J. Atmos. Oceanic Technol.* 22, 460–475. doi: 10.1175/JTECH1688.1

Jiang, L., and Wang, M. (2014). Improved near-infrared ocean reflectance correction algorithm for satellite ocean color data processing. *Opt. Express* 22, 21657–21678. doi: 10.1364/OE.22.021657

Kuchinke, C. P., Gordon, H. R., and Franz, B. A. (2009). Spectral optimization for constituent retrieval in case 2 waters I: implementation and performance. *Remote Sens. Environ.* 113, 571–587. doi: 10.1016/j.rse.2008.11.001

Liu, H., Hu, S., Zhou, Q., Li, Q., and Wu, G. (2019). Revisiting effectiveness of turbidity index for the switching scheme of NIR-SWIR combined ocean color atmospheric correction algorithm. *Int. J. Appl. Earth Obs. Geoinf.* 76, 1–9. doi: 10.1016/j.jag.2018.10.010

Mobley, C., Werdell, J., Franz, B., Ahmad, Z., and Bailey, S. (2016). *Atmospheric Correction for Satellite Ocean Color Radiometry*. Available online at: https://oceancolor.gsfc.nasa.gov/docs/technical/NASA-TM-2016-217551.pdf (accessed November 2018).

Morel, A., and Maritorena, S. (2001). Bio-optical properties of oceanic waters: a reappraisal. *J. Geophys. Res. Oceans* 106, 7163–7180. doi: 10.1029/2000JC000319

Nordkvist, K., Loisel, H., and Gaurier, L. D. (2009). Cloud masking of SeaWiFS images over coastal waters using spectral variability. *Opt. Express* 17, 12246–12258. doi: 10.1364/OE.17.012246

O'Reilly, J. E., Maritorena, S., Mitchell, B., Greg, S., David, A., Carder, K. L., et al. (1998). Ocean color chlorophyll algorithms for SeaWiFS. *J. Geophys. Res. Oceans* 103, 24937–24953. doi: 10.1029/98JC02160

Pahlevan, N., Roger, J.-C., and Ahmad, Z. (2017). Revisiting short-wave-infrared (SWIR) bands for atmospheric correction in coastal waters. *Opt. Express* 25, 6015–6035. doi: 10.1364/OE.25.006015

Rothman, L. S., Gordon, I. E., Babikov, Y., Barbe, A., Chris Benner, D., Bernath, P. F., et al. (2013). The HITRAN2012 molecular spectroscopic database. *J. Quant. Spectrosc. Radiat. Transfer* 130, 4–50. doi: 10.1016/j.jqsrt.2013.07.002

Ruddick, K., Ovidio, F., and Rijkeboer, M. (2000). Atmospheric correction of SeaWiFS imagery for turbid coastal and inland waters. *Appl. Opt.* 39:897. doi: 10.1364/AO.39.000897

Schroeder, T.h, Behnert, I., Schaale, M., Fischer, J., and Doerffer, R. (2007). Atmospheric correction algorithm for MERIS above case-2 waters. *Int. J. Remote Sens.* 28, 1469–86. doi: 10.1080/01431160600962574

Shi, W., and Wang, M. (2007). Detection of turbid waters and absorbing aerosols for the MODIS ocean color data processing. *Remote Sens. Environ.* 110, 149–161. doi: 10.1016/j.rse.2007.02.013

Siegel, D. A., Wang, M., Maritorena, S., and Robinson, W. (2000). Atmospheric correction of satellite ocean color imagery: the black pixel assumption. *Appl. Opt.* 39, 3582–3591. doi: 10.1364/AO.39.003582

Spurr, R., Stamnes, K., Eide, H., Li, W., Zhang, K., and Stamnes, J. (2007). Simultaneous retrieval of aerosols and ocean properties: a classic inverse modeling approach. I. Analytic Jacobians from the linearized CAO-DISORT model. *J. Quant. Spectrosc. Radiat. Transfer* 104, 428–449. doi: 10.1016/j.jqsrt.2006.09.009

Stamnes, K., Li, W., Yan, B., Eide, H., Barnard, A., Pegau, W. S., et al. (2003). Accurate and self-consistent ocean color algorithm: simultaneous retrieval of aerosol optical properties and chlorophyll concentrations. *Appl. Opt.* 42, 939–951. doi: 10.1364/AO.42.000939

Steinmetz, F., Deschamps, P.-Y., and Ramon, D. (2011). Atmospheric correction in presence of sun glint: application to MERIS. *Opt. Express* 19, 9783–9800. doi: 10.1364/OE.19.009783

Vanhellemont, Q., and Ruddick, K. (2015). Advantages of high quality SWIR bands for ocean colour processing: examples from Landsat-8. *Remote Sens. Environ.* 161, 89–106. doi: 10.1016/j.rse.2015.02.007

Wang, M., and Shi, W. (2006). Cloud masking for ocean color data processing in the coastal regions. *IEEE Trans. Geosci. Remote Sens.* 44, 3196–3105. doi: 10.1109/TGRS.2006.876293

Wang, M., and Shi, W. (2007). The NIR-SWIR combined atmospheric correction approach for MODIS ocean color data processing. *Opt. Express* 15, 15722–15733. doi: 10.1364/OE.15.015722

Wang, M., and Shi, W. (2012). Sensor noise effects of the SWIR bands on MODIS-derived ocean color products. *IEEE Trans. Geosci. Remote Sens.* 50, 3280–3292. doi: 10.1109/TGRS.2012.2183376

Wang, M., Shi, W., and Jiang, L. (2012). Atmospheric correction using near-infrared bands for satellite ocean color data processing in the turbid western Pacific region. *Opt. Express* 20, 741–753. doi: 10.1364/OE.20.000741

Wang, M., Son, S., and Shi, W. (2009). Evaluation of MODIS SWIR and NIR-SWIR atmospheric correction algorithms using SeaBASS data. *Remote Sens. Environ.* 113, 635–644. doi: 10.1016/j.rse.2008.11.005

Werdell, P. J., Franz, B. A., and Bailey, S. W. (2010). Evaluation of shortwave infrared atmospheric correction for ocean color remote sensing of Chesapeake Bay. *Remote Sens. Environ.* 114, 2238–2247. doi: 10.1016/j.rse.2010.04.027

Werdell, P. J., Franz, B. A., Bailey, S. W., Feldman, G. C., Boss, E., Brando, V. E., et al. (2013). Generalized ocean color inversion model for retrieving marine inherent optical properties. *Appl. Opt.* 52, 2019–2037. doi: 10.1364/AO.52.002019

Xiong, X., Sun, J., Xie, X., Barnes, W. L., and Salomonson, V. V. (2010). On-orbit calibration and performance of aqua MODIS reflective solar bands. *IEEE Trans. Geosci. Remote Sens.* 48, 535–546. doi: 10.1109/TGRS.2009.2024307

Conflict of Interest Statement: AI was employed by Science Systems and Applications Inc. and ZA was employed by Science Application International Corp. when this manuscript was being prepared.

The remaining authors declare that the research was conducted in the absence of any commercial or financial relationships that could be construed as a potential conflict of interest.

frontiers
in Earth Science

ORIGINAL RESEARCH
published: 18 June 2019
doi: 10.3389/feart.2019.00100

Modeling Atmosphere-Ocean Radiative Transfer: A PACE Mission Perspective

Jacek Chowdhary[1*†], Peng-Wang Zhai[2†], Emmanuel Boss[3], Heidi Dierssen[4], Robert Frouin[5], Amir Ibrahim[6], Zhongping Lee[7], Lorraine A. Remer[8], Michael Twardowski[9], Feng Xu[10], Xiaodong Zhang[11,12], Matteo Ottaviani[13], William Reed Espinosa[14] and Didier Ramon[15]

[1] Department of Applied Physics and Applied Mathematics, Columbia University, New York, NY, United States, [2] Department of Physics, University of Maryland, Baltimore, MD, United States, [3] School of Marine Sciences, University of Maine, Orono, ME, United States, [4] Department of Marine Sciences, University of Connecticut, Groton, CT, United States, [5] Scripps Institution of Oceanography, University of California, San Diego, San Diego, CA, United States, [6] SSAI, NASA Goddard Space Flight Center, Greenbelt, MD, United States, [7] School for the Environment, University of Massachusetts Boston, Boston, MA, United States, [8] Joint Center for Earth Systems Technology, University of Maryland, Baltimore, MD, United States, [9] Harbor Branch Oceanographic Institute, Florida Atlantic University, Fort Pierce, FL, United States, [10] Jet Propulsion Laboratory, California Institute of Technology, Pasadena, CA, United States, [11] Department of Earth System Science and Policy, University of North Dakota, Grand Forks, ND, United States, [12] Division of Marine Science, The University of Southern Mississippi, Stennis Space Center, Hattiesburg, MS, United States, [13] NASA Goddard Institute for Space Studies, New York, NY, United States, [14] NASA Goddard Space Flight Center, Greenbelt, MD, United States, [15] HYGEOS, Euratechnologies, Lille, France

OPEN ACCESS

Edited by:
Oleg Dubovik,
UMR8518 Laboratoire d'Optique Atmosphérique (LOA), France

Reviewed by:
Gian Luigi Liberti,
Italian National Research Council (CNR), Italy
Jose M. Baldasano,
Universitat Politecnica de Catalunya, Spain

***Correspondence:**
Jacek Chowdhary
Jacek.chowdhary@nasa.gov;
jacek.chowdhary@gmail.com

†Lead authors

Specialty section:
This article was submitted to Atmospheric Science, a section of the journal Frontiers in Earth Science

***Received:** 01 October 2018*
***Accepted:** 23 April 2019*
***Published:** 18 June 2019*

Citation:
Chowdhary J, Zhai P-W, Boss E, Dierssen H, Frouin R, Ibrahim A, Lee Z, Remer LA, Twardowski M, Xu F, Zhang X, Ottaviani M, Espinosa WR and Ramon D (2019) Modeling Atmosphere-Ocean Radiative Transfer: A PACE Mission Perspective. Front. Earth Sci. 7:100. doi: 10.3389/feart.2019.00100

The research frontiers of radiative transfer (RT) in coupled atmosphere-ocean systems are explored to enable new science and specifically to support the upcoming Plankton, Aerosol, Cloud ocean Ecosystem (PACE) satellite mission. Given (i) the multitude of atmospheric and oceanic constituents at any given moment that each exhibits a large variety of physical and chemical properties and (ii) the diversity of light-matter interactions (scattering, absorption, and emission), tackling all outstanding RT aspects related to interpreting and/or simulating light reflected by atmosphere-ocean systems becomes impossible. Instead, we focus on both theoretical and experimental studies of RT topics important to the science threshold and goal questions of the PACE mission and the measurement capabilities of its instruments. We differentiate between (a) forward (FWD) RT studies that focus mainly on sensitivity to influencing variables and/or simulating data sets, and (b) inverse (INV) RT studies that also involve the retrieval of atmosphere and ocean parameters. Our topics cover (1) the ocean (i.e., water body): absorption and elastic/inelastic scattering by pure water (FWD RT) and models for scattering and absorption by particulates (FWD RT and INV RT); (2) the air-water interface: variations in ocean surface refractive index (INV RT) and in whitecap reflectance (INV RT); (3) the atmosphere: polarimetric and/or hyperspectral remote sensing of aerosols (INV RT) and of gases (FWD RT); and (4) atmosphere-ocean systems: benchmark comparisons, impact of the Earth's sphericity and adjacency effects on space-borne observations, and scattering in the ultraviolet regime (FWD RT). We provide for each topic a summary of past relevant (heritage) work, followed by a discussion (for unresolved questions) and RT updates.

Keywords: radiative transfer, atmosphere, ocean surface, ocean body, PACE

1 INTRODUCTION

1.1 The PACE Mission

Plankton, Aerosol, Cloud ocean Ecosystem (PACE; see **Table 1** for a list of all acronyms used in this manuscript) is NASA's Plankton, Aerosol, Cloud, ocean Ecosystem mission[1], currently in the formulation phase of mission development. It is scheduled for launch in 2022 into a Sun synchronous, 676.5-km-high polar orbit with an inclination of 98° and a local equatorial crossing time of 1 pm. The science goals for this mission are (NASA, 2018a): (1) to extend past and current key systematic ocean color, aerosol, and cloud data records for Earth system and climate studies; and (2) to address new and emerging oceanic and atmospheric science questions using advanced instruments. To provide the requisite data for these goals, the PACE platform will carry three satellite instruments: the Ocean Color Instrument (OCI), the Spectro-Polarimeter for Planetary Exploration (SPEXone) (Hasekamp et al., 2019), and the Hyper Angular Rainbow Polarimeter (HARP2) (Martins et al., 2014). Together, these instruments will be the most advanced in NASA's history for the combined observation of ocean color and atmospheric aerosols, and will therefore provide unprecedented research opportunities. At the same time, the advanced remote sensing capabilities that these instruments offer places also require stringent requirements for forward and inverse radiative transfer (RT) modeling of light reflected by atmosphere-ocean systems. Before describing the status and various updates for such RT modeling, we summarize the measurement capabilities of OCI, SPEXone and HARP2 for PACE.

The width of an OCI image will be 2,663 km (which leads to a two-day ocean color coverage of the globe), and the spatial resolution will be 1 km for nadir viewing pixels. OCI will make single-view, hyperspectral radiance measurements for each pixel at a spectral resolution of 5 nm that cover the ultraviolet (UV) regime between 350 and 400 nm, the visible (VIS) between 400 and 700 nm, and the near infrared (NIR) regime between 700 and 885 nm. In addition, OCI will obtain single-view, narrow-band radiance measurements for each pixel in the short-wave infrared (SWIR) regime at nine wavelengths (940, 1038, 1250, 1378, 1615, 2130, and 2260 nm). The signal-to-noise ratio (SNR) for a typical ocean scene will be 1000 and 600 for the hyperspectral measurements in the UV-VIS and NIR regimes, respectively. These SNR values adhere to one of the threshold measurement requirements for PACE (NASA, 2018a), which is to retrieve the water-leaving radiance (that typically contributes less than 10% to space-borne radiance) with an accuracy in the VIS of the maximum of either 5%, or 0.002 for water reflectance ρ_w (see **Table 2** for definition and unit of all parameters used in this manuscript). Due to the high degree of empiricism present in retrieval algorithms of ocean inherent optical properties (IOP), the accuracy requirements for IOP retrievals are not defined for PACE. However, it is well established that the addition of bands and increase in SNR when compared to past ocean color missions should improve the retrievals relative to the current state of the art. The ultimate evaluation the IOP retrieval performance

TABLE 1 | List of acronyms.

Acronym	Description
3M	Multi-angle, Multi-spectral, Multi-Stokes-parameter
3MI	Multi-viewing Multi-channel Multi-polarisation Imager
AC	Atmospheric Correction
AERONET	Aerosol Robotic Network
AOS	Atmosphere-Ocean System
AVIRIS	Airborne Visible/Infrared Imaging Spectrometer
ARTS	Atmospheric Radiative Transfer Simulator
ATREM	Atmospheric Removal
AVHRR	Advanced Very High Resolution Radiometer
BrC	Brown Carbon
BRDF	Bidirectional Reflectance Distribution Function
CALIPSO	Cloud-Aerosol and Lidar Pathfinder Satellite Observation
CalNex	California Research at the Nexus of Air Quality and Climate Change
CARES	Carbonaceous Aerosols and Radiative Effects Study
CDOM	Colored Dissolved Organic Matter
CDM	Colored Detritus Matter
CWV	Column Water Vapor
CUDA	Compute Unified Device Architecture
CZCS	Coastal Zone Color Scanning experiment
DM	Detritus Matter
D-P	Detritus-Plankton
DoLP	Degree of Linear Polarization (see also **Table 2**)
DSCOVR	Deep Space Climate Observatory
EOS	Earth Observing System
EPIC	Earth Polychromatic Imaging Camera
FDOM	Fluorescence by Colored Dissolved Organic Matter
FWD	Forward
FWHM	Full Width at Half Maximum
GEOS-5	Goddard Earth Observing System Model, Version 5
GMAO	Global Modeling and Assimilation
GIOP-DC	Generalized Inherent Optical Properties – Default Configuration
GPU	Graphics Processing Unit
GRASP	Generalized Retrieval of Aerosol and Surface Properties
HARP2	Hyper Angular Rainbow Polarimeter 2
HICO	Hyperspectral Imager for Coastal Ocean
HITRAN	High-Resolution Transmission Molecular Absorption database
HSRL	High-Spectral Resolution Polarimeter
INV	Inverse
IOCCG	International Ocean Color Coordinating Group
IOP	Inherent Optical Properties
HULIS	Humic-like substances
LBL	Line-by-line
LOWTRAN	Low Resolution Atmospheric Transmission
LUTs	Look Up Tables
MASCOT	Multi-Angle Scattering Optical Tool
MC	Monte Carlo
MERIS	Medium Resolution Imaging Spetrometer
MISR	Multi-angle Imaging Spectroradiometer
MODIS	Moderate Resolution Imaging Spectroradiometer
MODTRAN	Moderate Resolution Atmospheric Transmission
MVSM	Multispectral Volume Scattering Meter
NAAMES	North Atlantic Aerosols and Marine Ecosystems Study
NAP	Non-algae particles
NIR	Near Infrared

(Continued)

---

[1] https://pace.gsfc.nasa.gov/

TABLE 1 | Continued

Acronym	Description
NPQ	Non-photochemical Quenching
OBPG	Ocean Biology Processing Group
OCI	Ocean Color Imager
OMI	Ozone Monitoring Instrument
OPE	Orientation of polarization ellipse
PACE	Plankton, Aerosol, Cloud ocean Ecosystems
PAR	Photosynthetically available radiation
POLDER	Polarization and Directionality of the Earth's Reflectances
PRISM	Portable Remote Imaging Spectrometer
RMS	Root-mean-square
RS	Remote Sensing
RSP	Research Scanning Polarimeter
RT	Radiative Transfer
SABOR	Ship-Aircraft Bio-Optical Research
SeaBASS	SeaWiFS Bio-optical Archive and Storage System
SEAC4RS	Studies of Emissions and Atmospheric Composition, Clouds, and Climate Coupling by Regional Surveys
SeaWiFS	Sea Viewing Wide-Filed-of-View Sensor
SML	Surface Micro-Layer
SNR	Signal-to-Noise ratio
SOS	Successive Orders of Scattering
SPEXone	Spectro-Polarimeter for Planetary Exploration
SRF	Ocean Surface
SWIR	Short-Wave Infrared
TCAP	Two-Column Aerosol Project
TOA	Top of Atmosphere
TOMS	Total Ozone Mapping Spectrometer
TOO	Top of Ocean
TSIS	Total and Spectral Solar Irradiance Sensor
UV	Ultra-Violet
VIIRS	Visible Infrared Imaging Spectrometer
VIS	Visible
VSF	Volume Scattering Function (β in **Table 2**)

will take place by comparing with co-located independent IOP measurement sets. More information on the measurement requirements for OCI, as well as the threshold and goal science questions targeted by these measurements, can be found in the Science Definition Report prepared for PACE (NASA, 2018a).

Both SPEXone and HARP2 instruments have smaller swaths and larger nadir-viewing pixel sizes, and they cover smaller parts of the UV-NIR spectrum, than the OCI. However, in addition to radiance measurements, SPEXone and HARP will also provide measurements of the linearly polarized radiance. Furthermore, both polarimeter instruments will look at each of their own pixels from multiple directions and will therefore capture angular features in the total and linearly polarized radiance. The swath for a SPEXone and HARP2 image will be 100 km and 1,556 km with a pixel resolution of $\sim$2.5 and $\sim$3.0 km, respectively. SPEXone will provide hyperspectral measurements of the total radiance at 2-nm spectral resolution, and of the Degree of Linear Polarization (DoLP) at 10–40 nm resolution, for the VIS-NIR regime covering 385–770 nm. On the other hand, HARP2 will provide measurements of the total and linearly polarized radiance in discrete narrow-bands (10–40 nm resolution) at four wavelengths in the VIS-NIR regime (440, 550, 670, and 870 nm). The radiometric SNR for an ocean scene in the VIS will be $>$800 and $>$200 at 10–40 nm resolution for SPEXone and HARP2, respectively. The corresponding DoLP accuracy for these instruments will be $\leq$0.3% and $\leq$1.0%. Each pixel of a SPEXone image will further be viewed from 5 angles at ±57°, ±20°, 0° from the satellite nadir view direction. HARP2 multi-angular measurements will cover the same angular range as SPEXone views but for more angles, i.e., for 60 angles at 670 nm and for 10 angles at the other three wavelengths.

SPEXone and HARP2 will therefore provide polarimetric data sets that have complementary strengths for better ocean, aerosol and cloud retrievals (see NASA, 2018b). That is, they complement each other in (i) swath coverage (ideally close to that of OCI for atmospheric correction); (ii) number of viewing angles (ideally $\geq$5 for atmospheric correction and for retrieval of aerosol properties and ice cloud scattering function, $\geq$10 for cloud thermodynamical phase retrievals, and $\geq$60 for water cloud droplet retrievals); (iii) spectral range (ideally include deep-blue channel for aerosol and cloud-top height retrievals) and spectral resolution (ideally matching OCI spectral resolution); (iv) SNR values (ideally matching OCI SNR); and (v) DoLP accuracy (ideally $\leq$ 0.5% for aerosol retrievals and $\leq$2% for cloud retrievals and atmospheric correction). Note that ideal polarimetric data sets could not have been achieved with a single instrument design at a practical cost; however, SPEXone and HARP2 will provide data sets that, when combined with OCI data, will help address the science goals for PACE well beyond its threshold requirements outlined in NASA (2018a).

1.2 Complexity of Atmosphere-Ocean Systems

Accurate calculations of the transport of solar radiant energy entering the Earth atmosphere are important for remote sensing of ocean color, aerosols, and clouds. They are needed to simulate the signal measured by an optical sensor, which may be carried onboard a satellite or deployed at any level in the ocean or atmosphere, to estimate the radiant contributions by various components in atmosphere-ocean systems, to characterize the properties (angular, spectral, and polarized) of the light field, and to develop inverse methods to retrieve the types and concentrations of optically active constituents. Diverse processes are involved and interact in various ways (e.g., elastic and inelastic scattering, absorption, fluorescence, and Fresnel reflection), which makes RT modeling of light in ocean-surface-atmosphere systems (AOS) a difficult issue. Realistic, precise, and reliable simulations depend on the proper treatment of the various processes and their interactions, all at the required spectral resolution (hyper-spectral in the case of PACE) and taking into account spatial heterogeneity.

In the following sections, we will focus on RT topics relevant to the work done by the 2014–2017 PACE Science Team for AOS

TABLE 2 | List of parameters.

Parameter	Description
A_{wc}	Albedo for whitecap, (dimensionless)
a, a_{tot}, a_{cdm}, a_{dm}, a_{ph}, a_w, a_{y}	Absorption coefficient, (m^{-1}) (generic, total, CDM, DM, phytoplankton, water, and CDOM, respectively)
$\hat{a}_{\mathrm{ph}}$	Specific absorption coefficient, ($\mathrm{m}^{-1}\ \mathrm{mg}^{-1}\ \mathrm{m}^3$), $a_{\mathrm{ph}} = \hat{a}_{\mathrm{ph}} \times [\mathrm{Chla}]$ (phytoplankton)
α_{cdm}, α_{y}	Absorption spectral slope, (dimensionless) (CDM and CDOM, respectively)
b, b_{p}	Scattering coefficient, (m^{-1}) (generic and particulate, respectively)
b_{b}, $b_{\mathrm{b,p}}$, $b_{\mathrm{b,dm}}$, $b_{\mathrm{b,ph}}$, $b_{\mathrm{b,w}}$,	Backscattering coefficient, (m^{-1}), $b_{\mathrm{b}} = \tilde{b} \times b$ (generic, particulate, DM, phytoplankton, and water, respectively)
$\tilde{b}$, $\tilde{b}_{\mathrm{p}}$, $\tilde{b}_{\mathrm{dm}}$, $\tilde{b}_{\mathrm{ph}}$	Backscattering efficiency, (dimensionless), $\tilde{b} = \int_{2\pi} \tilde{\beta}\ \mathrm{d}\Omega = b_{\mathrm{b}}/b$ (generic, particulate, DM, and phytoplankton, respectively)
β	Volume scattering function for hydrosols, ($\mathrm{sr}^{-1}\ \mathrm{m}^{-1}$), $\beta = b \times \tilde{\beta}$
$\tilde{\beta}$, $\tilde{\beta}_{\mathrm{p}}$	Normalized scattering (phase) function for hydrosols (scalar radiance operator), (sr^{-1})§† (generic and particulate, respectively)
$\tilde{\boldsymbol{\beta}}$	Normalized scattering matrix for hydrosols (4 × 4 vector radiance operator) (sr^{-1})§†
c	Extinction coefficient, (m^{-1}), $c = a + b$
[Chla]	Chlorophyll *a* concentration, ($\mathrm{mg\ m}^{-3}$)
DoLP	Degree of Linear Polarization, (dimensionless), DoLP = $(Q^2 + U^2)^{1/2}/(I)$
γ	Power-law exponent for Junge-type size distribution $n(r)$, (dimensionless), $\mathrm{d}n(r)/\mathrm{d}r = \mathrm{constant} \times r^{-\gamma}$
δ_{m}	Molecular depolarization ratio for pure seawater $\tilde{\beta}$, (dimensionless), $\delta_{\mathrm{m}} = \left\{\tilde{\beta}_{11}(\Theta = 90°) + \tilde{\beta}_{12}(\Theta = 90°)\right\} / \left\{\tilde{\beta}_{11}(\Theta = 90°) - \tilde{\beta}_{12}(\Theta = 90°)\right\}$
δ_{L}	Lidar depolarization ratio for marine particulate $\tilde{\beta}$, (dimensionless), $\delta_{\mathrm{L}} = \left\{\tilde{\beta}_{11}(\Theta = 180°) - \tilde{\beta}_{22}(\Theta = 180°)\right\} / \left\{\tilde{\beta}_{11}(\Theta = 180°) + \tilde{\beta}_{22}(\Theta = 180°)\right\}$
E_{d}	Downwelling irradiance reaching a unit horizontal area, ($\mathrm{W\ m}^{-2}\ \mathrm{nm}^{-1}$)
η	Height in atmosphere, normalized by the Earth's radius, (dimensionless)
Θ	Single scattering angle, (°)
θ, θ_0, θ_{b}	Angle, (°) (viewing with respect to the surface normal, solar zenith, and local Brewster, respectively)
F	Normalized scattering function for aerosols (scalar radiance operator), (dimensionless)§†
$\boldsymbol{F}$	Normalized scattering matrix for aerosols (4 × 4 vector radiance operator), (dimensionless)§†
f_{wc}	Spatial fraction of area covered by whitecaps, (dimensionless)
I, Q, U	Stokes parameters, ($\mathrm{W\ m}^{-2}\ \mathrm{sr}^{-2}\ \mathrm{nm}^{-1}$) (total intensity, and linear polarized intensity along 0° and 45° from reference plane, respectively)
K_{d}	Diffuse attenuation coefficient of downwelling irradiance, (m^{-1})
L, L_{w}, L_{tot}	Radiance, ($\mathrm{W\ sr}^{-1}\ \mathrm{m}^{-2}\ \mathrm{nm}^{-1}$) (generic, water-leaving, and TOA, respectively)
L_{atm}, L_{OC}, $L_{\mathrm{OC,dir}}$, $L_{\mathrm{OC,diff}}$, $L_{\mathrm{OC,rep}}$, $L_{\mathrm{srf-atm}}$	Radiance contribution to L_{tot}, ($\mathrm{W\ m}^{-2}\ \mathrm{sr}^{-1}\ \mathrm{nm}^{-1}$) (atmosphere, ocean color, ocean color direct, ocean color diffuse, ocean color residual, and atmosphere-surface, respectively)
λ	Wavelength, (nm)
m	Refractive index, (dimensionless)
μ, μ_0	Cosine of θ and of θ_0, (dimensionless)
$n(r)$	Normalized particle size distribution, ($\mathrm{m}^{-3}\ \mu\mathrm{m}^{-1}$)
Rrs	Remote sensing reflectance, (sr^{-1}), $\mathrm{Rrs} = L_{\mathrm{w}}/E_{\mathrm{d}}$
r_{e}	Effective radius of $n(r)$, (dimensionless)
r_{wlr}	Scalar Lambertian reflector for water-leaving radiance, (dimensionless)
ρ, $\Delta\rho$	Reflectance, (dimensionless)†, $\rho = \pi L/E_{\mathrm{d}}$ (generic and absolute difference, respectively)
ρ_{w}	Water reflectance, (dimensionless)†, $\rho_{\mathrm{w},} = \pi L_{\mathrm{w}}/E_{\mathrm{d}}$
S	Absolute Salinity, ($\mathrm{g\ kg}^{-1}$)

(Continued)

TABLE 2 | Continued

Parameter	Description
T	Temperature, (Celsius)
t_{atm}	Scalar diffuse transmittance for atmosphere, (dimensionless)
τ, τ_{aer}	Extinction optical depth, (dimensionless) (generic and aerosol, respectively)
φ	Azimuth angle, (°)
U_{10}, $U_{12.5}$	Wind speed above ocean surface, (m s^{-1}) (at 10 and 12.5 m, respectively)
v_{e}	Effective variance of $n(r)$, (dimensionless)
χ	Linear polarization angle, (°), $\tan(2\chi) = U/Q$
ω, ω_{aer}	Single scattering albedo, (dimensionless), $\omega = b/c$ (generic and aerosol, respectively)
Z_{aer}	Vertical distribution of aerosols, (dimensionless)
z	Height above sea surface, (km)

§ *Normalization of aerosol and hydrosol scattering functions differs by $(4\pi)^{-1}$: see Chowdhary et al. (2006).*
†*Using the convention [sr] for the dimension of π.*

models. The complexity of this work becomes apparent when listing some of the properties that have to be taken into account when performing RT computations in realistic AOS:

- Scattering and absorption by molecules, clouds and aerosols in the atmosphere
- Reflection and refraction by the ocean surface including the effects of surface roughness, shadowing, and multiple scattering
- Scattering by white caps, streaks, and floating substances such as oil slicks and biogenic films
- Scattering and absorption in the ocean by pure water, dissolved substances, and suspended matter
- Inelastic radiative processes including Raman scattering by ocean waters, fluorescence by dissolved organic matter, and fluorescence by chlorophyll.

Furthermore, there are geometric concerns that play a role such as the sphericity of the Earth, 3-dimensional variability in scattering properties such as isolated clouds and plankton blooms, azimuthal variability caused by e.g., oriented particles and wind-directionality of the ocean roughness, and the vicinity of land or sea-ice which leads to adjacency contamination of pixels viewed from space. Finally, there are numerical aspects that are important to consider for remote sensing (RS) applications such as the speed and validation of RT computations. The work done by our team touches upon many of these topics, the organization of which is presented as follows. In section “2 History of RT Methods for AOS: A Brief Overview,” we provide a brief historical overview of the RT methods applied to AOS during the last few decades. In section “3 Current RT Topics and Models: Heritage Studies, Discussions, and PACE Updates,” we focus on scattering in the ocean (“3.1 Ocean Body” section), by the ocean surface (“3.2 Ocean Surface” section), in the atmosphere (“3.3 Atmosphere” section), and by the entire AOS (“3.4 AOS models” section). In each of these subsections, we provide a brief overview of heritage work, followed by (when applicable) updated work performed by our team. For updated work, we differentiate between forward (FWD) RT studies that focus mainly on sensitivity analyses and/or simulating data sets, and inverse (INV) RT studies that involve also retrieval of PACE mission science products.

2 HISTORY OF RT METHODS FOR AOS: A BRIEF OVERVIEW

In what follows, we provide a brief historical overview of some of the RT studies performed on scattering of light in atmosphere-ocean systems. The list of studies does not do justice to the vast amount of work done on this topic by numerous researchers over a time span of many decades. For example this list focusses only on the progression of RT models and AOS models, i.e., models that provided a basis for subsequent refinements in FDW and INV RT models in other studies. Rather, the purpose of this list is to provide broad context for the research done by our team on RT methods and AOS properties to study PACE observations of oceans. We provide detailed historical information in the heritage overview part of each section. Methods and models that deal with RT in the atmosphere alone are reviewed by Hansen and Travis (1974), van de Hulst (1980), Lenoble (1985), and Stamnes (1986).

Chandrasekhar (1950) introduced methods to study reflected light and skylight of an atmosphere above a Lambertian surface. His methods were extended by Sekera (1961) to investigate scattering of polarized light in a Rayleigh atmosphere above a smooth ocean (see also Fraser and Walker, 1968). Later, Fraser (1981) and Ahmad and Fraser (1982) used another (i.e., Gauss-Seidel) method to study reflection of polarized light by a vertically inhomogeneous atmosphere that was bounded from below by a rough ocean surface.

A Monte Carlo approach was developed for an atmosphere above a smooth water surface plus water body (Plass and Kattawar, 1969, 1972), generalized later to include polarization (Kattawar et al., 1973) and a rough water surface (Plass et al., 1975, 1976; Tynes et al., 2001).

The method of successive orders of scattering without polarization was used by Raschke (1972) and later by Quenzel and Kaestner (1980) for RT computations in an atmosphere with aerosols and molecules above a rough ocean surface and ocean body. Chami et al. (2001) included polarization, but used a smooth ocean surface. (Chami et al., 2015) upgraded their code to include a rough ocean surface. Zhai et al. (2009, 2010) developed a polarized RT code based on this method that included both flat and rough ocean surfaces, which was later upgraded to account for inelastic radiative processes in ocean waters (Zhai et al., 2015, 2017a,b, 2018).

The adding method (van de Hulst, 1963) extended to include polarization by Hansen (1971) and Hovenier (1971) was used by Takashima (1974, 1975) for RT computations of polarized light in an atmosphere-surface system. This work was later updated to include an ocean body with a rough interface (Takashima, 1985; Takashima and Masuda, 1985; Masuda and Takashima, 1986, 1988).

Tanaka and Nakajima (1977) applied the matrix operator method, which is a variant of the adding method, without polarization for an atmosphere above a water body with a smooth surface. This method was later generalized to include a rough ocean surface by Nakajima and Tanaka (1983) and Fischer and Grassl (1984). Polarization was included for such systems by He et al. (2010) and Hollstein and Fischer (2012).

Dougherty (1989) used invariant imbedding techniques to study reflection without polarization by an ocean body covered by a smooth surface but no atmosphere. Mobley (1989, 1994) included a rough ocean surface in his Hydrolight program, and recently worked on including polarization for isolated rough ocean surfaces (Mobley, 2015) and ocean bodies (Mobley, 2018). Mishchenko and Travis (1997) employed a similar method including polarization for an atmosphere above a rough surface but no ocean body.

The Discrete-Ordinate RT method, introduced by Stamnes et al. (1988) for RT computations without polarization, was applied by Jin and Stamnes (1994) to an atmosphere above an ocean body with a smooth surface. Jin et al. (2004) subsequently included a rough ocean surface for such computations. Meanwhile Schultz et al. (1999) expanded this method to include polarization, which was applied by Sommersten et al. (2009, 2010) to atmosphere-ocean systems albeit with a smooth ocean surface.

Other authors opted to use a combination of the above-mentioned RT methods. For example, Chowdhary et al. (1995) applied the invariant imbedding method for the ocean body and used the adding method to include a rough ocean surface and atmosphere. Ota et al. (2010) used the Discrete-Ordinate RT method for homogeneous atmosphere and ocean layers, and used the matrix operator method to combine these results and to include a rough ocean surface. Xu et al. (2016) applied the Markov chain method for inhomogeneous layers and the adding method for homogeneous layers in the atmosphere and ocean, and used again the adding method to couple these layers and include a rough ocean surface. Polarization was taken into account in all of these combined RT methods.

The RT methods and AOS models listed above show a gradual trend from scalar computations for oceans with a smooth surface toward including polarization of light and considering rough ocean surfaces. However, most current RT methods still ignore inelastic radiative processes in the ocean, and most current AOS models still assume the atmosphere and ocean to be plane-parallel and horizontally homogeneous. In addition, most current RT methods apply (if not ignore altogether) simplified corrections for whitecaps, shadowing effects, and multiple scattering in rough ocean surfaces. Furthermore, much work still needs to be done in linking robust RT computations for realistic atmosphere-ocean systems to bio-optical modeling of ocean color. A driving constrain for PACE is to retrieve water-leaving radiance to better than 5% (10%) in the VIS (UV), and to retrieve properties of the atmosphere and ocean from this radiance with better accuracies than from heritage ocean color and atmosphere sensors. This requires among others more flexible bio-optical models that can also be applied to UV radiance, more realistic scattering matrices for marine particulates, better estimates of (in)elastic scattering and absorption by pure sea water, and less assumptions made for AOS models. Finally, there are no extended, peer-reviewed and accurate tabulated RT bench-mark results for fully coupled atmosphere-ocean models to validate any of the above-mentioned methods to accuracies consistent with PACE measurements. The next section provides a summary of work done by the 2014–2017 PACE Science Team that touches upon many of these topics.

3 CURRENT RT TOPICS AND MODELS: HERITAGE STUDIES, DISCUSSION, AND PACE UPDATES

3.1 Ocean Body

3.1.1 Particulate Scattering

Heritage studies: particulate scattering functions and scattering matrices

Radiative transfer models describing the angular distribution of the total and polarized radiance that is singly scattered by marine particulates can be classified into (**A**) those derived from measurements, (**B**) those computed for predefined particulates, and (**C**) those approximated with analytical expressions. Among the most widely used RT models belonging to class **A** are the early tabulated normalized scattering function ($\tilde{\beta}$) data provided by Petzold (1972), and the early tabulated normalized scattering matrix ($\tilde{\boldsymbol{\beta}}$) data provided by Voss and Fry (1984). Such models have the clear advantage of producing realistic bidirectional reflectance distribution functions (BRDFs) for water-leaving radiance in multiple scattering computations. However, due to their limited coverage of water types and/or averaging over data sets, they cannot replicate the variability in bidirectional scattering by marine particulates seen in laboratory (e.g., Volten et al., 1998; Witowski et al., 1998) or ocean (Mobley et al., 2002; Sullivan and Twardowski, 2009; Zhang et al., 2011; Twardowski et al., 2012) measurements. In addition, the Petzold volume scattering function data appear to be affected by an error such as stray light reflections in the near backward, which becomes prominent/obvious in his clear water dataset which do not agree with theory, other $\tilde{\beta}$ measurements, or satisfy closure with simulated apparent optical properties (i.e., properties that depend on the ambient light field). The work by Sullivan and Twardowski (2009) represents another example of Class **A** models. Here, the focus is placed on approximating the shape of the scattering function in the backscattering hemisphere based on extensive field measurements. Note that their results agree with the analytical Fournier-Forand scattering functions discussed below for Class **C** models.

Radiative transfer models belonging to class **B** typically assume the particles to be spheres that follow a Junge-type (power-law) size distribution with exponent γ (see **Table 2**) ranging between $3 \leq \gamma \leq 5$ (Stramski and Kiefer, 1991). Furthermore they typically assume such particles to be homogeneous with real refractives index m that can be grouped into two or more classes (Gordon and Brown, 1972; Zaneveld et al., 1974), i.e., either falling between $1.02 \leq m \leq 1.10$ for plankton-like organic particles (Spinrad and Brown, 1986; Aas, 1996) or between $1.15 \leq m \leq 1.25$ for mineral-like inorganic particles (Woźniak and Stramski, 2004). Variations in the distribution of singly scattered light can be replicated with these models by varying γ and/or m for a single polydisperse population (Twardowski et al., 2001), or by varying the mixing ratio of two (or more) modes of polydisperse particles that each have their own fixed set of (γ, m) values (Chowdhary et al., 2012; Kopelevich, 2012). Because of their variation with γ and m, class **B** models can be used to either mimic changes in particulate scattering functions in (empirical) remote sensing studies (Morel et al., 2002; Chowdhary et al., 2006; Ibrahim et al., 2016), or to retrieve m and/or γ from remote sensing observations (Loisel et al., 2008; Kostadinov et al., 2010). However, the goodness of RT and retrieval results obtained with class **B** models depends on the shape and internal structure assumed for marine particulates (Stramski et al., 2004). For example assuming spherical shapes for phytoplankton can create significant biases in the backscattering direction (Clavano et al., 2007), which become even larger when ignoring internal structures such as membrane walls and organelles (Kitchen and Zaneveld, 1992; Matthews and Bernard, 2013; Sun et al., 2016; Duforêt-Gaurier et al., 2018). Recently, Twardowski et al. (2012), Zhang et al. (2012, 2013, 2014b), Zhang and Gray (2015), and Xu G. et al. (2017) have started addressing the first issue by incorporating non-spherical (i.e., hexahedral) shapes for marine particulates in their retrieval studies of scattering functions. Other efforts to account for particle non-sphericity in RT simulations of underwater light are described by Gordon et al. (2009) and Gordon (2011) for the scattering properties of detached coccoliths, by Zhai et al. (2013) and Bi and Yang (2015) for the scattering properties of whole coccolithophores, and by Fournier and Neukermans (2017) and Neukermans and Fournier (2018) for the scattering properties of both detached coccoliths and whole coccolithophores. In addition, Organelli et al. (2018) started using coated spheres in RT computations to force closure with underwater light particulate backscattering and attenuation measurements, whereas Poulin et al. (2018) compared the performance of coated spheres and hexahedral shapes in closure studies of phytoplankton cultures.

Radiative transfer models belonging to class **C** use simple analytical expressions, instead of rigorous computations, to obtain scattering functions for marine particulates. Among the earliest and simplest models belonging to this class are (linear combinations of) Henyey-Greenstein functions (Henyey and Greenstein, 1941). These functions can be parameterized (Plass et al., 1985; Haltrin, 2002) in terms of the particulate backscattering efficiency $\tilde{b}_\mathrm{p}$ (defined in **Table 2**), but typically are not representative over the full angular range. Another, more widely used model belonging to this class is the Fournier-Forand scattering function (Fournier and Forand, 1994; Fournier and Jonasz, 1999; Mobley et al., 2002). This function is based on fundamental physical principles instead of empirical fitting, can be parameterized in terms of γ and m, and therefore retains the link to physical properties of marine particulates just like class **B** models. Mobley et al. (2002) further developed an approach to parameterize Fournier-Forand phase functions in terms of $\tilde{b}_\mathrm{p}$, where γ and m are effectively assumed to covary. Fournier-Forand phase functions are exceptionally accurate for a broad range of particle types. Sullivan and Twardowski (2009) showed a remarkably consistent shape for the particulate fraction in volume scattering function measurements collected in ten disparate field sites around the globe, including both Case I and II type waters. The observed phase function shape was consistent with analytical Fournier-Forand phase function shapes when the Mobley et al. (2002) approach was followed over the full natural range for polydispersions, i.e., $\tilde{b}_\mathrm{p}$ ranging from 0.003 to 0.03. The Sullivan and Twardowski (2009) phase functions shape has recently been shown to be applicable even in massive cyanobacterial blooms in Lake Erie (Moore et al., 2017). Simulations of BRDFs based on this single shape perform as well or better than more complex functions when compared to direct BRDF measurements, particularly in complex Case II waters (Gleason et al., 2012). This is consistent with previous works showing the BRDF for ocean color remote sensing is, to first order, controlled by the shape of scattering in the backward direction (Morel and Gentili, 1991, 1993; Gordon, 1993; Zaneveld, 1995; Morel et al., 2002). However, with the notable exception of Kokhanovsky (2003), class **C** models do not provide such parameterizations for the full (4 × 4) scattering matrix for representative polydispersions that are needed to perform RT computations of polarized underwater light. We remark that many models belonging to class **A** or **B** do provide scattering matrices, albeit not parameterized in terms of $\tilde{b}_\mathrm{p}$, γ or m.

Finally, there are hybrid RT models that use the scattering matrices of class **A** models except for first normalizing them by their scattering function, and then multiplying them by the parameterized functions of class **C** models (e.g., Adams and Kattawar, 1993; Zhai et al., 2010; You et al., 2011; Gu et al., 2016; Xu et al., 2016). Such hybrid models combine the advantages of class **A** for realistic scattering matrices and of class **C** models for variations in the scattering function. However, they still lack variability for the other scattering matrix elements. A potential solution to mitigate this problem is to adopt the parameterization provided by Kokhanovsky (2003) for the other scattering matrix elements. In this approach, taken by Zhai et al. (2015), the parameterization of the other scattering elements occurs in terms of the underwater light DoLP instead of $\tilde{b}_\mathrm{p}$, γ and m. But to make this approach completely self-consistent for all scattering matrix elements, one still needs to relate variations in DoLP to variations in $\tilde{b}_\mathrm{p}$, γ and m.

PACE updates (INV RT studies): plankton scattering matrices

To investigate the relative importance of plankton shapes and internal structures in INV RT studies of underwater light scattering, computations were initialized to compare the scattering matrices for four classes of particles: (**I**) homogeneous and spherical; (**II**) homogeneous and non-spherical; (**III**) inhomogeneous and spherical; and (**IV**) inhomogeneous and non-spherical (Chowdhary, Liu et al., unpublished). Class **I** particles are known to scatter less light in the backward direction than class **II**, **III**, and **IV** particles. It has been suggested that this plays a role in explaining the so-called missing backscattering enigma in underwater light scattering computations for micrometer-sized marine particles when compared to underwater light measurements (Stramski and Kiefer, 1991; Stramski et al., 2004). While scattering by sub-micron particles is favored by some to explain this enigma (Stramski and Wózniak, 2005) even when taking non-sphericity into account (Zhang and Gray, 2015, but see Clavano et al., 2007), one cannot ignore the large increase in backscattered light when taking internal structures such as wall membranes and organelles into account (Meyer, 1979; Bernard et al., 2009; Dall'Olmo et al., 2009; Sun et al., 2016; Duforêt-Gaurier et al., 2018; Organelli et al., 2018).

Details of the four classes of particles considered thus far are illustrated in **Figure 1A**. In this panel, *chloro*, *cyto*, *mito*, *nucl*, and *vac* stand for chloroplast, cytoplasma, mitochondria, nucleus, and vacuole, respectively. The surface-equivalent diameter of each particle is kept at 1 μm. The diameter of the organelles varies between 0.3 (*mito*), 0.4 (*nucl*, *vac*) and 0.5 μm (*chloro*), and thickness of the membrane wall (if present) is 0.1 μm. Also shown are scattering matrix examples in **Figure 1B** that were computed for some of these particles for a wavelength of 0.55 μm. These initial computations show that (i) internal structures increase the radiance scattered in the backward direction by several factors compared to variations in particle shape; and (ii) only variations in particle shape can create the magnitude of deviations from unity in the (2,2) scattering matrix element seen by Voss and Fry (1984). Observation (i) is consistent with the scattering matrix analyses by Quinby-Hunt et al. (1989). It strongly suggests that, in addition to colloid particles, one needs to consider internal structures of plankton-like particles when comparing underwater light scattering computations with backscattering efficiency $\tilde{b}_\mathrm{p}$ data for particulate scattering [this is also supported by the $b_{\mathrm{b,p}}$ (given in Eq. 1) data analyses in Dall'Olmo et al. (2009)]. Observation (ii) further suggests that ocean depth profiles of Lidar Depolarization Ratio δ_L (defined in **Table 2**) obtained from airborne observations (Hu et al., 2016) such as the one shown in **Figure 1C** are more sensitive to particle shape than to particle inhomogeneity. In addition, computations of $\tilde{b}_\mathrm{p}$ and δ_L performed for an ensemble of Class **II** particles with an equi-probable distribution of spheroid shapes show (see **Figure 1D**) that they exhibit quasi-orthogonal sensitivities to variations in the size and bulk composition of large marine particulates. Note also from **Figures 1C,D** that HSRL retrievals of δ_L are consistent with $\gamma > 4$ when assuming equi-probable distributions of spheroid shapes. The next steps in this line of research consist of obtaining representative and optically relevant shapes and internal structures of plankton particles that can be used in INV RT studies to retrieve $\tilde{b}$ and δ_L from *in situ* and lidar measurements, respectively. Emerging particle characterization methods such as *in situ* holographic imaging (Talapatra et al., 2013; Nayak et al., 2017) are also expected to aid in development and validation of such a model.

PACE updates (INV RT studies): particulate scattering functions, I

Recent work has verified the excellent accuracy of the Fournier-Forand analytical phase function in describing shapes of $\tilde{\beta}$ across the angular range near zero to 170°. Field measurements of the quantity $\beta \equiv b \times \tilde{\beta}$, i.e., of the volume scattering function (VSF), have been made using a combination of a custom Multi-Angle SCattering Optical Tool (MASCOT) resolving the VSF from 10° to 170° in 10° increments, and the Sequoia Type-B LISST resolving the near-forward VSF from 0.079° to 12.9° in 32 log-spaced increments. Fournier-Forand phase functions can be least-squares fit directly to these measured VSFs. When doing this, root-mean-square (RMS) errors <10% are typically observed over the full 6 order of magnitude VSF range. Despite the excellent accuracy of the Fournier-Forand analytical model, a systematic underestimation can still be observed in some cases in the $\sim$1° to 70° range. This underestimation was also recently noted by Harmel et al. (2016) in measurements of polydisperse Arizona Road Dust suspensions. The systematic nature of the bias indicated there may be the possibility of invoking a fitting method that may yet enhance accuracy. In collaboration with Dr. Tim Moore (UNH), a two cluster model was developed to fit VSFs that was able to effectively fit the mid-angle range, reducing RMS errors relative to fitting the Fournier-Forand function, with RMS errors in some cases decreasing from 17–18% to 3–7% (Twardowski et al., in preparation) (**Figure 2**). For INV RT models dependent on VSF shape (Zaneveld, 1995; Twardowski and Tonizzo, 2018), such a statistical model introduces one additional variable describing the mixing of the two clusters to reproduce the shape of the complete VSF, or it can be used to extrapolate or interpolate phase function shape from limited ancillary scattering measurements.

The two clusters are purely statistical quantities, i.e., they are two functions that, when mixed, minimized errors in describing the shapes of VSFs. Applying these functions to a much larger MASCOT VSF data set resulted in very low RMS errors, <10% in all cases except Hawaii, where signal-to-noise issues in very clear water are also significantly impacting RMS error (**Table 3**). Results suggest naturally observed VSFs in the 10° to 170° range may be represented with excellent accuracy with a function having only two degrees of freedom, with one variable being essentially a concentration metric and the other a mixing (shape) metric. While the two cluster fitting method provided optimal fits, a drawback is the loss of any physical meaning of the fit. The result of the two cluster fitting method are two amplitudes, one for each cluster, whereas the Fournier-Forand fits result in physically meaningful bulk refractive indices *m* and

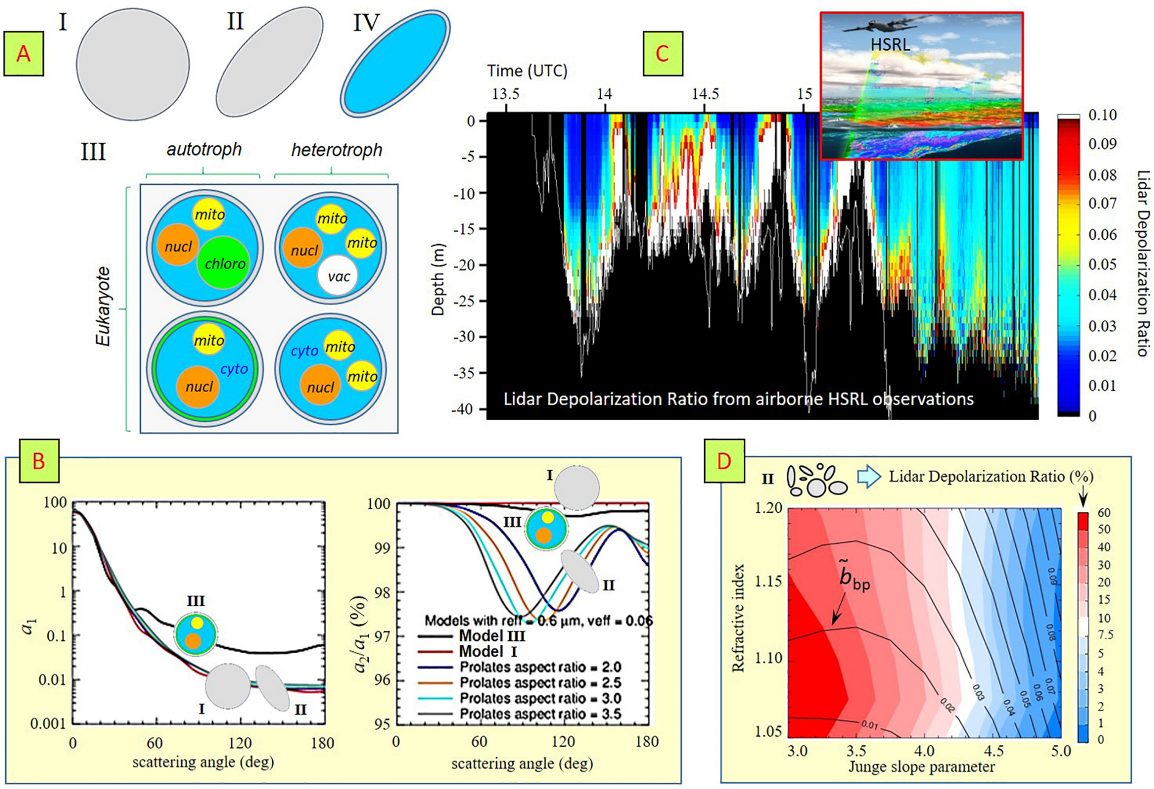

FIGURE 1 | (A) Particulate classes considered for plankton particles. Class **I** = spherical and homogeneous; Class **II** = non-spherical and homogeneous; Class **III** = spherical and inhomogeneous, Class **IV** = non-spherical and inhomogeneous. Class **III** and **IV** models contain a membrane wall and are filled with cytoplasm ("cyto"). Class **III** models contain one or more of the following organelles: chloroplast ("chloro"), mitochondria ("mito"), nucleus ("nucl"), vacuole ("vac"). **(B)** Scattering matrix element (1,1) (left diagram: a_1) and normalized scattering matrix element (2,2) (left diagram: a_2/a_1) computed for Class **I**, **II**, and **III** particles. **(C)** Ocean depth profile of lidar depolarization ratio δ_L example obtained by HSRL at $\lambda = 532$ nm during the NAAMES field campaign. The lower white curve marks the physical ocean bottom. **(D)** Lidar depolarization ratios and backscattering efficiencies computed at $\lambda = 550$ nm for randomly oriented Class **II** particles as a function of Junge size distribution exponent and refractive index.

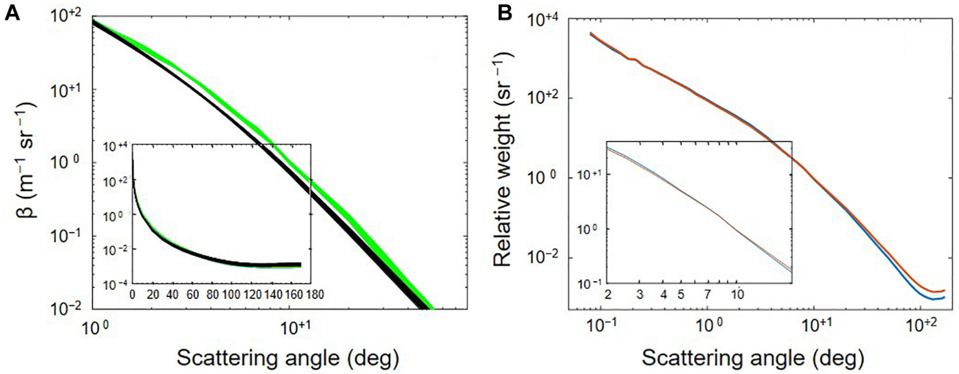

FIGURE 2 | (A) Fifteen, 1-m binned VSFs (green) from a single profile collected in the New York bight 11/2007, highlighting the ~1° to 70° range where Fournier-Forand phase function fits (black) systematically underestimate. Inset shows semi-log scale over full range. RMS error for the profile was 17.5%. **(B)** Two fitting clusters for data collected in the New York bight, derived using the method of Moore et al. (2009, 2014, see text). The vertical axis (i.e., relative weight) corresponds to β normalized by its integrated value over available scattering angles. One cluster exhibits about twice the amount of scattering in the backward direction relative to the other. There is also a cross-over point at 7° (see inset). Fitting the same profile data from panel **(B)** with the 2 clusters model results in an improved RMSE of 7%.

particle size distribution slopes γ, along with a scaling factor representing concentration.

PACE updates (INV RT studies): particulate scattering functions, II

Different from the idealized Fournier-Forand phase function (Fournier and Forand, 1994), simplified two-parameter models (Chowdhary et al., 2012; Kopelevich, 2012), or statistical two cluster approach described above, Zhang et al. (2011) and Twardowski et al. (2012) developed a theoretical approach to represent scattering functions using various particle subpopulations, each of which corresponds to an optically unique particle species that follows a log-normal size distribution $n(r)$. In Zhang et al. (2011), the particles assume spherical shapes and in Twardowski et al. (2012), the particles assume non-spherical shapes consisting of asymmetrical hexahedra for inorganic mineral particles (Bi et al., 2010) and Lorenz-Mie theory for coated bubbles (Czerski et al., 2011; Zhang et al., 2011). Later, asymmetrical hexahedra shape was applied to organic particles (Zhang et al., 2012). Through sensitivity analyses over the ranges of published size distributions and composition for oceanic particles, extensive libraries of distinctive particle phase functions have been built to represent the angular scattering and to serve as fingerprints for various oceanic particle species through inversion (Zhang et al., 2011, 2012; Twardowski et al., 2012).

With this particle phase function library, a measured VSF can be inverted to identify and quantify the scattering coefficient and the size distribution of the particle species (**Figure 3A**). The particle subpopulations or species identified via inversion represent the biogeochemical origin to the observed angular scattering. This approach has been applied to VSFs measured by the MASCOT mentioned above and another prototype volume scattering function sensor, Multispectral Volume Scattering Meter (MVSM), which resolves VSFs from 0.5° to 179° in 0.25° increments at eight wavelengths (Lee and Lewis, 2003). The results have been successfully validated in several studies with independent measurements. That is, the bulk particle size distribution $n(r)$ derived from the VSF-inversion is consistent with the Laser *in situ* Scattering and Transmissometery (LISST)-based estimates for particles of sizes greater than 2.5 μm, with an overall agreement of within 10% evaluated in three coastal waters (Chesapeake Bay, Monterey Bay, and Mobile Bay) (Zhang et al., 2012; also see **Figure 3C**). Czerski et al. (2011) and Twardowski et al. (2012) estimated the dynamics of bubble populations of sizes $< 30\ \mu$m during active wave breaking, where the optical volume scattering and acoustical determinations agreed well. Using the filter pore size as a threshold, Zhang et al. (2013) partitioned the inverted subpopulations into particulate and "dissolved" fractions (see **Figure 3B**), and further extracted phytoplankton particles using refractive indices $m = 1.04$ and 1.06 (Aas, 1996) from the particulate fraction. In support of their VSF inversions, Zhang et al. (2013, **Figure 2**) used an observed relationship between phytoplankton cell sizes and chlorophyll concentration to estimate the total chlorophyll concentration from their retrieved phytoplankton sizes and compared it favorably (Pearson correlation coefficient $r = 68\%$) with chlorophyll estimates obtained from High-Performance Liquid Chromatography (HPLC) measurements. Similarly, Zhang et al. (2014b) estimated the mass for particulate inorganic matter and particulate organic matter, with results comparing well with the laboratory gravimetric determinations in both Monterey Bay and Mobile Bay.

TABLE 3 | Percent (%) RMSE results after fitting two clusters to VSF data collected around the globe.

Data set	%RMSE	*n*
NY bight, 11/2007	1.3	296
NY bight, 07/2008	3.9	62
San Diego coast, 01/2008	8.7	34
Ligurian Sea, 10/2008	6.9	649
Hawaii, 09/2009	11.0	1575
Lake Erie, 08/2014	5.1	8
NW Atlantic, 08/2014	6.4	2117

Results apply to only MASCOT VSF data. All data binned to 1 m.

Over the entire angular range of the volume scattering, varying particle composition can change the particle VSF in terms of its shape. For example, the change of forward scattering VSF, when normalized by the total scattering coefficient could vary over 3–4 orders of magnitude. However, within the angular range of 90° to 180°, there are different findings regarding shape variability. Sullivan and Twardowski (2009) found that the backscattering shape as revealed from the MASCOT measurements was relatively constrained. That is, they found errors of 5% or less in fitting a single shape function from 90° to 170° for an extensive, global VSF data set, suggesting a more or less invariant backscattering shape. In contrast, Zhang et al. (2017) has recently found that backscattering shape, i.e., VSFs from 90° to 180°, as measured by the MVSM in three coastal waters around United States and in North Atlantic Ocean, varied up to a factor of two (**Figure 4B**). These disparate findings, which are based on measurements from two different prototype instruments over different waters, have yet to be resolved. The backward shape has a strong influence on the remote sensing BRDF, where about 97% of total variability observed in remote sensing reflectance (Rrs – see **Table 2**) over different viewing angles is due to the change in the detailed VSF shape over the backward angular range (Xiong et al., 2017). On the other hand, only 27% variability in the Rrs BRDF is attributable to the backscattering efficiency $\tilde{b}_\mathrm{b}$. Therefore, to meet the 5% PACE retrieval requirement for water-leaving radiance, we need to further improve our knowledge on backward variability of VSF to constrain the estimate of BRDF, which is particularly important for the PACE OCI instrument that has a wide field of view. Both field observations and theoretical studies have also found the backward shape of the VSFs of oceanic particles, defined as $\beta_\mathrm{p}(\theta)/b_{\mathrm{b,p}}$ (where $b_{\mathrm{b,p}}$ is the particulate backscattering coefficient, *cf.* "3.1.2 Bio-Optical Models" section), exhibits minimum shape variability in the backward direction (Oishi, 1990; Zhang et al., 2014a). Boss and Pegau (2001) showed that the minimum variability at 120° can be explained from mixing of particulate VSFs and salt water.

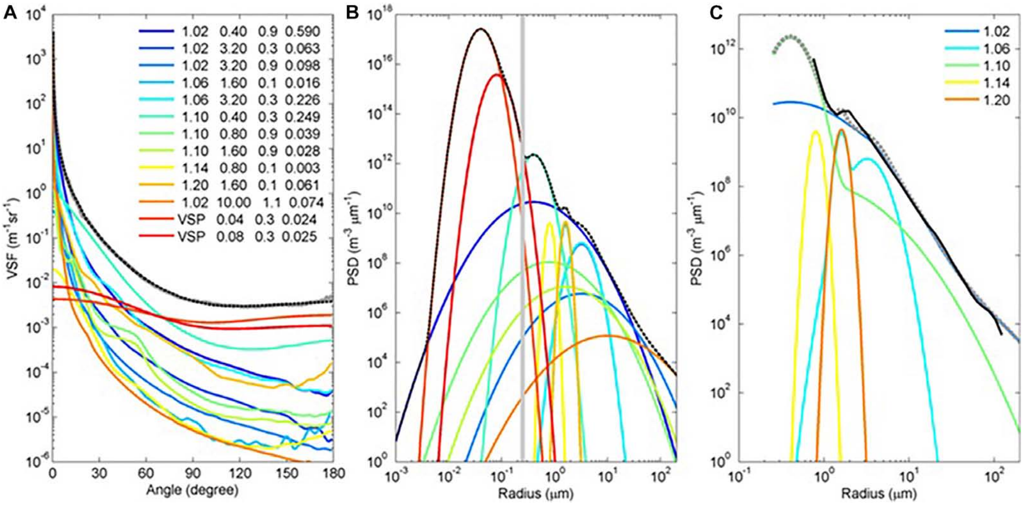

FIGURE 3 | An example demonstrating representing a measured VSF using various particle subpopulations. **(A)** The measured VSF (gray line) was disaggregated into subpopulations, whose corresponding refractive index, the mode size and standard deviation, and the scattering coefficient are shown in the legend. The dotted black line is the reconstructed VSF from these subpopulations. **(B)** Log-normal size distributions estimated for each of the subpopulations identified in panel **(A)**. The vertical gray line represents the filter size that commonly used in oceanography to partition particles into particulate and dissolved fractions. **(C)** The size distribution of subpopulations the particulate fraction are grouped by the refractive indices (shown in the legend). The dotted gray line is the bulk size distribution estimated by summing individual subpopulations. The black line is the size distribution independently derived from the LISST for comparison.

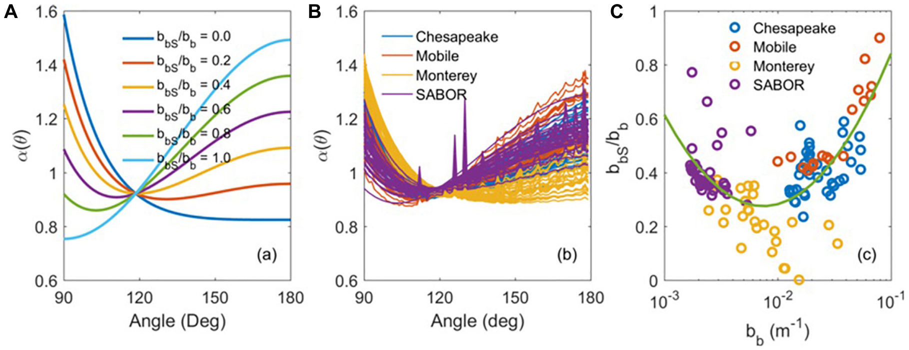

FIGURE 4 | (A) The variation of hypothetical particle scattering shapes (VSF at angles 90°–180° normalized by the backscattering coefficient) constructed by linear mixing of the two end members. The legend shows fractional b_b contributed by small particles. **(B)** The particle backscattering shapes measured in coastal waters of Chesapeake Bay, Mobile Bay, and Monterey Bay and during the SABOR cruise in North Atlantic Ocean. **(C)** The mixing ratios estimated by applying the two-component model in panel **(A)** to measured VSF shapes in panel **(B)** are shown as a function of particle backscattering coefficients.

Recently, however, Zhang et al. (2017) have suggested this minimum variability angle represents the intersection of two backscattering-normalized VSFs, one for particles of sizes smaller than the wavelength of light and the other for particulate sizes larger than the wavelength of light (**Figure 4A**). For each of the two end members, the backscattering shape can be analytically derived (Zhang et al., 2017). They also found that 90% of variability of the observed VSFs from 90° to 170° (**Figure 4B**) can be reproduced by this two-component model (**Figure 4C**). The minimum variability of scattering observed around 120° is intriguing and deserves further investigation.

Despite its fundamental role in ocean color remote sensing, the field-based observation of VSFs is still limited, which in turn circumscribes our understanding of the natural variability of angular scattering by oceanic particles and our ability to better model and/or retrieve these particles from the PACE mission. Efforts are being undertaken to expand the observation of particulate VSFs to a variety of waters with additional instruments and to improve our knowledge on the shape of particulate VSFs, particularly in the backward angles.

3.1.2 Bio-Optical Models

Heritage studies: parametrizations of RT quantities

Bio-optical models play a central role in characterizing ocean color spectra. Firstly, they identify inherent (i.e., independent) underwater light optical parameters that drive (and can therefore be retrieved from) the flux and spectrum of water-leaving radiance. These IOPs are (Gordon et al., 1975;

Preisendorfer, 1976; Morel and Prieur, 1977) the spectral absorption and scattering coefficients a and b, respectively (the sum of which gives the attenuation coefficient $c \equiv a + b$), and the backscattering efficiency $\tilde{b}$ which was mentioned earlier in section "3.1.1 Particulate Scattering". IOPs are tightly related to the fundamental RT quantities for underwater light scattering computations, i.e., the single scattering albedo ω ($\omega \equiv b/c$), the normalized scattering function $\tilde{\beta}$ ($\tilde{b} \equiv \int_{2\pi} \tilde{\beta}\, d\Omega$ where Ω stands for solid angle that is integrated over the backscattering hemisphere), and the optical thickness τ ($\tau \equiv \int c\, dz$ where z stands for physical thickness) of the ocean body. The RT quantities themselves vary with the abundance (i.e., number density), physical (e.g., size distribution and morphology) and chemical (e.g., organic versus inorganic) properties of suspended and dissolved marine matter. Hence, in principle, it is possible to retrieve e.g., the size distribution of marine particulates from IOPs. One of such retrieval was performed for phytoplankton by Kostadinov et al. (2009), who for this purpose assumed homogeneous spheres for the morphology of plankton particulates.

Secondly, bio-optical models provide a link between IOPs and the biological state of the ocean. That is, IOPs are commonly subdivided into contributions by water, phytoplankton, non-algal particles (NAP), and color dissolved organic matter (CDOM). Each of these contributions, except for water, are then represented by the product (or a sum of products) of a pre-defined specific spectrum (i.e., an eigenvector) and the amplitude of this spectrum (i.e., its eigenvalue). In the first generation of ocean color retrievals, it was customary (Morel, 1988; Morel and Maritorena, 2001) to parameterize the eigenvectors and eigenvalues of IOPs a, b and $\tilde{b}$ in terms of just 1 parameter: the concentration of Chlorophyll a ([Chla]), which is a photosynthetic pigment found in phytoplankton. Thus, the assumption made here was that the abundance and properties of each constituent in oceanic water (including NAP and CDOM) covaried with the concentration of phytoplankton. Such oceanic waters were collectively classified as Case I waters, while the remaining ocean waters, where the properties did not correlate well with chlorophyll and where inorganic matter could be important, were collectively classified as Case II waters. Case I waters were found to statistically represent open oceans well. Given that IOPs are tightly related to RT quantities (see discussion above), it is therefore possible for such oceanic waters to link variations in [Chla] to variations in the physical properties of marine particulates. For example, Kostadinov et al. (2009) found that their retrieval of pico (small-sized) and micro (large-sized) phytoplankton are highly correlated with small and large values of remotely sensed [Chla], respectively. However, bio-optical models are commonly derived from empirical fits to data that can be extremely noisy – see e.g., Bricaud et al. (1998) for phytoplankton absorption coefficient a_{ph}, and Huot et al. (2008) for b and $\tilde{b}$. Hence, the goodness and application of correlating the retrieval of physical properties such as phytoplankton size to the retrieval of biological properties such as [Chla] depends on the assumptions (e.g., plankton morphology) and uncertainties (e.g., scatter in bio-optical relations) associated with each retrieval.

The initial custom of classifying ocean waters into two opposite cases, and closely tying one of them to [Chla], has evolved over the past 2 decades (Mobley et al., 2004). For example, Aeolian dust storms are known to be an important source for suspended mineral particles in the open ocean (Johnson et al., 2010). The abundance and properties of these particles clearly do not co-vary with [Chla], although they provide nutrients that may lead to plankton blooms (Behrenfeld et al., 1996; Behrenfeld and Kolber, 1999; Boyd et al., 2000, 2009; Bishop et al., 2002). Plankton blooms themselves such as coccolithophore outbreaks can lead to excessive amounts of suspended mineral particulates whose scattering properties do not co-vary with [Chla] either (Balch et al., 2004). Furthermore, the bio-optical relationship between [Chla] and the absorption by CDOM, which is created by a variety of processes (Nelson and Siegel, 2013), is not only less tight than between e.g., [Chla] and b (Morel, 2009), but it also deteriorates quickly for UV wavelengths (Morel et al., 2007a). In addition, the temporal cycles of CDOM and [Chla] do not exactly match each other (Hu et al., 2006; Lee et al., 2010). The current generation of bio-optical models acknowledges these concerns by relaxing the interdependency of IOPs. Werdell et al. (2013a, 2018) provide an overview of the current state of bio-optical models. That is, eigenvalues of IOPs do not necessarily co-vary with [Chla] and eigenvectors may be either prescribed or retrieved/computed from ocean color data in real time. The implication is that the RT quantities $\{\omega, \tau, \tilde{\beta}\}$ used to perform underwater light scattering computations then also do not necessarily co-vary with [Chla] or even with one another. Such relaxations in IOPs remain to be adopted in current generation RT studies of polarized light emerging from AOS models (e.g., Chowdhary et al., 2006; Hasekamp et al., 2011; Knobelspiesse et al., 2012; Zhai et al., 2015). In addition, the (default) IOPs discussed in Werdell et al. (2013a) are for the wavelength (λ) range of 400–700 nm. This range, which was originally proposed by IOCCG (International Ocean Color Coordinating Group) in its *IOCCG report #5* (2005) for the creation of synthetic IOP data, needs to be extended into the UV for RT studies to be applicable to PACE observations (see Werdell et al., 2018).

PACE updates (INV RT studies): using ocean color to retrieve/constrain aerosol

Heritage bio-optical models have traditionally been used in RT studies to invert ocean spectra. For remote sensing observations from space, one has to first retrieve and subsequently subtract the contribution of atmospheric scattering in order to obtain these ocean spectra. Such retrievals of atmospheric scattering contribution are also a requirement for the inversion of aerosol properties from spaceborne observations over ocean. Two types of methods can be adopted to accomplish this separation of atmospheric and oceanic signals in space-borne observations. In the first method (called the 2-step approach), this is done by focusing on the spectral variation of radiance in the NIR and/or the SWIR where the ocean becomes black (because of strong absorption by pure sea water) to select an aerosol model that is capable of reproducing this radiance. This method, which has historically been used for atmospheric correction of spaceborne ocean color observations (Gordon and Wang, 1994b; Gao et al., 2000; Wang and Shi, 2007; Ahmad et al., 2010), does not require any *a priori* information of the ocean. Hence in this method, bio-optical models are only used to invert oceanic signals *after* characterizing the atmospheric signal. For more details on this method, see IOCCG (2010) and Frouin et al. (2019). In the second method (called the 1-step approach), the atmospheric scattering contribution is retrieved from the spectral variation of radiance in the NIR/SWIR *and* in the VIS. Here, one needs bio-optical models to account for the contribution of water-leaving radiance in the VIS *as part of* charactering atmospheric signals. The bio-optical models used in this second method can be divided into type (i) and type (ii) models, depending on their purpose. Type (i) models are used to only approximate water-leaving radiances for the purpose of improving the retrieval of aerosol properties in the VIS (note though that the results of such aerosol retrievals can subsequently be used to perform atmospheric correction for retrieval of the actual ocean color). Such use of bio-optical models is seen in Xu et al. (2016). On the other hand, the purpose of type (ii) models is to not only retrieve aerosol properties but to also retrieve ocean properties at the same time. This approach is used by Chowdhary et al. (2012). Type (ii) models are therefore similar to (if not the same as) the bio-optical models used to invert ocean spectra in the 2-step approach described above. Both Chowdhary et al. (2012) and Xu et al. (2016) pioneered the use bio-optical models to analyze polarimetric remote sensing observations over oceans. However, they both adopted a simple bio-optical model, i.e., one where all the IOPs are parameterized in terms of [Chla] only. Such models cannot account for natural variations in water-leaving radiances (which can be larger than PACE's retrieval threshold value of 5%; *cf.* "1.1 The PACE Mission" section) that occur for a given [Chla]. This does not necessarily pose a problem for type (i) bio-optical models that are only used to improve aerosol retrievals in the VIS. Note that to mitigate possible errors of single-parameter-based bio-optical models, Xu et al. (2016) allow adjustments of water-leaving radiance in their type (i) bio-optical model by adding Lambertian terms. However, type (ii) bio-optical models are used to also retrieve IOPs, and require therefore more parameters to describe complex waters. The accuracy requirements for IOP retrievals are not yet defined for PACE (*cf.* "1.1 The PACE Mission" section). Hence, evaluating the IOP retrieval performance of type (ii) bio-optical models occurs by comparing with co-located independent IOP measurement sets. Following the evolution of bio-optical models discussed in the preceding heritage section, the current PACE Science Team focused on incorporating more parameters in both type (i) and (ii) bio-optical models for analyses of VIS polarimetric observations.

The hydrosol model employed by Chowdhary et al. (2012) is based on using a [Chla]-driven type (ii) bio-optical model to constrain the RT properties of a mixture of plankton and detritus particles. This so-called D-P (Detritus-Plankton) hydrosol model, which can be applied to underwater scattering of polarized light and which reproduces classical (i.e., statistically averaged) "Case I" ocean color variations, is discussed in detail by Chowdhary et al. (2006). To relax the dependency on [Chla], the parameterizations of IOPs in the D-P hydrosol model were updated to accommodate the retrieval of three separate IOPs. The result of these updates is the second generation D-P model, hereafter referred to as the D-P II hydrosol model (see **Figures 5A,C**). The D-P II model adopts the following IOP parameterizations in terms of [Chla] and wavelength λ:

$$b_{b,p}(\lambda) \equiv \tilde{b}_p \times b_p(\lambda) = b_{b,p}(\lambda_0)\,(\lambda/\lambda_0)^k, \tag{1}$$

$$a_{ph}(\lambda) = \left[\mathrm{Chla}\right]\,\hat{a}_{ph}(\lambda), \tag{2}$$

$$a_{cdm}(\lambda) \equiv a_{dm}(\lambda) + a_y(\lambda) \cong a_{cdm}(\lambda_0)\exp\left\{-\alpha_{cdm}(\lambda-\lambda_0)\right\} \tag{3}$$

where the reference wavelength λ_0 is 443 nm, and from Morel and Maritorena (2001).

$$k = \begin{cases} 0.5\left(\log_{10}\left[\mathrm{Chla}\right] - 0.3\right), & 0.02 \leq \left[\mathrm{Chla}\right] \leq 2 \text{ mg m}^{-3} \\ 0, & \left[\mathrm{Chla}\right] > 2 \text{ mg m}^{-3}. \end{cases} \tag{4}$$

Subscripts "p," "ph," "cdm," "dm," and "y" denote particulate, phytoplankton, colored detrital matter, detrital matter, and yellow substance (i.e., CDOM), respectively. For example, a_{dm} is the absorption coefficient for detrital matter, i.e., for the sum of phytoplankton and NAP matter.

Chowdhary et al. (2012) follow Siegel et al. (2002) in assigning the same spectral variation to $a_{dm}(\lambda)$ and $a_y(\lambda)$ because of the difficulty to differentiate between these properties in the inversion of ocean color spectra. Furthermore,

$$\hat{a}_{ph}(\lambda) = A(\lambda)\left[\mathrm{Chla}\right]^{B(\lambda)-1}, \tag{5}$$

$$a_{cdm}(\lambda_0) = a_{dm}(\lambda_0) + a_y(\lambda_0). \tag{6}$$

The parameterization in Eq. 5 is taken from Bricaud et al. (1995), with constants $A(\lambda)$ and $B(\lambda)$ tabulated by Bricaud et al. (1998, 1999). Note that these constants cover only the spectrum between $400 \leq \lambda \leq 700$ nm. The free parameters (i.e., eigenvalues) for the D-P II model are the backscattering coefficient $b_{b,p}$ at λ_0 in Eq. 1; the Chlorophyll *a* concentration [Chla] in Eq. 2; and the absorption coefficient a_{cdm} at $\lambda_0 = 443$ nm in Eq. 3. The prescribed and [Chla]-driven parameters (i.e., eigenvectors) for this hydrosol model are the power law exponent k in Eq. 1, the specific phytoplankton absorption coefficient $\hat{a}_{ph}(\lambda)$ in Eq. 2, and the spectral decay constant α_{cdm} for absorption by non-algae and dissolved matter in Eq. 3.

The set of parameterizations chosen for $b_{b,p}(\lambda)$, $a_{ph}(\lambda)$, and $a_{cdm}(\lambda)$ is close to the default configuration (DC) used for the generalized inherent optical properties (GIOP) software database that was developed by Werdell et al. (2013a). The exception is the [Chla]-driven exponent k for $b_{b,p}$ in Eq. 1, which is taken from Morel and Maritorena (2001) instead of retrieving it from water-leaving radiance measurements as in Lee et al. (2002). The D-P II model further adopts the same value of 0.018 nm^{-1} for α_{cdm} in

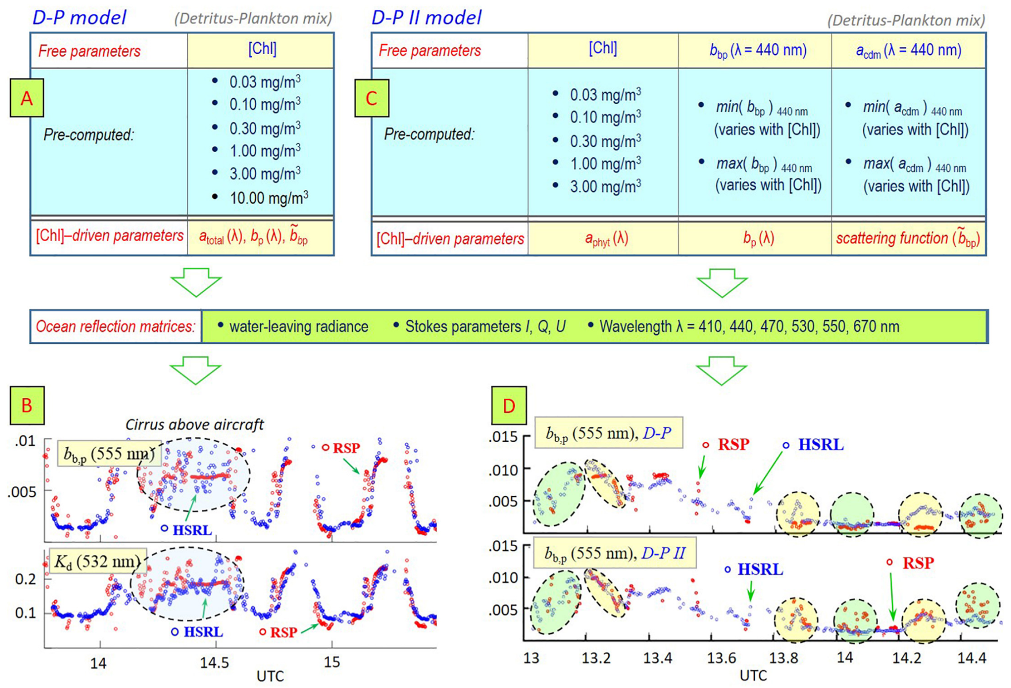

FIGURE 5 | (A) D-P model parameters used for RSP analyses. **(B)** Comparison for the SABOR campaign between $b_{\mathrm{b,p}}$ and K_{d} values that were retrieved from analyses of HSRL data and from analyses of RSP data using the D-P model. The scatter in the blue-shaded area coincides with the occurrence of cirrus clouds above the aircraft. **(C)** D-P II model parameters used for RSP analyses. **(D)** Comparison for the NAAMES campaign between $b_{\mathrm{b,p}}$ values that were retrieved from analyses of HSRL data and from analyses of RSP data using the D-P model (upper diagram) and the D-P II model (lower diagram). Yellow and green shaded areas correspond to regions of better and worse agreement when using the D-P II model.

Eq. 3 as was done for the GIOP-DC database. The RT quantities ω and $\tilde{\beta}$ for the D-P II model are computed in the same manner as for the D-P model (Chowdhary et al., 2006, 2012) except for (1) choosing Eqs 1–6 for the non-water absorption and scattering coefficients, and (2) using the ratio $b_{\mathrm{b,p}}/\tilde{b}_{\mathrm{p}}$ from Eq. 1 for the particulate scattering coefficient b_{p}.

To deploy the D-P II hydrosol model for analyses of air- and spaceborne polarimetric observations over oceans, rigorous underwater light computations were performed with the adding RT method to obtain reflection matrices of diffuse water-leaving radiance (that is, radiance that excludes the contribution of skylight reflected off the ocean surface alone). The ocean reflection matrices were computed only for Stokes parameters I, Q, and U (as defined in Hansen and Travis, 1974) that are measured by existing airborne multi-spectral, multi-angle polarimeters such as RSP (Cairns et al., 1999, 2003), airMSPI (Diner et al., 2013), HARP (Martins et al., 2014), and SPEX (Rietjens et al., 2015). Six wavelengths (410, 440, 470, 530, 550, and 670 nm), 60 viewing and 60 sun angles (both corresponding to 30 equidistant angles up to 64.8° and 30 Gauss integration points between 0° and 90°) were chosen for these matrices. For each wavelength and angle specification, 5 values were chosen for [Chla] (0.03, 0.1, 0.3, 1.0 and 3.0 mg/m^3), and 2 values were chosen for $b_{\mathrm{b,p}}(\lambda_0)$ and for $a_{\mathrm{cdm}}(\lambda_0)$ (corresponding to a lower and an upper limit for each of these parameters). The limits for $b_{\mathrm{b,p}}(\lambda_0)$ and $a_{\mathrm{cdm}}(\lambda_0)$, which are different for each [Chla] value, were determined from the synthetic IOP data sets computed in report #5 by IOCCG (2006). Underwater-light computations were performed using 60 Gauss integration points, and the D-P II scattering matrices were renormalized whenever necessary to conserve energy within 10^{-6}. Finally, each ocean reflection matrix was expanded in a Fourier series [using the supermatrix formalism described by de Haan et al. (1987)]. The terms in these allow the ocean reflection matrices to be obtained for arbitrary sun and viewing azimuth angle. Sixteen terms were used for this expansion to obtain an accuracy of 2×10^{-6} in reflectance units for the water-leaving radiance just above the ocean surface for all angles and [Chla] considered. This accuracy surpasses the PACE accuracy requirement of 5% (*cf.* "1.1 The PACE Mission" section) by at least an order of magnitude for all sun and viewing angles, all wavelengths, and all [Chla] values considered. In total, 1,728,000 (3×3) ocean reflection Fourier term matrices were produced. The D-P II ocean reflection matrices (as well as the matrices for the original D-P model) are publicly available on https://data.giss.nasa.gov/rad/ocean-matrices/, along with their performance analyses and a user manual.

Extensive numerical performance analyses demonstrated that the ocean color variations computed for the D-P II hydrosol model can reproduce those computed for the original D-P hydrosol model, which ensures consistency and continuity between past and future studies that use these detritus-plankton mixture models. Both the D-P and D-P II ocean reflection matrices are currently applied to analyses of concurrently obtained data by the Research Scanning Polarimeter (RSP) and the High-Spectral Resolution Lidar (HSRL) instruments in 3 field campaigns: the 2012 Two-Column Aerosol Project (TCAP) and the 2014 Ship-Aircraft Bio-Optical Research (SABOR) campaign (Stamnes et al., 2018), and the ongoing North Atlantic Aerosols and Marine Ecosystems Study (NAAMES) campaign. **Figure 5B** shows for SABOR a comparison between RSP and HSRL retrievals for the atmosphere and ocean. The agreement is surprisingly good (even for the indirect-retrieved diffuse attenuation coefficient K_{d}) given that the simple (1-parameter) D-P ocean reflection matrices were used for these retrievals. These data will be re-analyzed in the near future using the D-P II ocean reflection matrices. The same comparisons are shown in **Figure 5D** except for the NAAMES campaign using both the D-P (upper row charts) and D-P II (lower charts) ocean reflection matrices. The plankton particulates encountered during this campaign were noted to be unusually small for given [Chla]. This may explain why the RSP retrievals of $b_{\mathrm{b,p}}$ sometimes agree less well with the corresponding HSRL measurements (see green-shaded areas) when using the D-P II ocean reflection matrices than when using the D-P ocean reflection matrices. Note that the D-P and D-P II matrices reproduced the same water-leaving radiance for the NAAMES data analyses as evidenced by the retrieval of same aerosol properties (not shown here). Hence, trade-offs appear to be occurring between $b_{\mathrm{b,p}}$ and $\mathrm{a}_{\mathrm{cdm}}$ in the D-P II bio-optical model. More analyses of the data collected during NAAMES are currently being conducted to evaluate assumptions made for the IOPs in the D-P II hydrosol model (e.g., the spectral variation of $b_{\mathrm{b,p}}$ and a_{cdm} in Eqs 1 and 3, respectively).

Another remote sensing algorithm is being developed by a research group led by Peng-Wang Zhai at UMBC, which retrieves aerosols and water leaving radiance simultaneously. Their type (ii) bio-optical model is similar to the formulas outlined by Eqs 1–3, except that the scattering power law exponent k is treated as a retrieval free parameter. In addition, the α_{cdm} value is also treated as a free parameter. INV RT experiments are being performed to test the feasibility of retrieving the power law exponent for particle backscattering fraction. The ocean particulate scattering function are determined by the Founrier-Forand phase function based on backscattering fraction and the Mueller scattering matrix is determined by the measurements by Voss and Fry (1984). These adjustments are designed to accommodate different types of waters in which average laws are not followed. Numerical tests based on synthetic data generated by RT demonstrate that the algorithm can determine aerosol properties and water leaving radiance accurately even for ocean waters with significant sediment concentration (Gao et al., 2018).

PACE updates (FWD RT studies): synthetic data sets linking IOPs and Rrs

The performance of IOP inversion algorithms for PACE-like data will be evaluated by comparing the IOP retrievals with co-located independent IOP measurement sets (*cf.* "1.1 The PACE Mission" section). However, IOP measurement sets may not always be available for such performance evaluations. In addition, there are always measurement uncertainties which prevent conclusive evaluation of IOP inversion algorithms. To address these cases, the PACE Science Team created a synthetic dataset containing IOPs and remote-sensing reflectance Rrs. The overall scheme follows that adopted by the IOCCG Report 5 (IOCCG-OCAG, 2003; IOCCG, 2006), which was summarized in "*Models, parameters, and approaches that are used to generate wide range of absorption and backscattering spectra*," but here the spectral range is expanded (now 350–800 nm), along with wider variations of phytoplankton absorption spectra. Because Hydrolight (Mobley and Sundman, 2013) was used for the generation of Rrs from IOPs, the critical step for this synthetic dataset was the creation of reasonable IOPs spectra for both oceanic and coastal waters. Specifically and briefly, as articulated in IOCCG-OCAG (2003), the absorption (i.e., a) and backscattering (i.e., b_{b}) coefficients, the two key component IOPs for Rrs, were modeled as

$$a(\lambda) = a_{\mathrm{w}}(\lambda) + a_{\mathrm{ph}}(\lambda) + a_{\mathrm{dm}}(\lambda) + a_{\mathrm{y}}(\lambda) \tag{7a}$$

$$b_{\mathrm{b}}(\lambda) = b_{\mathrm{b,w}}(\lambda) + b_{\mathrm{b,ph}}(\lambda) + b_{\mathrm{b,dm}}(\lambda) \tag{7b}$$

Values of $a_{\mathrm{w}}(\lambda)$ were taken from combinations of Lee et al. (2015) (350–550 nm range), Pope and Fry (1997) (555–725 nm range), and Smith and Baker (1981) (730–800 nm range). From more than 4000 measured $a_{\mathrm{ph}}(\lambda)$ spectra (spanning 350–800 nm at 5 nm steps), 720 $a_{\mathrm{ph}}(\lambda)$ spectra were selected and divided into twelve groups with $a_{\mathrm{ph}}(440)$ ranging between $\sim$0.0014 and 39.0 m^{-1}, thus covering oligotrophic oceanic waters to waters with phytoplankton blooms.

Following IOCCG-OCAG (2003), a_{dm} and a_{y} were modeled as

$$a_{\mathrm{dm}}(\lambda) \equiv a_{\mathrm{dm}}(440)\exp\{-\alpha_{\mathrm{dm}}(\lambda - 440)\}, \tag{8a}$$

$$a_{\mathrm{y}}(\lambda) \equiv a_{\mathrm{y}}(440)\exp\left\{-\alpha_{\mathrm{y}}(\lambda - 440)\right\}, \tag{8b}$$

where the slope parameters α_{dm} and α_{y} were taken as constrained random values as in IOCCG-OCAG (2003), and $a_{\mathrm{dm}}(440)$ and $a_{\mathrm{y}}(440)$ were modeled as

$$a_{\mathrm{dm}}(440) = p_1 a_{\mathrm{ph}}(440), \tag{9}$$

$$a_{\mathrm{y}}(440) = p_2 a_{\mathrm{ph}}(440). \tag{10}$$

Parameters $p_1 \in \{0.1,\ 0.6\}$ and $p_2 \in \{0.1,\ 6.0\}$ were constrained random values so reasonable $a_{\mathrm{dm}}(440)$ and $a_{\mathrm{y}}(440)$ values were created for a given $a_{\mathrm{ph}}(440)$ (IOCCG-OCAG, 2003).

Values of $b_{\mathrm{b,w}}(\lambda)$ were taken from Zhang et al. (2009). Spectra of $b_{\mathrm{b,ph}}(\lambda)$ were also modeled as in IOCCG-OCAG (2003), where $b_{\mathrm{b,ph}}(\lambda)$ is

$$b_{\mathrm{b,ph}}(\lambda) = \tilde{b}_{\mathrm{ph}}\left(p_3\left[\mathrm{Chla}\right]^{0.63}\left[\frac{550}{\lambda}\right]^{n1} - a_{\mathrm{ph}}(\lambda)\right). \tag{11}$$

Here, $\tilde{b}_{\mathrm{ph}}$ is the backscattering efficiency of phytoplankton and a value of 1% was taken. Parameters $p_3 \in \{0.06,\ 0.6\}$ and

$n_1 \in \{-0.1,\ 2.0\}$ were random values as in IOCCG-OCAG (2003). Similarly, spectra of $b_{\mathrm{b,dm}}$ were modeled as

$$b_{\mathrm{b,dm}}(\lambda) = \tilde{b}_{\mathrm{dm}} \left(p_4 \left[\mathrm{Chla}\right]^{0.5} \left[\frac{550}{\lambda}\right]^{n2} \right) \tag{12}$$

where a value of 1.83% was assigned to the backscattering efficiency $\tilde{b}_{\mathrm{dm}}$ for detrital matter, with $p_4 \in \{0.06,\ 0.6\}$ and $n_2 \in \{-0.2,\ 2.2\}$ also random values, respectively.

3.1.3 Molecular Scattering

PACE discussions (FWD RT studies): pure seawater properties

A number of values for pure (sea)water absorption coefficient $a_{\mathrm{w}}(\lambda)$ have been estimated from laboratory measurements of pure water samples (Pope and Fry, 1997) or modeled using *in situ* measurements collected from hyper-oligotrophic regions of the ocean (Morel et al., 2007b; Lee et al., 2015). While recent work by Mason et al. (2016) have provided new, high accuracy measurements of *pure water* absorption in the UV and visible domain, these values are much lower than previously measured in the UV. On the other hand, Lee et al. (2015) have derived values for *seawater* in the UV that are significantly higher, which may be the result of UV absorption by dissolved inorganic constituents in seawater. Note that the Lee et al. (2015) coefficients were derived from optimizing a remote sensing reflectance inversion model instead of direct experimental measurement of water samples. The a_{w} values of Lee et al. (2015) and Mason et al. (2016) differ by several factors in the UV. The corresponding difference in water-leaving radiance (which is proportional to the inverse of total absorption a in Eq. 7) can for clear waters be much larger than the PACE retrieval requirements ("1.1 The PACE Mission" section). Hence, there is a clear need for research to better understand the role of absorption by dissolved inorganics in the UV such as oxygen, NO_3, Br^-, and other salt ions comprising sea salts that have significant absorption in the UV (Armstrong and Boalch, 1961; Ogura and Hanya, 1966; Johnson and Coletti, 2002; as cited in Lenoble, 1956; Copin-Montegut et al., 1971; Shifrin, 1988). These effects have received scarce attention in recent literature. At 230 nm, these constituents all have more than an order of magnitude higher absorption than the values of pure water absorption, with steeply increasing absorption at shorter UV wavelengths. An unresolved question is how much these constituents may absorb at wavelengths longer than 300 nm, as the tail absorption effects have typically not been studied with the required accuracy. Even relatively small contributions could be significant since pure water absorption is very low, particularly in the 320 to 420 nm range ($<\sim 0.005\ \mathrm{m}^{-1}$). Armstrong and Boalch (1961) found significant effects of sea salt absorption out to 400 nm, but rigorous purification steps were not taken, so it is unclear if their additions of artificial sea salts introduced organic contaminants.

In addition, the vibrational states and thermodynamic properties of seawater, and hence its optical properties, vary with changes in temperature (T) and/or salinity (S) in various regions of their spectra. Backscattering by pure seawater was often considered a "constant" and "well known" in remote sensing algorithms (e.g., Carder et al., 1999; Lee et al., 2002; Stramski et al., 2004; Twardowski et al., 2005; Werdell et al., 2013a), where common practice for several decades was to use a constant pure seawater backscattering spectra originating from Morel (1974). Note however, in the vast, clear oceanic waters, backscattering by pure seawater can contribute up to 90% to the total backscatter (Shifrin, 1988; Morel and Gentili, 1991; Twardowski et al., 2007). Therefore, uncertainties of just a few percent in $b_{\mathrm{b,w}}(\lambda)$ (the backscattering coefficient for water) can cause the water-leaving radiance to change by more than the 5% retrieval requirement for PACE (see section "1.1 The PACE Mission"). This also impacts estimating particulate backscatter $b_{\mathrm{b,p}}$ because backscattering by the pure seawater component must be subtracted from direct measurements or algorithm retrievals of total backscatter b_{b}. Accordingly, efforts have been made to measure and model the spectral T and S dependencies of $a_{\mathrm{w}}(\lambda)$ (Pegau et al., 1997; Twardowski et al., 1999; Sullivan et al., 2006; Jonasz and Fournier, 2007; Röttgers et al., 2014) and $\mathrm{b_{b,w}}(\lambda)$ (Morel, 1974; Buiteveld et al., 1994; Zhang et al., 2009). The importance of varying salinity and temperature in the computation of $b_{\mathrm{b,w}}(\lambda)$ has been investigated in Werdell et al. (2013b), and been found to have a noticeable effect on IOP retrieved (e.g., ∼3–10% change in retrieved particulate backscattering coefficient $b_{\mathrm{b,p}}$, 1–6% change in non-algae absorption coefficient a_{cdm}, and more importantly removal of a bias). About a decade ago, Zhang and Hu (2009) and Zhang et al. (2009) provided the most accurate theoretical description to date of pure seawater scattering as a function of the physical properties of water with variables of temperature, salinity, and pressure. Satellite observations of sea surface temperature (SST; Kilpatrick et al., 2001) and sea surface salinity (SSS; Lagerloef et al., 2008), as well as climatological values (Reynolds et al., 2002; Antonov et al., 2010), have made it now also possible to include T-S dependent $b_{\mathrm{b,w}}(\lambda)$ within inverse algorithms (Werdell et al., 2013b).

Another parameter that has a significant impact on $b_{\mathrm{b,w}}$ is the so-called depolarization ratio for pure seawater. The anisotropic nature of water molecules, which produces fluctuations in molecular orientations, is typically described in terms of the molecular depolarization ratio δ_{m}, which by definition is the ratio of horizontally polarized light to vertically polarized light at a scattering angle of 90° (see **Table 2**). The depolarization ratio values currently used by the optics community come from a single study conducted more than 40 years ago (Farinato and Rowell, 1976). In that work, three values were experimentally derived: $\delta_{\mathrm{m}} = 0.051$, 0.045, and 0.039, with progressively narrower filter bandwidth for stray light removal. Typically, the lowest one measured, $\delta_{\mathrm{m}} = 0.039$, is recommended because it was obtained with the least contamination of the stray light. This value is therefore, at this time, the accepted community value (Werdell et al., 2018). Pure water scattering in the blue decreases by more than 10% (which for clear ocean waters surpasses the PACE retrieval requirement for water-leaving radiance) when using $\delta_{\mathrm{m}} = 0.039$ relative to the $\delta_{\mathrm{m}} = 0.09$ value used by Morel (1974). The Zhang and Hu (2009) computations of pure water scattering with this value of 0.039 produces volume scattering functions that match experimental measurements by Morel (1968) within 2%. Nonetheless, this important parameter deserves additional experimental evaluation to further reduce uncertainties in pure water scattering values. Very recently, Zhang et al. (2019) measured, δ_m of pure water and seawater at various salinities. They obtained $\delta_m = 0.039 \pm 0.001$ for pure water, which supports the currently adopted value of 0.039. They also found the value of depolarization ratio increases slightly with salinity, by 10–20% at a salinity of 40 g/kg.

3.1.4 Inelastic Scattering

Heritage studies: Raman scattering and chlorophyll fluorescence in scalar RT codes

Inelastic radiative processes in ocean waters include Raman scattering by liquid water, fluorescence by colored dissolved organic matter (FDOM), and chlorophyll fluorescence. In what follows, we will use *inelastic scattering* to denote (any of) these processes. Raman scattering is mainly due to the OH bond stretch mode of water molecules (Walrafen, 1967), which absorbs light energy at higher frequency and reemit to lower frequency regions with fixed frequency shift spectra centered around 3400 cm^{-1}. It has been long recognized that the contribution of Raman scattering to the underwater radiation field is significant in the visible region for clear waters (Ge et al., 1995). Chlorophyll fluorescence and FDOM contributes to the water leaving radiance in variable amount depending on wavelengths and water turbidity (Preisendorfer and Mobley, 1988; Green and Blough, 1994). Raman scattering and chlorophyll fluorescence have also been used to better invert the oceanic remote sensing signal to biogeochemical parameters (Behrenfeld et al., 2009; Westberry et al., 2013).

The theoretical modeling of Raman scattering in ocean waters is mostly based on the Monte Carlo (MC) method (Kattawar and Xu, 1992; Gordon, 1999). Kattawar and Xu (1994) have included polarization in the simulation of Raman scattering, in which the radiance was averaged in bins of 30° of azimuth viewing angles to reduce statistical noise. Hydrolight, a commercial software based on the invariant embedding method, can simulate Raman scattering and fluorescence without considering the impacts of polarization (Mobley et al., 2002). Schroeder et al. (2003) have incorporated inelastic scattering in scalar RT models. Semianalytical models have also been developed for underwater reflectance to include Raman effects (Lee et al., 1994; Loisel and Stramski, 2000).

PACE updates (FWD RT models): Raman scattering and chlorophyll fluorescence in vector RT codes

As part of the PACE Science Team effort, Zhai et al. (2015) have implemented Raman scattering in the polarized RT code for atmosphere and ocean coupled systems based on the Successive Order of Scattering (SOS) method. Polarization due to Raman scattering has been preserved and the contribution of Raman scattering to the polarized water leaving radiance has been studied. The coupling mechanism between atmosphere and ocean are fully accounted for. Later Zhai et al. (2017a) added FDOM and chlorophyll fluorescence in their SOS RT code. Their polarized RT code simulation shows that FDOM contributes to the water radiation field in the broad visible spectral region, while chlorophyll fluorescence is limited in a narrow band centered at 685 nm. This is consistent with previous findings in the literature that were obtained with scalar RT codes. With the new polarized RT code, the impacts of fluorescence to the DoLP and orientation of the polarization ellipse (OPE) are studied. The underwater light DoLP is strongly influenced by inelastic scattering at wavelengths with strong inelastic scattering contribution. The OPE for underwater light is less affected by inelastic scattering but it has a noticeable impact, in terms of the angular region of positive polarization, in the backward direction. This effect is more apparent for deeper water depth. These results are important for analyses of underwater light DoLP measurements. The polarized RT code has also been used to study the contribution of polarized water leaving signals to the top of atmosphere in the visible spectra for a range of IOPs for open ocean and coastal waters (Zhai et al., 2017b). Below we discuss RT examples for the impact of inelastic scattering on underwater light radiance at zero water depth.

Figures 6A,B show examples of reflectance spectra with both elastic and inelastic scattering mechanisms included. The simulations are for a coupled atmosphere and ocean system, with the atmosphere characterized by a mixture of molecules and aerosols. The results are for a sensor that is located at the top of the ocean (TOO) just below the ocean surface and that is viewing in nadir direction the upwelling underwater light radiance. The aerosol optical depth at 550 nm is 0.15. Major gas absorptions have been included in the simulation, which include absorptions due to ozone, nitrogen dioxide, oxygen, and water vapor. The ocean optical properties are parameterized in terms of Chlorophyll *a* concentration [Chla]. The left axis of **Figure 6A** shows the reflectance (see definition in **Table 2**) with only elastic scattering included. The right axis of **Figure 6A** shows the total contribution of both elastic and inelastic scattering, which include Raman scattering, CDOM fluorescence, and chlorophyll fluorescence. The quantum yield of chlorophyll fluorescence used is 0.02, i.e., two percent of the absorbed photons are fluoresced. **Figure 6B** shows the absolute contribution of inelastic scattering as a function of wavelength.

Figure 6A shows the spectral behavior of TOO ocean reflectance as a function of [Chla]. There is an anchoring point close to 500 nm where the ocean reflectance is insensitive to the [Chla] values. When the wavelength is smaller than this anchoring point, the ocean reflectance for smaller [Chla] is larger and vice versa for wavelengths longer than the anchoring point. This changes the impact of inelastic scattering on TOO ocean reflectance. For example, ignoring inelastic scattering decreases the TOO radiance in the (deep) blue part of the spectrum by more than 10% if [Chla] becomes small. The corresponding decrease in water-leaving radiance is about 5%, which is equal to the retrieval accuracy requirement for PACE (*cf.* "1.1 The PACE Mission" section). The opposite trend is seen at 685 nm, where the impact of inelastic scattering causes a peak in TOO ocean reflectance to increase with increasing [Chla]. This peak, which is caused by chlorophyll fluorescence, is more clearly seen in **Figure 6B** and

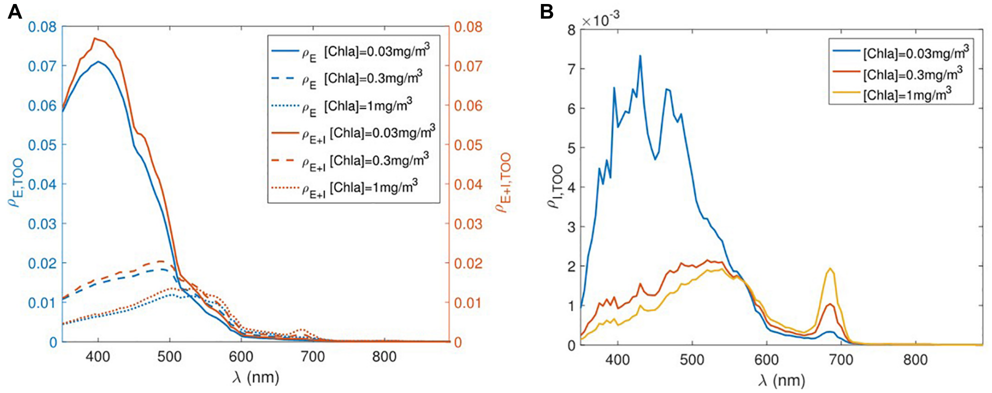

FIGURE 6 | (A) Ocean reflectance at nadir view at the top of the ocean (TOO) as a function of wavelength. **(B)** The absolute contribution of inelastic scattering to the TOO nadir reflectance as a function of wavelength. Subscripts E and I denote elastic and inelastic scattering, respectively.

the corresponding increase in water-leaving radiance surpasses the 5% retrieval accuracy for PACE. Between 400 and 600 nm, the inelastic scattering is still dominated by Raman scattering, whose contribution to TOO ocean reflectance remains large for clearer waters (smaller [Chla] values). These results illustrate the importance of accounting for inelastic scattering processes in polarized RT codes that are used to create synthetic data sets for PACE.

Raman scattering coefficients used in this work are based on measurements (Walrafen, 1967; Hu and Voss, 1997), which do not account for the temperature and salinity dependence. It is understood that the Raman spectra is sensitive to both temperature and salinity (Artlett and Pask, 2015, 2017). In future work, it will be important to systematically parameterize both Raman scattering coefficients and emission spectra in terms of temperature and salinity. For the simulation of FDOM, we have used the excitation – emission spectra from Hawes et al. (1992), which is based on the measurement of FDOM extracted from water samples. Green and Blough (1994) have pointed out that fluorescence is different for FDOM dissolved and extracted from water samples. Further investigation is needed to measure FDOM dissolved in water samples for different geographical and biological origins.

Another important subject on inelastic scattering in FWD RT models is to include non-photochemical quenching (NPQ) in chlorophyll fluorescence (Morrison, 2003). This would create synthetic data sets that allow us to better understand fluorescence signals in satellite observations and to develop more accurate remote sensing algorithm for chlorophyll fluorescence (Behrenfeld et al., 2009). Zhai et al. (2018) have implemented the quenching processes of the phytoplankton fluorescence in their polarized RT code. NPQ modulates the quantum yield of the chlorophyll fluorescence based on the photosynthetically available radiation (PAR), so that the quantum yield is not longer a prescribed parameter. It is a function of both the environmental factors and phytoplankton physiology. Zhai et al. (2018) have simulated the fluorescence for a variety of chlorophyll concentrations, solar zenith angles, and aerosol optical depths. A particularly interesting fact is that the fluorescence is actually higher for larger solar zenith angles or larger aerosol optical depth, which is because the smaller quantum yield due to photochemical and NPQ processes. This has also been observed by geostationary ocean observations (O'Malley et al., 2014)

3.2 Ocean Surface

3.2.1 Sunglint

Heritage studies: remote sensing and ocean surface roughness

Over cloud-free oceans, the remotely sensed signal contains contributions from atmospheric scattering, diffuse skylight reflected off the ocean surface, underwater light scattering and direct sun light reflected off the ocean surface (i.e., sunglint). Of all the contributions, sunglint unequivocally provides the brightest and most-recognizable signal: its radiance can exceed the radiance of off-sunglint observations by several factors in the VIS (Ottaviani et al., 2008; Chowdhary et al., 2012) and up to several orders of magnitude in the NIR/SWIR (Chowdhary et al., 2005). To a first order approximation, one can think of sunglint as a mirror-like reflection of the solar beam that is attenuated as light passes though the atmosphere. The extent and magnitude of such pattern depends on the ocean surface characteristics (i.e., wave slope distribution, refractive index), whereas the attenuation by the atmosphere depends on the amount and microphysical properties of aerosols. Remote sensing observations of sunglint can therefore provide information on aerosol properties (Kaufman et al., 2002; Ottaviani et al., 2008, 2013) and on ocean surface slicks when polarimetric measurements are available (Ottaviani et al., 2012). Similar results for oil slick properties were subsequently obtained by Lu et al. (2017) from spaceborne polarimetric observations by the POLDER (Polarization and Directionality of the Earth's Reflectances) instrument.

It is particularly difficult to retrieve ocean IOPs from spaceborne radiance observations when the scene is contaminated by sunglint. One approach that mitigates this problem is to use the radiance polarized along the meridional plane, which is much less affected by ocean surface reflectance but still provides useful information on ocean color variations (He et al., 2014; Liu et al., 2017). Another approach is to identify (and subsequently avoid) sunglint contaminated scenes by comparing aerosol optical thicknesses retrieved for the same pixel but from different viewing angles. In the latter approach, the sunglint-contaminated retrievals will lead to an identifiable overestimation of the aerosol optical thickness (Harmel and Chami, 2013). The advantage of both these approaches is that they do not require *a priori* information for the ocean surface roughness; however, they do require the use of multi-angle (and polarimetric) observations. Alternatively, if such observations are not available (e.g., at the edge of the swath monitored by the OCI instrument) then one must resort to ocean surface models to discard sunglint-contaminated scenes based on viewing geometry and surface waviness in space-borne IOP retrievals.

Cox and Munk (1954) were the first to systematically study the relation between the surface slope distribution and the ocean wind speed $U_{12.5}$ (measured at a height of 12.5 m). Based on airborne photographs of the sun glitter for wind speeds $U_{12.5} \leq 14$ m/s and moderate solar zenith angles, they provided an anisotropic surface slope distribution with a variance depending on the wind speed and wind direction. To a first-order approximation, this surface slope distribution becomes isotropic (Gaussian) with a variance that depends only on the wind speed. Their results have thereafter been adopted by the majority of remote sensing community as a standard model for the ocean surface roughness. Subsequent analyses of passive remote sensing observations from an ocean platform (Su et al., 2002), aircraft (Gatebe et al., 2005) and satellite (Ebuchi and Kizu, 2002; Bréon and Henriot, 2006; Zhang and Wang, 2010) have confirmed the two-dimensional Gaussian surface slope model fitted by Cox and Munk (1954) to a satisfactory/good degree except perhaps for large solar zenith angles. However, variations in the relation between wind speed and the variance of the surface slope distribution were observed. With realistic surface elevations (and hence including realistic surface wave shadowing and multiple reflections) that were obtained from wave variance spectra and Fourier transforms, Preisendorfer and Mobley (1986) and Mobley (2015) used ray tracing techniques to study the reflection and transmission properties of the *Cox and Munk* surface model with the implicit inclusion of shadowing and multiple reflections. Their studies indicate small difference in surface irradiance reflectance except perhaps for again large solar zenith angles.

When incorporating the *Cox and Munk* surface model in RT computations to identify sunglint contaminated scenes, there are some aspects to consider. Firstly, to compute the shape and angular extent of the sunglint, one needs wind speed and direction as auxiliary data, which may not always have the appropriate resolution to describe local conditions. Secondly, as mentioned before the relationship between the wind speed (and direction) and the variance of the ocean surface slope distribution can deviate from the relationship given by *Cox and Munk* (see Kay et al., 2009, and references therein). Thirdly, direct skylight reflected by the ocean surface will still be scattered by molecules and aerosols when propagating through the atmosphere towards the satellite sensor, and this aspect is often ignored when masking the sunglint *a priori*. For an atmosphere bounded from below by an isotropic rough ocean surface, Ottaviani et al. (2008) found that the error in simulated space-borne radiances may reach 90% (at 470 nm) around the edge of sunglint when ignoring these multiple-scattering effects.

The multiple scattering aspect of sunglint can be expected to be equally important for direct skylight reflected by anisotropic (i.e., wind-direction dependent) rough ocean surfaces. However, while atmospheric attenuation of sunglint reflected by anisotropic surfaces can be incorporated fairly easily in RT methods (Chowdhary et al., 2006; Lin et al., 2016), the inclusion of multiple scattering in the atmosphere of sunglint reflected by such surfaces remains a challenge for most of the RT methods reviewed in section "2 History of RT Methods for AOS: A Brief Overview." Masuda (1998) used the adding method to investigate this phenomenon, but he computed only up to three light interactions between the atmosphere and ocean, and he considered only the wavelength of 865 nm. Compared to heritage sensors, the hyperspectral measurements by the OCI and SPEXone instruments onboard the PACE mission will also include shorter wavelengths where light will undergo many more light interactions between the atmosphere and ocean, especially in the blue/UV part of the spectrum. The impact of those interactions on *a priori* sunglint masks used for aerosol and ocean color retrievals remains uncertain to this date.

PACE updates (INV RT studies): polarimetric remote sensing of SML refractive index

At any given viewing geometry, the surface properties determining the ocean surface total reflectance are solely the surface slope distribution and the refractive index m of the ocean-atmosphere interface. Furthermore the surface slope distribution affects the polarized surface reflectance in the same linear proportion as the total surface reflectance, so that the ratio of polarized to total reflectance (i.e., the DoLP) becomes independent of the surface roughness. Hence changes in surface DoLP only occur if the viewing geometry and/or m varies. For remote sensing of cloud-free oceans, this fact was demonstrated by Chowdhary et al. (2005) and Ottaviani et al. (2012), based on RSP observations of DoLP sunglint profiles. Small differences can still occur in airborne observations if the contribution of *diffuse* light scattered by high aerosol loads within the sunglint region is significant (Ottaviani et al., 2019).

The surface refractive index m varies throughout the global oceans in response to several factors. Firstly, m is determined by the dielectric constant which, for pure seawater and at any wavelength, varies with temperature T and salinity S (Röttgers et al., 2014). Variations in m caused by changes in T are relatively small, i.e., 0.002 in the VIS-NIR if T increases from 0 to 30°C. Similar variations are observed if S increases from 30 to 40 g/kg, a range which covers most of the global oceans except for the Arctic regions. Secondly, substances that cover the ocean surface such as floating seaweed, plastics, and slicks from biogenic origins (e.g., plankton and fish secretions) and anthropogenic origin (e.g., oil spills) affect *m* depending on the composition and thickness of the floating substance, and on the wavelength of light. For example, a thick oil slick can cause *m* to increase by 0.1–0.2 in the VIS-NIR depending on the oil type, refinement, wavelength, and temperature (Otremba, 2000; Carnesecchi et al., 2008). Thirdly, the uppermost 1–1000 μm of the ocean – referred to as the surface microlayer (SML) – has biological, chemical, and physical properties that are distinctly different from those of the underlying ocean body (Engel et al., 2017, and references therein). Little is known about the processes controlling the SML properties, yet the SML is a key player in gas exchanges between the atmosphere and ocean, and it is a major source of biogenic matter found in sea-spray aerosols. The high occurrence in the SML of marine gel particles (in addition to colloids, particulate matter, neuston assemblies, and CDOM) gives it a gelatinous nature, which in turn promotes aggregation of particulates and natural colonization of bacteria. Polarization measurements obtained by Kozarac et al. (2005) for *in situ* and *ex situ* SML samples show that the complex composition of SML has an impact on the surface *m*; however, the resulting absolute change in *m* remains unknown. Regarding the sunglint DoLP variations with *m* and with viewing geometry: consider for instance light illuminating an ocean surface at an angle θ_i (measured from the upward surface normal). When θ_i becomes equal to the Brewster angle $\theta_b \equiv arctan(m)$, the specularly reflected light becomes completely polarized (i.e., DoLP becomes 100%: Born and Wolf, 1999). Variations in *m* cause the angular location θ_b of maximum DoLP to shift and, as a consequence, the DoLP to change if the incident and viewing angles are kept constant.

Airborne multi-angle observations of the DoLP obtained with the RSP instrument in the SWIR are ideally suited to study variations in *m*. The penetration depth at SWIR wavelengths is of the order of tenths of a micrometer because of strong absorption by water, i.e., it appropriately targets slicks, films, and SML. In addition, the molecular and aerosol optical thicknesses are very small at these wavelengths, which enlarges the spatial dimension in airborne observations of sunglint-dominated scenes (i.e., of scenes that are least affected by diffuse atmospheric scattering). The multiangular (~150 views) capability of RSP allows sunglint to be sampled at high spatial resolution in transects flown near the principal plane. Finally, the high accuracy of RSP DoLP measurements (i.e., better than 0.2%) allows to identify changes in sunglint DoLP profiles caused by minuscule variations in *m* (as small as 1×10^{-4} under ideal experimental conditions). Using RSP data collected while flying over the Deepwater Horizon oil spill, Ottaviani et al. (2012) reported changes in *m* by 0.064 at λ = 2.2 μm for oil-affected scenes (*cf.* **Figure 7B**, and related discussion below).

Recently, we exploited a general algorithm based on a Levenberg–Marquardt type of inversion (Rodgers, 2000) to provide continuous retrievals of the refractive index along RSP flight transects. Using the average of 20 RSP scans at a time (corresponding to time intervals of ~15 s), the procedure starts with the identification of the sunglint-dominated views in the DoLP measured at 2.2 μm, achieved by selecting the series of consecutive views for which the DoLP is closest to that predicted by the Cox and Munk relation. The inversion is then launched with the refractive index as the sole free parameter. Even in this simplest version, the algorithm shows remarkable stability and accuracy as demonstrated in **Figure 7**. The transect in panel **(A)** belongs to a test flight during the SEAC4RS (Studies of

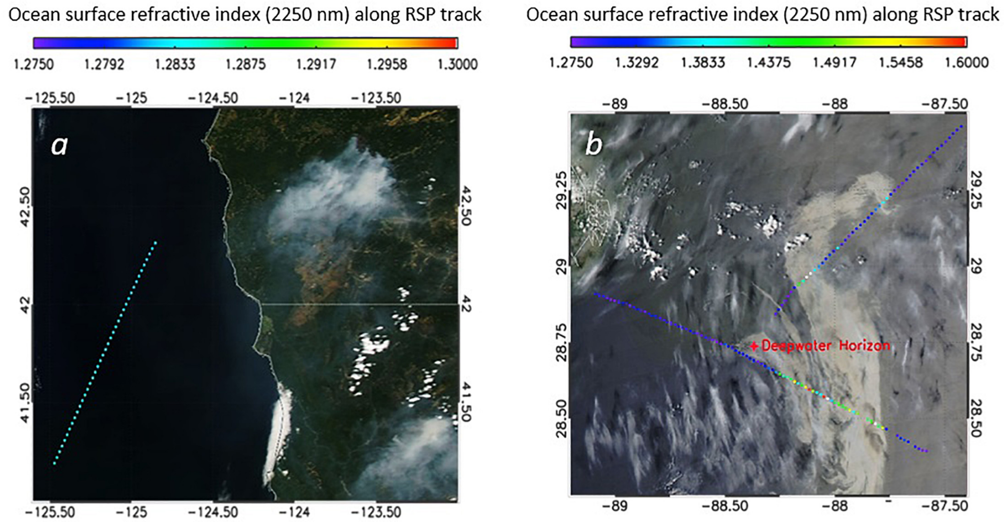

FIGURE 7 | Successful retrievals of the ocean surface refractive index from RSP measurements at 2.2 μm, over near-real-time imagery from the MODIS sensor. **(a)** SEAC4RS campaign (08/02/2013): test flight over pure seawater. Note that the color bar covers for this panel only a small range of the refractive index. **(b)** CARES/CalNEX campaign (05/11/2010): transects intersecting the oil spill caused by the explosion of the Deepwater Horizon offshore platform. The refractive index of pure seawater at 2.2 μm measured in laboratory experiments by Segelstein (1981) is 1.2815.

Emissions and Atmospherric Composition, Clouds, and Climate Coupling by Regional Surveys) campaign, when after sampling fires in Southern Oregon, the aircraft veered toward Case I waters off the Southern Oregon/Northern Californian coast. Panel **(B)** presents two flight legs obtained during the CARES/CalNex (Carbonaceous Aerosols and Radiative Effects Study/California Research at the Nexus of Air Quality and Climate Change) campaign that intersected the oil spill caused by the explosion of the Deepwater Horizon oil rig in 2010. For both these campaigns, where the RSP flew at two very different altitudes (∼20 km on an ER-2 aircraft during SEAC4RS, and ∼9 km on a B-200 aircraft during CARES/CalNex) and under very different atmospheric conditions, the algorithm retrieves very plausible refractive indices with high accuracy. In particular, note the small variability of the refractive index in panel (A), where the average over the whole leg is 1.2836 with a standard deviation of 0.0007. This result is particularly interesting in view of the possible detection of floating layers of biogenic materials. We further speculate that the temperature and salinity dependence of the refractive index can be observed in case of large gradients such as river waters flowing into oceans. The method also offers an alternative to measurements otherwise difficult to obtain, as is the case for the determination of the refractive index of oil (Ottaviani et al., 2012). Ottaviani et al. (2019) extended this method to a complete series of RSP transects, including a thorough assessment of the sensitivity to the residual aerosol effects and the inclusion of additional free parameters during the inversion.

The lessons learned from these RSP inversions will aid the interpretation of DoLP data obtained by PACE (see section "1.1 The PACE Mission") in sunglint regions. However, PACE polarimetry will occur at shorter wavelengths (i.e., in the NIR) than those of RSP. This means that aerosol scattering contributions may not be negligibly small. Furthermore, PACE polarimetry will occur at fewer viewing angles (i.e., ≤10), and at least for HARP2 at coarser DoLP accuracy (i.e., ≤1%). These reductions in measurement capabilities lead to a decrease in the retrieval accuracy of surface refractive indices from sunglint DoLP data, even in absence of aerosol scattering. Nevertheless, DoLP measurements of sunglint that were obtained by POLDER at a coarser accuracy (∼1%) in the NIR (870 nm) for ≤ 14 viewing angles have still proven useful in distinguishing between surface refractive indices retrieved for clean ocean waters and for oilslick covers (Lu et al., 2017). Hence, while PACE DoLP measurements of sunglint will not lead to the same retrieval accuracies for surface refractive index as RSP, they will likely contain information that can be used to not only detect and but also identify substances covering large sections of the ocean surface. This remains a research topic for the near future.

3.2.2 Whitecaps

Heritage studies: surface coverage and albedo models

Early quantitative work on oceanic whitecaps was initiated by Monahan (1971), who studied photographs of ocean surface in order to derive the spatial fraction f_{wc} of area covered by whitecaps. His results, which were obtained for wind speeds at 10 m above the sea surface, U_{10}, smaller than 10 m s^{-1}, set forth the functional form $f_{\mathrm{wc}} \sim (U_{10})^{k}$ where k is a constant. Wu (1979) argued on physical grounds that the exponent k should be 3.75, and fitted Monahan's (1971) results and other data to $f_{\mathrm{wc}} = 1.7 \times 10^{-6}\ U_{10}{}^{3.75}$. The same data sets were used by Monahan and O'Muircheartaigh (1980) to statistically analyze seven solutions for $f_{\mathrm{wc}} \sim (U_{10})^{k}$ proposed in the literature. They found Wu's (1979) expression to result in one of the best fits, and a linear regression analyses performed by these authors revealed an expression with only slightly smaller errors. Note, the scatter in the data from which to f_{wc} was retrieved is very large, i.e., of the order of f_{wc} itself. For many RT applications, it has been customary to adopt their expression of $f_{\mathrm{wc}} = 2.95 \times 10^{-6}\ U_{10}{}^{3.75}$, as a standard for the following decades. For remote sensing applications, other relationships have been used. Ocean color satellites currently employ an expression derived by Stramska and Petelski (2003) for undeveloped seas where $f_{\mathrm{wc}} = 8.75 \times 10^{-5}\ (U_{10}\text{-}6.33)^3$. At high wind speeds, however, a threshold equivalent to the whitecap fraction at 12 m s^{-1} is implemented in the operational code (see atmospheric correction section). Newer measurements of whitecaps under high wind situations in the polar seas suggest that f_{wc} does not follow a cubic relationship at high wind speeds $f_{\mathrm{wc}} = 7.38 \times 10^{-4}(U_{10}\text{-}4.23)^{1.42}$ (Brumer et al., 2017).

The whitecap albedo A_{wc} has also been the subject of various research. Whitlock et al. (1982), who studied laboratory-generated whitecap patches, found that the reflectance of whitecap varies significantly at wavelengths larger than 0.9 μm, but that it remains fairly constant at smaller wavelengths with $A_{\mathrm{wc}} \approx 50\%$ for freshly generated thick whitecap and $A_{\mathrm{wc}} \approx 10\%$ for a single bubble layer. Koepke (1984), who studied time-resolved pictures of whitecaps through a red filter, observed on the other hand that the reflectance of oceanic white caps decreased rapidly as they age. By averaging over time and setting limits to the whitecap reflectance based on the Whitlock measurements, he derived an effective white cap albedo of 22% ± 8%. Frouin et al. (1996) studied whitecap reflectance created by breaking waves, found that it decreased by 40–85% as the wavelength increased from 0.85 to 1.65 μm. They explained this spectral behavior by considering the nature of oceanic whitecap – i.e., air bubbles separated by a thin layer of water (surface foam), and bubbles injected into the upper layer of the ocean body. The spectral decrease in whitecap albedo A_{wc} could then qualitatively be described by the increase in absorption by water between the air bubbles. A similar spectral dependence of A_{wc} was also observed by Moore et al. (1998), who monitored whitecaps generated in the open ocean by the bow of a moving ship.

The relationship between whitecaps and liquid water absorption implies that these can be tied within the theoretical framework of RT modeling. Whitecaps belong to a broad class of strongly multiple-scattering media where the volumetric concentration of bubbles is greater than 70% (Kokhanovsky, 2004). RT modeling typically applies to media with low concentrations of scatterers (<1% by volume), but progress has been made in the development of RT theory of whitecaps (Kokhanovsky, 2004; Ma et al., 2015). However, more research is needed to validate the theoretical models with experimental measurements.

PACE updates (FWD RT studies): remote sensing of whitecap properties

The PACE mission aims to be hyperspectral from the UV into the NIR wavelengths and will require a more spectrally resolved whitecap reflectance. New spectral measurements of whitecap have been made across from 400 to 2500 nm (**Figure 8**). These measurements show that whitecaps are not featureless in the NIR but have dips in reflectance that largely correspond to the absorption features of liquid water. Reflectance dips occur particularly at 750, 980, and 1150 nm, which have enhanced liquid water absorption, a result of multiple scattering in and around the subsurface bubbles and surface foam (Dierssen, 2019). Following Whitlock et al. (1982), a simple model of whitecap reflectance based on the natural logarithm of water absorption can be used to describe the spectral shape of intense whitecaps generated by breaking waves into SWIR wavelengths (Dierssen, 2019). Moreover, the decrease in reflectance at these liquid water absorption bands is correlated with enhancements in reflectance of the whitecap across the spectrum. Dierssen (2019) found that more intense whitecap causes enhanced absorption by liquid water, likely as a result of enhanced multiple scattering within the surface foam and submerged bubbles, that is correlated with the reflectance of the whitecap feature.

Current FWD RT models based on wind speed and a single whitecap albedo cannot be used to accurately represent the diversity of whitecaps on the ocean. The manifestation of whitecaps and the amount of sea surface covered by surface foam and submerged bubbles are influenced by a variety of other factors including fetch and duration and the wind, water temperature, air temperature and stability of the lower atmosphere defined by the air/water temperature differential, salinity, current shear and long wave interaction, wave age, and the presence of surfactants such as organic films (e.g., Brumer et al., 2017). Furthermore, RT models should transition from using a single albedo to a more realistic framework that incorporates reflectance from actively breaking waves and residual bubble plumes and potential changes in albedo relating to the condition of the seas (Randolph et al., 2014, 2017; Xu et al., 2015). Potentially new RT models for estimating the contribution of whitecaps on the sea surface are presented in Dierssen (2019), including an effective whitecap factor that is based on optical reflectance rather than the traditional interpretation of whitecap fraction as an aerial average of bright features. Improving estimates of whitecap reflectance under high wind conditions will also improve the retrievals of aerosols, since presently the enhanced reflectance is incorrectly removed in the aerosol algorithms. The spectral aerosols models are not identical to whitecap reflectance and hence errors will be propagated from the NIR/SWIR to visible wavelengths under high wind conditions. Image-based retrievals of whitecap reflectance, rather than use of a windspeed climatology, should improve the PACE overall accuracy of retrievals of both oceanic and atmospheric constituents, particularly in high wind areas like the Southern Ocean.

With the addition of polarization capabilities on the PACE mission, future research is also warranted on the polarization effect of wind-roughened seas and whitecaps. Polarized reflectance has been considered for whitecap-free waters covered by ocean waves of various heights and periods, including wave shadowing at high incident angles (Mobley, 2015; Hieronymi, 2016). However, little research has been done on the polarization of light reflected by whitecaps. That is, surface foam is commonly modeled as a Lambertian reflector (Koepke, 1984; Gordon and Wang, 1994a) which renders unpolarized light. However, light scattered by a single submerged air bubble is highly polarized (akin to Raleigh scattering) because of a refractive index smaller than one relative to water (Mishchenko et al., 2002). Multiple scattering by a cloud of bubbles that make up whitecaps reduces the polarization, which is qualitatively consistent with analyses of CALIPSO (Cloud-Aerosol Lidar and Infrared Pathfinder Satellite

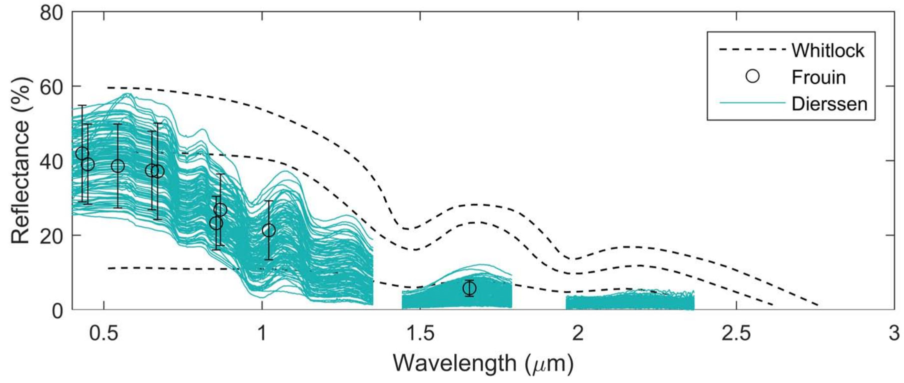

FIGURE 8 | Spectral reflectance of the whitecap of breaking waves measured from visible to short-wave infrared with black dashed lines from Whitlock et al. (1982, Figure 2a) and circles with error bars from Frouin et al. (1996). The different black-dashed lines correspond to different foam samples, with upper and lower curves corresponding to clear water foam patches with multiple- and single-bubble layer, respectively. Cyan lines are new hyperspectral measurements of breaking waves from Dierssen (2019) as part of the PACE project showing the liquid water absorption features at 0.750, 0.980, and 1.150 μm. The gaps in the measured spectrum correspond to regions where the atmosphere is opaque and downwelling irradiance is too low for a reliable signal.

Observation) data (Hu et al., 2008). However, there exist no model computations to provide quantitative corroborations. Hence this remains an important outstanding topic for future research.

3.3 Atmosphere

3.3.1 Aerosols

Heritage studies: remote sensing of aerosol properties

Aerosols originate from a wide range of sources including wind processes (Prospero et al., 2002; Carslaw et al., 2010; Burrows et al., 2014; Quinn et al., 2014), volcanic (Toohey et al., 2016) and biogenic emissions, combustion of fossil fuel and biomass (van der Werf et al., 2010; Lamarque et al., 2010; Bauer et al., 2016), and chemical processing of gaseous precursors. Once in the atmosphere particle properties can change during transport through such processes as hydration, evaporation, aging, chemical reactions, and coagulation (Ghan and Schwartz, 2007; Baker et al., 2014). Finally, aerosols are removed from the atmosphere by wet (in-cloud processing and rain) and dry (sedimentation and coagulation) deposition processes, which, in addition to environmental circumstances, depend on the particle physical and chemical properties (Bergametti and Forêt, 2014). The result of these multiple sources is to create a wide variety of aerosol types whose physical and optical properties vary widely with space and time.

Only space-borne observations can provide a global overview of the variability of aerosol properties. Remote sensing of aerosols from space requires accurate RT modeling of the atmosphere with aerosols properly represented in the model. The RT characteristics of aerosols that affect the reflected light measured by satellite sensors are their single scattering albedo ω, optical thickness τ, and scattering function F (or 4×4 scattering matrix $\boldsymbol{F}$ when accounting for the polarization of light). In the simplest case (i.e., single scattering by one aerosol type), the radiance emerging from the top of the atmosphere (TOA) becomes proportional to the product of these three RT quantities. Early studies showed that the linear relationship between the TOA radiance and τ can be preserved for multiple scattering (Griggs, 1983), and this formed the foundation for the first aerosol retrievals of τ from various satellite observations including AVHRR (Advanced Very High Resolution Radiometer) data (see Griggs, 1984). However, the radiances used for these retrievals were all measured at a single wavelength (centered close to 0.65 μm) and at a single viewing angle, i.e., they provided only a single data point from which only one aerosol RT quantity could be retrieved. Hence retrieving τ from these radiance measurements required that ω and F had to be assumed *a priori*, which is difficult given the large spatial and temporal variations in aerosol properties discussed above. Note that, even for the simplest case (i.e., one aerosol type consisting of homogeneous spherically shaped particles), ω and F in turn depend on 4 particle properties: the real and imaginary part of the refractive index m, and the effective radius r_e and effective variance v_e of the size distribution $n(r)$ [note from Hansen and Travis (1974), that r_e and v_e are not very sensitive to the shape of $n(r)$] – all of which are effectively assumed in AVHRR retrievals (Rao et al., 1989; Stowe et al., 1997). Higurashi and Nakajima (1999) reduced the assumption requirements by including the radiance measured at a second AVHRR channel (centered at 0.83 μm) to retrieve a measure for the size distribution (i.e., the Ångström exponent). However, the complex refractive index still needs to be assumed for such cases. Analyses performed by Mishchenko et al. (1999) show that erroneous assumptions made for the complex refractive index will significantly affect the τ values retrieved from AVHRR observations.

The need for more pieces of information measured by space-borne sensors was addressed by observations from a new generation of satellite instruments that were launched in succession (Kaufman et al., 1997), including those that are part of NASA's Earth Observing System (EOS) program. Specifically, the MODIS (Moderate Resolution Imaging Spectroradiometer) instrument onboard the Terra platform (launched in 1999) and Aqua platform (launched in 2002) provides radiance measurements in more wavelength bands that cover a larger spectrum than the AVHRR instrument (Barnes et al., 1998). Six of those bands, covering the spectrum 0.55–2.13 μm, are used to retrieve aerosol properties over ocean (Tanré et al., 1997; Levy et al., 2013). On the other hand, the MISR (Multi-angle Imaging Spectroradiometer) instrument onboard the Terra platform provides radiance measurements in nine viewing angles that cover a satellite viewing angle range of $\pm$ 70.5 Diner et al., 1998). The measurements in all nine directions are made in four wavelength bands, two of which (centered around 0.672 and 0.867 μm) are used for the standard aerosol retrieval over ocean (Martonchik et al., 1998; Kahn et al., 2001). Observations provided by the MODIS and MISR instruments have created to this date a wealth of new information on aerosol variability. Still, assumptions continue to be made about the RT properties of aerosol species, mainly derived from surface measurements and ground-based remote sensing retrievals. While considerable effort has been placed into matching these assumed particle properties to laboratory and field data, by definition they cannot replicate the full range of continuous temporal and spatial changes in ambient aerosol properties that is occurring in our Earth's atmosphere. Even if one were to adopt more elaborate retrieval algorithms such as GRASP (Generalized Retrieval of Aerosol and Surface Properties) (Dubovik et al., 2011, 2014) which does not rely on pre-defined discrete aerosol species, theoretical studies show (e.g., Knobelspiesse et al., 2012) that MODIS-like and MISR-like observations do not contain enough information to adequately capture (as defined in Mishchenko et al., 2004) these changes in ambient aerosol properties.

To improve the aerosol properties retrieved from instruments like the MODIS and MISR instruments, one must consider extending the spectral range monitored by these instruments and/or include measurements of the polarization of light. For example, the UV radiance provides more useful information on aerosol absorption than the VIS-SWIR radiance because of the rapid growth ($\sim\lambda^{-4}$) of the molecular optical depth with decreasing wavelength λ, which causes a substantial increase in multiply scattered (and hence in multiply absorbed) light.

Torres et al. (2005, 2007) and Satheesh et al. (2009) demonstrated this capability from analyses of space-borne observations in the near UV by the TOMS (Total Ozone Mapping Spectrometer) and OMI (Ozone Monitoring Instrument) instruments in the near-UV. The caveat in making practical use of the enhanced aerosol absorption in the near UV is that strong vertical variation in molecular scattering in the atmosphere introduces ambiguities in standard retrieval algorithms. Coupling between molecular scattering and aerosol absorption varies with the relative concentration of molecules and aerosols, which in turn is dependent on their vertical distribution. Thus, in practical terms a range of aerosol layer height/ absorption/optical thickness can produce the same measured radiance in the near UV. To unambiguously retrieve aerosol absorption properties, either layer height or aerosol optical depth must be constrained. Heritage studies approach this ambiguity by assuming layer height, usually through model output or climatology (Torres et al., 2005, 2007) or by introducing simultaneous observations at longer wavelengths that can be extrapolated to the UV wavelengths to constrain aerosol optical thickness (Satheesh et al., 2009; Gassó and Torres, 2016).

Even more promising, the linearly polarized radiance scattered by aerosol particles provides more information about the microphysical and chemical properties of these particles than their scattered radiance does. That is because (Hansen and Travis, 1974; Mishchenko and Travis, 1997):

i Radiance is described by just one measurable quantity, i.e., the Stokes parameter *I*, whereas linearly polarized radiance is described by two measurable quantities, i.e., (see also **Table 2**) the Stokes parameters *Q* and *U* (or, equivalently, the DoLP and the polarization angle χ);
ii The single-scattering angular features in *Q* and *U* are sharper, more numerous, and show larger sensitivity to variations in aerosol size distribution and complex refractive index than the corresponding single-scattering angular features in *I*;
iii The single-scattering angular features in *Q* and *U* are much better preserved in the presence of multiply scattered light than the corresponding features in *I*;
iv When *I*, *Q*, and *U* are measured simultaneously then the uncertainty in DoLP becomes independent of (and hence in degradations of) the absolute calibration uncertainty.

If the remaining uncertainty in DoLP is kept below 0.5%, then one can use multi-angle, multi-spectral measurements of *I*, *Q*, and *U* to retrieve aerosol properties (in real time, using no pre-defined aerosol models) with sufficient accuracies that meet the criteria for climate change studies. This has been demonstrated in numerous theoretical studies (Mishchenko and Travis, 1997; Hasekamp and Landgraf, 2005, 2007; Knobelspiesse et al., 2012), and is supported by analyses of actual, airborne, multi-angle, multi-spectral polarization measurements (Chowdhary et al., 2001, 2002, 2005, 2012; Wu et al., 2015, 2016; Xu et al., 2016). Of particular interest in these analyses are the first-in-kind retrievals of the spectral complex refractive index, which is a measure of aerosol composition. Spaceborne multi-angle, multi-spectral, multi-Stokes-parameter (3M) radiance measurements have been provided since 1996 in intermittent intervals by the POLDER-1, POLDER-2 and POLDER-3 instruments (Fougnie et al., 2007), but the DoLP uncertainty is larger than 0.5% (commonly assumed to be 1%) for these instruments (Knobelspiesse et al., 2012). Nevertheless, analyses of their measurements have produced new results for the optical properties of liquid clouds (e.g., Bréon and Goloub, 1998; Riedi et al., 2000; Bréon and Doutriaux-Boucher, 2005; Shang et al., 2015) and ice clouds (Chepfer et al., 2001; Baran and Labonnote, 2006; van Diedenhoven et al., 2014), of aerosols over cloud-free oceans (e.g., Tanré et al., 2001, 2011; Bellouin et al., 2003; Herman et al., 2005), and of aerosols above clouds (e.g., Waquet et al., 2013a,b; Peers et al., 2015) and in between clouds (van der Stap et al., 2015).

PACE discussions (INV and FWD RT studies): aerosol models and data, UV-A scattering in atmosphere

The prospect of using highly accurate 3M radiance and/or (hyperspectral) UV-SWIR radiance measurements to retrieve aerosol optical and physical properties also poses new challenges for the interpretation of these retrievals. For example, the majority of existing retrieval algorithms such as GRASP still assume a single complex refractive index for the fine mode aerosol, and a single complex refractive index for the coarse mode aerosol. In reality, each aerosol mode may consist of several components that are either internally or externally mixed. The challenge here is to extract those individual components from the retrieved m, ω, r_e, v_e, τ and particle shape. Internal mixtures come in many varieties that may involve both soluble and (non-spherical) insoluble components (Gibson et al., 2007; Wise et al., 2007; Freney et al., 2010). For such mixtures one may, under certain circumstances (Mishchenko et al., 2016), use the Maxwell Garnett effective medium approximation (Bohren and Huffman, 1983) to decompose the retrieved effective *m* into those of the individual components. Schuster et al. (2016) adopted such an approach (albeit for the spectral variation of the retrieved ω) to extract the relative proportion of carbonaceous aerosols and free iron minerals (hematite and goethite) in absorbing aerosols. Alternatively, one may use brute force, state-of-the-art RT methods to study (and possibly characterize) the scattering patterns of internally mixed complex components (Mishchenko and Dlugach, 2012; Mishchenko et al., 2013; Li and Mishchenko, 2016). The case for externally mixed components is more challenging, as there are no simple rules for the effective *m* and ω for such mixtures. Hasekamp et al. (2011) and Russell et al. (2014) use a particle volume-weighted approach to obtain an effective refractive index for an external mixture of a fine and a coarse mode aerosol. However, the validity and limits of this approach remain to be investigated for external mixtures. Alternatively, one may just simply want to flag the presence of externally mixed multiple aerosol types. The multi-parameter classification method described by Russell et al. (2014) for a dominating single aerosol type offers a possible venue for such tasks. Regardless of the aerosol mixture type, identifying the individual components will require an extensive database of their complex refractive indices that covers the full spectral range of UV-SWIR.

The PACE mission will continue to need well-defined characterization of aerosol optical properties for RT calculations, but will require those models to cover the expanded spectral range and spectral density of OCI. As explained above, even algorithms applied to a PACE polarimeter measuring 3M will require advanced (e.g., multi-component, inhomogeneous) aerosol models to test the remaining assumptions inherent in those algorithms. Thus, aerosol models for RT in the PACE era will need to be even more detailed, with greater characterization and better accuracy than they are now. These requirements and considerations apply across the board to the next generation of sensors intending to enhance aerosol characterization from space, not just to the three PACE instruments. For example the multi-viewing multi-channel multi-polarization imager (3MI) (Fougnie et al., 2018) will face the same challenges in validating retrievals and supporting remaining assumptions as the PACE polarimeters, and will require comprehensive measurement-based aerosol models.

Through the era of the Earth Observing System (EOS) that began with the launch of the Terra satellite, aerosol models for RT and remote sensing have become anchored in the statistics from the aerosol properties retrieved from the ground-based remote sensing measurements of the Aerosol Robotic Network (AERONET; Holben et al., 1998; Dubovik and King, 2000; Dubovik et al., 2000). The AERONET database provides a wealth of statistics of retrieved aerosol optical properties that cover a wide range of conditions, although the open ocean is not well sampled. This allows linking variability in optical properties to measurable or retrievable parameters, such as aerosol optical depth, or more recently to relative humidity (Ahmad et al., 2010). Furthermore, representations of aerosols in RT are moving away from assumptions of sphericity and Mie theory (Meng et al., 2010; Gassó and Torres, 2016; Lee et al., 2017).

However, remote sensing inversions from AERONET are inadequate by themselves to provide all the detailed characterization necessary for the PACE era. For example, the four discrete measured and inverted wavelengths from AERONET do not span the spectral range and resolution needed by PACE, and specifically do not include any characterization of the UV. The SkyNet network provides an alternative, though less widely distributed network of upward-looking radiometers and inversion products that include measurements and inversions at UV channels (Takamura and Nakajima, 2004), which will help, but again will not be adequate by themselves. Another example is the lack of models in AERONET inversion methods that properly characterize important aerosol types such as volcanic ash and biogenic particles. To obtain the necessary aerosol characterization from PACE we will require measurements made *in situ*, either in the laboratory or in the field. These should include spectral absorption/single scattering albedo and real part of the refractive index across the spectrum measured by PACE OCI and especially in the near-UV, particle size, and spectral elements of the scattering phase matrix including single scattering phase function/polarized single scattering phase function (Kahn et al., 2017). Then, to make use of these measurements for RT and remote sensing in the atmosphere, we need a set of complementary measurements to translate the *in situ* measurements to ambient conditions in the atmospheric column. These ancillary measurements should include aerosol layer height, particle hygroscopicity growth factor, among others, depending on the measurement situation (Kahn et al., 2017).

In addition, we foresee that new scrutiny of the FWD RT problem may be needed. Tolerable accuracy for analyses of past and current aerosol satellite sensors may no longer be sufficient to match PACE's accuracy requirements for hyperspectral radiometry and multi-angle polarimetry in the UV-VIS. To this end, we need benchmarking of RT codes for coupled AOS models that, in addition to hydrosol particulates (*cf.* "3.4.1 RT Validations" section), also include aerosol scenarios. It will also be necessary to re-evaluate modeled molecular scattering profiles that are important for the interpretation and retrieval of aerosols from measurements in the near-UV. Inclusion of inelastic atmospheric processes in atmospheric models has already begun (see e.g., Landgraf et al., 2004; Deelen et al., 2005; Spurr et al., 2008; Rozanov et al., 2014, 2017; Lelli et al., 2017). The point is that as space-based measurements improve and add capability for aerosol characterization, aspects of RT code that introduce uncertainties too small to affect simplistic aerosol retrievals may now create too much uncertainty to make use of the new measurements. Even the input solar spectrum becomes a source of unacceptable error, again in the near-UV where uncertainties in solar spectrum measurements are worse (see also discussion in section "3.4.3 UV Remote Sensing of AOS"). Finally, optimal estimation methods used to make use of the information data set provided by multi-angle polarimeters require on-line RT calculations, rather than Look-Up Tables. This requirement makes real-time aerosol retrievals cumbersome in an operational environment. Speeding up RT codes, without losing accuracy, will be a high priority.

PACE updates (INV RT studies): scattering property measurements, height retrievals

Laboratory and field measurements are beginning to meet the challenge of providing aerosol characterization with greater detail and accuracy, and for a wider variety of aerosol types. A new technique (Martins et al., 2009; Rocha-Lima et al., 2014, 2018), that is able to determine spectral absorption/single scattering albedo continuously from 300 to 2500 nm has been applied to volcanic ash and Saharan dust particles (**Figure 9**), although it is still unclear how to translate these laboratory measurements to ambient atmospheric conditions for RT. Another measurement innovation that can provide greater detail for aerosol models is airborne measurement of particle phase matrix elements (Dolgos and Martins, 2014). By measuring the single scattering function and polarized phase function across the range of scattering angles from 3° to 177° at 1° angular resolution, we can distinguish aerosol type, even separating similar fine mode types such as biogenics and biomass burning (**Figure 10**; Espinosa et al., 2017). Polarization is necessary to make that distinction and physically the differences lie mainly in differences in real part of the refractive index, not in size of the particles.

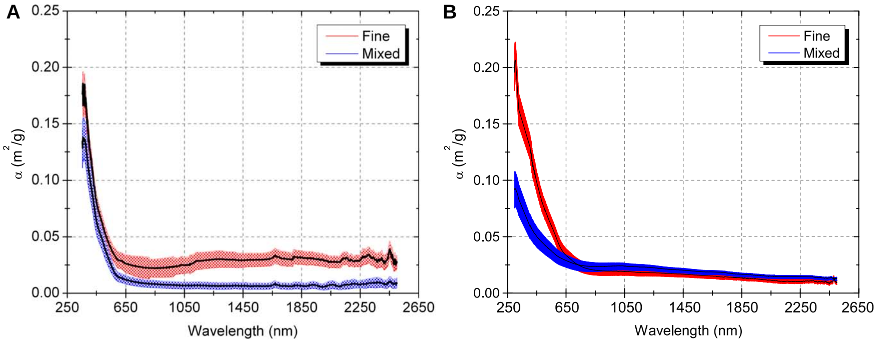

FIGURE 9 | Spectral mass absorption efficiency (m^2/g) for Saharan dust **(A)** and volcanic ash **(B)**, measured as a continuous spectrum from 300 to 2350 nm. The sampled particles were size separated into a fine mode (<1 µm: red) and all sizes (blue). Panels taken from Rocha-Lima et al. (2014, Figure 8) and Rocha-Lima et al. (2018, Figure 7).

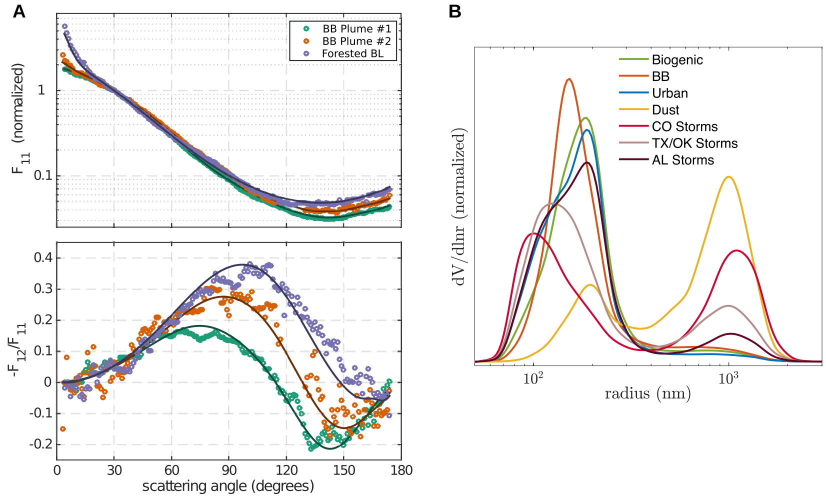

FIGURE 10 | (A) Measured phase function (F_{11}) in upper panel and degree of linear polarization ($-F_{12}/F_{11}$) in lower panel for three different samples encountered during the SEAC4RS campaign in North America in 2013. The samples include two different biomass burning plumes (BB plume) and a pass through a forest boundary layer heavy in biogenic aerosol (Forested BL). Shown are direct measurements from the UMBC PI-Neph, taken from Figure 5 in Espinosa et al. (2017). **(B)** Retrieved particle volume size distributions using the GRASP (Dubovik et al., 2014) retrieval software with PI-Neph inputs similar to those shown in the top panel. Different aerosol types after Espinosa et al. (2018) are shown. Data were collected during the DC3 (2012) and SEAC4RS (2013) field campaigns.

Then, similar to inversions applied to AERONET observations, inversions applied to these measured phase matrix elements can provide size distribution and real part of the refractive index (Espinosa et al., 2017). The scattering measurements are made *in situ* from aircraft and are subject to particle size limitations imposed by inlets and loss of volatiles as noted in other *in situ* measurements, but similar measurements can be made in ambient conditions with a specially designed open-path instrument mounted below the aircraft wing that eliminates the need for inlets or tubes. Direct measurements of scattering matrix elements depend on discrete laser wavelengths that inadequately span the spectral range of future space sensors. However, recently a custom instrument was used with laser wavelengths at 375 nm and 405 nm to characterize phase matrix elements of biomass burning aerosol in the deep blue and near-UV (Manfred et al., 2018), an important step forward toward providing the input to RT modeling in the PACE era. The recent work shown above is just a sample of the increased capability of laboratory and *in situ* field measurements of aerosol particle properties now reaching a mature stage. As deployment of these new measurement systems increases and the database of particle characterization grows, we can use these detailed measurements to guide the development of new aerosol models for RT that will span OCI's broad spectrum and represent new aerosol types. The challenge will be in translating these *in situ* measurements to represent aerosol properties of the total column in ambient conditions.

Advancements have also been made in aerosol height retrievals from OCI-like passive remote sensing data [e.g., Duforêt et al. (2007) and Dubuisson et al. (2009) from POLDER and MERIS (Medium Resolution Imaging Spectrometer) data]. Sensitivity studies on the information content of aerosol height over oceans in OCI's hyperspectral measurements of Oxygen A- and B-band radiance are reported by Davis and Kalashnikova (2019), Frouin et al. (2019), and Remer et al. (2019). In addition, Xu X. et al. (2017) studied aerosol height retrievals over vegetated land from actual Oxygen B-band radiance measured by the EPIC (Earth Polychromatic Imaging Camera) instrument onboard the DSCOVR (Deep Space Climate Observatory) platform. One drawback of aerosol height retrievals from Oxygen A- and B-band radiance is that the aerosol optical thickness has to be sufficiently large (i.e., $\geq$0.3) at 550 nm when over relatively bright surfaces. A solution is to use multi-angle polarization measurements in the deep-blue, exploiting the decrease caused by aerosol scattering in the polarization originating from pure molecular scattering. These measurements are less sensitive to the surface (see e.g., Chowdhary et al., 2012), and allow aerosol height to be retrieved at lower aerosol optical depths as demonstrated by Wu et al. (2016) (see also Chowdhary et al., 2005). More information on aerosol height retrievals from these and other passive remote sensing data (e.g., from multi-angle radiance-only data) is provided in Xu et al. (2018).

3.3.2 Gases

Heritage studies: gas absorption in the UV-SWIR spectrum

Retrievals of absorbing gas column concentrations are important for the atmospheric science discipline. The ocean discipline benefits equally, if not more, from such retrievals. That is because accounting for absorbing gases in the atmosphere is an important part of the atmospheric correction process in the retrieval of the ocean remote sensing reflectance (Rrs – see definition in **Table 2**) from satellite observations. That process requires a better understanding of modeling non-gray gas absorption in vertically inhomogenous atmosphere in RT simulations. In NASA's heritage ocean color retrievals, a simple gas correction of the TOA measurements, based on Beer's–Lambert law treatment, is performed using ancillary or climatology gas column concentration from NOAA's National Center of Environmental Predication (NCEP) (Derber et al., 1991; Gordon and Wang, 1994b; Kanamitsu et al., 2002; Ahmad et al., 2007; Dee et al., 2011). Traditional ocean color bands commonly are situated in atmospheric transparent windows to avoid the strong absorption features by O_2 (Oxygen) and H_2O (water vapor), which can not be treated with the simple Beer–Lambert RT equation. Nevertheless, the spectral bands of NASA's heritage multi-spectral ocean color sensors, such as SeaWiFS (Sea Viewing Wide Field-of-View Sensor), MODIS, and VIIRS (Visible Infrared Imaging Radiometer), are still impacted by the absorption of some atmospheric gases, mainly O_3 (Ozone) and NO_2 (Nitrogen Dioxide), within the broad UV-VIS spectrum. For hyperspectral sensors, such gaseous absorption in the UV-VIS spectrum can be erroneously attributed to plankton spectral signature, degrading the plankton type detection capabilities, which are central to the PACE mission. In addition, the hyperspectral detection capabilities of the OCI instrument on-board the PACE mission will require thorough corrections for absorption by O_2 and H_2O, most importantly in the plankton fluorescence spectral range (~685 nm). The O_3 correction is possible with the OCI UV capability; however, NO_2 correction is more challenging due to the insufficient spectral resolution in the UV. Since NO_2 concentration can be significantly higher in coastal industrial regions, it can have a significant impact on the ocean reflectance retrievals in the blue spectral range (Tzortziou et al., 2018). Future research is necessary to address these concerns. The retrieval of, and subsequent correction for absorption by, Column Water Vapor (CWV) is a challenging task due to (i) the complexity of the CWV profile; (ii) the spectrally variable nature of CWV absorption features; and (iii) the spatial heterogeneity of CWV concentration. Similarly, the Oxygen A- and B-bands (at ~760 nm and ~687 nm, respectively) can also be challenging to utilize for ocean color retrievals due to the presence of scattering aerosols near the boundary layer of the atmosphere. Thus, a Beer's–Lambert compensation of the water vapor and Oxygen bands, without consideration of the absorption-scattering coupling effects, the overlapping absorption of different gas species, and the inhomogeneous path, could lead to significant errors (Bouffiès et al., 1997; Dubuisson et al., 2004; Ibrahim et al., 2018).

The first challenge toward addressing the impact of absorption by H_2O and O_2 on OCI's hyperspectral data is to quantify this impact. This, in turn, requires the use of RT methods that can properly handle all absorbing gases within OCI's spectral coverage. That is, accurate RT simulations need to be performed at finer spectral resolutions than for heritage ocean color sensors to properly account for the narrow spectral features of H_2O and O_2. Brute force Line-by-Line (LBL) RT simulations are the most accurate (Gao et al., 2000, 2009), however, they are also very computational intensive. Several methods have been developed in the past to improve the efficiency of the LBL RT method, such as the *band model* method, the *k*-distribution method, the *correlated-k* distribution method, and the *double-k* method (Goody and Yung, 1989; Lacis and Oinas, 1991; Fu and Liou, 1992; Duan et al., 2005). The band model is the most efficient method since it analytically computes the transmittance of a homogenous path in the atmosphere for a wide range of absorber amounts. However, this method lacks sufficient accuracy for non-gray gaseous absorption, for vertically inhomogeneous atmospheres, and in the presence of scattering (Goody, 1952; Malkmus, 1967; Lacis and Oinas, 1991). The *k*-distribution method provides a highly accurate representation of the transmittance by grouping the gas LBL absorption features by strength within an arbitrary band, thus producing a smooth function that can be fitted with analytical expressions or represented by a relatively small number of bins. The *k*-distribution method is an exact alternative to the LBL method and the user can define the accuracy by defining the number of bins depending on the application with remarkable computational efficiency. To further increase the computational efficiency and accuracy in inhomogeneous atmosphere, the correlated-*k* method derives an analytical relationship between the *k*-distribution coefficients of multiple layers of the atmosphere at different pressure levels. Both the *k*-distribution and correlated-*k* provide accurate transmittance calculations for inhomogeneous atmosphere, overlapping gases, and in the presence of scattering in the atmosphere. However, the correlated-*k* method suffers in overlapping absorption between H_2O and CO_2 (Carbon Oxide) and in the Oxygen A-band (overlapping H_2O and O_2), where there is a poor vertical correlation (Lacis and Oinas, 1991). Note that Oxygen A- and B-bands are specifically important for PACE aerosol layer height retrievals and for the chlorophyll fluorescence detection, respectively (Dubuisson et al., 2001; Zhai et al., 2018). For example, Dubuisson et al. (2001) have utilized the Oxygen A-band to retrieve the aerosol layer height showing a significant underestimation of the scale height over dark ocean surfaces. Thus, Dubuisson et al. (2001) suggested a correction factor based on extensive RT simulations for varying aerosol optical depth and geometries, reducing the uncertainty by an order of magnitude. The importance of a correction factor due to the coupling effects was first highlighted by Frouin et al. (1990) to improve the CWV estimates over the dark ocean in the presence of scattering aerosols. Dubuisson et al. (2004) later formulated this method such that a correction factor as a function of geometry, aerosol optical depth and scale height is derived based on RT simulations to reduce CWV retrieval and correction uncertainties. A more recent method fits the hyperspectral measurements with analytical expressions involving both the total absorption optical depth and the absorption optical depth from TOA to the main scattering layer, which couples the absorption process with the scattering process in the atmosphere (Duan et al., 2005). A careful assessment of these methods in terms of numerical uncertainties and efficiencies are needed to determine an optimal method that can both satisfy the computational efficiency and accuracy conditions. In summary, the coupling effect of absorption and scattering in strongly absorbing spectral regions is problematic for ocean color remote sensing directly through imperfect correction of gas features that could be erroneously attributed to the ocean constituents or indirectly by impacting the assessment of the aerosol radiance necessary for the atmospheric correction (i.e., scale height, or out-of-band effects) (for example Dubuisson et al., 2001; Gordon, 1995). One suggestion to minimize these effects is to use a correction method as suggested by Dubuisson et al. (2001, 2004) for a large set of environmental conditions. Another possibility is to generate atmospheric correction algorithms (i.e., look-up tables, or LUTs) or gas retrieval algorithms with RT codes that inherently takes in consideration the strong gases absorption coupling with scattering; however, that could dramatically increase the dimension and complexity of the algorithm LUTs. A trade-off study would be necessary for such assessment in order to provide an optimal utilization to operationally capable algorithm for the PACE mission.

The second challenge toward addressing the impact of H_2O and O_2 absorption on OCI's hyperspectral data is to retrieve and compensate for the CWV transmittance. In the EOS era, NIR data have been utilized as an alternative to thermal IR data to retrieve CWV over land and ocean (Chesters et al., 1983; Susskind et al., 1984). The feasibility to retrieve CWV amount using 940-nm water vapor band was first demonstrated by Gao and Goetz (1990) and Gao et al. (1993) using data collected by AVIRIS (Airborne Visible/Infrared Imaging Spectrometer) onboard the ER-2 aircraft platform and independently by Frouin et al. (1990) using data collected by a dedicated, aircraft-mounted radiometer. The retrievals were based on the differential absorption technique, where the ratio of the TOA reflectance in a window channel to a water vapor channel (or more generally in two channels differentially affected by water vapor absorption) is correlated to the water vapor amount along the path. CWV retrievals using the 940-nm channel are also limited to bright surfaces, such as land, ice, and clouds – and, over oceans, to sun glint regions. Over dark surfaces, as indicated above, the coupling between aerosol scattering and water vapor absorption, modulated by water vapor content, can be exploited to yield sufficiently accurate retrievals (Dubuisson et al., 2004). The differential absorption technique has been extended for application to MODIS data, where three water vapor channels with different sensitivities to moisture (i.e., 905, 930, and 940 nm) are utilized to retrieve the CWV at different amounts. The method by Gao and Goetz (1990) utilizes two window channels and one water vapor channel to remove the spectral dependency of the surface. This is achieved in the Frouin et al. (1990) method by utilizing two channels, one narrow, the other wide, centered on the same wavelength at the maximum of water vapor absorption. The three-band ratio technique applied to MODIS data uses a LUT search of pre-computed three band ratios of the water vapor transmittance using either LBL, MODTRAN (Moderate Resolution Atmospheric Transmission), or LOWTRAN (Low Resolution Atmospheric Transmission) calculations. The OCI instrument will have one wide 940 nm band with a 50 nm FWHM (Full Width at Half Maximum) as opposed to MODIS three water vapor channels. This limitation will allow CWV retrievals albeit with a less dynamic range. However, the MODIS approach hints that such retrievals may be improved using other additional water vapor bands that lie within the OCI spectral range such as 720 nm and 820 nm spectral regions.

Additionally, OCI will have spectral measurements capability in the UV with high radiometric quality that will allow for ozone retrievals using the simple differential absorption algorithm used for OMI data, but instead at high spatial resolution (Veefkind et al., 2006 and references therein). However, the UV spectral range requires rigorous multiple scattering calculations, since the scattering and absorption of air molecules is significantly enhanced at shorter wavelengths. The ozone vertical profile is required as *a priori* in order to estimate the ozone concentration. A RT benchmark analysis is required to improve the algorithmic uncertainties for ozone retrievals and corrections.

PACE updates (FWD RT studies): accounting for absorbing gases in hyperspectral ocean color remote sensing

At the NASA Ocean Biology Processing Group (OBPG), FWD RT studies were conducted to test an operationally capable hyperspectral atmospheric correction (AC) method that accounts for gas absorption. A fully operational AC has been implemented and validated using proxy data sets from the HICO (Hyperspectral Imager for Coastal Ocean) and the AVIRIS instruments that resemble anticipated data from the OCI instrument (Ibrahim et al., 2018). This development was based on extending the multi-spectral AC algorithm to a hyperspectral one (Ahmad et al., 2010; Ibrahim et al., 2018). The main additional feature is the correction of water vapor, while other gases corrections are based on the ocean color heritage approach (Gordon and Wang, 1994b). The ATREM (ATmospheric REMoval) code was merged into the operational Level 1 to Level 2 (L2GEN) processing code, in order to primarily handle water vapor correction and CWV retrieval, for each pixel observation (Gao et al., 1993).

A *k*-distribution method was implemented in the current operational AC procedure to increase the computational efficiency of the LBL water vapor transmittance calculations without compromising the accuracy (Lacis and Oinas, 1991; Kato et al., 1999). A pre-computed table of *k*-distribution coefficients was stored for every band and layer of the atmosphere, and the corresponding AC method was tested and validated by applying the algorithm to HICO proxy data retrievals and comparing against *in situ* observations of the ocean remote sensing reflectance Rrs obtained from SeaBASS (SeaWiFS Bio-optical Archive and Storage System) and AERONET-OC(Ocean Color). Note that while the *k*-distribution ignores coupling effects between gaseous absorption and scattering in narrow spectral features such as the O_2 bands, its implementation proved to be simple and accurate for band-averaged transmittances. As an illustration, **Figure 11** below shows the retrieval of the hyperspectral Rrs from HICO observations at the Chesapeake Bay region on the east coast of the United States, as compared to MODIS Aqua multi-spectral retrievals. The Rrs retrievals are shown for three different locations in the Bay water. Note that the agreement seen for the MODIS and HICO retrievals of Rrs is desirable and expected for a wide dynamic range, since both sensors are vicariously calibrated at the same site and processed with the same atmospheric correction algorithm. However, the wealth of the hyperspectral Rrs information from HICO or OCI is expected to significantly improve ocean color products provided that AC includes a proper handling of gases absorption for all wavelengths.

The OCI instrument will continue the heritage CWV retrieval using the 940-nm band. However, compared to MODIS' three bands near the 940 nm regions (905 nm, 935 nm, and 940 nm) that each have different sensitivities to water vapor amount, OCI's 940-nm band has a wider spectral resolution and will be less sensitive to large water vapor amounts over dark surfaces due to saturation of absorbing amounts and small SNR. Water vapor correction using OCI's 940-nm band over the dark ocean is therefore not optimal. However, Ibrahim et al. (2018) showed a better water vapor correction can be obtained by utilizing the less saturated 720 nm and 820 nm bands (or a combination of both) on OCI, especially for large water vapor amounts. The analysis shows less systematic bias in CWV retrievals over the ocean than using only the 940-nm band. Based on extensive RT simulations, the retrieval error using a combination of 940 and 820 nm, 720 and 820 nm, and 720 nm only is 19, 8.5, and 9%, respectively. CWV retrievals uncertainty using the 720 and 820 nm bands corroborates with the ones retrieved by microwave radiometry over dark oceans (Gao and Kaufman, 2003). A combination of the three strongly absorbing water vapor bands (720, 820, and 940 nm) within the OCI spectral coverage will therefore allow retrievals of CWV with large dynamic range, over land and ocean. It is important to note that retrieving the CWV using NIR bands does not necessarily mean a proper compensation of the water vapor transmittance at some of the visible bands. This is primarily due to the dependence of the water vapor transmittance on the vertical profile of water vapor and temperature/pressure, which is currently assumed to be the US standard 1976 (Anderson et al., 1986). Current efforts within the PACE team are being taken to supplement the vertical profile information from ancillary sources such as NASA's Goddard Earth Observing System Model, Version 5 (GEOS-5) provided by the Global Modeling and Assimilation Office (GMAO) which provides 3-h instantaneous vertically resolved specific humidity that can scale the observed data (Gelaro et al., 2017).

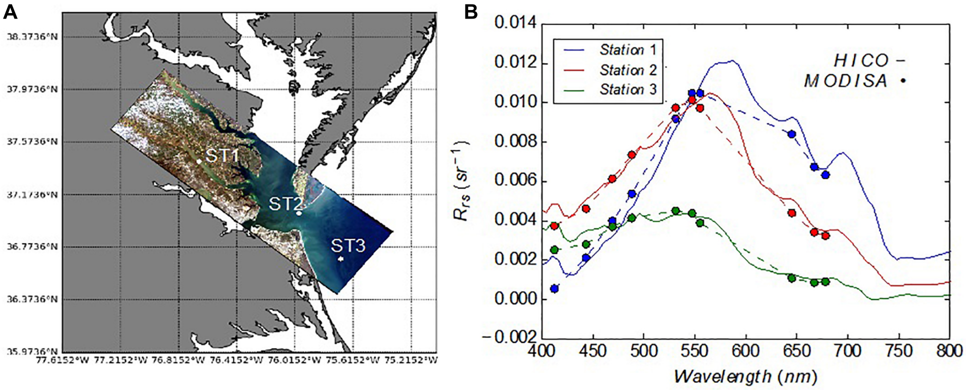

FIGURE 11 | (A) HICO true color image at the Chesapeake Bay waters. **(B)** the retrieved Rrs at three different locations from HICO and MODIS Aqua after atmospheric correction and water vapor correction using the *k*-distribution method for gaseous absorption. This figure has been adapted from Ibrahim et al. (2018).

Synthetic data generated by RT solvers will be used to test future PACE atmospheric correction algorithms. It is important for such data to properly account for gas absorption in cases of (i) non-narrow (e.g., overlapping) absorption bands, and (ii) particle scattering interaction. These cases are not well handled by the *k*-distribution. The double-*k* method has been applied to a RT model that accounts for all major light matter interaction mechanisms, including gas absorption, scattering and absorption by particulates in atmosphere and ocean, atmosphere and ocean coupling, and inelastic scattering mechanisms in ocean waters. The base line of the model is the RT model developed by Zhai et al. (2010, 2015, 2017a). Gas absorption from water vapor, oxygen, ozone, nitrogen dioxide, methane, and carbon dioxide are included. First, hyperspectral lookup tables of gas absorption coefficients have been built using the atmospheric radiative transfer simulator (ARTS) (Buehler et al., 2011) based on the HITRAN (HIgh Resolution TRANsmission molecular database) 2012 database (Rothman et al., 2013) for water vapor, oxygen, carbon dioxide, and methane. Absorptions by ozone and nitrogen dioxide are included separately using measurements of Daumont et al. (1992) and Bogumil et al. (2003). For each measurement channel, we choose several representative gas absorption optical depths, and run the full RT that couples gas absorption and scattering. We then apply the double-*k* method (Duan et al., 2005) to fit the full hyperspectral line-by-line radiance using the radiance values at wavelengths with known absorption optical depth. The instrument radiance is found by integrating the fitted spectral radiance with the instrument line shape function. Generally a high accuracy of 0.1% can be achieved using the double-*k* method in comparison to the exact line-by-line RT simulations. In Ibrahim et al. (2018), we used this implementation to show that ignoring the coupling between water vapor absorption and particulate scattering in simulating spaceborne NIR radiance between 600 and 800 nm leads to an error between 0 and 10% for one particular case with an aerosol optical depth of 0.2 at 550 nm. The error becomes larger for more absorptive bands. This highly accurate model is therefore suitable to generate synthetic PACE science data for studies on CWV retrievals in the NIR and/or correction for gaseous absorption in the VIS.

3.4 AOS Models

3.4.1 RT Validations

Heritage studies: benchmark results

The current literature contains a multitude of benchmark results to validate vector RT computations in isolated slabs of atmosphere. Tabulated results can be found for homogeneous atmospheres containing molecules only (Coulson et al., 1960; Stammes et al., 1989; Mishchenko, 1990; Natraj et al., 2009; Natraj and Hovenier, 2012), for (in-) homogeneous atmospheres containing (molecules and) aerosols (de Haan et al., 1987; Wauben and Hovenier, 1992; Siewert, 2000), and for homogeneous atmospheres consisting of cloud droplets (Kokhanovsky et al., 2010). However, there exist no tables for the polarized radiance computed for AOS models. Although comparisons for polarized RT computations using different RT codes have been reported (e.g., Zhai et al., 2010; Hollstein and Fischer, 2012; Chami et al., 2015), the results are *drawn* as a function of viewing angle which limits the accuracy that can be extracted to validate other RT codes. Current and future remote sensing polarimeters can measure the DoLP to an accuracy of 0.1–0.5%, which requires that the RT codes used to analyze these measurements must be validated to at least the same accuracy. Even quantitative RT results for just the intensity of light computed for AOS models are rare to find (Mobley et al., 1993; Bulgarelli and Doyle, 2004).

PACE updates (FWD RT studies): tabulated benchmark results

To provide accurate tabulated results for the total and linear polarized upwelling radiance just above the ocean surface (SRF) and at the top of the atmosphere (TOA), RT computations were performed (Chowdhary et al., "Benchmark results for scalar and vector radiative transfer computations of light in atmosphere-ocean systems", unpublished) for different viewing geometries, wavelengths, and AOS models (see **Figure 12**). The viewing geometries for these tables scan the upwelling radiance in the solar principal plane (azimuth angle $\varphi = 0°$ and 180°) and in an off-principal plane (azimuth angle $\varphi = 60°$ and 240°) for viewing angle θ that ranges between 0° and 60° (measured with respect to the surface normal) in steps of 5°. Two sun angles ($\theta_0 = 30°$ and 60°) are considered for each scan; hence, the viewing geometries include the backscattering direction, the sun glint region, and observations that graze neutral polarization points seen in actual airborne observations (Kawata and Yakazaki, 1998) and in simulations (Adams and Kattawar, 1997; Chowdhary et al., 2012). Four wavelengths (350, 450, 550, and 650 nm) are chosen for these tables to sample the UV-VIS-NIR part of the spectrum that is monitored by the PACE mission. Furthermore, four hypothetical AOS models are used for our computations. They increase gradually in complexity from (i) a purely molecular atmosphere above a wind-ruffled ocean surface (taken from Cox and Munk, 1954) with no ocean body (*AOS-I* model); to (ii) a pure ocean water body below a wind-ruffled ocean surface with no atmosphere (*AOS-II* model); onward to (iii) a fully coupled simple atmosphere-ocean system body (*AOS-III* model) containing a molecular atmosphere, wind-ruffled ocean surface and pure ocean water; and finally to (iv) a coupled complex atmosphere-ocean system (*AOS-IV* model), that includes scattering by molecules, wind-ruffled ocean surface, pure ocean water, and sharp forward-scattering marine particulates [i.e., the D-P mixture taken from Chowdhary et al. (2012), with [Chla] = 0.03 mg/m^3 at 350 and 450 nm and [Chla] = 3.00 mg/m^3 at 550 and 650 nm]. Some results presented for the *AOS-I* model can be compared with those reported for an isolated molecular atmosphere by Natraj et al. (2009) if the optical thickness is set to 0.5 (this model is denoted by *AOS-I**), whereas the purpose of the advanced *AOS-IV* model is to produce realistic values for SRF and TOA observations. All computations were performed thrice using RT codes that are based on different RT methods, i.e., the

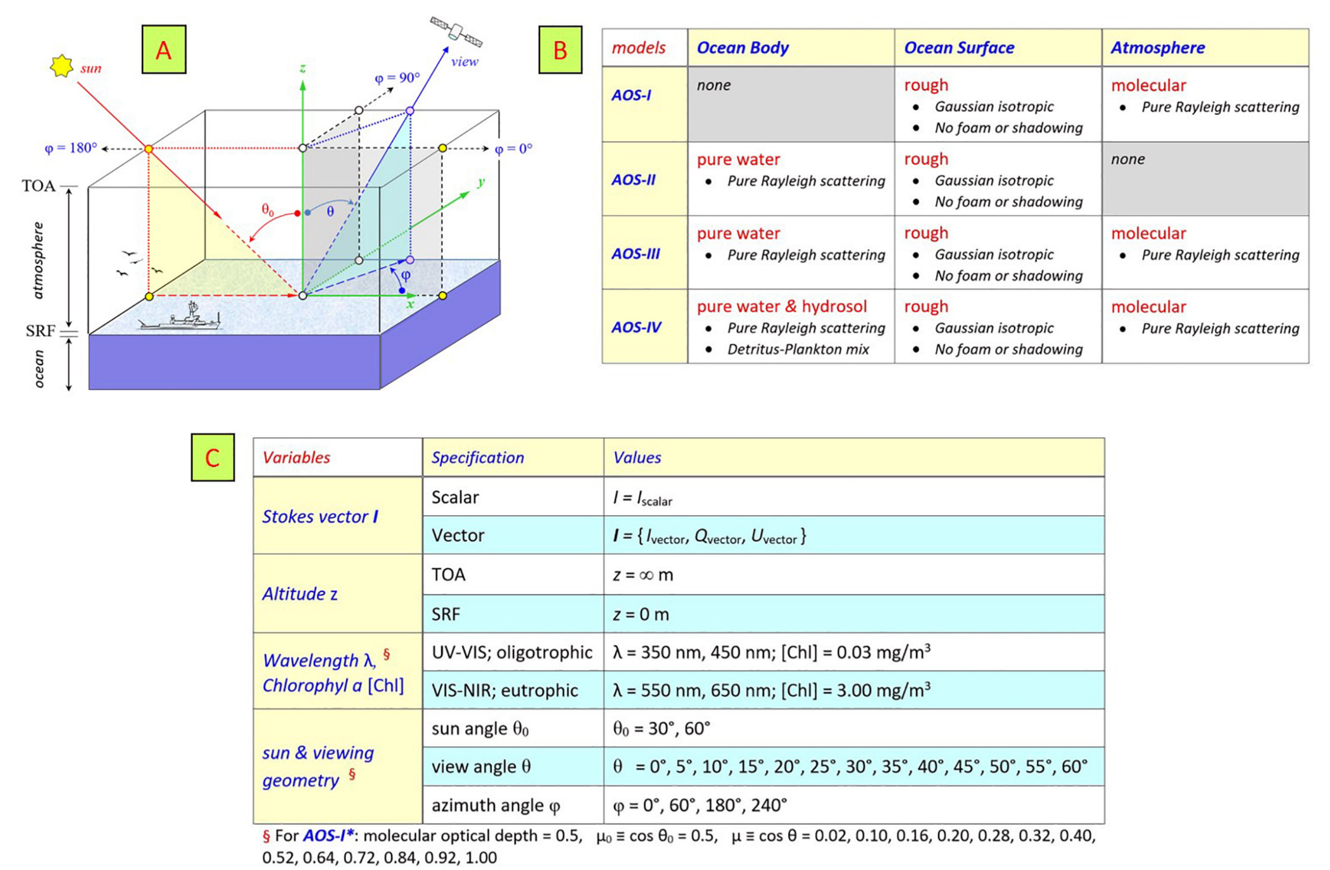

models	Ocean Body	Ocean Surface	Atmosphere
AOS-I	none	rough • Gaussian isotropic • No foam or shadowing	molecular • Pure Rayleigh scattering
AOS-II	pure water • Pure Rayleigh scattering	rough • Gaussian isotropic • No foam or shadowing	none
AOS-III	pure water • Pure Rayleigh scattering	rough • Gaussian isotropic • No foam or shadowing	molecular • Pure Rayleigh scattering
AOS-IV	pure water & hydrosol • Pure Rayleigh scattering • Detritus-Plankton mix	rough • Gaussian isotropic • No foam or shadowing	molecular • Pure Rayleigh scattering

Variables	Specification	Values
Stokes vector ***I***	Scalar	$I = I_{\text{scalar}}$
	Vector	$\boldsymbol{I} = \{I_{\text{vector}}, Q_{\text{vector}}, U_{\text{vector}}\}$
Altitude z	TOA	$z = \infty$ m
	SRF	$z = 0$ m
Wavelength λ, § Chlorophyl *a* [Chl]	UV-VIS; oligotrophic	λ = 350 nm, 450 nm; [Chl] = 0.03 mg/m^3
	VIS-NIR; eutrophic	λ = 550 nm, 650 nm; [Chl] = 3.00 mg/m^3
sun & viewing geometry §	sun angle θ_0	θ_0 = 30°, 60°
	view angle θ	θ = 0°, 5°, 10°, 15°, 20°, 25°, 30°, 35°, 40°, 45°, 50°, 55°, 60°
	azimuth angle φ	φ = 0°, 60°, 180°, 240°

§ For ***AOS-I****: molecular optical depth = 0.5, $\mu_0 \equiv \cos\theta_0 = 0.5$, $\mu \equiv \cos\theta$ = 0.02, 0.10, 0.16, 0.20, 0.28, 0.32, 0.40, 0.52, 0.64, 0.72, 0.84, 0.92, 1.00

FIGURE 12 | (A) Schematic illustration of Atmosphere-Ocean System (AOS) model and scattering geometries used for RT benchmark computations. **(B)** Specification of AOS models shown in sub-panel **(A)**. **(C)** Specification of variables used for each AOS model computation.

Doubling-Adding RT code *eGAP* described in Chowdhary et al. (2006), the Successive-Order-of-Scattering RT code *SOS-CAOS* described in Zhai et al. (2009, 2010), and the hybrid Markov-Chain-Adding-Doubling RT code *MarCH-AD* described in Xu et al. (2016). For these computations, the number of underwater light quadrature points used for *AOS-I* and *AOS-III* models was set at 80 to adequately capture refraction of light by the ocean surface, while in *AOS-IV* model it was set at 300 to capture the sharp unnormalized diffraction peaks (corresponding asymmetry parameters ≥ 0.95) for scattering by D-P particulates. A fourth code, i.e., the Monte Carlo RT code *SMART-G* described in Ramon et al. (2019), was also used for *OAS-I* model computations in which the rough ocean surface was treated as a BRDF surface. The number of photons used for the latter computations was set at 3×10^{11}. In total, Chowdhary et al. ("Benchmark results for scalar and vector radiative transfer computations of light in atmosphere-ocean systems", unpublished) provide more than 25,000 tabulated RT results in units of reflectance. The stated reflectance accuracies for these tables, based on the maximum absolute difference in reflectance values obtained from the 3+ RT code computations, is better than 10^{-5} for *AOS-I* and *AOS-IV* models, and better than 10^{-6} for *AOS-II* and *AOS-III* models. The corresponding DoLP values vary by less than 0.2% for a handful of tabulated reflectance values, and by less than 0.1% for all other scattering geometries, atmosphere-ocean systems, wavelengths, and altitudes considered in this work. This satisfies the forward RT accuracy requirement to match the measurement accuracy for all PACE satellite instruments (*cf.* "1.1 The PACE Mission" section).

3.4.2 Horizontal Variations

Heritage studies: horizontal variations

All the RT and retrieval studies mentioned thus far in this chapter approximate AOS models to be plane-parallel and horizontally homogeneous, i.e., they ignore the Earth's curvature and horizontal variations in the atmosphere (e.g., small-scale aerosol plumes and broken clouds) and ocean (e.g., turbid eddies, isolated sea ice patches, and land-water boundaries). These approximations simplify, and therefore speed up, the numerical implementation of RT computations and retrieval algorithms. Cases for which these simplifications are not valid are either avoided or require addition numerical corrections.

Monte Carlo RT methods have a natural ability to handle 3-dimensional scattering media, and are therefore are particularly well suited to study light propagation in spherical AOS models. However, the large computational effort required for these methods can become burdensome, especially if the need for higher accuracy and/or smaller spatial resolution increases. One approach to reduce this burden is to trace the light backward from the detector to the source. This so-called Backward Monte Carlo method has been used in a number of studies (Collins et al., 1972; Adams and Kattawar, 1978; Ding and Gordon, 1994; Oikarinen et al., 1999) to examine scattering of light in spherical atmospheres. Such studies and other ones based on different RT methods (e.g., Herman et al., 1995; Rozanov et al., 2001; Doicu and Trautmann, 2009) show that the radiance emerging from spherical atmospheres can deviate noticeably from the one for plane-parallel approximated atmospheres even for small viewing angles θ (measured with respect to the surface normal), that deviations increase with solar zenith angle θ_0 for $\theta_0 \geq 60°$, and that (depending on the aerosol type and load) these deviations cannot be ignored anymore if the solar zenith angle θ_0 becomes larger than 70°.

A commonly used correction for deviations occurring at large solar zenith angles is to only attenuate the direct solar beam by a spherical atmosphere while still using the plane-parallel approximation to compute the contribution of light scattered in the atmosphere (Dahlback and Stamnes, 1991). To improve the accuracy, single scattering may further be calculated in full spherical geometry (Spurr, 2002). Such pseudo-spherical approaches may still fail at solar zenith angles $\theta_0 \geq 85°$ (Caudill et al., 1997). More importantly, they do not address deviations from RT results obtained for plane-parallel atmospheres that can occur at small solar zenith angles. Another approach, described by Ding and Gordon (1994), is to only replace the radiance scattered by molecules in a plane-parallel atmosphere by the corresponding radiance scattered in a spherical atmosphere. This approach works well for solar zenith angles $\theta_0 > 70°$, but again does not affect much the RT results obtained for small solar zenith angles. Finally, we remark that while some of the above-mentioned studies (Rozanov et al., 2001; Doicu and Trautmann, 2009) consider the presence of a Lambertian ground surface (albeit ignoring the polarization of light in RT computations), none of them consider an ocean surface below a spherical atmosphere. The bidirectional and polarizing properties of an ocean surface strongly affects the radiance and polarization of light emerging from the top of the atmosphere, and may therefore change the impact that a spherical atmosphere has on RT computations for AOS models. There are RT methods available to study such phenomena (e.g., Xu et al., 2013), but they have not yet been applied to OCI studies for Earth.

AOS scenes exhibiting horizontal variations pose yet another problem in RT simulations. For atmospheric correction of ocean-color imagery, it is generally assumed that the target is horizontally homogeneous, or equivalently that the target is infinitely large. This "large target" formalism is generally appropriate in the open ocean, sufficiently far from clouds and land, since the intrinsic atmospheric reflectance (i.e., the signal that has not interacted with the water body) is the main perturbing signal. In the vicinity of land, near sea ice or clouds, and even where horizontal heterogeneity is large (case of upwelling areas), the impact of photons reflected by the environment of the target and scattered into the field of view may not be negligible and may yield erroneous water reflectance retrievals and derived biogeochemical variables (e.g., Tanré et al., 1981; Santer and Schmechtig, 2000). The problem is not only the adjacency effect at the wavelength of interest, i.e., UV to visible, but also (in some cases more importantly) the propagation to shorter wavelengths of errors in the determination of aerosol scattering in the red and NIR. At these wavelengths the environment reflectance is seen in the atmospheric correction scheme as part of the aerosol reflectance. The atmospheric variables controlling the adjacency effect are the aerosol amount (optical thickness) and altitude, and to a lesser extent the aerosol model (see Frouin et al., 2019).

PACE updates (FWD RT studies): spherical shells

The *SMART-G* radiation transfer code (Ramon et al., 2019) was used to examine the effects of Earth's sphericity on the radiance emerging from the atmosphere. This code is based on the Monte Carlo technique, works in either plane-parallel or in spherical-shell geometry, and accounts for polarization. A local estimate variance reduction technique (Marchuk et al., 1980; Rakimgulov and Ukhinov, 1994) is implemented for the radiance calculations. In spherical mode, the change in photon path due to index of refraction variations with altitude is neglected, which reduces accuracy at grazing angles and in twilight conditions. Inelastic processes (e.g., Raman scattering) are not taken into account. *SMART-G* is written in CUDA (Compute Unified Device Architecture) and runs on GPUs (Graphic Processing Units). For typical simulations, an acceleration factor of several hundred is obtained using the GPU-based code compared with CPU (Central Processing Unit) computing. This makes *SMART-G* competitive, in terms of computational burden, with codes based on other RT methods (e.g., discrete ordinate, doubling-adding, successive orders of scattering), while allowing maximum flexibility.

SMART-G was run with 1 billion photons in backward mode (to avoid common problems associated with forward calculations, see above) for benchmark model *AOS-I**, i.e., a pure Rayleigh atmosphere with optical thickness of 0.5 (see section "3.4.3 RT Validations"). The top of the atmosphere was at 120 km and molecule concentration decreased exponentially with increasing altitude (scale height is 8 km). **Figures 13**, **14** display some of the results, i.e., for Stokes parameters I, Q, and U (normalized into reflectance units) and the DoLP as a function of viewing angle θ (measured with respect to the surface normal) for the 0°–180° and 60°–120° azimuth planes. Cosine of the sun zenith angle θ_0 is set to 0.6. Absolute and relative differences with respect to benchmark results (Chowdhary et al., "Benchmark results for scalar and vector radiative transfer computations of light in atmosphere-ocean systems", unpublished) are also displayed. In the plane-parallel approximation, the reflectance values for I, Q, and U generated by the two codes agree to better than 0.00002 (absolute), and the corresponding DoLP values to better than 0.01 (absolute). For Stokes parameter I, the relative difference is less than 0.01%. The typical effect of sphericity is to lower intensity I by 0.3–0.5% for viewing angles $\theta < 50°$ and up to

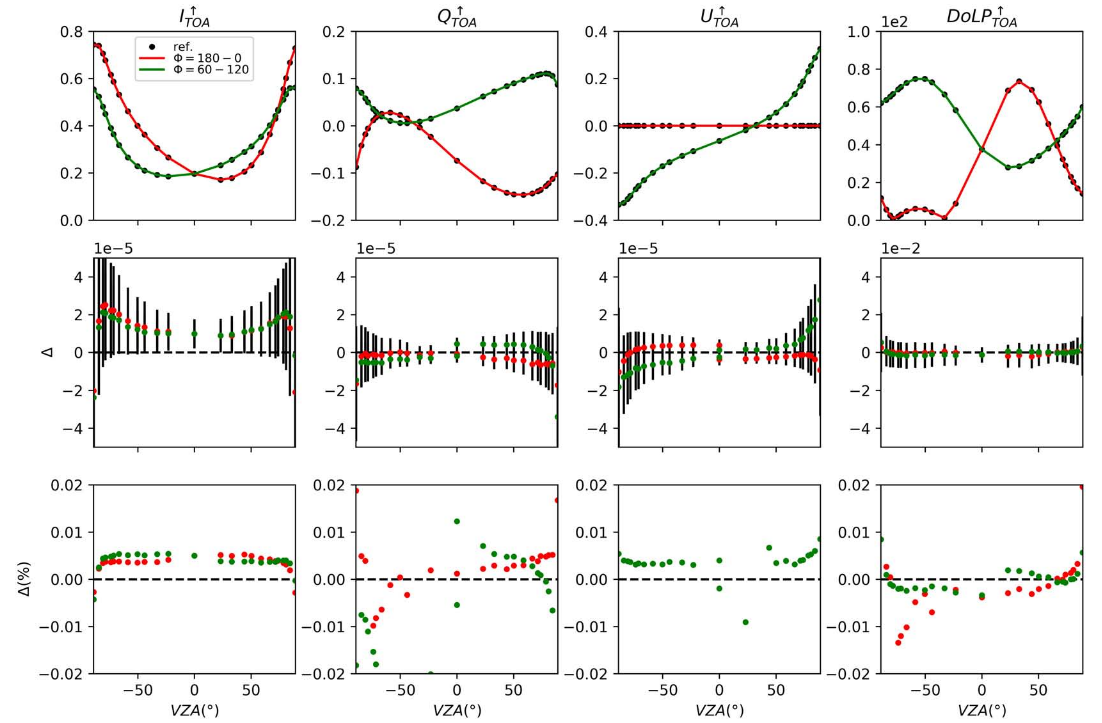

FIGURE 13 | Comparison of benchmark results for AOS-I* model (Chowdhary et al., "Benchmark results for scalar and vector radiative transfer computations of light in atmosphere-ocean systems", unpublished) computed with the NASA/GISS RT code and the Monte Carlo code (plane-parallel atmosphere) as a function of view angle θ (measured with respect to the surface normal) for relative azimuth angles of 0°, 60°, 120°, and 180° (red and green curves). Absolute differences are <0.00002 for the reflectance values of *I*, *Q*, and *U*, and relative differences are generally <0.02% for DoLP.

2% at larger viewing angles, and to change the polarization ratio DoLP by 0.3–0.4%. This is due to a reduced illuminated volume in spherical-shell approximation (smaller optical path, all the more as the view angle is large). Note that this view angle (θ) effect, which in first approximation varies as the ratio of the spherical-shell and plane-parallel optical paths, i.e., $\cos(\theta)[(\cos^2(\theta) + 2\eta + \eta^2)^{1/2} - \cos(\theta)]/\eta$, where η is equal to h/R_E with h the height of the atmosphere and R_E the Earth radius, would appear negligible at small view angles if h is not large enough. For example $h = 20$ km, used in the simulations performed by Ding and Gordon (1994), is too small (at $\theta = 30°$, the ratio would be 0.9995 for $h = 20$ km instead of 0.9969 for $h = 120$ km). The other important effect of sphericity (well known but not illustrated here) is an intensity increase at grazing solar zenith angles ($\theta_0 > 80°$) due to the smaller attenuation of the direct solar beam, again because of the smaller optical path. In view of the accuracy requirement for water reflectance ρ_w, i.e., ±5% or ± 0.002 in the blue for clear waters ("1.1 The PACE Mission" section), and since at blue wavelengths typically 90% of the signal observed from space originates from the atmosphere, mostly due to molecular scattering, the above results indicate that neglecting Earth's sphericity in generating Rayleigh look-up tables may introduce errors comparable to (i.e., up to 5% for $\theta < 50°$) or even larger than (i.e., up to 20% for $\theta_0 > 80°$) the PACE accuracy requirement for ρ_w. Earth's sphericity, therefore, needs to be taken into account in the molecular scattering calculations, even at small viewing angle θ, for accurate ocean-color remote sensing from space, in addition to molecular number density, index of refraction, and anisotropy of molecules.

PACE updates (FWD RT studies): adjacency effects

Adjacency effects, due in particular to horizontal heterogeneity of surface reflectance, can be simulated with a Monte Carlo code such as *SMART-G*. The typical procedure consists in applying, in backward mode, a given 2-dimensional surface reflectance function that depends on the photon's horizontal coordinates. The photons are injected from the viewing direction toward the surface point of Cartesian coordinates (x, y) for which the adjacency effect is to be estimated (the target). This point is considered at the center of the x–y plane. Then using the local estimate method (or a cone sampling method), the Stokes parameters are computed for the solar geometry. Due to atmospheric scattering, some of the photons exiting the atmosphere in the solar direction experience one or multiple reflections at the surface outside the target, and may not interact with the target. The atmospheric spread function $f(x, y)$, i.e., the fraction of radiance that leaves the surface at (x, y) and scatters within the field of view when targeting the point (0, 0), can also be computed (photons experiencing surface reflection can be counted), allowing calculation of the environment reflectance and, therefore, the adjacency effect.

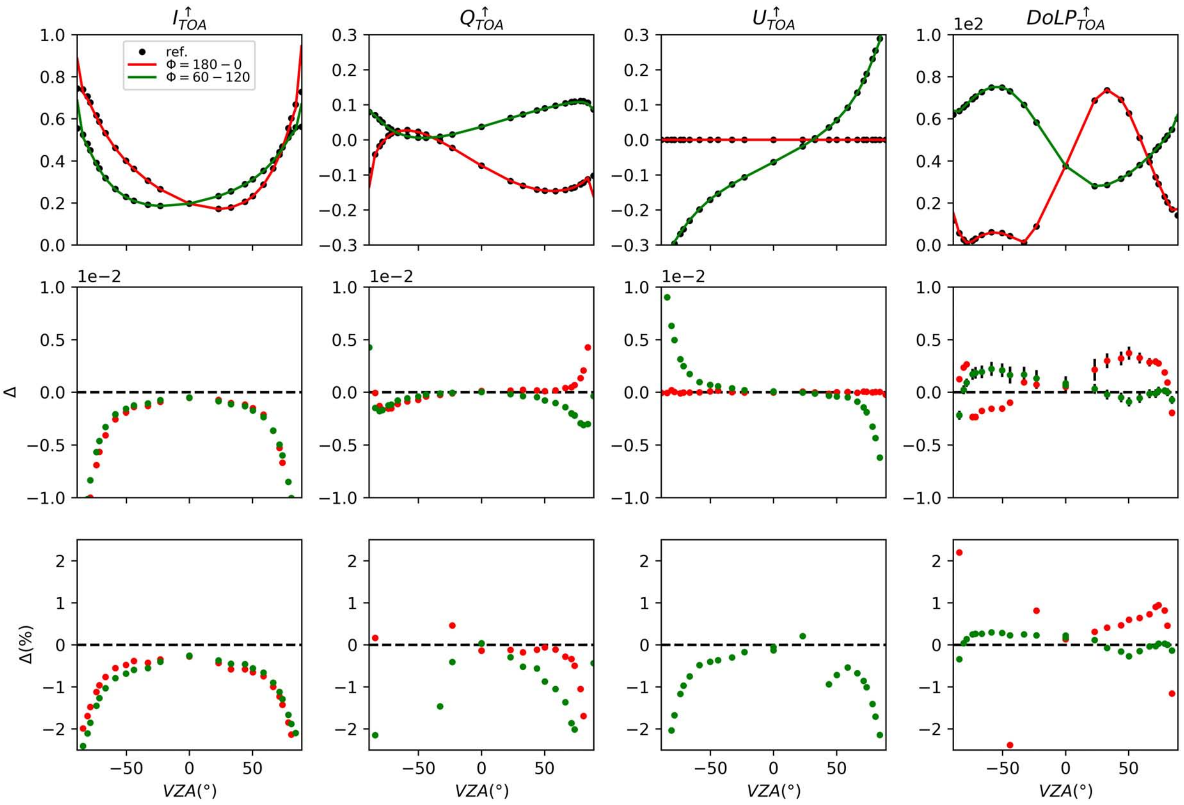

FIGURE 14 | Same as **Figure 13**, but spherical-shell atmosphere for Monte Carlo code. The effect of sphericity is to lower intensity I by 0.3–0.5% for viewing angles θ < 50° and up to 2% at larger viewing angles, and to change polarization ratio DoLP by 0.3–0.4%.

Figure 15 displays *SMART-G* simulations in the plane-parallel approximation of the adjacency effect on the TOA reflectance at 412, 670, and 865 nm of a water target next to a rectilinear coastline separating land and ocean. [The adjacency effect, Δρ, is indicated as the difference between the actual reflectance (defined in **Table 2**) at TOA and the reflectance that would be measured if the surface were horizontally homogeneous.] The reflectance of the land surface, assumed Lambertian, is 0.05, 0.1, and 0.3, respectively (typical green vegetation), and phytoplankton chlorophyll concentration is 0.1 mg/m^3 (Case I waters). Aerosol are of maritime type, with an optical thickness of 0.2 at 550 nm and an aerosol scale height of 2 km (exponential profile), and the ocean surface wind speed is 5 m/s. View zenith angle is 45° and relative azimuth angle is 90°. The azimuth angle of the Sun is along the coastline. At 2 km from the coast, i.e., right panels, Δρ is generally positive, especially in the NIR where vegetation reflectance is high compared to that of the water (negligible). For small Sun angles (<20°), Δρ is about 0.005, 0.002, and 0.001 at 865, 670, and 412 nm, which represents about 25, 5 and <1% of the actual reflectance. The effect decreases with increasing Sun angle θ_0 with increasing view angle θ, due to increasing diffuse atmospheric transmittance. Using TOA observations in the red and NIR for atmospheric correction, the impact of Δρ on water reflectance retrieval at 412 nm is expected to be large, much larger than the Δρ at 412 nm caused by adjacency effect. Note that Δρ also depends on the sensor location (over the ocean or over land), an effect due to Fresnel reflection that may be masked for some angular configurations (Santer and Schmechtig, 2000). This masking effect would be more pronounced if the principal plane were perpendicular to the coast. Regarding polarization, the adjacency effect is opposite (more light, less polarization), i.e., the difference in DoLP (denoted by ΔDoLP) is generally negative, about 3% at 865 nm. For a given geometry, i.e., solar angle θ of 56° in the left panels, Δρ decreases in magnitude with increasing distance from the coast (same for ΔDoLP*)*, but the effect is still felt at 10 km (4% at 865 nm), which is sufficient to yield unacceptable errors (i.e., > 0.002) on retrieved water reflectance at 412 nm (*cf.* "1.1 The PACE Mission" section). Only effects of distance and geometry for a typical aerosol are displayed in **Figure 15**, but aerosol parameters, especially vertical distribution (not easy to estimate from passive radiometry) also affect Δρ and ΔDoLP.

3.4.2 UV Remote Sensing of AOS

PACE discussions (INV RT studies): UV solar spectra, aerosol height retrievals

Including hyperspectral UV-A radiance in observations by the OCI and SPEXone instruments offers new opportunities for atmospheric correction and ocean color product retrievals that were not possible with heritage ocean color missions. But

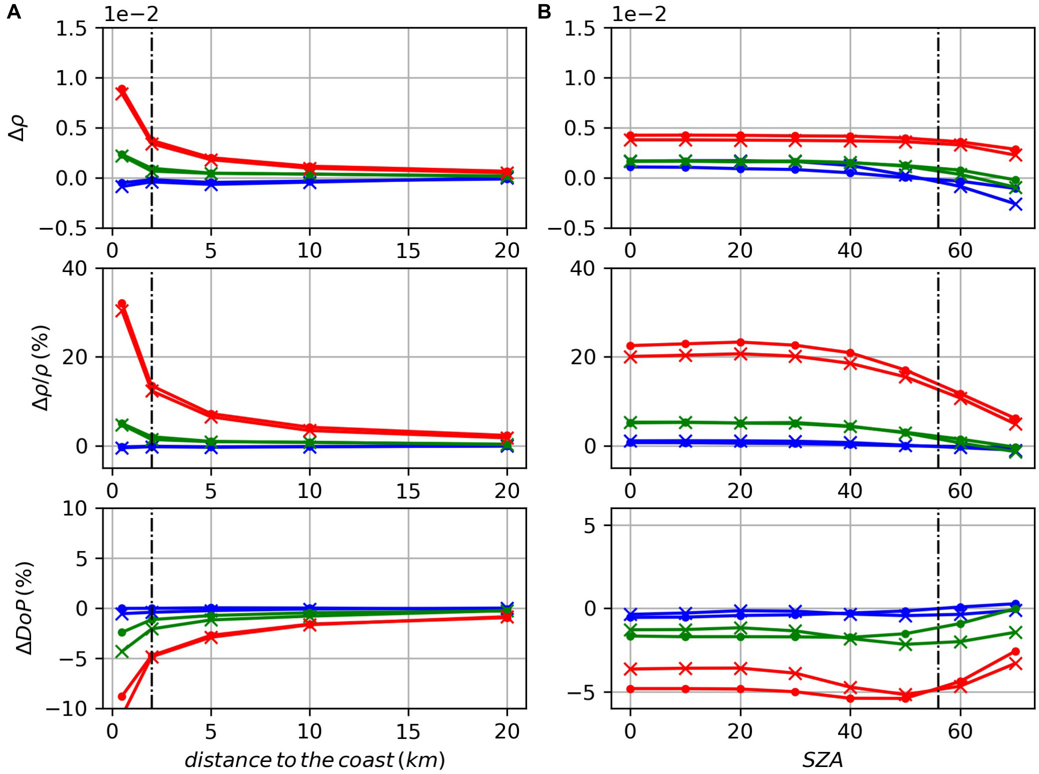

FIGURE 15 | Monte Carlo simulations of adjacency effects on the TOA reflectance of a water target next to a rectilinear coastline. Wavelengths are 412, 670, and 865 nm (blue, green, and red curves). **(A)** Absolute and relative TOA reflectance and degree of linear polarization differences between cases of heterogeneous and homogenous surface as a function of distance to the coast. Solar and view angle are 56° and 45°, and relative azimuth angle is 90°. **(B)** Same as panel **(A)**, but as a function of the Sun zenith angle (SZA, in degrees) for a distance to the coast of 2 km. Curves with solid circles correspond to the sensor located over ocean and curves with crosses to the sensor located over land.

studying these new opportunities by means of RT computations for UV-A radiance comes also with the need to more carefully consider (i) enhanced scattering in atmosphere and ocean of UV-A radiance; and (ii) changes in UV-A atmosphere and ocean scattering properties. In addition, one needs to consider variations in UV solar irradiance, which can happen on timescales of days (Lean, 1987) and which exceed those for the VIS-NIR spectrum by an order of magnitude (Lean and DeLand, 2012). Using prescribed solar irradiance spectra that do not incorporate such short-term temporal variations may lead to hyperspectral artifacts in retrieved water-leaving radiance that, in the UV-A toward the blue, easily exceed 0.002 in reflectance units. This was demonstrated by Thompson et al. (2015) in analyses of airborne hyperspectral data from the PRISM (Portable Remote Imaging Spectrometer) instrument. One of the requirements for PACE observations in the UV-A (toward the blue) is to retrieve water-leaving radiance within 10%. Determining the contribution of UV solar irradiance variations to the uncertainty in water leaving radiance, and its reduction through the use of TSIS (Total Solar Irradiance Sensor) observations if available, remains a subject for future studies. Here, we focus on subjects concerning RT of UV-A radiance in coupled atmosphere-ocean systems. In what follows, we will first summarize some of the main benefits of OCI/UV-A radiance for retrieving ocean and atmosphere properties before discussing concerns for simulating and analyzing TOA observations of UV-A radiance.

A major challenge in traditional atmospheric correction methods (i.e., methods that rely on NIR-SWIR radiance to constrain and remove aerosol scattering contributions in VIS space-borne radiance observations) is identifying the single scattering albedo (ω_{aer}) and vertical distribution (Z_{aer}) of aerosols (see Frouin et al., 2019). Changes in ω_{aer} affect the amount of radiance absorbed in a single-scattering event before reaching the TOA. In the VIS, the impact of ω_{aer} on TOA radiance is further enhanced by repeated aerosol-molecule light interactions. Because the molecular density decreases with height z, the amount of repeated aerosol-molecule light interactions becomes also dependent on the vertical location of aerosols. To properly extract ocean contributions from TOA radiance in the VIS therefore requires knowledge of both ω_{aer} and Z_{aer}. Section "3.3.1 Aerosols" discusses examples of using Oxygen A- and B-bands in the NIR, and of polarization in the deep blue, to obtain information on Z_{aer}. That section touches also on using UV-A radiance to retrieve on Z_{aer}. UV-A radiance becomes very sensitive – even more than VIS radiance – to variations in ω_{aer} and Z_{aer} because the molecular optical depth increases at a rate proportional to λ^{-4} (Bodhaine et al., 1999). This was confirmed by Levelt et al. (2006) and Torres et al. (2005, 2007) in analyses of UV observations by the TOMS and OMI instruments. In a follow-up study, Satheesh et al. (2009) demonstrated that one can retrieve both ω_{aer} and Z_{aer} from OMI/UV radiance if one uses MODIS/NIR-SWIR radiance to constrain τ_{aer}. Note that MODIS and OMI measurements do not occur simultaneous which can cause retrieval biases in the presence of clouds that evolve in the time lag between those measurements. This was demonstrated in a recent work by Gassó and Torres (2016). However, retrievals of ω_{aer} and Z_{aer} from OCI radiance measurements in the UV-A will not suffer from this limitation because OCI provides simultaneous radiance measurements in the NIR/SWIR to constrain τ_{aer}.

Historically, Chlorophyll *a* concentration [Chla] has been the most common property retrieved from heritage ocean color satellite data – and it continues to be one of the core ocean color products for the PACE mission (NASA, 2018a). Chlorophyll *a* affects the color of the ocean in the VIS by absorbing in the blue part of this spectrum – specifically, by its absorption peak at 443 nm. Most heritage [CZCS (Coastal Zone Color Scanning Experiment), SeaWiFS] and current [MERIS, MODIS, VIIRS] ocean color satellite instruments therefore measure radiance at, amongst others, a wavelength band centered at around 440 nm. The retrieval of [Chla] then proceeds (Blondeau-Patissier et al., 2014, and references therein) by using empirical relationships that fit either (i) so-called band ratios that consist of the ratio of the radiance at ∼443 nm and a radiance obtained in the green part of the VIS (Dierssen, 2010), or (ii) the IOPs retrieved from the radiance at ∼443 nm and at other wavelengths (the empirical relationships used in this approach are the bio-optical equations discussed in section "3.1.2 Bio-Optical Models"). However, as is shown explicitly in Eqs 9 and 10, detrital matter and CDOM also absorb at 440 nm. Of these two ocean constituents, CDOM can absorb as much (if not more) as [Chla] at ∼443 nm, and its absorption decreases with increasing wavelength just like the absorption spectrum of [Chla] (Nelson and Siegel, 2013). This makes it particularly difficult to separate changes in [Chla] from variations in CDOM using the above-mentioned band ratio algorithms (see, e.g., Siegel et al., 2005). Bio-optical equations such as those discussed in section "3.1.2 Bio-Optical Models" explicitly separate absorption by [Chla] (using pre-described Chla-specific phytoplankton absorption coefficients $\hat{a}_{\mathrm{ph}}$) from absorption by CDOM (which, in practice, is often combined with a relatively small contribution of absorption by detrital particulate matter). However, bio-optical equations are used for analyses of *absolute* water-leaving radiance measurements which are more susceptible to errors in atmospheric correction than the *ratio* of such radiance measurements. The aforementioned difficulties in constraining ω_{aer} and Z_{aer} from NIR-SWIR radiance will therefore impact bio-optical equations-based ocean product retrievals more than band ratio-based ocean product retrievals. In either retrieval method, UV-A radiance offers a better alternative to separate CDOM absorption than the radiance at 443 nm. That is because CDOM absorption continues to increase with decreasing wavelength (see, e.g., Eq. 8b), whereas Chlorophyll *a* absorption decreases in the UV-A. As a result, the relative contribution of CDOM absorption to total underwater light absorption (i.e., including absorption by Chlorophyll *a*, detrital matter, and water) increases from about 50% at 400 nm to >70% at 300 nm (Nelson and Siegel, 2013). Indeed, Morel et al. (2007a) conclude in their analyses of irradiance measurements obtained for two extreme open ocean regimes (i.e., South Pacific and Mediterranean waters) that the dominance of [Chla] in modeling bio-optical properties in the VIS is replaced by that of CDOM in the UV.

PACE updates (FWD RT studies): RT coupling of scattering in atmosphere and ocean

Light scattering contributions to TOA observations over oceans also exhibit regime changes when comparing VIS to UV-A radiance. **Figure 16** illustrates these changes for an extreme case, i.e., for surface waters of the eastern South Pacific Gyre which have anomalously low [Chla] (Morel et al., 2007b; Claustre et al., 2008) and CDOM amounts (Morel et al., 2007a; Nelson and Siegel, 2013). The left and right half-hemisphere in each diagram of this figure provides a contour plot of a radiance ratio quantity at λ = 385 and 490 nm, respectively. The plots are given as a function of two polar viewing angles: the viewing angle θ measured with respect to the surface normal (shown by the radial coordinate, which ranges from 0° at the center point to 60° at the outer boundary); and the viewing azimuth angle φ (shown by the angular coordinate, which ranges from 0° in the upward direction to 180 in the downward direction). The convention for the azimuth angle is chosen such that the $\varphi = 0°$ half-plane contains the sunglint, and the $\varphi = 180°$ half-plane contains the backscattering direction. The location of the sun (denoted by a yellow star in the backscattering direction) is set at solar zenith angle $\theta_0 = 10°$, 30° and 50° for the first, second, and third row of plots, respectively. The radiance ratio quantities depicted in these plots describe relative contributions to the TOA total radiance $L_{\mathrm{tot}}(\theta, \varphi)$ (first column) and to the TOA ocean color radiance $L_{\mathrm{OC}}(\theta, \varphi)$ (second to fourth columns). That is, $L_{\mathrm{tot}}(\theta, \varphi)$ can be decomposed as follows:

$$L_{\mathrm{tot}}(\theta, \varphi) = L_{\mathrm{atm}}(\theta, \varphi) + L_{\mathrm{atm-srf}}(\theta, \varphi) + L_{\mathrm{OC}}(\theta, \varphi) \tag{13}$$

where $L_{\mathrm{atm}}(\theta, \varphi)$ is the contribution of light scattered only in the atmosphere, $L_{\mathrm{srf-atm}}(\theta, \varphi)$ is the contribution of light scattered in the atmosphere *and* reflected (once or more times) by the ocean surface, and L_{OC} is the ocean color contribution defined as light that has been scattered in the ocean body (but *may* also have been scattered in the atmosphere before entering, or after exiting, the ocean body). For simplicity, we will omit hereafter the dependence on θ and φ of radiance quantities and operators. To compute L_{atm}, we used an efficient adding/doubling method described in detail by de Haan et al. (1987) for isolated atmospheres. We assumed for these computations a homogeneous atmosphere consisting of molecules (with optical thickness and depolarization ratio δ_{m} taken from Bodhaine et al., 1999) and a background fine-mode aerosol (with effective radius $r_{\mathrm{e}} = 0.1\ \mu\mathrm{m}$ as defined in Hansen and Travis, 1974; a spectrally constant refractive index $m = 1.45$; and optical thickness τ_{aer} = 0.10 at 550 nm). For the ocean surface in the computation of $L_{srf-atm}$, we used the isotropic Gaussian surface slope distribution from Cox and Munk (1954) with surface wind speed $U_{12.5}$ = 7 m/s, and included whitecaps with albedo A_{wc} = 40% in the UV-A and VIS. To compute L_{OC}, we used [Chla] = 0.03 mg/m^3 as input for the D-P hydrosol model mentioned in section "3.1.2 Bio-Optical Models" (see also Chowdhary et al., 2012), and adjusted the total underwater absorption coefficient a_{tot} to fit the anomalously low K_d values given by Morel et al. (2007a) for the South Pacific Gyre.

The plots in the first column of **Figure 16** show (L_{OC}/L_{tot}), i.e., they depict (see thin contour lines; given in percent of L_{tot}) the relative contribution to TOA radiance of light that has been scattered under water. Superimposed on these plots are outlines (see thick contour line; given at 10% level of $L_{tot} - L_{OC}$) of the sunglint radiance contribution. There are several conclusions that can be drawn from these plots. Firstly, the underwater light scattering contribution can (at θ_0 = 10°) become larger than 16% of the TOA radiance at 385 nm, whereas at 490 nm it remains less than 13% in spite of the atmosphere being optical thinner in the VIS (due to decrease in molecular scattering) than in the UV-A. The L_{OC} contribution decreases at both wavelengths with increasing solar zenith angle, but it remains always larger at 385 nm than at 490 nm. This result differs from the one reported by Zhai et al. (2017a) – i.e., for the same [Chla] = 0.03, they report relative L_{OC} contributions that are larger at 490 nm than at 385 nm for θ_0 = 45°. The difference between our and their results can be attributed to variations in CDOM amount. That is, our and their underwater light absorption coefficients a_{tot} lead to diffuse attenuation coefficients K_d that (according to **Figure 2** in Morel et al., 2007a) are typical for CDOM-poor Pacific Gyre waters and CDOM-rich Mediterranean waters, respectively. This comparison of RT results simply confirms (albeit for oligotrophic oceans) the sensitivity of UV-A radiance to retrieve variations in CDOM.

The first column of **Figure 16** further shows that, regardless of CDOM amount, oligotrophic oceans can be sufficiently bright in the UV-A to contribute noticeable to the TOA radiance. This implies that any inversion algorithm that uses spaceborne UV-A radiance to constrain aerosol properties ω_{aer} and Z_{aer} (see discussion above on atmospheric correction) must also

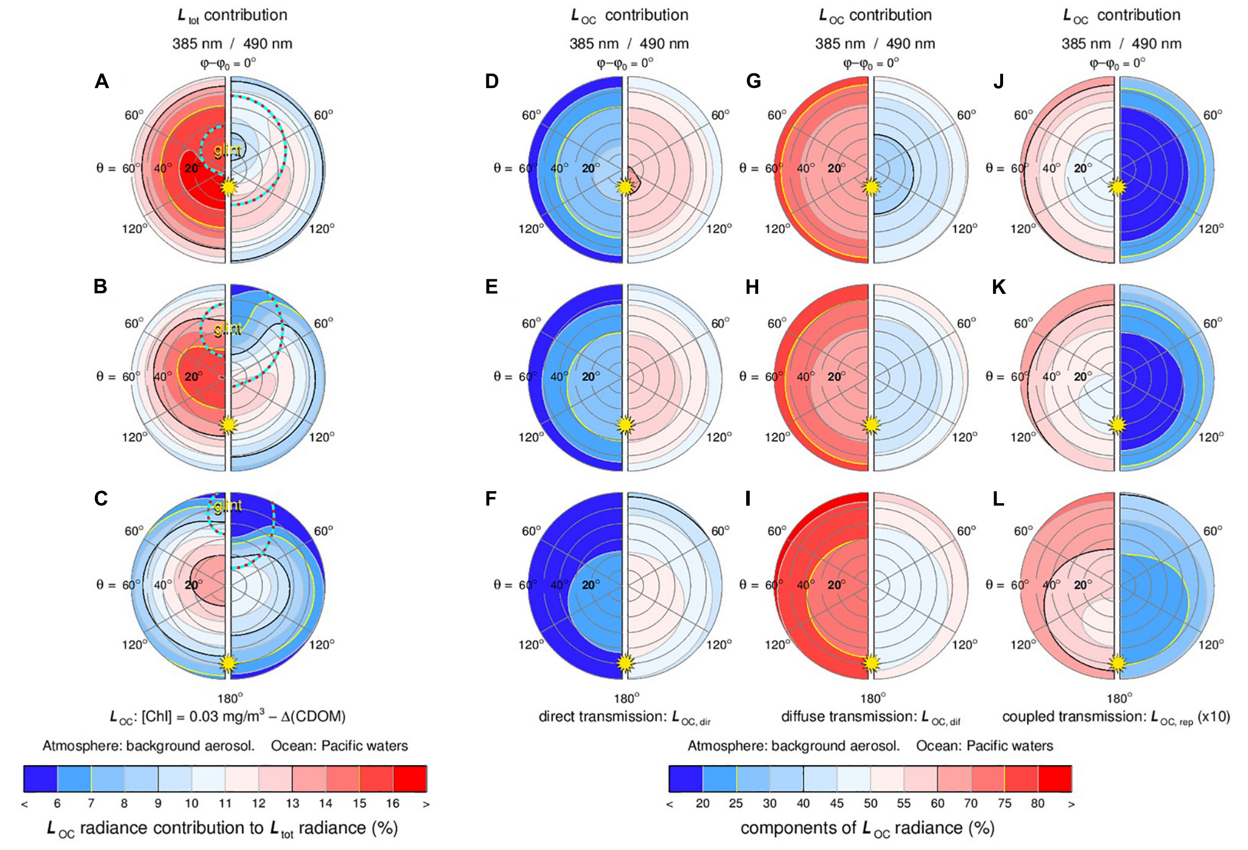

FIGURE 16 | Radiative transfer simulations of radiance contributions to TOA observations. First column shows underwater light scattering radiance (L_{OC}) contribution to TOA radiance (L_{tot}). Left and right hemispheres are for 385 and 490 nm, respectively. The sun (denoted by a yellow star in the backscattering direction) is located at 10° (first row), 30° (second row) and 50° (third row). Second, third and fourth columns show contributions to radiance (L_{OC}) of direct transmitted water-leaving radiance ($L_{OC,dir}$), diffuse transmitted radiance ($L_{OC,dif}$), and coupled water-leaving radiance ($L_{OC,rep}$), respectively.

consider variations in ocean color that are caused by changes in [Chla] and/or CDOM. That may lead to challenging cases when inverting scenes that contain brown carbon (BrC) aerosols. Like CDOM (and unlike black carbon aerosols), BrC aerosols exhibit absorption spectra that increase rapidly toward the UV-A (Kirchstetter et al., 2004; Sun et al., 2007; Chen and Bond, 2010). Although the optical properties of CDOM and BrC particles vary in space and time, and although specifying their chemical structures remains an active field of research, CDOM and BrC have been associated with substances that have similar composition, i.e., marine humic matter (Boyle et al., 2009; Nelson and Siegel, 2013) and humic-like substances (HULIS) (Hoffer et al., 2006, 2016; George et al., 2015; Laskin et al., 2015), respectively. This may, at least in part, explain the similarity between CDOM and BrC absorption spectra. The ability to distinguish the impact on TOA radiance of such similarities in AOS absorption spectra is an outstanding question. Hence, retrieving ω_{aer} (and Z_{aer}) from spaceborne UV-A radiance observations over oceans is not always a trivial matter, and needs to be carefully examined in future studies.

The first column of **Figure 16** also shows that the sunglint outline in L_{tot} becomes much smaller at 385 nm than at 490 nm. This is a direct result of the atmospheric optical depth becoming larger with decreasing wavelength, which causes the direct atmospheric attenuation of sunglint to decrease by a factor of up to two, and the diffuse atmospheric transmission to scatter the sunglint over a wider range of viewing angles. Furthermore, we found (not shown here) that when increasing the surface wind speed from 2 to 7 m/s, the sunglint outline in L_{tot} varies significantly less at 385 nm (spatial coverage changes by less than 10%) than at 490 nm (spatial coverage changes by up to 70%). That is because the diffuse transmission of sunglint through the atmosphere (i) contributes several factors more to the sunglint outline in L_{tot} at 385 nm than at 490 nm, and (ii) reduces the sensitivity of this glint to surface wind properties. The corresponding impact on the polarized component in L_{tot} remains to be studied, but will be of particular interest to spaceborne polarimetry of aerosols and hydrosols. That is, numerical studies show (see e.g., Chowdhary et al., 2006; Zhai et al., 2017b) that the polarized component L_{tot} becomes most sensitive to variations in underwater light scattering properties when approaching sunglint viewing angles for moderate to large solar zenith angles. Similar sensitivities can be expected for variations in aerosol scattering that in the UV-A will mostly perturb the large polarization of light scattered by molecules at 90°. However, the perturbations in UV-A polarized radiance caused by variations in aerosols and hydrosols will have different angular and spectral patterns (one of the reasons for this difference is the change in underwater light polarization pattern when this light crosses the ocean surface). Modern-age multi-angle and multi-spectral polarimeters such as SPEXone can distinguish such patterns with very high accuracies (i.e., with DoLP uncertainties <0.3%). This may offer a feasible pathway toward distinguishing variations caused by BrC aerosols and CDOM in the inversion of UV-A radiance (see discussion above on BrC aerosols).

We discussed above that the L_{OC} radiance increases toward the UV-A for oligotrophic oceans. The L_{OC} radiance itself can be further decomposed into several contributions that depend on the pathway of light taken through the atmosphere. Let $L_{\text{OC,dir}}$ and $L_{\text{OC,dif}}$ denote, respectively, the *direct* contribution (i.e., only attenuated by the atmosphere along the path to and from the ocean body) and the *diffuse* contribution (i.e., scattered in the atmosphere along the path to and/or from the ocean body) to L_{OC}. Furthermore, let $L_{\text{OC,rep}}$ describe the residual contribution to L_{OC} of light that has *repeatedly* interacted with the atmosphere and the ocean system (i.e., the system consisting of the ocean body and ocean surface). One can then write:

$$L_{\text{OC}} = L_{\text{OC, dir}} + L_{\text{OC, dif}} + L_{\text{OC, rep}}. \tag{14}$$

The plots in the second column of **Figure 16** depict ($L_{\text{OC, dir}}/L_{\text{OC}}$), i.e., they show the contribution to L_{OC} of underwater light that has never been scattered in the atmosphere. This contribution can be as large as 60% at 490 nm, but it decreases rapidly toward the UV-A where it is ≤30% at 385 nm. Hence most of the contribution to L_{OC} in the UV-A has at some point been scattered in the atmosphere. The plots in the third column of **Figure 16** depict ($L_{\text{OC, dif}}/L_{\text{OC}}$), and they show that the contribution to L_{OC} in the UV-A comes mostly from $L_{\text{OC,dif}}$. In the VIS, $L_{\text{OC,dif}}$ is often approximated by Gordon (1997) and Gao et al. (2007).

$$\begin{aligned} L_{\text{OC,diff}} = {} & [(t_{\text{atm}}) \times (r_{\text{wlr}}) \times (e^{\tau/\mu_0}) + (e^{\tau/\mu} + t_{\text{atm}}) \times \\ & (r_{\text{wlr}}) \times (t_{\text{atm}})]\, L_0 \end{aligned} \tag{15}$$

where L_0 is the solar radiance illuminating the AOS, r_{wlr} is a Lambertian reflector for water-leaving radiance, and $e^{\tau/\mu}$ and t_{atm} are the scalar direct and diffuse transmittance factors for the atmosphere, respectively. Here, τ is the optical thickness of the atmosphere, and μ_0 and μ are the cosine of the sun and viewing angles, respectively. Hence r_{wlr} ignores the facts that the water-leaving radiance is bidirectional (Morel and Gentili, 1993; Morel et al., 2002; Fan et al., 2015) and highly polarized (Chowdhary et al., 2006; Tonizzo et al., 2011; Zhai et al., 2017b). Furthermore t_{atm} ignores the impact of polarization (not just of light in the atmosphere but also of water-leaving radiance) on RT computations for the atmosphere, which can lead to substantial errors in transmitted radiance (Lacis et al., 1998). Some inversion methods go a step further by modifying the direct transmittance factor $e^{\tau/\mu}$ to include t_{atm} (Gordon et al., 1983; Gordon (1997)), and by inserting empirically derived coefficients to improve the accuracy of such modifications (Wang, 1999). Given the dominant contribution of $L_{\text{OC,dif}}$ to L_{OC} in the UV-A, such approximations need to be re-examined and evaluated against PACE's accuracy requirements (*cf.* "1.1 The PACE Mission" section, see also NASA, 2018a) for retrievals of L_{OC}.

The fourth column of **Figure 16** shows plots of ($L_{\text{OC, rep}}/L_{\text{OC}}$). Note that the values in these plots, which describe the contribution to L_{OC} of light that is repeatedly reflected between the atmosphere and ocean system, are multiplied by a factor of 10 to magnify their magnitude. This light contributes (much) less than 4% to L_{OC} at 490 nm because of the low albedo of the ocean and of the atmosphere at this wavelength. Some inversion methods for L_{OC} radiance therefore ignore this contribution altogether in the VIS (e.g., Gordon et al., 1983; Gordon, 1997; Wang, 1999). Other inversion methods still include this contribution albeit only for light that is transmitted (not reflected) back and forth by the ocean surface (e.g., Gao et al., 2000, 2007, 2009). At 385 nm, radiance $L_{\mathrm{OC,\,rep}}$ increases in absolute terms by a *factor of more 50* when compared to its absolute value at 490 nm (not shown here). From **Figure 16**, we see that $L_{\mathrm{OC,\,rep}}$ now contributes up to 7% to L_{OC}. This contribution originates from a complex coupling of light scattered by the atmosphere and ocean system, e.g., it includes water-leaving radiance that is scattered by the atmosphere back to the ocean surface and that is subsequently reflected back to sky by this surface. This coupling cannot be simplified even when using a Lambertian reflector r_{wlr} for water-leaving radiance. Therefore any inversion algorithm that uses spaceborne UV-A radiance to simultaneously retrieve aerosol and ocean properties (see, e.g., previous discussion on constraining BrC aerosol and CDOM over oligotrophic waters) must also consider truly coupled atmosphere-ocean systems if $L_{\mathrm{OC,\,rep}}$ is deemed too large to ignore. Note that $L_{\mathrm{OC,\,rep}}$ will decrease in magnitude if [Chla] or CDOM increases (which darkens the ocean in the UV), or if the amount of back-scattering in the atmosphere decreases (e.g., because of a change in aerosol properties). On the other hand, the vicinity of bright surfaces in the UV-A such as sea ice or snow-covered land will not only exuberate adjacency effects that were discussed in the section "3.4.2 Horizontal Variations," but will also increase in particular $L_{\mathrm{OC,\,rep}}$ radiance because of repeated skylight reflections off such surfaces.

4 CONCLUDING REMARKS

This paper summarizes research frontiers on RT in coupled ocean and atmosphere systems to enable new ocean-atmosphere science and specifically to support the PACE mission development. RT is an essential tool in remote sensing of atmosphere and ocean components, and in furthering our understanding of the coupled system. It is used to facilitate designing new retrieval algorithms; providing validation datasets for satellite data products; and performing sensitivity to different components of the Earth system. In anticipation of the advanced remote sensing capabilities of the instruments onboard the PACE spacecraft, the PACE Science Team has performed novel FWD RT and INV RT studies on different components of the atmosphere-ocean system. This work included examining the representation of hydrosols, aerosols, gases, surface whitecaps and sunglint in these models. In addition, bio-optical models, the key element in practical RT for ocean applications, were investigated from several perspectives. The team also has evaluated fundamental processes and assumptions of common RT models including inelastic scattering, and 3D effects such as spherical shells and adjacency effects. This has resulted in a set of calculations from state-of-the-art RT models that have been published to serve as a benchmark for future coupled ocean and atmosphere RT applications.

4.1 Optical Properties of Hydrosols, Aerosols, Gases, Surface Whitecaps and Surface Slicks

To better represent hydrosol optical properties in RT, Chowdhary, Liu et al. (unpublished) have studied the impacts of particle shape and inhomogeneity on scattering matrices of hydrosols. Their study suggests that internal structures of plankton-like particles need to be considered when using RT computations to analyze backscattering radiance. Furthermore, they suggest that there is information content on plankton morphology in ocean depth profiles of depolarization ratios δ_L obtained from air- and space-borne lidars. On modeling the phase function of hydrosols, Twardowski et al. (unpublished) have used a linear combination of two cluster representations, which has been verified by a large collection of volume scattering function measurements. This method can show an improvement of RMS errors of several percent relative to Fournier-Forand phase functions when considering the full VSF angular range, but, unlike the latter function, has no physical meaning. The phase function of hydrosols in the backward directions, as shown recently by Zhang et al. (2017), can be approximated by a linear combination of two end members, one representing the scattering by particles of sizes much smaller than the wavelength of light and the other by particles of sizes much greater than the wavelength of light.

Another approach to analyze measured hydrosol phase functions was taken by Zhang et al. (2011) and Twardowski et al. (2012) who computed an extensive library of optically unique phase functions that serve as fingerprints for various oceanic particle species. Each particle species represented by this library has its own refractive index and its own log-normal size distribution, both of which were determined through sensitivity analyses over the ranges of published size distributions and composition for oceanic particles. In Zhang et al. (2011) the particle species are assumed spherical, whereas in Twardowski et al. (2012) the particles assume non-spherical shapes consisting of asymmetrical hexahedra for inorganic mineral particles (Bi et al., 2010). Both studies used coated spheres (Czerski et al., 2011; Zhang et al., 2011) to represent air bubbles. This library of phase functions has subsequently been used to invert measured hydrosol phase functions into the scattering coefficient and size distribution of particle subpopulations (Twardowski et al., 2012; Zhang et al., 2012, 2013, 2014b).

We note at this point that while each of the above-mentioned approaches for hydrosol scattering (i.e., internal structure of plankton, non-spherical shape of marine particulates, submicron-sized marine particulates, VSF decomposition) may provide a reasonable or partial solution for the "missing particulate backscattering enigma" (see discussions in Stramski et al., 2004; Organelli et al., 2018; Poulin et al., 2018), a particle model that incorporates all these approaches to study their combined impact on backscattering remains an outstanding topic of research. Such a model could validate, or lead to adjustments of, parameter choices made for each approach such as refractive index and shape distributions of marine particles. We anticipate that further measurement and experimentation with VSFs including underwater light polarization and lidar depolarization measurements will provide additional information to help constrain, and perhaps even reduce, the parameters of such a complex model. Emerging particle characterization methods such as *in situ* holographic imaging (Talapatra et al., 2013; Nayak et al., 2017) are also expected to aid in development and validation of such a model.

Unlike hydrosols and aerosols, the absorption properties of gases are well known. The advances reported in this work concern expanding the representation of gaseous absorption in RT modeling in a practical sense to high spectral resolution across the full solar spectrum. At NASA's OBPG, and as part of the PACE ST activities, a hyperspectral atmospheric correction algorithm was developed, based on the well-established heritage algorithm in combination with the ATREM algorithm for gas correction, to derive the hyperspectral water-leaving reflectance from airborne and spaceborne hyperspectral sensors. The AC algorithm was tested and validated using HICO data as a proxy for anticipated OCI observations. The results show the consistency and feasibility of the hyperspectral AC process including the gas absorption correction (Ibrahim et al., 2018). However, several gaps in the RT developments still exist, such as modeling efficiently the fine absorption features of water vapor and Oxygen, and the coupling between gas absorption features and molecular and aerosol scattering. The development of such capabilities will be needed to fully utilize OCI's hyperspectral coverage, such as the Oxygen A-band for the aerosol layer height and the plankton fluorescence retrieval.

The PACE Science Team also investigated the reflectance of whitecaps due to wave breaking, and how to represent this reflectance in RT. New spectral measurements of whitecaps have been made across from 400 to 2500 nm (Dierssen, 2019). These measurements show that whitecaps reflectances have spectral dips in the NIR spectrum that largely correspond to the absorption features of liquid water. Reflectance dips occur particularly at 750, 980, and 1150 nm, which have enhanced liquid water absorption, a result of multiple scattering in and around subsurface bubbles and surface foam. Following Whitlock et al. (1982), a simple model of whitecap reflectance based on the natural logarithm of water absorption can be used to describe the spectral shape of intense whitecaps generated by breaking waves into SWIR wavelengths. Moreover, the decrease in reflectance at these liquid water absorption bands is correlated with enhancements in reflectance of the whitecap across the spectrum. The conclusion drawn by this PACE Science Team is that current models based on wind speed and a single whitecap albedo cannot be used to accurately represent the diversity of whitecaps on the ocean.

Another RT topic that was reexamined by the PACE team is the information contained in sunglint observations. Obtaining that information requires vector RT with polarization. In the SWIR (where the interaction of light with the atmosphere and ocean body is minimized) the DoLP within sunglint is only sensitive to the ocean surface refractive index, m. Variations in m occur throughout the global ocean for large changes in sea surface temperature and salinity, but also in the presence of substances covering the ocean surface such as slicks from biogenic origin (e.g., plankton and fish secretions) and anthropogenic origin (e.g., oil spills). An intriguing application involves the detection of variations in the uppermost 1–1000 μm of the ocean, which is referred to as the surface microlayer and which has biological, chemical, and physical properties that are distinctively different from those of the underlying ocean body. Ottaviani et al. (2019) developed an inversion algorithm to provide continuous (i.e., along aircraft ground track) retrievals of m from airborne sunglint DoLP observations by the RSP instrument at 2.2 μm. They demonstrate that the multi-angle views and high DoLP accuracy of RSP measurements allows m to be retrieved within 5×10^{-4} under ideal experimental conditions. Actual retrieval examples are shown for pristine sea surfaces and the Deepwater Horizon oil spill.

4.2 Bio-Optical Models in Radiative Transfer

In ocean color remote sensing, bio-optical models are needed to correlate water leaving radiance at different wavelengths. The correlation occurs by means of prescribing variations in the magnitude and spectra of IOPs. For traditional "Case I" waters, one can – *to a first order approximation* – parameterize IOPs in terms of the Chlorophyll *a* concentration [Chla]. This is a strong constraint though, which often fails in coastal waters. Considerable efforts have been made to relax the dependence of IOPs on [Chla] (Werdell et al., 2013a). However, bio-optical models developed for analyzing *polarized* water-leaving radiance spectra still use [Chla] to parameterize IOPs (Chowdhary et al., 2006; Zhai et al., 2010; Hasekamp et al., 2011; Xu et al., 2016). Chowdhary, Stamnes et al. (unpublished) have taken the next step in developing the Detritus-Plankton (D-P) II hydrosol model, where the backscattering coefficient for particulate matter and absorption coefficient for colored detrital matter are allowed to vary independently of [Chla]. More than 1.7 million reflection matrices for water-leaving radiance were computed with this model, and are now available at https://data.giss.nasa.gov/rad/ocean-matrices/. These matrices are currently used to analyze airborne polarimetric (RSP) and lidar (HSRL) data obtained during the 2012 TCAP and the 2014 SABOR campaign (Stamnes et al., 2018), and the ongoing NAAMES campaign. In addition, Ibrahim et al. (2016) and Zhai et al. (2017b) have adopted a bio-optical model that added sediment concentration to parameterize IOPs. This philosophy has been adopted to design an inversion algorithm that retrieves aerosol and hydrosol parameters simultaneously (Gao et al., 2018).

In addition to extending the number of parameters used to prescribe variations in IOPs for analyses of polarized water-leaving radiance, the PACE Science Team also extended the spectral range in prescribed IOP variations for analyses of total water-leaving radiance. Specifically, the IOCCG Report 5 (IOCCG-OCAG, 2003; IOCCG, 2006) prescribed variations in IOPs from 400 to 800 nm, and created synthetic data sets to test the performance of IOPs inversion algorithms. This spectral range has now been extended down to 350 nm to produce synthetic data sets for UV-A radiance from PACE/OCI. In addition, wider variations are now adopted for phytoplankton absorption spectra a_{ph} (using a larger range at 440 nm, and more normalized spectral shapes) to cover oceans ranging from oligotrophic to waters with plankton blooms. Updates are also made in the absorption coefficient a_{w} for pure sea water based on the work by Lee et al. (2015), and in the backscattering coefficient $b_{\mathrm{b,w}}$ for pure sea water based following Zhang et al. (2009). Finally, slightly different variations with [Chla] (compared to the parameterizations in IOCCG (2006) are now used for the attenuation coefficient c_{ph} and the scattering coefficient $b_{\mathrm{d,m}}$ for phytoplankton and non-algae particulate matter, respectively, at 550 nm.

4.3 Radiative Transfer of Light in Atmosphere-Ocean Systems

Radiative transfer simulations for the atmosphere and for the ocean have prioritized the modeling of different phenomena. Atmospheric modeling almost always includes polarization but rarely inelastic scattering, while ocean RT modeling often ignores polarization, but does address inelastic scattering. At the onset of the PACE Science Team in 2015, no coupled ocean-atmosphere RT model that addressed both polarization and inelastic scattering in the ocean could be identified. Since then, Zhai et al. (2015, 2017a) have developed a RT model based on the successive order of scattering method that can accurately handle polarization, atmosphere and ocean coupling, elastic and inelastic scattering. The inelastic scattering mechanisms include Raman scattering due to ocean waters, fluorescent dissolved organic matter, and fluorescence by chlorophyll. Furthermore, the photochemical and NPQ processes of the chlorophyll fluorescence have been accounted for in Zhai et al. (2018). The RT model has been used to study the sensitivity of TOA polarized radiance to contributions originating from underwater light scattering in open and coastal ocean waters, which can be used to design new atmospheric correction algorithms (Zhai et al., 2017b).

Another common omission in RT is Earth curvature that may affect significantly the TOA signal, not only at large solar zenith and viewing angles, but also at small viewing angle. It needs to be taken to account in RT simulations for accurate water reflectance retrievals, especially at high latitudes. Two processes are essentially at play in a spherical-shell atmosphere: 1) reduced illumination volume and 2) reduced attenuation of the downward solar beam. The earth curvature effect at low viewing angle has been largely ignored, since it is relatively small compared with the effect at large viewing angle, but neglecting it may not yield the rather demanding accuracy required for PACE science objectives. Pseudo-spherical corrections (e.g., just accounting for air mass change in the incident solar beam) may be sufficient at large solar zenith angle, but they do not capture effects at low viewing angle. Monte Carlo codes operated in backward mode are tools of predilection to quantify "exactly" spherical effects and generate look-up tables (e.g., molecule and aerosol scattering) for atmospheric correction algorithms. Adjacency effects due to the proximity of land, sea ice, or clouds, on the other hand, can be felt at relatively far distances (>10 km), their magnitude depending on the contrast between the reflectance of the target and its surroundings and the optical thickness of the atmosphere. Monte Carlo codes allow simulations for any spatial heterogeneity configuration; they offer a great deal of flexibility. Impacts on TOA measurements are calculated precisely, as well as the atmospheric spread function, which can be used in efficient corrective schemes, allowing image processing in the usual "large target" RT formalism.

4.4 Benchmarking, Path Forward and Conclusion

Because of the wide variety of ocean, atmosphere and coupled RT models in current use, each with their own representation of optically active components and their own set of assumptions, there is a spread of solutions resulting from these models. We require a set of calculations, agreed upon by multiple RT codes to set a benchmark for future RT results for the ocean and atmosphere coupled system. In the PACE Science Team, a set of typical ocean and atmosphere coupled systems have been designed to perform polarized RT simulations. Several RT models have been used to perform the simulations and the inter-comparison has led to 25,000+ RT results with an accuracy ranging between 10^{-5} and 10^{-6} in terms of reflectance (Chowdhary et al., "Benchmark results for scalar and vector radiative transfer computations of light in atmosphere-ocean systems", unpublished). This benchmark has exceeded any previous dataset for the coupled ocean and atmosphere system.

Despite the advances described above, gaps remain in RT topics that require continued research in the near future. Several topics were identified by the PACE Science Team:

- For RT of light in the ocean, these topics are (i) better understanding of the role of absorption by dissolved inorganics in the UV (FWD RT studies); (ii) better understanding of variability in backscattering shape of VSF (FWD and INV RT studies); (iii) developing particulate models that combine non-sphericity and inhomogeneity (FWD and INV RT studies); (iv) accounting for temperature and salinity dependence of Raman scattering and emission (FWD RT studies).
- For ocean surface reflection, outstanding topics are (i) impact of anisotropic surface roughness on the reflection of diffuse skylight (FWD RT studies); (ii) polarization properties of whitecaps in the UV-SWIR (FWD RT studies).
- For RT of light in the atmosphere, more research is needed on (i) retrieving multiple aerosol species that within a given size mode co-exist as external or internal mixtures (INV RT studies); (ii) characterizing aerosol properties in

the UV (INV RT studies); (iii) retrieving aerosol vertical distribution from UV polarimetry (INV RT studies).
- For UV remote sensing of AOS, attention should be given to (i) approximations made for the coupling of atmosphere and ocean (FWD RT studies); (ii) accounting for simultaneous variations in absorbing aerosols and absorbing oceanic matter (INV RT studies); (iii) accounting for short-term variations of solar irradiance (INV RT studies).

This list, which is not all-inclusive, should be viewed within the context of advancement of accuracies in FWD and INV RT modeling for ensuring the fidelity to nature and/or meeting the radiometric (NASA, 2018a) and polarimetric (NASA, 2018b) measurement targets and products for PACE. Development of new technologies with subsequent experimentation will be required to address many of these gaps. Note that PACE data and products will serve many communities, and that these communities participate in research of interdisciplinary fields. Hence it is not possible to assign an order of importance to the above-mentioned topics. Furthermore, both numerical accuracy and efficiency are major concerns for making advances in INV RT modeling. Depending on the information content contained in an instrument with specific combinations of spectral, angular and polarimetric measurements and uncertainties, one often needs to makes trade-offs between accuracy and efficiency by considering approximation. So the development of retrieval oriented RT modeling approaches is another task for ocean color remote sensing and should be done in the next stage.

Overall, we conclude that RT modeling of multi-spectral polarized light in atmosphere-ocean systems has made significant forward progress during the tenure of the first PACE Science Team. While there are facets that will require further development to meet the capabilities required of the PACE and other missions, and to push ocean and atmospheric science forward, we are confident that the new results presented here will help both the atmosphere and ocean color communities make progress to meet these challenges. In addition, we strongly encourage these communities to view their challenges as a coupled problem, affecting both ocean and atmosphere that can only be met by working together. Thus, coupled science and effort must go hand-in-hand with improved coupled RT modeling. This is an essential step toward approaching the focus questions that are posed in the Aerosol-Ocean Interactions science traceability matrix (STM) for Aerosols, Cloud and Ecosystem (ACE) (Behrenfeld and Meskhidze, 2017), and solving some of the most pressing problems threatening the sustainability of our planet.

MEMBERS OF 2014–2017 PACE SCIENCE TEAM

Jacek Chowdhary, Emmanuel Boss, Heidi Dierssen, Robert Frouin, Amir Ibrahim, Zhongping Lee, Lorraine Remer, Michael Twardowski, Feng Xu and Xiaodong Zhang.

AUTHOR CONTRIBUTIONS

JC and P-WZ were responsible for the overall structure and flow of the manuscript. JC was a co-lead author for sections “1 Introduction,” “1.1 The PACE Mission,” “1.2 Complexity of Atmosphere-Ocean Systems,” “2 History of RT Methods for OAS: A Brief Overview,” “3 Current RT Topics and Models: Heritage Studies, Discussion, and PACE Updates,” “3.1 Ocean Body,” “3.1.1 Particulate Scattering,” “3.1.2 Bio-Optical Models,” “3.2.1 Sunglint,” “3.3.1 Aerosols,” “3.4.1 RT Validations,” “3.4.2 Horizontal Variations,” and “3.4.2 UV Remote Sensing of AOS.” P-WZ was a co-lead author for sections “1 Introduction,” “1.1 The PACE Mission,” “1.2 Complexity of Atmosphere-Ocean Systems,” “2 History of RT Methods for OAS: A Brief Overview,” “3.1.4 Inelastic Scattering,” “3.3.2 Gases,” and “3.4.1 RT Validations.” EB was a co-lead author for sections “3.1.2 Bio-Optical Models” and “3.1.3 Molecular Scattering.” HD was a co-lead author for section “3.2.2 Whitecaps.” RF was a co-lead author for section “3.4.2 Horizontal Variations.” AI was a co-lead author for section “3.3.2 Gases.” MT was a co-lead author for sections “3.1.1 Particulate Scattering” and “3.1.3 Molecular Scattering.” MO was a co-lead author for section “3.2.1 Sunglint.” LAR was a co-lead author for section “3.3.1 Aerosols.” ZL was a co-lead author for sections “3.1.1 Particulate Scattering” and “3.1.2 Bio-Optical Models.” FX was a co-lead author for section “3.4.1 RT Validations.” XZ was a co-lead author for section “3.1.1 Particulate Scattering.” DR contributed to section “3.4.2 Horizontal Variations.” WRE contributed to section “3.3.1 Aerosols.” All authors contributed to section “4 Concluding Remarks” and approved the submitted version of the manuscript.

FUNDING

This work was supported by NASA Grant NNH13ZDA001N-PACEST. In addition, P-WZ was partially supported by additional funds from the NASA PACE Project and also acknowledged support by NASA Grants (NNX15AB94G and 80NSSC18K0345). MT further acknowledged additional support from the HBOI Foundation, and XZ from NASA (NNX13AN72G and 0NSSC17K0656) and from NSF (1355466 and 1459168).

ACKNOWLEDGMENTS

The authors thank the reviewers for their constructive comments on an earlier version of this manuscript, and greatly appreciate the discussions with Otto Hasekamp and Jeremy Werdell on specifics of the PACE mission, and the discussions with Ziauddin Ahmad, Brian Cairns, and Bo-Cai Gao on UV-A solar spectra.

REFERENCES

Aas, E. (1996). Refractive index of phytoplankton derived from its metabolite composition. *J. Plankton Res.* 18, 2223–2249. doi: 10.1093/plankt/18.12.2223

Adams, C. D., and Kattawar, G. W. (1978). Radiative transfer in spherical shell atmospheres I. Rayleigh scattering. *Icarus* 35, 139–151. doi: 10.1016/0019-1035(78)90067-2

Adams, C. N., and Kattawar, G. W. (1993). Effect of volume-scattering function on the errors induced when polarization is neglected in radiance calculations in an atmosphere-ocean system. *Appl. Opt.* 32, 4610–4617.

Adams, J. T., and Kattawar, G. W. (1997). Neutral points in an atmosphere–ocean system. 1: upwelling light field. *Appl. Opt.* 36, 1976–1986.

Ahmad, Z., Franz, B. A., McClain, C. R., Kwiatkowska, E. J., Werdell, J., Shettle, E. P., et al. (2010). New aerosol models for the retrieval of aerosol optical thickness and normalized water-leaving radiances from the SeaWiFS and MODIS sensors over coastal regions and open oceans. *Appl. Opt.* 49:5545. doi: 10.1364/AO.49.005545

Ahmad, Z., and Fraser, R. S. (1982). An iterative transfer code for atmosphere-ocean systems. *J. Atm. Sci.* 39, 656–665. doi: 10.1175/1520-0469(1982)039<0656:airtcf>2.0.co;2

Ahmad, Z., Mc Clain, C. R., Herman, J. R., Franz, B. A., Kwiatkowska, E., Robinson, W. D., et al. (2007). Atmospheric correction for NO2 absorption in retrieving water-leaving reflectances from the SeaWiFS and MODIS measurements. *Appl. Opt.* 46, 6504–6512.

Anderson, G., Clough, S., Kneizys, F., Chetwynd, J., and Shettle, E. (1986). *AFGL Atmospheric Constituent Profiles (0 - 120 Km), 1-TR-86-0110*. Hanscom AFB, MA: U.S. Air Force Geophysics Laboratory. Optical Physics Division.

Antonov, J. I., Seidov, D., Boyer, T. P., Locarnini, R. A., Mishonov, A. V., Garcia, H. E., et al. (2010). "World ocean atlas 2009, volume 2: salinity," in *NOAA NESDIS 68*, ed. S. Levitus (Washington, DC: U.S. Government Printing Office), 39.

Armstrong, F. A. J., and Boalch, G. T. (1961). The ultra-violet absorption of sea watter. *J. Mar. Biol. Assoc.* 41, 591–597.

Artlett, C. P., and Pask, H. M. (2015). Optical remote sensing of water temperature using Raman spectroscopy. *Opt. Express* 23, 31844–31856. doi: 10.1364/OE.23.031844

Artlett, C. P., and Pask, H. M. (2017). New approach to remote sensing of temperature and salinity in natural water samples. *Opt. Express* 25, 2840–2851. doi: 10.1364/OE.25.002840

Baker, A. R., Laskina, O., and Grassian, V. H. (2014). "Processing and ageing in the atmosphere, in mineral dust," in *A Key Player in the Earth System*, eds P. Knippertz and J.-B. W. Stuut (Berlin: Springer), 75–92. doi: 10.1007/978-94-017-8978-3_4

Balch, W. M., Vaughn, J. M., Drapeau, D. T., Bowler, B. C., Booth, E., Vining, C. L., et al. (2004). "Case I/II ambiguities in algal blooms: the case for minerals and viruses," in *Proceedings of the American Society of Limnology and Oceanography/The Oceanography Society, Ocean Research 2004 Conference*, (Honolulu).

Baran, A. J., and Labonnote, L. C. (2006). On the reflection and polarization properties of ice clouds. *J. Quant. Spectrosc. Radiat. Transf.* 100, 41–54.

Barnes, W. L., Pagano, T. S., and Salomonson, V. V. (1998). Prelaunch characteristics of the moderate resolution imaging spectroradiometer (MODIS). on EOS-AM1. *IEEE Trans. Geosci. Remote Sens.* 36, 1088–1100. doi: 10.1109/36.700993

Bauer, S. E., Tsigaridis, K., and Miller, R. L. (2016). Significant atmospheric aerosol pollution caused by world food cultivation. *Geophys. Res. Lett.* 43, 5394–5400. doi: 10.1002/2016GL068354

Behrenfeld, M., and Meskhidze, N. (2017). Response to the 2017 NRC Decadal Survey Request for Information Regarding the OCEAN ECOSYSTEM and OCEAN-AEROSOL INTERACTIONS Components of the Aerosol, Cloud, and Ocean Ecosystem (ACE). Mission. Available at: https://acemission.gsfc.nasa.gov/documents/whitepapers/RFI-2c%20Ocean.pdf. doi: 10.1002/2016gl068354 (accessed May 11, 2019).

Behrenfeld, M. J., Bale, A. J., Kolber, Z. S., Aiken, J., and Falkowski, P. G. (1996). Confirmation of iron limitation of phytoplankton photosynthesis in the equatorial Pacific ocean. *Nature* 383, 508–511. doi: 10.1038/383508a0

Behrenfeld, M. J., and Kolber, Z. S. (1999). Widespread iron limitation of phytoplankton in the South Pacific Ocean. *Science* 283, 840–884.

Behrenfeld, M. J., Westberry, T. K., Boss, E. S., O'Malley, R. T., Siegel, D. A., Wiggert, J. D., et al. (2009). Satellite-detected fluorescence reveals global physiology of ocean phytoplankton. *Biogeosciences* 6, 779–794. doi: 10.5194/bg-6-779-2009

Bellouin, N., Boucher, O., Tanré, D., and Dubovik, O. (2003). Aerosol absorption over the clear-sky oceans deduced from POLDER-1 and AERONET observations. *Geophys. Res. Lett.* 30:1748.

Bergametti, G., and Forêt, G. (2014). "Dust deposition, in mineral dust," in *A Key Player in the Earth System*, eds P. Knippertz and J.-B. W. Stuut (Berlin: Springer), 179–196.

Bernard, S., Probyn, T. A., and Quiantes, A. (2009). Simulating the optical properties of phytoplankton cells using a two-layered spherical geometry. *Biogeosci. Discuss.* 6, 1497–1563. doi: 10.5194/bgd-6-1497-2009

Bi, L., and Yang, P. (2015). Impact of calcification state on the inherent optical properties of coccoliths and coccolithophores. *J. Quant. Spectrosc. Radiat. Transf.* 155, 10–21. doi: 10.1016/j.jqsrt.2014.12.017

Bi, L., Yang, P., Kattawar, G. W., and Kahn, R. (2010). Modeling optical properties of mineral aerosol particles by using nonsymmetric hexahedra. *Appl. Opt.* 49, 334–342. doi: 10.1364/AO.49.000334

Bishop, J. K., Davis, R. E., and Sherman, J. T. (2002). Robotic observations of dust storm enhancement of Carbon biomass in the North Pacific. *Science* 298, 817–821. doi: 10.1126/science.1074961

Blondeau-Patissier, D., Gower, J. F. R., Dekker, A. G., Phinn, S. R., and Brando, V. E. (2014). A review of ocean color remote sensing methods and statistical techniques for the detection, mapping and analysis of phytoplankton blooms in coastal and open oceans. *Progr. Oceanogr.* 123, 123–144. doi: 10.1016/j.pocean.2013.12.008

Bodhaine, B. A., Wood, N. B., Dutton, E. G., and Slusser, J. R. (1999). On rayleigh optical depth calculations. *J. Atmos. Ocean. Technol.* 16, 1854–1861. doi: 10.1175/1520-0426(1999)016<1854:orodc>2.0.co;2

Bogumil, K., Orphal, J., Homann, T., Voigt, S., Spietz, P., Fleischmann, O. C., et al. (2003). Measurements of molecular absorption spectra with the SCIAMACHY pre-flight model: instrument characterization and reference data for atmospheric remote-sensing in the 230–2380 nm region. *J. Photochem. Photobiol. A* 157, 167–184. doi: 10.1016/s1010-6030(03)00062-5

Bohren, C., and Huffman, D. (1983). *Absorption and Scattering of Light by Small Particles*. New York, NY: Wiley.

Born, M., and Wolf, E. (1999). *Principles of Optics. Electromagnetic Theory of Propagation, Interference and Diffraction of Light*. Cambridge: Cambridge University Press.

Boss, E., and Pegau, W. S. (2001). Relationship of light scattering at an angle in the backward direction to the backscattering coefficient. *Appl. Opt.* 40, 5503–5507.

Bouffiès, S., Bréon, F. M., Tanré, D., and Dubuisson, P. (1997). Atmospheric water vapor estimate by a differential absorption technique with the polarisation and directionality of the Earth reflectances (POLDER). instrument. *J. Geophys. Res.* 102, 3831–3841. doi: 10.1029/96JD03126

Boyd, P. W., Mackie, D. S., and Hunter, K. A. (2009). Aerosol iron deposition to the surface ocean – Modes of iron supply and biological responses. *Mar. Chem.* 10, 128–143. doi: 10.1016/j.marchem.2009.01.008

Boyd, P. W., Watson, A. J., Law, C. S., Abraham, E. R., Trull, T., Murdoch, R., et al. (2000). A mesoscale phytoplankton bloom in the polar southern ocean stimulated by iron fertilization. *Nature* 407, 695–702. doi: 10.1038/35037500

Boyle, E. S., Guerriero, N., Thiallet, A., Del Vecchio, R., and Blough, N. V. (2009). Optical properties of humic substances and CDOM: relation to structure. *Environ. Sci. Technol.* 43, 2262–2268. doi: 10.1021/es803264g

Bréon, F. M., and Doutriaux-Boucher, M. (2005). A comparison of cloud droplet radii measured from space. *IEEE Trans Geosci. Remote Sens.* 43, 1796–1805. doi: 10.1109/tgrs.2005.852838

Bréon, F.-M., and Goloub, P. (1998). Cloud droplet effective radius from spaceborne polarization measurements. *Geophys. Res Lett.* 25, 1879–1882. doi: 10.1029/98gl01221

Bréon, F. M., and Henriot, N. (2006). Spaceborne observations of ocean glint reflectance and modeling of wave slope distributions. *J. Geophys. Res.* 11:C06005. doi: 10.1029/2005JC003343

Bricaud, A., Babin, M., Morel, A., and Claustre, H. (1995). Variability in the chlorophyll-specific absorption coefficients of natural phytoplankton: analyses and parameterization. *J. Geophys. Res.* 100, 13321–13332.

Bricaud, A., Morel, A., Babib, M., Allali, K., and Claustre, H. (1999). Erratum: variations of light absorption by suspended particles with chlorophyll a concentrations in oceanic (case 1). waters: analysis and implications for bio-optical models. *J. Geophys. Res.* 104:8025. doi: 10.1029/1999jc900030

Bricaud, A., Morel, M., Babin, M., Allali, K., and Claustre, H. (1998). Variations of light absorption by suspended particles with Chlorophyll a concentration in oceanic (case 1). Waters: analyses and implications for bio-optical models. *J. Geophys. Res.* 103, 31033–31044. doi: 10.1029/98jc02712

Brumer, S. E., Zappa, C. J., Brooks, I. M., Tamura, H., Brown, S. M., Blomquist, B. W., et al. (2017). Whitecap coverage dependence on wind and wave statistics as observed during SO GasEx and HiWinGS. *J. Phys. Oceanogr.* 47, 2211–2235. doi: 10.1175/jpo-d-17-0005.1

Buehler, S. A., Eriksson, P., and Lemke, O. (2011). Absorption lookup tables in the radiative transfer model ARTS. *J. Quant. Spectrosc. Radiat. Transf.* 112, 1559–1567. doi: 10.1016/j.jqsrt.2011.03.008

Buiteveld, H., Hakvoort, J. H. M., and Donze, M. (1994). The optical properties of pure water. *SPIE Ocean Optics XII* 2258, 174–183.

Bulgarelli, B., and Doyle, J. P. (2004). Comparison between numerical models for radiative transfer simulation in the atmosphere-ocean system. *J. Quant. Spectrosc. Radiat. Transf.* 86, 315–334. doi: 10.1016/j.jqsrt.2003.08.009

Burrows, S. M., Ogunro, O., Frossard, A. A., Russell, L. M., Rasch, P. J., and Elliot, S. M. (2014). A physically-based framework for modelling the organic fractionation of sea spray aerosol from bubble film Langmuir equilibria. *Atmos. Chem. Phys. Discuss.* 14, 5375–5443. doi: 10.5194/acpd-14-5375-2014

Cairns, B., Russell, E. E., LaVeigne, J. D., and Tennant, P. M. W. (2003). "Research scanning polarimeter and airborne usage for remote sensing of aerosols," in *Proceedings of the Polarization Science and Remote Sensing*, (San Diego, CA).

Cairns, B., Russell, E. E., and Travis, L. D. (1999). The research scanning polarimeter: calibration and ground-based measurements. *Proc. SPIE* 3754, 186–197.

Carder, K. L., Chen, F. R., Lee, Z. P., Hawes, S., and Kamykowski, D. (1999). Semi-analytic MODIS algorithms for chlorophyll a and absorption with bio-optical domains based on nitrate-depletion temperatures. *J. Geophys. Res.* 104, 5403–5421. doi: 10.1029/1998jc900082

Carnesecchi, F., Byfield, V., Cipollini, P., Corsini, G., and Diani, M. (2008). "An optical model for the interpretation of remotely sensed multispectral images of oil spill," in *Proceedings of the Remote Sensing of the Ocean, Sea Ice, and Large Water Regions*, (San Diego, CA).

Carslaw, K. S., Boucher, O., Spracklen, D. V., Mann, G. W., Rae, J. G. L., Woodward, S., et al. (2010). A review of natural aerosol interactions and feedbacks within the Earth system. *Atmos. Chem. Phys.* 10, 1701–1737. doi: 10.5194/acp-10-1701-2010

Caudill, T. R., Flitter, D. E., and Herman, B. M. (1997). Evaluation of the pseudo-spherical approximation for backscattered ultraviolet radiances and ozone retrieval. *J. Geophys. Res.* 102, 3881–3890. doi: 10.1029/96jd03266

Chami, M., Lafrance, B., Fougnie, B., Chowdhary, J., Harmel, T., and Waquet, F. (2015). OSOAA: a vector radiative transfer model of coupled atmosphere-ocean system for a rough sea surface application to the estimates of the directional variations of the water leaving reflectance to better process multi-angular satellite sensors data over the ocean. *Opt. Express* 23, 27829–27852. doi: 10.1364/OE.23.027829

Chami, M., Santer, R., and Dillegeard, E. (2001). Radiative transfer model for the computation of radiance and polarization in an atmosphere-ocean system: polarization properties of suspended matter for remote sensing. *Appl. Opt.* 40, 2398–2416.

Chandrasekhar, S. (1950). *Radiative Transfer*. Oxford: Oxford University Press.

Chen, Y., and Bond, T. C. (2010). Light absorption by organic carbon from wood combustion. *Atmos. Chem. Phys.* 10, 1773–1787. doi: 10.5194/acp-10-1773-2010

Chepfer, H., Goloub, P., Reidi, J., De Haan, J., Hovenier, J., and Flamant, P. H. (2001). Ice crystal shapes in cirrus clouds derived from POLDER-1/ADEOS-1. *J. Geophys. Res. Atmos.* 106, 7955–7966. doi: 10.1029/2000jd900285

Chesters, D., Uccellini, L. W., and Robinson, W. D. (1983). Low-level water vapor fields from the VISSR atmospheric sounder (VAS). split window channels. *J. Clim. Appl. Meteorol.* 22, 725–743. doi: 10.1175/1520-0450(1983)022<0725:llwvff>2.0.co;2

Chowdhary, J., Cairns, B., Mishchenko, M. I., Hobbs, P. V., Cota, G. F., Redemann, J., et al. (2005). Retrieval of aerosol scattering and absorption properties from photopolarimetric observations over the ocean during the CLAMS experiment. *J. Atmos. Sci.* 62, 1093–1117. doi: 10.1175/jas3389.1

Chowdhary, J., Cairns, B., Mishchenko, M. I., and Travis, L. D. (2001). Retrieval of aerosol properties over the ocean using multispectral and multiangle photopolarimetric measurements from the Research Scanning Polarimeter. *Geophys. Res. Lett.* 28, 234–246.

Chowdhary, J., Cairns, B., and Travis, L. (2002). Case studies of aerosol retrievals from multi-angle, multi-spectral photo-polarimetric remote sensing data. *J. Atmos. Sci.* 59, 383–397.

Chowdhary, J., Cairns, B., and Travis, L. D. (2006). Contribution of water-leaving radiance to multiangle, multispectral polarimetric observations over the open ocean: bio-optical model results for case 1 waters. *Appl. Opt.* 45, 5542–5587.

Chowdhary, J., Cairns, B., Waquet, F., Knobelspiesse, K., Ottaviani, M., Redemann, J., et al. (2012). Sensitivity of multiangle, multispectral polarimetric remote sensing over open oceans to water-leaving radiance: analyses of RSP data acquired during the MILAGRO campaign. *Remote Sens. Environ.* 118, 284–308. doi: 10.1016/j.rse.2011.11.003

Chowdhary, J., Travis, L. D., and Lacis, A. A. (1995). "Incorporation of a rough ocean surface and semi-infinite water body in multiple scattering computations of polarized light in an atmosphere-ocean system," in *Proceedings of the Atmospheric Scattering and Modelling* (Rome: Proceedings of SPIE), 2311:58. doi: 10.1117/12.198585

Claustre, H., Sciandra, A., and Vaulot, D. (2008). Introduction to the special section bio-optical and biochemical conditions in the South East Pacific in late 2014: the BIOSCOPE program. *Biogeosciences* 5, 679–691. doi: 10.5194/bg-5-679-2008

Clavano, W. R., Boss, E., and Karp-Boss, L. (2007). Inherent optical properties of non-spherical marine-like particles – from theory to observations. *Oceanogr. Mar. Biol.* 45, 1–45.

Collins, D. G., Blättner, W. G., Wells, M. B., and Horak, H. G. (1972). Backward monte carlo calculations of the polarization characteristics of the radiation emerging from spherical-shell atmospheres. *Appl. Opt.* 1, 2684–2696. doi: 10.1364/AO.11.002684

Copin-Montegut, G., Ivanoff, A., and Saliot, A. (1971). Coefficient d'atténuation des eaux de mer dans l'ultra-viole. CR Acad. *Sci. Paris* 272, 1453–1456.

Coulson, K. L., Dave, J. V., and Sekera, Z. (1960). *Tables Related to Radiation Emerging From a Planetary Atmosphere With Rayleigh Scattering*. Berkeley, CA: University of California Press.

Cox, C., and Munk, W. (1954). Statistics of the sea-surface derived from sun-glitter. *J. Mar. Res.* 13, 198–227.

Czerski, H., Twardowski, M., Zhang, X., and Vagle, S. (2011). Resolving size distributions of bubbles with radii less than 30 microns with optical and acoustical methods. *J. Geophys. Res.* 116:C00H11. doi: 10.1029/2011JC007177

Dahlback, A., and Stamnes, K. (1991). A new spherical model for computing the radiation field available for photolysis and heating at twilight'. *Planet. Space Sci.* 39, 671–683. doi: 10.1016/0032-0633(91)90061-e

Dall'Olmo, G., Westberry, T. K., Behrenfeld, M. J., Boss, E., and Slade, W. H. (2009). Significant contribution of large particles to optical backscattering in the open ocean. *Biogeosciences* 6, 947–967. doi: 10.5194/bg-6-947-2009

Daumont, D., Brion, J., Charbonnier, J., and Malicet, J. (1992). Ozone UV spectroscopy I: absorption cross-sections at room temperature. *J. Atmos. Chem.* 15:145. doi: 10.1021/acs.est.5b04379

Davis, A. B., and Kalashnikova, O. V. (2019). "Aerosol layer height over water via O2 A-band observations from space: a tutorial," in *Springer Series in Light Scattering, vol. 3: Radiative Transfer and Light Scattering*, ed. A. A. Kokhanovsky (Heidelberg: Springer), 133–166. doi: 10.1007/978-3-030-03445-0_4

de Haan, J. F., Bosma, P. B., and Hovenier, J. W. (1987). The adding method for multiple scattering computations of polarized light. *Astron. Astrophys.* 183, 371–391.

Dee, D. P., Uppala, S. M., Simmons, A. J., Berrisford, P., Poli, P., Kobayashi, S., et al. (2011). The ERA-Interim reanalysis: configuration and performance of the data assimilation system. *Q. J. R. Meteorol. Soc.* 137, 553–597. doi: 10.1002/qj.828

Deelen, V. R., Landgraf, J., and Aben, I. (2005). Multiple elastic and inelastic light scattering in the Earth's atmosphere: a doubling-adding method to include Raman scattering by air. *J. Quant. Spectrosc. Radiat. Transf.* 95, 309–330. doi: 10.1016/j.jqsrt.2004.11.002

Derber, J. C., Parrish, D. F., and Lord, S. J. (1991). The new global operational analysis system at the national meteorological center. *Weather Forecast* 6, 538–547. doi: 10.1175/1520-0434

Dierssen, H. M. (2010). Perspectives on empirical approaches for ocean color remote sensing of chlorophyll in a changing climate. *PNAS* 107, 17073–17078. doi: 10.1073/pnas.0913800107

Dierssen, H. M. (2019). Hyperspectral measurements, parameterizations, and atmosphericcorrection of whitecaps and foam from visible to shortwave infrared for ocean color remote sensing. *Front. Earth Sci.* 7:14. doi: 10.3389/feart.2019.00014

Diner, D. J., Beckert, J. C., Reilly, T. H., Bruegge, C. J., Conel, J. E., Kahn, R. A., et al. (1998). Multi-angle imaging spectroradiometer (MISR). instrument description and experiment overview. *IEEE Trans. Geosci. Remote Sens.* 36, 1072–1087. doi: 10.1109/36.700992

Diner, D. J., Xu, F., Garay, M. J., Martonchik, J. V., Rheingans, B. E., Geier, S., et al. (2013). The airborne multiangle spectropolarimetric imager (AirMSPI): a new tool for aerosol and cloud remote sensing. *Atmos. Meas. Tech.* 6, 2007–2025. doi: 10.5194/amt-6-2007-2013

Ding, K., and Gordon, H. R. (1994). Atmospheric correction of ocean-color sensors: effects of the Earth's curvature. *Appl. Opt.* 33, 7096–7106. doi: 10.1364/AO.33.007096

Doicu, A., and Trautmann, T. (2009). Picard iteration methods for a spherical atmosphere. *J. Quant. Spectrosc. Radiat. Transf.* 110, 1851–1863. doi: 10.1016/j.jqsrt.2009.04.002

Dolgos, G., and Martins, J. V. (2014). Polarized imaging nephelometer for in situ airborne measurements of aerosol light scattering. *Opt. Express* 22, 21972–21990. doi: 10.1364/OE.22.021972

Dougherty, R. L. (1989). Radiative transfer in a semi-infinite absorbing/scattering medium with reflective boundary. *J. Quant. Spectrosc. Radiat. Transf.* 41:55. doi: 10.1016/0022-4073(89)90021-6

Duan, M., Min, Q., and Li, J. (2005). A fast radiative transfer model for simulating high-resolution absorption bands. *J. Geophys. Res. Atmos.* 110:D15201.

Dubovik, O., Herman, M., Holdak, A., Lapyonok, T., Tanre, D., Deuze, J. L., et al. (2011). Statistically optimized inversion algorithm for enhanced retrieval of aerosol properties from spectral multi-angle polarimetric satellite observations. *Atmos. Meas. Tech.* 4, 975–1018. doi: 10.5194/amt-4-975-2011

Dubovik, O., and King, M. (2000). A flexible inversion algorithm for retrieval of aerosol optical properties from Sun and sky radiance measurements. *J. Geophys. Res.* 105, 20673–20696. doi: 10.1029/2000jd900282

Dubovik, O., Lapyonok, T., Litvinov, P., Herman, M., Fuertes, D., Ducos, F. M., et al. (2014). GRASP: a versatile algorithm for characterizing the atmosphere. *SPIENewsroom* 28, 2–5. doi: 10.1117/2.1201408.005558

Dubovik, O., Smirnov, A., Holben, B. N., King, M. D., Kaufman, Y. J., Eck, T. F., et al. (2000). Accuracy assessments of aerosol optical properties retrieved from aerosol robotic network (AERONET). Sun and sky radiance measurements. *J. Geophys. Res.* 105, 9791–9806. doi: 10.1029/2000JD900040

Dubuisson, P., Borde, R., Schmechtig, C., and Santer, R. (2001). Surface pressure estimates from satellite data in the oxygen A-band: applications to the MOS sensor over land J. *Geophys. Res. Atmos.* 106, 27277–27286. doi: 10.1029/2001jd000401

Dubuisson, P., Dessailly, D., Vesperini, M., and Frouin, R. (2004). Water vapor retrieval over ocean using near-infrared radiometry. *J. Geophys. Res. Atmos.* 109:D19106.

Dubuisson, P., Frouin, R., Dessailly, D., Duforêt, L., Léon, J.-F., Voss, K., et al. (2009). Estimating the altitude of aerosol plumes over the ocean from reflectance ratio measurements in the O2 A-band. *Rem. Sen. Environ.* 113, 1899–1911. doi: 10.1016/j.rse.2009.04.018

Duforêt, L., Frouin, R., and Dubuisson, P. (2007). Importance and estimation of aerosol vertical structure in satellite ocean-color remote sensing. *Appl. Opt.* 46, 1107–1119.

Duforêt-Gaurier, L., Dessailly, D., Moutier, W., and Loisel, H. (2018). Assessing the impact of a two-layered spherical geometry of phytoplankton cells on the bulk backscattering ratio of marine particulate matter. *Appl. Sci.* 8:2689. doi: 10.3390/app8122689

Ebuchi, N., and Kizu, S. (2002). Probability distribution of surface wave slope derived using sun glitter images from geostationary meteorological satellite and surface vector winds from scatterometers. *J. Oceanogr.* 58, 477–486.

Engel, A., Bange, H. W., Cunliffe, M., Burrows, S. M., Friedrichs, G., Galgani, L., et al. (2017). The ocean's vital skin: toward an integrated understanding of the sea surface microlayer. *Front. Mar. Sci.* 4:165. doi: 10.3389/fmars.2017.00165

Espinosa, W. R., Martins, J. V., Remer, L. A., Puthukkudy, A., Orozco, D., and Dolgos, G. (2018). In situ measurements of angular dependent light scattering by aerosols over the contiguous United States. *Atmos. Chem. Phys.* 18, 3737–3754. doi: 10.5194/acp-18-3737-2018

Espinosa, W. R., Remer, L. A., Dubovik, O., Ziemba, L., Beyersdorf, A., Orozco, D., et al. (2017). Retrievals of aerosol optical and microphysical properties from imaging polar nephelometer scattering measurements. *Atmos. Meas. Tech.* 10:811. doi: 10.5194/amt-10-811-2017

Fan, Y., Li, W., Voss, K. J., Gatebe, C. K., and Stamnes, K. (2015). Neural network method to correct bidirectional effects in water-leaving radiance. *Appl. Opt.* 55, 10–21. doi: 10.1364/AO.55.000010

Farinato, R. S., and Rowell, R. L. (1976). New values of the light scattering depolarization and anisotropy of water. *J. Chem. Phys.* 65, 593–595. doi: 10.1063/1.433115

Fischer, J., and Grassl, H. (1984). Radiative transfer in an atmosphere-ocean system: and azimuthally dependent matrix-operator approach. *Appl. Opt.* 23:1032. doi: 10.1364/ao.23.001032

Fougnie, B., Bracco, G., Lafrance, B., Ruffel, C., Hagolle, O., and Tinel, C. (2007). PARASOL in-flight calibration and performance. *Appl. Opt.* 46, 5435–5451.

Fougnie, B., Marbach, T., Lacan, A., Lang, R., Schlüssel, P., Poli, G., et al. (2018). The multi-viewing multi-channel multi-polarisation imager–Overview of the 3MI polarimetric mission for aerosol and cloud characterization. *J. Quant. Spectrosc. Radiat. Transf.* 219, 23–32. doi: 10.1016/j.jqsrt.2018.07.008

Fournier, G., and Forand, J. L. (1994). "Analytical phase function for ocean water," in *Proceedings of the Ocean Optics XII SPIE*, ed. J. S. Jaffe (Bellingham, DC), 194–201.

Fournier, G., and Jonasz, M. (1999). "Computer-based underwater imaging analyses," in *Proceedings of the Airborne and In-water Underwater Imaging SPIE*, Vol. 3761, ed. G. Gilbert (Bellingham, DC), 62–77.

Fournier, G., and Neukermans, G. (2017). An analytical model for light backscattering by coccoliths and coccospheres of *Emiliania huxleyi*. *Opt. Expr.* 25, 14999–15009. doi: 10.1364/OE.25.014996

Fraser, R. S. (1981). Atmospheric neutral points outside of the principal plane. *Contrib. Atm. Phys.* 58:286.

Fraser, R. S., and Walker, W. H. (1968). Effect of specular reflection at the ground on light scattered from a Rayleigh atmosphere. *J. Opt. Soc. Am.* 58:636. doi: 10.1364/josa.58.000636

Freney, E. J., Adachi, K., and Buseck, P. R. (2010). Internally mixed atmospheric aerosol particles: hygroscopic growth and light scattering. *J. Geophys. Res.* 115:D19210.

Frouin, R., Deschamps, P.-Y., and Lecomte, P. (1990). Determination from space of atmospheric total water vapor amounts by differential absorption near 940 nm: theory and airborne verification. *J. Appl. Meteorol.* 29, 448–460. doi: 10.1175/1520-0450(1990)029<0448:dfsoat>2.0.co;2

Frouin, R., Franz, B., Ibrahim, A., Knobelspiesse, K., Ahmad, Z., Cairns, B., et al. (2019). Atmospheric correction of satellite ocean-color imagery during the PACE era. *Front. Earth Sci.* (in press). doi: 10.3389/feart.2019.00145

Frouin, R., Schwindling, M., and Deschamps, P.-Y. (1996). Spectral reflectance of sea foam in the visible and near-infrared: in situ measurements and remote sensing applications. *J. Geophys. Res.* 101, 14361–14371. doi: 10.1029/96jc00629

Fu, Q., and Liou, K. N. (1992). On the correlated k-distribution method for radiative transfer in nonhomogeneous atmospheres. *J. Atmos. Sci.* 49, 2139–2156. doi: 10.1175/1520-0469(1992)049<2139:otcdmf>2.0.co;2

Gao, B.-C., and Goetz, A. F. H. (1990). Column atmospheric water vapor and vegetation liquid water retrievals from Airborne Imaging Spectrometer data. *J. Geophys. Res.* 95, 3549–3564.

Gao, B.-C., Heidebrecht, K. B., and Goetz, A. F. H. (1993). Derivation of scaled surface reflectances from AVIRIS data. *Remote Sens. Environ.* 44, 165–178. doi: 10.1016/0034-4257(93)90014-o

Gao, B. C., and Kaufman, Y. J. (2003). Water vapor retrievals using Moderate Resolution Imaging Spectroradiometer (MODIS) near-infrared channels. *J. Geophys. Res.* 108:4389. doi: 10.1029/2002JD003023

Gao, B.-C., Montes, M. J., Ahmad, Z., and Davis, C. O. (2000). Atmospheric correction algorithm for hyperspectral remote sensing of ocean color from space. *Appl. Opt.* 39:887. doi: 10.1364/AO.39.000887

Gao, B.-C., Montes, M. J., Davis, C. O., and Goetz, A. F. H. (2009). Atmospheric correction algorithms for hyperspectral remote sensing data of land and ocean. *Remote Sens. Environ.* 113(Suppl. 1), S17–S24. doi: 10.1016/j.rse.2007.12.015

Gao, B.-C., Montes, M. J., Li, R.-R., Dierssen, H. M., and Davis, C. (2007). An Atmospheric Correction Algorithm for Remote Sensing of Bright Coastal Waters Using MODIS Land and Ocean Channels in the Solar Spectral Region. *IEEE Trans. Geosci. Remote Sens.* 45, 1835–1843. doi: 10.1109/tgrs.2007.895949

Gao, M., Zhai, P., Franz, B., Hu, Y., Knobelspiesse, K., Werdell, P. J., et al. (2018). Retrieval of aerosol properties and water-leaving reflectance from multi-angular polarimetric measurements over coastal waters. *Opt. Express* 26, 8968–8989. doi: 10.1364/OE.26.008968

Gassó, S., and Torres, O. (2016). The role of cloud contamination, aerosol layer height and aerosol model in the assessment of the OMI near-UV retrievals over the ocean. *Atmos. Meas. Techniques* 9, 3031–3052. doi: 10.5194/amt-9-3031-2016

Gatebe, C. K., King, M. D., Lyapustin, A. I., Arnold, G. T., and Redemann, J. (2005). Airborne spectral measurements of ocean directional reflectance. *J. Atmos. Sci.* 62, 1072–1092. doi: 10.1175/jas3386.1

Ge, Y., Voss, K. J., and Gordon, H. R. (1995). Insitu measurements of inelastic scattering in Monterey Bay using solar Fraunhofer lines. *J. Geophys. Res.* 100, 13227–13236.

Gelaro, R., McCarty, W., Suárez, M. J., Todling, R., Molod, A., Takacs, L., et al. (2017). The modern-era retrospective analysis for research and applications, version 2 (MERRA-2). *J. Climate* 30, 5419–5454. doi: 10.1175/jcli-d-16-0758.1

George, C., Ammann, M., D'Anna, B., Donaldson, D. J., and Nizkorodov, S. A. (2015). Heterogeneous photochemistry in the atmosphere. *Chem. Rev.* 115, 4218–4258. doi: 10.1021/cr500648z

Ghan, S. J., and Schwartz, S. E. (2007). Aerosol properties and processes: a path from field and laboratory measurements to global climate models. *Bull. Am. Meteorol. Soc.* 88, 1059–1083.

Gibson, E. R., Gierlus, K. M., Hudson, P. K., and Grassian, V. H. (2007). Generation of internally mixed insoluble and soluble aerosol particles to investigate the impact of atmospheric aging and heterogeneous processing on the CCN activity in mineral dust aerosol. *Aerosol Sci. Technol.* 41, 914–924. doi: 10.1080/02786820701557222

Gleason, A. C. R., Voss, K. J., Gordon, H. R., Twardowski, M. T., Sullivan, J., Trees, C., et al. (2012). Detailed validation of the bidirectional effect in various Case I and Case II waters. *Opt. Expr.* 20, 7630–7645. doi: 10.1364/OE.20.007630

Goody, R. M. (1952). A statistical model for water-vapour absorption. *Q. J. R. Meteorol. Soc.* 78, 165–169. doi: 10.1002/qj.49707833604

Goody, R. M., and Yung, Y. L. (1989). *Atmospheric Radiation. Theoretical Basis*. Oxford: Oxford University Press.

Gordon, H. (1995). Remote sensing of ocean color: a methodology for dealing with broad spectral bands and significant out-of-band response. *Appl. Opt.* 34, 8363–8374. doi: 10.1364/AO.34.008363

Gordon, H. R. (1993). Sensitivity of radiative transfer to small-angle scattering in the ocean: quantitative assessment. *Appl. Opt.* 32, 7505–7511. doi: 10.1364/AO.32.007505

Gordon, H. R. (1997). Atmospheric correction of ocean color imagery in the Earth Observing System era. *J. Geophys. Res.* 112, 17081–17106. doi: 10.1029/96jd02443

Gordon, H. R. (1999). Contribution of Raman scattering to water-leaving radiance: a reexamination. *Appl. Opt.* 38, 3166–3174.

Gordon, H. R. (2011). Light scattering and absorption by randomly-oriented cylinders: dependence on aspect ratio for refractive indices applicable for marine particles. *Opt. Express* 19, 4673–4691. doi: 10.1364/OE.19.004673

Gordon, H. R., and Brown, O. B. (1972). A theoretical model of light scattering by Sargasso Sea particulates. *Limnol. Oceanogr.* 17, 826–832. doi: 10.4319/lo.1972.17.6.0826

Gordon, H. R., Brown, O. B., and Jacobs, M. M. (1975). Computed relationships between the inherent and apparent optical properties of a flat homogeneous ocean. *Appl. Opt.* 14, 417–427. doi: 10.1364/AO.14.000417

Gordon, H. R., Clark, D. K., Brown, J. W., Brown, O. B., Evans, R. H., and Broenkow, W. W. (1983). Phytoplankton pigment concentrations in the middle atlantic bight: comparison of ship determinations and CZCS estimates. *Appl. Opt.* 22, 20–36.

Gordon, H. R., Smyth, T. J., Balch, W. M., Boynton, G. C., and Tarran, G. A. (2009). Light scattering by coccolith detached from *Emiliania huxleyi*. *Appl. Opt.* 48, 6059–6073. doi: 10.1364/AO.48.006059

Gordon, H. R., and Wang, M. (1994a). Influence of oceanic whitecaps on atmospheric correction for ocean color sensors. *Appl. Opt.* 33, 7754–7763. doi: 10.1364/AO.33.007754

Gordon, H. R., and Wang, M. (1994b). Retrieval of water-leaving radiance and aerosol optical thickness over the oceans with SeaWiFS: a preliminary algorithm. *Appl. Opt.* 33, 443–452. doi: 10.1364/AO.33.000443

Green, S. A., and Blough, N. V. (1994). Optical absorption and fluorescence properties of chromophoric dissolved organic matter in natural waters. *Limnol. Oceanogr.* 39, 1903–1916.

Griggs, M. (1983). Satellite measurements of tropospheric aerosols. *Adv. Space Res.* 5, 109–118. doi: 10.1016/0273-1177(82)90335-0

Griggs, M. (1984). A comparison of atmospheric aerosol measurements by various satellite sensors. *Adv. Space Res.* 4, 33–39. doi: 10.1016/0273-1177(84)90426-5

Gu, Y., Carrizo, C., Gilerson, A. A., Brady, P., Cummings, M., Twardowski, M., et al. (2016). Polarimetric imaging and retrieval of target polarization characteristics in underwater environment. *Appl. Opt.* 55, 626–637. doi: 10.1364/AO.55.000626

Haltrin, V. (2002). One-parameter two-term Henyey-Greenstein phase function for light scattering in Sea Water. *Applied Opt.* 41, 1022–1028.

Hansen, J. E. (1971). Multiple scattering of polarized light in planetary atmospheres. Part II. Sunlight reflected by terrestrial water clouds. *J. Atm. Sci.* 28, 1400–1426. doi: 10.1175/1520-0469(1971)028<1400:msopli>2.0.co;2

Hansen, J. E., and Travis, L. D. (1974). Light scattering in planetary atmospheres. *Space Sci. Rev.* 16:527.

Harmel, T., and Chami, M. (2013). Estimation of the sunglint radiance field from optical satellite imagery over open ocean: multidirectional approach and polarization aspects. *J. Geophys. Res.* 118, 76–90. doi: 10.1029/2012JC008221

Harmel, T., Hieronymi, M., Slade, W., Röttgers, R., Roullier, F., and Chami, M. (2016). Laboratory experiments for inter-comparison of three volume scattering meters to measure angular scattering properties of hydrosols. *Opt. Express* 24, A234–A256. doi: 10.1364/OE.24.00A234

Hasekamp, O. P., Fu, G., Rusli, S. P., Wu, L., Di Noia, A., Brugh, J., et al. (2019). Aerosol measurements by SPEXone on the NASA PACE mission: expected retrieval capabilities. *J. Quant. Spectros. Radiat. Transf.* 227, 170–184. doi: 10.1016/j.jqsrt.2019.02.006

Hasekamp, O. P., and Landgraf, J. (2005). Retrieval of aerosol properties over the ocean from multispectral single-viewing-angle measurements of intensity and polarization: retrieval approach, information content, and sensitivity study. *J. Geophys. Res.* 110:D20207. doi: 10.1029/2005JD006212

Hasekamp, O. P., and Landgraf, J. (2007). Retrieval of aerosol properties over land surfaces: capabilities of multiple-viewing-angle intensity and polarization measurements. *Appl. Opt.* 46, 3332–3344.

Hasekamp, O. P., Litvinov, P., and Butz, A. (2011). Aerosol properties over the ocean from PARASOL multiangle photometric measurements. *J. Geophys. Res.* 116:D14204.

Hawes, S. K., Carder, C. K., and Harvey, G. R. (1992). Quantum fluorescence efficiencies of fulvic and humic acids: effects on ocean color and fluorometric detection. *Proc. SPIE* 1750, 212–223.

He, X., Bai, Y., Zhu, Q., and Gong, F. (2010). A radiative transfer model of coupled ocean-atmosphere system using matrix operator method for rough sea-surface. *J. Quant. Spectrosc. Radiat. Transf.* 111, 1426–1448. doi: 10.1016/j.jqsrt.2010.02.014

He, X., Pan, D., Bai, Y., Wang, D., and Hao, Z. (2014). A new simple concept for ocean colour remote sensing using parallel polarization radiance. *Sci. Rep.* 4:3748. doi: 10.1038/srep03748

Henyey, L. C., and Greenstein, J. L. (1941). Diffuse radiation in the galaxy. *Astrophys. J.* 93, 70–83.

Herman, B. M., Caudill, T. R., Flittner, D. E., Thome, K. J., and Ben-David, A. (1995). Comparison of the Gauss-Seidel spherical polarized radiative transfer code with other radiative transfer codes. *Appl. Opt.* 34, 4563–4572. doi: 10.1364/AO.34.004563

Herman, M., Deuzé, J.-L., Marchand, A., Roger, B., and Lallart, P. (2005). Aerosol remote sensing from POLDER/ADEOS over the ocean: improved retrieval using a nonspherical particle model. *J. Geophys. Res.* 110:D10S02. doi: 10.1029/2004JD004798

Hieronymi, M. (2016). Polarized reflectance and transmittance distribution functions of the ocean surface. *Opt. Express* 24, A1045–A1068. doi: 10.1364/OE.24.0A1045

Higurashi, A., and Nakajima, T. (1999). Two-channel aerosol retrieval algorithm on a global scale using MOAA AVHRR. *J. Atmos. Sci.* 56, 924–941. doi: 10.1175/1520-0469(1999)056<0924:doatca>2.0.co;2

Hoffer, A., Gelencsér, A., Guyon, P., Kiss, G., Schmid, O., Frank, G. P., et al. (2006). Optical properties of humic-like substances (HULIS). in biomass-burning aerosols. *Atmos. Chem. Phys.* 6, 3563–3570. doi: 10.1021/acs.est.8b01251

Hoffer, A., Tóth, A., Nyirõ-Kósa, I., Pósfai, M., and Gelenscér, A. (2016). Light absorption properties of laboratory-generated tar ball particles. *Atmos. Chem. Phys.* 16, 239–246. doi: 10.5194/acp-16-239-2016

Holben, B. N., Eck, T., Slutsker, I., Tanre, D., Buis, J., Setzer, A., et al. (1998). Aeronet: a federated instrument network and data archive for aerosol characterization. *Remote Sens. Environ.* 66, 1–16. doi: 10.1016/s0034-4257(98)00031-5

Hollstein, A., and Fischer, J. (2012). Radiative transfer solutions for coupled atmosphere ocean systems using the matrix operator technique. *J. Quant. Spectrosc. Radiat. Transf.* 113, 536–548. doi: 10.1016/j.jqsrt.2012.01.010

Hovenier, J. W. (1971). Multiple scattering of polarized light in planetary atmospheres. *Astron. Astrophys.* 13, 7–29.

Hu, C., Lee, Z., Muller-Karger, E., Carder, L., and Walsh, J. J. (2006). Ocean color reveals phase shift between marine plants and yellow substance. *IEEE Geosci. Remote Sens. Lett.* 3, 262–266. doi: 10.1109/lgrs.2005.862527

Hu, C., and Voss, K. J. (1997). In situ measurements of Raman scattering in clear ocean water. *Appl. Opt.* 36, 6962–6967.

Hu, Y., Behrenfeld, M., Hostetler, C., Pelon, J., Trepte, C., Hair, J., et al. (2016). Ocean lidar measurements of beam attenuation and a roadmap to accurate phytoplankton biomass estimates. *EPJ Web Conf.* 119:22003. doi: 10.1051/epjconf/201611922003

Hu, Y., Stamnes, K., Vaughan, M., Pelon, J., Weimer, C., Wu, D., et al. (2008). Sea surface wind speed estimation from space-based lidar measurements. *Atmos. Chem. Phys.* 8, 3593–3601. doi: 10.5194/acp-8-3593-2008

Huot, Y., Morel, A., Twardowski, M. S., Stramski, D., and Reynolds, R. A. (2008). Particle optical backscattering along a chlorophyll gradient in the upper layer of the eastern South Pacific Ocean. *Biogeosciences* 5, 495–507. doi: 10.5194/bg-5-495-2008

Ibrahim, A., Franz, B., Ahmad, Z., Healy, R., Knobelspiesse, K., Gao, B.-G., et al. (2018). Atmospheric correction for hyperspectral ocean color retrieval with application to the Hyperspectral Imager for Coastal Ocean (HICO). *Remote Sens. Environ.* 204, 60–75. doi: 10.1016/j.rse.2017.10.041

Ibrahim, A., Gilerson, A., Chowdhary, J., and Ahmed, S. (2016). Retrieval of macro- and micro-physical properties of oceanic hydrosols from polarimetric observations. *Remote Sens. Environ.* 186, 548–566. doi: 10.1016/j.rse.2016.09.004

IOCCG (2006). "Remote sensing of inherent optical properties: fundamentals, tests of algorithms, and applications," in *Reports of the International Ocean-Colour Coordinating Group, No. 5*, ed. Z.-P. Lee (Dartmouth, NS: IOCCG), 126.

IOCCG (2010). "Atmospheric correction for remotely-sensed ocean-colour products," in *Reports of the International Ocean-Colour Coordinating Group*, No. 10, ed. M. Wang (Dartmouth, NS: IOCCG).

IOCCG-OCAG (2003). *Model, Parameters, and Approaches That Used to Generate Wide Range of Absorption and Backscattering Spectra*. (Dartmouth, NS: International Ocean Colour Coordinating Group)

Jin, Z., Charlock, T. P., Smith, W. L. Jr., and Rutledge, K. (2004). A parameterization of ocean surface albedo. *Geophys. Res. Lett.* 31:L22301.

Jin, Z., and Stamnes, K. (1994). Radiative transfer in nonuniformly refracting layered media: atmosphere-ocean system. *Appl. Opt.* 33, 431–442. doi: 10.1364/AO.33.000431

Johnson, K. S., and Coletti, L. J. (2002). In situ ultraviolet spectro-photometry for high resolution and long term monitoring of nitrate, bromide and bisulfide in the ocean. *Deep-Sea Res. I* 49, 1291–1305. doi: 10.1016/s0967-0637(02)00020-1

Johnson, M. S., Meskhidze, N., Solmon, F., Gassó, S., Chuang, P., Gaiero, D. M., et al. (2010). Modeling dust and soluble iron deposition to the South Atlantic. *J. Geophys. Res.* 115:D15202. doi: 10.1029/2009JD013311

Jonasz, M., and Fournier, G. R. (2007). *Light Scattering by Particles in Water: Theoretical and Experimental Foundations*. New York, NY: Academic Press.

Kahn, R., Banerjee, P., and McDonald, D. (2001). Sensitivity of multiangle imaging to natural mixtures of aerosols over ocean. *J. Geophys. Res.* 106, 18219–18238. doi: 10.1029/2000jd900497

Kahn, R. A., Berkoff, T. A., Brock, C., Chen, G., Ferrare, R. A., Ghan, S., et al. (2017). SAM-CAAM: a concept for acquiring systematic aircraft measurements to characterize aerosol air masses. *Bull. Am. Meteor. Soc.* 98, 2215–2228. doi: 10.1175/BAMS-D-16-0003.1

Kanamitsu, M., Ebisuzaki, W., Woollen, J., Yang, S.-K., Hnilo, J. J., Fiorino, M., et al. (2002). NCEP–DOE AMIP-II Reanalysis (R-2). *Bull. Am. Meteorol. Soc.* 83, 1631–1643. doi: 10.1175/BAMS-83-11-1631

Kato, S., Ackerman, T. P., Mather, J. H., and Clothiaux, E. E. (1999). The k-distribution method and correlated-k approximation for a shortwave radiative transfer model. *J. Quant. Spectrosc. Radiat. Transf.* 62, 109–121. doi: 10.1016/S0022-4073(98)00075-2

Kattawar, G. W., Plass, G. N., and Guinn, A. Jr. (1973). Monte Carlo calculations of the polarization of radiation in the Earth's atmosphere-ocean system. *J. Phys. Oceanogr.* 3, 353–372. doi: 10.1175/1520-0485(1973)003<0353:mccotp>2.0.co;2

Kattawar, G. W., and Xu, X. (1992). Filling in of Fraunhofer lines in the ocean by Raman scattering. *Appl. Opt.* 31, 6491–6500. doi: 10.1364/AO.31.006491

Kattawar, G. W., and Xu, X. (1994). *Detecting Raman Scattering in the Ocean by Use of Polarimetry*. Bergen: Ocean Optics XII, 222–233. doi: 10.1117/12.190066

Kaufman, Y. J., Martins, J. V., Remer, L. E., Schoeberl, M. R., and Yamasoe, M. A. (2002). Satellite retrieval of aerosol absorption over the oceans using sunglint. *Geophys. Res. Lett.* 29:1928. doi: 10.1029/2002GL015403

Kaufman, Y. J., Tanré, D., Gordon, H. R., Nakajima, T., Lenoble, J., Frouin, R., et al. (1997). Passive remote sensing of tropospheric aerosol and atmospheric correction for the aerosol effect. *J. Geophys. Res.* 102, 16815–16830. doi: 10.1029/97JD01496

Kawata, Y., and Yakazaki, A. (1998). "Multiple scattering analysis of airborne POLDER image DATA over the sea," in *IEEE Transactions on Geoscience and Remote Sensing* (Piscataway, NJ)

Kay, S., Hedley, J., and Lavender, S. (2009). Sun glint correction of high and low spatial resolution images of aquatic scenes: a review of methods for visible and near-infrared wavelengths. *Remote Sens.* 1, 697–730. doi: 10.3390/rs1040697

Kilpatrick, K. A., Podestá, G. P., and Evans, R. (2001). Overview of the NOAA/NASA advanced very high resolution radiometer Pathfinder algorithm for sea surface temperature and associated matchup database. *J. Geophys. Res.* 106, 9179–9197. doi: 10.1029/1999jc000065

Kirchstetter, T. W., Novakov, T., and Hobbs, P. V. (2004). Evidence that the spectral dependence of light absorption by aerosols is affected by organic carbon. *J. Geophys. Res.* 109:D21208. doi: 10.1029/2004JD004999

Kitchen, J. K., and Zaneveld, J. R. V. (1992). A three-layered sphere model of the optical properties of phytoplankton. *Limnol. Oceanogr.* 37, 1680–1690. doi: 10.4319/lo.1992.37.8.1680

Knobelspiesse, K., Cairns, B., Mishchenko, M., Chowdhary, J., Tsigaridid, K., van Diedenhoven, B., et al. (2012). Analyses of fine-mode aerosol retrieval capabilities by different passive remote sensing instrument designs. *Opt. Express* 20, 21457–21484. doi: 10.1364/OE.20.021457

Koepke, P. (1984). Effective reflectance of oceanic whitecaps. *Appl. Opt.* 23:1816. doi: 10.1364/ao.23.001816

Kokhanovsky, A. A. (2003). Parameterization of the Mueller matrix of oceanic waters. *J. Geophys. Res.* 108:3175. doi: 10.1029/2001JC001222

Kokhanovsky, A. A. (2004). Spectral reflectance of whitecaps. *J. Geophys. Res.* 109:C05021. doi: 10.1029/2003JC002177

Kokhanovsky, A. A., Budak, V. P., Cornet, C., Duan, M., Emde, C., Katsev, I. L., et al. (2010). Benchmark results in vector atmospheric radiative transfer. *J. Quant. Spectrosc. Radiat. Transf.* 111, 1931–1946. doi: 10.1016/j.jqsrt.2010.03.005

Kopelevich, O. V. (2012). Application of data on seawater light scattering for the study of marine particles: a selective review focusing on Russian literature. *Geo Mar. Lett.* 32, 183–193. doi: 10.1007/s00367-012-0278-y

Kostadinov, T. S., Siegel, D. A., and Maritorena, S. (2009). Retrieval of the particle size distribution from satellite ocean color observations. *J. Geophys. Res.* 114:C09015. doi: 10.1029/2009JC005303

Kostadinov, T. S., Siegel, D. A., and Maritorena, S. (2010). Global variability of phytoplankton functional types from space: assessment via the particle size distribution. *Biogeosciences* 7, 3239–3257. doi: 10.5194/bg-7-3239-2010

Kozarac, Z., Risoviæ, D., Frka, S., and Möbius, D. (2005). Reflection of light from the air/water interface covered with sea-surface microlayers. *Mar. Chem.* 96, 99–113. doi: 10.1016/j.marchem.2004.12.003

Lacis, A. A., Chowdhary, J., Mishchenko, M. I., and Cairns, B. (1998). Modeling errors in diffuse-sky radiation: vector vs. scalar treatment. *Geophys. Res. Lett.* 25, 135–138. doi: 10.1029/97gl03613

Lacis, A. A., and Oinas, V. (1991). A description of the correlated k distribution method for modeling nongray gaseous absorption, thermal emission, and multiple scattering in vertically inhomogeneous atmospheres. *J. Geophys. Res. Atmos.* 96, 9027–9063. doi: 10.1029/90JD01945

Lagerloef, G., Colomb, F. R., Le Vine, D., Wentz, F., Yueh, S., Ruf, C., et al. (2008). The AQUARIUS/SAC-D mission designed to meet the salinity remote sensing challenge. *Oceanography* 21, 68–81. doi: 10.5670/oceanog.2008.68

Lamarque, J.-F., Bond, T. C., Eyring, V., Granier, C., Heil, A., Klimont, Z., et al. (2010). Historical (1850–2000). gridded anthropogenic and biomass burning emissions of reactive gases and aerosols: methodology and application. *Atmos. Chem. Phys.* 10, 7017–7039. doi: 10.5194/acp-10-7017-2010

Landgraf, J., Hasekamp, O. P., van Deelen, R., and Aben, I. (2004). Rotational Raman scattering of polarized light in the Earth atmosphere: a vector radiative transfer model using the radiative transfer perturbation theory approach. *J. Quant. Spectrosc. Radiat. Transf.* 87, 399–433. doi: 10.1016/j.jqsrt.2004.03.013

Laskin, A., Laskin, J., and Nizkorodov, S. A. (2015). Chemistry of atmospheric brown carbon. *Chem. Rev.* 115, 4335–4382. doi: 10.1021/cr5006167

Lean, J. (1987). Solar ultraviolet irradiance variations: a review. *J. Geophys. Res.* 92, 839–868.

Lean, J., and DeLand, M. T. (2012). How does the Sun's spectrum vary? *J. Clim.* 25, 2555–2559. doi: 10.1175/JCLI-D-11-00571.1

Lee, J., Hsu, N. C., Sayer, A. M., Bettenhausen, C., and Yang, P. (2017). AERONET-based nonspherical dust optical models and effects on the VIIRS deep Blue/SOAR over water aerosol product. *J. Geophys. Res. Atmos.* 122, 10384–10401. doi: 10.1002/2017jd027258

Lee, M. E., and Lewis, R. M. (2003). A new method for the measurement of the optical volume scattering function in the open ocean. *J. Atm. Ocean. Techn.* 20, 563–571. doi: 10.1175/1520-0426(2003)20<563:anmftm>2.0.co;2

Lee, Z., Wei, J., Voss, K., Lewis, M., Bricaud, A., and Huot, Y. (2015). Hyperspectral absorption coefficient of pure seawater in the range of 350–550 nm inverted from remote sensing reflectance. *Appl. Opt.* 54, 546–558.

Lee, Z.-P., Carder, K. L., and Arnone, R. (2002). Deriving inherent optical properties from water color: a multi-band quasianalytical algorithm for optically deep waters. *Appl. Opt.* 41, 5755–5772.

Lee, Z.-P., Carder, K. L., Hawes, S. K., Steward, R. G., Peacock, T. G., and Davis, C. O. (1994). Model for the interpretation of hyperspectral remote-sensing reflectance. *Appl. Opt.* 33, 5721–5732. doi: 10.1364/AO.33.005721

Lee, Z. P., Shang, S., Hu, C., Lewis, M., Arnone, R., Li, Y., et al. (2010). Time series of bio-optical properties in a subtropical gyre: implications for the evaluation of interannual trends of biogeochemical properties. *J. Geophys. Res. Oceans* 115:C09012.

Lelli, L., Rozanov, V. V., Vountas, M., and Burrows, J. P. (2017). Polarized radiative transfer through terrestrial atmosphere accounting for rotational Raman scattering. *J. Quant. Spectrosc. Radiat. Transf.* 200, 70–89. doi: 10.1016/j.jqsrt.2017.05.027

Lenoble, J. (1956). Etude de la penetration de l'ultraviolet dans la mer. *Ann. Geophys.* 12, 16–31.

Lenoble, J. (1985). *Radiative Transfer in Scattering and Absorbing Atmospheres: Standard Computational Procedures*. Hampton, VA: A. Deepak Publishing.

Levelt, P. F., van den Oord, G. H. J., Dobber, M. R., Maälkki, A., Visser de Vries, H. J., Stammes, P., et al. (2006). The ozone monitoring instrument. *IEEE Trans. Geosci. Remote Sens.* 44, 1093–1101. doi: 10.1109/TGRS.2006.872333

Levy, R. C., Mattoo, S., Munchak, L. A., Remer, L. A., Sayer, A. M., Patadia, F., et al. (2013). The Collection 6 MODIS aerosol products over land and ocean. *Atmos. Meas. Tech.* 6, 2989–3034. doi: 10.5194/amt-6-2989-2013

Li, L., and Mishchenko, M. I. (2016). Optics of water microdroplets with soot inclusions: exact versus approximate results. *J. Quant. Spectrosc. Radiat. Transf.* 178, 255–262. doi: 10.1016/j.jqsrt.2015.12.025

Lin, Z., Li, W., Gatebe, C., Poudyal, R., and Stamnes, K. (2016). Radiative transfer simulations of the two-dimensional ocean glint reflectance and determination of the sea surface roughness. *Appl. Opt.* 55, 1206–1215. doi: 10.1364/AO.55.001206

Liu, J., He, X., Liu, J., Bai, Y., Wang, D., Chen, T., et al. (2017). Polarization-based enhancement of ocean color signal for estimating suspended particulate matter: radiative transfer simulations and laboratory measurements. *Opt. Express* 25, A323–A337. doi: 10.1364/OE.25.00A323

Loisel, H., Duforêt, L., Dessailly, D., Chami, M., and Dubuisson, P. (2008). Investigation of the variations in the water leaving polarized reflectance from the POLDER satellite data over two biogeochemical contrasted oceanic areas. *Opt. Express* 16, 12905–12918.

Loisel, H., and Stramski, D. (2000). Estimation of the inherent optical properties of natural waters from the irradiance attenuation coefficient and reflectance in the presence of Raman scattering,". *Appl. Opt.* 39, 3001–3011.

Lu, Y., Zhou, Y., Liu, Y., Mao, Z., Qian, W., Wang, M., et al. (2017). Using remote sensing to detect the polarized sunglint reflected from oil slicks beyond the critical angle. *J. Geophys. Res. Oceans* 122, 6342–6354. doi: 10.1002/2017jc012793

Ma, L. X., Wang, F. Q., Wang, C. A., Wang, C. C., and Tan, J. Y. (2015). Investigation of the spectral reflectance and bidirectional reflectance distribution function of sea foam layer by the Monte Carlo method. *Appl. Opt.* 54, 9863–9874. doi: 10.1364/AO.54.009863

Malkmus, W. (1967). Random lorentz band model with exponential-tailed S-1 line-intensity distribution function*. *J. Opt. Soc. Am.* 57, 323–329.

Manfred, K. M., Washenfelder, R. A., Wagner, N. L., Adler, G., Erdesz, F., Womack, C. C., et al. (2018). Investigating biomass burning aerosol morphology using a laser imaging nephelometer. *Atmos. Chem. Phys.* 18, 1879–1894. doi: 10.5194/acp-18-1879-2018

Marchuk, G. I., Mikhailov, G. A., Nazaraliev, M. A., Barbinian, R. A., Kargin, B. A., and Elepov, B. S. (1980). *The Monte Carlo Methods in Atmospheric Optics*. Berlin: Springer Series in Optical Sciences.

Martins, J. V., Artaxo, P., Kaufman, Y. J., Castanho, A. D., and Remer, L. (2009). Spectral absorption properties of aerosol particles from 350–2500nm. *Geophys. Res. Lett.* 36:L13810. doi: 10.1029/2009GL037435

Martins, J. V., Nielsen, T., Fish, C., Sparr, L., Fernandez-Borda, R., Schoeberl, M., et al. (2014). "HARP CubeSat–An innovative hyperangular imaging polarimeter for earth science applications," in *Proceedings of the Small Sat Pre-Conference Workshop*, (Logan).

Martonchik, J. V., Diner, D. J., Kahn, R., Verstraete, M. M., Pinty, B., Gordon, H. R., et al. (1998). Techniques for the retrieval of aerosol properties over land and ocean using multiangle imaging. *IEEE Trans. Geosci. Remote Sens.* 36, 1212–1227. doi: 10.1109/36.701027

Mason, J. D., Cone, M. T., and Fry, E. S. (2016). Ultraviolet (250–550 nm). absorption spectrum of pure water. *Appl. Opt.* 55, 7163–7172. doi: 10.1364/AO.55.007163

Masuda, K. (1998). Effects of the speed and direction of surface winds on the radiation in the atmosphere-ocean system. *Remote Sens. Environ.* 64:5363.

Masuda, K., and Takashima, T. (1986). Computational accuracy of radiation emerging from the ocean surface in the model atmosphere-ocean system. *Pap. Meteor. Geophys.* 37:1. doi: 10.2467/mripapers.37.1

Masuda, K., and Takashima, T. (1988). Dependence of the radiation just above and below the ocean surface on atmospheric and oceanic parameters. *Appl. Opt.* 27:4891. doi: 10.1364/AO.27.004891

Matthews, M. W., and Bernard, S. (2013). Using a two-layered sphere model to investigate the impact of gas vacuoles on the inherent optical properties of *M. aeruginosa*. *Bioeosci. Dis.* 10, 10531–10579. doi: 10.5194/bgd-10-10531-2013

Meng, Z., Yang, P., Kattawar, G. W., Bi, L., Liou, K. N., and Laszlo, I. (2010). Single-scattering properties of tri-axial ellipsoidal mineral dust aerosols: a database for application to radiative transfer calculations. *J. Aerosol. Sci.* 41, 501–512. doi: 10.1016/j.jaerosci.2010.02.008

Meyer, R. A. (1979). Light-scattering from biological cells – Dependence of backscatter radiation on membrane thickness and refractive index. *Appl. Opt.* 18, 585–588.

Mishchenko, M., Cairns, B., Hansen, J., Travis, L., Kaufman, Y., Martins, J. V., et al. (2004). Monitoring of aerosol forcing of climate from space: analysis of measurement requirements. *J. Quant. Spectrosc. Radiat. Transf.* 88, 149–161. doi: 10.1016/j.jqsrt.2004.03.030

Mishchenko, M. I. (1990). The fast invariant imbedding method for polarized light: computational aspects and numerical results for Rayleigh scattering. *J. Quant. Spectrosc. Radiat. Transf.* 43, 163–171. doi: 10.1016/0022-4073(90)90045-8

Mishchenko, M. I., and Dlugach, J. M. (2012). Adhesion of mineral and soot aerosols can strongly affect their scattering and absorption properties. *Opt. Lett.* 37, 704–706. doi: 10.1364/OL.37.000704

Mishchenko, M. I., Dlugach, J. M., and Liu, L. (2016). Applicability of the effective-medium approximation to heterogeneous aerosol particles. *J. Quant. Spectrosc. Radiat. Transf.* 178, 284–294. doi: 10.1016/j.jqsrt.2015.12.028

Mishchenko, M. I., Geogdzhayev, I. V., Cairns, B., Rossow, W. B., and Lacis, A. L. (1999). Aerosol retrievals over the ocean by use of channels 1 and 2 AVHRR data: sensitivity analysis and preliminary results. *Appl. Opt.* 38, 7325–7341.

Mishchenko, M. I., Liu, L., and Mackowski, D. W. (2013). T-matrix modeling of linear depolarization by morphologically complex soot and soot-containing aerosols. *J. Quant. Spectrosc. Radiat. Transf.* 123, 135–144. doi: 10.1016/j.jqsrt.2012.11.012

Mishchenko, M. I., and Travis, L. D. (1997). Satellite retrieval of aerosol properties over the ocean using measurements of reflected sunlight: effect of instrumental errors and aerosol absorption. *J. Geophys. Res.* 102, 13543–13553. doi: 10.1029/97jd01124

Mishchenko, M. I., Travis, L. D., and Lacis, A. A. (2002). *Scattering, Absorption, and Emission of Light by Small Particles*. Cambridge: Cambridge University Press.

Mobley, C. D. (1989). A numerical method for the computation of radiance distributions in natural waters with wind-roughened surfaces. *Limnol. Oceanogr.* 34, 1473–1483. doi: 10.4319/lo.1989.34.8.1473

Mobley, C. D. (1994). *Light and Water. Radiative Transfer in Natural Waters*. San Diego, CA: Academic Press.

Mobley, C. D. (2015). Polarized reflectance and transmittance properties of windblown sea surface. *Appl. Opt.* 54, 4828–4849. doi: 10.1364/AO.54.004828

Mobley, C. D. (2018). "Invariant imbedding theory for the vector radiative transfer equation," in *Series in Light Scattering*, ed. A. Kokhanovsky (Cham: Springer).

Mobley, C. D., Gentili, B., Gordon, H. R., Jin, Z., Kattawar, G. W., Morel, A., et al. (1993). Comparison of numerical models for computing underwater light fields. *Appl. Opt.* 32, 7484–7504. doi: 10.1364/AO.32.007484

Mobley, C. D., Stramski, D., Bisset, W. P., and Boss, E. (2004). Optical modeling of ocean waters. is the case 1 – case 2 classification still useful? *Oceanograpohy* 17, 60–67. doi: 10.5670/oceanog.2004.48

Mobley, C. D., and Sundman, L. K. (2013). *HydroLight 5.2 User's Guide*. Bellevue, DC: Sequoia Scientific. Inc.

Mobley, C. D., Sundman, L. K., and Boss, E. (2002). Phase function effects on oceanic fields. *Appl. Opt.* 41, 1035–1050.

Monahan, E. C. (1971). Oceanic whitecaps. *J. Phys. Oceanogr.* 1:139.

Monahan, E. C., and O'Muircheartaigh, I. (1980). Optimal power-law description of oceanic whitecap coverage dependence on windspeed. *J. Phys. Oceanogr.* 10:2094. doi: 10.1175/1520-0485(1980)010<2094:opldoo>2.0.co;2

Moore, K. D., Voss, K. J., and Gordon, H. R. (1998). Spectral reflectance of whitecaps: instrumentation, calibration, and performance in coastal waters. *J. Atm. Oceanic Techn.* 15:496. doi: 10.1175/1520-0426(1998)015<0496:srowic>2.0.co;2

Moore, T., Campbell, J., and Dowell, M. (2009). A class-based approach to characterizing and mapping the uncertainty of the MODIS ocean chlorophyll product. *Remote Sens. Environ.* 113, 2424–2430. doi: 10.1016/j.rse.2009.07.016

Moore, T., Dowell, M., Bradt, S., and Verdu, A. R. (2014). An optical water type framework for selecting and blending retrievals from bio-optical algorithms in lakes and coastal waters. *Remote Sens. Environ.* 143, 97–111. doi: 10.1016/j.rse.2013.11.021

Moore, T., Mouw, C. B., Sullivan, J., Twardowski, M., Burtner, A. M., Ciochetto, A. B., et al. (2017). Bio-optical properties in western Lake Erie during intense summertime algal blooms: impacts for remote sensing applications. *Front. Mar. Sci.* 4:300. doi: 10.3389/fmars.2017.00300

Morel, A. (1968). Note au sujet des constants de diffusion de la lumiere pour l'eau et l'eau de mer optiquement pures. *Cahiers Oceanogr.* 20, 157–162.

Morel, A. (1974). "Optical properties of pure water and pure sea water," in *Optical Aspects of Oceanography*, eds N. G. Jerlov and E. S. Nielsen (New York, NY: Academic Press), 1–24.

Morel, A. (1988). Optical modeling of the upper ocean in relation to its biogenous matter content (Case I waters). *J. Geophys. Res.* 93, 10749–10768.

Morel, A. (2009). Are the empirical relationships describing the bio-optical properties of case 1 waters consistent and internally compatible? *J. Geophys. Res.* 114:C01016. doi: 10.1029/2008JC004803

Morel, A., Antoine, D., and Gentili, B. (2002). Bidirectional reflectance of oceanic waters: accounting for Raman emission and varying particle scattering phase function. *Appl. Opt.* 41, 6289–6306.

Morel, A., and Gentili, B. (1991). Diffuse reflectance of oceanic waters: its dependence on sun angle as influenced by the molecular scattering contribution. *Appl. Opt.* 30, 4427–4438. doi: 10.1364/AO.30.004427

Morel, A., and Gentili, B. (1993). Diffuse reflectance of oceanic waters. II. Bidirectional aspects. *Appl. Opt.* 32, 6864–6879. doi: 10.1364/AO.32.006864

Morel, A., and Prieur, L. (1977). Analysis of variations in ocean color. *Limnol. Oceanogr.* 22, 709–722. doi: 10.4319/lo.1977.22.4.0709

Morel, M., and Maritorena, S. (2001). Bio-optical properties of oceanic waters: a reappraisal. *J. Geophys. Res.* 106, 7163–7180. doi: 10.1029/2000jc000319

Morel, A., Claustre, D., and Gentili, B. (2007a). Natural variability of bio-optical properties in Case 1 waters: attenuation and reflectance within the visible and near-UV spectral domains, as observed in South Pacific and Mediterranean waters. *Biogeosciences* 4, 913–925. doi: 10.5194/bg-4-913-2007

Morel, A., Gentili, B., Claustre, H., Babin, M., Bricaud, A., Ras, J., et al. (2007b). Optical properties of the clearest natural waters. *Limnol. Oceanogr.* 52, 217–229. doi: 10.1364/AO.20.000177

Morrison, J. R. (2003). In situ determination of the quantum yield of phytoplankton chlorophyll a fluorescence: a simple algorithm, observations, and a model. *Limnol. Oceanogr.* 48, 618–631. doi: 10.4319/lo.2003.48.2.0618

Nakajima, T., and Tanaka, M. (1983). Effect of wind-generated waves on the transfer of solar radiation in the atmosphere-ocean system. *J. Quant. Spectrosc. Radiat. Transf.* 29:521. doi: 10.1016/0022-4073(83)90129-2

NASA (2018a). *PACE Science Definition Team Report*. Available at: https://pace.oceansciences.org/docs/PACE_TM2018-219027_Vol_2.pdf (accessed May 11, 2019).

NASA (2018b). *Polarimetry in the PACE Mission: Science Team Consensus Document. PACE Technical Report Series*. Available at: https://pace.oceansciences.org/docs/TM2018219027Vol.3.pdf (accessed May 11, 2019).

Natraj, V., Li, K.-F., and Yung, Y. L. (2009). Rayleigh scattering in planetary atmospheres: corrected tables through accurate computation of *X* and *Y* functions. *Astrophys. J.* 691, 1909–1920. doi: 10.1088/0004-637x/691/2/1909

Nayak, A., McFarland, M., Sullivan, J., and Twardowski, M. (2017). Evidence for ubiquitous preferential particle orientation in representative oceanic shear flows. *Limnol. Oceanogr.* 63, 122–143. doi: 10.1002/lno.10618

Nelson, N. B., and Siegel, D. A. (2013). The global distribution and dynamics of chromophoric dissolved organic matter. *Annu. Rev. Mar. Sci.* 5, 447–476. doi: 10.1146/annurev-marine-120710-100751

Neukermans, G., and Fournier, G. (2018). Optical modeling of spectral backscattering and remote sensing reflectance from *Emiliania huxleyi* blooms. *Front. Mar. Sci.* 5:146. doi: 10.3389/fmars.2018.00146

Natraj, V., and Hovenier, J. W. (2012). Polarized light reflected and transmitted by thick Rayleigh scattering atmospheres. *Astrophys. J.* 748:16. doi: 10.1088/0004-637X/748/1/28

Ogura, N., and Hanya, T. (1966). Nature of ultra-violet absorption of sea water. *Nature* 212:758. doi: 10.1038/212758a0

Oikarinen, L., Sihvola, E., and Kyröllä, E. (1999). Multiple scattering in limb-viewing geometry. *J. Geophys. Res.* 104, 31261–31274. doi: 10.1029/1999jd900969

Oishi, T. (1990). Significant relationship between the backward scattering coefficient of sea water and the scatterance at 120°. *Appl. Opt.* 29, 4658–4665. doi: 10.1364/AO.29.004658

O'Malley, R. T., Behrenfeld, M. J., Westberry, T. K., Milligan, A. J., Shang, S., and Yan, J. (2014). Geostationary satellite observations of dynamic phytoplankton photophysiology. *Geophys. Res. Lett.* 41, 5052–5059. doi: 10.1002/2014gl060246

Organelli, E., Dall'Olmo, G., Brewin, R. J. W., Tarran, G. A., Boss, E., and Bricaud, A. (2018). The open-ocean missing structural complexity of particles. *Nat. Commun.* 9:5439. doi: 10.1038/s41467-018-07814-6

Ota, Y., Higurashi, A., Nakajima, T., and Yokota, T. (2010). Matrix formulations of radiative transfer including the polarization effect in a coupled atmosphere-ocean system. *J. Quant. Spectrosc. Radiat. Transf.* 111, 878–894. doi: 10.1016/j.jqsrt.2009.11.021

Otremba, Z. (2000). The impact on the reflectance in VIS of a type of crude oil film floating on the water surface. *Opt. Express* 7, 129–134.

Ottaviani, M., Cairns, B., van Diedenhoven, B., Knobelspiesse Hostetler, C., Ferrare, R., Burton, S., et al. (2012). Polarimetric retrievals of surface and cirrus clouds properties in the region affected by the Deepwater Horizon oil spill. *Remote Sens. Environ.* 121, 389–403. doi: 10.1016/j.rse.2012.02.016

Ottaviani, M., Chowdhary, J., and Cairns, B. (2019). Remote sensing of the ocean surface refractive index via short-wave infrared polarimetry. *Remote Sens. Environ.* 221, 14–23. doi: 10.1016/j.rse.2018.10.016

Ottaviani, M., Knobelspiesse, K., Cairns, B., and Mishchenko, M. (2013). Information content of aerosol retrievals in the sunglint region. *Geophys. Res. Lett.* 40, 631–634. doi: 10.1002/grl.50148

Ottaviani, M., Spurr, R., Stamnes, K., Li, W., Su, W., and Wiscombe, W. (2008). Improving the description of sunglint for accurate prediction of remotely sensed radiances. *J. Quant. Spectrosc. Radiat. Transf.* 109, 2364–2375. doi: 10.1016/j.jqsrt.2008.05.012

Peers, F., Waquet, F., Cornet, C., Dubuisson, P., Ducos, F., Goloub, P., et al. (2015). Absorption of aerosols above clouds from POLDER/PARASOL measurements and estimation of their direct radiative effect. *Atmos. Chem. Phys.* 15, 4179–4196. doi: 10.5194/acp-15-4179-2015

Pegau, W. S., Gray, D., and Zaneveld, J. R. V. (1997). Absorption and attenuation of visible and near-infrared light in water: dependence on temperature and salinity. *Appl. Opt.* 36, 6035–6046.

Petzold, T. J. (1972). *Volume Scattering Functions for Selected Ocean Waters*. La Jolla, CA: Scripps Institution of Oceanography.

Plass, G. N., and Kattawar, G. W. (1969). Radiative transfer in an atmosphere-ocean system. *Appl. Opt.* 8, 455–466.

Plass, G. N., and Kattawar, G. W. (1972). Monte Carlo calculations of radiative transfer in the Earth's atmosphere-ocean system: I. Flux in the atmosphere and ocean. *J. Phys. Oceanogr.* 8, 139–145. doi: 10.1175/1520-0485(1972)002<0139:mccort>2.0.co;2

Plass, G. N., Kattawar, G. W., and Guinn, J. A. Jr. (1975). Monte Carlo calculations of radiative transfer in the Earth's atmosphere and ocean: influence of ocean waves. *Appl. Opt.* 14, 1924–1936. doi: 10.1364/AO.14.001924

Plass, G. N., Kattawar, G. W., and Guinn, J. A. Jr. (1976). Radiance distribution over a ruffled sea: contributions from glitter. *Appl. Opt.* 15, 3161–3165. doi: 10.1364/AO.15.003161

Plass, G. N., Kattawar, G. W., and Humphreys, T. (1985). Influence of the oceanic scattering phase function on the radiance. *J. Geophys. Res.* 90, 3347–3351.

Pope, R., and Fry, E. (1997). Absorption spectrum (380 - 700 nm). of pure waters: II. Integrating cavity measurements. *Appl. Opt.* 36, 8710–8723.

Poulin, C., Zhang, X., Yang, P., and Huot, Y. (2018). Diel variations of the attenuation, backscattering and absorption coefficients of four phytoplankton species and comparison with spherical, coated spherical and hexahedral particle optical models. *J. Quant. Spectrosc. Radiat. Transf.* 217, 288–305.

Preisendorfer, R. W. (1976). *Hydrologic Optics Vol. 1: Introduction. National Technical Information Service*. Springfield: Office of Naval Research.

Preisendorfer, R. W., and Mobley, C. D. (1986). Albedos and glitter patterns of a wind-roughened sea surface. *J. Phys. Oceanogr.* 16:1293. doi: 10.1175/1520-0485(1986)016<1293:aagpoa>2.0.co;2

Preisendorfer, R. W., and Mobley, C. D. (1988). Theory of fluorescent irradiance fields in natural waters. *J. Geophys. Res.* 93D, 10831–10855.

Prospero, J. M., Ginoux, P., Torres, O., Nicholson, S. E., and Gill, T. E. (2002). Environmental characterization of global sources of atmospheric soil dust identified with the nimbus 7 total ozone mapping spectrometer (TOMS). absorbing aerosol product. *Rev. Geophys.* 40:1002. doi: 10.1029/2000RG000095

Quenzel, H., and Kaestner, M. (1980). Optical properties of the atmosphere: calculated variability and application to satellite remote sensing of phytoplankton. *Appl. Opt.* 19:1338. doi: 10.1364/AO.19.001338

Quinby-Hunt, M. S., Hunt, A. J., Lofftus, K., and Shapiro, D. (1989). Polarized-light scattering studies of marine Chlorella. *Limnol. Oceanogr.* 34, 1587–1600. doi: 10.4319/lo.1989.34.8.1587

Quinn, P. K., Bates, T. S., Schulz, K. S., Coffman, D. J., Forssard, A. A., Russell, L. M., et al. (2014). Contribution of sea surface carbon pool to organic matter enrichment in sea spray aerosol. *Nat. Geosci.* 7, 228–232. doi: 10.1038/srep36675

Rakimgulov, K. B., and Ukhinov, S. A. (1994). Local estimates in Monte calro method for the ocean-atmosphere system with a random interface. *J. Numer. Anal. Math. Model.* 9, 547–564.

Ramon, D., Steinmetz, F., Jolivet, D., Compiègne, M., and Frouin, R. (2019). Modeling polarized radiative transfer in the ocean-atmosphere system with the GPU-accelerated SMART-G Monte Carlo code. *J. Quant. Spec. Rad. Transf.* 22, 89–107. doi: 10.1016/j.jqsrt.2018.10.017

Randolph, K., Dierssen, H. M., and Cifuentes-Lorenzen, A. (2017). Novel methods for optically measuring whitecaps under natural wave-breaking conditions in the Southern Ocean. *J. Atmos. Oceanic Technol.* 34, 533–554. doi: 10.1175/jtech-d-16-0086.1

Randolph, K., Dierssen, H. M., Twardowski, M., Cifuentes-Lorenzen, A., and Zappa, C. J. (2014). Optical measurements of small deeply penetrating bubble populations generated by breaking waves in the Southern Ocean. *J. Geophys. Res.* 119, 757–776. doi: 10.1002/2013JC009227

Rao, C. R. N., Stow, L. L., and McClain, E. P. (1989). Remote sensing of aerosols over the ocean using AVHRR data. Theory, practice, and applications. *Int. J. Remote Sens.* 10, 743–749. doi: 10.1080/01431168908903915

Raschke, E. (1972). Multiple scattering calculation of the transfer of solar radiation in an atmosphere-ocean system. *Beitr. Phys. Atmos.* 45, 1–19.

Remer, L. A., Davis, A. B., Mattoo, S., Levy, R. C., Kalashnikova, O., Chowdhary, J., et al. (2019). Retrieving aerosol characteristics from the PACE mission, Part 1: ocean color instrument. *Front. Earth Sci.* (in press). doi: 10.3389/feart.2019.00152

Reynolds, R. W., Rayner, N. A., Smith, T. M., Stokes, D. C., and Wang, W. (2002). An improved in situ and satellite SST analysis for climate. *J. Clim.* 15, 1609–1625. doi: 10.1175/1520-0442(2002)015<1609:aiisas>2.0.co;2

Riedi, J., Doutriaux-Boucher, M., Goloub, P., and Couvert, P. (2000). Global distribution of cloud top phase from POLDER/ADEOS1. *Geophys. Res. Lett.* 27, 1707–1710. doi: 10.1029/1999gl010921

Rietjens, J. H. H., Smit, M., van Harten, G., Di Noia, A., Hasekamp, O. P., de Boer, J., et al. (2015). "Accurate spectrally modulating polarimeters for atmospheric aerosol characterization," in *Proceedings of the SPIE 9613, Polarization Science and Remote Sensing VII*, (Bellingham, DC), doi: 10.1117/12.2188024

Rocha-Lima, A., Martins, J. V., Remer, L. A., Krotkov, N. A., Tabacniks, M. H., Ben-Ami, Y., et al. (2014). Optical, microphysical and compositional properties of the Eyjafjallajökull volcanic ash. *Atmos. Chem. Phys.* 14, 10649–10661. doi: 10.5194/acp-14-10649-2014

Rocha-Lima, A., Martins, J. V., Remer, L. A., Todd, M., Marsham, J. H., Engelstaedter, S., et al. (2018). A detailed characterization of the Saharan dust collected during the Fennec campaign in 2011: in situ ground-based and laboratory measurements. *Atmos. Chem. Phys.* 18, 1023–1043. doi: 10.5194/acp-18-1023-2018

Rodgers, C. D. (2000). *Inverse Methods for Atmospheric Sounding Theory and Practice*. Singapore: World Scientific Publishing Company.

Rothman, L. S., Gordon, I. E., Babikov, Y., Barbe, A., Benner, D. C., Bernath, P. F., et al. (2013). The HITRAN2012 molecular spectroscopic database. *J. Quant. Spectrosc. Radiat. Transf.* 130, 4–50.

Röttgers, R., Dupouy, C., Taylor, B. B., Bracher, A., and Wozniak, S. B. (2014). Mass-specific light absorption coefficients of natural aquatic particles in the near-infrared spectral region. *Limnol. Oceanogr.* 59, 1449–1460. doi: 10.4319/lo.2014.59.5.1449

Rozanov, A. V., Rozanov, V. V., and Burrows, J. P. (2001). A radiative transfer model for a spherical planetary atmosphere: combined differential-integral approach involving the Picard iterative approximation. *J. Quant. Spectrosc. Radiat. Transf.* 69, 491–512. doi: 10.1016/s0022-4073(00)00100-x

Rozanov, V. V., Dinter, T., Rozanov, A. V., Wolanin, A., Bracher, A., and Burrows, J. P. (2017). Radiative transfer modeling through terrestrial atmosphere and ocean accounting for inelastic processes: software package SCIATRAN. *J. Quant. Spectrosc. Radiat. Transf.* 194, 65–85. doi: 10.1016/j.jqsrt.2017.03.009

Rozanov, V. V., Rozanov, A. V., Kokhanovsky, A. A., and Burrows, J. P. (2014). Radiative transfer through terrestrial atmosphere and ocean: software package SCIATRAN. *J. Quant. Spectrosc. Radiat. Transf.* 133, 13–71. doi: 10.1016/j.jqsrt.2013.07.004

Russell, P. B., Kacenelenbogen, M., Livingston, J. M., Hasekamp, O. P., Burton, S. P., Schuster, G. L., et al. (2014). A multiparameter aerosol classification method and its application to retrievals from spaceborne polarimetry. *J. Geophys. Res. Atmos.* 119, 9838–9863. doi: 10.1002/2013JD021411

Santer, R., and Schmechtig, C. (2000). Adjacency effect on water surfaces: primary scattering approximation and sensitivity study. *Appl. Opt.* 39, 361–375.

Satheesh, S. K., Torres, O., Remer, L. A., Suresh Babu, S., Vinoj, V., Eck, T. F., et al. (2009). Improved assessment of aerosol absorption using OMI-MODIS joint retrieval. *J. Geophys. Res.* 114:D05209. doi: 10.1029/2008JD011024

Schroeder, M., Barth, H., and Reuter, R. (2003). Effect of inelastic scattering on underwater daylight in the ocean: model evaluation, validation, and first results. *Appl. Opt.* 42, 4244–4260.

Schultz, F. M., Stamnes, K., and Weng, F. (1999). VDISORT: an improved and generalized discrete ordinate method for polarized (vector). radiative transfer. *J. Quant. Spectrosc. Radiat. Transf.* 61, 105–122. doi: 10.1016/s0022-4073(97)00215-x

Schuster, G. I., Dubovik, O., and Arola, A. (2016). Remote sensing of soot carbon – Part 1: distinguishing different absorbing aerosol species. *Atmos. Chem. Phys.* 16, 1565–1585. doi: 10.5194/acp-16-1565-2016

Segelstein, D. J. (1981). *The Complex Refractive Index of Water*. Ph.D thesis, Department of Physics, University of Missouri, Kansas.

Sekera, Z. (1961). Union géodésique géophys. *Intern. Monogram* 10:66.

Shang, H., Chen, L., Breon, F. M., Letu, H., Li, S., Wang, Z., et al. (2015). Impact of cloud horizontal inhomogeneity and directional sampling on the retrieval of cloud droplet size by the POLDER instrument. *Atmos. Meas. Tech.* 8, 4931–4945. doi: 10.5194/amt-8-4931-2015

Shifrin, K. S. (1988). *Physical Optics of Ocean Water*. Berlin: Springer Science & Business Media.

Siegel, D. A., Maritorena, S., Nelson, N. B., Hansell, D. A., and Lorenzi-Kayser, M. (2002). Global distribution and dynamics of colored dissolved and detrital organic materials. *J. Geophys. Res.* 107:3228. doi: 10.1029/2001JC000965

Siegel, D. A., Maritorena, S., and Nelson, N. (2005). Independence and interdependencies among global ocean color properties: reassessing the bio-optical assumption. *J. Geophys. Res.* 110:C07011. doi: 10.1029/2004JC002527

Siewert, C. E. (2000). A discrete-ordinates solution for radiative-transfer models that include polarization effects. *J. Quant. Spectrosc. Radiat. Transf.* 64, 227–254. doi: 10.1016/s0022-4073(99)00006-0

Smith, R. C., and Baker, K. S. (1981). Optical properties of the clearest natural waters (200-800 nm). *Appl. Opt.* 20, 177–184. doi: 10.1364/AO.20.000177

Sommersten, E. R., Lotsberg, J. K., Stamnes, K., and Stamnes, J. (2009). "Vector discrete-ordinate radiative transfer in the coupled atmosphere-ocean system: CAO-VDISORT," in *AIP Conference Proceedings 1100*, ed. A. Waldron (College Park: American Institute of Physics). doi: 10.1063/1.3116923

Sommersten, E. R., Lotsberg, J. K., Stamnes, K., and Stamnes, J. J. (2010). Discrete ordinate and Monte Carlo simulations for polarized light radiative transfer in a coupled system consisting of two media with different refractive indices. *J. Quant. Spectrosc. Radiat. Transfer* 111, 616–633. doi: 10.1016/j.jqsrt.2009.10.021

Spinrad, R. W., and Brown, J. F. (1986). Relative real refractive index of marine microorganisms: a technique for flow cytometric estimations. *Appl. Opt.* 25, 1930–1934.

Spurr, R. J. D. (2002). Simultaneous derivation of intensities and weighting functions in a general pseudo-spherical discrete ordinate radiative transfer treatment. *J. Quant. Spectrosc. Radiat. Transf.* 75, 129–175. doi: 10.1016/s0022-4073(01)00245-x

Spurr, R., de Haan, J., Roueland, V. O., and Vasilkov, A. (2008). Discrete-ordinate radiative transfer in a stratified medium with first-order rotational Raman scattering. *J. Quant. Spectrosc. Radiat. Transf.* 109, 404–425. doi: 10.1016/j.jqsrt.2007.08.011

Stamnes, K. (1986). The theory of multiple scattering of radiation in plane parallel atmospheres. *Rev. Geophys.* 24, 299–310. doi: 10.1029/RG024i002p00299

Stamnes, K., Tsay, S.-C., Wiscombe, W., and Yayaweera, K. (1988). Numerically stable algorithm for discrete-ordinate-method radiative transfer in multiple scattering and emitting layered media. *Applied Optics* 27, 2502–2509. doi: 10.1364/AO.27.002502

Stammes, P., de Haan, J. F., and Hovenier, J. W. (1989). The polarized internal radiation field of a planetary atmosphere. *Astron. Astroph.* 225, 239–259.

Stamnes, S., Hostetler, C., Ferrare, R., Burton, S., Liu, X., Wasilewski, A., et al. (2018). Simultaneous polarimeter retrievals of microsphysical aerosol and ocean color parameters with comparison to high spectral resolution lidar atmosphere and ocean products: the MAPP algorithm. *Appl. Opt.* 57, 2394–2413. doi: 10.1364/AO.57.002394

Stowe, L. L., Ignatov, M., and Singh, R. R. (1997). Development, validation, and potential enhancements to the second-generation operational aerosol product at the national environment satellite, data, and information service of the national oceanic and atmospheric administration. *J. Geophys. Res.* 102, 16923–16934. doi: 10.1029/96jd02132

Stramska, M., and Petelski, T. (2003). Observations of oceanic whitecaps in the north polar waters of the Atlantic. *J. Geophys. Res. Oceans* 108, 1978–2012.

Stramski, D., and Kiefer, D. A. (1991). Light scattering by microorganisms in the open ocean. *Prog. Oceanog.* 28, 343–381.

Stramski, D., Boss, E., Bogucki, D., and Voss, K. J. (2004). The role of seawater constituents in light backscattering in the ocean. *Progr. Oceanogr.* 61, 27–56. doi: 10.1016/j.pocean.2004.07.001

Stramski, D., and Wózniak, S. B. (2005). On the role of colloidal particles in light scattering in the ocean. *Limnol. Oceanogr.* 50, 1581–1591. doi: 10.4319/lo.2005.50.5.1581

Sun, H., Biederman, L., and Bond, T. C. (2007). Color of brown carbon: a model for ultraviolet and visible light absorption by organic carbon. *Geophys. Res. Lett.* 34:L17813. doi: 10.1029/2007GL029797

Susskind, J., Rosenfield, J., Reuter, D., and Chahine, M. T. (1984). Remote sensing of weather and climate parameters from HIRS2/MSU on TIROS-N. *J. Geophys. Res. Atmos.* 89, 4677–4697.

Su, W., Charlock, T. P., and Rutledge, K. (2002). Observations of reflectance distribution around sunglint from a coastal ocean platform. *Appl. Opt.* 41, 7369–7383.

Sullivan, J. M., Twardowski, M. S., Zaneveld, J. R., Moore, C., Barnard, A., Donaghay, P. L., et al. (2006). The hyper-spectral temperature and salinity dependent absorption of pure water, salt water and heavy salt water in the visible and near-IR wavelengths (400 - 750 nm). *Appl. Opt.* 45, 5294–5309.

Sullivan, J. M., and Twardowski, M. T. (2009). Angular shape of the oceanic particulate volume scattering function in the backward direction. *Appl. Opt.* 46, 6811–6819. doi: 10.1364/AO.48.006811

Sun, B., Kattawar, G. W., Yang, P., Twardowski, M. S., and Sullivan, J. M. (2016). Simulation of the optical properties of ocean diatom chains. *J. Quant. Spectrosc. Radiat. Transf.* 178, 390–399.

Takamura, T., and Nakajima, T. (2004). Overview of SKYNET and its activities. *Opt. Pura Appl.* 37, 3303–3308.

Takashima, T. (1974). Method of computing the effect of surface reflection on the atmospheric radiation. *Publ. Astron. Soc. Japan* 36:361.

Takashima, T. (1975). A new approach of the adding method for the computations of emergent radiation of an inhomogeneous plane-parallel planetary atmosphere. *Astrophys. Space Sci.* 36:319. doi: 10.1007/bf00645257

Takashima, T. (1985). Polarization effect on radiative transfer in planetary composite atmospheres with interacting interface. *Earth Moon Planets* 33:59. doi: 10.1007/bf00054709

Takashima, T., and Masuda, K. (1985). Degree of radiance and polarization of the upwelling radiation from an atmosphere-ocean system. *Appl. Opt.* 24:2423. doi: 10.1364/ao.24.002423

Tanaka, M., and Nakajima, T. (1977). Effects of oceanic turbidity and index of hydrosols on the flux of solar radiation in the atmosphere-ocean system. *J. Quant. Spectrosc. Radiat. Transf.* 18:93. doi: 10.1016/0022-4073(77)90130-3

Talapatra, S., Hong, J., McFarland, M., Nayak, A. R., Zhang, C., Katz, J., et al. (2013). Characterization of biophysical interactions in the water column using in situ digital holography. *Mar. Ecol. Progr. Ser.* 473, 29–51. doi: 10.3354/meps10049

Tanré, D., Herman, M., and Deschamps, P. Y. (1981). Influence of the background contribution upon space measurements of ground reflectance. *Appl. Opt.* 20, 3676–3684. doi: 10.1364/AO.20.003676

Tanré, D., Kaufman, Y. J., Herman, M., and Mattoo, S. (1997). Remote sensing of aerosol properties over oceans using the MODIS/EOS spectral radiances. *J. Geophys. Res.* 102, 16971–16988. doi: 10.1029/96jd03437

Tanré, D., Bréon, F. M., Deuzé, J. L., Herman, M., Goloub, P., Nadal, F., et al. (2001). Global observation of anthropogenic aerosols from satellite. *Geophys. Res. Lett.* 28, 4555–4558. doi: 10.1029/2001gl013036

Tanré, D., Bréon, F. M., Deuzé, J. L., Dubovik, O., Ducos, F., François, P., et al. (2011). Remote sensing of aerosols by using polarized, directional and spectral measurements within the A-Train: the PARASOL mission. *Atmos. Meas. Tech.* 4, 1383–1395. doi: 10.5194/amt-4-1383-1395-2011

Thompson, D. R., Seidel, F. C., Gao, B. C., Gierach, M. M., Green, R. O., Kudela, R. M., et al. (2015). Optimizing irradiance estimates for coastal and inland water imaging spectroscopy. *Geophys. Res. Lett.* 42, 4116–4123. doi: 10.1002/2015GL063287

Tonizzo, A. T., Gilerson, A., Harmel, T., Ibrahim, A., Chowdhary, J., Gross, B., et al. (2011). Estimating particle composition and size distribution from polarized water-leaving radiance. *Appl. Opt.* 50, 5047–5058.

Toohey, M., Stevens, B., Schmidt, H., and Timmreck, C. (2016). Easy Volcanic Aerosol (EVA v1.0): an idealized forcing generator for climate simulations. *Geosci. Model Dev.* 9, 4049–4070. doi: 10.5194/gmd-9-4049-2016

Torres, O., Bhartia, P. K., Sinyuk, A., Welton, E. J., and Holben, B. (2005). Total ozone mapping spectrometer measurements of aerosol absorption from space: comparison to SAFARI 2000 ground-based observations. *J. Geophys. Res.* 110:D10S18. doi: 10.1029/2004JD004611

Torres, O., Tanskanen, A., Veihelmann, B., Ahn, C., Braak, P. K., Veefkind, P., et al. (2007). Aerosols and surface UV products from ozone monitoring instrument observations: an overview. *J. Geophys. Res.* 112:D24S47. doi: 10.1029/2007JD008809

Twardowski, M. S., Sullivan, J. M., Donaghay, P. L., and Zaneveld, J. R. V. (1999). Microscale quantification of the absorption by dissolved and particulate material in coastal waters with an ac-9. *J. Atmos. Oceanic Tech.* 16, 691–707. doi: 10.1175/1520-0426(1999)016<0691:mqotab>2.0.co;2

Twardowski, M. S., Boss, E., Macdonald, J. B., Pegau, W. S., Barnard, A. H., and Zaneveld, R. V. (2001). A model for estimating refractive index from the optical backscattering ratio and the implications for understanding particle composition in case I and case II waters. *J. Geophys. Res.* 106, 14129–14142. doi: 10.1029/2000jc000404

Twardowski, M. S., Lewis, M., Barnard, A., and Zaneveld, J. R. V. (2005). "In-water instrumentation and platforms for ocean color remote sensing applications," in *Remote Sensing of Coastal Aquatic Waters*, eds R. Miller, C. Del Castillo, and B. McKee (Dordrecht: Springer Publishing), 69–100. doi: 10.1007/1-4020-3100-9_4

Twardowski, M., Claustre, H., Freeman, S. A., Stramski, D., and Huot, Y. (2007). Optical backscattering properties of the clearest natural waters. *Biogeosci. Discuss.* 4, 2441–2491. doi: 10.5194/bgd-4-2441-2007

Twardowski, M., Zhang, X., Vagle, S., Sullivan, J., Freeman, S., Czerski, H., et al. (2012). The optical volume scattering function in a surf zone inverted to derive sediment and bubble particle subpopulations. *J. Geophys. Res.* 117:C00h17. doi: 10.1029/2011JC007347

Twardowski, M., and Tonizzo, A. (2018). Ocean color analytical model explicitly dependent on the volume scattering function. *Appl. Sci.* 8:2684. doi: 10.3390/app8122684

Tynes, H. H., Kattawar, G. W., Zege, E. P., Katsev, I. L., Prikhach, A. S., and Chaikovskaya, L. I. (2001). Monte Carlo and multicomponent approximation methods for vector radiative transfer by use of effective Mueller matrix calculations. *Appl. Opt.* 40, 400–412.

Tzortziou, M., Parker, O., Lamb, B., Herman, J. R., Lamsal, L., Stauffer, R., et al. (2018). Atmospheric Trace Gas (NO2 and O3) variability in South Korean coastal waters, and implications for remote sensing of coastal ocean color dynamics. *Remote Sens.* 10:1587. doi: 10.3390/rs10101587

van Diedenhoven, B., Fridlind, A. M., Cairns, B., and Ackerman, A. S. (2014). Variation of ice crystal size, shape and asymmetry parameter in tops of tropical deep convective clouds. *J. Geophys. Res. Atmos.* 119, 11809–11825. doi: 10.1002/2014JD022385

Veefkind, J. P., de Haan, J. F., Brinksma, E. J., Kroon, M., and Levelt, O. F. (2006). Total ozone from the ozone monitoring instrument (OMI) using the DOAS technique. *IEEE Trans. Geosci. Remote Sens.* 44, 1239–1244.

Volten, H., de Haan, J. F., Hovenier, J. W., Schreurs, R., Vassen, W., Dekker, A. G., et al. (1998). Laboratory measurements of angular distributions of light scattering by phytoplankton and silt. *Limnol. Oceanogr.* 43, 1180–1197. doi: 10.4319/lo.1998.43.6.1180

van de Hulst, H. C. (1963). *A New Look at Multiple Scattering.* New York, NY: NASA Institute for Space Studies.

van de Hulst, H. C. (1980). *Multiple Light Scattering*. New York, NY: Academic Press.

van der Stap, F. A., Hasekamp, O. P., and Röckmann, T. (2015). Sensitivity of PARASOL multi-angle photopolarimetric aerosol retrievals to cloud contamination. *Atmos. Meas. Tech.* 8, 1287–1301. doi: 10.5194/amt-8-1287-2015

van der Werf, G. R., Randerson, J. T., Giglio, L., Collatz, G. J., Mu, M., Kasibhatla, P. S., et al. (2010). Global fire emissions and the contribution of deforestation, savanna, forest, agricultural, and peat fires (1997-2009). *Atmos. Chem. Phys.* 10, 11707–11735. doi: 10.5194/acp-10-11707-2010

Voss, K. J., and Fry, E. S. (1984). Measurements of the Mueller matrix for ocean water. *Appl. Opt.* 23, 4427–4439.

Walrafen, G. E. (1967). Raman spectral studies of effects of temperature on water structure. *J. Chem. Phys.* 47, 114–126.

Wang, M. (1999). Modeling errors in diffuse-sky radiation: vector vs. scalar treatment. *Appl. Opt.* 38, 451–455.

Wang, M., and Shi, W. (2007). The NIR-SWIR combined atmospheric correction approach for MODIS ocean color data processing. *Opt. Express* 15, 15722–15733.

Wauben, W. M. F., and Hovenier, J. W. (1992). Polarized radiation of an atmosphere containing randomly-oriented spheroids. *J. Quant. Spectrosc. Radiat. Transf.* 47, 491–504. doi: 10.1016/0022-4073(92)90108-G

Waquet, F., Cornet, C., Deuzé, J.-L., Dubovik, O., Ducos, F., Goloub, P., et al. (2013a). Retrieval of aerosol microphysical and optical properties above liquid clouds from POLDER/PARASOL polarization measurements. *Atmos. Meas. Tech.* 6, 991–1016. doi: 10.5194/amt-6-991-2013

Waquet, F., Peers, F., Ducos, F., Goloub, P., Platnick, S., Riedi, J., et al. (2013b). Global analysis of aerosol properties above clouds. *Geophys. Res. Lett.* 40, 5809–5814. doi: 10.1002/2013gl057482

Werdell, P. J., Franz, B. A., Bailey, S. W., Feldman, G. C., Boss, E., Brando, V. E., et al. (2013a). Generalized ocean color inversion model for retrieving marine inherent optical properties. *Appl. Opt.* 52, 2019–2037. doi: 10.1364/AO.52.002019

Werdell, P. J., Franz, B. A., Lefler, J. T., Robinson, W. D., and Boss, E. (2013b). Retrieving marine inherent optical properties from satellites using temperature and salinity-dependent backscattering by seawater. *Opt. Express* 21, 32611–32622. doi: 10.1364/OE.21.032611

Werdell, P. J., McKinna, L. I. W., Boss, E., Ackleson, S. G., Craig, S. E., Gregg, W. W., et al. (2018). An overview of approaches and challenges for retrieving marine inherent optical properties from ocean color remote sensing. *Progr. Oceanogr.* 160, 186–212. doi: 10.1016/j.pocean.2018.01.001

Westberry, T. K., Boss, E., and Lee, Z.-P. (2013). Influence of Raman scattering on ocean color inversion models. *Appl. Opt.* 52, 5552–5561. doi: 10.1364/AO.52.005552

Whitlock, C. H., Barlett, D. S., and Gurganus, E. A. (1982). Sea foam reflectance and influence on optimum wavelength for remote sensing of ocean aerosols. *Geophys. Res. Lett.* 9:719. doi: 10.1029/gl009i006p00719

Wise, M. E., Semeniuk, T. A., Bruintjes, R., Martin, S. T., Russel, L. M., and Buseck, P. R. (2007). Hygroscopic behavior of NaCl-bearing natural aerosol particles using environmental transmission electron microscopy. *J. Geophys. Res.* 112:D10224. doi: 10.1029/2006JD007678

Witowski, K., Król, T., Zieliński, A., and Kuteń, E. (1998). A light-scattering matrix for unicellular marine phytoplankton. *Limnol. Oceanogr.* 43, 859–869. doi: 10.4319/lo.1998.43.5.0859

Woźniak, S., and Stramski, D. (2004). Modeling the optical properties of mineral particles suspended in seawater and their influence on ocean reflectance and chlorophyll estimation from remote sensing algorithms. *Appl. Opt.* 43, 3489–3503.

Wu, J. (1979). Oceanic Whitecaps and Sea State. *J. Phys. Oceanogr.* 9, 1064–1068. doi: 10.1175/1520-0485(1979)009<1064:owass>2.0.co;2

Wu, L., Hasekamp, O., van Diedenhoven, B., and Cairns, B. (2015). Aerosol retrieval from multiangle, multispectral photopolarimetric measurements: importance of spectral range and angular resolution. *Atmos. Meas. Tech.* 8, 2625–2638. doi: 10.5194/amt-8-2625-2015

Wu, L., Hasekamp, O., van Diedenhoven, B., Cairns, B., Yorks, J. E., and Chowdhary, J. (2016). Passive remote sensing of aerosol layer height using near-UV multi-angle polarization measurements. *Geophys. Res. Lett.* 43, 8783–8790. doi: 10.1002/2016GL069848

Xiong, Y., Zhang, X., He, S., and Gray, D. J. (2017). Re-examining the effect of particle phase functions on the remote-sensing reflectance. *Appl. Opt.* 56, 6881–6888. doi: 10.1364/AO.56.006881

Xu, F., West, R. A., and Davis, A. B. (2013). A hybrid method for modeling polarized radiative transfer in a spherical-shell planetary atmosphere. *J. Quant. Spectrosc. Radiat. Transf.* 117, 59–70. doi: 10.1016/j.jqsrt.2012.10.013

Xu, Z., Zhou, W., Sun, Z., Yang, Y., Lin, J., Wang, G., et al. (2015). Estimating the augmented reflectance ratio of the ocean surface when whitecaps appear. *Remote Sens.* 7, 13606–13625. doi: 10.3390/rs71013606

Xu, F., Dubovik, O., Zhai, P.-W., Diner, D. J., Kalashnikova, O. V., Seidel, F. C., et al. (2016). Joint retrieval of aerosol and water-leaving radiance from multispectral, multiangular and polarimetric measurements over ocean. *Atmos. Meas. Tech.* 9, 2877–2907. doi: 10.5194/amt-9-2877-2016

Xu, G., Sun, B., Brooks, S. D., Yang, P., Kattawar, G. W., and Zhang, X. (2017). Modeling the ninherent optical properties of aquatic particles using an irregular hexahedral ensemble. *J. Quant. Spectrosc. Radiat. Transf.* 191, 30–39. doi: 10.1016/j.jqsrt.2017.01.020

Xu, X., Wang, J., Wang, Y., Zeng, J., Torres, O., Yang, Y. K., et al. (2017). Passive remote sensing of altitude and optical depth of dust plumes using the oxygen A and B bands: first results from EPIC/DSCOVR at Lagrange-1 point. *Geophys. Res. Lett.* 44, 7544–7554. doi: 10.1002/2017gl073939

Xu, X., Wang, J., Wang, Y., and Kokhanovsky, A. (2018). "Passive remote sensing of aerosol height," in *Remote Sensing of Aerosols, Clouds, and Precipitation*, eds T. Islam, et al. (Amsterdam: Elsevier), 1–22. doi: 10.1016/b978-0-12-810437-8.00001-3

You, Y., Tonizzo, A., Gilerson, A. A., Cummings, M. E., Brady, P., Sullivan, J. M., et al. (2011). Measurements and simulations of polarization states of underwater light in clear oceanic waters. *Opt. Express* 50, 4873–4893. doi: 10.1364/AO.50.004873

Zaneveld, J. R. V., Roach, D. M., and Pak, H. (1974). The determination of the index of refraction distribution of oceanic particulates. *J. Geophys. Res.* 79, 4091–4095. doi: 10.1029/jc079i027p04091

Zaneveld, J. R. V. (1995). A theoretical derivation of the dependence of the remotely sensed reflectance of the ocean on the inherent optical properties. *J. Geophys. Res.* 100, 113135–113142. doi: 10.1364/AO.21.004146

Zhai, P., Hu, Y., Trepte, C. R., and Lucker, P. L. (2009). A vector radiative transfer model for coupled atmosphere and ocean systems based on successive order of scattering method. *Opt. Express* 17, 2057–2079.

Zhai, P., Hu, Y., Chowdhary, J., Trepte, C. R., Lucker, P. L., and Josset, D. B. (2010). A vector radiative transfer model for coupled atmosphere and ocean systems with a rough interface. *J. Quant. Spectrosc. Radiat. Transf.* 111, 1025–1040. doi: 10.1016/j.jqsrt.2009.12.005

Zhai, P., Hu, Y., Trepte, C. R., Winker, D. M., Josset, D. B., Lucker, P. L., et al. (2013). Inherent optical properties of the coccolithophore: *Emiliania huxleyi*. *Opt. Express* 21, 17625–17638. doi: 10.1364/OE.21.017625

Zhai, P., Hu, Y., Winker, D. M., Franz, B., and Boss, E. (2015). Contribution of Raman scattering to polarized radiation field in ocean waters. *Opt. Express* 23, 23582–23596. doi: 10.1364/OE.23.023582

Zhai, P., Hu, Y., Winker, D. M., Franz, B., Werdell, J., and Boss, E. (2017a). A vector radiative transfer model for coupled atmosphere and ocean systems including inelastic sources in ocean waters. *Opt. Express* 25, A223–A239. doi: 10.1364/OE.25.00A223

Zhai, P., Knobelspiesse, K., Ibrahim, A., Franz, B., Hu, Y., Gao, M., et al. (2017b). Water-leaving contribution to polarized radiation field over ocean. *Opt. Express* 25, A689–A708. doi: 10.1364/OE.25.00A689

Zhai, P., Boss, E., Franz, B., Werdell, P. J., and Hu, Y. (2018). Radiative transfer modeling of phytoplankton fluorescence quenching processes. *Remote Sens.* 10:1309. doi: 10.3390/rs10081309

Zhang, X., and Hu, L. (2009). Estimating scattering of pure water from density fluctuation of the refractive index. *Opt. Express* 17, 1671–1678.

Zhang, X., Hu, L., and He, M.-X. (2009). Scattering by pure seawater: effect of salinity. *Opt. Express* 17, 5698–5710.

Zhang, X., and Gray, D. J. (2015). Backscattering by very small particles in coastal waters. *J. Geophys. Res.* 120, 6914–6926. doi: 10.1002/2015JC010936

Zhang, H., and Wang, M. (2010). Evaluation of sun glint models using MODIS measurements. *J. Quant. Spectrosc. Radiat. Transf.* 111, 492–506. doi: 10.1016/j.jqsrt.2009.10.001

Zhang, X., Twardowski, M., and Lewis, M. (2011). Retrieving composition and sizes of oceanic particle subpopulations from the volume scattering function. *Appl. Opt.* 50, 1240–1259. doi: 10.1364/AO.50.001240

Zhang, X., Gray, D., Huot, Y., You, Y., and Bi, L. (2012). Comparison of optically derived particle size distributions: scattering over the full angular range versus diffraction at near forward angles. *Appl. Opt.* 51, 5085–5099. doi: 10.1364/AO.51.005085

Zhang, X., Huot, Y., Gray, D. J., Weidemann, A., and Rhea, W. J. (2013). Biogeochemical origins of particles obtained from the inversion of the volume scattering function and spectral absorption in coastal waters. *Biogeosciences* 10, 6029–6043. doi: 10.5194/bg-10-6029-2013

Zhang, X., Boss, E., and Gray, D. J. (2014a). Significance of scattering by oceanic particles at angles around 120 degree. *Opt. Express* 22, 31329–31336. doi: 10.1364/OE.22.031329

Zhang, X., Stavn, R. H., Falster, A. U., Gray, D., and Gould, R. W. Jr. (2014b). New insight into particulate mineral and organic matter in coastal ocean waters through optical inversion. *Estuar. Coast. Shelf Sci.* 149, 1–12. doi: 10.1016/j.ecss.2014.06.003

Zhang, X., Fournier, G. R., and Gray, D. J. (2017). Interpretation of scattering by oceanic particles around 120 degrees and its implication in ocean color studies. *Opt. Expr.* 25, A191–A199. doi: 10.1364/OE.25.00A191

Zhang, X., Stramski, D., Reynolds, R. A., and Blocker, E. R. (2019). Light scattering by pure water and seawater: the depolarization ratio and its variation with salinity. *Appl. Opt.* 58, 991–1004. doi: 10.1364/AO.58.000991

Conflict of Interest Statement: The authors declare that the research was conducted in the absence of any commercial or financial relationships that could be construed as a potential conflict of interest.

frontiers in Earth Science

METHODS
published: 18 July 2019
doi: 10.3389/feart.2019.00176

Approach for Propagating Radiometric Data Uncertainties Through NASA Ocean Color Algorithms

Lachlan I. W. McKinna[1,2]*, Ivona Cetinić[2,3], Alison P. Chase[4] and P. Jeremy Werdell[2]

[1] Go2Q Pty Ltd., Buderim, QLD, Australia, [2] Ocean Ecology Laboratory, NASA Goddard Space Flight Center, Greenbelt, MD, United States, [3] GESTAR/Universities Space Research Association, Columbia, MD, United States, [4] School of Marine Sciences, University of Maine, Orono, ME, United States

Spectroradiometric satellite observations of the ocean are commonly referred to as "ocean color" remote sensing. NASA has continuously collected, processed, and distributed ocean color datasets since the launch of the Sea-viewing Wide-field-of-view Sensor (SeaWiFS) in 1997. While numerous ocean color algorithms have been developed in the past two decades that derive geophysical data products from sensor-observed radiometry, few papers have clearly demonstrated how to estimate measurement uncertainty in derived data products. As the uptake of ocean color data products continues to grow with the launch of new and advanced sensors, it is critical that pixel-by-pixel data product uncertainties are estimated during routine data processing. Knowledge of uncertainties can be used when studying long-term climate records, or to assist in the development and performance appraisal of bio-optical algorithms. In this methods paper we provide a comprehensive overview of how to formulate first-order first-moment (FOFM) calculus for propagating radiometric uncertainties through a selection of bio-optical models. We demonstrate FOFM uncertainty formulations for the following NASA ocean color data products: chlorophyll-a pigment concentration (*Chl*), the diffuse attenuation coefficient at 490 nm ($K_{d,490}$), particulate organic carbon (*POC*), normalized fluorescent line height (*nflh*), and inherent optical properties (IOPs). Using a quality-controlled *in situ* hyperspectral remote sensing reflectance ($R_{rs,i}$) dataset, we show how computationally inexpensive, yet algebraically complex, FOFM calculations may be evaluated for correctness using the more computationally expensive Monte Carlo approach. We compare bio-optical product uncertainties derived using our test R_{rs} dataset assuming spectrally-flat, uncorrelated relative uncertainties of 1, 5, and 10%. We also consider spectrally dependent, uncorrelated relative uncertainties in R_{rs}. The importance of considering spectral covariances in R_{rs}, where practicable, in the FOFM methodology is highlighted with an example SeaWiFS image. We also present a brief case study of two *POC* algorithms to illustrate how FOFM formulations may be used to construct measurement uncertainty budgets for ecologically-relevant data products. Such knowledge, even if rudimentary, may provide useful information to end-users when selecting data products or when developing their own algorithms.

Keywords: ocean color, remote sensing, bio-optics, uncertainties, oceanography, radiometry, biogeochemistry

Edited by:
David Antoine,
Curtin University, Australia

Reviewed by:
Constant Mazeran,
Solvo (Europe), France
Frederic Melin,
Joint Research Centre, Italy

***Correspondence:**
Lachlan I. W. McKinna
lachlan.mckinna@go2q.com.au

Specialty section:
This article was submitted to Atmospheric Science, a section of the journal Frontiers in Earth Science

Received: *30 November 2018*
Accepted: *21 June 2019*
Published: *18 July 2019*

Citation:
McKinna LIW, Cetinić I, Chase AP and Werdell PJ (2019) Approach for Propagating Radiometric Data Uncertainties Through NASA Ocean Color Algorithms. Front. Earth Sci. 7:176. doi: 10.3389/feart.2019.00176

INTRODUCTION

NASA has continually collected, processed, archived, and distributed global ocean color data since the launch of the Sea-viewing Wide Field-of-View Sensor (SeaWiFS) in 1997. This two decades-long multi-sensor data climatology continues to provide unprecedented synoptic-scale insight into near-surface oceanographic processes. Some of the satellite-derived variables, such as chlorophyll-a pigment concentration Chl (mg m^{-3}), are considered as Essential Climate Variables (ECV) and are widely used by the oceanographic community to study phytoplankton ecology, marine biogeochemistry, and ecosystem responses to climate change (IOCCG, 2008; McClain, 2009; Franz et al., 2017).

Following formal definitions outlined in the Guide to Uncertainty in Measurement (JCGM, 2008), we can outline the objective of ocean color remote sensing as, to *measure* oceanographic quantities or *measurands*. We note that the *measurement procedure* involves a number of mathematical steps and assumptions that derive the *measurand* from sensor-observed top-of-atmosphere radiances. Thus, a derived ocean color data product is a *result of measurement* and should always be treated as an estimate of the *measurand* which has inherent *uncertainty*.

Quantifying uncertainty in derived ocean color data products (i.e., measurands) is highly valuable, allowing end-users to: assess if datasets are fit-for-purpose, assess if observed temporal change is greater than uncertainty, assimilate uncertainties into climate models, and assess consistency among sensors (Maritorena et al., 2010; Gould et al., 2014). Additionally, a thorough understanding of uncertainty sources within a model may help guide the decisions of scientists when developing new satellite algorithms.

The measurement uncertainty ($u_{measurement}$), in an ocean color data product, y, can be expressed as the following:

$$u_{measurement}(y) = \sqrt{u^2_{data}(y) + u^2_{model}(y)}, \qquad (1)$$

where $u_{model}(y)$ represents uncertainties in y due to inherent inaccuracies/limitations in the algorithm (e.g., model coefficients), and $u_{data}(y)$ represents uncertainties in y due to uncertainties in sensor-observed radiometry (data). In this paper we focus on $u_{data}(y)$, that is, the propagation of radiometric uncertainties through bio-optical algorithms. For brevity, we shorten $u_{data}(y)$ to $u(y)$ throughout this paper unless otherwise stated.

For the ocean color community, much of our understanding of measurement uncertainty in derived data products is sourced from validation exercises using *in situ* datasets (Bailey and Werdell, 2006; Antoine et al., 2008; Melin, 2010; Mélin et al., 2016) or from Monte Carlo-type simulations (Wang et al., 2005). We note that advanced statistical methodologies have also emerged for predicting uncertainties in derived ocean color products (Moore et al., 2009; Salama et al., 2009; Jay et al., 2018). While validation studies remain critical for appraising the absolute skill of an ocean color algorithm, such datasets themselves have their own measurement uncertainty associated with *in situ* observations (including uncertainties associated with subpixel temporal/spatial/environmental variability). Monte Carlo-type analyses are particularly useful for understanding measurement uncertainty, however, these approaches can be computationally expensive and are impracticable to implement within pixel-by-pixel ocean color processing.

More recently, analytical first-order first moment (FOFM) methods have been proposed that can directly propagate radiometric uncertainty through an ocean color algorithm to estimate derived data product uncertainty (Neukermans et al., 2009; Salama et al., 2009, 2011; Lee et al., 2010; Maritorena et al., 2010; Lamquin et al., 2013; Qi et al., 2017). These approaches are based on the *law of propagation of uncertainty* according to JCGM (2008). A FOFM methodology benefits from being computationally efficient, thereby allowing it to be implemented in pixel-by-pixel ocean color data processing software (Lamquin et al., 2013). In addition, FOFM calculations can be used to estimate the relative contribution of individual sources to total measurement uncertainty.

Work presented here is the first comprehensive examination of methods that can be used to estimate uncertainties in NASA's standard bio-optical data products. In this study we aim to demonstrate the feasibility of using a FOFM uncertainty framework to approximate ocean color data uncertainty in derived data products. The FOFM method, which itself is an analytical approximation, is first appraised by comparing FOFM-derived uncertainties with Monte Carlo-derived uncertainties. We demonstrate how this approach can be used as a method to check the correctness of FOFM calculations. Second, using FOFM propagation theory, we estimate uncertainty in derived ocean color products given spectrally-flat, uncorrelated relative uncertainties of 1, 5, and 10% in spectral remote-sensing reflectances, $R_{rs,i}$ (sr^{-1}). We also consider spectrally-dependent, uncorrelated relative uncertainties in $R_{rs,i}$ published by Hu et al. (2013). Third, we consider how inclusion of covariances affect uncertainty estimates. A sample SeaWiFS scene of the Hawaiian Islands is used in this case study. Finally, we demonstrate how the FOFM approach may be used to estimate measurement uncertainty budgets. In our case study we consider two algorithms for estimating particulate organic carbon (POC; mg m^{-3}), a key metric used to understand oceanic biomass and the carbon cycle.

In this work, we utilize a high quality *in situ* hyperspectral $R_{rs,i}$ dataset that can be spectrally subsampled to match the spectral characteristics of most existing and future ocean color sensors. This includes NASA's Plankton, Aerosol, Cloud, ocean Ecosystem (PACE) mission that is currently under development and will carry the first dedicated hyperspectral ocean color sensor.

DATA AND METHODS

Bio-optical Algorithms and Data Products

The NASA Ocean Biology Data Archive and Active Distribution Center (OB.DAAC) distribute a number of derived marine data products in two separate data suites: (i) the standard ocean color (OC) data product suite and, (ii) the inherent optical properties (IOP) product suite. The OC suite comprises established (legacy) ocean color data products that were developed during the SeaWiFS (1997–2010) and Moderate

TABLE 1 | Bio-optical ocean color data products.

Product name	Product suite	Symbol	Units	References
Chlorophyll-a pigment concentration*	OC	*Chl*	mg m^{-3}	O'Reilly et al., 1998; Hu et al., 2012b
Chlorophyll-a derived from band ratio	–	Chl_{BR}	mg m^{-3}	O'Reilly et al., 1998
Chlorophyll-a derived from line height	–	Chl_{LH}	mg m^{-3}	Hu et al., 2012b
Diffuse attenuation coefficient at 490 nm	OC	$K_{d,490}$	m^{-1}	Mueller, 2000
Particulate organic carbon	OC	POC	mg m^{-3}	Stramski et al., 2008a
Normalized fluorescent line height	OC	nflh	mW cm^{-2} μm^{-1} sr^{-1}	Behrenfeld et al., 2009
Absorption coefficient of total non-water components 443 nm	IOP	$a_{nw,443}$	m^{-1}	Werdell et al., 2013
Absorption coefficient of phytoplankton at 443 nm	IOP	$a_{\phi,443}$	m^{-1}	Werdell et al., 2013
Absorption coefficient of colored dissolved and detrital matter at 443 nm	IOP	$a_{dg,443}$	m^{-1}	Werdell et al., 2013
Particulate backscattering coefficient at 443 nm	IOP	$b_{bp,443}$	m^{-1}	Werdell et al., 2013

**Note that NASA's standard Chl product is a dynamic blend of Chl_{BR} and Chl_{LH}.*

Resolution Imaging Spectroradiometer aboard Aqua (MODISA 2002–present) missions. The IOP suite comprises spectral component absorption and backscattering coefficients derived using the default configuration of the Generalized Inherent Optical Properties (GIOP) algorithm framework (Werdell et al., 2013). A selection of the OC suite and IOP suite products were used in this study (**Table 1**). More comprehensive detail of the bio-optical algorithms used to derive these data products and their associated uncertainties are given in Appendices A–E (**Supplementary Material**). We note that in this study the GIOP used a spectral subset of our R_{rs} evaluation dataset (described in section Evaluation R_{rs} Dataset) spanning 412–655 nm.

Modeling Bio-Optical Data Product Uncertainty

In this study we used the analytical law of propagation of uncertainty (JCGM, 2008) to propagate radiometric uncertainties through models used to derive bio-optical quantities. We follow the notation conventions outlined by JCGM (2008) where the uncertainty of a measured quantity, y, is denoted as $u(y)$ and is the positive square root of the variance, $u^2(y)$. We note that y is derived from a model, f, of N input quantities, x_i. Following (JCGM, 2008), for uncorrelated input quantities, $u^2(y)$ can be calculated as:

$$u^2(y) = \sum_{i=1}^{N} \left(\frac{\partial f}{\partial x_i} \right)^2 u^2(x_i) \tag{2}$$

where, $u(x_i)$ is the 1-σ uncertainty in the input quantity x_i. For our notation of spectral properties used in ocean color remote sensing, subscripts i correspond to wavelength. In this study, partial derivatives of target parameters were calculated analytically, however, these could also be computed numerically. For the situation where uncertainties of input quantities are correlated, Equation 2 is extended to:

$$u^2(y) = \sum_{i=1}^{N} \left(\frac{\partial f}{\partial x_i} \right)^2 u^2(x_i) + 2 \sum_{i=1}^{N-1} \sum_{j=i+1}^{N} \frac{\partial f}{x_i} \frac{\partial f}{x_j} u(x_i, x_j) \tag{3}$$

where $u(x_i, x_j) = u(x_j, x_i)$ denotes the estimated error covariance associated with the quantities x_i and x_j. Comprehensive details of partial derivative calculations for each bio-optical algorithm in **Table 1** are given in Appendices A–E (**Supplementary Material**).

Monte Carlo (MC) methods are routinely used to perform sensitivity analyses as well as quantify model output uncertainties (Refsgaard et al., 2007). In this study, we have utilized a MC approach to appraise FOFM calculations. As the partial derivative calculus within FOFM uncertainty estimates can be complex, we have used MC-to-FOFM comparisons as a means of checking calculations.

The MC estimates of uncertainties in this study were computed as follows:

(i) A given bio-optical model, f, that derives an output y, that is considered a function of n spectral remote sensing reflectance bands, $R_{rs,i}$, is run 5,000 times.
(ii) Upon each iteration, each $R_{rs,i}$ is perturbed by a factor $\Delta r_{,i}$ which is randomly sampled from a Gaussian distribution $\Delta r_{,i} \sim N(0, u(R_{rs,i}))$, in which the mean is zero and the standard deviation, $u(R_{rs,i})$, is known or assumed. No spectral correlations are assumed.
(iii) The MC simulation then generates a probability density function (*PDF*) for y. From the *PDF*, the mean value, $\hat{y}$ and the standard deviation, σ_y, can be computed.

We note that the MC method captures non-linear effects and thus we cannot always expect direct agreement between σ_y^2 and FOFM-derived $u^2(y)$. Indeed, even if a bio-optical model contains weak non-linearities and MC model input uncertainties are normally distributed, the number of MC iterations still needs to be suitably large for σ_y^2 to agree with $u^2(y)$.

Evaluation R_{rs} Dataset

To evaluate our FOFM uncertainty method, we used a dataset of high quality hyperspectral $R_{rs,i}$ spectra ($N = 1124$). Hyperspectral radiometric measurements were collected *in situ* during three different expeditions, representing a range of oligotrophic to mesotrophic waters: the SABOR experiment in the Gulf of Maine/North Atlantic/Mid-Atlantic coast (July–August 2014); AE1319 in the North Atlantic and Labrador

Sea (August–September 2013); and NH1418 in the Equatorial Pacific (September–October 2014). A HyperOCR system (Sea-Bird Scientific) deployed on a tethered profiler in "buoy mode" was used to collect upwelling radiance, $L_{u,i}$ (W m^{-2} μm^{-1} sr^{-1}), and downwelling irradiance, $E_{d,i}$ (W m^{-2}), spectra during deployments lasting ~5 min. During sample collection, the instrument was allowed to drift far enough from the boat to avoid the ship's shadow.

The spectra were dark and tilt-corrected, and the upper and lower 25th percentile of the $E_{d,i}$ spectra were removed from both $E_{d,i}$ and $L_{u,i}$. The mean of the remaining spectra was used in subsequent analysis, providing one spectrum per deployment, and with uncertainties calculated as the standard deviation of the same spectra used to calculate the mean (N.B. uncertainties here represent only the experimental portion of the uncertainties, and calibration bias has not been accounted for). The $L_{u,i}$ measurements were extrapolated to and across the air-water interface to obtain the water-leaving radiance, $L_{w,i}$ (W m^{-2} sr^{-1}), which were then used to calculate remote-sensing reflectance ($R_{rs,i}$), defined as:

$$R_{rs,i} = \frac{L_{w,i}}{E_{d,i}} \tag{4}$$

The spectra were additionally corrected for Raman scattering following methods in Westberry et al. (2013), which was necessary to compensate for the scattering that water molecules themselves can contribute to $L_{w,i}$, especially at the blue wavelengths in very clear waters (McKinna et al., 2016). Finally, the R_{rs} spectra were normalized to remove the angular effect of the sun position in the sky relative to nadir, following methods in Lee et al. (2011). For a more detailed description of the $R_{rs,i}$ calculations and processing, see Data and Methods section in Chase et al. (2017). All hyperspectral $R_{rs,i}$ used in this study are shown in **Figure 1**.

Finally, each hyperspectral R_{rs} spectrum was spectrally sub-sampled. The resulting multiband $R_{rs,i}$ dataset had sixteen 10 nm-wide spectral bands centered on: 412, 425, 443, 460, 475, 490, 510, 532, 555, 583, 617, 640, 655, 665, 678, and 710 nm. This multispectral subset spanned the visible domain and included bands from both past and present NASA sensors (e.g., SeaWiFS and MODIS).

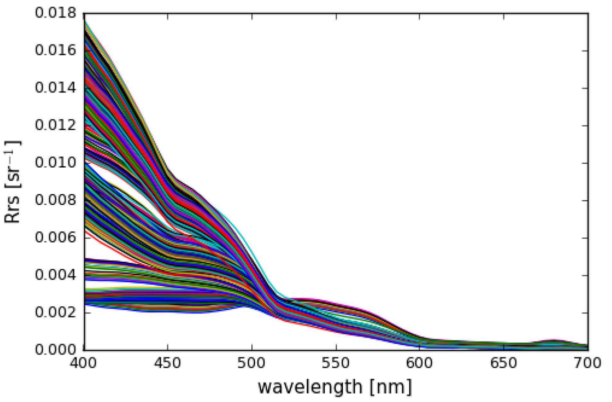

FIGURE 1 | Hyperspectral remote-sensing reflectances ($N = 1124$) used in this study.

Radiometric Uncertainties

Spectrally Flat R_{rs} Uncertainties

For NASA ocean color bio-optical algorithms, model input quantities are typically remote sensing reflectances, $R_{rs,i}$ (sr^{-1}), which are derived from measured top-of-atmosphere radiances, $L_{t,i}$ (W m^{-2} μm^{-1} sr^{-1}), via atmospheric correction (AC) algorithms. Historically, a desirable science requirements for NASA ocean color missions has been $R_{rs,i}$ with relative uncertainty of 5% (spectrally flat) or less (Hooker et al., 1992; Hooker and McClain, 2000; McClain et al., 2004; PACE Science Definition Team, 2018). Whilst not directly representative of a true sensor (see section Spectrally-Dependent R_{rs} Uncertainties), treating relative uncertainties in $R_{rs,i}$ as spectrally flat is still useful under circumstances where detailed knowledge of sensor performance characteristics is limited, such as during pre-launch scoping studies, to provide rudimentary uncertainty estimates. In this study we first consider 5% relative uncertainty in $R_{rs,i}$ to compare FOFM-to-MC calculations. We next use the FOFM method consider how spectrally flat relative uncertainties in R_{rs} of 1, 5, and 10% impact estimated OC and IOP uncertainties. Note, we treat spectrally flat relative uncertainties in R_{rs} of 1, 5, and 10% as spectrally uncorrelated.

Spectrally-Dependent R_{rs} Uncertainties

We note that on-orbit uncertainties in $L_{t,i}$ and $R_{rs,i}$ have previously been quantified for NASA's SeaWiFS and MODISA missions (Eplee et al., 2007; Hu et al., 2012a, 2013; Angal et al., 2015). Whilst historically 5% has been the desired accuracy goal for R_{rs} in the blue-green spectral range, work by Hu et al. (2013) reported that relative uncertainties of $R_{rs,i}$ for SeaWiFS and MODISA increase monotonically with wavelength, and that $R_{rs,i}$ relative uncertainty also varies as a function of *Chl*, or water-column optical complexity. To extend this study beyond spectrally flat relative uncertainties, we utilized the relative uncertainties for MODISA $R_{rs,i}$ estimated for the North Atlantic Ocean (see Table 2 of Hu et al., 2013). To estimate relative uncertainty for a given $R_{rs,i}$ spectra, we followed three steps: (i) linearly interpolate tabulated relative uncertainties to match the spectral resolution of our *in situ* $R_{rs,i}$ dataset, (ii) estimate *Chl* concentration using NASA's standard OC algorithm, and (iii) linearly interpolate the spectrally tabulated relative uncertainties to estimate relative uncertainty for observed $R_{rs,i}$ based on the respective *Chl* concentration. Note, where estimated *Chl* exceeded 0.2 mg m^{-3} [beyond values reported by Hu et al. (2013)] we linearly extrapolated tabulated relative uncertainties. **Figure 2** shows the spectral relative uncertainties in $R_{rs,i}$ [*sensu* Hu et al. (2013)] used in this study and how they vary with *Chl* concentration. Note, spectrally-dependent relative uncertainties in R_{rs} computed as a function of *Chl* were treated as spectrally uncorrelated.

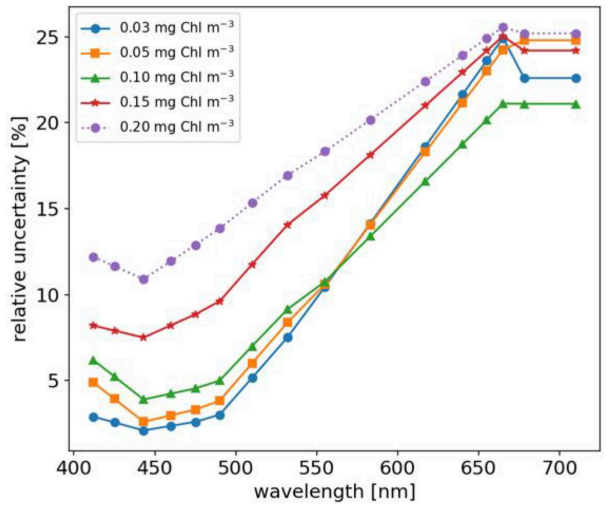

FIGURE 2 | Relative uncertainties of R_{rs} varying with Chl concentration. Original data taken from Hu et al. (2013) and interpolated to the multispectral resolution used in this study.

Spectrally-Correlated R_{rs} Uncertainties

Our initial analyses treated R_{rs} spectral uncertainties as uncorrelated, which in practice is an oversimplification. Indeed, AC algorithms utilize near-infrared bands to make assumptions about the contribution of atmospheric aerosols to L_t (Gordon and Wang, 1994; Bailey et al., 2010). Thus, $R_{rs,i}$ uncertainties are inherently spectrally correlated. While much work has been done to characterize radiometric uncertainties of NASA sensors used for ocean color (Eplee et al., 2007; Hu et al., 2012a, 2013), few studies have quantified off-diagonal elements of the variance-covariance matrices for top-of-atmosphere radiance, $\mathbf{V}_{Lt}$, and remote sensing reflectances, $\mathbf{V}_{Rrs}$, respectively. We note that while beyond the scope of this work, parallel efforts are underway by the research community to derive pixel-by-pixel estimates of $u(R_{rs,i})$ by propagating radiometric uncertainties through ocean color atmospheric correction algorithms (Gillis et al., 2018).

Recently, Lamquin et al. (2013) demonstrated a methodology to estimate $\mathbf{V}_{Lt}$ for MERIS data and propagate these through ESA's clear water branch AC algorithm and into bio-optical data products. Critically, Lamquin et al. (2013) demonstrated that ignoring covariances can lead to overestimated data product uncertainties. In this study, using a similar methodology to Lamquin et al. (2013), we estimate $\mathbf{V}_{Lt}$ for SeaWiFS and then using a numerical approximation estimate $\mathbf{V}_{Rrs}$. A full description of this method can be found in Appendix F (**Supplementary Material**). We note that while our estimates of $\mathbf{V}_{Rrs}$ are somewhat rudimentary, they are still useful for demonstrating the importance of including covariance terms in FOFM-based uncertainty estimates.

Satellite Data Processing

A SeaWiFS image of Hawaii captured on 1 December 2000 was used to demonstrate the FOFM methodology when applied to ocean color imagery. SeaWiFS Level-1 data was downloaded from NASA's Ocean Biology Distributed Active Archive Center (NASA OB.DAAC) Level 1 and 2 Browser website (https://oceancolor.gsfc.nasa.gov/)[1]. Data were then processed from Level 1 to Level 2 using NASA Ocean Color Science Software (OCSSW). These processing steps include radiometric calibration, geolocation, and atmospheric correction. A prototype version of OCSSW code was used to compute $u(Chl)$ using FOFM methodology where $u(R_{rs,i})$ was estimated using an empirical methodology described in Appendix F (**Supplementary Material**).

RESULTS

Appraisal of Methodology

The MC methodology, while computationally expensive, was expected to give robust estimates of measurand uncertainties. Thus, MC outputs provided a benchmark to which the FOFM uncertainty estimates could be compared with for correctness. Direct calculations of FOFM uncertainties, $u(y)$, were compared with MC output uncertainties, σ_y. To compare MC and FOFM calculations we used 5% spectrally flat relative uncertainty in R_{rs} and computed the following comparison statistics: bias and Type II linear regression slope. When computing these statistics for the purpose of FOFM-to-MC comparisons, we assume that MC-estimated uncertainties were quasi-truth. We note that variables were log-transformed for these calculations following Seegers et al. (2018). Bias was computed as:

$$bias = 10^\wedge \left\{ \sum_{k=1}^{N} \frac{\log_{10}(MC_k) - \log_{10}(FOFM_k)}{N} \right\}, \qquad (5)$$

where $N = 1124$ is the number of input spectra. Given that bias was computed using log-transformed variables, it becomes interpretable as multiplicative metrics (Seegers et al., 2018). We note that our bias calculations assume estimated OC and IOP uncertainties follow log-normal distributions; a property that is demonstrated later in the paper (e.g., **Figures 4**, **5**).

The MC and FOFM estimation of derived product uncertainties were in good agreement for the following OC products: $K_{d,490}$, POC, and $nflh$. This was indicated by slope and bias and statistics (**Table 2**) having values of, or near to, 1.0. However, regression statistics indicated Chl uncertainties derived using the FOFM method did not completely agree with the MC method (**Table 2**). To assess this discrepancy more closely, uncertainties in each component of the Chl algorithm were inspected, namely the band ratio (BR), line height (LH), and blended components. Regression statistics indicated that FOFM estimates of Chl_{blend} product uncertainties did not agree well with MC values and were typically biased low by 27%, visualized further by the color-coded scatter plot in **Figure 3A**.

Derived uncertainties for IOP products generally agreed with MC simulations. Specifically, **Table 2** shows FOFM estimates of

---

[1] NASA Goddard Space Flight Center, Ocean Ecology Laboratory, & Ocean Biology Processing Group. Sea-viewing Wide Field-of-view Sensor (SeaWiFS) L1 Data (data/10.5067/ORBVIEW-2/SEAWIFS/L1/DATA/1).

uncertainties with respect to MC estimates for $a_{nw,443}$, $a_{\phi,443}$, $a_{dg,443}$, and $b_{bp,443}$ were biased low by 1%, low by 2%, low by 2% and, high by 2%, respectively. Slight disagreement between MC and FOFM estimates of $u(b_{bp,443})$ can be visualized in **Figure 3** when $u(b_{bp,443}) > 2.0 \times 10^{-3}$ m^{-1}. In addition, MC and FOFM estimates of $u(a_{\phi,443})$ showed slight disagreement when $u(a_{\phi,443}) > 1.0 \times 10^{-2}$ m^{-1}.

TABLE 2 | Log-normal statistics comparing Monte Carlo (MC) and first-order first-moment (FOFM) uncertainty calculations for R_{rs} with spectrally flat, uncorrelated 5% relative uncertainty.

	Derived product uncertainty	
Product	**Bias**	**Slope**
Chl (all)	0.95	0.96
Chl_{BR}	1.00	1.00
Chl_{LH}	0.99	1.00
$Chl_{blended}$*	0.73	0.72
$K_{d,490}$	0.99	1.00
POC	0.99	1.00
nflh	0.99	1.00
$a_{nw,443}$	0.99	1.00
$a_{\phi,443}$	0.98	1.00
$a_{dg,443}$	0.98	1.00
$b_{bp,443}$	0.99	0.98

Blended LH and BR Chl product span 0.134–0.165 mg m^{-3}.

These results demonstrate that while FOFM uncertainty calculations are computationally inexpensive, they serve as approximations only, especially in the case of *Chl*. Indeed, while FOFM-derived uncertainties can be expected to agree with MC-derived values for simple functions that vary linearly, it may not be unusual for FOFM-derived uncertainties to differ from MC-derived values; particularly when analyzing complicated non-linear problems (Putko et al., 2001; Mekid and Vaja, 2008). For example, with the IOPs we found slight differences in the order of 1% between MC and FOFM uncertainty estimates. For such mathematical functions, higher order methods such as Second Order First Moment (SOFM) methods may be useful, however, the added mathematical complexity may be prohibitive.

Uncertainties Estimated From *in situ* Radiometric Data

OC Product Uncertainties

Using the multispectral R_{rs} evaluation dataset, uncertainties in derived OC products associated with 5% spectrally-flat relative, uncorrelated uncertainty in R_{rs} were computed. **Figure 4** shows histograms of derived OC products, absolute uncertainties, and relative uncertainties. MC computations are summarized in **Table 3**, while FOFM computations are provided for comparative purposes in **Table 4**.

The range of derived *Chl* confirmed that the dataset spans oligotrophic (0.04 mg m^{-3}) to mesotrophic conditions (1.28 mg m^{-3}) with a median value of 0.11 mg m^{-3}. Values of $u(Chl)$ span four orders of magnitude and have median values of 7.00

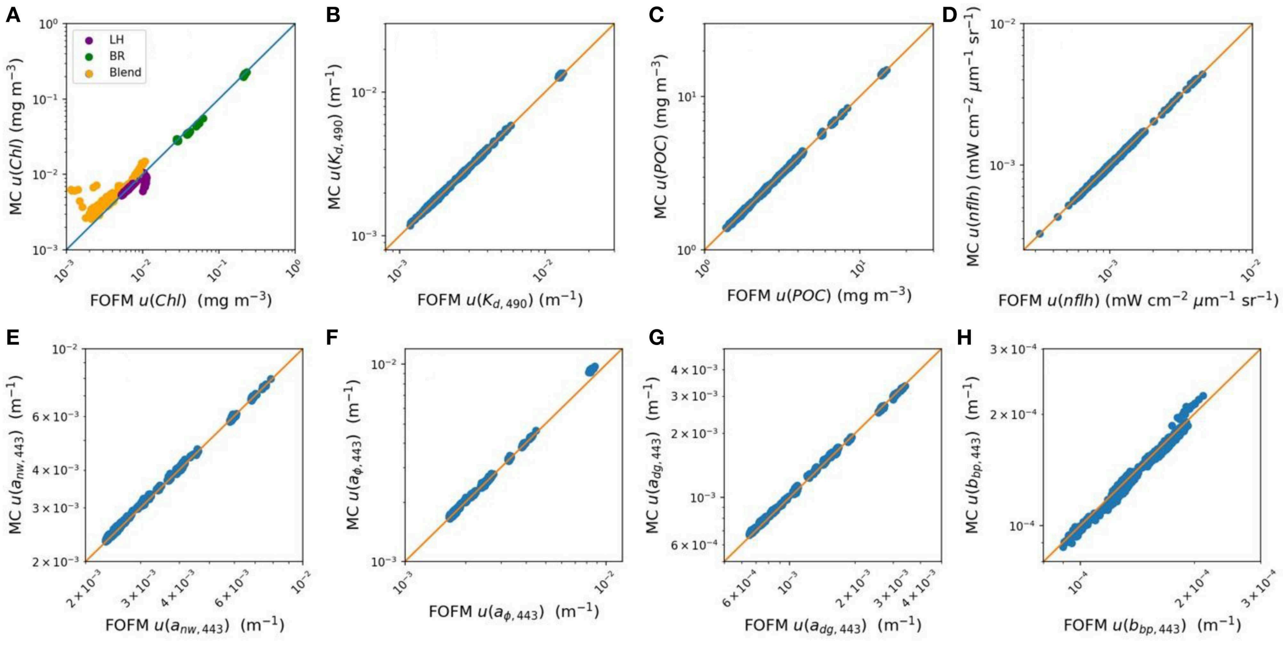

FIGURE 3 | Scatter plot comparisons of data product uncertainties estimated from FOFM with those estimated from Monte Carlo (MC) simulations. **(A–D)** OC products Chl, $K_{d,490}$, POC, and nflh, respectively. Note that the scatter plot of Chl uncertainty is color coded with respect to the method use to derive the output product (line height: purple, band ratio: green, blended: yellow). **(E–H)** IOP products $a_{nw,443}$, $a_{\phi,443}$, $a_{dg,443}$, and $b_{bp,443}$, respectively.

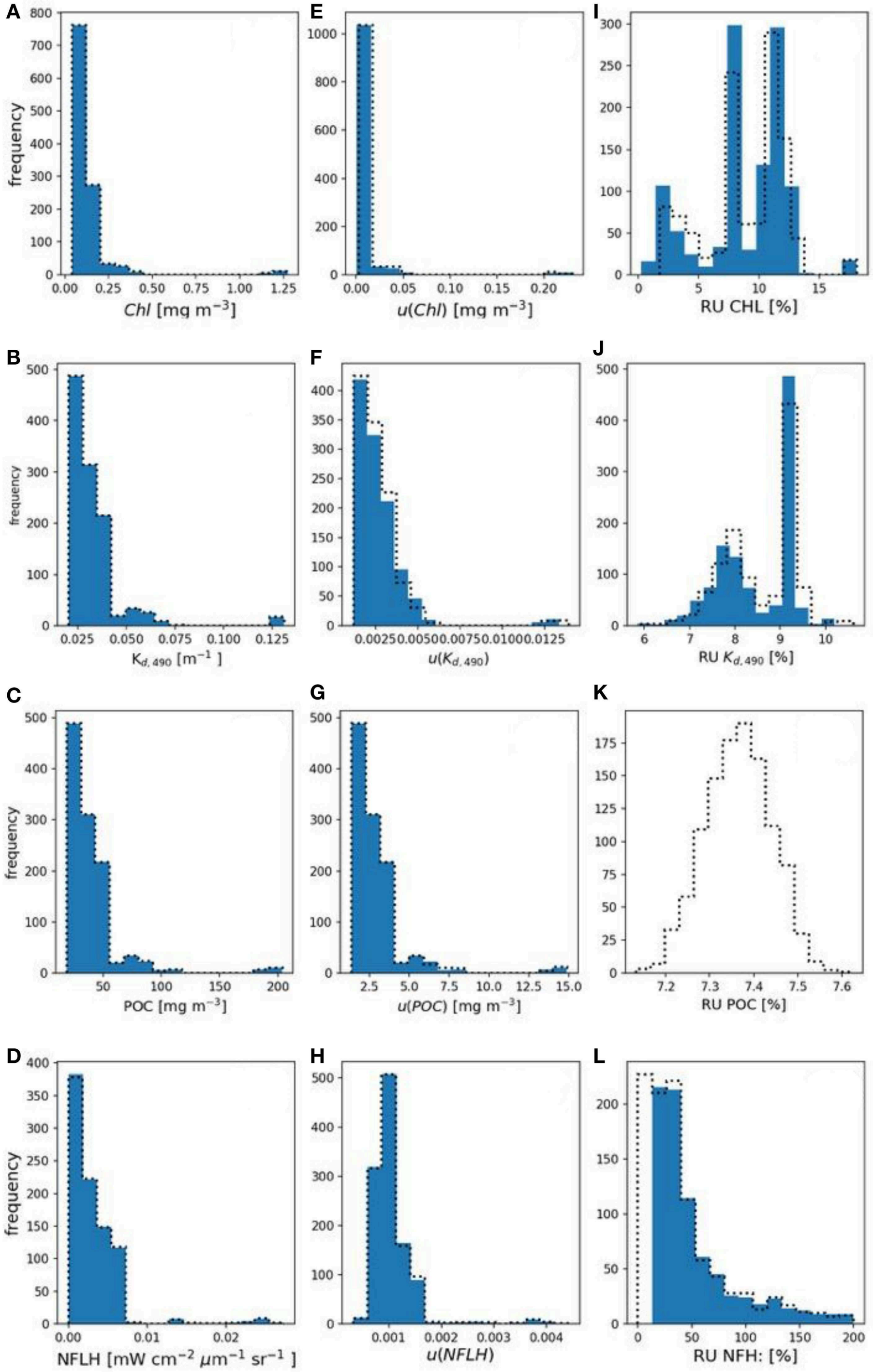

FIGURE 4 | (A–D) Histograms of derived Chl, $K_{d,490}$, POC, and nflh, respectively. **(E–H)** Histograms of FOFM-estimated uncertainties in derived Chl, $K_{d,490}$, POC, and nflh, respectively computed using 5% spectrally flat, uncorrelated uncertainty in input R_{rs}. **(I–L)** Histograms of FOFM-estimated relative uncertainties in derived Chl, $K_{d,490}$, POC, and nflh, respectively. Note: FOFM-estimates of POC relative uncertainties in this example were invariant. Dashed curves represent MC results, solid blue bars represent FOFM results.

$\times\ 10^{-3}$ and 6.70 $\times\ 10^{-3}$ mg m^{-3} for the MC and FOFM methods, respectively. The relative uncertainties for *Chl* span a single order of magnitude and have median values of 9.74 and 9.67% for the MC and FOFM methods, respectively. Although the histogram of derived *Chl* in **Figure 4** appears log-normally distributed, two distinct peaks are present; a low peak (ranging

TABLE 3 | OC products and associated uncertainties derived via MC method with 5%, uncorrelated relative uncertainty in R_{rs}.

	Derived value		Absolute uncertainty		Relative uncertainty (%)	
Product	**Range**	**Median**	**Range**	**Median**	**Range**	**Median**
Chl (mg m^{-3})	3.96×10^{-2}–1.27	0.110	2.56×10^{-5}-0.231	7.00×10^{-3}	1.73–18.2	9.74
$K_{d,490}$ (m^{-1})	2.01×10^{-2}–0.131	2.91 x10^{-2}	1.19×10^{-3}–1.36×10^{-2}	2.68×10^{-3}	5.92–10.5	8.94
POC (mg m^{-3})	18.8–203.4	33.1	1.37–14.6	2.44	7.11–7.60	7.37
nflh (mW cm^{-2} μm^{-1} sr^{-1})	5.25×10^{-6}–2.74×10^{-2}	2.20×10^{-3}	3.18×10^{-4}-4.47×10^{-3}	9.86×10^{-4}	14.8–1.7×10^{4}	41.9

TABLE 4 | OC products and associated uncertainties derived via FOFM method with 5%, uncorrelated relative uncertainty in R_{rs}.

	Derived value		Absolute uncertainty		Relative uncertainty (%)	
Product	**Range**	**Median**	**Range**	**Median**	**Range**	**Median**
Chl (mg m^{-3})	3.96×10^{-2}–1.28	0.110	3.89×10^{-5}-0.230	6.70×10^{-3}	0.26–18.7	9.67
$K_{d,490}$ (m^{-1})	2.01×10^{-2}–0.131	2.91×10^{-2}	1.18×10^{-3}–1.33×10^{-2}	2.68×10^{-3}	5.86–10.2	8.91
POC (mg m^{-3})	18.8–203.4	33.1	1.37–14.9	2.42	7.31*	7.31
nflh (mW cm^{-2} μm^{-1} sr^{-1})	2.05×10^{-6}–2.73×10^{-2}	2.19E $\times 10^{-3}$	3.21×10^{-4}–4.43×10^{-3}	9.87×10^{-4}	15.1–3.24×10^{4}	42.1

**Relative uncertainties in POC computed using FOFM method were constant over the dynamic range.*

from 0 to 0.5 mg m^{-3}) and a high peak (centered on 1.1 mg m^{-3}). Since bio-optical properties are log-normally distributed in the ocean (Campbell, 1995), the peaks observed in the distributions of derived bio-optical variables are probably due to the limited size of the hyperspectral R_{rs} dataset ($N = 1124$), that does not uniformly span the entire range of oceanic conditions (see Figure 1A in Chase et al., 2017).

The range of derived $K_{d,490}$ spans an order of magnitude with a median value of 0.0291 m^{-1}. The values of $u(K_{d,490})$ also span an order of magnitude with median values of 2.68×10^{-3} m^{-1} for both MC and FOFM calculations. The relative uncertainties for $K_{d,490}$ span a single order of magnitude and have a median value of 8.94 and 8.91% for MC and FOFM calculations, respectively. The range of derived *POC* spans two orders of magnitude with a median value of 33.1 mg m^{-3}. The values of $u(POC)$ span an order of magnitude and have median values of 2.44 and 2.42 mg m^{-3} for MC and FOFM calculations, respectively. The relative uncertainties in *POC* have a value of 7.37 and 7.31% for MC and FOFM calculations, respectively. We note that the relative uncertainty in *POC* as computed by FOFM method exhibits no spread. For uncorrelated, spectrally flat relative uncertainties, $u(POC)/POC$ is a function of $u(R_{rs,443})/R_{rs,443}$ and $u(R_{rs,555})/R_{rs,555}$. Thus, when $u(R_{rs,443})/R_{rs,443}$ and $u(R_{rs,555})/R_{rs,555}$ are fixed (e.g., at 5%), $u(POC)/POC$ is fixed. In practice, this will not always hold true, particularly when relative uncertainties in R_{rs} are variable and spectrally dependent. We note that in **Figure 4** the MC-derived relative uncertainties for *POC* are normally distributed over a narrow range centered on 7.37%.

The range of *nflh* spans three orders of magnitude with an MC-estimated median value of 2.20×10^{-3} mW cm^{-2} μm^{-1} sr^{-1}. We note that direct calculations of *nflh* resulted in a median value of 2.19×10^{-3} mW cm^{-2} μm^{-1} sr^{-1}. The values of $u(nflh)$ span an order of magnitude with median values of 9.86×10^{-4} and 9.87×10^{-4} mW cm^{-2} μm^{-1} sr^{-1} for MC and FOFM calculations, respectively. The median relative uncertainty in *nflh* was 41.9 and 42.1% for MC and FOFM calculations, respectively (**Figure 4**). We note that the range of relative errors for *nflh* is very large (for MC calculations: 14.8–1.7×10^{4}%), and these should be interpreted with a caution. Low values of *nflh*, in the order of 1×10^{-6} mW cm^{-2} μm^{-1} sr^{-1}, were derived from the evaluation dataset which in most likelihood would be beyond the detection limit of existing ocean color sensors. Further, while the absolute uncertainties associated with these low *nflh* values may also be small in magnitude, they can still manifest as large relative uncertainties.

IOP Product Uncertainties

Using the radiometric evaluation dataset, uncertainties in derived IOP products associated with 5% relative, uncorrelated uncertainty in $R_{rs,i}$ were computed following the methodology in Appendix E (**Supplementary Material**). **Figure 5** shows histograms of derived IOP products, absolute uncertainties, and relative uncertainties. MC computations are summarized in **Table 5** while FOFM computations are provided for comparative purposes in **Table 6**.

The range of derived $a_{nw,443}$ spans two orders of magnitude with a median value of 0.0185 m^{-1}. Values of $u(a_{nw,443})$ span an order of magnitude with median values of 2.31×10^{-3} and 2.26×10^{-3} m^{-1} for MC and FOFM methods, respectively. The median relative uncertainty in $a_{nw,443}$ spans a single order of magnitude and has median values of 12.6 and 12.2% for MC and FOFM methods, respectively. The range of $a_{\phi,443}$, $a_{dg,443}$, and $b_{bp,443}$ all span a single order of magnitude with median values of 9.6×10^{-3}, 8.71×10^{-3}, and 1.08×10^{-3} m^{-1}, respectively. Absolute uncertainties in IOPs all span two orders of magnitude apart from $u(a_{\phi,443})$ which spanned a single order of magnitude. Highest relative uncertainties of all GIOP-derived products are for $a_{\phi,443}$ (∼20%), whereas $a_{nw,440}$, $a_{dg,440}$, and

TABLE 5 | IOP products and associated uncertainties derived using MC method with 5%, uncorrelated relative uncertainty in R_{rs}.

	Derived value		Absolute uncertainty		Relative uncertainty (%)	
Product	**Range**	**Median**	**Range**	**Median**	**Range**	**Median**
$a_{nw}(443)$ (m^{-1})	9.40×10^{-3}–0.127	0.0185	1.79×10^{-3}–$1.13\text{x}10^{-2}$	2.31×10^{-3}	8.16–19.4	12.6
$a_{\phi}(443)$ (m^{-1})	5.80×10^{-3}–$9.43\ \text{x}10^{-2}$	9.60×10^{-3}	1.63×10^{-3}–9.68×10^{-3}	2.04×10^{-3}	10.0–29.2	21.4
$a_{dg}(443)$ (m^{-1})	3.50×10^{-3}–$3.72\ \text{x}10^{-2}$	8.71×10^{-3}	6.66×10^{-4}–5.90×10^{-3}	1.07×10^{-3}	7.92–19.9	14.5
$b_{bp}(443)$ (m^{-1})	4.18×10^{-4}–4.00×10^{-3}	1.08×10^{-3}	8.98×10^{-5}–$2.25\text{E} \times 10^{-4}$	1.34×10^{-4}	5.57–34.1	13.8

TABLE 6 | IOP products and associated uncertainties derived using FOFM method with 5%, uncorrelated relative uncertainty in R_{rs}.

	Derived value		Absolute uncertainty		Relative uncertainty (%)	
Product	**Range**	**Median**	**Range**	**Median**	**Range**	**Median**
$a_{nw,443}$ (m^{-1})	9.42×10^{-3}–0.127	0.0185	1.79×10^{-3}-1.03×10^{-2}	2.26×10^{-3}	8.12–19.1	12.2
$a_{\phi,443}$ (m^{-1})	5.86×10^{-3}–9.45×10^{-2}	9.63E-3	1.64×10^{-4}–8.73×10^{-3}	2.00×10^{-3}	9.02–28.6	20.8
$a_{dg,443}$ (m^{-1})	3.51×10^{-3}–3.70×10^{-2}	8.73E-3	6.51×10^{-4}–5.63×10^{-3}	1.05×10^{-3}	7.93–18.9	14.1
$b_{bp,443}$ (m^{-1})	4.16×10^{-4}–$4.01\text{x}10^{-3}$	1.00E-3	9.00×10^{-5}–2.11×10^{-4}	1.33×10^{-4}	5.25–34.1	13.9

$b_{bp,440}$ have relative uncertainties of similar magnitude that are all <15%.

Summary of MC and FOFM Comparisons

FOFM and MC estimates of OC and IOP uncertainties were generally in good agreement. This provides confidence that our FOFM analytical formulations were correct. However, FOFM-to-MC comparisons of *Chl* and IOP uncertainties, whilst similar in magnitude, exhibited a degree of scatter around the one-to-one line. We expect that these differences may be due to the MC method's ability to handle non-linearity and discontinuities in the models more robustly than the FOFM approach. For example, the *Chl* model has several complex features such: switching between Chl_{BR} *and* Chl_{LH}, the Chl_{BR} model's selection of maximum band ratios, and the blending of Chl_{BR} *and* Chl_{LH}, which may not be fully captured by the FOFM method.

We thus found FOFM-to-MC comparisons to be useful as a "quick acceptability checking" of FOFM calculations. In practice, however, one should not always assume the two methods will closely agree as the MC model may handle non-linearities and discontinuities more robustly than the FOFM method. The FOFM and MC calculations also indicate that for normally distributed radiometric input uncertainties, the estimated output uncertainties for OC and IOP were log-normally distributed (as per **Figures 4**, **5**). Such highly dynamic and variable nature of uncertainties in ocean color data products highlights the need for these estimates to be done on a pixel-by-pixel basis, rather than a single scene-wide estimate, further justifying the need for simplified, computationally inexpensive approach (i.e., FOFM).

We note that our FOFM uncertainty formulation for the GIOP currently does not consider uncertainty in spectral shape models [i.e., $u(a^*_{\phi,i})$ and $u(b^*_{bp,i})$]. Indeed, we believe that this may be why there were some noticeable differences when comparing FOFM and MC methods, for example: when $u(b_{bp,443}) > 2.00 \times 10^{-4}\ \text{m}^{-1}$ (**Figure 3H**). In a cursory study, we re-ran both FOFM and MC calculations with the shape models parametrized as spectral constants (i.e., having no uncertainties). This resulted in improved FOFM-to-MC comparisons (results not shown) and further highlighted how spectral shape uncertainties impact our FOFM uncertainty estimates. As part of future work, we thus plan to extend our current GIOP FOFM uncertainty formulation to include the spectral shape uncertainties. Additionally, we note that $u(a^*_{\phi,i})$ and $u(b^*_{bp,i})$, computed as functions of *Chl* and a red-green $R_{rs,i}$ ratio, respectively, are also correlated. Thus, an improved GIOP FOFM uncertainty formulation should also consider covariances between spectral shape models.

GIOP Model Misfit Uncertainties

In this analysis we used our high-quality evaluation R_{rs} dataset to approximate GIOP model misfit uncertainties. Our assumptions in this exercise were: (i) the uncertainties in our R_{rs} dataset are small, and (ii) the least squares residual of the optimal solution (model misfit) are thus due to an imperfect model.

In this analysis we first computed the error-covariance matrix, $\mathbf{E}_{\text{rrs}}$, for each R_{rs} observation as follows: (i) employ the Levenberg-Marquardt non-linear least squares optimization to iteratively find an optimal solution for the free variables x_{ϕ}, x_{dg}, and x_p which correspond to *Chl* concentration, $a_{dg,440}$, and $b_{bp,440}$, respectively (see Appendix E in **Supplementary Material** for further detail). We note that in the standard implementation of the GIOP, the cost function (Chi-squared) is unweighted. (ii) feed the optimal set of x_{ϕ}, x_{dg}, and x_p back in the forward reflectance model to compute a best-fit spectral sub-surface remote sensing reflectance, $r^{\text{mod}}_{rs,i}$. (iii) calculate the spectral residual, $\varepsilon_{rrs,i}$, between $r^{\text{mod}}_{rs,i}$ and sensor-observed subsurface

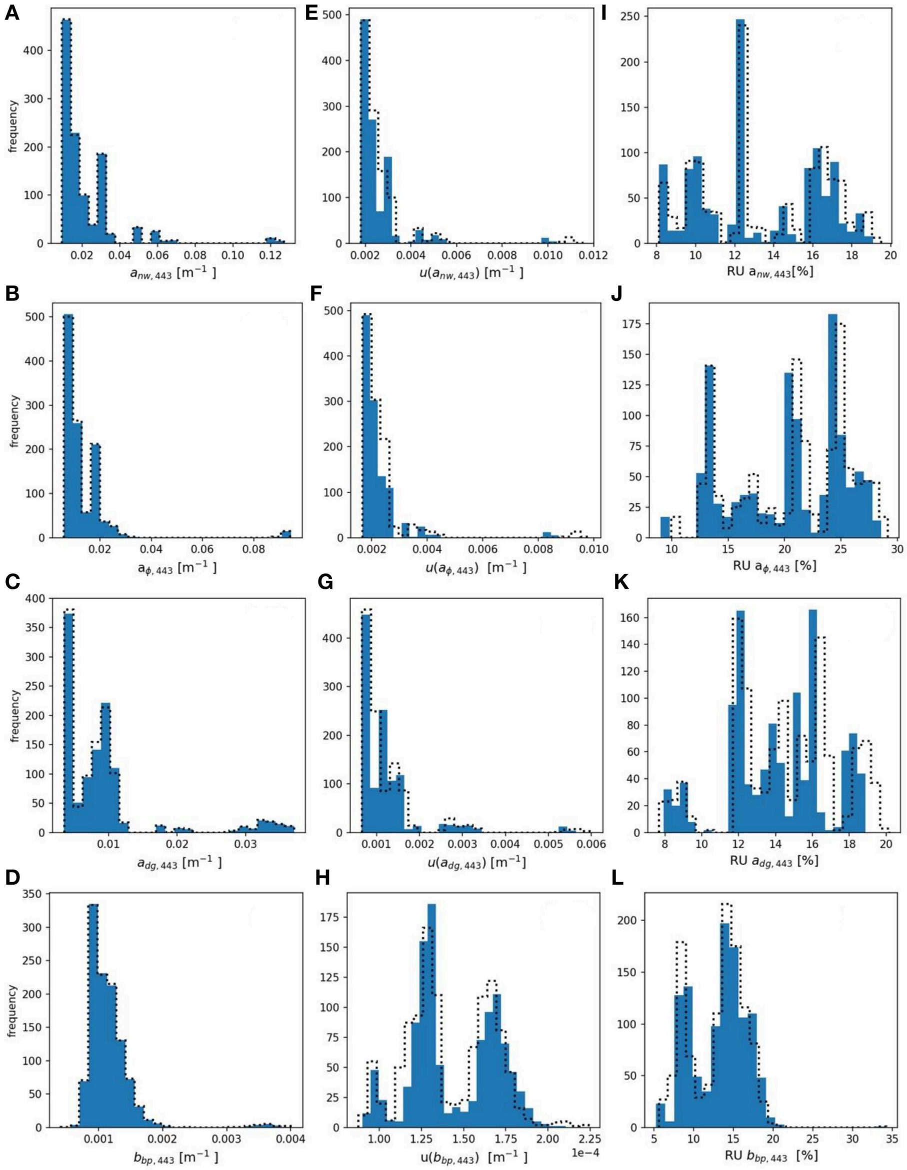

FIGURE 5 | (A–D) histograms of derived $a_{nw,443}$, $a_{dg,443}$, $a_{\phi,443}$, and $b_{bp,443}$, respectively. **(E–H)** histograms of FOFM-estimated uncertainties in derived $a_{nw,443}$, $a_{dg,443}$, a_{ϕ},443, and $b_{bp,443}$, respectively, computed using 5% spectrally flat, uncorrelated uncertainty in input R_{rs}. **(I–L)** histograms of FOFM-estimated relative uncertainties in derived $a_{nw.443}$, $a_{dg,443}$, a_{ϕ},443, and $b_{bp,443}$, respectively. Dashed curves represent MC results, solid blue bars represent FOFM results.

remote sensing reflectance. (iv) set the diagonal elements of $\mathbf{E}_{\mathrm{rrs}}$ as the square of $\varepsilon_{rrs,i}$.

Next, by substituting $\mathbf{E}_{\mathrm{rrs}}$ for $\mathbf{V}_{\mathrm{rrs}}$ in Equation E13 the parameter error-covariance matrix, $\mathbf{E}_{\mathrm{x}}$, can be computed as:

$$\mathbf{E_x} = \mathbf{J}^{-1}\mathbf{E_{rrs}}(\mathbf{J}^{\mathrm{T}})^{-1} \qquad (6)$$

Where **J** is the Jacobian matrix of the forward model (see Appendix E in **Supplementary Material** for derivation). Finally, the estimates of parameter uncertainties due to model misfit were calculated as the square root of the diagonal elements of $\mathbf{E}_{\mathrm{x}}$. The model-misfit uncertainties are summarized in **Table 7** and compared to parameter uncertainties due to Hu spectrally-dependent radiometric uncertainties (as per **Table 6**).

We found that estimated GIOP model misfit uncertainties were 60–90% smaller than those imparted by radiometric uncertainty. Thus, by combining the two during pixel-by-pixel processing, it would be possible to more completely estimate $u_{measurement}(y)$ for IOPs. However, we accept that our FOFM model-data misfit approach is approximate only and does not consider all uncertainties in the GIOP model formulation.

TABLE 7 | GIOP model-misfit uncertainties estimated using the evaluation R_{rs} dataset.

Product	Absolute uncertainty (m^{-1})		Relative uncertainty (%)		Difference between absolute data and absolute model misfit uncertainties* (%)
	Range	Median	Range	Median	Median
$a_{tw,443}$ (m^{-1})	3.88×10^{-4} –5.71×10^{-3}	4.87×10^{-4}	1.26–5.70	3.15	−77
$a_{\phi,443}$ (m^{-1})	3.67×10^{-4}–5.25×10^{-3}	4.54×10^{-4}	3.02–9.09	4.68	−77
$a_{dg,443}$ (m^{-1})	1.07×10^{-4}–2.26×10^{-3}	1.434×10^{-4}	0.81–7.48	2.86	−86
$b_{bp,443}$ (m^{-1})	2.94×10^{-5}–2.17×10^{-4}	5.22×10^{-5}	1.57–9.58	4.52	−61

*Differences between median absolute model uncertainties in this table and median absolute radiometric (data) uncertainties (column RU: Hu in **Table 9**).

Comparing Product Uncertainties Due to Various Radiometric Input Uncertainties

In order to evaluate the impact of different R_{rs} uncertainty values on derived product uncertainties, using the FOFM method we: (i) propagated spectrally flat, uncorrelated R_{rs} relative uncertainties of 1, 5, and 10% through OC and IOP models, and (ii) propagated spectrally-dependent, uncorrelated $u(R_{rs})$ through OC and IOP models by linearly interpolating/extrapolating tabulated data published by Hu et al. (2013), referred to as "Hu uncertainties" (see **Figure 2**). Summary results of this analysis are given in **Tables 8**, **9**. As expected, introducing spectrally flat, uncorrelated R_{rs} uncertainties of lower and higher value than the previously evaluated 5%, resulted in respectively, lower and higher uncertainties in data products, while the distribution of uncertainties kept the same shape as for the 5% run (**Figure 6**). For the product uncertainties derived using the "Hu R_{rs} uncertainties," both the shape of the distribution and median values changed from the 5% run (**Figure 6**). These results demonstrate the importance of considering spectral dependence in radiometric uncertainties. Notably, considering spectrally flat 5% relative uncertainties in R_{rs} for a data product such as *nflh*, which utilizes red-end bands, may result in significant underestimation of likely data product uncertainties.

Spectrally flat relative uncertainty in R_{rs} (e.g., 5% in the blue-green region) is a commonly used accuracy goal for ocean color missions. However, we know from on-orbit data that sensors such as SeaWiFS and MODIS have largely not achieved their desired accuracy goals over the full spectral range (Hu et al., 2013), particularly at red wavelengths. In lieu of any knowledge of a sensor's radiometric uncertainty characteristics (e.g., during design trade studies), one might decide to utilize desired relative radiometric accuracy goals to approximate ocean color data product uncertainties. However, our results have shown spectrally flat (5%) and spectrally-dependent (Hu) relative R_{rs} uncertainties lead to different estimates of OC and IOP uncertainties. Indeed, for improved uncertainty estimates, we recommend the use of more representative spectrally-dependent $u(R_{rs})/R_{rs}$, if known.

Application to Satellite Chlorophyll Image

The potential impact that spectrally-correlated uncertainties in R_{rs} have upon ocean color data product uncertainties was evaluated using a scene of the southern Hawaiian Islands captured on 1 December 2000 (**Figure 7**). We have estimated on a pixel-by-pixel basis the covariance matrix of remote sensing reflectances, $\mathbf{V}_{\mathrm{Rrs}}$, as per the methodology described in Appendix F (**Supplementary Material**). Estimates of $u(Chl)$ were then calculated both with- and without the off-diagonal terms in $\mathbf{V}_{\mathrm{Rrs}}$ to demonstrate the impact of incorporating covariance terms (if known) when estimating uncertainties.

The sample SeaWiFS *Chl* image (**Figure 7A**) shows that the clearest waters occurred southeast of Island of Hawaii (largest island) with two large eddies to the west. Regions of elevated *Chl* concentration are also visible along the northeast coast of the Island of Hawaii, and also adjacent to coastal waters of four islands (Maui, Lanai, Molokai, and Kahoolawe) to the northwest of Hawaii. Derived Chl_{blend} ranges from 1.83×10^{-3} to 0.498 mg m^{-3} with a median of 0.066 mg m^{-3}. When the off-diagonal terms in $\mathbf{V}_{\mathrm{Rrs}}$ were considered, the estimated values of $u(Chl)$ ranged from 1.30×10^{-3} to 0.075 mg m^{-3} with a scene-wide median of 5.20×10^{-3} mg m^{-3} (**Figure 7B**) and the relative uncertainties spanned 0.84–38.6% with a median of 7.89% (**Figure 7C**). When the off-diagonal terms in $\mathbf{V}_{\mathrm{Rrs}}$ were not considered (i.e., set to zero), estimated values of $u(Chl)$ ranged from 1.30×10^{-3} to 0.109 mg m^{-3} with a scene-wide median of 5.50×10^{-3} mg m^{-3} (**Figure 7D**) and relative uncertainties spanning 0.85–46.1 % with a median of 8.27% (**Figure 7E**). Note, these image statistics were computed with standard NASA level-2 quality control flags applied to remove the effect of: land, clouds, sun glint, atmospheric correction failure, product failure, and straylight contamination.

These results demonstrate how a FOFM method can be utilized in operational processing code to estimate uncertainties in derived bio-optical data products. The FOFM method was straightforward to implement within l2gen code and did not add any appreciable processing overhead. Whilst our estimation of $\mathbf{V}_{\mathrm{Rrs}}$ is rudimentary (Appendix F in **Supplementary Material**), it allowed us to consider the covariance terms in the FOFM derivation of $u(Chl)$. Critically, we demonstrated that the inclusion of off-diagonal covariance terms from $\mathbf{V}_{\mathrm{Rrs}}$ led to lower estimates of both $u(Chl)$ and $u(Chl)/Chl$ when compared to the same calculations performed with off-diagonal elements of $\mathbf{V}_{\mathrm{Rrs}}$ set to zero; a result consistent with findings of Lamquin et al. (2013). Additionally, this example was done with an operational processing code, demonstrating the easiness of implementing a FOFM method within day-to-day ocean color processing.

TABLE 8 | Median OC data product uncertainties computed as relative uncertainties (RU) in R_{rs} vary.

	Median absolute uncertainties				Median relative uncertainties (%)			
	RU: 1%	**RU: 5%**	**RU: 10%**	**RU: Hu**	**RU: 1%**	**RU: 5%**	**RU: 10%**	**RU: Hu**
Product								
Chl (mg m^{-3})	1.52×10^{-3}	6.70×10^{-3}	1.46×10^{-2}	6.50×10^{-3}	1.96	9.67	19.35	8.29
$K_{d,490}$ (m^{-1})	5.37×10^{-4}	2.68×10^{-3}	5.36×10^{-3}	5.07×10^{-3}	1.78	8.91	17.8	17.3
POC (mg m^{-3})	4.84×10^{-1}	2.42	4.84	4.38	1.46	7.31	14.6	13.1
nflh (mW cm^{-2} μm^{-1} sr^{-1})	1.97×10^{-4}	9.87×10^{-4}	1.97×10^{-3}	4.47×10^{-3}	8.41	42.1	84.1	197.6

TABLE 9 | Median IOP data product uncertainties computed as relative uncertainties (RU) in R_{rs} vary.

	Median absolute uncertainties				Median relative uncertainties (%)			
	RU: 1%	**RU: 5%**	**RU: 10%**	**RU: Hu**	**RU: 1%**	**RU: 5%**	**RU: 10%**	**RU: Hu**
Product								
$a_{tw,443}$ (m^{-1})	4.52×10^{-4}	2.26×10^{-3}	4.52×10^{-3}	2.76×10^{-3}	2.45	12.2	24.5	15.1
$a_{\phi,443}$ (m^{-1})	4.00×10^{-4}	2.00×10^{-3}	4.00×10^{-3}	2.42×10^{-3}	4.15	20.8	41.6	23.8
$a_{dg,443}$ (m^{-1})	2.11×10^{-4}	1.05×10^{-3}	2.11×10^{-3}	1.33×10^{-3}	2.82	14.1	28.2	15.9
$b_{bp,443}$ (m^{-1})	2.67×10^{-5}	1.33×10^{-4}	2.67×10^{-4}	1.73×10^{-4}	2.78	13.9	27.9	17.9

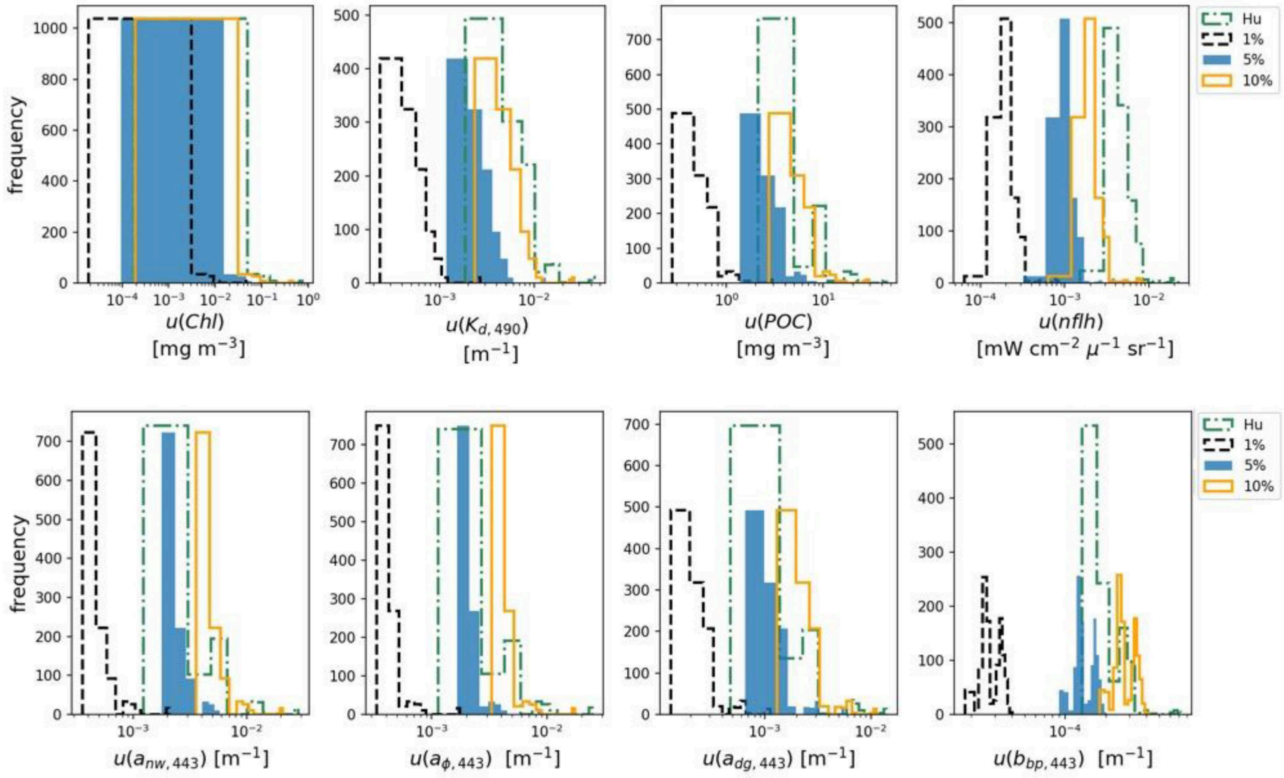

FIGURE 6 | Upper row are histograms of derived OC data products uncertainties estimated using the FOFM method. Bottom row are histograms of derived IOP data product uncertainties estimated using the FOFM method. The four histograms in each subplot correspond to four different input u(R_{rs}): spectrally flat R_{rs} relative uncertainties of 1% (dashed black), 5% (blue), and 10% (orange) as well as spectrally dependent relative uncertainties taken from Hu et al. (2013) outlined in green dashed line.

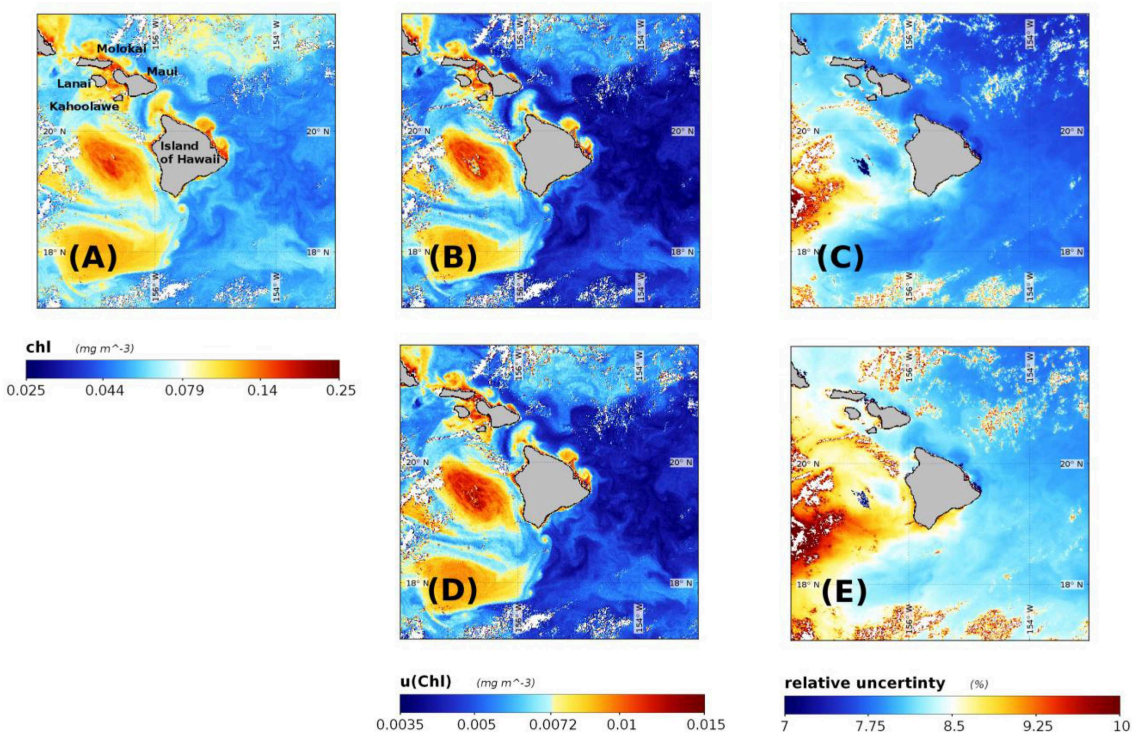

FIGURE 7 | Derived data products for a SeaWiFS image of waters surrounding the Hawaii Islands captured on 1 December 2000. **(A)** Chl concentration derived using OCI algorithm, **(B)** u(Chl) computed with covariances included, **(C)** relative uncertainty in Chl computed with estimated R_{rs} covariances included, **(D)** u(Chl) calculated without estimated R_{rs} covariances included, and **(E)** relative uncertainty in Chl computed without estimated R_{rs} covariances included.

POC Algorithm Case Study

Recall from Equation 1, we broadly defined measurement uncertainty as having two sources: data uncertainty and model uncertainty. Throughout this paper we have focused heavily on deriving data uncertainties (i.e., propagation of radiometric uncertainty) which is useful if one is trying understand how a specific sensor's noise characteristics may impact derived data product uncertainties. However, this information alone does not provide a complete picture of measurement uncertainty; model uncertainty also needs to be considered. We thus wish to demonstrate how with knowledge of model uncertainties one can draw more complete conclusions about biogeochemically-relevant data product uncertainties. As such, we present a case study in which we estimate *POC* measurement uncertainty for two different algorithms: (i) Stramski et al. (2008a) and (ii) Rasse et al. (2017).

Our motivation here is to solely demonstrate how one might develop algorithm uncertainty budgets (data and model uncertainty as per Equation 1) using a FOFM framework. Our calculations, however, are limited by: (i) the representativeness of our *in situ* R_{rs} dataset which does not encompass all optical water-types found in the World's oceans, (ii) our spectral $u(R_{rs})$ values which are estimated from data published by Hu et al. (2013) for a MODIS-like sensor without co-variance terms, and (iii) our knowledge of model uncertainties, such as coefficients uncertainties, which is limited to those reported in literature and/or our best-guess estimates. We hence caution the reader should not use our reported numbers as a basis for algorithm selection.

POC Measurement Uncertainty Estimates

In this exercise, we performed rudimentary calculations to estimate measurement uncertainty budgets for two *POC* algorithms: (i) NASA's standard *POC* algorithm (Stramski et al., 2008a) and (ii) the IOP-based model of Rasse et al. (2017). Conveniently for this exercise, both *POC* models have a power law formulation:

$$POC = a_{poc} X^{b_{poc}} \tag{7}$$

where X in Stramski et al. (2008a) is a blue-to-green reflectance ratio ($R_{rs,443}/R_{rs,555}$, as per Appendix C in **Supplementary Material**) and the coefficients a_{poc} and b_{poc} have the values of 203.2 and −1.034, respectively. For the approach of Rasse et al. (2017) X is $b_{bp,470}$ and the coefficients a_{poc} and b_{poc} have the values of 141,253 and 1.18, respectively. Note, in this case study we use GIOP-derived estimates of $b_{bp,470}$ as inputs to the Rasse et al. (2017) model.

First, let us consider the model uncertainty component due to imperfect model coefficients. For both *POC* algorithms, with the coefficients a_{poc} and b_{poc} and their assigned uncertainties of $u_{model}(a_{poc})$ and $u_{model}(b_{poc})$, respectively, we can estimate the model variance for *POC* as:

$$
\begin{aligned}
u^2_{\mathrm{model}}(POC) = {} & \left(X^{b_{poc}}\right)^2 u^2_{\mathrm{model}}(a_{poc}) \\
& + \left(a_{poc} X^{b_{poc}} \log(X)\right)^2 u^2_{\mathrm{model}}(b_{poc}) \\
& + \left(a_{poc} b_{poc} X^{b_{poc}-1}\right)^2 u^2_{\mathrm{model}}(X)
\end{aligned} \tag{8}
$$

In the third term on the right-hand side of Equation 8, we set $u_{model}(X) = 0$ and $u_{model}(X) = u_{model}(b_{bp,470})$ for Stramski et al. (2008a) and Rasse et al. (2017), respectively. We have also assumed the covariance of the coefficients a_{poc} and b_{poc}, which are determined by regression fit, is zero. For the Rasse et al. (2017) model, the reported model coefficient uncertainties $u_{model}(a_{poc})$ and $u_{model}(b_{\mathrm{poc}})$ are 45,534 and 0.046, respectively. For the Stramski et al. (2008a) model, values of $u_{model}(a_{poc})$ and $u_{model}(b_{\mathrm{poc}})$ were not reported. We did, however, estimate these model uncertainties by reanalyzing the original published dataset (Stramski et al., 2008b) and considering the likely uncertainty introduced by not accounting for the effect of filter pad absorption of *POC* (Novak et al., 2018). Following this cursory analysis (results not shown), we estimated $u_{model}(a_{poc})$ and $u_{model}(b_{\mathrm{poc}})$ for the Stramski et al. (2008a) model to be ~2.20 and 0.015, respectively.

Next, we considered the data uncertainty component. The Stramski et al. (2008a) model's data uncertainty FOFM calculus was formulated in Appendix C (**Supplementary Material**). For the Rasse et al. (2017) model, we first estimated $u_{data}(b_{bp},_{470})$. To do so, $b_{bp},_{470}$ was calculated from GIOP-derived $b_{bp},_{440}$ as:

$$b_{bp,470} = b_{bp,440} \times \left(\frac{440}{470}\right)^{\gamma} \tag{9}$$

The variance in $b_{bp},_{470}$ due to data uncertainty was then estimated as:

$$
\begin{aligned}
u^2_{data}(b_{bp,470}) = {} & \left(\frac{\partial b_{bp,470}}{\partial b_{bp,440}}\right)^2 u^2_{data}(b_{bp,440}) + \left(\frac{\partial b_{bp,470}}{\partial \gamma}\right)^2 u^2_{data}(\gamma) \\
& + 2\frac{\partial b_{bp,470}}{\partial b_{bp,440}} \frac{\partial b_{bp,470}}{\partial \gamma} u^2_{data}(b_{bp,440}, \gamma)
\end{aligned} \tag{10}
$$

For this exercise, we used GIOP-derived values of $u_{data}(b_{bp},_{470})$ and $u(\gamma)$. The correlation between derived values of b_{bp},547 and γ was used to estimate the covariance term $u(b_{bp},_{547,}\ \gamma)$ as $-1.64 \times 10^{-6}\ \mathrm{m}^{-1}\ \mathrm{nm}^{-1}$. Using, the GUM methodology the variance in the Rasse et al. (2017) *POC* model due to data uncertainty was then estimated as:

$$u^2_{data}(POC) = \left(a_{poc} b_{poc} (b_{bp,470})^{b_{poc}-1}\right)^2 u^2_{data}(b_{bp,470}) \tag{11}$$

We finally estimated the measurement uncertainty budgets for both *POC* models using our R_{rs} evaluation dataset and with Hu spectrally-dependent, uncorrelated radiometric uncertainties (results are shown in **Table 10**).

TABLE 10 | Simplified random uncertainty budgets for two POC models.

Algorithm	**Median derived value (mg m^{-3})**	**Median absolute uncertainty in mg m^{-3} (median relative uncertainty in %)**		
		Data	**Model**	**Measurement**
Stramski et al., 2008a	33.1	4.40 (13.1)	0.94 (2.85)	4.50 (16.6)
Rasse et al., 2017	37.8	6.96 (18.4)	17.30 (45.8)	18.6 (49.2)

Median absolute uncertainties and median relative uncertainties were computed using our R_{rs} evaluation dataset with Hu spectrally-dependent, uncorrelated radiometric uncertainties and basic knowledge of model coefficient uncertainty. We note that these data are intended to illustrate how one might formulate measurement uncertainty budgets. These data are not intended for algorithm comparison purposes.

In our rudimentary measurement uncertainty budget for the Stramski et al. (2008a) *POC* algorithm, we found the contribution of data (radiometric) uncertainty was larger than model uncertainty. Conversely, for the Rasse et al. (2017) *POC* algorithm, the contribution of model uncertainty was larger than data uncertainty. Whilst these *POC* algorithm uncertainty budgets may not be fully representative due to the assumptions we partook here, the exercise nonetheless demonstrates an important point: data and model uncertainties should both be considered if one wishes to use uncertainties as a means of benchmarking/comparing ocean color algorithms.

From an algorithm development perspective one can also use FOFM method to explore the relative contribution of individual uncertainty sources to the combined measurement uncertainty. We have graphically displayed the estimated component uncertainty contribution for each *POC* algorithm using pie charts (**Figure 8**). Such information may assist algorithm designers identify and minimize uncertainty sources within a model.

Summary of POC Case Study

Our brief example demonstrates the benefits of using the FOFM method for analytically estimating measurement uncertainty in *POC*. From an ecological perspective, this is particularly useful if one is trying to understand the variability in observed patterns, and distinguish real change from variation in uncertainty. Additionally, it allows for sensitivity analysis, thereby providing a guideline for improving model parameterization. The case study demonstrates how an uncertainty budget can provide additional information to end-users regarding data product quality, potentially informing algorithm selection, and/or guiding new algorithm development. Although ocean color algorithms are typically benchmarked based upon validation matchup metrics (Seegers et al., 2018), we expect model selection and development may be better guided by considering how data and model uncertainties manifest in derived data products.

This case study highlights a challenge if one wishes to compare/benchmark legacy ocean color algorithms based on their measurement uncertainty; one must have reasonable and complete knowledge of both data and model uncertainties to do so. Whilst we have demonstrated that it is possible to

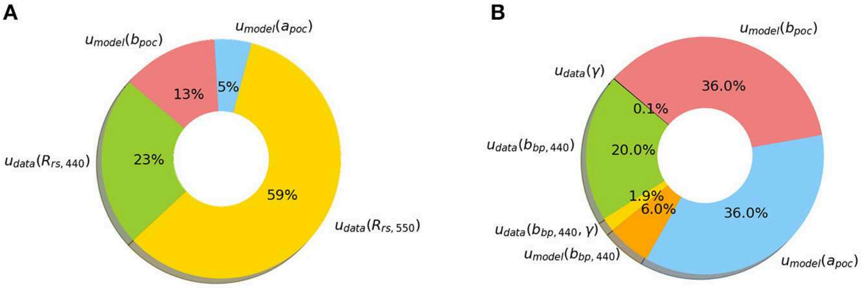

FIGURE 8 | Pie charts demonstrate how individual uncertainty sources contribute to estimates of total measurement uncertainty. Here we consider: **(A)** a blue-green band-ratio *POC* algorithm and **(B)** an IOP-based *POC* algorithm. We note that these examples are intended to illustrate how one might visualize source contributions to measurement uncertainty. These plots are not intended for algorithm comparison purposes.

estimate and propagate random radiometric uncertainties using the FOFM framework, estimating model uncertainties remains a challenge. This is because model component uncertainties (e.g., model coefficient uncertainties) of legacy ocean color algorithms were not routinely reported. To address this, re-analysis of the structure of legacy ocean color algorithms using high quality bio-optical datasets, such as NASA's bio-Optical Marine Algorithm Dataset (NOMAD; Werdell and Bailey, 2005), may be necessary. Without such knowledge, it remains a challenge to formulate complete measurement uncertainty budgets for legacy ocean color algorithms.

CONCLUSIONS

In this paper we demonstrated a FOFM-based method for estimating uncertainties in a selection of NASA OC and IOP products, namely: *Chl*, $K_{d,490}$, *POC*, *nflh*, $a_{nw,440}$, $a_{\phi,440}$, $a_{dg,440}$, and $b_{bp,440}$, due to sensor-observed radiometric uncertainty. Using a high quality hyperspectral R_{rs} dataset subsampled to our target wavelengths, we first appraised the FOFM methodology by comparing FOFM-derived uncertainty estimates with uncertainties estimated from MC simulations with an assumed relative spectrally flat, uncorrelated uncertainty in R_{rs} of 5%. Our analyses showed that OC and IOP uncertainties estimated using the FOFM method generally agreed with MC simulations. Collectively, the FOFM-to-MC comparisons provided a basis for checking the correctness of the FOFM formulations, which are often algebraically complex. Further, we demonstrated that the FOFM formulation, which is computationally inexpensive, can be applied in routine pixel-by-pixel data processing for estimating uncertainties in derived ocean color data products.

This paper has primarily focused on propagating radiometric uncertainties through bio-optical models ($u_{data}(y)$ in Equation 1). In practice, the combined measurement uncertainty in derived ocean color data products is expected to be larger once model uncertainties are included. In this study, we have broadly assumed that coefficients within the bio-optical algorithms themselves are errorless, which is not the case. Indeed, most coefficients in bio-optical algorithms have been derived empirically using *in situ* oceanographic datasets, which themselves have inherent uncertainties due to measurement method and environmental variability. The GIOP, for example, makes assumptions about spectral shapes of IOPs, utilizes an approximate forward reflectance model (Gordon et al., 1988), and employs a model to convert $R_{rs,i}$ to $r_{rs,i}$ (Lee et al., 2002). Thus, there are a number of GIOP model components whose uncertainties, if characterized, may improve the overall estimate of IOP measurement uncertainty. Our case study of *POC* algorithms also highlighted how the addition of model (e.g., coefficient) uncertainties can further inform end-users, and may potentially guide algorithm development and/or selection.

Although this work represents a first step toward implementing pixel-by-pixel uncertainty estimates in NASA operational ocean color processing code, we recognize that continued effort is required. For example, strategies for quantifying uncertainties in look-up-table (LUT) based models, such as the two-band particulate inorganic carbon (PIC) algorithm (Balch et al., 2005) and bidirectional reflectance distribution function (BRDF) correction (Morel et al., 2002), are needed. Globally, there are a multitude of ocean color algorithms maintained by various researchers and/or institutes and formulating uncertainty estimates must be a collective effort. While the community continues to innovate new bio-optical algorithms, we strongly encourage model developers to characterize uncertainties as a matter of routine.

As we enter the hyperspectral world of PACE, it is credible to expect an evolutionary leap in remote sensing observation of ocean processes detailing, for example, phytoplankton diversity, physiological preferences, and ecology from space. This, parallel to the increase in computational power of the day-to-day data processing, will allow for more complex algorithms; algorithms which will need detailed evaluation of uncertainty budgets, to understand what is real, and what is hidden under the dashed line.

AUTHOR CONTRIBUTIONS

LM, IC, and PW: conceptualization, methodology, simulations, and data analysis. AC and IC: hyperspectral dataset. LM, IC, PW, and AC: original draft, reviewing, and editing.

FUNDING

This research was funded by the National Aeronautics and Space Administration (NASA) Ocean Biology and Biogeochemistry Program via an award under the solicitation *The Science of Terra, Aqua, and Suomi NPP*, Ocean Biology and Biogeochemistry (NNX13AC42G), and PACE mission.

ACKNOWLEDGMENTS

Many thanks to NASA Ocean Biology Processing Group staff for their advice during the preparation of this manuscript. The authors are thankful for all the scientists that contributed to collection of this dataset, especially Wayne Slade and Nicole Poulton, and captains and crews of the UNOLS research vessels. We are also very grateful to the two reviewers for their detailed and insightful comments which have greatly improved this work.

SUPPLEMENTARY MATERIAL

The Supplementary Material for this article can be found online at: https://www.frontiersin.org/articles/10.3389/feart.2019.00176/full#supplementary-material

REFERENCES

Angal, A., Xiong, X., Sun, J., and Geng, X. (2015). On-orbit noise characterization of MODIS reflective solar bands. *J. Appl. Remote Sens.* 9:094092.

Antoine, D., d'Ortenzio, F., Hooker, S. B., Bécu, G., Gentili, B., Tailliez, D., et al. (2008). Assessment of uncertainty in the ocean reflectance determined by three satellite ocean color sensors (MERIS, SeaWiFS and MODIS-A) at an offshore site in the Mediterranean Sea (BOUSSOLE project). *J. Geophys. Res. Oceans* 113, 1–22. doi: 10.1029/2007JC004472

Bailey, S. W., Franz, B. A., and Werdell, P. J. (2010). Estimation of near-infrared water-leaving reflectance for satellite ocean color data processing. *Opt. Express* 18, 7521–7527. doi: 10.1364/OE.18.007521

Bailey, S. W., and Werdell, P. J. (2006). A multi-sensor approach for the on-orbit validation of ocean color satellite data products. *Remote Sens. Environ.* 102, 12–23. doi: 10.1016/j.rse.2006.01.015

Balch, W. M., Gordon, H. R., Bowler, B. C., Drapeau, D. T., and Booth, E. S. (2005). Calcium carbonate measurements in the surface global ocean based on Moderate-Resolution Imaging Spectroradiometer data. *J. Geophys. Res. Oceans* 110, 1–21. doi: 10.1029/2004JC002560

Behrenfeld, M. J., Westberry, T. K., Boss, E. S., O'Malley, R. T., Siegel, D. A., Wiggert, J. D., et al. (2009). Satellite-detected fluorescence reveals global physiology of ocean phytoplankton. *Biogeosciences* 6, 779–794. doi: 10.5194/bg-6-779-2009

Campbell, J. W. (1995). The lognormal distribution as a model for bio-optical variability in the sea. *J. Geophys. Res. Oceans* 100, 13237–13254. doi: 10.1029/95JC00458

Chase, A. P., Boss, E., Cetinić, I., and Slade, W. (2017). Estimation of phytoplankton accessory pigments from hyperspectral reflectance spectra: toward a global algorithm. *J. Geophys. Res. Oceans* 122, 9725–9743. doi: 10.1002/2017JC012859

Eplee, J. R. E., Patt, F. S., Barnes, R. A., and McClain, C. R. (2007). SeaWiFS long-term solar diffuser reflectance and sensor noise analyses. *Appl. Opt.* 46, 762–773. doi: 10.1364/AO.46.000762

Franz, B. A., Behrenfeld, M. J., Siegel, D. A., and Signorini, S. R. (2017). Global ocean phytoplankton [in: State of the Climate in 2016]. *Bull. Amer. Meteor. Soc.* 99, S94–S96. doi: 10.1175/2018BAMSStateoftheClimate.1

Gillis, D. B., Bowles, J. H., Montes, M. J., and Moses, W. J. (2018). Propagation of sensor noise in oceanic hyperspectral remote sensing. *Opt. Express* 26, A818–A831. doi: 10.1364/OE.26.00A818

Gordon, H. R., Brown, O. B., Evans, R. H., Brown, J. W., Smith, R. C., Baker, K. S., et al. (1988). A semianalytic radiance model of ocean color. *J. Geophys. Res. Atmos.* 93, 10909–10924. doi: 10.1029/JD093iD09p10909

Gordon, H. R., and Wang, M. (1994). Retrieval of water-leaving radiance and aerosol optical thickness over the oceans with SeaWiFS: a preliminary algorithm. *Appl. Opt.* 33, 443–452. doi: 10.1364/AO.33.000443

Gould, W. G., McCarthy, S. E., Coelho, E., Shulman, I., and Richman, J. G. (2014). Combining satellite ocean color and hydrodynamic model uncertainties in bio-optical forecasts. *J. Appl. Remote Sens.* 8:083652 doi: 10.1117/1.JRS.8.083652

Hooker, S. B., Esaias, W. E., Feldman, G. C., Gregg, W. W., and McClain, C. R. (1992). *An Overview of SeaWiFS and Ocean-Color, NASA Tech. Memo. 104566*, Vol. 1, eds S. B. Hooker, and E. R. Firestone. Greenbelt, MD: NASA Goddard Space Flight Center, 24.

Hooker, S. B., and McClain, C. R. (2000). The calibration and validation of SeaWiFS data. *Prog. Oceanogr.* 45, 427–465. doi: 10.1016/S0079-6611(00)00012-4

Hu, C., Feng, L., and Lee, Z. (2013). Uncertainties of SeaWiFS and MODIS remote sensing reflectance: implications from clear water measurements. *Remote Sens. Environ.* 133, 168–182. doi: 10.1016/j.rse.2013.02.012

Hu, C., Feng, L., Lee, Z., Davis, C. O., Mannino, A., McClain, C. R., et al. (2012a). Dynamic range and sensitivity requirements of satellite ocean color sensors: learning from the past. *Appl. Opt.* 51, 6045–6062. doi: 10.1364/AO.51.006045

Hu, C., Lee, Z., and Franz, B. (2012b). Chlorophyll a algorithms for oligotrophic oceans: a novel approach based on three-band reflectance difference. *J. Geophys. Res. Oceans* 117(C1), 1–25. doi: 10.1029/2011JC007395

IOCCG (2008). *Why Ocean Colour? The Societal Benefits of Ocean- Colour Technology*, Vol. 7. Dartmouthn, NS: IOCCG.

Jay, S., Guillaume, M., Chami, M., Minghelli, A., Deville, Y., Lafrance, B., et al. (2018). Predicting minimum uncertainties in the inversion of ocean color geophysical parameters based on Cramer-Rao bounds. *Opt. Express* 26, A1–A18. doi: 10.1364/OE.26.0000A1

JCGM (2008). *Evaluation of Measurement Data - Guide to the Expression of Uncertainty in Measurement*. JCGM 100:2008.

Lamquin, N., Mangin, A., Mazeran, C., Bourg, B., Bruniquel, V., and D'Andon, O. F. (2013). *OLCI L2 Pixel-by-Pixel Uncertainty Propagation in OLCI Clean Water Branch*. ESA ATBD ref. S3-L2-SD-01-C01-ACR-TN.

Lee, Z., Arnone, R., Hu, C., Werdell, P. J., and Lubac, B. (2010). Uncertainties of optical parameters and their propagations in an analytical ocean color inversion algorithm. *Appl. Opt.* 49, 369–381. doi: 10.1364/AO.49.000369

Lee, Z., Carder, K. L., and Arnone, R. A. (2002). Deriving inherent optical properties from water color: a multiband quasi-analytical algorithm for optically deep waters. *Appl. Opt.* 41, 5755–5772. doi: 10.1364/AO.41.005755

Lee, Z., Du, K., Voss, K. J., Zibordi, G., Lubac, B., Arnone, R., et al. (2011). An inherent-optical-property-centered approach to correct the angular effects in water-leaving radiance. *Appl. Opt*. 50, 3155–3167. doi: 10.1364/AO.50.003155

Maritorena, S., d'Andon, O. H. F., Mangin, A., and Siegel, D. A. (2010). Merged satellite ocean color data products using a bio-optical model: characteristics, benefits and issues. *Remote Sens. Environ.* 114, 1791–1804. doi: 10.1016/j.rse.2010.04.002

McClain, C. R. (2009). A decade of satellite ocean color observations. *Ann. Rev. Mar. Sci.* 1, 19–42. doi: 10.1146/annurev.marine.010908.163650

McClain, C. R., Feldman, G. C., and Hooker, S. B. (2004). An overview of the SeaWiFS project and strategies for producing a climate research quality global ocean bio-optical time series. *Deep Sea Res. Part II Topical Stud. Oceanogr.* 51, 5–42. doi: 10.1016/j.dsr2.2003.11.001

McKinna, L. I. W., Werdell, P. J., and Proctor, C. W. (2016). Implementation of an analytical Raman scattering correction for satellite ocean-color processing. *Opt. Express* 24, A1123–A1137. doi: 10.1364/OE.24.0A1123

Mekid, S., and Vaja, D. (2008). Propagation of uncertainty: expressions of second and third order uncertainty with third and fourth moments. *Measurement* 41, 600–609. doi: 10.1016/j.measurement.2007.07.004

Melin, F. (2010). Global distribution of the random uncertainty associated with satellite-derived Chl a. *IEEE Geosci. Remote Sens. Lett.* 7, 220–224. doi: 10.1109/LGRS.2009.2031825

Mélin, F., Sclep, G., Jackson, T., and Sathyendranath, S. (2016). Uncertainty estimates of remote sensing reflectance derived from comparison of ocean color satellite data sets. *Remote Sens. Environ.* 177, 107–124. doi: 10.1016/j.rse.2016.02.014

Moore, T. S., Campbell, J. W., and Dowell, M. D. (2009). A class-based approach to characterizing and mapping the uncertainty of the MODIS ocean chlorophyll product. *Remote Sens. Environ.* 113, 2424–2430. doi: 10.1016/j.rse.2009.07.016

Morel, A., Antoine, D., and Gentili, B. (2002). Bidirectional reflectance of oceanic waters: accounting for Raman emission and varying particle scattering phase function. *Appl. Opt.* 41, 6289–6306. doi: 10.1364/AO.41.006289

Mueller, J. L. (2000). "SeaWiFS algorithm for the diffuse attenuation coefficient, K(490), using water-leaving radiances at 490 and 555 nm," in eds S. B. Hooker and E. Firestone, R *NASA Technical Memorandum 2000-206829*, Vol. 11 (Greenbelt, MD: NASA Goddard Space Flight Center), 51.

Neukermans, G., Ruddick, K., Bernard, E., Ramon, D., Nechad, B., and Deschamps, P.-Y. (2009). Mapping total suspended matter from geostationary satellites: a feasibility study with SEVIRI in the Southern North Sea. *Opt. Express* 17, 14029–14052. doi: 10.1364/OE.17.014029

Novak, M. G., Cetinić, I., Chaves, J. E., and Mannino, A. (2018). The adsorption of dissolved organic carbon onto glass fiber filters and its effect on the measurement of particulate organic carbon: a laboratory and modeling exercise. *Limnol. Oceanogr. Methods* 16, 356–366. doi: 10.1002/lom3.10248

O'Reilly, J. E., Maritorena, S., Mitchell, B. G., Siegel, D. A., Carder, K. L., Garver, S. A., et al. (1998). Ocean color chlorophyll algorithms for SeaWiFS. *J. Geophys. Res. Oceans* 103, 24937–24953. doi: 10.1029/98JC02160

PACE Science Definition Team (2018). *Pre-Aerosol, Clouds, and ocean Ecosystem (PACE) Mission Science Definition Team Report*. Greenbelt, MD.

Putko, M. M., Taylor, I. I. I. A. C., Newman, P. A., and Green, L. L. (2001). Approach for input uncertainty propagation and robust design in CFD using sensitivity derivatives. *J. Fluids Eng.* 124, 60–69. doi: 10.1115/1.1446068

Qi, L., Lee, Z., Hu, C., and Wang, M. (2017). Requirement of minimal signal-to-noise ratios of ocean color sensors and uncertainties of ocean color products. *J. Geophys. Res. Oceans* 122, 2595–2611. doi: 10.1002/2016JC012558

Rasse, R., Dall'Olmo, G., Graff, J., Westberry, T. K., van Dongen-Vogels, V., and Behrenfeld, M. J. (2017). Evaluating optical proxies of particulate organic carbon across the surface atlantic ocean. *Front. Marine Sci.* 4, 1–18. doi: 10.3389/fmars.2017.00367

Refsgaard, J. C., van der Sluijs, J. P., Højberg, A. L., and Vanrolleghem, P. A. (2007). Uncertainty in the environmental modelling process – a framework and guidance. *Environ. Model. Softw.* 22, 1543–1556. doi: 10.1016/j.envsoft.2007.02.004

Salama, M. S., Dekker, A., Su, Z., Mannaerts, C. M., and Verhoef, W. (2009). Deriving inherent optical properties and associated inversion-uncertainties in the Dutch Lakes. *Hydrol. Earth Syst. Sci.* 13, 1113–1121. doi: 10.5194/hess-13-1113-2009

Salama, M. S., Mélin, F., and Van der Velde, R. (2011). Ensemble uncertainty of inherent optical properties. *Opt. Express* 19, 16772–16783. doi: 10.1364/OE.19.016772

Seegers, B. N., Stumpf, R. P., Schaeffer, B. A., Loftin, K. A., and Werdell, P. J. (2018). Performance metrics for the assessment of satellite data products: an ocean color case study. *Opt. Express* 26, 7404–7422. doi: 10.1364/OE.26.007404

Stramski, D., Reynolds, R. A., Babin, M., Kaczmarek, S., Lewis, M. R., Rottgers, R., et al. (2008a). Relationships between the surface concentration of particulate organic carbon and optical properties in the eastern South Pacific and eastern Atlantic Oceans. *Biogeosciences* 5, 171–201. doi: 10.5194/bg-5-171-2008

Stramski, D., Reynolds, R. A., Babin, M., Kaczmarek, S., Lewis, M. R., Röttgers, R., et al. (2008b). Concentration of particulate organic carbon and optical properties in the eastern South Pacific and eastern Atlantic Oceans. Supplement to: Stramski, D et al. (2008): Relationships between the surface concentration of particulate organic carbon and optical properties in the eastern South Pacific and eastern Atlantic Oceans. *Biogeosciences* 5, 171–201. doi: 10.5194/bg-5-171-2008

Wang, P., Boss, E. S., and Roesler, C. (2005). Uncertainties of inherent optical properties obtained from semianalytical inversions of ocean color. *Appl. Opt.* 44, 4074–4085. doi: 10.1364/AO.44.004074

Werdell, P. J., and Bailey, S. W. (2005). An improved *in-situ* bio-optical data set for ocean color algorithm development and satellite data product validation. *Remote Sens. Environ.* 98, 122–140. doi: 10.1016/j.rse.2005.07.001

Werdell, P. J., Franz, B. A., Bailey, S. W., Feldman, G. C., Boss, E., Brando, V. E., et al. (2013). Generalized ocean color inversion model for retrieving marine inherent optical properties. *Appl. Opt.* 52, 2019–2037. doi: 10.1364/AO.52.002019

Westberry, T. K., Boss, E., and Lee, Z. (2013). Influence of Raman scattering on ocean color inversion models. *Appl. Opt.* 52, 5552–5561. doi: 10.1364/AO.52.005552

Conflict of Interest Statement: LM was employed by company Go2Q Pty Ltd.

The remaining authors declare that the research was conducted in the absence of any commercial or financial relationships that could be construed as a potential conflict of interest.

frontiers
in Earth Science

REVIEW
published: 23 July 2019
doi: 10.3389/feart.2019.00152

Retrieving Aerosol Characteristics From the PACE Mission, Part 1: Ocean Color Instrument

Lorraine A. Remer[1]*, Anthony B. Davis[2], Shana Mattoo[3,4], Robert C. Levy[4], Olga V. Kalashnikova[2], Odele Coddington[5], Jacek Chowdhary[6], Kirk Knobelspiesse[7], Xiaoguang Xu[1], Ziauddin Ahmad[7,8], Emmanuel Boss[9], Brian Cairns[10], Heidi M. Dierssen[11], David J. Diner[2], Bryan Franz[7], Robert Frouin[12], Bo-Cai Gao[13], Amir Ibrahim[3,7], J. Vanderlei Martins[14], Ali H. Omar[15], Omar Torres[16], Feng Xu[2] and Peng-Wang Zhai[14]

[1] Joint Center for Earth Systems Technology, University of Maryland, Baltimore County, Baltimore, MD, United States, [2] Jet Propulsion Laboratory, California Institute of Technology, Pasadena, CA, United States, [3] Science Systems and Applications, Inc., Lanham, MD, United States, [4] Climate and Radiation Laboratory, NASA Goddard Space Flight Center, Greenbelt, MD, United States, [5] Laboratory for Atmospheric and Space Physics, University of Colorado, Boulder, Boulder, CO, United States, [6] NASA Goddard Institute for Space Studies, Columbia University, New York, NY, United States, [7] Ocean Ecology Laboratory, NASA Goddard Space Flight Center, Greenbelt, MD, United States, [8] Science Application International Corporation, NASA Goddard Space Flight Center, Greenbelt, MD, United States, [9] School of Marine Sciences, University of Maine, Orono, ME, United States, [10] NASA Goddard Institute for Space Studies, New York, NY, United States, [11] Department of Marine Sciences, University of Connecticut, Groton, CT, United States, [12] Scripps Institution of Oceanography, University of California, San Diego, La Jolla, CA, United States, [13] United States Naval Research Laboratory, Washington, DC, United States, [14] Department of Physics, University of Maryland, Baltimore County, Baltimore, MD, United States, [15] Chemistry and Dynamics Branch, NASA Langley Research Center, Hampton, VA, United States, [16] Atmospheric Chemistry and Dynamics Laboratory, NASA Goddard Space Flight Center, Greenbelt, MD, United States

OPEN ACCESS

Edited by:
David Antoine,
Curtin University, Australia

Reviewed by:
Howard R. Gordon,
University of Miami, United States
Barbara Bulgarelli,
Joint Research Centre (Italy), Italy

***Correspondence:**
Lorraine A. Remer
remer@umbc.edu

Specialty section:
This article was submitted to
Atmospheric Science,
a section of the journal
Frontiers in Earth Science

Received: 30 November 2018
Accepted: 03 June 2019
Published: 23 July 2019

Citation:
Remer LA, Davis AB, Mattoo S, Levy RC, Kalashnikova OV, Coddington O, Chowdhary J, Knobelspiesse K, Xu X, Ahmad Z, Boss E, Cairns B, Dierssen HM, Diner DJ, Franz B, Frouin R, Gao B-C, Ibrahim A, Martins JV, Omar AH, Torres O, Xu F and Zhai P-W (2019) Retrieving Aerosol Characteristics From the PACE Mission, Part 1: Ocean Color Instrument. Front. Earth Sci. 7:152. doi: 10.3389/feart.2019.00152

NASA's Plankton, Aerosol, Clouds, ocean Ecosystem (PACE) satellite mission is scheduled to launch in 2022, with the Ocean Color Instrument (OCI) on board. For the first time reflected sunlight from the Earth across a broad spectrum from the ultraviolet (UV: 350 nm) to the short wave infrared (SWIR: 2260 nm) will be measured from a single instrument at 1 km spatial resolution. While seven discrete bands will represent the SWIR, the spectrum from 350 to 890 nm will be continuously covered with a spectral resolution of 5 nm. OCI will thus combine in a single instrument (and at an enhanced spatial resolution for the UV) the heritage capabilities of the Moderate resolution Imaging Spectroradiometer (MODIS) and the Ozone Monitoring Instrument (OMI), while covering the oxygen A-band (O2A). Designed for ocean color and ocean biology retrievals, OCI also enables continuation of heritage satellite aerosol products and the development of new aerosol characterization from space. In particular the combination of MODIS and OMI characteristics allows deriving aerosol height, absorption and optical depth along with a measure of particle size distribution. This is achieved by using the traditional MODIS visible-to-SWIR wavelengths to constrain spectral aerosol optical depth and particle size. Extrapolating this information to the UV channels allows retrieval of aerosol absorption and layer height. A more direct method to derive aerosol layer height makes use of O2A absorption methods, despite the relative coarseness of the nominal 5 nm spectral resolution of OCI. Altogether the PACE mission with OCI will be an unprecedented opportunity for aerosol characterization that will continue climate data records from the past decades and propel aerosol science forward toward new opportunities.

Keywords: aerosol, oxygen A-band, hyperspectral, PACE, remote sensing, UV

INTRODUCTION AND OVERVIEW

Uncertainty in Understanding Aerosol Processes

Aerosols contribute the largest uncertainties in estimating climate forcing (Boucher et al., 2013). Reducing these uncertainties requires knowing global aerosol concentrations and distribution, and aerosol chemical, physical and optical properties. We also need to understand how aerosols affect other atmospheric constituents, especially clouds (Boucher et al., 2013). The process in which aerosols modify clouds to affect Earth's energy budget is still poorly understood (Rosenfeld et al., 2014a; Seinfeld et al., 2016; Fan et al., 2016). Even more uncertain is how aerosol-cloud interaction affects precipitation onset and amount, influencing floods, droughts and the availability of fresh water (Andreae and Rosenfeld, 2008; Tao et al., 2012; Rosenfeld et al., 2014b).

The challenge to understanding these processes lies within the multiple pathways that aerosols, clouds and Earth's energy balance intertwine (Koren et al., 2008; Stevens and Feingold, 2009; Morrison and Grabowski, 2011; Altaratz et al., 2014). Aerosols can act as cloud condensation nuclei (CCN) or as ice nuclei (IN), which means that variation on the concentrations or composition of aerosols can exert an influence on cloud evolution through a microphysical path (Koren et al., 2008; Altaratz et al., 2014). Observational and modeling studies have found a myriad of resulting changes in clouds linked to changes in aerosols via this microphysical path including changes to cloud albedo, cloud macrophysical properties, cloud "lifetime," lightning and precipitation (Twomey, 1977; Albrecht, 1989; Kaufman and Nakajima, 1993; Rosenfeld and Woodley, 2001; Kaufman et al., 2005a; Khain et al., 2005; Koren et al., 2005, 2010, 2012; Rosenfeld et al., 2008; Li et al., 2011; Van den Heever et al., 2011; Yuan et al., 2011, 2012; Shi et al., 2014). Furthermore, because aerosols alter radiative absorption and scattering they can change atmospheric heating rates that will affect atmospheric stability and surface heat fluxes, which in turn affect cloud formation and evolution (Johnson et al., 2004; Koren et al., 2004, 2008; Feingold et al., 2005; Kaufman and Koren, 2006; Altaratz et al., 2014; Shi et al., 2014). We also know that aerosol-cloud interaction is a two-way street. Clouds can produce aerosols via nucleation in aqueous chemistry (Eck et al., 2014), and clouds can remove aerosols from the atmosphere through wet deposition (Chin et al., 2000). These intertwined processes occur in regimes that span 12 orders of magnitude from the microscale (aerosols $\sim$0.1 μm) to the synoptic scale (global $\sim 10^5$ km). Mapping and understanding cloud, aerosol and energy balance processes across 12 orders of magnitude of spatial scale is required to fully understand today's climate. The next challenge is to understand how these processes will evolve in a future changed climate.

In addition to their role in climate and hydrological processes, aerosols pose a serious global health threat. Particulate matter (PM) and aerosols that pollute ambient air are a major global cause of death and disease, having been found responsible for 3.2 million deaths per year as well as being the 9th leading risk factor for premature death globally (Lim et al., 2012). The relative toxicity of specific PM types — components having different size and chemical composition—is still poorly understood (Franklin et al., 2017). However, it has been shown that smaller (sub-micron) particles could be especially harmful since they can penetrate deeper into the lung (Franck et al., 2011). Aerosol particles can be lofted far from their sources and even transported across oceans to other continents (Kaufman et al., 2005b; Yu et al., 2012, 2013). Therefore, air pollution mitigation is a global problem because local air quality can be affected by sources far upwind. Some aerosols contain valuable minerals needed by terrestrial and marine plant life and, therefore, the transport and deposition of these aerosols can be an important source of micronutrients for otherwise nutrient-limited biomes (Jickells et al., 2005; Yu et al., 2015), or modify ocean chemistry and impact ocean biology (Ito et al., 2016).

Abbreviations: AATSR, Advanced Along Track Scanning Radiometer; ABI, Advanced Baseline Imager; AERONET, Aerosol Robotics Network; AI, Aerosol Index; AirMSPI, Airborne Multiangle SpectroPolarimetric Imager; ALH, aerosol layer height; AOD, aerosol optical depth; AVIRIS Airborne Visible InfraRed Imaging Spectrometer; BRF, bidirectional reflection function; CALIOP, Cloud-Aerosol Lidar with Orthogonal Polarization; CALIPSO, Cloud-Aerosol Lidar and Infrared Pathfinder Satellite Observations; CCN, cloud condensation nuclei; CPL, Cloud Physics Lidar; DOAS, differential optical absorption spectroscopy; DoF, degrees of freedom; DSCOVR, Deep Space Climate Observatory; DT, Dark Target; EPIC, Earth Polychromatic Imaging Camera; FMF, fine mode fraction; GOES, Geostationary Operational Environmental Satellite; HICO, Hyperspectral Imager for Coastal Ocean; IN, ice nuclei; IR, InfraRed; LUT, Look Up Table; M_C6, MODIS Collection 6; MAIAC, Multi-Angle Implementation of Atmospheric Correction; MAP, multi-angle imaging polarimeters; MERIS, Medium Resolution Imaging Spectrometer; MISR, Multi-angle Imaging SpectroRadiometer; ML_M, MODIS-Like applied to MODIS inputs; ML_V, MODIS-Like applied to VIIRS inputs; MODIS, Moderate Resolution Imaging Spectroradiometer; MSI, Multi-Spectral Instrument; NASA, National Aeronautics Space Administration; NIR, Near InfraRed; O2A, oxygen A-band; OCI, Ocean Color Instrument; OCO, Orbiting Carbon Observatory; OLCI, Ocean and Land Color Instrument; OMI, Ozone Monitoring Instrument; OMPS, Ozone Mapping and Profiling Suite; PACE, Plankton, Aerosols, Clouds, Ocean Ecosystems; PARASOL, Polarization and Anisotropy of Reflectances for Atmospheric Sciences coupled with Observations from a Lidar; PM, particulate matter; POLDER, Polarization and Directionality of the Earth's Reflectance; RMSE, Root Mean Square Error; SLSTR, Sea and Land Surface Temperature Radiometer; SPEXone, Spectro-Polarimeter for Planetary Exploration-1; SSA, single scattering albedo; SWIR, Short Wave Infra Red; TANSO-CAI, Thermal And Near infrared Sensor for Carbon Observation - Cloud and Aerosol Imager; TOA, top of atmosphere; TOMS, Total Ozone Mapping Spectrometer; TropOMI, Tropospheric Ozone Monitoring Instrument; UV, ultraviolet; VIIRS, Visible Infrared Imaging Radiometer Suite.

An Integrated Approach to Characterizing Aerosol

An integrated approach is required to achieve sufficient understanding of the processes that aerosols affect. The approach requires modeling at all scales and observational data to inform and constrain these models. *In situ* data collection provides indispensable information about aerosol composition and detailed particle properties, but is limited to the surface layer or is brought aloft by infrequent aircraft or balloon sampling. Ground-based remote sensing observations such as the AERONET (Holben et al., 1998), other sun/sky radiometer networks, and lidars provide frequent measures of total column or vertically resolved aerosol properties However, these instrumented stations are typically limited geographically to continental land masses of wealthy countries, hence leaving the developing world and much of the world's oceans undersampled (Knobelspiesse et al., 2004; Smirnov et al., 2009). Global statistics are beyond reach of these ground, aircraft or balloon observational systems, and models would be under-constrained if relying only on ground or suborbital observations. Only space-based remote sensing provides relatively frequent and consistent observations of the total atmospheric column.

Satellite Aerosol Remote Sensing Since 2000 With Imaging Spectro-Radiometry

Since the launch of Terra and the A-train constellation of satellites starting at the end of 1999, aerosol remote sensing reached a new era. The MODerate resolution Imaging Spectroradiometer (MODIS) and Multiangle Imaging SpectroRadiometer (MISR) on Terra, MODIS on Aqua, Ozone Monitoring Instrument (OMI) on Aura, Medium Resolution Imaging Spectrometer (MERIS), Sentinel-3 Ocean and Land Color Instrument (OLCI), Sentinel-2 Multi-Spectral Instrument (MSI), Polarization and Directionality of the Earth's Reflectance (POLDER) on the Polarization and Anisotropy of Reflectances for Atmospheric Sciences coupled with Observations from a Lidar (PARASOL) and Cloud-Aerosol Lidar with Orthogonal Polarization (CALIOP) on Cloud-Aerosol Lidar and Infrared Pathfinder Satellite Observations; have combined to provide an unprecedented view of the global aerosol system. Focusing on passive remote sensing from radiometers, algorithms have extracted information from spectral measurements in the visible and shortwave infrared (SWIR) portions of the spectrum (i.e., MODIS), from spectral measurements in the ultraviolet (UV) portion of the spectrum (i.e., OMI and the earlier Total Ozone Mapping Spectrometer (TOMS) instrument from which OMI draws its heritage), and from multi-angular measurements in the visible and near-infrared (NIR) [i.e., MISR, Advanced Along Track Scanning Radiometer (AATSR) and POLDER]. Algorithms have also extracted information from multi-angular measurements of polarized reflectance in the visible (POLDER), but discussion of polarimetry is outside the scope of this review and will be covered in a companion paper by Remer et al. (2019), hereafter referred to as "Part 2." The different information acquired by these different satellite sensors has enabled the community to produce reliable measures of total column ambient aerosol loading (aerosol optical depth - AOD) over a variety of land types and over the ocean (Boucher et al., 2013; Myhre et al., 2013), and even recently AOD in the column above clouds (Torres et al., 2012; Jethva et al., 2013, 2014a,b, 2016; Meyer and Platnick, 2015; Sayer et al., 2016). In addition, space-based measurements have produced information on aerosol microphysical properties: particle size parameter (Remer et al., 2005), single scattering albedo (SSA) (e.g., Jethva and Torres, 2011; Torres et al., 2013), particle non-sphericity (deviation from spherical shape, e.g., Kalashnikova and Kahn, 2006; Kalashnikova et al., 2013), and combinations of size, absorption and shape to categorize aerosol type (e.g., Kahn and Gaitley, 2015). Note, however, that, despite the unprecedented view from space, uncertainties remain because these retrievals are fundamentally underdetermined, contributing to large differences among satellite products in regional and seasonal patterns. Additionally, differences and uncertainties in calibration, sampling, cloud screening, treatment of the surface reflectivity, and aerosol retrieval algorithms contribute to overall retrieval uncertainty (e.g., Li et al., 2009; Kokhanovsky et al., 2010).

Limitations of Current Aerosol Satellite Remote Sensing

The information content of a single-look multispectral or hyperspectral sensor such as MODIS or OMI is limited, especially when neither spans the entire solar spectrum. MODIS does not measure in the UV, while OMI measures in the UV, but misses all wavelengths longer than 500 nm. In addition, OMI's 13 km × 24 km footprint makes quantitative aerosol retrievals in all but the most cloud-free situations impossible. Both MODIS and OMI standard aerosol retrieval algorithms must rely on a series of assumptions in order to retrieve AOD and any other aerosol property. Multi-angle measurements of the same scene such as MISR or AATSR increase the information content because the instrument becomes sensitive to a wider array of aerosol properties with fewer assumptions. Even so, MISR and AATSR still are limited to determining "aerosol type," a qualitative constraint based on a combination of size, absorption and shape. Aerosol type, while important for a wide range of applications, is not the same as determining quantitative particle properties such as size distribution, SSA or complex refractive index.

For retrieving these quantitative particle properties from space even more information is needed, such as with a multi-wavelength, multi-angle polarimeter of sufficient accuracy, wavelength range and resolution (Mishchenko et al., 2004; Cairns et al., 2010; Knobelspiesse et al., 2012; Kokhanovsky, 2015). Such instruments will be discussed more fully in Part 2 (Remer et al., 2019).

New contemporary algorithms applied to the traditional sensors are enhancing aerosol retrieval capabilities despite the inherent limitations. For example, an advanced type of algorithm only now making its way toward operations is a multi-pixel algorithm called the MAIAC (Lyapustin et al., 2011). MAIAC requires multiple days of views of the same scene in order to constrain surface reflectance for the aerosol retrieval. At the beginning of the MODIS era 18 years ago, holding onto a week's worth of information at each pixel would have overwhelmed computer resources. In addition to computer resources, some algorithmic options require a data base containing, for example, spectral surface reflectance characteristics to be acquired for a particular sensor and then used in the operational forward processing stream. Thus, these algorithms generally are not optimal at launch and only achieve high accuracy and precision after the statistics of the data base have been acquired. The Deep Blue family of algorithms is an example of this type of algorithm (Hsu et al., 2004, 2013). For some purposes waiting for an algorithm to mature is entirely appropriate (e.g., accumulating long-term data records, offering constraint on aerosol and climate models). For other purposes such as near real-time hazards warning and other aerosol air quality applications, at-launch algorithms are highly desirable.

Single-view radiometers (e.g., MODIS and OMI) have provided decades of insight into the global aerosol system and new observational methods to constrain estimates of climate change (Boucher et al., 2013), study aerosol-cloud interaction (Koren et al., 2005, 2010, 2012), follow intercontinental transport of particles (Yu et al., 2012, 2013) and improve particulate air pollution forecasts (Al-Saadi et al., 2005). Enhancement to these heritage capabilities using single-view radiometry, even at launch, is possible, despite the limitations of the viewing geometry and lack of polarization information, but will require sensors that measure in additional wavelengths, cover a broader spectral range and/or at a finer spectral, spatial or temporal resolution.

Outline

This paper explores the potential for aerosol remote sensing and characterization in the PACE era, primarily from the OCI that has been designed to continue and even enhance heritage aerosol algorithms over both ocean and land. Section "Aerosol Remote Sensing for the PACE Mission" begins with a brief description of the PACE observatory, the two types of instruments on the observatory and the possibility for remote sensing of aerosols from the observatory. This is followed by discussion on the abilities and challenges of adapting current aerosol algorithms to OCI measurements in order to continue heritage aerosol time series beyond the lifetimes of today's sensors and missions. Section "Advances Beyond Heritage. 1: Broad Spectral Range Retrievals From OCI" explores the potential of using OCI's broad spectrum from the UV to the SWIR to retrieve an enhanced set of aerosol characterization products. These products include spectral AOD, a measure of particle size, SSA and aerosol layer height (ALH). Section "Advances Beyond Heritage, 2: Oxygen A-band Information Content on Aerosol Profiling" describes advances beyond heritage remote sensing by exploring the possibilities of retrieving ALH by capitalizing on OCI's 5 nm spectral resolution through the oxygen A-band (O2A). In Section "Advances Beyond Heritage, 2: Oxygen A-band Information Content on Aerosol Profiling," we also broach the possibility of improved aerosol profile retrievals from the combination of multiangle observations in the O_2 A-band. Part 2 of this study (Remer et al., 2019) explores this in more detail. Finally in Section "Discussion and the Path Forward," we discuss the results, identify the gaps that still exist before OCI's full potential as an aerosol instrument can be realized, and provide suggestions for the path forward.

The algorithm concepts presented in this paper illustrate the potential for aerosol remote sensing from OCI. These concepts are not the official, operational, set of algorithms as these will require additional vetting. The focus of this paper is OCI. For further analysis of PACE aerosol remote sensing with multi-angle and polarimetry, we refer the reader to the companion paper in this same issue (Remer et al., 2019).

AEROSOL REMOTE SENSING FOR THE PACE MISSION

The PACE mission offers the aerosol community new opportunities for retrieving and characterizing aerosol from space. There are two levels of opportunity based on the two types of instruments the mission intends to fly. First there is OCI (Del Castillo et al., 2012) that will measure reflected sunlight from the Earth across the broad spectrum from the UV (350 nm) to the SWIR (2250 nm) all at nominally 1 km spatial resolution. The spectrum from 345 to 890 nm will be spectrally continuous with a spectral resolution of 5 nm, while the SWIR wavelengths will be measured in seven discrete bands. Opportunities from OCI will be based on the heritage of products already being produced from similar instruments such as MODIS and OMI. **Table 1**

TABLE 1 | Instrument specifications for MODIS, OMI, and OCI.

	MODIS	OMI	OCI
UV to NIR bands	0.41, 0.44, 0.47, 0.49, 0.53, 0.55, 0.55, 0.66, 0.67, 0.68, 0.75, 0.85, 0.87, 0.91, 0.94, 0.94 µm	Hyperspectral continuous 0.264–0.504 µm	Continuous 0.345–0.89 µm plus discrete bands at 0.94 and 1.04 µm
SWIR to Thermal infrared	1.24, 1.63, 2.13, 3.7, 3.9, 3.9, 4.05, 4.46, 4.5, 1.38, 6.6, 7.2, 8.5, 9.7, 11.0, 12.0, 13.2, 13.6, 14.1 µm	None	1.25, 1.38, 1.62, 2.13, 2.25 µm
Swath width	2330 km	2600 km	2660 km
Global coverage	2 days	1 day	1 – 2 days
Ground pixel	0.25, 0.5, and 1 km	13 × 24 km	1 km

compares the characteristics of MODIS, OMI and OCI. At the very least OCI will be able to continue the aerosol record begun from MODIS and OMI, providing opportunity to collocate and compare with similar aerosol algorithms applied to the Visible Infrared Imaging Reflectance Suite (VIIRS) and the constellation of geosynchronous satellites planned for the PACE time frame [Advanced Baseline Imager (ABI) on Geostationary Operational Environmental Satellite – Series R (GOES-R), etc.]. In addition to continuity, aerosol science from PACE OCI will advance beyond the capabilities provided by heritage instruments because OCI offers moderate spatial resolution in the UV region and fine spectral resolution through the oxygen-A band.

The second type of PACE instrument will be a pair of multi-wavelength, Mulit-Angle Polarimeters (MAPs). The PACE MAPs have the high potential to push beyond traditional limitations in characterizing aerosol retrievals with new capabilities that include retrievals of particle size distribution, complex refractive index, SSA, aerosol height distribution and simultaneous retrievals of aerosol properties with surface (ocean and land) reflectance (Waquet et al., 2009; Chowdhary et al., 2012; Xu et al., 2016, Xu F. et al., 2017; Gao et al., 2018; Stamnes et al., 2018).

Aerosol products for the PACE mission will be derived from OCI alone and from the MAPs alone. However, there is also opportunity to develop and use advanced algorithms that make use of all instruments in synergy. PACE aerosol products will at minimum, match aerosol products currently available from the OMI, MODIS and VIIRS sensors, and include the UV aerosol index (AI), spectral AOD over land and ocean, and fine mode fraction (FMF) over ocean. The FMF is a measure of the relative effect that this mode has on the reflectance at top-of-atmosphere as compared with the effect of the total aerosol of all sizes on the reflectance (Remer et al., 2005). Note that in the MODIS aerosol context the fine mode refers to a lognormal particle size distribution with effective radius less than 0.5 μm. Advances from this minimum set will depend on algorithm development as applied to OCI and the PACE polarimeters.

Masking and Other Preliminary Necessities

Fundamental to any aerosol retrieval is the need to identify scenes applicable for useful retrievals. This process, called masking, includes identifying and excluding scenes containing clouds, snow/ice, sun glint, and more from retrievals. In the PACE mission some masking will improve, others will be worse, while some will remain essentially the same as heritage aerosol algorithms. With the added information content for PACE, some retrievals that would have been masked for the heritage algorithms, may be able to proceed. For example, aerosol retrievals above clouds and otherwise unfavorable surfaces may be possible.

OCI lacks thermal infrared (IR) observations, which in terms of clouds, will lead to a degraded cloud masking capability compared to heritage MODIS and VIIRS datasets. However, compared to heritage OMI/TOMS-alone datasets, improved spatial resolution and expanded wavelengths into the SWIR will allow for significantly improved cloud masking. The OCI 1.38 μm channel is especially important for detecting thin cirrus clouds. In addition, the 1.38 μm channel may offer possibilities for "correction" rather than blunt masking by removing the net radiative effect of the cirrus in an adjustment of the measured top-of-atmosphere radiances, and then using those previously cirrus-affected pixels to derive information about the aerosol and/or surface beneath. Furthermore, the pair of SWIR channels centered at 2.135 and 2.25 μm will provide information on cloud thermodynamic phase unavailable from previous sensors (Coddington et al., 2017).

Masking is also typically required to remove the impact of the direct and diffuse solar radiation reflected by the sea surface and other sea surface features that can significantly enhance NIR and SWIR. Highly scattering non-aerosol targets on the ocean surface include whitecaps, foam and bubbles, sea ice, floating vegetation, high calcite waters, high sediment waters, optically shallow waters (e.g., with bright coral or sand) and regions with concentrated floating plastics (Frouin et al., 1996; Li et al., 2003; Marmorino and Smith, 2005; Balch et al., 2011; Dierssen et al., 2015; Fogarty et al., 2017; Garaba and Dierssen, 2018; Garaba et al., 2018; Perry et al., 2018). The most widespread of these is enhanced reflectance due to the production of whitecaps that occur over vast regions of the global ocean, particularly in the Southern Ocean (Albert et al., 2016). The heritage approach to mask whitecaps uses wind speed measurements to estimate the whitecap fraction, but such relationships are only climatological and do not predict instantaneous whitecap fields. Moreover, new measurements of whitecaps indicate that they have more spectral features across the visible to SWIR and new approaches are being tested to predict their contribution to at-sensor radiance without the reliance on climatological wind speeds (Dierssen, 2019). It is expected that improvements in assessments of wave conditions and whitecap fraction will help constrain the large uncertainty in emission fluxes for sea spray aerosols (Albert et al., 2010).

OCI Continuation of TOMS/OMI Heritage

OCI, like OMI, is a hyperspectral resolution imager with continuous spectral coverage at 5 nm spectral resolution that spans a wavelength range from the UV into the NIR. From an aerosol retrieval perspective OCI is an improvement on OMI as its spatial resolution will nominally be 1 km instead of 13 km × 24 km, and its continuous spectral range extends to 885 nm, while OMI's ends at 500 nm. However, OCI's spectral resolution of its contiguous channels is 10 times coarser than OMI's in the UV and visible.

The TOMS/OMI heritage products include both the qualitative UV AI (Herman and Celarier, 1997; Herman et al., 1997) and the quantitative suite of aerosol characteristics that include extinction AOD and SSA at 380 nm (Torres et al., 1998, 2002, 2005, 2007). The quantitative OMI aerosol retrieval fits two measured UV channels to the values of pre-computed reflectances stored in a Look Up Table (LUT). Aerosol type and layer height are constrained from ancillary information, leaving the algorithm to choose between different values of AOD and aerosol absorption (Torres et al., 1998, 2002, 2007). In the case of OMI-like aerosol algorithms applied to OCI inputs, we can expect a direct translation of the OMI technique to OCI measurements. There is already experience in porting the basic UV algorithm from its original application with TOMS observations to OMI. OCI's coarser spectral resolution should not be a detrimental factor in applying the heritage algorithm, and because OCI has much finer spatial resolution than OMI, clouds should be less of a factor in the retrieval. This should significantly increase the overall availability of high quality retrievals, especially in cloudier conditions.

In addition, the wavelength pairs in the OCI oxygen A- and B-band spectral regions (∼690 and ∼765 nm) and in their adjacent continuous regions (∼680 and ∼780 nm) will allow the retrieval of the height of desert dust and carbonaceous aerosol layers using inversion schemes developed for the Earth Polychromatic Imaging Camera (EPIC) sensor (Xu X. et al., 2017; Xu et al., 2018b) (see Discussion and the Path Forward). The retrieved ALH will better constrain the OMI-like AOD/SSA retrieval resulting in more accurate products than current attainable from the OMI inversion. Thus, the OMI-like approach will be optimized on the account of OCI's both fine spatial resolution and extended spectral coverage.

OCI Continuation of MODIS/VIIRS Heritage

Multiple heritage aerosol algorithms are encompassed by the MODIS/VIIRS era. Of these, the most pertinent to the discussion that follows is the Dark Target (DT) over ocean retrieval (Tanré et al., 1997; Remer et al., 2005; Levy et al., 2013). In this algorithm measured top-of-atmosphere reflectances in six spectral bands (0.55, 0.66, 0.87, 1.24, 1.63, and 2.13 μm) are fit to calculated reflectances in a LUT. The table is constructed under the assumption that the aerosol size distribution can be represented by two lognormal distributions, one with effective radius larger than 0.5 μm (the coarse mode) and one with effective radius smaller than 0.5 μm (the fine mode). A successful match yields the spectral AOD and one or two size distribution parameters. Greater detail of this method will be given in Section "Advances Beyond Heritage. 1: Broad Spectral Range Retrievals From OCI" as this heritage algorithm forms the basis of Step 1 of the proto-algorithm developed for application to OCI inputs.

OCI's hyperspectral range spans four of the MODIS bands used by the MODIS DT aerosol over ocean algorithm and further extends to include six discrete bands in the SWIR thereby spanning the range of wavelengths needed by any of the heritage aerosol algorithms, even those not specifically discussed in this paper. OCI spatial resolution of 1 km is less desirable than MODIS' 0.5 km, and OCI is missing MODIS' thermal IR channels used in cloud masking. Recent studies have shown that this could make a difference in maintaining continuity, but still achieve desired accuracy of key retrieved aerosol parameters (Levy et al., 2015). Thus, the OCI configuration of wavelengths, spatial resolution, swath width and temporal sampling is sufficient to produce AOD over land and ocean, from the UV to the SWIR, and the MODIS FMF over ocean to the accuracies and precisions of heritage MODIS products.

Even though the OCI configuration spans the same parameter space of heritage MODIS algorithms, a seamless continuation of the heritage product time series is not guaranteed. Experience in porting MODIS retrievals to VIIRS has revealed the subtleties of the transfer. Issues arise in translating band spectral response functions from old sensor to new sensor, changes in gas corrections resulting from differences in spectral response function and the creation of specific LUTs for the new sensor. Other issues are introduced by differences in spatial resolution and lack of auxiliary channels used for masking (e.g., clouds). Finally, calibration of radiances from one sensor to the next may differ, introducing offsets that may either be static from pre-launch differences and also time-dependent from on-orbit corrections.

Figure 1 illustrates some of these issues based on experience in porting the MODIS DT algorithm to VIIRS. The porting process consisted of (1) creating a LUT for VIIRS based on the VIIRS channels that paralleled the LUT used by the MODIS retrieval, (2) degrading the MODIS spatial resolution to match the VIIRS spatial resolution, and (3) applying a cloud mask to both MODIS and VIIRS inputs that used only wavelengths and spatial resolution common to both sensors. Then the MODIS algorithm could be applied to the (spatially) degraded MODIS inputs using the MODIS LUT. This resulted in a product labeled "MODIS-like on MODIS" (ML_M). "MODIS-like" is not the same as the operational Collection 6 MODIS algorithm (M_C6) because ML_M used different spatial resolution and different masking than M_C6. **Figure 1A** shows the seasonal mean AOD (March–April–May) of the MODIS-like algorithm applied to MODIS inputs, and **Figure 1C** shows the difference between the MODIS-like algorithm and the original operational true MODIS algorithm. Differences in algorithm applied to the same inputs are small, but regionally can reach magnitudes of ±0.05 AOD. These differences are attributed mostly to differences in sampling caused by masking differences.

Figure 1B shows the seasonal mean AOD for the same MODIS-like algorithm applied to VIIRS inputs. Comparing **Figures 1A,B** demonstrates the consistency in the products after the porting. **Figure 1D** is the difference between applying exactly the same algorithm to the inputs of the two sensors. Here, differences in AOD can be as large as ±0.07 AOD over land, and systematically biased 0.02 to 0.10 over ocean. The take home message from **Figure 1** is in comparing **Figures 1C,D**. **Figure 1C** shows the difference in retrieved AOD due to algorithmic difference (with same inputs) is relatively small, while **Figure 1D** shows relatively large differences in AOD due to different inputs (with same algorithm). Input reflectances, not the algorithm, are the major challenge to overcome in matching retrieved AOD data sets from different sensors. The differences in **Figure 1D** have been traced to fundamental biases in the input radiances of specific channels and could be eliminated with calibration that forces the instruments to be the same. Achieving continuity in the aerosol record between any two sensors, such as MODIS and VIIRS, requires a period of overlap during which differences can be identified and calibration adjusted, if necessary.

In **Figure 1** we demonstrate differences in the results of applying the same algorithm to both MODIS and VIIRS input

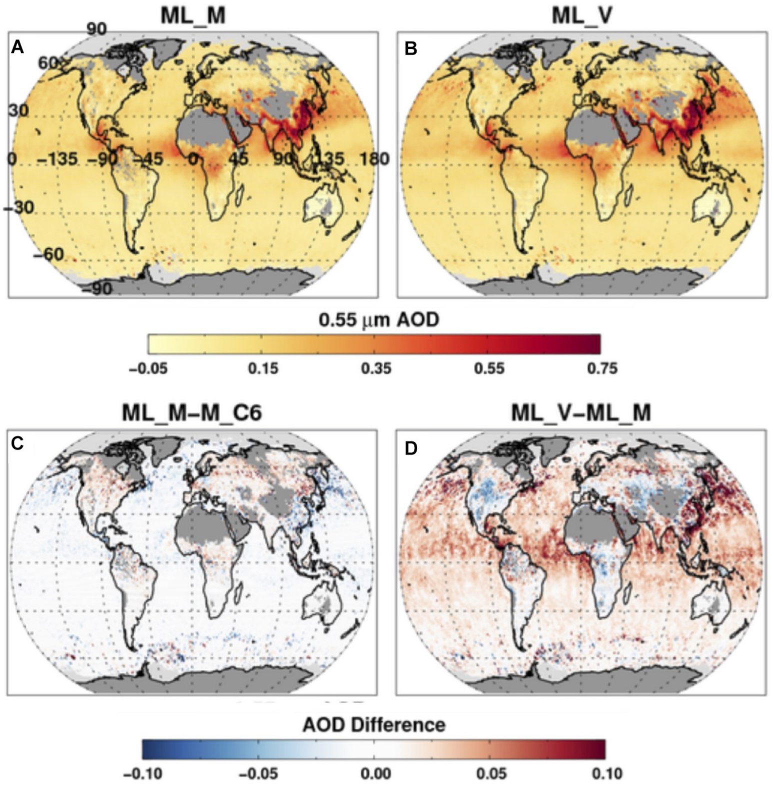

FIGURE 1 | (A,B) Global seasonal mean AOD at 550 nm (March–April–May) as derived from the MODIS-like retrieval algorithm applied to MODIS input radiances **(A)** and applied to VIIRS input radiances **(B)**. **(C)** Difference between **(A)** and the corresponding seasonal mean AOD at 550 nm produced from the operational MODIS aerosol retrieval algorithm. **(D)** Difference between **(B)** and **(A)**. Reprinted from Levy et al. (2015), under Creative Commons Attribution 3.0 License.

reflectances. Now we attempt to determine which of the two satellite sensors is returning the more accurate AOD product by comparing satellite retrievals against collocated ground-based AERONET measurements. **Figure 2** shows the differences between satellite retrieval and AERONET AOD as a function of AERONET AOD. In **Figure 2B**, we can see the same positive bias of ML_V for ocean retrievals against AERONET as we saw ML_V against ML_M in **Figure 1D**. This suggests that the VIIRS radiances are the ones requiring calibration adjustment. We note that the MODIS and MODIS-like algorithms employ a different set of wavelengths in their retrievals over ocean and land. Calibration biases in particular wavelengths will not necessarily affect AOD retrievals the same over ocean and land.

If all reflectance measurements made by OCI are well-calibrated, we anticipate similar magnitude differences between heritage aerosol products and OCI aerosol products based on heritage algorithms as is illustrated in **Figure 1C**. These small differences, due to the coarser spatial resolution of OCI and its lack of IR channels that MODIS uses for masking, are unbiased and within the expected uncertainty of heritage products. However, as **Figures 1D**, **2** demonstrate, inexact instrument calibration, even within specified uncertainties of sensor characterization teams, has the potential to increase differences in retrieved AOD and create biases that are outside heritage expectations.

ADVANCES BEYOND HERITAGE. 1: BROAD SPECTRAL RANGE RETRIEVALS FROM OCI

Irrespective of the challenges described above, OCI-alone can still advance aerosol characterization beyond heritage expectations by allowing for new algorithms that make use of the information content available from a broad spectrum spanning the UV to the SWIR. This is essentially merging the capabilities of OMI and MODIS into a single sensor with common geometry and spatial resolution, instantaneous viewing and the same calibration. This configuration will permit retrieval of aerosol loading (spectral AOD), a measure of particle size (FMF), a measure of aerosol absorption (SSA), and ALH. Thus, OCI should be able to retrieve four parameters to characterize aerosol, while OMI and MODIS heritage algorithms separately could each only retrieve two of the four parameters, while assuming values for the remaining two. Aerosol layer in this context is an optically effective scale height. Other satellite sensors past and present have also measured reflectances from the UV to the SWIR. These include the Thermal And Near infrared Sensor for Carbon Observation – Cloud and Aerosol Imager (TANSO-CAI) with four wavelengths (380, 674, 870, and 1620 nm) at 1 km spatial resolution (eoPortal directory: GOSAT) and the Tropospheric Ozone Monitoring

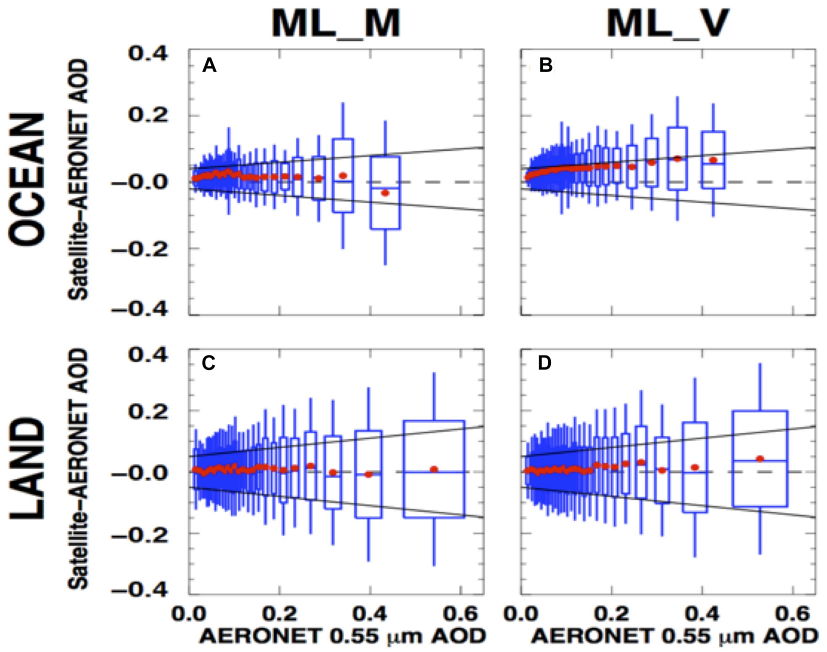

FIGURE 2 | Differences between satellite retrieval of AOD and collocated AERONET measurements of AOD from a global data set of satellite-AERONET collocations, sorted according to AERONET AOD and binned with equal number of collocations in each bin. Red dots indicate mean of each bin, boxes enclose one standard deviation in each bin, whiskers extend to two standard deviations and blue center line of each box denotes the median. **(A,C)** Is for the MODIS-like retrieval algorithm applied to MODIS input radiances. **(B,D)** Is for the same MODIS-like retrieval algorithm applied to VIIRS input radiances. **(A,B)** is for aerosol retrievals over ocean, and **(C,D)** is for retrievals over land. Reprinted from Levy et al. (2015), under Creative Commons Attribution 3.0 License.

Instrument; (TropOMI) with three spectral regions (270–495 nm, 710–775 nm, and 2305–2385 nm) at 7 km spatial resolution (European Space Agency [ESA], 2013). Data from TANSO-CAI and TropOMI may be able to provide a test bed for OCI algorithm development, although to date, there are no published studies describing full spectrum aerosol retrievals from these sensors.

Reflectances in the UV spectrum (e.g., those used in the OMI aerosol algorithms) are primarily sensitive to three aerosol characteristics: aerosol loading (AOD), aerosol absorption, and height of the aerosol layer. Unfortunately, heritage measurements in the UV provide only two pieces of independent information. Thus, retrievals are unconstrained, requiring assumptions to constrain one of the three aerosol parameters in order to retrieve the other two. The traditional tactic taken and applied to TOMS and OMI aerosol algorithms is to constrain aerosol height with assumptions based on climatology and then retrieve loading and absorption in the form of AOD and SSA. The retrievals, especially SSA, are also susceptible to assumptions of (i) surface reflectances, particularly in extremely oligotrophic oceans, and (ii) aerosol particle properties used by the retrieval, including particle size and most importantly the spectral signature of absorption through the UV and blue regions of the spectrum.

Meanwhile, aerosol retrievals based on the visible-NIR-SWIR spectrum (e.g., those applied in the MODIS and VIIRS aerosol algorithms) are primarily sensitive to only two aerosol characteristics: aerosol loading (AOD) and a measure of relative particle size based on spectral AOD. In addition to spectral AOD, particle size can be represented by a parameter denoted as FMF, which is usually thought of in terms of the ratio of fine mode AOD at 550 nm to total AOD at 550 nm. The retrieval in the visible-NIR-SWIR is less sensitive to ALH or aerosol absorption. Some MODIS algorithms that make use of the blue wavelengths retrieve and report SSA, but those products have not been validated.

Making use of the complementary capabilities of OMI and MODIS was an early goal of both science teams. Soon after the OMI-alone aerosol retrieval had been validated, attempts were made to join OMI's sensitivity to absorption and layer height with MODIS' sensitivity to loading and size. With both instruments being in the A-Train, and measuring less than 8-minutes apart, it was theoretically possible to create such a combined OMI-MODIS retrieval. However, the endeavor to merge Level 1 radiance data from the two instruments faced significant challenges in terms of non-uniform calibration, spatial resolution and viewing geometry. Instead, a retrieval was devised that used Level 2 retrieval products from each instrument. MODIS spectral AOD was extrapolated into the UV, thereby constraining the UV AOD and allowing OMI to return a constrained SSA and ALH that compared well to independent observations (Satheesh et al., 2009). This tactic was never implemented operationally, due to lack of investment to bring the idea to maturity. Recently Gassó and Torres (2016) provides additional demonstration of the concept.

The EPIC sensor on Deep Space Climate Observatory (DSCOVR) currently deployed on the L1 point (Marshak et al., 2018) merged measuring capabilities in the near UV, visible and NIR (including channels in the oxygen-A and B-bands) into a single instrument. A successful method to derive ALH from EPIC's oxygen A- and B- channels was developed (Xu X. et al., 2017) and the results compared to independent observations over the oceans. Most recently, Xu et al. (2018b) also demonstrated the method over dark vegetated surfaces. The application of this inversion technique to OCI observations will go a long way into addressing the need of constraining the ALH in OMI-like near UV retrieval applications. We will further address O2A retrievals for OCI in section "Advances Beyond Heritage, 2: Oxygen A-band Information Content on Aerosol Profiling."

OCI Broad-Spectrum Prototype Algorithm

Here we present a novel, OCI prototype algorithm developed specifically for a single instrument spanning the complete range from the UV to the SWIR and therefore moves beyond the Satheesh et al. (2009) technique. The algorithm requires a uniform calibration, spatial resolution and viewing geometry across the broad spectrum. The algorithm is based on the DT aerosol over ocean algorithm (Tanré et al., 1997; Remer et al., 2005; Levy et al., 2013) that was developed for MODIS, and has since been ported to VIIRS and other sensors. The prototype algorithm expands the DT algorithm to include UV channels that are used to retrieve SSA. This prototype algorithm is presented here for the first time.

The OCI prototype algorithm begins first by identifying applicable ocean scenes for retrieval and discarding non-applicable scenes with clouds/cirrus, ice, glint or suspended sediments in the water. The algorithm then ingests reflectances of the identified ocean scene in six wavelengths (550, 650, 880, 1240, 1640, and 2110 nm), as well as ancillary data in the form of total column ozone and surface wind speed. The water leaving radiance is assumed null at all wavelengths, except at 550 nm, where it is assumed equal to 0.005. The measured reflectances are compared with modeled top-of-atmosphere (TOA) reflectances, and the best fit between satellite-measured and modeled TOA spectral reflectances is used to determine the aerosol characteristics and aerosol loading (AOD) of the scene. Modeled TOA reflectances are computed for a combination of one fine mode model (out of four) and one coarse mode model (out of five). In all nine models aerosols are assumed to be spherical particles with minimal absorption. The latter assumption is justified by the fact that the algorithm at these wavelengths is not sensitive to particle absorption. Thus the DT retrieval returns the AOD, a choice of a fine mode and a coarse mode, each defined with a specific size distribution, and also the relative weighting between fine and coarse modes, resulting in a bimodal size distribution.

The first step, as described above, is unchanged from the traditional DT algorithm first developed for MODIS. To the first order, because of the selected wavelengths, the DT algorithm is sensitive to aerosol loading and to particle size distribution but insensitive to absorption variation (Tanré et al., 1996, 1997). The nine DT aerosol models represent particles with minimal absorption with imaginary parts of the refractive index spanning 0.001–0.0035 (Remer et al., 2005). The choice of the imaginary part of the refractive index in these wavelengths was based on ground-based measurements, evaluated later by total column sky radiometer retrievals (Tanré et al., 1997; Dubovik et al., 2002). However, because the primary sensitivity of the retrieval using wavelengths of 0.55 μm and longer is to aerosol loading and size distribution, the effect of uncertainties in assumed absorption properties is to introduce manageable uncertainty in the retrieval of the primary aerosol characteristics. The traditional DT algorithm was not able to distinguish between particles of the same size, but different absorptions, nor able to retrieve a quantitative measure of absorption.

The creation of a second step, an appendage to the traditional DT algorithm that uses the returns from the first step, provides quantitative measures of aerosol absorption from measured UV reflectances. The other inputs are OCI-measured reflectances at 354 and 388 nm. In this second step we use expanded LUTs of the nine traditional models to include the two new UV wavelengths, and in addition allow the imaginary part of the refractive index to vary between four distinct values in these two new wavelengths. Size distribution and the real part of the refractive index are spectrally extrapolated to the UV from the original values assigned to each of the nine models for visible and SWIR wavelengths, and are kept constant as those models' imaginary parts of the refractive index are allowed to vary between four different values. These four imaginary parts of the refractive index represent four different models representative of different degrees of aerosol absorption. These are referred to as "absorption models," even though one is purposely non-absorbing. The range of the imaginary part of the refractive index varies from 0.000 to 0.011. Thus the prototype algorithm LUT consists of 36 models: nine original DT models, each expanded into four possible absorption models in the UV spectrum.

The LUT of step 2 consists of top-of-atmosphere reflectances at 354 and 388 nm for a variety of geometries, a variety of AODs at 0.55 μm extrapolated to the UV wavelengths using the extinction optical properties of each of the 36 models and for four ALHs.: 1.5, 3, 6, and 10 km. Thus for a specific geometry and a specific AOD at 0.55 μm determined from step 1, there are computed reflectances from 144 possible situations (36 models × 4 layer heights). Note that the expansion into multiple absorption properties and layer heights for each size distribution only affects the computed top-of-atmosphere reflectance in the two UV wavelengths. There is no change in the LUT values of the original six wavelength bands of the first step. As such, step 1 and step 2 are only linked because the outputs of step 1 become the inputs to step 2. Step 1 already has determined the size distribution that best fits the observations, choosing one fine mode and one coarse mode from the nine possible models and combining them into a bimodal distribution with a retrieved reflectance weighting parameter (FMF). This retrieved bimodal size distribution and the retrieved spectral AOD are the outputs from step 1 that are input into step 2. These inputs from step 1 constrain the step 2 retrieval in the UV into just 16 possibilities (4 absorption levels × 4 layer heights) out of the original 144.

In the traditional UV aerosol retrievals (Torres et al., 1998) the measured reflectance in the UV wavelengths is sensitive to four aerosol properties: loading (AOD), absorption, layer height and aerosol type (size distribution). The retrieval then assumes two of the four properties and uses the spectral dependence of the UV reflectances to determine the remaining two parameters. For example, the retrieval might assume aerosol type and layer height to retrieve AOD and absorption (Torres et al., 1998). The *spectral dependence* of the UV reflectances is key in pulling out two pieces of information in the retrieval. Here in the OCI proto-algorithm, we do not need to *assume* two properties because Step 1 provides that information, and we use the spectral dependence of the UV reflectances to determine both absorption and layer height from the 16 possibilities in the LUT. The proto-algorithm returns the interpolated layer height and interpolates the SSA from the values of the two absorption models closest to the observations.

Figure 3 demonstrates this prototype algorithm applied to custom granules of merged MODIS and OMI Level 1 radiances.

We tested the algorithm through a series of experiments in which we simulate TOA spectral reflectance from forward calculations using the aerosol models described above, and then retrieve from these calculated reflectances using the proto-algorithm. Doing such an experiment for a range of AOD at 550 nm (0–3.0) and doubling the normalized water leaving radiance to 0.010 from the UV to 0.66 μm, we found the algorithm retrieved the correct input parameters in 100% of the cases when AOD > 0.30, but only 56% of the cases when the AOD was less. This suggests that we can expect little sensitivity to ocean color as long as AOD at 550 nm exceeds about 0.30. When AOD is less than this threshold, preliminary results obtained from theoretical studies suggest that absorbing aerosol can still be identified and separated from non-absorbing marine aerosol, even if the absorption cannot be quantified. Identifying absorbing aerosol depends on spectral signatures in the UV region that differ from spectral signatures of chlorophyll in Case I (open ocean) waters.

One of the expected products from this prototype algorithm is an optically effective aerosol layer scale height. Retrieving this parameter should be possible, given that the AOD and aerosol model are sufficiently constrained by Step 1 of the algorithm. However, this algorithm will not be the only means of obtaining height from PACE instruments. As will be shown in Section "Advances Beyond Heritage, 2: Oxygen A-band Information Content on Aerosol Profiling," there is sufficient information in the OCI channels that cover the O2A to constrain aerosol height independently. In addition one of the MAPs on PACE will be measuring the polarized signal in the UV and deep blue wavelengths. ALH can also be retrieved from the polarized signal in these wavelengths (Wu et al., 2016). Thus, there will be at least three independent methods for characterizing ALH from PACE. Not only will this redundancy confirm the OCI broad spectrum retrieval of layer height, but in doing so, it will also increase confidence in the retrievals of the other parameters produced by the proto-algorithm.

Validation of the prototype retrieval demonstrated in **Figure 3** is based on collocations with SKYNET retrievals. SKYNET is a

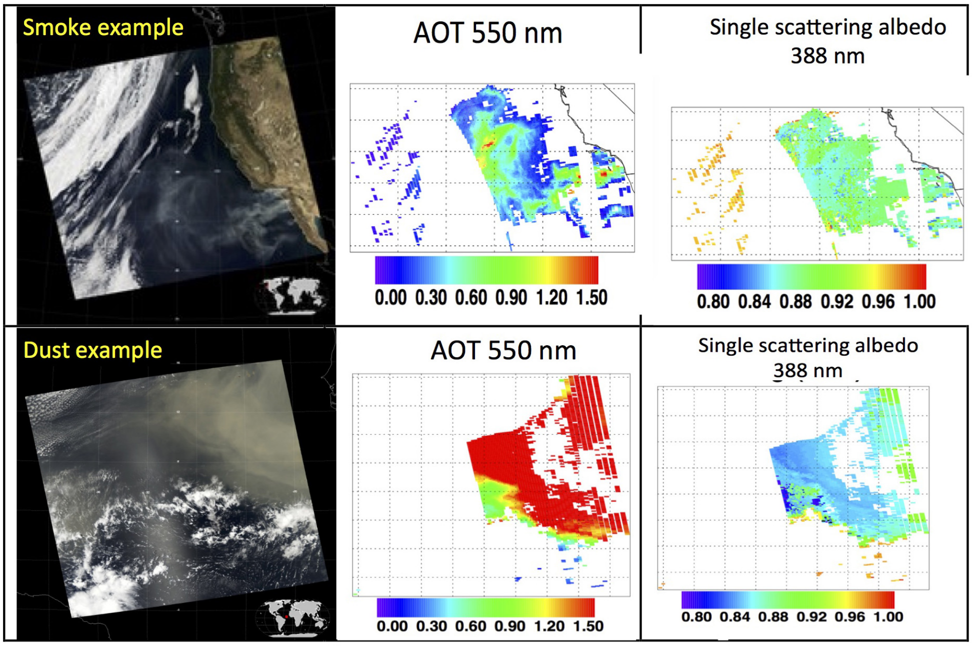

FIGURE 3 | Examples of the proto-type OCI algorithm described in the text applied to custom-built collocated MODIS-OMI granules where the OMI reflectances are mapped to the MODIS granule at the MODIS spatial resolution, although the OMI reflectances maintain their original geometric meta data. The **(left)** column shows the true color MODIS granules. **(Center)** Shows the standard MODIS AOD at 550 nm retrievals and the **(right)** column shows the resulting single scattering albedo at 388 nm using the OMI UV reflectances. **(Top)** Row is for a smoke case over the ocean (23 October 2007, 21:40 UTC). **(Bottom)** Row is for a dust case over ocean (13 March 2006, 15:25 UTC).

ground-based network of autonomous sun/sky radiometers, like AERONET, except SKYNET also makes sky scans in the UV, and retrieves SSA in the UV. This provides a direct comparison with the satellite retrieval's primary product without spectral extrapolation to the visible. Collocations with SKYNET retrievals are rare, and so far validation of the prototype algorithm has been inconclusive. The reason SKYNET was selected for validation and not AERONET is that originally AERONET instruments did not perform a sky scan at 380 nm and therefore no absorption retrieval was produced in the UV. Subsequently some AERONET stations do produce absorption products in the UV, but the same problems encountered with SKYNET collocations would also apply to AERONET.

Part of the difficulty in proving this retrieval with the merged MODIS-OMI data sets is the original problem of possible inconsistent calibration, spatial resolution and geometry. The work done so far demonstrates feasibility and identifies/quantifies sensitivities. The exact retrieval algorithm to be applied to actual OCI observations may take advantage of advanced computer power and two decades of experience and need not follow the MODIS or OMI heritage procedures, as was presented here. Although any OCI aerosol algorithm will make use of the same information content and be challenged by the similar uncertainties.

ADVANCES BEYOND HERITAGE, 2: OXYGEN A-BAND INFORMATION CONTENT ON AEROSOL PROFILING

OCI offers two new capabilities that permit advancing aerosol retrievals beyond heritage. In Section "Advances Beyond Heritage. 1: Broad Spectral Range Retrievals from OCI" we explored the first of these capabilities: the broad spectrum from the UV through the SWIR at a common 1 km spatial resolution and in a single instrument. In Section "Advances Beyond Heritage, 2: Oxygen A-band Information Content on Aerosol Profiling" we explore the second of these capabilities: the continuous 5 nm spectral resolution through the O2A (758–778 nm) region. This capability through the O2A can be mined from the single-view OCI measurements to retrieve ALH, but if it can be measured from a multi-angle instrument, such as the PACE MAPs, information on aerosol layering in the atmosphere increases. Both of these situations will be addressed in this section.

Oxygen A-Band Absorption From Single- and Multi-View Radiometry

Radiance measurements in the O2A are sensitive to the vertical distribution of atmospheric scatterers, which in principle allows for the retrieval of aerosol height from future instruments with hyperspectral capability. OCI has continuous spectral measurements through the O2A and, while much coarser than an ideal (quasi-line-by-line) hyperspectral coverage such as by Orbiting Carbon Observatory (OCO)-2/3 sensors (Crisp et al., 2004), it may have sufficient spectral resolution to achieve similar results. We therefore address here aerosol height estimation via spectral analysis of O_2 absorption in the visible-NIR spectral region. The O2A method to be shown in this section is governed by spectral gas *absorption*, and not the interplay of Rayleigh and aerosol *scattering* used by radiometric and polarimetric UV and blue-channel visible measurements (Torres et al., 1998; Wu et al., 2016). The spectral gas absorption method is less affected by confounding factors that create ambiguities in the scattering methods (Kalashnikova et al., 2011; Wu et al., 2016). For example, in the prototype algorithm described in Section "Advances Beyond Heritage. 1: Broad Spectral Range Retrievals from OCI," retrieval of ALH can be confounded by unknown AOD, absorption or particle size distribution. Determination of the height of a layer of scattering particles using spectral analysis of an absorbing gas is grounded in differential optical absorption spectroscopy (DOAS) (Hebestreit et al., 1999). DOAS is normally used to infer the *unknown* amount of absorbing gas of *known* cross-section across a *known* path. If, as is the case for atmospheric O_2, where both the amount and cross-section of the gas are accurately known, one can infer the effective path through the gas. This in turn becomes a means of locating the layer of the aerosol scattering contributions in the atmospheric column.

The ability to use oxygen absorption for the retrieval of aerosol height from passive sensors has been described extensively in the literature (Gabella et al., 1999; Min and Harrison, 2004; Corradini and Cervino, 2006; Pelletier et al., 2008; Dubuisson et al., 2009; Kokhanovsky and Rozanov, 2010; Frankenberg et al., 2012; Sanghavi et al., 2012; Ding et al., 2016; Xu X. et al., 2017, Xu et al., 2018a,b, Zeng et al., 2018; and others). Therein, the need for the highest possible spectral resolution has been clearly demonstrated. Indeed, the better the spectral resolution, the more samples of weak to strong absorption there are, yielding better vertical resolution in the scattering layer height estimate, and possibly its thickness as well. In other words, a coarse aerosol profiling becomes possible using a passive sensor system. However, compared with active (lidar) approaches to aerosol profiling, the complications of passive DOAS-based methods, including multiple scatterings and surface reflections, increase retrieval uncertainty. To ensure detectability, the aerosol loadings should therefore be significant. Previous theoretical and observational studies (Corradini and Cervino, 2006; Dubuisson et al., 2009; Kokhanovsky and Rozanov, 2010) have suggested an AOD at 550 nm in excess of $\approx$0.3 is necessary to infer height to within a few hundred meters. Our present analysis shows that AOD in the O2A bands $> \approx 0.1$ (equivalent to $\approx$0.15 at 550 nm for an Angstrom exponent of about unity) may suffice over a dark surface such as water.

OCI, at a nominal resolution of 5 nm, will have 3 or 4 spectral bands in the O2A, but only at a single viewing angle. One of the proposed PACE MAPs, Spectro-Polarimeter for Planetary Exploration-1 (SPEXone) (Hasekamp et al., 2019) has hyperspectral radiometry at 2 nm resolution up to 770 nm for five viewing angles. However, SPEXone would provide only one piece of O2A information per pixel, namely, the ratio of a continuum channel and an in-band channel, but will be available at five viewing angles. One of the questions that we explore here is whether observing at different view angles is essentially equivalent to sensing of different penetration depths in the atmosphere above the layer, assuming a plane-parallel atmosphere? In other words will SPEXone or another multi-angle instrument enhance OCI's ability to use DOAS to profile aerosol layers, or will the information content from both sensors essentially over lap? However, first we demonstrate that OCI alone has sufficient spectral resolution to discriminate between different ALHs for less aerosol loading than literature suggests. Then we will proceed with a more formal analysis of DoF for both OCI and a MAP modeled on SPEXone. The point of that exercise is to see if OCI can *profile* aerosol layers on its own, in addition to discriminating layer top height, and then see if merged OCI and MAP O2A observations can improve the aerosol profiling offered by OCI alone.

To begin we examine whether or not OCI will be able to discriminate ALH. The upper-left panel of **Figure 4** illustrates the O2A spectrum displayed as a DOAS ratio for a single surface reflection (where surface albedo is immaterial). That is, spectral radiance normalized by the continuum value ($\lambda = 754$ nm), in this case, for nadir viewing and a solar zenith angle of 60°. Notional bandpasses for a (mono-view) hyperspectral sensor with 5 nm resolution are also shown (top) along with that of a plausible in-band MAP channel (bottom).

When this study was performed, the rational hypothesis is that we will have no control over how OCI will sample the O2A spectral region.[1] Our operative assumption for this study is that it will be a randomly positioned overlay of adjacent 5-nm-wide channels. The upper-right panel of **Figure 4** therefore shows how the oxygen DOAS ratio spectrally averaged in the upper-left panel varies as a function of where the first hyperspectral channel starts. We see that there are cases when the three values required to cover the A-band are quite widely separated; there are also cases are when two of the three values nearly coincide, thus leaving effectively only two effective O_2 optical depths to use. We proceed with the simulation below using an in-between sampling where two of the three available DOAS ratios are relatively close.

In the lower-left panel of **Figure 4**, we used the most likely spectral sampling of the A-band by the OCI ($\lambda_{\text{start}} = 756.5$ nm) to compute signals for two ALH s, along with the anticipated measurement error bars. These synthetic reflected spectra are for optically thin (single-scattering, AOD at the O2A band = 0.1) aerosol layers in 0–2 and 3–5 km altitude ranges. Notice the lesser absorptance (larger in-band radiance) for the elevated layer. Instrumental uncertainties at the 2% level are shown for the two DOAS signals, noting that such radiance ratios are typically more precisely known than are the individual radiances where absolute radiometric error is typically 3% or more. This is because some part of radiometry error (e.g., calibration drift) is the same across (in this case, spectral) pixels. The difference between the two spectra is clearly outside the anticipated measurement error, and we can conclude that there is sensitivity to ALH, at least at this coarse level of discrimination.

This impact of aerosol height on the measured signal will naturally be stronger as the AOD and SSA increase, with the usual tradeoff between the two aerosol optical properties (scattering and absorption). In short, if AOD and SSA are reasonably well quantified from other spectral regions/channels of OCI and/or MAP instruments, we anticipate workable retrieval accuracy for ALH from the O2A, at least sufficient to discriminate between low altitude (background and/or near sources) and high altitude (long-range transported) aerosol scenarios.

To rigorously quantify the retrievability of parameterized aerosol profile using O2A spectroscopy, supplemented or not with simultaneous multi-angle observations, we use Rodgers (2000) Bayesian formalism. Specifically, we use the non-dimensional DoF for retrieved parameter x, $A_\text{x} = 1–\sigma_\text{x}{}^2/\sigma_{\text{a,x}}{}^2$, where x can be either aerosol layer top pressure p_top or its pressure thickness Δp. We use $\sigma_{\text{a,x}}$ to denote the "*a priori*" uncertainty expressed as a standard deviation that quantifies our uncertainty about the parameter before making the radiance measurements and performing the retrieval; similarly, σ_x denotes the "a posteriori" (post-observation/retrieval) uncertainty on the targeted parameter. The DoF varies, by definition, between 0 and 1. If A_x approaches unity, then we have considerably reduced the uncertainty on x thanks to the observation and retrieval; conversely, if A_x approaches 0, then we have gained very little new information and the uncertainty remains almost as large as the prior value. We have assumed $\sigma_{\text{a,pt}} = 250$ hPa (layer top is anywhere between, say, ≈1 to ≈6 km in altitude), and $\sigma_{\text{a},\Delta\text{p}} = 150$ hPa (translates to ≈1.2 km in physical layer thickness near the surface, and ≈2.5 km at 6 km altitude). Measurement error on the DOAS ratios used in the retrieval was set at ±1.5% and error assigned to the non-retrieved (actually, otherwise-retrieved) aerosol optical thickness τ_a was set to ±0.025, while τ_a itself was set to 0.1 in accord with the simple black-surface/single-scattering forward model $\mathbf{f}(\mathbf{x})$ for any given "state vector" $\mathbf{x} = (p_\text{top}, \Delta p)$. The vector-valued function $\mathbf{f}(\mathbf{x})$ contains all the DOAS ratios across the OCI spectral channels that cover the significantly absorbing parts of the O2A (cf. **Figure 4**, lower-left panel), as predicted by the simplified (black-surface/single-scattering) radiative transfer model. In a separate simulation discussed in Section "Aerosol Layer Height Retrievals Using EPIC/DSCOVR's Oxygen A- and B-band Channels," $\mathbf{f}(\mathbf{x})$ predicts DOAS ratios for *both* the OCI and the MAP, assuming five angles are used in the principal plane (0°, $\pm 30^\circ$, $\pm 60^\circ$). In this case, the forward model $\mathbf{f}(\mathbf{x})$ is thus a function of $n = 2$ variables, plus another aerosol parameter (AOD) assumed known but within known uncertainty; $\mathbf{f}(\mathbf{x})$ maps these aerosol properties to DOAS ratios, formally in a vector space with either $m = 3$ dimensions (one for each of OCI's A-band spectral channels). For details about how to derive σ_x and A_x from the above information, we refer to Rodgers (2000). For details about the adopted radiative transfer model, we refer to Davis and Kalashnikova (2019), who also summarize the required elements of optimal estimation theory from Rodgers (2000).

Figure 5 shows A_x for $x = p_\text{top}$ (upper panels) and $x = \Delta p$ (lower panels). On the left, the retrieval uses only OCI spectral

---

[1] At the time of finalizing this report, it has since been decided that OCI's on-board spectral sampling at 2.5 nm will be used to optimize the information content of the A-band channels. Gao and Davis (1997) show how Nyquist (or better) sub-sampling can be used to reconstruct exactly any version of the spectral registration at 5 nm resolution. This means that the conclusions we reach here about OCI's aerosol profiling capability are to be considered as a worse-case scenario from which we can build as the PACE mission is implemented.

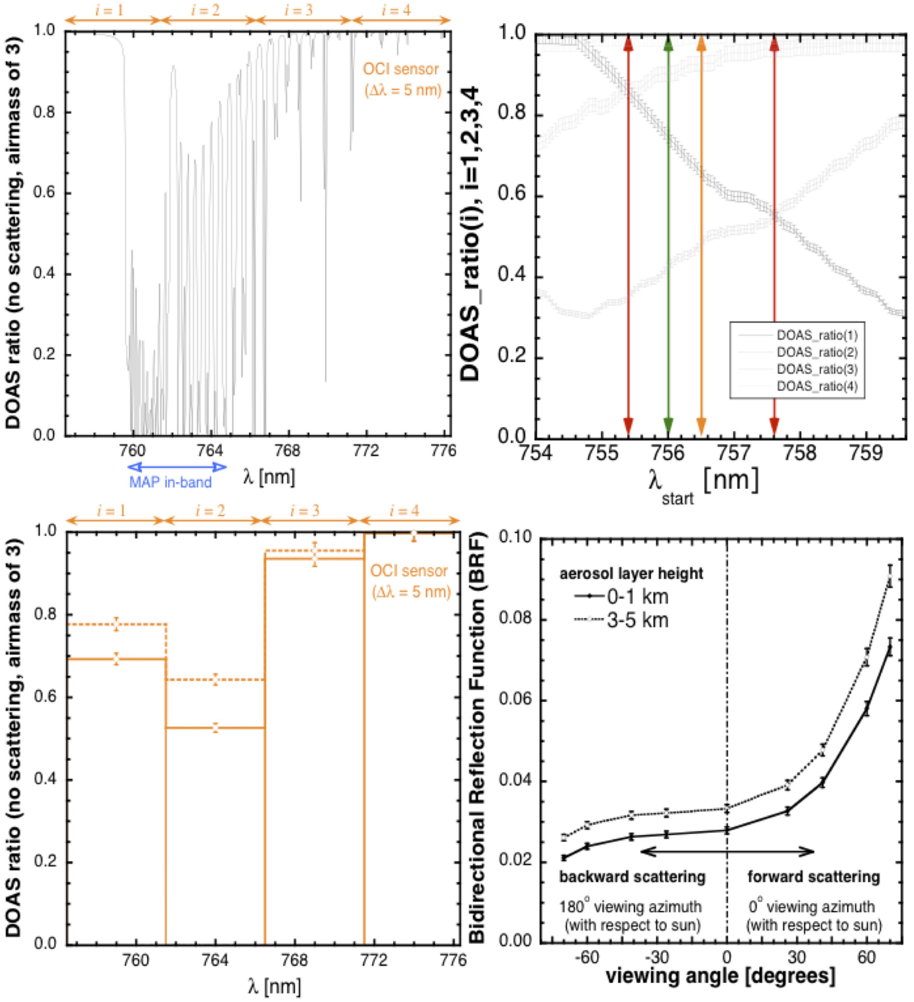

FIGURE 4 | (Upper left) Synthetic spectrum of the O_2 A-band at 0.05 nm resolution, normalized in DOAS-style to continuum level, for a typical airmass of 3 (e.g., sun at 60°, nadir view). An anticipated spectral coverage by the OCI hyperspectral sensor (4 channels, each 5 nm wide) is indicated above in orange, and a reasonable assumption for the single MAP channel is indicated below in blue. **(Upper right)** Evolution of DOAS ratios with 2% error for an airmass of 3 for the 4 hyperspectral OCI channels needed to completely cover the A-band as a function of where the 1st one starts. One good, two bad, and one average scenarios in terms of ratio separations are color-coded in green, red and orange, and the latter values are used in the lower left-hand panel. **(Lower left)** Reflected DOAS ratios for optically thin [AOD(O2A) = 0.1] boundary layer and lofted aerosol layer in the 0–2 km (solid) and 3–5 km (dashed) zones, respectively, assuming the sun is 60° from zenith and nadir viewing geometry. **(Lower right)** Bidirectional reflection function (BRF) for the MAP signal as a function of view angle. Even at typical radiometric noise levels, assumed to be 3%, the two aerosol layer elevations are easier to distinguish here than in lower-left, using instrument error magnitude as unit of signal distance. Reprinted by permission from Springer Nature: Davis and Kalashnikova (2019).

data. In all cases, A_x is plotted as a function of the aerosol layer's top pressure (horizontally) and pressure thickness (vertically). We note that there is some dependence on the latter but none on the former. We also note that much information is gained from the spectroscopy about p_{top}. Specifically, we have $A_{\text{a,pt}}$ in the interval [0.922, 0.928], hence $\sigma_{\text{a,pt}}$ in the range of 67–70 hPa. In turn, this yields an error in aerosol layer top altitude of $\approx$100 m for low altitude aerosol scenarios to $\approx$150 m for lofted layers, which is somewhat better or comparable to accuracy estimates in the above-cited literature. In contrast, **Figure 5**'s lower left-hand panel shows that very little information is gained about Δp since its DoF is in a very low range of 0.0690–0.0735.

The result of these sensitivity studies shows that the top pressure, hence altitude, of an aerosol layer can be retrieved using O2A spectroscopy at the relatively modest spectral resolution (5 nm) of the OCI sensor that is planned to launch on PACE. The often-stated lower limit of $\approx$0.3 in AOD at 550 nm may be relaxed to $\approx$0.1, as long as the underlying surface is very dark, to achieve an uncertainty of $\approx$0.15 km on aerosol layer height.

Now the question is whether or not DOAS applied to a multi-angle instrument improves on OCI's abilities.

Returning to **Figure 4**, the lower right-hand panel shows DOAS ratios for multi-angle measurements for the boundary layer (0–2 km) aerosol and its lofted (3–5 km) counterpart for

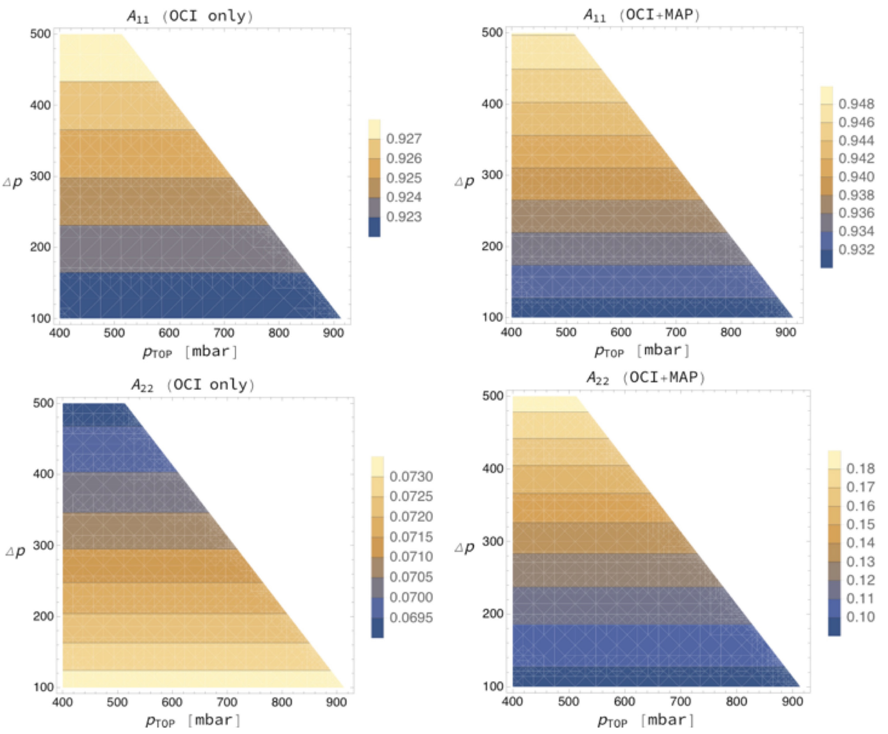

FIGURE 5 | (Upper left) Degree of freedom A_{pt} (denoted A/d11/n) associated with aerosol layer top pressure p_{top} (which has index $i = 1$ in the state vector/bx/n) as retrieved by OCI only with a posterior uncertainty of σ_{pt} based on a prior uncertainty of $\sigma_{a,pt} = 250$ hPa; DOAS ratio measurement uncertainty is assumed to be 1.5% and aerosol optical depth is taken to be 0.1 at O2A wavelengths, with ±0.025 error. **(Lower left)** Same as upper-left, but for $A_{\Delta p}$ (denoted A/d22/n) associated with aerosol layer pressure thickness Δp (which has index $i = 2$ in the state vector/bx/n), using $\sigma_{a,\Delta p} = 150$ hPa. **(Upper right)** As for **(upper left)** but with additional information from collocated multi-angle observations. **(Lower right)** As for **(upper right)**, but for Δp rather than p_{top}. Details explained in Davis and Kalashnikova (2019).

a sensor with just one in-band channel, as indicated in the upper-left panel. Viewing angle is sampled in the MISR pattern (Diner et al., 1998): nadir, ±26.1°, ±45.6°, ±60°, and ±70.5°, with "+" meaning "fore" and "−" meaning "aft" looks that correspond respectively to forward and backward scattering in the northern hemisphere for in MISR's descending sun-synchronous orbit. Again, the anticipated DOAS ratio measurement error of 2% is indicated, demonstrating that, here too, there is sensitivity to ALH, in addition to the one conveyed by OCI spectroscopy.

Moving on to **Figure 5** where DoFs are displayed, we used a separate simulation where $\mathbf{f}(\mathbf{x})$ predicts DOAS ratios for *both* the OCI and the MAP, assuming five angles are used in the principal plane (0°, ±30°, ±60°). In this case, the forward model $\mathbf{f}(\mathbf{x})$ is still a function of $n = 2$ aerosol profile variables, plus AOD (assumed known but with known uncertainty). In this set-up, $\mathbf{f}(\mathbf{x})$ is a formal measurement vector with $m = 8$ dimensions (OCI's and MAP's A-band observations).

What happens to the above DoF assessment if the spectrometer is supplemented by a multi-angle radiometer with non-polarized O2A band channels? We assume an in-band channel as shown at the bottom of the upper left-hand panel of **Figure 4**, and an out-of-band/continuum channel that can combined into a DOAS ratio for each of the sampled viewing angles. The outcome is displayed in the right two panels of **Figure 5** for five angles (nadir, ±30°, ±60°). We note the similarity with the left-hand panels but the ranges for the DoFs are different. In the upper panels, the range of A_{pt} increases from [0.922, 0.928] to [0.930, 0.950], which corresponds to a modest reduction of $\sigma_{\text{a,pt}}$ by ≈10%. In contrast, $A_{\Delta\text{p}}$ increases quite dramatically from [0.0690, 0.0735] to [0.09, 0.19] and, moreover, the trend of $A_{\Delta\text{p}}$ with Δp has changed direction. This range, however, is still not enough to build a credible retrieval of Δp with any confidence. Rather, we can interpret it as a gain in information that can be used to constrain somewhat better the uncertainty on Δp that, in the retrieval of its top pressure p_{top}, should be treated as a non-retrieved (hence necessarily prescribed but uncertain) property of the aerosol layer under consideration.

The bottom line of this theoretical exploration is that PACE will be able to discriminate different altitudes of ALH, but will not be able to profile that height, even by combining OCI with multi-angle measurements.

Aerosol Layer Height Retrievals Using EPIC/DSCOVR's Oxygen A- and B-Band Channels

Oxygen A-band techniques have already been adapted to other sensors currently taking data, and results validated. For example, Xu X. et al. (2017) have retrieved ALHs over ocean surfaces using radiances measured in the oxygen A- and B-bands from the EPIC sensor on the DSCOVR satellite. EPIC measures earth-reflected solar radiances in ten narrow bands. Two of these bands are located in the oxygen A- and B-bands centered at 764 and 688 nm with bandwidth of 0.8 and 1.0 nm, respectively. Two corresponding continuum bands are placed at 680 and 780 nm. The ALH retrieval uses DOAS ratios as described above providing one piece of information by comparing an in-band value with the continuum in both the oxygen A- and B-bands, **Figure 6A** shows the results plotted against collocated CALIOP-measured ALH s over ocean. Most recently, Xu et al. (2018b) extended the retrieval algorithm for smoke ALH over vegetated land surfaces (**Figure 6B**). Assuming that CALIOP-derived aerosol extinction profiles represent an accurate representation of ALH the retrieval accuracy from EPIC's oxygen bands was 0.45 km over ocean and 0.58 km over vegetated land surfaces. Although OCI has a spectral resolution ($\sim$ 5 nm) coarser than the spectral width of EPIC's oxygen A and B channels, theoretical studies show that OCI can resolve oxygen absorption signals and infer ALH. The addition of SPEXone, one of the PACE MAPs with finer spectral resolution through the O2A region, may improve the situation, but the study we have done suggests limited enhancement to OCI's basic sensitivity from the MAP. Furthermore, SPEXone's narrow swath width will not cover the entire OCI domain. Therefore, the ability to infer ALH from OCI-alone will be important to constrain retrievals of other aerosol parameters from the PACE broad swath instruments, including retrievals of aerosol absorption information as described in Section 3, microphysical retrievals from the other PACE polarimeter without O2A capability and will also benefit atmospheric correction for OCI, especially through the shortwave end of its spectrum.

DISCUSSION AND THE PATH FORWARD

PACE offers multi-tiered opportunities for aerosol remote sensing. At the most basic level, OCI will allow continuation of heritage aerosol retrieval algorithms developed for and applied to MODIS, VIIRS and OMI. Continuation aerosol algorithms include the MODIS/VIIRS DT and Deep Blue family of algorithms and products, the OMI UV AI, the OMI UV-derived aerosol products, and new algorithms such as MODIS MAIAC. There are no foreseen barriers to porting these algorithms directly to OCI and we anticipate comparable validation results over both ocean and land surfaces. However, experience in porting aerosol retrievals from MODIS to VIIRS, or OMI to EPIC, suggest points of difficulty that will need to be addressed. Shifts in wavelengths will require new gas corrections and re-calculation of any empirical spectral relationships in the algorithm. Algorithms that depend on acquisition of statistics of surface characteristics will require time to acquire and build these new LUTs. Absence of thermal IR channels may affect cloud masking and introduce differences from heritage sensor results. Furthermore, consistency of sensor characterization will be a significant issue. Homogenizing calibration from existing sensors to new sensors, such as OCI will be necessary in order to maintain consistency across aerosol Climate Data Records. We recommend planning for collocations between OCI and other satellite sensors in the overall mission strategy. All of these recommendations are supported by first-hand experience in the transfer from MODIS to VIIRS, or in OMI to EPIC.

In addition, OCI alone offers a step up from current sensors in terms of its broad spectrum and 5 nm spectral resolution. These additional abilities show promise of obtaining new information on aerosol absorption and ALH. OCI is equivalent to merging MODIS and OMI into a single instrument and extending OMI's spectral range into the SWIR, co-registered and with common calibration and common moderate spatial resolution. For the first time we will have UV channels available for aerosol retrievals at the same resolution as the visible-SWIR channels. Note that OMI's spatial resolution is 13 × 24 km, and the Ozone Mapping and Profiling Suite (OMPS) is 50 km, whereas OCI's spatial resolution is 1 km. Using the broad-spectrum retrieval we will be able to characterize aerosol absorption, layer height, AOD and a measure of particle size across the broad OCI swath, over ocean. Meanwhile, OCI's spectral resolution of 5 nm is sufficient to resolve the signal through the oxygen-A band, and will permit independent retrievals of ALH. Independent retrievals of aerosol height from the UV and oxygen-A band offer an opportunity for redundancy. However, these advances are only possible when aerosol loading is sufficiently high, so that the aerosol signal overwhelms ocean variability. This is more important to the UV to SWIR retrieval than it is when applying O2A algorithms. We also see that oxygen-A band retrievals can be applied to multi-angle measurements that increase confidence in the OCI-alone retrieval of ALH, but still do not allow for profiling of aerosol layers.

A potential limitation to applying the UV proto-algorithm to the aerosol over global oceans is the requirement of moderate to high aerosol loading (AOD at 550 nm > 0.30). We need this requirement to be assured that the atmosphere dominates the OCI-measured signal in the UV and is not affected by variable conditions in the ocean. In testing, we found that the retrieval correctly identified input aerosol absorption 100% of the time despite perturbation to ocean spectral reflectance when AOD > 0.30, but only 56% of the time when the AOD was less. The fraction of retrievals that meet this threshold and would be available for retrieval is small, globally. According to the first 5–7 years of MODIS aerosol product over ocean, only about 10% of the 1 degree grid squares met this requirement (Remer et al., 2008). However in certain regions and seasons, namely March through May in the north Pacific, March through August in the north tropical Atlantic, and December through August in the north Indian Ocean, the seasonal regional mean AOD approaches or exceeds 0.25, suggesting a significant number of retrievals would be possible. Even in the vast areal extent of the ocean where seasonal mean AOD is near background levels, an occasional aerosol event from volcano or wildfire would likely exceed the threshold and be retrievable. These belts of persistent moderate to high aerosol loading are key regions where better characterization of aerosol absorption properties and height will constrain estimates of aerosol effects on regional circulations, cloud processes and the hydrological system (Samset et al., 2018).

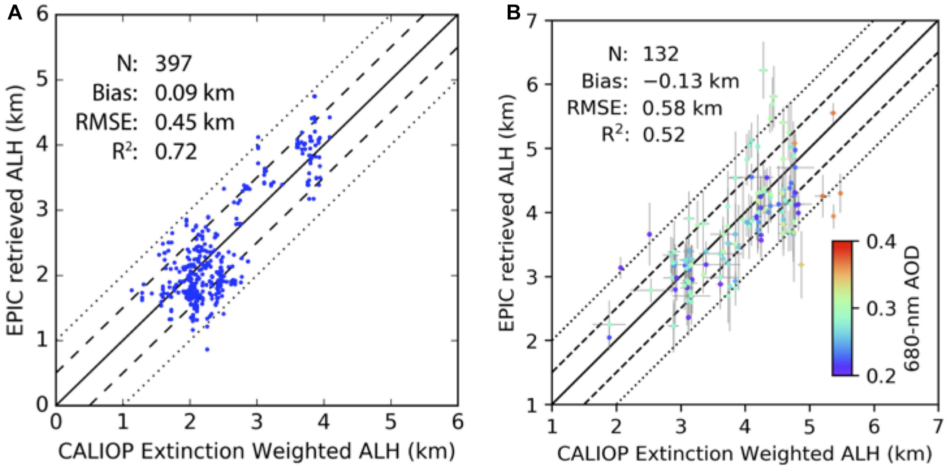

FIGURE 6 | Scatterplots of EPIC retrieved aerosol layer height (ALH) versus CALIOP extinction-weighted ALH. **(A)** For a dust plume over the Atlantic Ocean on 17 – 18 April 2016. Adapted from Xu X. et al. (2017) with permission from John Wiley and Sons. **(B)** For smoke plumes over Canada and Northeastern United States on 25 – 26 August 2017. Adapted from Xu et al. (2018a) with permission under Creative Commons Attribution 4.0 License. Also plotted on each panel are the one-to-one line (solid), ±0.5 km (dashed) and ±1.0 km (dotted) envelopes, the number of samples (N), bias, root-mean-square error (RMSE), and coefficient of determination (R^2). On **(B)**, color of each scatter indicates EPIC retrieved 680-nm AOD values, and error bars of each scatter indicates standard deviations for ALH values of the collocated EPIC and CALIOP pixels.

Heritage and new aerosol algorithms can be developed from PACE sensor measurements for both ocean and land surfaces, and in some cases over clouds, as well. The PACE mission will be able to produce global aerosol products. However, because of the high interest in the mission's ocean objectives, we comment now specifically on the aerosol over ocean retrieval. Heritage aerosol algorithms have served us well and "heritage plus" algorithms will continue to serve us well when applied to OCI measurements over open ocean in Case 1 waters. However, in coastal regions, where traditional assumptions of the ocean spectral signal breaks down, backscattering from suspended hydrosol particles (e.g., phytoplankton and sediment) in unanticipated spectral ranges can be misinterpreted as aerosols, leading to overestimation of AOD at low aerosol loading and interfering with new retrievals making use of the UV and hyperspectral capabilities. Furthermore, adjacency effects between water and shore also add to the complexity in near-shore regions (Bulgarelli et al., 2014). These greater challenges in complex situations require a new instrument, and that is the MAP. While not completely immune from these complex situations, the MAP increases information content, which can be exploited to better separate atmospheric from oceanic and land signals. The MAP is the subject of a companion paper in this same issue (Remer et al., 2019).

There exists strong synergy between atmosphere and ocean retrievals, for PACE. Products derived from each sensor and from each discipline will provide essential information to each other's algorithms, constraining aerosol characteristics and ocean properties for each other, either in near real time, statistically over time, or for reprocessing. The aerosol loading limitations of the above described methods prevents their direct use for atmospheric correction over most of the world's oceans, but does not prevent exploration of more sophisticated methods that might retrieve aerosol and ocean properties together. Simultaneous retrievals of aerosol and ocean properties, or aerosol and land properties are possible. We did not deliberate on the aerosol/land retrievals, but we did consider the possibilities of aerosol/ocean retrievals. These possibilities are discussed more fully in other papers appearing in this special issue (Chowdhary et al., 2019; Frouin et al., 2019; Remer et al., 2019).

Currently there is a severe lack of appropriate space or field data to use as a test bed for algorithm development. Hyperspectral data to simulate OCI observations can be provided by spaceborne HICO or AVIRIS, but neither cover the full spectral range of OCI, and both sensors tend to target scenes when and where aerosol loading is minimal. High altitude hyperspectral imagery that extends into the UV, and is complemented by bands in the SWIR, similar to the OCI design will be essential for preparation of the PACE mission. Such imagery should target aerosol events and various cloudy scenes, over land and ocean, as well as oceanic targets. These images will aid PACE cloud, atmospheric correction and Inherent Optical Property algorithm development, as well as aerosol algorithms. We note that maintaining calibration of such an instrument, especially in the deep blue and UV part of the spectrum is currently challenging, with commonly used sensors such as AVIRIS declaring known issues in this spectral range. Not having reliable full spectrum test data is a serious technical gap in preparing for the PACE mission. Furthermore, such instruments are rarely deployed with airborne MAPs. Existing data in cloud free conditions for with both types of instruments are extremely rare (Gao et al., 2018). We note that AVIRIS, CPL and the Airborne Multiangle SpectroPolarimetric Imager (AirMSPI: a MAP) will fly together during the FIREX-AQ campaign, which should begin to build the necessary test bed for algorithm development, but it is only a start from what will actually be needed.

The PACE mission will be an unprecedented opportunity for aerosol characterization. The combination of the broad-spectrum hyperspectral radiometer and multi-angle polarimeters, used independently or synergistically, will be able to continue heritage global aerosol remote sensing while opening up new opportunities for aerosol characterization on several levels. In addition, the PACE mission unites aerosol, cloud and ocean communities as they work towards meeting intertwined technical and research challenges. We anticipate PACE leading a surge of new understanding that crosses traditional atmosphere-ocean boundaries, leading to new science and societal benefits.

AUTHOR CONTRIBUTIONS

This work represents part of the overall consensus statement agreed to by the first NASA PACE Science Team and includes contributions from the Principal Investigators of the Atmospheric Correction subgroup of that Science Team, along with their associates involved with the aerosol characterization focus of that subgroup. All authors of this manuscript were part of the discussions of that subgroup and Science Team from 2014 to 2018. In addition, LR was the Deputy Lead of the Science Team and Leader of the subgroup. She organized this particular manuscript and consolidated the input from all authors. In addition she led the effort in creating the prototype broad-spectrum algorithm. SM, RL, and OT all contributed directly in obtaining the results of the heritage and broad-spectrum algorithms and writing of those sections. AD along with OK led the O2A work presented herein. KK and JC were active participants in commenting on early versions of this manuscript and helped to clarify several sections. ZA, EB, BC, OC, HD, DD, BF, RF, B-CG, AI, JM, AO, FX, and P-WZ were active participants during the years of discussion that resulted in this manuscript, and each has made contributions, edited, or commented on this manuscript.

FUNDING

This work was supported by the NASA Grants under the solicitation NNH13ZDA001N-PACEST. In addition, LR, SM, RL, and OT acknowledge funding from the NASA grant NNX15AD15G. AD acknowledge funding from the NASA grant NN105525. P-WZ acknowledges funding from the NASA grant 80NSSC18K0345.

ACKNOWLEDGMENTS

Portions of this work were carried out by OK, AD, and DD at the Jet Propulsion Laboratory, California Institute of Technology, under a contract with the National Aeronautics and Space Administration. JPL work was supported by the PACE science team grant, under Paula Bontempi.

REFERENCES

Albert, M. F., Anguelova, M. D., Manders, A. M., Schaap, M., and De Leeuw, G. (2016). Parameterization of oceanic whitecap fraction based on satellite observations. *Atmos. Chem. Phys.* 16, 13725–13751. doi: 10.5194/acp-16-13725-2016

Albert, M. F. M. A., Schaap, M., de Leeuw, G., and Builtjes, P. J. H. (2010). Progress in the determination of the sea spray source function using satellite data. *J. Integr. Environ. Sci.* 7, 159–166. doi: 10.1080/1943815100362146

Albrecht, B. A. (1989). Aerosols, cloud microphysics and fractional cloudiness. *Science* 245, 1227–1230. doi: 10.1126/science.245.4923.1227

Al-Saadi, J., Szykman, J., Pierce, R. B., Kittaka, C., Neil, D., Chu, D. A., et al. (2005). Improving national air quality forecasts with satellite aerosol observations. *Bull. Am. Meteor. Soc.* 86, 1249–1262. doi: 10.1175/BAMS-86-9-1249

Altaratz, O., Koren, I., Remer, L., and Hirsh, E. (2014). Review: cloud invigoration by aerosols – coupling between microphysics and dynamics. *Atmos. Res.* 140-141, 38–60. doi: 10.1016/j.atmosres.2014.01.009

Andreae, M. O., and Rosenfeld, D. (2008). Aerosol-cloud-precipitation interactions. Part 1. The nature and sources of cloud-active aerosols. *Earth Sci. Rev.* 89, 13–41. doi: 10.1016/j.earscirev.2008.03.001

Balch, W. M., Drapeau, D. T., Bowler, B. C., Lyczskowski, E., Booth, E. S., and Alley, D. (2011). The contribution of coccolithophores to the optical and inorganic carbon budgets during the southern ocean gas exchange experiment: new evidence in support of the "Great Calcite Belt" hypothesis. *J. Geophys. Res.* 116:C00F06.

Boucher, O., Randall, P., Artaxo, C., Bretherton, G., Feingold, P., Forster, V.-M., et al. (2013). "Clouds and aerosols," in *Proceedings of the Climate Change 2013: The Physical Science Basis. Contribution of Working Group I to the Fifth Assessment Report of the Intergovernmental Panel on Climate Change*, eds T. F. Stocker, D. Qin, G.-K. Plattner, M. Tignor, S. K. Allen, J. Boschung, et al. (Cambridge: Cambridge University Press).

Bulgarelli, B., Kiselev, V., and Zibordi, G. (2014). Simulation and analysis of adjacency effects in coastal waters: a case study. *Appl. Opt.* 53, 1523–1545. doi: 10.1364/AO.53.001523

Cairns, B., Mishchenko, M. I., Maring, H., Fafaul, B., and Pszcolka, S. (2010). "Accurate monitoring of terrestrial aerosols and total solar irradiance: the NASA Glory mission," in *Proceedings of the SPIE Sensors, Systems, and Next-Generation Satellites XIV*, (Toulouse).

Chin, M., Rood, R. B., Lin, S.-J., Mller, J.-F., and Thompson, A. M. (2000). Atmospheric sulfur cycle simulated in the global model GOCART: model description and global properties. *J. Geophys. Res.* 105, 24671–24687. doi: 10.1029/2000jd900384

Chowdhary, J., Cairns, B., Waquet, F., Knobelspiesse, K., Ottaviani, M., Redemann, J., et al. (2012). Sensitivity of multiangle, multispectral polarimetric remote sensing over open oceans to water-leaving radiance: analyses of RSP data acquired during the MILAGRO campaign. *Rem. Sens. Envir.* 118, 284–308. doi: 10.1016/j.rse.2011.11.003

Chowdhary, J., Zhai, P., Boss, E., Dierssen, H., Frouin, R., Ibrahim, A., et al. (2019). Radiative transfer in atmosphere-ocean systems. *Remote. Sens. Environ.* doi: 10.1016/j.rse.2011.11.003

Coddington, O. M., Vukicevic, T., Schmidt, K. S., and Platnick, S. (2017). Characterizing the information content of cloud thermodynamic phase retrievals from the notional PACE OCI shortwave reflectance measurements. *J. Geophys. Res. Atmos.* 122, 8079–8100. doi: 10.1002/2017JD026493

Corradini, S., and Cervino, M. (2006). Aerosol extinction coefficient profile retrieval in the oxygen A-band considering multiple scattering atmosphere. Test case: SCIAMACHY nadir simulated measurements. *J. Quant. Spectrosc. Radiat. Transf.* 97, 354–380. doi: 10.1016/j.jqsrt.2005.05.061

Crisp, D., Atlas, R. M., Bréon, F.-M., Brown, L. R., Burrows, J. P., Ciais, P., et al. (2004). The orbiting carbon observatory (OCO) mission. *Adv. Space Res.* 34, 700–709.

Davis, A. B., and Kalashnikova, O. V. (2019). "Aerosol layer height over water via O2 A-band observations from space: a tutorial," in *Springer Series in Light Scattering, vol. 3: Radiative Transfer and Light Scattering*, ed. A. A. Kokhanovsky (Heidelberg: Springer), 133–166. doi: 10.1007/978-3-030-03445-0_4

Del Castillo, A., Platnick, S., and the Pace Science Definition Team (2012). *The Pre-ACE Aerosols, Clouds and Ocean Ecosystems Mission Science Definition Team Report*. Available at: https://pace.oceansciences.org/docs/pace_sdt_report_final.pdf (accessed June 13, 2019).

Dierssen, H. M. (2019). Spectral characterization of whitecaps reveals new hyperspectral methods for estimating whitecap and foam in ocean color imagery. *Front. Earth Sci. Atmos. Sci.* 7.

Dierssen, H. M., Chlus, A., and Russell, B. (2015). Hyperspectral discrimination of floating mats of seagrass wrack and the macroalgae Sargassum in coastal waters of Greater Florida Bay using airborne remote sensing. *Remote Sens. Environ.* 167, 247–258. doi: 10.1016/j.rse.2015.01.027

Diner, D. J., Beckert, J. C., Reilly, T. H., Bruegge, C. J., Conel, J. E., Kahn, R. A., et al. (1998). Multi-angle imaging spectroradiometer (MISR) instrument description and experiment overview. *IEEE Trans. Geosci. Remote Sens.* 36, 1072–1087. doi: 10.1109/36.700992

Ding, S., Wang, J., and Xu, X. (2016). Polarimetric remote sensing in oxygen A and B bands: sensitivity study and information content analysis for vertical profile of aerosols. *Atmos. Meas. Tech.* 9, 2077–2092. doi: 10.5194/amt-9-2077-2016

Dubovik, O., Holben, B. N., Lapyonok, T., Sinyuk, A., Mishchenko, M. I., Yang, P., et al. (2002). Non-spherical aerosol retrieval method employing light scattering by spheroids. *Geophys. Res. Lett.* 29, 54-1, 54-4. doi: 10.1029/2001GL014506

Dubuisson, P., Frouin, R., Duforêt, L., Dessailly, D., Voss, K. J., and Antoine, D. (2009). Estimating the altitude of aerosol plumes over the ocean from reflectance ratio measurements in the O2 A-band. *Remote Sens. Environ.* 113, 1899–1911. doi: 10.1016/j.rse.2009.04.018

Eck, T. F., Holben, B. N., Reid, J. S., Arola, A., Ferrare, R. A., Hostetler, C. A., et al. (2014). Observations of rapid aerosol optical depth enhancements in the vicinity of polluted cumulus clouds. *Atmos. Chem. Phys.* 14, 11633–11656. doi: 10.5194/acp-14-11633-2014

European Space Agency [ESA] (2013). *Sentinel-5 Precursor. Copernicus Low Earth Orbit Atmosphere Mission*. Available at: http://esamultimedia.esa.int/docs/S5-prec_Data_Sheet.pdf (accessed June 13, 2019).

Fan, J., Wang, Y., Rosenfeld, D., and Liu, X. (2016). Review of aerosol-cloud interactions: mechanisms, significance and challenges. *J. Atmos. Sci.* 73, 4221–4252. doi: 10.1175/JAS-D-16-0037.1

Feingold, G., Jiang, H. L., and Harrington, J. Y. (2005). On smoke suppression of clouds in Amazonia. *Geophys. Res. Lett.* 32:L02804. doi: 10.1029/2004GL021369

Fogarty, M. C., Fewings, M. R., Paget, A. C., and Dierssen, H. M. (2017). The Influence of a sandy substrate, seagrass, or highly turbid water on albedo and surface heat flux. *J. Geophys. Res. Oceans* 123, 53–73. doi: 10.1016/j.scitotenv.2017.06.249

Franck, U., Odeh, S., Wiedensohler, A., Wehner, B., and Herbarth, O. (2011). The effect of particle size on cardiovascular disorders – the smaller the worse. *Sci. Total Environ.* 409, 4217–4221. doi: 10.1016/j.scitotenv.2011.05.049

Frankenberg, C., Hasekamp, O., O'Dell, C., Sanghavi, S., Butz, A., and Worden, J. (2012). Aerosol information content analysis of multi- angle high spectral resolution measurements and its benefit for high accuracy greenhouse gas retrievals. *Atmos. Meas. Tech.* 5, 1809–1821. doi: 10.5194/amt-5-1809-2012

Franklin, M. O., Kalashnikova, V., and Garay, M. J. (2017). Size-resolved particulate matter concentrations derived from 4.4 km-resolution size-fractionated multi-angle imaging spectroradiometer (MISR) aerosol optical depth over Southern California. *Remote Sens. Environ.* 196, 312–323. doi: 10.1016/j.rse.2017.05.002

Frouin, R., Schwindling, M., and Deschamps, P.-Y. (1996). Spectral reflectance of sea foam in the visible and near-infrared: in situ measurements and remote sensing implications. *J. Geophys. Res. Oceans* 101, 14361–14371. doi: 10.1029/96jc00629

Frouin, R. J., Franz, B. A., Ibrahim, A., Knobelspiesse, K., Ahmad, Z., Cairns, B., et al. (2019). Atmospheric correction of satellite ocean-color imagery during the PACE Era. *Front. Earth Sci.* doi: 10.3389/feart.2019.00145

Gabella, M., Kisselev, V., and Perona, G. (1999). Retrieval of aerosol profile variations from reflected radiation in the oxygen absorption A band. *Appl. Opt.* 38, 3190–3195.

Gao, B.-C., and Davis, C. O. (1997). Development of a line-by-line-based atmosphere removal algorithm for airborne and spaceborne imaging spectrometers. *SPIE Proc.* 3118, 132–141.

Gao, M., Zhai, P.-W., Franz, B., Hu, Y., Knobelspiesse, K., Werdell, P. J., et al. (2018). Retrieval of aerosol properties and water-leaving reflectance from multi-angular polarimetric measurements over coastal waters. *Opt. Exp.* 26, 8968–8989. doi: 10.1364/OE.26.008968

Garaba, S., Aitken, J., Slat, B., Dierssen, H. M., Lebreton, L., Zielinski, O., et al. (2018). Sensing ocean plastics with an airborne hyperspectral shortwave IR imager. *Env. Sci. Technol.* 52, 11699–11707. doi: 10.1021/acs.est.8b02855

Garaba, S. P., and Dierssen, H. M. (2018). An airborne remote sensing case study of synthetic hydrocarbon detection using short wave infrared absorption features identified from marine-harvested macro-and microplastics. *Remote Sens. Environ.* 205, 224–235. doi: 10.1016/j.rse.2017.11.023

Gassó, S., and Torres, O. (2016). The role of cloud contamination, aerosol layer height and aerosol model in the assessment of the OMI near-UV retrievals over the ocean. *Atmos. Meas. Tech.* 9, 3031–3052. doi: 10.5194/amt-9-3031-2016

Hasekamp, O. P., Fu, G., Rusli, S. P., Wu, L., Di Noia, A., de Brugh, J., et al. (2019). Aerosol measurements by SPEXone on the NASA PACE mission: expected retrieval capabilities. *J. Quant. Spectrosc. Radiat. Transf.* 227, 170–184. doi: 10.1016/j.jqsrt.2019.02.006

Hebestreit, K., Stutz, J., Rosen, D., Matveiv, V., Peleg, M., Luria, M., et al. (1999). DOAS measurements of tropospheric bromine oxide in mid-latitudes. *Science* 283, 55–57. doi: 10.1126/science.283.5398.55

Herman, J. R., and Celarier, E. A. (1997). Earth surface reflectivity climatology at 340 nm to 380 nm from TOMS data. *J. Geophys. Res.* 102, 28,003–28,011.

Herman, J. R., Bhartia, P. K., Torres, O., Hsu, C., Seftor, C., and Celarier, E. (1997). Global distribution of UV-absorbing aerosols from Nimbus 7/TOMS data. *J. Geophys. Res. Atmos.* 102, 16911–16922. doi: 10.1029/96JD03680

Holben, B. N., Eck, T., Slutsker, I., Tanré, D., Buis, J., Setzer, A., et al. (1998). Aeronet: a federated instrument network and data archive for aerosol characterization. *Rem. Sens. Environ.* 66, 1–16. doi: 10.1016/s0034-4257(98)00031-5

Hsu, N. C., Jeong, M.-J., Bettenhausen, C., Sayer, A. M., Hansell, R., Seftor, C. S., et al. (2013). Enhanced deep blue aerosol retrieval algorithm: the second generation. *J. Geophys. Res. Atmos.* 118, 9296–9315. doi: 10.1002/jgrd.50712

Hsu, N. C., Tsay, S. C., King, M. D., and Herman, J. R. (2004). Aerosol properties over bright-reflecting source regions. *IEEE Trans. Geosci. Rem. Sens.* 42, 557–569. doi: 10.1109/TGRS.2004.824067

Ito, T., Nenes, A., Johnson, M. S., Meskhidze, N., and Deutsch, C. (2016). Acceleration of oxygen decline in the tropical Pacific over the past decades by aerosol pollutants. *Nat. Geosci.* 9, 443. doi: 10.1038/ngeo2717

Jethva, H., and Torres, O. (2011). Satellite-based evidence of wavelength-dependent aerosol absorption in biomass burning smoke inferred from ozone monitoring instrument. *Atmos. Chem. Phys.* 11, 10541–10551. doi: 10.5194/acp-11-10541-2011

Jethva, H., Torres, O., and Ahn, C. (2014a). Global assessment of OMI aerosol single-scattering albedo using ground-based AERONET inversion. *J. Geophys. Res. Atmos.* 119, 9020–9040. doi: 10.1002/2014JD021672

Jethva, H., Torres, O., Waquet, F., Chand, D., and Hu, Y. (2014b). How do A-train sensors intercompare in the retrieval of above-cloud aerosol optical depth? A case study-based assessment. *Geophys. Res. Lett.* 41, 186–192. doi: 10.1002/2013GL058405

Jethva, H., Torres, O., Remer, L., and Bhartia, P. (2013). A color ratio method for simultaneous retrieval of aerosol and cloud optical thickness of above-cloud absorbing aerosols from passive sensors: application to MODIS measurements. *IEEE Trans. Geosci. Rem. Sens.* 51, 3862–3870. doi: 10.1109/TGRS.2012.2230008

Jethva, H., Torres, O., Remer, L., Redemann, J., and Livingston, J. (2016). Validating MODIS above-cloud aerosol optical depth retrieved from "color ratio" algorithm using direct measurements made by NASA's airborne AATS and 4STAR sensors. *Atmos. Meas. Tech* 9, 5053–5062. doi: 10.5194/amt-9-5053-2016

Jickells, T. D., An, Z. S., and Andersen, K. K. (2005). Global iron connections between desert dust, ocean biogeochemistry, and climate. *Science* 308, 67–71. doi: 10.1126/science.1105959

Johnson, B. T., Shine, K. P., and Forster, F. M. (2004). The semi-direct aerosol effect: impact of absorbing aerosols on marine stratocumulus. *Q. J. R. Meteorol. Soc.* 130, 1407–1422. doi: 10.1256/qj.03.61

Kahn, R. A., and Gaitley, B. J. (2015). An analysis of global aerosol type as retrieved by MISR. *J. Geophys. Res. Atmos*. 120, ,4248–4281. doi: 10.1002/2015JD02332

Kalashnikova, O. V., Garay, M. J., Davis, A. B., Diner, D. J., and Martonchik, J. V. (2011). Sensitivity of multi-angle photo-polarimetry to vertical layering and mixing of absorbing aerosols: quantifying measurement uncertainties. *J. Quat. Spectrosc. Radiat. Trans.* 112, 2149–2163. doi: 10.1016/j.jqsrt.2011.05.010

Kalashnikova, O. V., Garay, M. J., Martonchik, J. V., and Diner, D. J. (2013). MISR dark water aerosol retrievals: operational algorithm sensitivity to particle non-sphericity. *Atmos. Meas. Tech.* 6, 2131–2154. doi: 10.5194/amt-6-2131-2013

Kalashnikova, O. V., and Kahn, R. (2006). Ability of multiangle remote sensing observations to identify and distinguish mineral dust types: part 2. Sensitivity over dark water. *J. Geophys. Res.* 111, D11207. doi: 10.1029/2005JD00675

Kaufman, Y. J., and Koren, I. (2006). Smoke and pollution aerosol effect on cloud cover. *Science* 313, 655–658. doi: 10.1126/science.1126232

Kaufman, Y. J., Koren, I., Remer, L. A., Rosenfeld, D., and Rudich, Y. (2005a). The effect of smoke, dust and pollution aerosol on shallow cloud development over the atlantic ocean. *Proc. Nat. Acad. Sci. U.S.A.* 102, 11207–11212. doi: 10.1073/pnas.0505191102

Kaufman, Y. J., Koren, I., Remer, L. A., Tanré, D., Ginoux, P., and Fan, S. (2005b). Dust transport and deposition observed from the Terra-MODIS spacecraft over the Atlantic Ocean. *J. Geophys. Res.* 110:D10S12. doi: 10.1029/2003JD004436

Kaufman, Y. J., and Nakajima, T. (1993). Effect of Amazon smoke on cloud microphysics and albedo. *J. Appl. Meteor*. 32, 729–744. doi: 10.1175/1520-0450(1993)032<0729:eoasoc>2.0.co;2

Khain, A., Rosenfeld, D., and Pokrovsky, A. (2005). Aerosol impact on the dynamics and microphysics of deep convective clouds. *Q. J. R. Meteorol. Soc.* 131, 2639–2663. doi: 10.1256/qj.04.62

Knobelspiesse, K., Cairns, B., Mishchenko, M., Chowdhary, J., Tsigaridis, K., van Diedenhoven, B., et al. (2012). Analysis of fine-mode aerosol retrieval capabilities by different passive remote sensing instrument designs. *Opt. Exp.* 20, 21457–21484. doi: 10.1364/OE.20.021457

Knobelspiesse, K. D., Pietras, C., Fargion, G. S., Wang, M., Frouin, R., Miller, M. A., et al. (2004). Maritime aerosol optical thickness measured by handheld sun photometers. *Remote Sens. Environ.* 93, 87–106. doi: 10.1016/j.rse.2004.06.018

Kokhanovsky, A. A. (2015). The modern aerosol retrieval algorithms based on the simultaneous measurements of the intensity and polarization of reflected solar light: a review. *Front. Environ. Sci.* 3:4. doi: 10.3389/fenvs.2015.00004

Kokhanovsky, A. A., Deuzé, J. L., Diner, D. J., Dubovik, O., Ducos, F., Emde, C., et al. (2010). The inter-comparison of major satellite aerosol retrieval algorithms using simulated intensity and polarization characteristics of reflected light. *Atmos. Meas. Tech.* 3, 909–932. doi: 10.5194/amt-3-909-2010

Kokhanovsky, A. A., and Rozanov, V. V. (2010). The determination of dust cloud altitudes from a satellite using hyperspectral measurements in the gaseous absorption band. *Int. J. Remote Sens.* 31, 2729–2744. doi: 10.1080/01431160903085644

Koren, I., Altaratz, O., Remer, L. A., Feingold, G., Martins, J. V., and Heiblum, R. H. (2012). Aerosol-induced intensification of rain from the tropics to the mid-latitudes. *Nat. Geosci.* 5, 118–122. doi: 10.1038/ngeo1364

Koren, I., Kaufman, Y. J., Remer, L. A., and Martins, J. V. (2004). Measurement of the effect of amazon smoke on inhibition of cloud formation. *Science* 303, 1342–1345. doi: 10.1126/science.1089424

Koren, I., Kaufman, Y. J., Rosenfeld, D., Remer, L. A., and Rudich, Y. (2005). Aerosol invigoration and restructuring of Atlantic convective clouds. *Geophys. Res. Lett.* 32:LI4828. doi: 10.1029/2005GL023187

Koren, I., Martins, J. V., Remer, L. A., and Afargan, H. (2008). Smoke invigoration versus inhibition of clouds over the amazon. *Science* 321, 946–949. doi: 10.1126/science.1159185

Koren, I., Remer, L. A., Altaratz, O., Martins, J. V., and Davidi, A. (2010). Aerosol-induced changes of convective cloud anvils produce strong climate warming. *Atmos. Chem. Phys.* 10, 5001–5010. doi: 10.5194/acp-10-5001-2010

Levy, R. C., Mattoo, S., Munchak, L. A., Remer, L. A., Sayer, A. M., Patadia, F., et al. (2013). The Collection 6 MODIS aerosol products over land and ocean. *Atmos. Meas. Tech.* 6, 2989–3034. doi: 10.5194/amt-6-2989-2013

Levy, R. C., Munchak, L. A., Mattoo, S., Patadia, F., Remer, L. A., and Holz, R. E. (2015). Towards a long-term global aerosol optical depth record: applying a consistent aerosol retrieval algorithm to MODIS and VIIRS-observed reflectance. *Atmos. Meas. Tech.* 8, 4083–4110. doi: 10.5194/amt-8-4083-2015

Li, R.-R., Kaufman, Y. J., Gao, B.-C., and Davis, C. O. (2003). Remote sensing of suspended sediments and shallow coastal waters. *IEEE Trans. Geosci. Remote Sens.* 41, 559–566. doi: 10.1007/s10661-017-5905-7

Li, Z., Niu, F., Fan, J., Liu, Y., Rosenfeld, D., and Ding, Y. (2011). Long-term impacts of aerosols on the vertical development of clouds and precipitation. *Nat. Geosci.* 4, 888–894. doi: 10.1038/ngeo1313

Li, Z., Zhao, X., Kahn, R., Mishchenko, M., Remer, L., Lee, K.-H., et al. (2009). Uncertainties in satellite remote sensing of aerosols and impact on monitoring its long-term trend: a review and perspective. *Ann. Geophys.* 27, 2755–2770. doi: 10.5194/angeo-27-2755-2009

Lim, S. S., Vos, T., and Flaxman, A. D. (2012). A comparative risk assessment of burden of disease and injury attributable to 67 risk factors and risk factor clusters in 21 regions, 1990-2010: a systematic analysis for the Global Burden of Disease Study 2010. *Lancet* 380, 2224–2260. doi: 10.1016/S0140-6736(12)61766-8

Lyapustin, A., Wang, Y., Laszlo, I., Kahn, R., Korkin, S., Remer, L., et al. (2011). Multiangle implementation of atmospheric correction (MAIAC): 2. Aerosol algorithm. *J. Geophys. Res.* 116:D03211. doi: 10.1029/2010JD014986

Marmorino, G. O., and Smith, G. B. (2005). Bright and dark ocean whitecaps observed in the infrared. *Geophys. Res. Lett.* 32:L11604. doi: 10.1029/2005GL023176

Marshak, A., Herman, J., Adam, S., Karin, B., Carn, S., Cede, A., et al. (2018). Earth observations from DSCOVR EPIC Instrument. *Bull. Amer. Meteor. Soc.* 99, 1829–1850. doi: 10.1175/BAMS-D-17-0223.18

Meyer, K. G., and Platnick, S. E. (2015). Simultaneously inferring above-cloud absorbing aerosol optical thickness and underlying liquid phase cloud optical and microphysical properties using MODIS. *J. Geophys. Res. Atmos* 120, 5524–5547. doi: 10.1002/2015JD023128

Min, Q., and Harrison, L. C. (2004). Retrieval of atmospheric optical depth profiles from downward-looking high-resolution O2 A-band measurements: optically thin conditions. *J. Atmos. Sci.* 61, 2469–2477. doi: 10.1175/1520-0469(2004)061<2469:roaodp>2.0.co;2

Mishchenko, M. I., Cairnsa, B., Hansen, J. E., Travis, L. D., Burgc, R., Kaufman, Y. J., et al. (2004). Monitoring of aerosol forcing of climate from space: analysis of measurement requirements. *J. Quant. Spectrosc. Radiat. Transf.* 88, 149–161. doi: 10.1016/j.jqsrt.2004.03.030

Morrison, H., and Grabowski, W. W. (2011). Cloud-system resolving model simulations of aerosol indirect effects on tropical deep convection and its thermodynamic environment. *Atmos. Chem. Phys.* 11, 10503–10523. doi: 10.5194/acp-11-10503-2011

Myhre, G., Bréon, F.-M., Collins, W., Fuglestvedt, J., Huang, J., Koch, D., et al. (2013). "Anthropogenic and natural radiative forcing," in *Proceedings of the Climate Change 2013: The Physical Science Basis. Contribution of Working Group I to the Fifth Assessment Report of the Intergovernmental Panel on Climate Change*, eds T. F. Stocker, D. Qin, G.-K. Plattner, M. Tignor, S. K. Allen, J. Boschung, et al. (Cambridge: Cambridge University Press).

Pelletier, B., Frouin, R., and Dubuisson, P. (2008). "Retrieval of the aerosol vertical distribution from atmospheric radiance," in *Proceedings of the SPIE*, (Noumea), 71501R.

Perry, R. A., Vaudrey, J. M., and Dierssen, H. M. (2018). Long range transport and carbon and nitrogen dynamics of floating seagrass wracks in Greater Florida Bay. *Estuar. Coast. Shelf Sci.* 209, 7–17. doi: 10.1016/j.ecss.2018.05.006

Remer, L. A., Kaufman, Y. J., Tanré, D., Mattoo, S., Chu, D. A., Martins, J. V., et al. (2005). The MODIS aerosol algorithm, products, and validation. *Atmos. J. Sci.* 62, 947–973.

Remer, L. A., Kleidman, R. G., Levy, R. C., Kaufman, Y. J., Tanré, D., Mattoo, S., et al. (2008). Global aerosol climatology from the MODIS satellite sensors. *J. Geophys. Res.: Atmos.* 113. doi: 10.1029/2007JD009661

Remer, L. A., Knobelspiesse, K., Zhai, P.-W., Xu, F., Kalashnikova, O. V., Chowdhary, J., et al. (2019). Retrieving aerosol characteristics from the PACE mission, Part 2: multi-angle and polarimetry. *Front. Earth Sci.* doi: 10.3389/fenvs.2019.00094

Rodgers, C. D. (2000). *Inverse Methods for Atmospheric Sounding: Theory and Practice*. Singapore: World Scientific.

Rosenfeld, D., Lohmann, U., Raga, G. B., O'Dowd, C. D., Kulmala, M., Fuzziet, S., et al. (2008). Flood or drought: how do aerosols affect precipitation? *Science* 321, 1309–1313. doi: 10.1126/science.1160606

Rosenfeld, D., Sherwood, S., Wood, R., and Donner, L. (2014b). Climate effects of aerosol-cloud interactions. *Science* 343, 379–380. doi: 10.1126/science.1247490

Rosenfeld, D., Andreae, A., and Asmi, A. (2014a). Global observations of aerosol-cloud-precipitation-climate interactions. *Rev. Geophys.* 52, 750–808. doi: 10.1002/2013RG000441

Rosenfeld, D., and Woodley, W. L. (2001). Pollution and clouds. *Phys. World* 14, 33–37.

Samset, B. H., Stjern, C. W., and Andrews, E. (2018). Aerosol absorption: progress towards global and regional constraints. *Curr. Clim. Change Rep*. 4:65. doi: 10.1007/s40641-018-0091-4

Sanghavi, S., Martonchik, J. V., Landgraf, J., and Platt, U. (2012). Retrieval of the optical depth and vertical distribution of particulate scatterers in the atmosphere using OA- and B-band SCIAMACHY observations over Kanpur: a case study. *Atmos. Meas. Tech.* 5, 1099–1119. doi: 10.5194/amt-5-1099-2012

Satheesh, S. K., Torres, O., Remer, L. A., Suresh Babu, S., Vinoj, V., Eck, T. F., et al. (2009). Improved assessment of aerosol absorption using OMI-MODIS joint retrieval. *J. Geophys. Res.* 114:D05209. doi: 10.1029/2008JD011024

Sayer, A. M., Hsu, N. C., Bettenhausen, C., Lee, J., Redemann, J., Schmid, B., et al. (2016). Extending "Deep Blue" aerosol retrieval coverage to cases of absorbing aerosols above clouds: sensitivity analysis and first case studies. *J. Geophys. Res. Atmos.* 121, 4830–4854. doi: 10.1002/2015JD024729

Seinfeld, J. H., Bretherton, C., Carslaw, K. S., Coe, H., DeMott, P. J., Dunlea, E. J., et al. (2016). Improving our fundamental understanding of the role of aerosol- cloud interactions in the climate system. *Proc. Nat. Acad. Sci. U.S.A.* 113, 5781–5790. doi: 10.1073/pnas.1514043113

Shi, J. J., Matsui, T., Tao, W.-K., Peters-Lidard, C., Chin, M., Tan, Q., et al. (2014). Implementation of an aerosol-cloud microphysics-radiation coupling into the NASA Unified WRF: simulation results for the 6-7 August 2006 AMMA special observing period. *Quart. J. R. Meteor. Soc.* 140, 2158–2175. doi: 10.1002/qj.2286

Smirnov, A., Holben, B. N., Slutsker, I., Giles, D. M., McClain, C. R., Eck, T. F., et al. (2009). Maritime aerosol network as a component of aerosol robotic network. *J. Geophys. Res. Atmos.* 114:D06204.

Stamnes, S., Hostetler, C., Ferrare, R., Burton, S., Liu, X., Hair, J., et al. (2018). Simultaneous polarimetric retrievals of microphysical aerosol and ocean color parameters from the "MAPP" algorithm with comparison to high spectral resolution lidar aerosol and ocean products. *Appl. Opt.* 57, 2394–2413. doi: 10.1364/AO.57.002394

Stevens, B., and Feingold, G. (2009). Untangling aerosol effects on clouds and precipitation in a buffered system. *Nature* 461, 607–613. doi: 10.1038/nature08281

Tanré, D., Herman, M., and Kaufman, Y. J. (1996). Information on aerosol size distribution contained in solar reflected spectral radiances. *Geophys. J. Res.* 101, 43–19.

Tanré, D., Kaufman, Y. J., Herman, M., and Mattoo, S. (1997). Remote sensing of aerosol properties over oceans using the MODIS/EOS spectral radiances. *J. Geophys. Res.* 102, 971–916.

Tao, W. K., Chen, J.-P., Li, Z., Wang, C., and Zhang, C. (2012). Impact of aerosols on convective clouds and precipitation. *Rev. Geophys.* 50:RG2001. doi: 10.1029/2011RG000369

Torres, O., Ahn, C., and Chen, Z. (2013). Improvements to the OMI near-UV aerosol algorithm using A-train CALIOP and AIRS observations. *Atmos. Meas. Tech.* 6, 3257–3270. doi: 10.5194/amt-6-3257-2013

Torres, O., Bhartia, P. K., Herman, J. R., Ahmad, Z., and Gleason, J. (1998). Derivation of aerosol properties from satellite measurements of backscattered ultraviolet radiation: theoretical basis. *Geophys. J. Res.* 103, 99–17.

Torres, O., Bhartia, P. K., Herman, J. R., Sinyuk, A., and Holben, B. (2002). A long term record of aerosol optical thickness from TOMS observations and comparison to AERONET measurements. *Atmos. J. Sci.* 59, 398–413. doi: 10.1175/1520-0469(2002)059<0398:altroa>2.0.co;2

Torres, O., Bhartia, P. K., Syniuk, A., and Welton, E. (2005). TOMS Measurements of aerosol absorption from space: comparison to SAFARI 2000 ground based observations. *Geophys. J. Res.* 110, D10S18. doi: 10.10129/2004JD004611

Torres, O., Jethva, H., and Bhartia, P. K. (2012). Retrieval of aerosol optical depth above clouds from omi observations: sensitivity analysis and case studies. *J. Atmos. Sci.* 69, 1037–1053. doi: 10.1175/JAS-D-11-0130.1

Torres, O., Tanskanen, A., Veihelman, B., Ahn, C., Braak, R., Bhartia, P. K., et al. (2007). Aerosols and surface UV products from OMI observations: an overview. *Geophys. J. Res.* 112, D24S47. doi: 10.1029/2007JD008809

Twomey, S. (1977). Influence of pollution on shortwave albedo of clouds. *Atmos. J. Sci.* 34, 1149–1152. doi: 10.1175/1520-0469(1977)034<1149:tiopot>2.0.co;2

Van den Heever, S. C., Stephens, G. L., and Wood, N. B. (2011). Aerosol indirect effects on tropical convection characteristics under conditions of radiative convective equilibrium. *Atmos. J. Sci.* 68, 699–718. doi: 10.1175/2010JAS3603.1

Waquet, F., Cairns, B., Knobelspiese, K., Chowdhary, J., Travis, L. D., Schmid, B., et al. (2009). Polarimetric remote sensing of aerosols over land. *Geophys. J. Res.* 114:D01206. doi: 10.1029/2008JD010619

Wu, L., Hasekamp, O., van Diedenhoven, B., Cairns, B., Yorks, J. E., and Chowdhary, J. (2016). Passive remote sensing of aerosol layer height using near-UV multi-angle polarization measurements. *Geophys. Res. Lett.* 43, 8783–8790. doi: 10.1002/2016GL069848

Xu, F., Dubovik, O., Zhai, P.-W., Diner, D. J., Kalashnikova, O. V., Seidel, F. C., et al. (2016). Joint retrieval of aerosol and water-leaving radiance from multispectral, multiangular and polarimetric measurements over ocean. *Atmos. Meas. Tech.* 9, 2877–2907. doi: 10.5194/amt-9-2877-2016

Xu, F., van Harten, G., Diner, D. J., Kalashnikova, O. V., Seidel, F. C., Bruegge, C. J., et al. (2017). Coupled retrieval of aerosol properties and land surface reflection using the airborne multiangle spectropolarimetric imager (AirMSPI). *J. Geophys. Res. Atmos.* 122, 7004–7026. doi: 10.1002/2017JD026776

Xu, X., Wang, J., Wang, Y., Zeng, J., Torres, O., Yang, Y., et al. (2017). Passive remote sensing of altitude and optical depth of dust plumes using the oxygen A and B bands: first results from EPIC/DSCOVR at Lagrange-1 point. *Geophys. Res. Lett.* 44, 7544–7554. doi: 10.1002/2017GL073939

Xu, X., Wang, J., Wang, Y., Zeng, J., Torres, O., Reid, J. S., et al. (2018b). Detecting layer height of smoke aerosols over vegetated land and water surfaces via oxygen absorption bands: hourly results from EPIC/DSCOVR satellite in deep space. *Atmos. Meas. Tech.*

Xu, X., Wang, J., Wang, Y., and Kokhanovsky, A. (2018a). "Passive remote sensing of aerosol height," in *Remote Sensing of Aerosols, Clouds, and Precipitation*, ed. T. Islam (Amsterdam: Elsevier), 1–22. doi: 10.1016/b978-0-12-810437-8.00001-3

Yu, H., Chin, M., Yuan, T. L., Bian, H., Remer, L. A., Prospero, J. M., et al. (2015). The fertilizing role of African dust in the Amazon rainforest: a first multiyear assessment based on data from cloud-aerosol lidar and infrared pathfinder satellite observations. *Geophys. Res. Lett.* 42, 1984–1991. doi: 10.1002/2015GL063040

Yu, H., Remer, L. A., Chin, M., Bian, H., Tan, Q., Yuan, T., et al. (2012). Aerosols from overseas rival domestic emissions over North America. *Science* 337, 566–569. doi: 10.1126/science.1217576

Yu, H., Remer, L. A., Kahn, R. A., Chin, M., and Zhang, Y. (2013). Satellite perspective of aerosol intercontinental transport: from qualitative tracking to quantitative characterization. *Atmos. Res.* 124, 73–100. doi: 10.1016/j.atmosres.2012.12.013

Yuan, T., Remer, L., and Yu, H. (2011). Microphysical, macrophysical and radiative signatures of volcanic aerosols in trade wind cumulus observed by the A-Train. *Atmos. Chem. Phys.* 11, 7119–7132. doi: 10.5194/acp-11-7119-2011

Yuan, T., Remer, L. A., Bian, H., Ziemke, J. R., Albrecht, R., Pickering, K. E., et al. (2012). Aerosol indirect effect on tropospheric ozone via lightning. *J. Geophys. Res.* 117, D18212. doi: 10.1029/2012JD017723

Zeng, Z.-C., Natraj, V., Xu, F., Pongetti, T. J., Shia, R.-L., Kort, E. A., et al. (2018). Constraining aerosol vertical profile in the boundary layer using hyperspectral measurements of oxygen absorption. *Geophys. Res. Lett.* 45, 10772–10780. doi: 10.1029/2018GL079286

Conflict of Interest Statement: AI was employed by Science Application International Inc.

The remaining authors declare that the research was conducted in the absence of any commercial or financial relationships that could be construed as a potential conflict of interest.

frontiers in Environmental Science

REVIEW
published: 23 July 2019
doi: 10.3389/fenvs.2019.00094

Retrieving Aerosol Characteristics From the PACE Mission, Part 2: Multi-Angle and Polarimetry

Lorraine A. Remer[1]*, Kirk Knobelspiesse[2], Peng-Wang Zhai[3], Feng Xu[4], Olga V. Kalashnikova[4], Jacek Chowdhary[5], Otto Hasekamp[6], Oleg Dubovik[7], Lianghai Wu[6], Ziauddin Ahmad[2,8], Emmanuel Boss[9], Brian Cairns[10], Odele Coddington[11], Anthony B. Davis[4], Heidi M. Dierssen[12], David J. Diner[4], Bryan Franz[2], Robert Frouin[13], Bo-Cai Gao[14], Amir Ibrahim[2,15], Robert C. Levy[16], J. Vanderlei Martins[3], Ali H. Omar[17] and Omar Torres[17]

[1] Joint Center for Earth System Technology, University of Maryland Baltimore County, Baltimore, MD, United States, [2] Ocean Ecology Laboratory, NASA Goddard Space Flight Center, Greenbelt, MD, United States, [3] Department of Physics, University of Maryland Baltimore County, Baltimore, MD, United States, [4] Jet Propulsion Laboratory, California Institute of Technology, Pasadena, CA, United States, [5] NASA Goddard Institute for Space Studies, Columbia University, New York, NY, United States, [6] Earth Science Group, SRON Netherlands Institute for Space Research, Utrecht, Netherlands, [7] Laboratoire d'Optique Atmosphérique, Université de Lille, Villeneuve d'Ascq, France, [8] NASA Goddard Space Flight Center, Science Application International Corp., Greenbelt, MD, United States, [9] School of Marine Sciences, University of Maine, Orono, ME, United States, [10] NASA Goddard Institute for Space Studies, New York, NY, United States, [11] Laboratory for Atmospheric and Space Physics, University of Colorado, Boulder, CO, United States, [12] Departments of Marine Science and Geography, University of Connecticut, Groton, CT, United States, [13] Scripps Institution of Oceanography, University of California, San Diego, La Jolla, CA, United States, [14] Naval Research Laboratory, Washington, DC, United States, [15] Science Systems and Applications, Inc., Lanham, MD, United States, [16] Laboratory for Climate and Radiation, NASA Goddard Space Flight Center, Greenbelt, MD, United States, [17] Chemistry and Dynamics Branch, NASA Langley Research Center, Hampton, VA, United States

Edited by:
David Antoine,
Curtin University, Australia

Reviewed by:
Fischer Juergen,
Freie Universität Berlin, Germany
Bertrand Fougnie,
European Organisation for the Exploitation of Meteorological Satellites, Germany

***Correspondence:**
Lorraine A. Remer
remer@umbc.edu

Specialty section:
This article was submitted to Atmospheric Science, a section of the journal Frontiers in Environmental Science

Received: 30 November 2018
Accepted: 03 June 2019
Published: 23 July 2019

Citation:
Remer LA, Knobelspiesse K, Zhai P-W, Xu F, Kalashnikova OV, Chowdhary J, Hasekamp O, Dubovik O, Wu L, Ahmad Z, Boss E, Cairns B, Coddington O, Davis AB, Dierssen HM, Diner DJ, Franz B, Frouin R, Gao B-C, Ibrahim A, Levy RC, Martins JV, Omar AH and Torres O (2019) Retrieving Aerosol Characteristics From the PACE Mission, Part 2: Multi-Angle and Polarimetry. Front. Environ. Sci. 7:94. doi: 10.3389/fenvs.2019.00094

The Plankton, Aerosol, Clouds, ocean Ecosystem (PACE) mission presents new opportunities and new challenges in applying observations of two complementary multi-angle polarimeters for the space-based retrieval of global aerosol properties. Aerosol remote sensing from multi-angle radiometric-only observations enables aerosol characterization to a greater degree than single-view radiometers, as demonstrated by nearly two decades of heritage instruments. Adding polarimetry to the multi-angle observations allows for the retrieval of aerosol optical depth, Angstrom exponent, parameters of size distribution, measures of aerosol absorption, complex refractive index and degree of non-sphericity of the particles, as demonstrated by two independent retrieval algorithms applied to the heritage POLarization and Directionality of the Earth's Reflectance (POLDER) instrument. The reason why this detailed particle characterization is possible is because a multi-angle polarimeter measurement contains twice the number of Degrees of Freedom of Signal (DFS) compared to an observation from a single-view radiometer. The challenges of making use of this information content involve separating surface signal from atmospheric signal, especially when the surface is optically complex and especially in the ultraviolet portion of the spectrum where we show the necessity of polarization in making that separation. The path forward is likely to involve joint retrievals that will simultaneously retrieve aerosol and surface properties, although advances will be required in radiative transfer modeling and in representing optically complex constituents in those models. Another challenge is in having the processing capability that can keep pace with the output of these instruments in an operational environment. Yet, preliminary algorithms applied to airborne multi-angle polarimeter observations offer encouraging results that demonstrate the advantages of these instruments to retrieve aerosol layer height, particle single scattering albedo, size distribution and spectral optical depth, and also show the necessity of polarization measurements, not just multi-angle radiometric measurements, to achieve these results.

Keywords: aerosol, multi-angle, polarimeter, PACE, remote sensing, multi-wavelength

INTRODUCTION

NASA's Plankton, Aerosols, Clouds, ocean Ecosystems (PACE) mission offers unique and new opportunities for characterizing aerosol from space. Part of the challenge of PACE will be to advance and combine our current infrastructure and algorithms to take advantage of PACE's new and unique observations from a combination of synergistic satellite instruments.

PACE will carry three instruments. The primary instrument is the Ocean Color Instrument (OCI). This is a radiometer that spans the spectral range, hyperspectrally, from near 350 to 885 nm, measuring at 5 nm spectral resolution. OCI also includes seven discrete bands in the shortwave infrared (SWIR) centered at 940, 1,038, 1,250, 1,378, 1,615, 2,130, and 2,260 nm. In addition to OCI, PACE is expected to carry two multi-wavelength, multi-angle imaging polarimeters (MAPs). One of these is Spectro-Polarimeter for Planetary Exploration-1 (SPEXone: Hasekamp et al., 2019), an instrument contributed by the Netherlands. The other is Hyper Angle Rainbow Polarimeter-2 (HARP2), an instrument contributed by the University of Maryland Baltimore County (UMBC). SPEXone uses the spectral modulation technique (Snik et al., 2009) to achieve a highly accurate hyperspectral polarization from 385 to 770 nm. Spectral resolution for scalar radiometric intensity is 5 nm in the continuum and 2 nm in the Oxygen-A band, and for polarization 15–45 nm (polarimetric spectral resolution increases with wavelength). SPEXone's swath width is 100 km, with 5 × 5 km spatial resolution sampled at 2.5 × 2.5 km pixel resolution, and it views each Earth target at five different angles. HARP2 uses a Philips prism beam splitting technique with stripe filters to achieve accurate polarization in four discrete wavelengths (440, 550, 670, and 870 nm), but across a broad swath of 1,550 km. HARP2 is hyperangular, viewing each nominally 2.5 km pixel at 10–60 different angles. Thus, the two polarimeters together offer synergistic opportunities, compensating for wide vs. narrow swaths, and hyperangle vs. hyperspectral capabilities. **Table 1** shows the characteristics of each MAP, including the differences in polarimetric accuracy.

In this paper, we present an overview of the opportunities and challenges of using a multi-angle polarimeter (MAP) for aerosol characterization in a PACE context. We will briefly review our heritage operational space-based multi-angle radiometers and polarimeters, and how they have contributed to our current understanding of aerosol characterization. We will present an analysis of information content for aerosol characterization from a MAP, as compared to a radiometer like OCI, and then discuss specific issues of making a MAP retrieval of aerosol. Throughout this paper we will refer to a generic MAP that is neither SPEXone nor HARP2 but can be applied to either sensor or to others that might participate in other missions. Because the emphasis of PACE, as a mission, has been focused on ocean biology, we will address the specific challenges of retrieving aerosol characteristics over oceans, although observations from the PACE MAPs will be used to characterize aerosol over land, as well. Despite the focus in the over ocean retrievals of aerosols here, this paper does not directly address atmospheric correction. Instead, Frouin et al. (2019) explores atmospheric correction or the retrieval of normalized water-leaving radiance in the PACE era. The at-launch aerosol retrieval algorithms to be applied to the individual PACE MAPs have not been formulated in detail at this time, and therefore, this paper cannot provide specifics on the eventual operational algorithms or exact final PACE aerosol products.

Abbreviations: 3D, Three dimensional; 3MI, Multi-viewing, Multi-channel, Multi-polarization Imager; AAOD, Absorbing Aerosol Optical Depth; AATSR, Advanced Along Track Scanning Radiometer; ACE, Aerosol Cloud Ecosystems; ACEPOL, Aerosol Characterization from Polarimeter and Lidar; ADEOS, Advanced Earth Observation Satellite; AERONET, Aerosol Robotics Network; AirHARP, Airborne version of Hyper Angle Rainbow Polarimeter; AirMSPI, Airborne Multiangle SpectroPolarimetric Imager; AirSPEX, Airborne version of Spectro-Polarimeter for Planetary Exploration; AMS, Aerosol Mass Spectrometer; AOD, Aerosol Optical Depth; AOT, Aerosol Optical Thickness; ATSR-2, Along Track Scanning Radiometer 2; BC, Black Carbon; BIOSOPE, BIogeochemistry and Optics SOuth Pacific Experiment; BRDF, Bi-Reflection Directional Function; CDOM, Colored Dissolved Organic Material; Chla, Chlorophyll-*a;* CPL, Cloud Physics Lidar; DFS, Degrees of Freedom for Signal; DoLP, Degree of Linear Polarization; ER-2, Earth Research-2; ESA, European Space Agency; FF, Fournier-Forand; GRASP, Generalized Retrieval for Aerosol and Surface Properties; HARP2, Hyper Angle Rainbow Polarimeter-2; IOP, Inherent Optical Properties; MAIA, Multi-Angle Imager for Aerosols; MAN, Maritime Aerosol Network; MAP, Multi-Angle imaging Polarimeters; MISR, Multi-angle Imaging SpectroRadiometer; MODIS, MODerate resolution Imaging Spectroradiometer; NAP, Non-Algae Particle concentration; NASA, National Aeronautics Space Administration; NDW, Non-algae Dominated Water; NIR, Near InfraRed; OCI, Ocean Color Instrument; OMI, Ozone Monitoring Instrument; PACE, Plankton, Aerosols, Clouds, ocean Ecosystems; PARASOL, Polarization and Anisotropy of Reflectances for Atmospheric Sciences coupled with Observations from a Lidar; PDW, Phytoplankton Dominated Water; PODEX, Polarimeter Definition Experiment; POLDER, POLarization and Directionality of the Earth's Reflectance; PSD, Particle Size Distribution; RSP, Research Scanning Polarimeter; SEAC4RS, Studies of Emissions, Atmospheric Composition, Clouds and Climate Coupling by Regional Surveys; SLSTR, Sea and Land Surface Temperature Radiometer; SP2, Soot Photometer; SPEXone, Spectro-Polarimeter for Planetary Exploration-1; SRON, Netherlands Institute for Space Research; SSA, Single Scattering Albedo; TOA, Top Of Atmosphere; UV, Ultraviolet; VIS, Visible.

TABLE 1 | Characteristics of the two PACE MAPs.

MAP characteristics	SPEXone	HARP-2
Spectral range	385-770 nm	440, 550, 670, 870 nm
Spectral resolution	Scalar radiometric intenstiy: 5 nm O_2A band: 2 nm Polarized: 15–45 nm, increasing with wavelength	All bands polarized. 440, 550, 670 nm bands: 10 nm 870 nm band: 40 nm
Polarimetric accuracy (DoLP)	0.0025	<0.005
# viewing angles	5 (−57°, −20°, 0°, 20°, 57°)	10 for 440, 550, 870 nm + 60 for 670 nm (114°)
Swath width	9° (100 km)	94° (1,550 km)
Ground sample distance	2.5 × 2.5 km	1.3 × 2.0 km
Heritage	GroundSPEX, SPEX airborne	AirHARP, cubesat HARP

One of the challenges of PACE will be the attempt to extract additional information from the ultraviolet (UV) wavelengths. The use of UV observations by the OCI radiometer for aerosol retrievals is addressed in this issue in a separate paper (Remer et al., 2019), but here we present a summary of the results of a theoretical sensitivity study (Zhai et al., 2017b) that highlights the importance of polarimetry to constrain the uncertainty introduced by the UV (Kahn et al., 2016). Note that we discuss these results from the perspective of aerosol characterization. Frouin et al. (2019) addresses the challenges of the UV specifically for atmospheric correction, whereas Chowdhary et al. (2019) touches upon ocean color contributions to spaceborne UV observations.

The inclusion of MAPs in the mission has elevated PACE capabilities for global aerosol characterization to new levels. While the focus of this paper is aerosol characterization, a MAP, with its enhanced information content, provides the opportunity for simultaneous retrievals of aerosols and surface properties. Success of a simultaneous retrieval depends on the availability of radiative transfer models that are sufficiently accurate to make use of the full information content measured by a MAP. Such radiative transfer models need to couple ocean and atmosphere and need to represent all processes and constituents appropriately. An extensive exploration of the current state of ocean and atmospheric radiative transfer modeling is presented in Chowdhary et al. (2019) and will only be briefly discussed here in the context of aerosol characterization.

HERITAGE MULTI-ANGLE AND POLARIMETER AEROSOL CHARACTERIZATION

Cloud Masking and Other Scene Selection Processes

Heritage quantitative aerosol remote sensing algorithms, especially those applied to single-view radiometers like the MODerate resolution Imaging Spectroradiometer (MODIS) and the Ozone Monitoring Instrument (OMI), needed to constrain their retrievals by making assumptions regarding the scene observed by the instrument. A scene with clouds or certain surface types such as snow/ice that does not conform to algorithm assumptions will be identified and then excluded from retrieval. Included in that screening for single-view radiometers would be sun glint over water. Recent algorithms for these single-view heritage instruments have begun to retrieve aerosol above clouds (Waquet et al., 2009b; Torres et al., 2012; Jethva et al., 2013, 2014, 2016; Meyer and Platnick, 2015; Sayer et al., 2016), but these algorithms still require identification of the cloud scene in order to choose the correct algorithmic path. Single-view polarimetry will not add much value for cloud identification, as polarimetry is not sensitive to water droplet clouds, except by accident when the single-view coincides with the rainbow peak.

The situation has been less restrictive for heritage multiangle radiometers and polarimeters. Multiangular satellite observations, such as from Multi-angle Imaging SpectroRadiometer (MISR) instrument (Diner et al., 1998) provide additional information for scene selection that cannot be discerned from single-view radiometers. For example, MISR uses multi-angular smoothness and spatial correlation tests to assist in cloud screening as part of the aerosol retrieval algorithm (Martonchik et al., 2002). Multi-angle instruments also have the advantage that some of the view angles always avoid glint so that every scene can be viewed at some non-glint geometry (see e.g., Harmel and Chami, 2013). An example using MISR to fill in glint-induced gaps in MODIS-Terra aerosol optical depth (AOD) product over the ocean is shown in **Figure 1**. This increases the availability of retrieved aerosol characteristics over oceans. The information contained in multi-angle polarimetry has also been shown to be sufficient to perform masking by simply assessing the goodness of fit in the retrieval process, thereby avoiding deterministic thresholds inherent to single-view techniques, which may inadvertently over- or under-screen the data (Stap et al., 2015). The PACE MAPs have the capabilities to make use of new techniques that avoid masking, and to have the capabilities to mask when needed. Advanced algorithms developed for these instruments should address scene selection with the same rigor as they apply to characterizing the aerosol once scene selection has been accomplished.

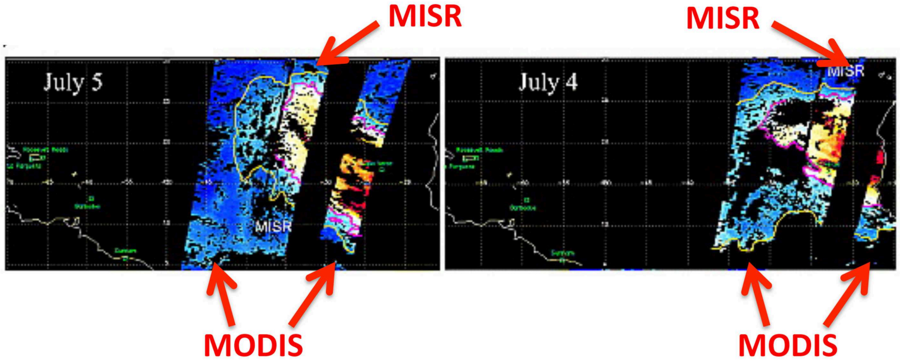

FIGURE 1 | Complementary MISR and MODIS coverage over dust plumes transported over the Atlantic. The narrower MISR swath partly fills in areas that would otherwise be lost to sun glint masking in the broader MODIS swath. MODIS AOD data (right and left of the MISR swath) is plotted together with the narrower MISR swath for two successive days in this dust plume event. AOD data in the middle of the MODIS swath is missing because of glint masking. MISR can retrieve AOD despite glint because only 2–3 out of nine MISR cameras view the scene in glint while other cameras point at the same scene, but at non-glint angles. These can be used for retrievals. Adapted with permission from Kalashnikova and Kahn (2008), John Wiley & Sons.

A comprehensive study of cloud detection by PACE that includes discussion of both OCI and MAP capabilities and limitations can be found in Platnick et al. (2018).

Heritage Aerosol Retrievals From Multi-Spectral Multi-Angular Radiance Measurements

The concept of using satellite multi-angle measurements to derive aerosol properties over land and ocean has a long history (Martonchik and Diner, 1992; Wang and Gordon, 1994). The first satellite sensor providing opportunity to test the concept was the dual angle Along Track Scanning Radiometer 2 (ATSR-2) that surveyed each pixel twice, once in the forward direction at 52–55° view angle and then near nadir at 0–22° view angle (Flowerdew and Haigh, 1995). Aerosol retrievals were devised to make use of the dual-look information to separate aerosol signal from surface reflectance and bi-reflection directional function (BRDF) over land (Flowerdew and Haigh, 1996). Soon after an algorithm making use of both multi-angle and spectral information was applied to ATSR-2 data and validated (Veefkind et al., 1998). Since then a series of algorithms have been applied to the multi-angle observations of ATSR-2 and its successors (e.g., Holzer-Popp et al., 2002; Kokhanovsky et al., 2009; Kolmonen et al., 2016; de Leeuw et al., 2018).

While the European multi-angle aerosol retrieval effort has focused on ATSR-2 and its successors, NASA's primary heritage multi-angle instrument is MISR. MISR has been on orbit, observing Earth and retrieving aerosol characteristics since soon after Terra launch in 2000. Besides retrieving AOD, MISR's multi-angle capability has been used for additional aerosol characterization. Previous MISR studies demonstrate the ability of multi-angular radiances to distinguish dust from other airborne particles (e.g., Kalashnikova and Kahn, 2006; Kalashnikova et al., 2013) over the ocean surfaces, and show the value of such observations for separating aerosol and surface scattering over non-black ocean waters (where the red and near infrared radiance emanating from the ocean is not zero, Limbacher and Kahn, 2017). As a demonstration of multi-angular capabilities, Limbacher and Kahn (2017) introduced a coupled, self-consistent retrieval of aerosols over open oceans with Chlorophyll-*a* concentration [Chla] < 1.5 mg/m^3, with a primary goal to correct MISR ocean retrievals of AOD at low aerosol loadings. Because MISR-based ocean reflectance is derived self-consistently with aerosol amount and type in a physical retrieval, it can potentially provide a more robust atmospheric correction for collocated MODIS-Terra ocean retrievals.

Currently, the only plans to continue multi-angle radiometry without polarization after MISR are with the European Sea and Land Surface Temperature Radiometer (SLSTR) instrument, a follow-on of the Advanced Along Track Scanning Radiometer (AATSR), on the European Space Agency (ESA) Sentinel-3 mission, which was launched in 2016. These instruments measure the same scene at two view angles (Grey et al., 2006), which is less advantageous than a 9-camera MISR-like observation. Future multi-angle sensors will combine multi-angle capability with polarimetry. However, there are paths forward for multi-angle radiometry beyond MISR and AATSR that would provide additional capability for aerosol characterization that do not require polarimetry. One such configuration would be for a multi-angle instrument with hyperspectral capabilities. Such a configuration could resolve the Oxygen A-band signal through different slant paths from multi-angle views and enhance the ability to derive the heights of cloud (Ferlay et al., 2010) and aerosol (Davis and Kalashnikova, 2019) layers. There are no current plans for such an instrument featuring radiometry alone. Instead, all multi-angle instruments in the queue are combined with polarimetric capability, although SPEXone on PACE will combine polarimetry with multi-angle hyperspectral views out to 770 nm, and may provide the information described by Davis and Kalashnikova (2019) on coarser resolution. Currently, SPEXone, HARP2, NASA's Multi-Angle Imager for Aerosols (MAIA), and the European Multi-viewing, Multi-channel, Multi-polarization

Imager (3MI) are the only planned instruments with multi-angle capability that could continue the NASA MISR aerosol record. These are all multi-angle polarimeters (MAPs) that exceed MISR's capabilities by adding information for aerosol characterization associated with polarimetric measurements and enhanced spectral coverage, though MAIA will not provide continuous, near-global coverage, and instead will observe a globally distributed set of discrete target areas (Diner et al., 2018).

Heritage Multi-Angular and Polarimetric Observations

The POLarization and Directionality of the Earth's Reflectance (POLDER) (Deschamps et al., 1994) instrument, was a MAP that enjoyed three deployments into space. The first two were relatively short due to catastrophic failures in its spacecraft (Advanced Earth Observation Satellite—ADEOS), not in the sensor itself. The third POLDER, aboard the Polarization and Anisotropy of Reflectances for Atmospheric Sciences coupled with Observations from a Lidar space craft (PARASOL) (Tanré et al., 2011), produced a 9-year data record. POLDER could potentially retrieve AOD and ocean reflectance simultaneously, and, to some extent, could characterize absorbing aerosol amount. POLDER's first-generation aerosol retrieval was the very first attempt to use polarization measurements. The standard aerosol algorithm was originally very conservative in its output, limiting itself to producing only MODIS-like aerosol products (AOD and size) and using simplified radiative transfer assumptions (Deuzé et al., 2000).

In addition to the original operational stream, a more comprehensive, although computationally expensive, retrieval algorithm (Dubovik et al., 2011, 2014) has been applied to POLDER measurements, This is the Generalized Retrieval for Aerosol and Surface Properties (GRASP) that produces an expanded product line that includes additional quantitative aerosol properties (size, complex refractive index, fraction of non-sphericity, and scale height). This algorithm uses a multi-pixel approach that assumes limited temporal variability of surface reflectance (over land) or limited spatial variability of aerosol characteristics (over both land and ocean). Progress has been made in speeding up processing, and at present, the whole archive of 9 years (2004–2013) POLDER-3/PARASOL data and 18 months of POLDER-1,2/ADEOS-1,2 have been processed (Dubovik et al., 2019). **Figure 2** illustrates the retrieval results for single scattering albedo. These results are preliminary in that complex situations have not yet been properly addressed, and thus, snow/ice, heterogeneous scenes, and clouds are likely introducing errors in the plotted values. Even so, the GRASP/POLDER products are showing, over all expected global patterns, good agreement with the Aerosol Robotics Network (AERONET) inversions and have recently been used for the quantification of emissions of biomass burning and mineral dust aerosols over Africa (Chen et al., 2018).

A separate POLDER algorithm development effort is also underway at SRON, the Netherlands Institute for Space Research (Hasekamp et al., 2011; Fu and Hasekamp, 2018), which like GRASP is computationally expensive but more fully exploits the information content inherent in a POLDER observation than did the first generation algorithm (Tanré et al., 2011). For example, the SRON algorithm produces aerosol size, single scattering albedo (SSA) or absorbing AOD (AAOD), complex refractive index, and degree of particle non-sphericity. An example of the algorithm to characterize global aerosol particle absorption (AAOD) is shown in **Figure 2** (Lacagnina et al., 2017). Both the GRASP and SRON retrievals have been validated against direct sun measurements and compared with inverted sky radiances from AERONET, and both report a significant ability to quantify column aerosol particle properties. The advances represented by GRASP and SRON to more fully exploit the multi-angle and polarimetric capabilities of POLDER and increase its aerosol characterization ability are already offering new insight in a variety of long-standing global aerosol questions. These include quantifying of emissions of biomass burning and mineral dust aerosols over Africa (Chen et al., 2018), evaluating global model aerosol absorption (Lacagnina et al., 2015), computing the direct radiative effect of aerosols (Lacagnina et al., 2017), and aerosol typing (Russell et al., 2014).

MULTI-ANGULAR POLARIMETRIC INFORMATION CONTENT FOR AEROSOL RETRIEVAL OVER OCEAN

There is strong consensus within the aerosol community that a multi-angle polarimeter is part of the essential next step in improving our understanding of the global aerosol system, reducing uncertainty in estimates of aerosol forcing of climate, improving knowledge of aerosol-cloud processes, advancing space-based air quality monitoring and forecasting, and documenting important aerosol events. The POLDER missions provided the first taste of multi-angle polarimetry. As technology advances to include hyperspectral capability, possibly broader wavelength ranges and higher polarimetric accuracy, the expectation is that aerosol characterization will also advance. As noted above, multi-angle radiometry is an important step up from the single-look instruments, and polarimetry allows even better characterization of particle properties from space.

Tanré et al. (1996) quantified the information content or degrees of freedom inherent in a 6-wavelength, single look, unpolarized satellite observation of aerosol over Case 1 ocean waters using principal component analysis. Their conclusion is that these six wavelengths resulted in only 2–3 degrees of freedom, expressed as the aerosol loading, the weighting between modes and if one mode was dominant, then also the effective radius of the dominant mode. The six wavelengths spanned the MODIS spectrum (0.55–2.13 μm). OCI, extending to hyperspectral and into the UV, should add information content to the MODIS-like measurements, and the possibility of using this information to retrieve absorption and aerosol layer height was explored in a companion paper (Remer et al., 2019). However, the most significant increase in information content (often expressed as Degrees of Freedom for Signal, DFS) can be made with multi-angle polarimetry, thus offering the potential for more complete, and accurate, aerosol characterization

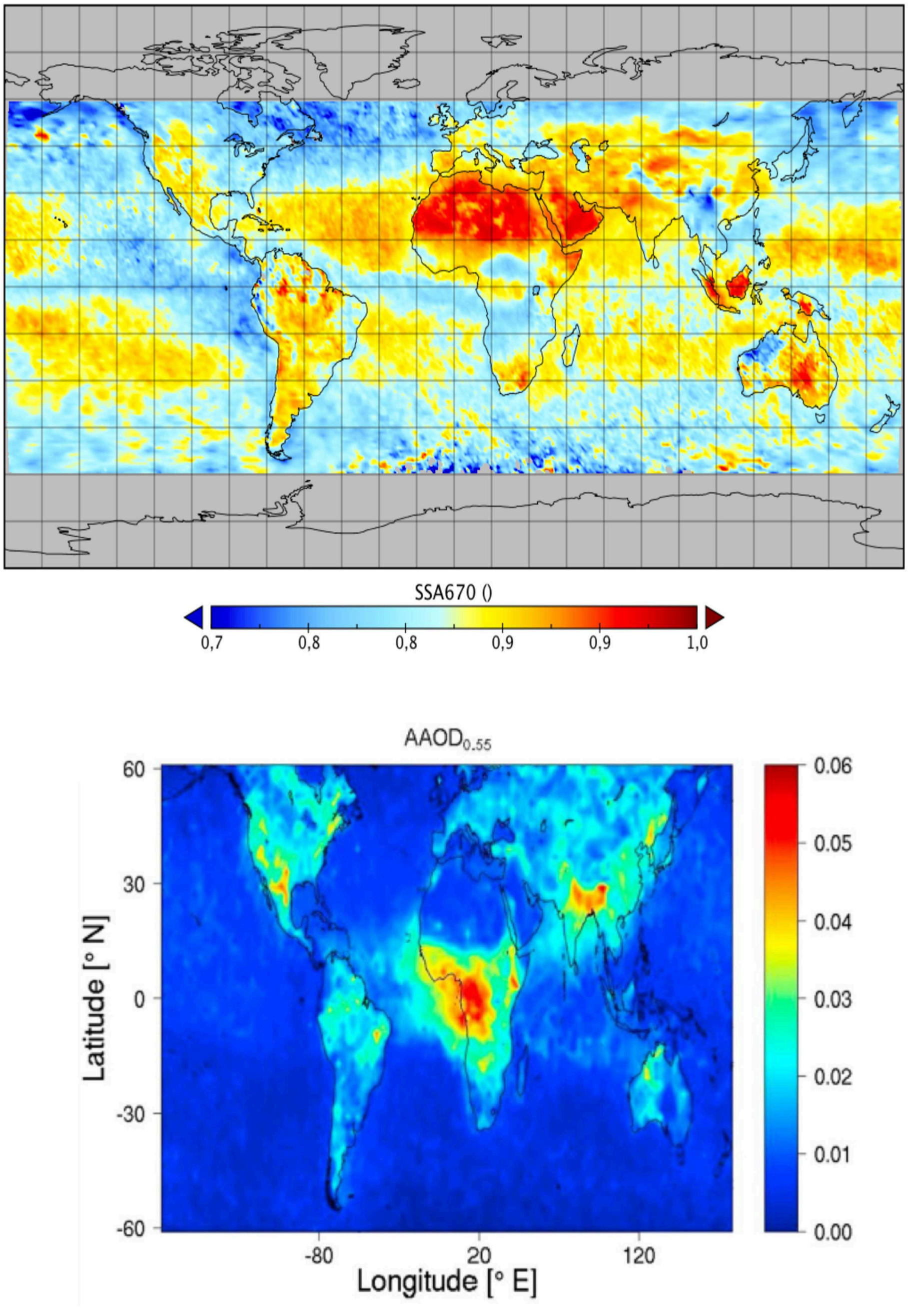

FIGURE 2 | Annual mean aerosol absorption properties for 2006 derived from PODER-3/PARASOL observations using the GRASP algorithm reporting single scattering albedo (SSA) at 670 nm **(Top)** and using the SRON retrieval algorithm (Hasekamp et al., 2011; Fu and Hasekamp, 2018) reporting absorbing aerosol optical depth (AAOD) at 550 nm **(Bottom)**. Adapted with permission from Lacagnina et al. (2017), John Wiley & Sons. Note that SSA is an intrinsic aerosol property while AAOD is dependent also on the aerosol loading. Direct comparisons of the two maps are not possible. However, very high AAOD should roughly correspond to low SSA, and vice-versa. Also, please note that the GRASP results are still preliminary and may be affected by cloud, snow/ice, surface heterogeneity, and other contamination issues.

(Hasekamp and Landgraf, 2005; Hasekamp, 2010; Knobelspiesse et al., 2012).

Figure 3 shows the results of a study that compares the information contained in an observation by an example multi-angle polarimeter, the European 3MI instrument (Manolis et al., 2017; Fougnie et al., 2018) to that of OCI. For this study, we assumed 3MI has a polarimetric accuracy (expressed in terms of Degree of Linear Polarization—DoLP) of 1%. This study was performed for a scene parameterized from the "maritime" aerosol model in Smirnov et al. (2003) and a simple Case-I

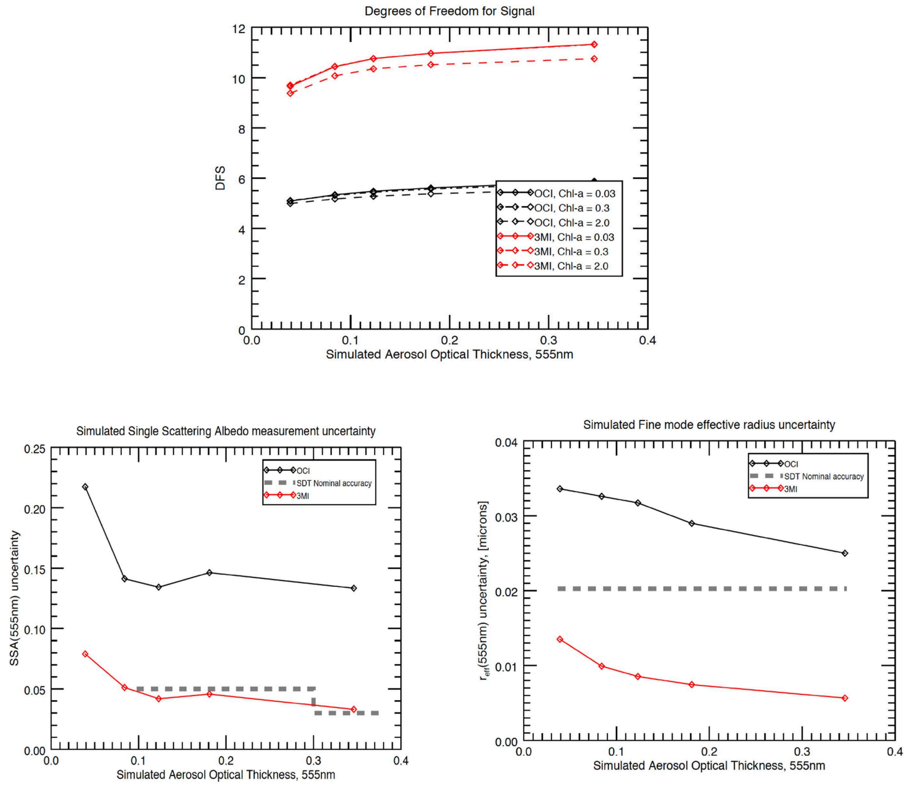

FIGURE 3 | (Top) Calculated degrees of freedom (information content) from OCI (black) and a multi-angle polarimeter, the European 3MI instrument (red), as function of calculated Aerosol Optical Thickness (AOT). The different lines represent different chlorophyll concentrations in the simulated ocean. Note that 3MI is used as a generic example of a MAP, and is not expected to fly on PACE. **(Bottom)** Calculated uncertainties in simultaneous retrievals of single scattering albedo (bottom left) and fine mode effective radius (bottom right) for the two instruments, following the same color scheme. The dashed line indicates the uncertainty requirements of these parameters, defined by the PACE Science Definition Team report (NASA, 2012).

ocean reflectance model based on Chlorophyll-a and wind speed, as described in **Table 2**. Note that the (isotropic) wind speed parameterizes both the ocean surface reflected sunglint (Cox and Munk, 1954), and the spectra and quantity of sea foam (Koepke, 1984; Frouin et al., 1996). It follows the Bayesian information content methods described in Rodgers (2000) and implemented for aerosol and ocean scenes as in Knobelspiesse et al. (2012). This type of analysis can also be used to determine the expected measurement uncertainty of other parameters not included as free parameters (italicized in **Table 2**), so long as they uniquely express the derived parameter. We used this property to derive Single Scattering Albedo for the combined aerosol state, which is a function determined largely by the imaginary refractive index, but also depends on other properties (real refractive index, size distribution and fine mode fraction). See section 2.1 in Knobelspiesse et al. (2012) for more details.

The top plot in **Figure 3** shows the DFS for each instrument for aerosol retrieval over ocean, given 12 free parameters describing the aerosol and ocean state (as in **Table 2**; the maximum DFS value is 12). Since the aerosol loading in a scene determines how well microphysical properties can be retrieved, this analysis has been repeated for five different AOT's, represented as the abscissa in each plot. This analysis is an expression of measurement uncertainty in terms of desired retrieval parameters and is therefore independent of the retrieval algorithm method. Like any simulation, this represents a parameterization that may not span the entire range of geophysical reality. However, these simplifications are consistent for all tested measurement systems, so this is a powerful means to compare in a relative sense, and to some extent covers differences for varying geometries. Furthermore, Knobelspiesse et al. (2012) has shown that calculated uncertainties are insensitive to the simulated value of aerosol intensive properties (size distribution and complex refractive index) so this analysis is representative of most scenes, as long as the extensive properties (AOT, Chl-a) are assessed at various values. This is why we chose to represent our results in terms of varying AOT, and for different magnitudes of [Chl-a]. These results show that the 3MI DFS is much higher than that of OCI alone. This means that 3MI can independently determine most of the aerosol and ocean parameters in the simulation, while OCI would need to "add" information via the use of assumptions of particle properties based on empirical information. The ability to determine SSA (bottom left) and fine size mode effective radius (bottom right) are shown as predicted uncertainties. The gray dashed lines indicate the MAP uncertainty requirements for these parameters

TABLE 2 | Scene parameterization for results in **Figure 3**.

	Aerosol fine mode	Aerosol coarse mode
Effective radius (r_e)	*0.135 μm*	*3.63 μm*
Effective variance (v_e)	*0.193*	*0.704*
Real refractive index (m_r)	*1.37*	*1.37*
Imaginary refractive index (m_i)	*0.001*	*0.001*
AOT(555 nm) fine mode fraction	*36%*	
Aerosol optical thickness (555 nm)	*0.039, 0.084, 0.123, 0.181, 0.346*	
Chlorophyll-a concentration	*0.03, 0.3, 2.0 mg/m³*	
Wind speed (isotropic)	*8 m/s*	
Solar zenith angle	45°	
Solar-sensor relative azimuth angle	45°	
Aerosol vertical distribution	Surface to 1 km	

*Italics indicates free parameters in a simultaneous retrieval (12 total). The single scattering albedo (SSA) depicted in **Figure 3** is computed from r_e, v_e, m_r, and m_i in this Table using Mie theory.*

from the PACE Science Definition Team report (NASA, 2012). Thus, 3MI with an assumed polarimetric accuracy of 1% would meet those requirements for simple scenes such as this, while OCI alone would not be able to do so. The PACE MAPs are expected to have even better polarimetric accuracy and should perform as well, or better, even in more complex situations than the simple case presented in **Table 2** and shown in **Figure 3**.

CHALLENGES IN EXPLOITING MAP INFORMATION CONTENT OVER OCEAN

Full exploitation of MAP information content faces several challenges. The relative newness of such algorithms, and the complexity of simultaneous retrieval of multiple parameters, is a barrier to full operational exploitation. This complexity can lead to computationally expensive algorithms that are difficult to implement on a global scale. Radiative transfer calculations at the heart of retrieval algorithms must be confirmed as being appropriate for the measurement uncertainty of a MAP instrument, and these measurement uncertainty models need to be developed, validated, and incorporated into a retrieval. Furthermore, validation of aerosol optical properties retrieved from these algorithms can be challenging for some parameters. Fortunately, the PACE mission can benefit from the history of such development for POLDER, the Aerosol Cloud Ecosystems (ACE) mission study, and the variety of MAP prototypes that have been deployed on aircraft for research field campaigns, and other instruments (Dubovik et al., 2019).

The difficulty of aerosol retrieval algorithm development is illustrated with the data processing experience of the POLDER mission, which in the original operational algorithm over the ocean reported a limited parameter set (Aerosol Optical Thickness and the Ångström exponent) and relied on only two of the three polarimetric channels (670 and 865 nm) (Deuzé et al., 1999, 2000). Many algorithms have been developed since that time, and some of them (such as GRASP) have specifically tackled the issue of computational expense. A complete review of such algorithms can be found in Kokhanovsky et al. (2015), and descriptions of more recent algorithms include those by Gao et al. (2018) and Stamnes et al. (2018). In addition to modern advancements of computational power since the era of original POLDER algorithms, some have investigated the exploitation of alternate methods to converge to a retrieval solution efficiently, such as utilizing fast Neural Networks (Di Noia et al., 2017). In some ways, the algorithms required for proper exploitation of MAP information content may require different paradigms than those that were appropriate for the era of single view angle multi-spectral instruments.

Measurement uncertainty, and the estimated uncertainty of retrieved aerosol products, is of particular importance to MAPs. This is because the retrieval algorithms mentioned above must weigh the relative importance of the hundreds or thousands of individual observations (at various geometries, spectral channels, and polarimetric states) that comprise a "measurement" of a scene. Polarimetric observations of DoLP are several factors more accurate than the corresponding radiometric observations and have an entirely different relationship with regards to systematic and random errors. The relative importance of these errors and the correlations between errors of different observations can have an impact on the uncertainty of the retrieved geophysical products (Knobelspiesse et al., 2012). Measurement uncertainty has been characterized for some airborne polarimetric instruments (Diner et al., 2010; Harten et al., 2018; Stamnes et al., 2018), but coordinated validation of these uncertainty models is difficult and limited (Knobelspiesse et al., 2019).

Validation of aerosol products beyond Aerosol Optical Thickness and Ångström exponent also presents a challenge. While AERONET (Holben et al., 1998) represents the standard to which most aerosol satellite products over land are compared, and its extension, the Maritime Aerosol Network (MAN, Smirnov et al., 2009), can be used over the oceans, both are limited in the validation capability for other aerosol optical properties. AERONET does not measure aerosol optical properties directly, and AERONET aerosol optical property retrieval quality is highest for AOD > 0.4 (Dubovik et al., 2000); MAN instruments do not have sky scanning capabilities, and cannot be used for aerosol retrievals. While other measurements besides these networks do exist, they are limited by the same fundamental information constraints. *In situ* observations, on the other hand, must contend with the difficulties of accounting for temporal and spatial scale, and have their own measurement uncertainties. Aerosol chemical properties from commonly used *in-situ* sensors are measured with 15–30% accuracy, for example, size-resolved aerosol black carbon (BC) mass from Soot Photometer (SP2) has 30% relative uncertainty, while bulk aerosol chemical composition from Aerosol Mass Spectrometer (AMS) has 17–19% relative uncertainty (Ryerson et al., 2013; Kalashnikova et al., 2018).

The Coupled Atmospheric-Oceanic System

Retrieving aerosol properties over ocean requires separating atmosphere and ocean signals. This is a significant challenge given that the atmospheric and ocean systems are coupled physically, chemically, biologically—and most pressing for PACE, radiatively. The radiative coupling of the atmosphere and ocean, and the consequences for PACE remote sensing is explored in depth in Chowdhary et al. (2019). Here, we briefly discuss approaches that are used to manage this coupling in the retrieval of aerosol characteristics from MAP observations.

One approach to isolate the atmospheric signal for aerosol characterization is to focus on observations that are minimally affected by ocean scattering contributions. This can be done spectrally, by focusing on the near infrared (NIR) part of the spectrum where absorption by pure sea water becomes very large (Smith and Baker, 1981), and geographically by focusing on Case 1 (open ocean) waters where scattering by the ocean in the NIR part becomes negligible (Morel and Maritorena, 2001). The former choice further avoids scattering contributions by phytoplankton and their by-products that vary with biomass and can become large in the visible (VIS)/UV (see again Morel and Maritorena, 2001), while the latter choice avoids complex ocean scenes, such as coasts and estuaries, where scattering contributions vary e.g., suspended sediments and can become large even in the NIR (Li et al., 2003). These choices have been necessary in heritage algorithms for inversions of spaceborne single-view radiance observations to either retrieve aerosols properties (Tanré et al., 1997), or to simply account for aerosol scattering in atmospheric correction (Gordon, 1997). However, as we move into the PACE era, the expectation is to expand aerosol property inversions spectrally into the shorter wavelengths (UV, blue and green) and geographically into the near-shore environment. In addition, for ocean color retrievals from PACE there will be a need to expand atmospheric correction spectrally into the UV. This will require a new way of approaching the atmospheric-ocean system.

The process for more sophisticated aerosol retrieval over ocean is to make use of a MAP's large information content to retrieve aerosol and ocean properties simultaneously. Joint retrieval of aerosol and hydrosol properties requires a sophisticated and computationally efficient inverse model to disentangle their contributions to top-of-atmosphere (TOA) radiometry and polarimetry. Currently, several approaches are developed for the open ocean applications. For example, Chowdhary et al. (2002, 2012) used a simple, 1-parameter bio-optical model (i.e., varying only with [Chla]) for Case 1 waters to characterize water reflectance and retrieved aerosol properties using least squares fitting of the Research Scanning Polarimeter (RSP: an airborne multi-angle polarimeter: Cairns et al., 1999) data. Xu et al. (2016) developed an optimization approach for joint aerosol and water-leaving radiance retrieval with the constraints of multi-pixel measurements and a simplified bio-optical model for open ocean, and tested the retrieval with data from the Airborne Multiangle SpectroPolarimetric Imager (AirMSPI: see Diner et al., 2013). Hasekamp et al. (2011) have developed aerosol retrieval algorithms over ocean using PARASOL data for a radiatively coupled atmosphere-ocean system using PARASOL data, also with the simple case 1 water bio-optical model of Chowdhary et al. (2012).

The problem with using a simple 1-parameter bio-optical model for case 1 waters is that it is inappropriate for coastal and inland waters, or even case 1 waters that vary from the ideal (e.g., Mobley et al., 2004). When the inherent optical properties (IOP) do not tightly co-vary with [Chla], more sophisticated bio-optical models (i.e., that include more free parameters such as marine particulate scattering and Colored Dissolved Organic Material - CDOM), absorption coefficients; Werdell et al., 2013) are needed to simultaneously retrieve aerosol and ocean properties. Stamnes et al. (2018) and Gao et al. (2018) have taken the first steps toward including more free parameters in the joint retrieval of aerosol and hydrosol properties from MAP data. However, additional research is needed to quantify polarimetric properties of plankton and suspended mineral particles for such waters, such that these more sophisticated bio-optical models can take fullest advantage of MAP data for joint aerosol-ocean retrievals over complex (coastal) waters.

Aerosol retrieval algorithms that use only the polarized reflectance measured by a MAP in the VIS offer an alternative, albeit partial solution, for open ocean observations. They rely less on the goodness of bio-optical models but are also less sensitive to some aerosol properties, such as SSA and AOD. These types of algorithms are based on our understanding of the absolute and relative magnitudes of intensity and polarized contributions to the TOA radiance, especially in parsing the contributions from ocean and atmosphere. We have acquired this information from various sources. Chowdhary et al. (2006) have studied the magnitude and angular variation of the total and polarized water-leaving reflectances, based on bio-optical models of case 1 waters, in which inherent optical properties (IOPs) are parameterized in terms of [Chla]. The wavelength range was from 400 to 600 nm and for [Chla] spanning 0.03–3.0 mg/m^3. Chami (2007) has studied the importance of the top-of-atmosphere polarized reflectance for both open ocean and coastal waters. The wavelength range was from 443 to 870 nm. Chami (2007) suggested that the polarized signal may be preferred for aerosol retrieval because the top-of-atmosphere polarized signal is insensitive to variations in open ocean water properties. This has been verified by PARASOL measurements (Harmel and Chami, 2008). However, these conclusions do not hold for modern-age polarimetric observations with higher accuracy than PARASOL (Mishchenko et al., 2007) in the short-wave visible part of the spectrum (Chowdhary et al., 2012) or for waters dominated by algal blooms or sediments (Chami, 2007; Loisel et al., 2008). Because extending this type of analysis spectrally and for more complex waters will be necessary to make full use of PACE capabilities, we summarize a specific study of this type in section Characterizing Signal in the UV and Over Complex Waters.

Meanwhile, we note that a joint retrieval, that includes total reflectance measurements contains its own challenges for retrieving accurate ocean parameters (including normalized ocean leaving radiance) because an overwhelming portion of the signal measured by the MAP originates in the atmosphere not from the ocean. Small errors in forward modeling will translate into a large, errors in retrieved ocean parameters. These small errors could be introduced from cloud contamination, trace gas, or adjacency effects, or from inaccurate assumptions of aerosol optical properties, atmospheric profiles, horizontal homogeneity or ocean salinity. Even basic radiative transfer assumptions, such as plane parallel assumptions, truncating scattering diffraction peaks, using limited number of streams and Fourier terms, ignoring inelastic scattering processes, or using inaccurate solar spectra can affect the robustness of the joint retrieval, especially the retrieval of the ocean parameters.

Although the retrieved aerosol parameters are less susceptible to these small errors than the ocean parameters, these errors in the forward model can also affect the aerosol retrieval accuracy or the number of aerosol parameters that can be retrieved with confidence. Case I waters will always be easier than complex waters, and the stronger the aerosol loading, the more reliable the aerosol retrieval. At low aerosol loading over coastal regions, even a MAP may not return much more additional aerosol information beyond what we have come to expect from heritage instruments. However, we expect progress over the next few years that will address these sources of error in forward models and provide more sophisticated bio-optical models and better representation of polarimetric properties of hydrosols. Thus, in the PACE era, we expect to see attempts of simultaneous retrievals of aerosol and ocean properties, and better realization of the information content measured by the PACE MAPs.

Characterizing Signal in the UV and Over Complex Waters

The PACE MAPs will cover the spectrum from 385 to 870 nm, which will surpass the wavelength range studied in the above-mentioned literature (Chowdhary et al., 2006; Chami, 2007; Harmel and Chami, 2008). In order to gain a better understanding of the water-leaving contribution to the TOA radiances in the UV and the deep blue part of the spectrum, Zhai et al. (2017b) performed a sensitivity study for a set of wavelengths from 340 to 865 nm. This study uses a vector radiative transfer model for coupled atmosphere and ocean systems based on the successive order of scattering method (Zhai et al., 2009, 2010). All inelastic scattering processes in ocean waters are accounted for in this study, which include Raman scattering, fluorescence from CDOM and chlorophyll (Zhai et al., 2015, 2017a). In order to be realistically representative, two water types are employed: one is dominated by phytoplankton particles (hereafter referred as PDW), and the other is dominated by non-algae particles (hereafter referred as NDW). In this way, this study fills in several holes that earlier studies missed.

PDW consists of three components: pure sea water with absorption and scattering coefficients based on (Pope and Fry, 1997; Zhang and Hu, 2009), phytoplankton particles with IOPs parameterized in terms of [Chla] (Voss, 1992; Bricaud et al., 1998, 2010), and CDOM with absorption coefficients increasing exponentially as wavelength decrease (Morel and Maritorena, 2001). Specifically, the absorption coefficient of phytoplankton particles in the UV is from the BIogeochemistry and Optics SOuth Pacific Experiment (BIOSOPE) (Bricaud et al., 2010), which is combined with the visible data (Bricaud et al., 1998) to form a complete dataset. The scattering of light by CDOM is neglected. The scattering phase function of phytoplankton particles is characterized by the Fournier-Forand (FF) phase function, whose shape is dominated by the backscattering fraction (Fournier and Forand, 1994; Mobley et al., 2002). The scattering matrix of phytoplankton particles is based on the measurement reported by Voss and Fry (1984). In addition to the three components of PWD, NWD contains non-algae particles with IOPs characterized by the non-algae particle concentration [NAP]. Similar to CDOM, the absorption coefficient of NAP increases exponentially as wavelength decreases, though the spectral slope is different from that of CDOM (Babin et al., 2003). The scattering coefficient and scattering matrix for NAP are calculated using Mie theory assuming spherical particles. The particle size distribution (PSD) used for this calculation is a Junge size distribution with a slope of 4, and the refractive index for the calculation is assumed to be 1.2 relative to water. Readers are referred to Zhai et al. (2017b) for more details of the bio-optical model used in this work.

We studied both the reflectances at the TOA and just above the ocean surface. The TOA total reflectance is defined as: $\rho_t = \pi L_t/E_d$, where L_t is the total radiance exiting the whole atmosphere and ocean system, and E_d is the downwelling irradiance at the TOA. The water leaving signal is $\rho_w^{'} = \pi(L_t - L_t^n)/E_d$, where L_t^n is the TOA radiance for the system with the same atmosphere and ocean surface but without ocean water. The following wavelengths are simulated: 340, 354, 388, 416, 442, 452, 470, 510, 551, 670, 765, and 865 nm. These span the spectral range from UV to NIR, in which water leaving radiance is significant. **Figure 4** shows that the total reflectance ρ_t decreases with increasing wavelength due to the decrease of molecular and aerosol scattering as wavelength increases. The water signal in the total reflectance is noticeable, but subtle, between 400 and 600 nm for phytoplankton (quantified by chlorophyll and designated by PDW) and non-algal particle concentrations (NDW), with the signal from NDW being more prominent.

For the water signal, ρ_w' (maroon curves in **Figure 4**) with PDW, there is an inflection wavelength between 510 and 550 nm where ρ_w' does not change for different [Chla] values. When the wavelength is shorter than this inflection wavelength, ρ_w' is larger for smaller [Chla] values. This trend is reversed when wavelength is longer than the inflection wavelength. In contrast to PDW, the NDW water signal ρ_w' does not have an inflection wavelength. The NDW water signal is larger for larger [NAP] across the whole spectral interval 400–600 nm, and the wavelength of the ρ_w' maximum remains almost constant for a wide range of [NAP]. For both PDW and NDW, the ρ_w' values are smaller in both UV and NIR than in the visible bands. The small-to-negligible ρ_w' values in the NIR are common for open (and many coastal) waters, and form the basis for heritage atmospheric correction schemes using NIR bands to constrain aerosol for retrievals in the VIS (Gordon and Wang, 1994). However, note that for NWD, that reflectance ρ_w' at 865 nm becomes about 0.001 for [NAP] = 10 g/m^3, which is small but not negligible in terms of an aerosol retrieval or atmospheric correction. Furthermore, the small ρ_w' values in the UV for PDW can become very large (and even superceed the ρ_w' values in the VIS) if the amount of CDOM becomes very low (Chowdhary et al., 2019). Such low CDOM values can be found in extreme oligotrophic waters, such as the South Pacific (Morel et al., 2007). The small ρ_w' values at 340 nm

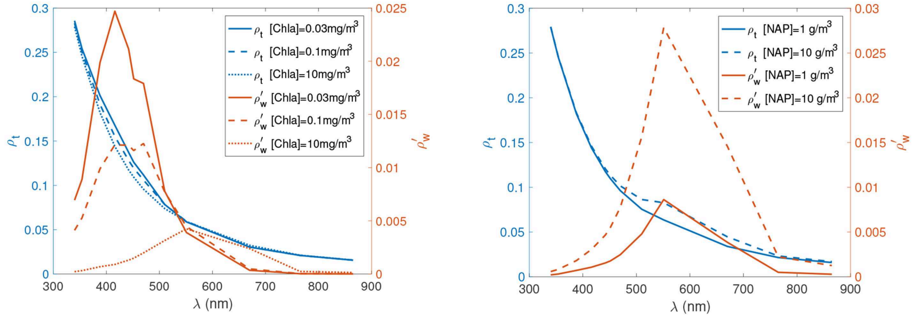

FIGURE 4 | TOA Reflectance at nadir as a function of wavelength. The total reflectance is shown in blue by the left y axis and the water leaving signal is shown in maroon by the right y axis. The differences between heavy, solid and dashed lines are due to differences in chlorophyll amounts **(left)** or non-algal particle concentrations **(right)**. The solar zenith angle is 45 degrees and the aerosol optical depth at 550 nm is 0.15. Reprinted with permission from Zhai et al. (2017a), The Optical Society (OSA).

for NDW, the water-type of which is more characteristic for coastal (eutropic) environments, is around the same level as in the NIR.

Figure 5 shows the relative contribution $\eta = 100\rho'_w/\rho_t$ of water leaving signal at the TOA for PDW and NDW at nadir, respectively. For PDW, the maximum fraction decreases from 16 to 8%, and the wavelength corresponding to the maximum fraction shifts from 470 to 670 nm, as [Chla] increases from 0.03 to 10 mg/m^3, respectively. Note that, for [Chla] $=$ 0.03 mg/m^3, the wavelength of maximum occurrence shifts into the UV if CDOM becomes very low (Chowdhary et al., 2019). At both sides of the maximum peak, the fraction decreases as wavelength decreases toward the UV or increases toward NIR. The fraction is around or $<$2% at wavelengths shorter than 354 nm or longer than 760 nm. For NDW, the maximum relative contribution occurs around 550 nm, and this peak does not shift spectrally as [NAP] values change. However, the relative contribution does increase in magnitude from around 15–35%, when [NAP] increases from 1 to 10 g/m^3. As wavelength approaches the UV, the fraction decreases at a faster rate than that of PDW due to the light absorption in that part of the spectrum by the NAP constituents in the water. In the NIR, the water-leaving fraction is still significant for NDW, which is around 8% or less at nadir.

Figure 5 also illustrates the reasons why traditional algorithms, needing to separate atmospheric and oceanic signals in the radiometric measurements have made use of the NIR. See section The Coupled Atmospheric-Oceanic System. In this wavelength range, η is much lower than in the visible, allowing characterization of the atmospheric constituents including aerosol without much contribution from the ocean. From **Figure 5**, we can also anticipate similar advantages for aerosol characterization by using the UV wavelengths. Without a MAP, the recommendation is to make use of careful spectral range selection to separate ocean and atmospheric signals. However, there remains some sensitivity to [Chla] and [NAP] in both the UV and in the NIR radiometric quantities, which can be reduced by working with polarized measurements.

Figure 6 show the relative percentage contribution of the *polarized* water leaving signal to the TOA *polarized* radiance field for the same case shown in **Figure 4**. The spectral variation of the polarized water-leaving fraction is due to the different bio-optical properties of the PDW and NDW waters, as the atmosphere properties are kept the same for these cases. The spectral behavior is similar to that of the total reflectance, but the magnitude of relative contribution is much less. Note the different scales on the y-axes of **Figure 6** vs. **Figure 5**. The wavelength of the PDW maximum fraction strongly depends on [Chla], but the wavelength of the NDW maximum fraction is less sensitive to [NAP]. The PDW maximum fraction is larger for smaller [Chla]; while the NDW maximum fraction is larger for larger [NAP]. The PDW maximum fraction increases only from 2 to 5.5% for [Chla] decreasing from 10 to 0.03 mg/m^3; while the NDW maximum fraction increases only from 6 to 16% for [NAP] increasing from 1 to 10 g/m^3. Note that these increases will become larger if the amount of CDOM in the ocean becomes less (see Chowdhary et al., 2012, which was computed for smaller amounts of CDOM). Nevertheless, the satellite-measured *polarized* signal will be much less affected by variability in oceanic constituents than the total radiometric signal. The sensitivity study shown in **Figures 4–6** did not include the viewing angular variation of water leaving contributions to the TOA signals, which was previously studied in Chowdhary et al. (2006) for open ocean waters.

These results are important for designing algorithms for PACE MAPs, either for retrieving aerosol or for atmospheric correction. In terms of retrieving aerosol, these results show an interplay in the UV and shortwave blue range between the effects of chlorophyll and non-algal particle concentrations. Adding non-algal particles will increase the absorption in that range, and offset the scattering expected from PDW. This oceanic complexity in this spectral range adds to the already complex atmospheric situation in the shortwave in which there is interplay between the spectral aerosol absorption, aerosol particle size, and height of the aerosol layer. Furthermore, there are aerosols (specifically: brown carbon particulates) that exhibit the same spectral increase in absorption toward the UV as CDOM in the ocean, which complicates separating the atmospheric and oceanic contribution to TOA radiance in the UV (Chowdhary et al., 2019). Together these oceanic and atmospheric properties

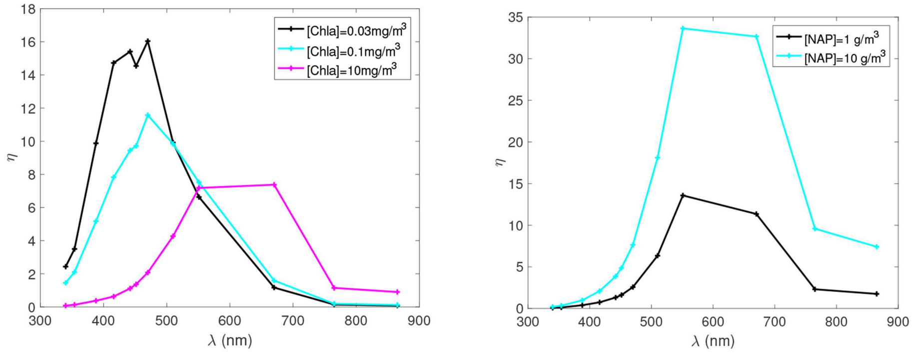

FIGURE 5 | Water-leaving relative percentage contribution in the TOA reflectance for the same case as in **Figure 4**. Reprinted with permission from Zhai et al. (2017a), The Optical Society (OSA).

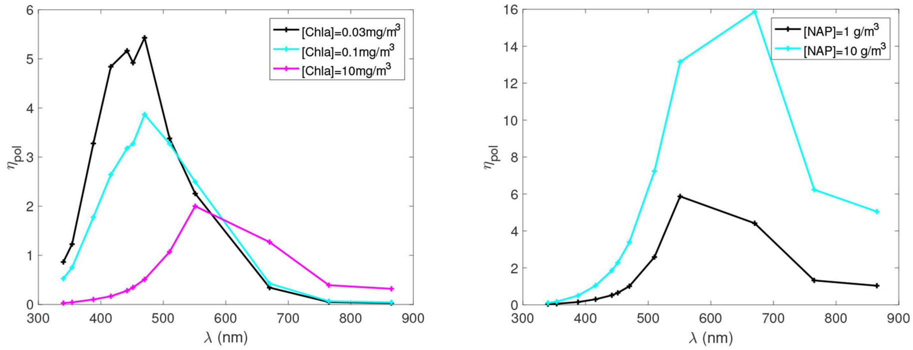

FIGURE 6 | Polarized water-leaving relative percentage contribution in the TOA polarized reflectance for the same case as **Figure 4**. Reprinted with permission from Zhai et al. (2017a), The Optical Society (OSA).

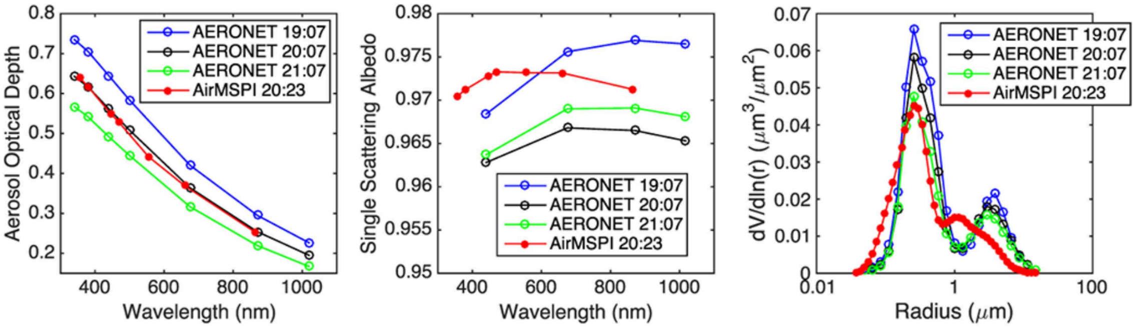

FIGURE 7 | AirMSPI-retrieved aerosol optical depth (AOD), single scattering albedo (SSA), and volume-weighted aerosol size distribution collocated with the Fresno AERONET site on January 6, 2012, compared to the AERONET-derived values. Different times of observation noted. Adapted with permission from Xu F. et al. (2017), John Wiley & Sons.

will introduce significant uncertainty in making use of the shortwave observations in these wavelengths (Kahn et al., 2016).

An encouraging outcome from these results is that the relative and absolute magnitudes of the different contributions from PDW, and non-algal particles show that the *polarized* water signal contributes <1/3 the signal to TOA measurements than does the *total* water signal, across all wavelengths and for both PDW and non-algal water constituents. This suggests aerosol-retrieval algorithms based on polarized measurements or joint atmospheric-oceanic retrievals that exploit both polarized and total TOA measurements from the UV to the NIR should find adequate constraints on the ocean signal to better characterize aerosol properties than non-polarized sensors. In addition, we note that this sensitivity study was conducted at only one geometry and does not illustrate the added capability of combining polarimetry with multi-angle views. However, this theoretical study only touches upon the complexities exhibited by total and polarized spectral water reflectances. In practice, the uncertainties introduced by these complexities may hinder some of the advantages suggested by **Figure 6** for optimized joint atmosphere-ocean retrievals.

MULTI-ANGLE POLARIMETER AEROSOL RETRIEVALS OVER OCEAN AND LAND

Multiangular polarimetric observations of the coupled atmosphere-ocean system offer unique opportunities to separate and retrieve variations in the oceanic and atmospheric properties that otherwise lead to similar spectral signatures in TOA total radiance. As noted above, given that some aerosols show a strong spectral increase in absorption coefficient in the near-UV (e.g., Koven and Fung, 2006; Bergstrom et al., 2007; Russell et al., 2010) that also occurs for oceanic non-algal particles and CDOM (e.g., Jerlov, 1976; Bricaud and Stramski, 1990; Nelson and Siegel, 2013; Wei et al., 2016), their impact on spaceborne measurements of intensity will be difficult to distinguish or might even cancel each other out. On the other hand, variations in absorbing aerosols and non-algal particles will likely lead to different changes in angular features of TOA polarized light that can be distinguished even if these changes occur simultaneously (Chowdhary et al., 2019).

A multi-angle polarimeter inversion is different from the types of retrievals applied to radiometers for the past 15 years. Heritage aerosol retrievals must use a priori assumptions about the aerosol and surface properties plus a pre-calculated Look Up Table, and are often limited to only retrieving aerosol loading and some information about aerosol type and height for general aerosol conditions. In contrast, the simultaneous inversion of multiple wavelengths, angles and polarization states, with a minimum of constraints, can retrieve aerosol optical thickness, particle shape, size distribution and complex refractive index, while simultaneously constraining parameters of the surface beneath, even if a full simultaneous retrieval of the surface characteristics is not made (Mishchenko et al., 2007; Waquet et al., 2009a; Dubovik et al., 2011; Knobelspiesse et al., 2012; Wu et al., 2015). Some of this potential is illustrated in **Figure 3**. Multi-angle radiance and polarimetric observation improves upon radiometry alone in reducing the number of a priori assumptions required for aerosol retrieval and allows a more physical characterization of the scene.

An early example of the power of multi-angle polarimetry is the use of ocean glint as a bright backdrop from which to accurately retrieve aerosol absorption. The success of this retrieval depends on first constraining the aerosol scattering properties, including the real part of the refractive index. This can only be done with multi-angle looks at the same aerosol, with at least one view in glint and one not in glint, and to achieve the required accuracy in the scattering properties retrieval, only polarimetry provides sufficient information (Kaufman et al., 2002; Ottaviani et al., 2013).

Other examples, based on analyses of airborne MAP data, have shown that not only can a multi-angle polarimeter retrieve a comprehensive set of aerosol properties in cloud-free scenes over open ocean waters (Chowdhary et al., 2001, 2002, 2005; Xu et al., 2016; Stamnes et al., 2018), they can do the same for coastal waters (Gao et al., 2018, 2019). Moreover, MAP can be used to characterize aerosol properties above clouds and below thin cirrus clouds, at least in some situations, because aerosols and clouds have different polarimetric signatures (Knobelspiesse et al., 2011; Waquet et al., 2013; Peers et al., 2015; Xu et al., 2018). In principle, aerosol retrievals within broken cloud fields may also be possible (Hasekamp, 2010), although three dimensional (3D) effects may seriously hamper the accuracy (Davis et al., 2013; Stap et al., 2016). To overcome this limitation, substantial development of 3D multi-angle/multi-pixel algorithms will be required (Martin et al., 2014; Levis et al., 2015; Martin and Hasekamp, 2018). The ability of a MAP to retrieve in traditionally cloud-masked scenes increases the availability of the aerosol characterization and provides a more accurate global picture of aerosol forcing. We expect improvement from MAPs in this respect despite new algorithms applied to heritage radiometers or to the PACE OCI that are allowing for aerosol retrievals above clouds (Jethva et al., 2013, 2014, 2016; Meyer and Platnick, 2015; Sayer et al., 2016; Remer et al., 2019).

While we have focused this study mostly on retrieving aerosol characteristics over ocean, a MAP represents opportunity to step up from heritage capabilities in retrieving aerosol properties over land as well (Waquet et al., 2009b; Dubovik et al., 2011; Wu et al., 2015; Xu F. et al., 2017; among others). As an example, **Figure 7** shows a comparison of retrieved aerosol optical depth (AOD), single scattering albedo (SSA), and size distributions with collocated AERONET Level 1.5 aerosol products. The MAP measurements resulting in these retrievals are from AirMSPI, which has 8 aerosol bands in the UV to near infrared, 7 of which are used for aerosol retrieval (Diner et al., 2013). The AirMSPI retrievals demonstrate a reasonable agreement except for the coarse particle size mode, likely due to the lack of shortwave infrared bands on AirMSPI. Overall, AirMSPI AOD validation with 27 cases of available field observations shows a spectrally mean R^2 of 0.95, linear regression mean slope of 0.97, and mean intercept of 0.01, reflecting high retrieval quality (Xu F. et al., 2017).

There are some limitations to using polarimetry for aerosol characterization. All aerosol retrieval procedures using polarimetry require measurements over specific ranges of scattering angles, depending on the retrieval approach. The ranges and values of scattering angles that would be measured by a polar orbiting instrument will vary with solar and viewing geometries. Thus, the availability and quality of derived products will vary with location and time, especially for the outer portions of an instrument's swath. However, as demonstrated in **Figure 8**, polarimetry yields still substantial improved capability over radiometry even for less favorable or reduced scattering angles.

In addition to characterizing aerosol microphysical and optical properties, MAP measurements at 410 nm also provide information on aerosol layer height. The reason is that,

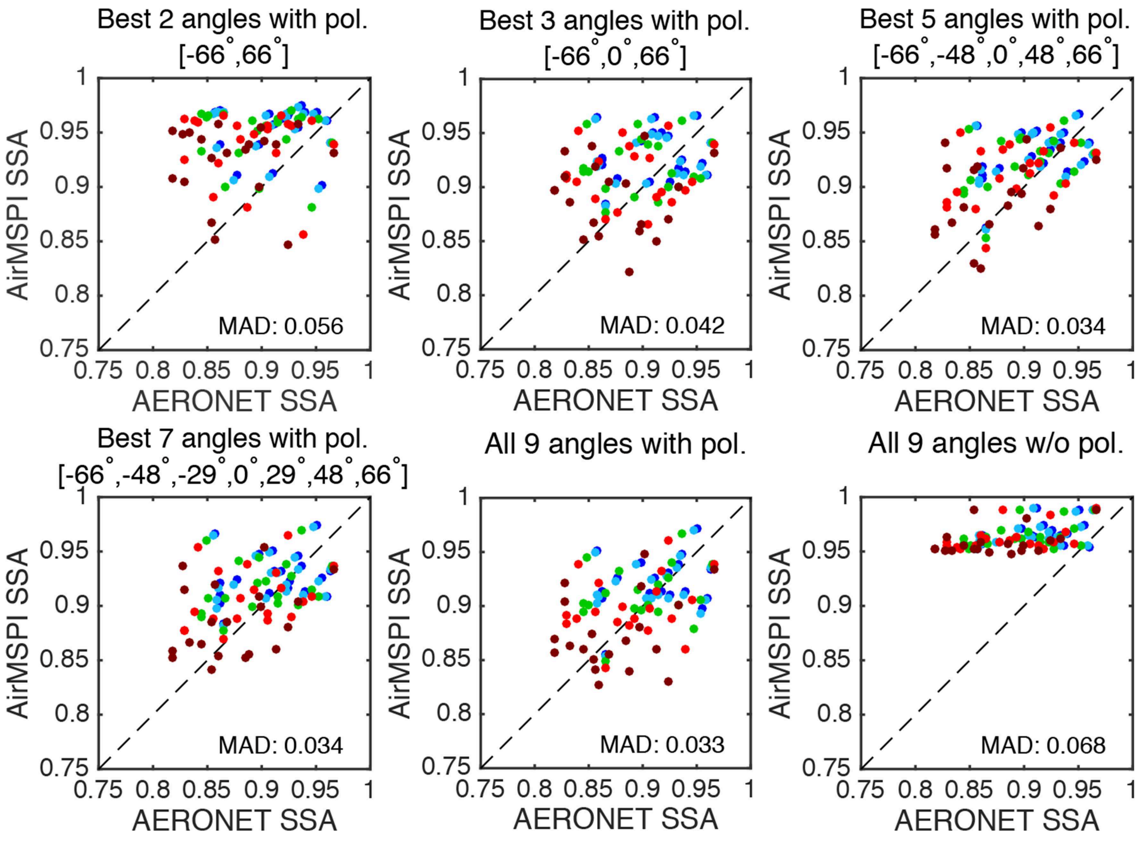

FIGURE 8 | Scatter plots of AirMSPI-retrieved SSA against collocated AERONET values using a different number of viewing angles and polarization features. The results of SSA are plotted in different colors for five wavelengths from visible to near-infrared: dark blue (445 nm), light blue (470 nm), green (555 nm), red (660 nm), and brown (865 nm). The mean absolute difference (MAD) between the two retrievals is listed in the bottom right of each subplot. "Best angles" are identified as the subset of AirMSPI viewing angles that gives the best agreement with AERONET derived values. Reprinted with permission from Xu F. et al. (2017), John Wiley & Sons.

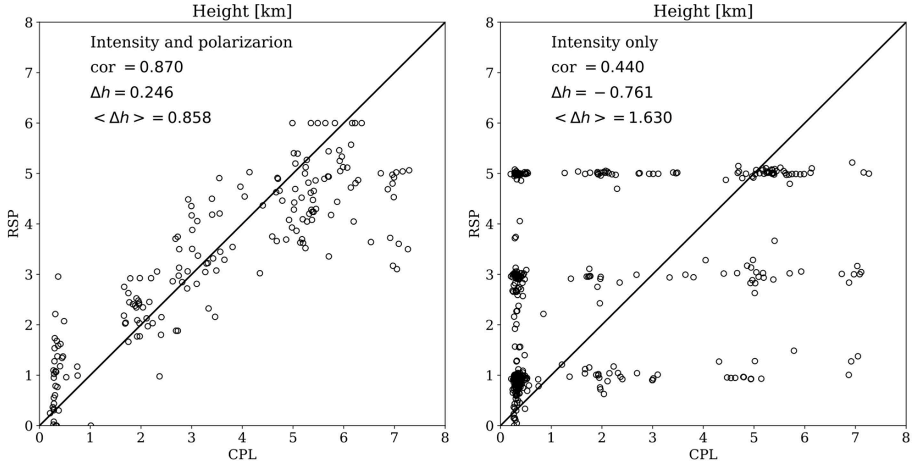

FIGURE 9 | Retrieved aerosol layer height from the Research Scanning Polarimeter (RSP) vs. the same derived from the Cloud Physics Lidar (CPL) using both radiance and polarization measurements **(left)**, and using only radiance measurements **(right)**. Measurements were obtained during the Polarimeter Definition Experiment (PODEX) and the Studies of Emissions, Atmospheric Composition, Clouds and Climate Coupling by Regional Surveys (SEAC4RS) measurement campaigns. Adapted with permission from Wu et al. (2016), John Wiley & Sons.

depending on its altitude, an elevated aerosol layer shields the strong polarization signal from Rayleigh scattering by air molecules. The potential of aerosol layer height retrievals from MAP measurements has been demonstrated by Wu et al. (2016) using airborne measurements from the Research Scanning Polarimeter (RSP: Cairns et al., 1999). They found good agreement between the aerosol layer height retrieved from RSP and measurements from the Cloud Physics Lidar (CPL: McGill et al., 2002) flying on the same platform. The left panel of **Figure 9** shows the comparison between aerosol layer heights derived from RSP and CPL measurements, and the right panel shows the comparison if only radiance (intensity) measurements of RSP are used. Clearly, without the polarization measurements the information on aerosol height is virtually absent. Wu et al. (2016) also showed that the availability of 410 nm polarization measurements and a high polarimetric accuracy are the most important factors determining the capability to retrieve aerosol layer height. These results do not invalidate the possibility that other methods without polarization, such as Oxygen A-band retrievals, may also deliver similar information on aerosol layer height (Xu X. G. et al., 2017; Davis and Kalashnikova, 2019). Nevertheless, one advantage of using polarimetry to retrieve aerosol height is that it is uses observations in the blue-UV, where aerosol optical depths are larger than in the Oxygen A-band, which may allow height retrievals in situations with less aerosol loading.

The caveats to relying on multi-angle polarimetry for characterizing aerosol from the PACE mission include the details of the limitations of an individual instrument's swath, spectral coverage, spatial resolution and polarimetric accuracy. By flying two complementary polarimeters on PACE, namely SPEXone and HARP2, the mission somewhat compensates individual instrument limitations. At the very least, the instrument teams intend to use their collocation on the PACE observatory to cross calibrate radiometric and polarimetric measurements. Furthermore, comparison of instrument-specific retrievals of aerosol properties, made by each sensor along the SPEXone narrow swath, will aid in evaluating individual sensor performance and algorithms. Actual retrieval applied to the joint simultaneous measurements of both PACE MAPs is challenging. Despite having two MAPs on the same platform, PACE will fly with no polarimetric measurements at wavelengths longer than 850 nm, which may affect accuracy of aerosol coarse mode characterization and overall abilities over land surfaces. Algorithms used to fully exploit the advantages of polarimetry for aerosol retrievals are complex, requiring effort to develop and maintain. Moreover, existing approaches are currently computationally costly, although we expect computational power to increase substantially by the time the PACE mission launches. Furthermore, development of more computationally efficient retrieval algorithms is also underway (Dubovik et al., 2014; Di Noia et al., 2017).

In summary, despite the caveats, the potential PACE mission benefits of multi-angle polarization in characterizing aerosol are substantial, proven and documented.

SYNERGY BETWEEN OCI AND MAP FOR AEROSOL RETRIEVALS

The primary PACE instrument is the Ocean Color Instrument (OCI), a 5-nm spectral resolution single-view radiometric sensor, that will share the satellite with the two secondary contributed MAPs. Collocated data from OCI and the multi-angle polarized measurements will provide a rich dataset for Earth system exploration, however, new retrieval techniques still need to be developed to take advantage of the large information content of such datasets.

OCI's capabilities could aid aerosol retrievals from the MAPs in the realm of radiometric calibration, gaseous correction and constraints on aerosol height and coarse mode particles. OCI's well-calibrated 5-nm measurements allow for better radiometric calibration of both PACE MAPs if the MAPs are designed to match OCI's measurements. For example, to make optimal use of the high radiometric accuracy of OCI, SPEXone has chosen two of its viewing angles at $+20^\circ$ and -20° to overlap with OCI views. Note that OCI is a single view instrument but will not point nadir. In order to avoid ocean sun glint, OCI will perform a tilt maneuver every orbit at the sub-solar point so that it will point 20° forward in the northern hemisphere and 20° aft in the southern hemisphere. Also, OCI, with its 5-nm resolution, will quantify and subsequently correct for absorbing gases and retrieve information on aerosol height across HARP2's wide swath. OCI provides more bands in the chlorophyll absorption peak, which is useful in validating and/or better constraining a rudimentary ocean reflectance model for constraining ocean reflectance for aerosol retrievals, again across the broad swath. SPEXone also observes at 5 nm resolution, but only in its much narrower swath. Also, OCI provides information on aerosol absorption further into the UV than the MAPs allowing for better constraint on the direct radiative effect of aerosols. Lacagnina et al. (2017) have used a similar synergy between POLDER and OMI.

However, most of the synergy between PACE instruments flows in the other direction with the MAPs aiding OCI in separating the aerosol signal from the ocean signal, and vice-versa. Conversely, MAP's information content as compared with OCI will allow for much better characterization of aerosol properties. This will help to constrain OCI aerosol characterization and atmospheric correction (Frouin et al., 2019). Additionally, because large amounts of sediments and CDOM in coastal waters can masquerade as absorbing aerosols in the satellite-measured signal in the UV/shortwave visible range, algorithms applied to OCI alone will find it difficult to isolate the atmospheric signal to make use of the aerosol signal there, or to isolate the ocean signal to derive water-leaving radiance. This is when making use of MAP observations can help separate and characterize the aerosol scattering contributions for aerosol retrievals.

Another synergy between OCI and the MAPs is the quantification of the direct radiative effect of aerosols above clouds by calculating the difference between the total outgoing irradiance and the outgoing irradiance for an atmosphere with no aerosol and only the cloud (de Graaf et al., 2014). Here, the total outgoing irradiance can be estimated from the measured spectral radiance. Currently, this is being done from single viewing angle radiance measurements, but this estimate can be significantly improved using multi-angle measurements. To best estimate the outgoing irradiance combined measurements of cloud and aerosol properties are needed, and it will take the combination of both PACE MAPs with the PACE OCI to deliver the required characterization.

DISCUSSION

The PACE mission will be an opportunity to expand characterization of global aerosols with the Ocean Color Instrument (OCI), a single-view broad spectrum, wide swath, radiometer and two complementary multi-angle polarimeters (MAPs). For aerosols, OCI primarily has the capability to continue the heritage retrieval algorithms associated with heritage sensors such as MODIS and OMI. OCI also has the potential to enhance aerosol characterization by means of its broad spectrum and fine spectral resolution through the oxygen A band (Davis and Kalashnikova, 2019; Remer et al., 2019). However, any OCI aerosol retrieval algorithm will require a priori assumptions because its single view radiometric measurements are limited in information content.

Multi-Angle Polarimeters will dramatically increase the information content of the PACE mission to produce a more complete characterization of aerosol parameters not possible today. The challenge in making use of the full information content of a MAP is in the separation of satellite-measured signal into atmospheric and oceanic components. One approach to retrieving aerosol properties from satellite is to avoid the ocean signal as much as possible by using wavelengths that are assumed to be dark in water leaving reflectance and avoiding situations that do not meet this assumption. This will often regulate the aerosol retrieval to Case I waters, far from estuaries and coastlines, sometimes where the most societally relevant aerosol occurs.

The alternative to this limiting set of assumptions is to approach the atmospheric-oceanic decoupling with a joint retrieval that returns both aerosol and ocean color properties together. The requisite radiative transfer models that can accurately (i.e., consistent with current and future MAP accuracies) and realistically (e.g., including inelastic underwater light scattering, scattering by complex inhomogeneous particles, and light propagation in horizontally inhomogeneous media) simulate radiative transfer of polarized light through atmosphere-ocean systems are now becoming feasible (Chowdhary et al., 2019). Such joint retrievals are possible (e.g., Chowdhary et al., 2012; Stamnes et al., 2018; Gao et al., 2019), but come with challenges. One of the requirements is that oceanic bio-optical models that were used in past polarimetric retrievals need to catch up (i.e., incorporate more inherent optical parameters, e.g., parameterization of the oceanic Mueller matrix in terms of oceanic constituents) with those used for modern-age radiometric ocean color retrievals. There is also a need to better characterize the scattering matrices of suspended hydrosols. Both of these requirements are currently in the process of being addressed (Chowdhary et al., 2019). We need to continue our research on these issues in the next few years, in order to be prepared for the PACE mission and the simultaneous inversions that such a mission will support.

While the expectations are high for the PACE MAPs' aerosol characterization capabilities, this enthusiasm does not negate the need to continue and expand upon aerosol retrievals from radiometry. In particular, the PACE OCI with its fine spectral resolution measurements and broad spectral range offers an alternative and complementary path forward for aerosol characterization during the PACE era (Remer et al., 2019). Single-view radiometry for aerosol retrieval enjoys a long heritage, and while algorithms applied to radiometers require greater reliance on assumptions to constrain the retrieval, those assumptions are based in physical understanding and experience acquired over decades. As research continues to meet the challenges to obtain joint atmospheric-oceanic retrievals from the PACE MAPs, we must not neglect preparation for OCI-centered aerosol characterization.

Sensitivity studies have been conducted using coupled radiative transfer modeling during the tenure of this PACE science team. These studies model the contribution of water-leaving radiance to the TOA signal, across the spectrum, for both total radiance and polarimetric radiance for a variety of water constituents. The results indicate that polarized radiance is much less affected by variability of chlorophyll-containing and non-algal constituents in the water than is total radiance (intensity). Thus, when attempting retrievals of aerosol properties over water with unconstrained water-leaving radiances, using the polarized signal instead of intensity should introduce much less uncertainty.

To prepare for PACE, a test bed of multi-angle polarimeter data is needed to verify the sensitivity studies and to prepare and test algorithms. There are now several airborne MAPs flying and making measurements that could be used as test cases. Recently, four different airborne MAPs flew on the NASA ER-2 as part of the Aerosol Characterization from Polarimeter and Lidar (ACEPOL) campaign. These data span the specific capabilities expected of any MAP that would fly on the PACE mission, and therefore provide adequate test data for algorithm development. This is in addition to new algorithms being developed and applied to POLDER/PARASOL observations The effort should be placed in continuing to fly these airborne instruments over scenes of particular interest to PACE, including aerosol events and clouds, over land and ocean, and to collocate these scenes with ancillary data that can be used to verify proto-algorithm retrievals. Also, effort should be directed toward processing the collected data and making it quickly available for algorithm development, as well as to use POLDER/PARASOL data as an opportunity to explore MAP information content with actual space borne measurements.

Retrievals applied to real observations show that MAP-retrieved aerosol parameters match ground truth to accuracies within expectations, and also demonstrate the relative importance of polarization to multi-angle capabilities. We expect a PACE MAP to improve accuracy of the global aerosol parameters that we now retrieve, expand the type of parameters that we can retrieve, and extend retrievals to situations previously unattainable from heritage aerosol satellite missions. In summary, the potential PACE mission benefits of multi-angle polarization in characterizing aerosol are substantial, proven, and documented.

AUTHOR CONTRIBUTIONS

This work represents part of the overall consensus statement agreed to by the first NASA PACE Science Team and includes contributions from the Principal Investigators of the Atmospheric Correction subgroup of that Science Team, along with their associates involved with the aerosol characterization focus of that subgroup. All authors of this paper were part of the discussions of that subgroup and Science Team from 2014 to 2018. In addition, LR was Deputy Lead of the Science Team and Leader of the subgroup. She organized this particular paper and consolidated the input from all authors. KK made significant contributions to the discussion and writing of all sections, but was primarily responsible for the information content study and the section that discusses the challenges in realizing the value of that content. P-WZ was responsible for the analysis and writing of the section that explored the sensitivity of using the UV part of the spectrum for aerosol retrieval over complex water. FX did the analysis and provided the figures that show AirMSPI retrievals validated against AERONET. He was supported in that effort by OK, who also took responsibility for the multi-angle radiometer-only section. JC provided much of the material in the section that discusses the issues with separating aerosol signal from ocean signal. OH and OD provided most of the material for the section on heritage retrievals using POLDER. OH and LW gave us the aerosol height retrieval information and figures. ZA, EB, BC, OC, AD, HD, DD, BF, RF, B-CG, AI, RL, JM, AO, and OT were active participants during the years of discussion that resulted in this paper, and each has made contributions, edited, or commented on this manuscript.

FUNDING

This work was supported by NASA Grants under the solicitation NNH13ZDA001N-PACEST. In addition, LR, RL, and OT acknowledge funding from NASA grant NNX15AD15G. OK and AD contribution was supported by the PACE science team grant, under Paula Bontempi. P-WZ acknowledges funding from NASA grant 80NSSC18K0345. OC acknowledges funding from NASA grant NNX15AC78G.

ACKNOWLEDGMENTS

Portions of this work were performed by OK, AD and DD at the Jet Propulsion Laboratory, California Institute of Technology, under a contract with the National Aeronautics and Space Administration.

REFERENCES

Babin, M., Stramski, D., Ferrari, G. M., Claustre, H., Bricaud, A., Obolensky, G., et al. (2003). Variations in the light absorption coefficients of phytoplankton, nonalgal particles, and dissolved organic matter in coastal waters around Europe. *J. Geophys. Res*. 108:3211. doi: 10.1029/2001JC000882

Bergstrom, R. W., Pilewskie, P., Russell, P. B., Redemann, J., Bond, T. C., Quinn, P., et al. (2007). Spectral absorption properties of atmospheric aerosols. *Atmos. Chem. Phys*. 7, 5937–5943. doi: 10.5194/acp-7-5937-2007

Bricaud, A., Babin, M., Claustre, H., Ras, J., and Tie'che, F. (2010). Light absorption properties and absorption budget of Southeast Pacific waters. *J. Geophys. Res*. 115:C08009. doi: 10.1029/2009JC005517

Bricaud, A., Morel, A., Babin, M., Allali, K., and Claustre, H. (1998). Variations of light absorption by suspended particles with chlorophyll a concentration in oceanic (case 1) waters: analysis and implications for bio-optical models. *J. Geophys. Res*. 103, 31033–31044. doi: 10.1029/98JC02712

Bricaud, A., and Stramski, D. (1990). Spectral absorption coefficients of living phytoplankton and nonalgal biogenous matter: a comparison between the Peru upwelling area and the Sargasso Sea. *Limnol. Oceanogr*. 35, 562–582. doi: 10.4319/lo.1990.35.3.0562

Cairns, B., Travis, L. D., and Russel, E. E. (1999). The Research Scanning Polarimeter: Calibration and ground-based measurements. *Proc. SPIE* 3754, 186–196. doi: 10.1117/12.366329

Chami, M. (2007). Importance of the polarization in the retrieval of oceanic constituents from the remote sensing reflectance. *J. Geophys. Res*. 112:C05026. doi: 10.1029/2006JC003843

Chen, C., Dubovik, O., Henze, D. K., Lapyonak, T., Chin, M., Ducos, F., et al. (2018). Retrieval of desert dust and carbonaceous aerosol emissions over Africa from POLDER/PARASOL products generated by the GRASP algorithm. *Atmos. Chem. Phys*. 18, 12551–12580. doi: 10.5194/acp-18-12551-2018

Chowdhary, J., Cairns, B., Mishchenko, M., and Travis, L. (2001). Retrieval of aerosol properties over the ocean using multispectral and multiangle photopolarimetric measurements from the Research Scanning Polarimeter. *Geophys. Res. Lett*. 28, 243–246. doi: 10.1029/2000GL011783

Chowdhary, J., Cairns, B., Mishchenko, M. I., Hobbs, P. V., Cota, G. F., Redemann, J., et al. (2005). Retrieval of aerosol scattering and absorption properties from photopolarimetric observations over the ocean during the CLAMS experiment. *J. Atmos. Sci*. 62, 1093–1117. doi: 10.1175/JAS3389.1

Chowdhary, J., Cairns, B., and Travis, L. D. (2002). Case studies of aerosol retrievals over the ocean from multiangle, multispectral photopolarimetric remote sensing data. *J. Atmos. Sci*. 59, 383–397. doi: 10.1175/1520-0469(2002)059%3C0383:CSOARO%3E2.0.CO;2

Chowdhary, J., Cairns, B., and Travis, L. D. (2006). Contribution of water-leaving radiances to multiangle, multispectral polarimetric observations over the open ocean: bio-optical model results for case 1 waters. *Appl. Opt*. 45, 5542–5567. doi: 10.1364/AO.45.005542

Chowdhary, J., Cairns, B., Waquet, F., Knobelspiesse, K., Ottaviani, M., Redemann, J., et al. (2012). Sensitivity of multiangle, multispectral polarimetric remote sensing over open oceans to water-leaving radiance: analyses of RSP data acquired during he MILAGRO campaign. *Remote Sens. Environ*. 118, 284–308. doi: 10.1016/j.rse.2011.11.003

Chowdhary, J., Zhai, P., Boss, E., Dierssen, H., Frouin, R., Ibrahim, A., et al. (2019). Radiative transfer in atmosphere-ocean systems. *Front. Earth Sci*. 7:100. doi: 10.3389/feart.2019.00100

Cox, C., and Munk, W. (1954). Measurement of the roughness of the sea surface from photographs of the sun's glitter. *Opt. Soc. Amer*. 44, 838–850. doi: 10.1364/JOSA.44.000838

Davis, A. B., Garay, M. J., Xu, F., Qu, Z., and Emde, C. (2013). "3D radiative transfer effects in multi-angle/multi-spectral radio-polarimetric signals from a mixture of clouds and aerosols viewed by a non-imaging sensor," in *S.P.I.E. Proceedings, Vol. 8873, Polarization Science and Remote Sensing VI,* eds J. A. Shaw and D. A. LeMaster (San Diego, CA). doi: 10.1117/12.2023733

Davis, A. B., and Kalashnikova, O. V. (2019). "Aerosol layer height over water via O_2 A-band observations from space: a tutorial," in *Springer Series in Light Scattering, Vol. 3: Radiative Transfer and Light Scattering*, ed A. A. Kokhanovsky (Heidelberg: Springer), 133–166. doi: 10.1007/978-3-030-03445-0_4

de Graaf, M., Bellouin, N., Tilstra, L. G., Haywood, J., and Stammes, P. (2014). Aerosol direct radiative effect of smoke over clouds over the southeast Atlantic Ocean from 2006 to 2009. *Geophys. Res. Lett.* 41, 7723–7730. doi: 10.1002/2014GL061103

de Leeuw, G., Sogacheva, L., Rodriguez, E., Kourtidis, K., Aristeidis, K., Georgoulias, G., et al. (2018). Two decades of satellite observations of AOD over mainland China using ATSR-2, AATSR and MODIS/Terra: data set evaluation and large-scale patterns. *Atmos. Chem. Phys.* 18:1573. doi: 10.5194/acp-18-1573-2018

Deschamps, P. Y., Breon, F. M., Leroy, M., Podaire, A., Bricaud, A., Buriez, J. C., et al. (1994). The POLDER mission: instrument characteristics and scientific objectives. *IEEE Trans. Geosci. Rem. Sens*. 32, 598–615. doi: 10.1109/36.297978

Deuzé, J. L., Goloub, P., Herman, M., Marchand, A., Perry, G., Susana, S., et al. (2000). Estimate of the aerosol properties over the ocean with POLDER. *J. Geophys. Res*. 105, 15329–15346. doi: 10.1029/2000JD900148

Deuzé, J. L., Herman, M., Goloub, P., Tanr,é, D., and Marchand, A. (1999). Characterization of aerosols over ocean from POLDER/ADEOS-1. *Geophys. Res. Lett.* 26, 1421–1424. doi: 10.1029/1999GL900168

Di Noia, A., Hasekamp, O. P., Wu, L., van Diedenhoven, B., Cairns, B., and Yorks, J. E. (2017). Combined neural network/Phillips-Tikhonov approach to aerosol retrievals over land from the NASA Research Scanning Polarimeter. *Atmos. Meas. Tech.* 10, 4235–4252. doi: 10.5194/amt-10-4235-2017

Diner, D. J., Beckert, J. C., Reilly, T. H., Bruegge, C. J., Conel, J. E., Kahn, R. A., et al. (1998). Multi-angle Imaging SpectroRadiometer (MISR) instrument description and experiment overview. *IEEE Trans. Geosci. Remote Sens.* 36, 1072–1087. doi: 10.1109/36.700992

Diner, D. J., Boland, S. W., Brauer, M., Bruegge, C., Burke, K. A., Chipman, R., et al. (2018). Advances in multiangle satellite remote sensing of speciated airborne particulate matter and association with adverse health effects: from MISR to MAIA. *J. Appl. Remote Sens.* 12:042603. doi: 10.1117/1.JRS.12.042603

Diner, D. J., Davis, A., Hancock, B., Geier, S., Rheingans, B., Jovanovic, V., et al. (2010). First results from a dual photoelastic-modulator-based polarimetric camera. *Appl. Opt.* 49, 2929–2946. doi: 10.1364/AO.49.002929

Diner, D. J., Xu, F., Garay, M. J., Martonchik, J. V., Rheingans, B. E., Geier, S., et al. (2013). The Airborne Multiangle SpectroPolarimetric Imager (AirMSPI): a new tool for aerosol and cloud remote sensing. *Atmos. Meas. Tech*. 6, 2007–2025. doi: 10.5194/amt-6-2007-2013

Dubovik, O., Herman, M., Holdak, A., Lapyonok, T., Tanr,é, D., Deuz,é, J. L., et al. (2011). Statistically optimized inversion algorithm for enhanced retrieval of aerosol properties from spectral multi-angle polarimetric satellite observations. *Atmos. Meas. Tech.* 4, 975–1018. doi: 10.5194/amt-4-975-2011

Dubovik, O., Lapyonok, T., Litvinov, P., Herman, M., Fuertes, D., Ducos, F., et al. (2014). "GRASP: a versatile algorithm for characterizing the atmosphere," in *SPIE: Newsroom* (Bellingham, WA). doi: 10.1117/2.1201408.005558

Dubovik, O., Li, Z., Mishchenko, M. I., Tanré, D., Karol, Y., and Yin, D. (2019). Polarimetric remote sensing of atmospheric aerosols: Instruments, methodologies, results, and perspectives. *J. Quant. Spectrosc. Radiat. Trans*. 224, 474–511. doi: 10.1016/j.jqsrt.2018.11.024

Dubovik, O., Smirnov, A., Holben, B. N., King, M. D., Kaufman, Y. J., Eck, T. F., et al. (2000). Accuracy assessments of aerosol optical properties retrieved from Aerosol Robotic Network (AERONET) Sun and sky radiance measurements. *J. Geophys. Res.* 105, 9791–9806. doi: 10.1029/2000JD900040

Ferlay, N., Thieuleux, F., Cornet, C., Davis, A. B., Dubuisson, P., Ducos, F., et al. (2010). Toward new inferences about cloud structures from multidirectional measurements in the oxygen A band: middle-of-cloud pressure and cloud geometrical thickness from POLDER-3/PARASOL. *J. Appl. Meteorol. Climatol.* 49, 2492–2507. doi: 10.1175/2010JAMC2550.1

Flowerdew, R. J., and Haigh, J. D. (1995). An approximation to improve accuracy in the derivation of surface reflectances from multi-look satellite radiometers. *Geophys. Res. Lett.* 22, 1693–1696. doi: 10.1029/95GL01662

Flowerdew, R. J., and Haigh, J. D. (1996). Retrieval of aerosol optical thickness over land using the ATSR-2 Dual-Look Satellite Radiometer. *Geophys. Res. Lett.* 23, 351–354. doi: 10.1029/96GL00153

Fougnie, B., Marbach, T., Lacan, A., Lang, R., Schlüssel, P., Poli, G., et al. (2018). The multi-viewing multi-channel multi-polarisation imager–overview of the 3MI polarimetric mission for aerosol and cloud characterization. *J. Quant. Spectrosc. Radiat. Trans.* 219, 23–32. doi: 10.1016/j.jqsrt.2018.07.008

Fournier, G. R., and Forand, J. L. (1994). "Analytic phase function for ocean water," in *Ocean Optics XII, Vol. 2258* (Bergen: International Society for Optics and Photonics), 194–202. doi: 10.1117/12.190063

Frouin, R., Schwindling, M., and Deschamps, P. Y. (1996). Spectral reflectance of sea foam in the visible and near-infrared: *in situ* measurements and remote sensing implications. *J. Geophys. Res.* C6, 14361–14371. doi: 10.1029/96JC00629

Frouin, R. J., Franz, B. A., Ibrahim, A., Knobelspiesse, K., Ahmad, Z., Cairns, B., et al. (2019). Atmospheric correction of satellite ocean-color imagery during the PACE era. *Front. Earth Sci*. doi: 10.3389/feart.2019.00145

Fu, G., and Hasekamp, O. (2018). Retrieval of aerosol microphysical and optical properties over land using a multimode approach. *Atmos. Meas. Tech.* 11, 6627–6650. doi: 10.5194/amt-11-6627-2018

Gao, M., Zhai, P., Franz, B., Hu, Y., Knobelspiesse, K., Werdell, P. J., et al. (2018). Retrieval of aerosol properties and water-leaving reflectance from multi-angular polarimetric measurements over coastal waters. *Opt. Express* 26, 8968–8989. doi: 10.1364/OE.26.008968

Gao, M., Zhai, P., Franz, B., Hu, Y., Knobelspiesse, K., Werdell, P. J., et al. (2019). Inversion of multi-angular polarimetric measurements over open and coastal ocean waters: a joint retrieval algorithm for aerosol and water leaving radiance properties. *Atmos. Meas. Tech. Discuss.* doi: 10.5194/amt-2019-67. [Epub ahead of print].

Gordon, H. R. (1997). Atmospheric correction of ocean color imagery in the Earth observing era. *J. Geophys. Res.* 102, 17081–17106. doi: 10.1029/96JD02443

Gordon, H. R., and Wang, M. (1994). Retrieval of water-leaving radiance and aerosol optical thickness over the oceans with SeaWiFS: a preliminary algorithm. *Appl. Opt.* 33, 443–452. doi: 10.1364/AO.33.000443

Grey, W. M., North, P. R., Los, S. O., and Mitchell, R. M. (2006). Aerosol optical depth and land surface reflectance from multiangle AATSR measurements: global validation and intersensor comparisons. *IEEE Trans. Geosci. Remote Sens.* 44, 2184–2197. doi: 10.1109/TGRS.2006.872079

Harmel, T., and Chami, M. (2008). Invariance of polarized reflectance measured at the top of atmosphere by PARASOL satellite instrument in the visible range with marine constituents in open ocean waters. *Opt. Express* 16, 6064−6080. doi: 10.1364/OE.16.006064

Harmel, T., and Chami, M. (2013). Estimation of the sunglint radiance field from optical satellite imagery over open ocean: multidirectional approach and polarization aspects. *J. Geophys. Res.* 118, 76–90. doi: 10.1029/2012JC008221

Harten, G. V., Diner, D. J., Daugherty, B. J., Rheingans, B. E., Bull, M. A., Seidel, F. C., et al. (2018). Calibration and validation of Airborne Multiangle SpectroPolarimetric Imager (AirMSPI) polarization measurements. *Appl. Opt.* 57, 4499–4513. doi: 10.1364/AO.57.004499

Hasekamp, O. P. (2010). Capability of multi-viewing-angle photo-polarimetric measurements for the simultaneous retrieval of aerosol and cloud properties. *Atmos. Meas. Tech.* 3, 839–851. doi: 10.5194/amt-3-839-2010

Hasekamp, O. P., Fu, G., Rusli, S. P., Wu, L., Di Noia, A., and de Brugh, J., et al. (2019). Aerosol measurements by SPEXone on the NASA PACE mission: expected retrieval capabilities. *J. Quant. Spectrosc. Radiat. Transf.* 227, 170–184. doi: 10.1016/j.jqsrt.2019.02.006

Hasekamp, O. P., and Landgraf, J. (2005). Retrieval of aerosol properties over the ocean from multispectral single-viewing-angle measurements of intensity and polarization: retrieval approach, information content, and sensitivity study. *J. Geophys. Res.* 110:D20207. doi: 10.1029/2005JD006212

Hasekamp, O. P., Litvinov, P., and Butz, A. (2011). Aerosol properties over the ocean from PARASOL multiangle photopolarimetric measurements. *J. Geophys. Res.* 116:D14204. doi: 10.1029/2010JD015469

Holben, B. N., Eck, T. F., Slutsker, I., Tanre, D., Buis, J. P., Setzer, A., et al. (1998). AERONET—A federated instrument network and data archive for aerosol characterization. *Remote Sens. Environ.* 66, 1–16. doi: 10.1016/S0034-4257(98)00031-5

Holzer-Popp, T., Schroedter, M., and Gesell, G. (2002). Retrieving aerosol optical depth and type in the boundary layer over land and ocean from simultaneous GOME spectrometer and ATSR-2 radiometer measurements, 1, Method description. *J. Geophys. Res.* 107, AAC16-1–AAC16-17. doi: 10.1029/2001JD002013

Jerlov, N. G. (1976). *Marine Optics*. New York, NY: Elsevier Scientific.

Jethva, H., Torres, O., Remer, L., and Bhartia, P. (2013). A color ratio method for simultaneous retrieval of aerosol and cloud optical thickness of above-cloud absorbing aerosols from passive sensors: application to MODIS measurements. *IEEE Trans. Geosci. Remote Sens*. 51, 3862–3870. doi: 10.1109/TGRS.2012.2230008

Jethva, H., Torres, O., Remer, L., Redemann, J., Livingston, J., Dunagan, S., et al. (2016). Validating MODIS above-cloud aerosol optical depth retrieved from "color ratio" algorithm using direct measurements made by NASA's airborne AATS and 4STAR sensors. *Atmos. Meas. Tech*. 9, 5053–5062. doi: 10.5194/amt-9-5053-2016

Jethva, H., Torres, O., Waquet, F., Chand, D., and Hu, Y. (2014). How do A-train sensors intercompare in the retrieval of above-cloud aerosol optical depth? A case study-based assessment. *Geophys. Res. Lett.* 41, 186–192. doi: 10.1002/2013GL058405

Kahn, R. A., Sayer, A. M., Ahmad, Z., and Franz, B. A. (2016). The sensitivity of SEAWIFS ocean color retrievals to aerosol amount and type. *J. Atmos. Ocean. Technol*. 33, 1185–1209. doi: 10.1175/JTECH-D-15-0121.1

Kalashnikova, O. V., Garay, M. J., Bates, K. H., Kenseth, C. M., Kong, W., Cappa, C. D., et al. (2018). Photo-polarimetric sensitivity to black carbon content of wildfire smoke: results from the 2016 IMPACT-PM field campaign. *J. Geophys. Res.* 123, 5376–5396. doi: 10.1029/2017JD028032

Kalashnikova, O. V., Garay, M. J., Martonchik, J. V., and Diner, D. J. (2013). MISR Dark Water aerosol retrievals: operational algorithm sensitivity to particle non-sphericity. *Atmos. Meas. Tech.* 6, 2131–2154. doi: 10.5194/amt-6-2131-2013

Kalashnikova, O. V., and Kahn, R. (2006). Ability of multiangle remote sensing observations to identify and distinguish mineral dust types: 2. Sensitivity over dark water. *J. Geophys. Res.* 111:D11207. doi: 10.1029/2005JD006756

Kalashnikova, O. V., and Kahn, R. A. (2008). Mineral dust plume evolution over the Atlantic from combined MISR/MODIS aerosol retrievals. *J. Geophys. Res.* 113:D24204. doi: 10.1029/2008JD010083

Kaufman, Y. J., Martins, J. V., Remer, L. A., Schoeberl, M. R., and Yamasoe, M. A. (2002). Satellite retrieval of aerosol absorption over the oceans using sunglint. *Geophys. Res. Lett.* 29:1928. doi: 10.1029/2002GL015403

Knobelspiesse, K., Cairns, B., Mishchenko, M., Chowdhary, J., Tsigaridis, K., van Diedenhoven, B., et al. (2012). Analysis of fine-mode aerosol retrieval capabilities by different passive remote sensing instrument designs. *Opt. Express* 20, 21457–21484. doi: 10.1364/OE.20.021457

Knobelspiesse, K., Cairns, B., Redemann, J., Bergstrom, R. W., and Stohl, A. (2011). Simultaneous retrieval of aerosol and cloud properties during the MILAGRO field campaign. *Atmos. Chem. Phys.* 11, 6245–6263. doi: 10.5194/acp-11-6245-2011

Knobelspiesse, K., Tan, Q., Bruegge, C., Cairns, B., Chowdhary, J., van Diedenhoven, B., et al. (2019). Intercomparison of airborne multi-angle polarimeter observations from the Polarimeter Definition Experiment (PODEX). *Appl. Opt.* 58, 650–669. doi: 10.1364/AO.58.000650

Koepke, P. (1984). Effective reflectance of oceanic whitecaps. *Appl. Opt.* 23,1816–1824. doi: 10.1364/AO.23.001816

Kokhanovsky, A. A., Curier, R. L., De Leeuw, G., Grey, W. M. F., Lee, K.-H., Bennouna, Y., et al. (2009). The inter-comparison of AATSR dual-view aerosol optical thickness retrievals with results from various algorithms and instruments. *Int. J. Remote Sens.* 30, 4525–4537. doi: 10.1080/01431160802578012

Kokhanovsky, A. A., Davis, A. B., Cairns, B., Dubovik, O., Hasekamp, O., Sano, I., et al. (2015). Space-based remote sensing of atmospheric aerosols: the multi-angle spectro-polarimetric frontier. *Earth Sci. Rev*. 145, 85–116. doi: 10.1016/j.earscirev.2015.01.012

Kolmonen, P., Sogacheva, L., Virtanen, T. H., de Leeuw, G., and Kulmala, M. (2016). The ADV/ASV AATSR aerosol retrieval algorithm: current status and presentation of a full-mission AOD dataset. *Int. J. Digital Earth* 9, 545–561. doi: 10.1080/17538947.2015.1111450

Koven, C. D., and Fung, I. (2006). Inferring dust composition from wavelength-dependent absorption in Aerosol Robotic Network (AERONET) data. *J. Geophys. Res.* 111:D14205 doi: 10.1029/2005JD006678

Lacagnina, C., Hasekamp, O. P., Bian, H., Curci, G., Myhre, G., Van Noije, T., et al. (2015). Aerosol single-scattering albedo over the global oceans: comparing PARASOL retrievals with AERONET, OMI, and AeroCom models estimates. *J. Geophys. Res. Atmos.* 120, 9814–9836. doi: 10.1002/2015JD023501

Lacagnina, C., Hasekamp, O. P., and Torres, O. (2017). Direct radiative effect of aerosols based on PARASOL and OMI satellite observations. *J. Geophys. Res. Atmos.* 122, 2366–2388. doi: 10.1002/2016JD025706

Levis, A., Aides, A., Schechner, Y. Y., and Davis, A. B. (2015). "Airborne three-dimensional cloud tomography," in *Proceedings of the IEEE International Conference on Computer Vision* (Santiago Chile), 3379–3387. doi: 10.1109/ICCV.2015.386

Li, R.-R., Kaufman, Y. J., Gao, B.-C., and Davis, C. O. (2003). Remote sensing of suspended sediments and shallow coastal waters. *IEEE Trans. Geosci. Remote Sens.* 41, 559–566. doi: 10.1109/TGRS.2003.810227

Limbacher, J. A., and Kahn, R. A. (2017). Updated MISR dark water research aerosol retrieval algorithm – Part 1: coupled 1.1 km ocean surface chlorophyll *a* retrievals with empirical calibration corrections. *Atmos. Meas. Tech.*10, 1539–1555. doi: 10.5194/amt-10-1539-2017

Loisel, H., Duforet, L., Dessailly, D., Chami, M., and Dubuisson, P. (2008). Investigation of the variations in the water leaving polarized reflectance from the POLDER satellite data over two biogeochemical contrasted oceanic areas. *Opt. Express* 16, 12905–12918. doi: 10.1364/OE.16.012905

Manolis, I., Bézy, J.-L., Meynart, R., Porciani, M., Loiselet, M., Mason, G., et al. (2017). "The 3MI instrument on the Metop second generation," in *Proceedings of SPIE 10563, International Conference on Space Optics — ICSO 2014* (Tenerife).

Martin, W., Cairns, B., and Bal, G. (2014). Adjoint methods for adjusting three-dimensional atmosphere and surface properties to fit multi-angle/multi-pixel polarimetric measurements. *J. Quant. Spectrosc. Radiat. Trans.* 144, 68–85. doi: 10.1016/j.jqsrt.2014.03.030

Martin, W. G., and Hasekamp, O. P. (2018). A demonstration of adjoint methods for multi-dimensional remote sensing of the atmosphere and surface. *J. Quant. Spectrosc. Radiat. Trans.* 204, 215–231. doi: 10.1016/j.jqsrt.2017.09.031

Martonchik, J. V., and Diner, D. J. (1992). Retrieval of Aerosol optical properties from multi-angle satellite imagery. *IEEE Trans. Geosci. Remote Sens*. 30, 223–230. doi: 10.1109/36.134073

Martonchik, J. V., Diner, D. J., Crean, K. A., and Bull, M. A. (2002). Regional aerosol retrieval results from MISR. *IEEE Trans. Geosci. Remote Sens.* 40, 1520–1531. doi: 10.1109/TGRS.2002.801142

McGill, M., Hlavka, D., Hart, W., Scoutt, V. S., Spinhirne, J., and Schmid, B. (2002). Cloud physics lidar: instrument description and initial measurement results. *Appl. Opt*. 41, 3725–3734. doi: 10.1364/AO.41.003725

Meyer, K. G., and Platnick, S. E. (2015). Simultaneously inferring above-cloud absorbing aerosol optical thickness and underlying liquid phase cloud optical and microphysical properties using MODIS. *J. Geophys. Res. Atmos.* 120, 5524–5547. doi: 10.1002/2015JD023128

Mishchenko, M. I., Cairns, B., Kopp, G., Schueler, C. F., Fafaul, B. A., Hansen, J. E., et al. (2007). Accurate monitoring of terrestrial aerosols and total solar irradiance: introducing the Glory mission. *Bull. Amer. Meteorol. Soc.* 88, 677–691. doi: 10.1175/BAMS-88-5-677

Mobley, C. D., Stramski, D., Bissett, W. P., and Boss, E. (2004). Optical modeling of ocean waters: is the case 1 - case 2 classification still useful? *Oceanography* 17, 60–67. doi: 10.5670/oceanog.2004.48

Mobley, C. D., Sundman, L. K., and Boss, E. (2002). Phase function effects on oceanic light fields. *Appl. Opt*. 41, 1035–1050. doi: 10.1364/AO.41.001035

Morel, A., Gentili, B., Claustre, H., Babin, M., Bricaud, A., Ras, J., et al. (2007). Optical properties of the “clearest” natural waters. *Limnol. Oceanogr.* 52, 217–229. doi: 10.4319/lo.2007.52.1.0217

Morel, M., and Maritorena, S. (2001). Bio-optical properties of oceanic waters: a reappraisal. *J. Geophys. Res.* 106, 7163–7180. doi: 10.1029/2000JC000319

NASA (2012). *PACE Science Definition Team Report*. Available online at: https://pace.oceansciences.org/docs/pace_sdt_report_final.pdf

Nelson, N. B., and Siegel, D. A. (2013). The global distribution and dynamics of chromophoric dissolved organic matter. *Annu. Rev. Mar. Sci.* 5, 447–476. doi: 10.1146/annurev-marine-120710-100751

Ottaviani, M., Knobelspiesse, K., Cairns, B., and Mishchenko, M. (2013). Information content of aerosol retrievals in the sunglint region. *Geophys. Res. Lett.* 40, 631–634. doi: 10.1002/grl.50148

Peers, F., Waquet, F., Cornet, C., Dubuisson, P., Ducos, F., Goloub, P., et al. (2015). Absorption of aerosols above clouds from POLDER/PARASOL measurements and estimation of their direct radiative effect. *Atmos. Chem. Phys.* 15, 4179–4196. doi: 10.5194/acp-15-4179-2015

Platnick, S., Coddington, O., Ackerman, S. A., Frey, R., Heidinger, A., Walter, A., et al. (2018). *Cloud Retrievals in the PACE Mission: PACE Science Team Consensus Document.* PACE Technical Report Series, Volume 4, NASA/TM-2018-219027. Available online at: https://pace.oceansciences.org/docs/TM2018219027Vol.4.pdf

Pope, R. M., and Fry, E. S. (1997). Absorption spectrum (380–700 nm) of pure water. II Integrating measurements. *Appl. Opt.* 36, 8710–8723. doi: 10.1364/AO.36.008710

Remer, L. A., Davis, A. B., Mattoo, S., Levy, R. C., Kalashnikova, O. V., Chowdhary, J., et al. (2019). Retrieving aerosol characteristics from the PACE mission, Part 1: Ocean Color Instrument. *Front. Earth Sci*. doi: 10.3389/feart.2019.00152

Rodgers, C. D. (2000). *Inverse Methods for Atmospheric Sounding: Theory and Practice, Vol. 2.* Singapore: World Scientific. doi: 10.1142/9789812813718

Russell, P. B., Bergstrom, R. W., Shinozuka, Y., Clarke, A. D., DeCarlo, P. F., Jimenez, J. L., et al. (2010). Absorption Ångstrom Exponent in AERONET and related data as an indicator of aerosol composition. *Atmos. Chem. Phys.* 10, 1155–1169. doi: 10.5194/acp-10-1155-2010

Russell, P. B., Kacenelenbogen, M., Livingston, J. M., Hasekamp, O. P., Burton, S. P., Schuster, G. L., et al. (2014). A multiparameter aerosol classification method and its application to retrievals from spaceborne polarimetry. *J. Geophys. Res.* 119, 9838–9863. doi: 10.1002/2013JD021411

Ryerson, T. B., Andrews, A. E., Angevine, W. M., Bates, T. S., Brock, C. A., Cairns, B., et al. (2013). The 2010 California research at the nexus of air quality and climate change (CalNex) field study. *J. Geophys. Res.* 118, 5830–5866. doi: 10.1002/jgrd.50331

Sayer, A. M., Hsu, N. C., Bettenhausen, C., Lee, J., Redemann, J., Schmid, B., et al. (2016). Extending “Deep Blue” aerosol retrieval coverage to cases of absorbing aerosols above clouds: sensitivity analysis and first case studies. *J. Geophys. Res.* 121, 4830–4854. doi: 10.1002/2015JD024729

Smirnov, A., Holben, B. N., Dubovik, O., Frouin, R., Eck, T. F., and Slutsker, I. (2003). Maritime component in aerosol optical models derived from Aerosol Robotic Network data. *J. Geophys. Res.* 108, AAC14-1–AAC14-11. doi: 10.1029/2002JD002701

Smirnov, A., Holben, B. N., Slutsker, I., Giles, D. M., McClain, C. R., Eck, T. F., et al (2009). Maritime aerosol network as a component of aerosol robotic network. *J. Geophys. Res.* 114:D06204. doi: 10.1029/2008JD011257

Smith, R. C., and Baker, K. S. (1981). Optical properties of the clearest natural waters (200-800 nm). *Appl. Opt*. 20, 177–184. doi: 10.1364/AO.20.000177

Snik, F., Karalidi, T., and Keller, C. (2009). Spectral modulation for full linear polarimetry. *Appl. Opt.* 48, 1337–1346. doi: 10.1364/AO.48.001337

Stamnes, S., Hostetler, C., Ferrare, R., Burton, S., Liu, X., Wasilewski, A., et al. (2018). Simultaneous polarimeter retrievals of microsphysical aerosol and ocean color parameters with comparison to high spectral resolution lidar atmosphere and ocean products: the MAPP algorithm. *Appl. Opt.* 57, 2394–2413. doi: 10.1364/AO.57.002394

Stap, F. A., Hasekamp, O. P., Emde, C., and Roeckmann, T. (2016). Influence of 3D effects on 1D aerosol retrievals in synthetic, partially clouded scenes. *J. Quant. Spectrosc. Radiat. Trans*. 170, 54–68. doi: 10.1016/j.jqsrt.2015.10.008

Stap, F. A., Hasekamp, O. P., and Röckmann, T. (2015). Sensitivity of PARASOL multi-angle photopolarimetric aerosol retrievals to cloud contamination. *Atmos. Meas. Tech.* 8, 1287–1301. doi: 10.5194/amt-8-1287-2015

Tanré, D., Bréon, F. M., Deuzé, J. L., Dubovik, O., Ducos, F., François, P., et al. (2011). Remote sensing of aerosols by using polarized, directional and spectral measurements within the A-Train: the PARASOL mission. *Atmos. Meas. Tech.* 4, 1383–1395. doi: 10.5194/amt-4-1383-2011

Tanré, D., Herman, M., and Kaufman, Y. J. (1996). Information on aerosol size distribution contained in solar reflected spectral radiances. *J. Geophys. Res*. 101, 19043–19060. doi: 10.1029/96JD00333

Tanré, D., Kaufman, Y. J., Herman, M., and Mattoo, S. (1997). Remote sensing of aerosol properties over oceans using the MODIS/EOS spectral radiances. *J. Geophys. Res.* 102, 16971–16988. doi: 10.1029/96JD03437

Torres, O., Jethva, H., and Bhartia, P. K. (2012). Retrieval of aerosol optical depth above clouds from OMI observations: sensitivity analysis and case studies. *J. Atmos. Sci*. 69, 1037–1053. doi: 10.1175/JAS-D-11-0130.1

Veefkind, J. P., de Leeuw, G., and Durkee, P. A. (1998). Retrieval of aerosol optical depth over land using two-angle view satellite radiometry during TARFOX. *Geophys. Res. Lett.* 25, 3135–3138. doi: 10.1029/98GL02264

Voss, K. J. (1992). A spectral model of the beam attenuation coefficient in the ocean and coastal areas. *Limnol. Oceanogr.* 37, 501–509. doi: 10.4319/lo.1992.37.3.0501

Voss, K. J., and Fry, E. S. (1984). Measurement of the Mueller matrix for ocean water. *Appl. Opt.* 23, 4427–4439. doi: 10.1364/AO.23.004427

Wang, M., and Gordon, H. R. (1994). Estimating aerosol optical properties over the oceans with the multiangle imaging sprectroradiometer: some preliminary studies. *Appl. Opt.* 33, 4042–4057. doi: 10.1364/AO.33.004042

Waquet, F., Cairns, B., Knobelspiesse, K., Chowdhary, J., Travis, L. D., Schmid, B., et al. (2009a). Polarimetric remote sensing of aerosols over land. *J. Geophys. Res.* 114:D01206. doi: 10.1029/2008JD010619

Waquet, F., Peers, F., Ducos, F., Goloub, P., Platnick, S., Riedi, J., et al. (2013). Global analysis of aerosol properties above clouds. *Geophys. Res. Lett.* 40, 5809–5814. doi: 10.1002/2013GL057482

Waquet, F., Riedi, J., Labonnote, L. C., Goloub, P., Cairns, B., and Tanre, J. L.' (2009b). Aerosol remote sensing over clouds using A-Train observations. *J. Atmos. Sci*. 66, 2468–2480. doi: 10.1175/2009JAS3026.1

Wei, J., Lee, Z., Ondrusek, M., Mannino, A., Tzortziou, M., and Armstrong, R. (2016). Spectral slopes of the absorption coefficient of colored dissolved and detrital material inverted from UV-visible remote sensing reflectance. *J. Geophys. Res. Oceans* 121, 1953–1969. doi: 10.1002/2015JC011415

Werdell, P. J., Franz, B. A., Bailey, S. W., Feldman, G. C., Boss, E., Brando, V. E., et al. (2013). Generalized ocean color inversion model for retrieving marine inherent optical properties. *Appl. Opt*. 52, 2019–2037. doi: 10.1364/AO.52.002019

Wu, L., Hasekamp, O., van Diedenhoven, B., and Cairns, B. (2015). Aerosol retrieval from multiangle, multispectral photopolarimetric measurements: importance of spectral range and angular resolution. *Atmos. Meas. Tech*. 8, 2625–2638. doi: 10.5194/amt-8-2625-2015

Wu, L., Hasekamp, O., van Diedenhoven, B., Cairns, B., Yorks, J. E., and Chowdhary, J. (2016). Passive remote sensing of aerosol layer height using near-UV multi-angle polarization measurements. *Geophys. Res. Lett.* 43, 8783–8790. doi: 10.1002/2016GL069848

Xu, F., Dubovik, O., Zhai, P.-W., Diner, D. J., Kalashnikova, O. V., Seidel, F. C., et al. (2016). Joint retrieval of aerosol and water-leaving radiance from multispectral, multiangular and polarimetric measurements over ocean. *Atmos. Meas. Tech.* 9, 2877–2907. doi: 10.5194/amt-9-2877-2016

Xu, F., van Harten, G., Diner, D. J., Davis, A. B., Seidel, F., Rheingans, B., et al. (2018). Coupled retrieval of liquid water cloud and aerosol above cloud properties using the Airborne Multiangle SpectroPolarimetric Imager (AirMSPI). *J. Geophys. Res. Atmos.* 123, 3175–3204. doi: 10.1002/2017JD027926

Xu, F., van Harten, G., Diner, D. J., Kalashnikova, O. V., Seidel, F. C., Bruegge, C. J., et al. (2017). Coupled retrieval of aerosol properties and land surface reflection using the Airborne Multiangle SpectroPolarimetric Imager. *J. Geophys. Res. Atmos.* 122, 7004–7026. doi: 10.1002/2017JD026776

Xu, X. G., Wang, J., Wang, Y., Zeng, J., Torres, O., Yang, Y. K., et al. (2017). Passive remote sensing of altitude and optical depth of dust plumes using the oxygen A and B bands: first results from EPIC/DSCOVR at Lagrange-1 point. *Geophys. Res. Lett.* 44, 7544–7554. doi: 10.1002/2017GL073939

Zhai, P., Hu, Y., Trepte, C. R., and Lucker, P. L. (2009). A vector radiative transfer model for coupled atmosphere and ocean systems based on successive order of scattering method. *Opt. Express* 17, 2057–2079. doi: 10.1364/OE.17.002057

Zhai, P.-W., Hu, Y., Chowdhary, J., Trepte, C. R., Lucker, P. L., and Josset, D. B. (2010). A vector radiative transfer model for coupled atmosphere and ocean systems with a rough interface. *J. Quant. Spectrosc. Radiat. Trans*. 111, 1025–1040. doi: 10.1016/j.jqsrt.2009.12.005

Zhai, P.-W., Hu, Y., Winker, D. M., Franz, B., and Boss, E. (2015). Contribution of Raman scattering to polarized radiation field in ocean waters. *Opt. Express* 23, 23582–23596. doi: 10.1364/OE.23.023582

Zhai, P.-W., Hu, Y., Winker, D. M., Franz, B., Werdell, J., and Boss, E. (2017a). A vector radiative transfer model for coupled atmosphere and ocean systems including inelastic sources in ocean waters. *Opt. Express* 25, A223–A239. doi: 10.1364/OE.25.00A223

Zhai, P. W., Knobelspiesse, K., Ibrahim, A., Franz, B. A., Hu, Y., Gao, M., et al. (2017b). Water-leaving contribution to polarized radiation field over ocean. *Opt. Express* 25, A689–A708. doi: 10.1364/OE.25.00A689

Zhang, X., and Hu, L. (2009). Scattering by pure seawater at high salinity. *Opt. Express* 17, 12685–12691. doi: 10.1364/OE.17.012685

Conflict of Interest Statement: AI was employed by Science Application International Inc.

The remaining authors declare that the research was conducted in the absence of any commercial or financial relationships that could be construed as a potential conflict of interest.

The handling editor is currently co-organizing a Research Topic with one of the authors OD, and confirms the absence of any other collaboration.

frontiers in Earth Science

ORIGINAL RESEARCH
published: 26 July 2019
doi: 10.3389/feart.2019.00145

Atmospheric Correction of Satellite Ocean-Color Imagery During the PACE Era

Robert J. Frouin[1]*, Bryan A. Franz[2], Amir Ibrahim[2,3], Kirk Knobelspiesse[2], Ziauddin Ahmad[2,4], Brian Cairns[5], Jacek Chowdhary[5,6], Heidi M. Dierssen[7], Jing Tan[1], Oleg Dubovik[8], Xin Huang[8], Anthony B. Davis[9], Olga Kalashnikova[9], David R. Thompson[9], Lorraine A. Remer[10], Emmanuel Boss[11], Odele Coddington[12], Pierre-Yves Deschamps[8], Bo-Cai Gao[13], Lydwine Gross[14], Otto Hasekamp[15], Ali Omar[16], Bruno Pelletier[17], Didier Ramon[18], François Steinmetz[18] and Peng-Wang Zhai[19]

[1] Scripps Institution of Oceanography, University of California, San Diego, La Jolla, CA, United States, [2] Ocean Ecology Laboratory, NASA Goddard Space Flight Center, Greenbelt, MD, United States, [3] Science Systems and Applications Inc., Lanham, MD, United States, [4] Science Application International Corporation, McLean, VA, United States, [5] NASA Goddard Institute for Space Studies, New York, NY, United States, [6] Department of Applied Physics and Applied Mathematics, Columbia University, New York, NY, United States, [7] Department of Marine Sciences, University of Connecticut, Groton, CT, United States, [8] Laboratoire d'Optique Atmosphérique, Université de Lille, Villeneuve d'Ascq, France, [9] Jet Propulsion Laboratory, California Institute of Technology, Pasadena, CA, United States, [10] Joint Center for Earth System Technology, University of Maryland Baltimore County, Baltimore, MD, United States, [11] School of Marine Sciences, University of Maine, Orono, ME, United States, [12] Laboratory for Atmospheric and Space Physics, University of Colorado, Boulder, CO, United States, [13] Naval Research Laboratory, Washington, DC, United States, [14] Pixstart, Toulouse, France, [15] Earth Science Group, Netherlands Institute for Space Research, Utrecht, Netherlands, [16] Atmospheric Composition Branch, NASA Langley Research Center, Hampton, VA, United States, [17] Institut de Recherche Mathématique, Université de Rennes, Rennes, France, [18] HYGEOS, Euratechnologies, Lille, France, [19] Department of Physics, University of Maryland Baltimore County, Baltimore, MD, United States

OPEN ACCESS

Edited by:
Paulo Artaxo,
University of São Paulo, Brazil

Reviewed by:
Roland Doerffer,
Brockmann Consult, Germany
Jae-Hyun Ahn,
Korea Institute of Ocean Science and Technology, South Korea

***Correspondence:**
Robert J. Frouin
rfrouin@ucsd.edu

Specialty section:
This article was submitted to Atmospheric Science, a section of the journal Frontiers in Earth Science

Received: *19 December 2018*
Accepted: *21 May 2019*
Published: *26 July 2019*

Citation:
Frouin RJ, Franz BA, Ibrahim A, Knobelspiesse K, Ahmad Z, Cairns B, Chowdhary J, Dierssen HM, Tan J, Dubovik O, Huang X, Davis AB, Kalashnikova O, Thompson DR, Remer LA, Boss E, Coddington O, Deschamps P-Y, Gao B-C, Gross L, Hasekamp O, Omar A, Pelletier B, Ramon D, Steinmetz F and Zhai P-W (2019) Atmospheric Correction of Satellite Ocean-Color Imagery During the PACE Era. Front. Earth Sci. 7:145. doi: 10.3389/feart.2019.00145

The Plankton, Aerosol, Cloud, ocean Ecosystem (PACE) mission will carry into space the Ocean Color Instrument (OCI), a spectrometer measuring at 5 nm spectral resolution in the ultraviolet (UV) to near infrared (NIR) with additional spectral bands in the shortwave infrared (SWIR), and two multi-angle polarimeters that will overlap the OCI spectral range and spatial coverage, i. e., the Spectrometer for Planetary Exploration (SPEXone) and the Hyper-Angular Rainbow Polarimeter (HARP2). These instruments, especially when used in synergy, have great potential for improving estimates of water reflectance in the post Earth Observing System (EOS) era. Extending the top-of-atmosphere (TOA) observations to the UV, where aerosol absorption is effective, adding spectral bands in the SWIR, where even the most turbid waters are black and sensitivity to the aerosol coarse mode is higher than at shorter wavelengths, and measuring in the oxygen A-band to estimate aerosol altitude will enable greater accuracy in atmospheric correction for ocean color science. The multi-angular and polarized measurements, sensitive to aerosol properties (e.g., size distribution, index of refraction), can further help to identify or constrain the aerosol model, or to retrieve directly water reflectance. Algorithms that exploit the new capabilities are presented, and their ability to improve accuracy is discussed. They embrace a modern, adapted heritage two-step algorithm and alternative schemes (deterministic, statistical) that aim at inverting the TOA signal in a single step. These schemes, by the nature of their construction, their robustness, their generalization properties, and their ability to associate uncertainties, are expected to become the new standard in the future. A strategy for atmospheric correction is presented that ensures continuity and consistency with past and present ocean-color missions while enabling full exploitation of the new dimensions and possibilities. Despite the major improvements anticipated with the PACE instruments, gaps/issues remain to be filled/tackled. They include dealing properly with whitecaps, taking into account Earth-curvature effects, correcting for adjacency effects, accounting for the coupling between scattering and absorption, modeling accurately water reflectance, and acquiring a sufficiently representative dataset of water reflectance in the UV to SWIR. Dedicated efforts, experimental and theoretical, are in order to gather the necessary information and rectify inadequacies. Ideas and solutions are put forward to address the unresolved issues. Thanks to its design and characteristics, the PACE mission will mark the beginning of a new era of unprecedented accuracy in ocean-color radiometry from space.

Keywords: ocean color, aerosols, atmospheric correction, hyper-spectral remote sensing, multi-angle polarimetry, PACE mission

INTRODUCTION

Importance of Water Reflectance

The electromagnetic radiation (radiance) emanating from a water body at solar wavelengths, or water-leaving radiance, normalized by the incident solar irradiance at the surface defines "remote sensing" reflectance and, to an angular factor, water reflectance. Water body refers to oceans, seas, lakes, ponds, wetlands, rivers, and smaller pools of water, and the terminology marine reflectance is often used for oceanic and coastal waters. Water reflectance depends on light-matter interactions, therefore on the concentration and type of optically active constituents present in the water column and on the state of the air-water interface. The optically active constituents include water molecules, bubbles, and a variety of hydrosols and dissolved organic and inorganic materials (bacteria, viruses, phytoplankton, organic detritus, minerals, nitrates, bromides, and humic and fulvic acids). The radiative processes involved are elastic and inelastic scattering by water molecules (Rayleigh and Raman, respectively), elastic scattering by bubbles and hydrosols, absorption by water molecules and hydrosols, absorption by dissolved substances, fluorescence by phytoplankton and dissolved compounds, photoluminescence and bioluminescence by a variety of marine organisms, and Fresnel reflection/refraction at the wavy surface. These processes are generally fast, i.e., quasi instantaneous, but some are slow (phosphorescence). They interact in emitting, transmitting, absorbing, and reflecting light, contributing to the final reflectance. Water reflectance is an apparent, not intrinsic, optical property (depends on geometry), but its value is largely determined by the inherent properties of the water body, i.e., absorption and scattering coefficients, not by variations in directional illumination (angular distribution of downward radiance) or the viewing direction, providing a good—certainly convenient—way to characterize a water body.

Owing to this link to optical and biogeochemical variables, and despite the relatively small penetration depth of solar radiation in the water column, observations of spectral water reflectance, commonly referred to as "water color" (or "ocean color" in the case of marine waters), constitute a major tool to gather information about water constituents and associated processes (e.g., primary production), complementing traditional physical, biological, and chemical measurements of the euphotic zone. Spectral water reflectance gives access to chlorophyll-a, -b, and –c and other phytoplankton pigment concentrations, diffuse attenuation coefficient, euphotic depth, inherent optical properties (absorption and scattering coefficients), dissolved organic matter, total suspended matter, particulate organic and inorganic carbon, phytoplankton physiological properties (carbon-to-chlorophyll ratio, fluorescence quantum yield), phytoplankton taxonomic groups (based on size and/or pigments), and primary production (see, IOCCG, 2012). Knowing these parameters is essential to advance our understanding of the biological pump and carbon/nutrient cycling, i.e., processes that affect the ocean uptake of atmospheric carbon dioxide and the functioning of aquatic ecosystems. The information allows one to confront biogeochemical models with actual data, assimilate optical properties in ecosystem models, quantify complex evolutionary rates, determine biological-physical interactions, and clarify the photochemistry of dissolved organic matter, and it provides key water quality and ecological indicators for managing aquatic environments. Applications and societal benefits of ocean color radiometry are discussed with illustrative examples in IOCCG (2008). The retrieval methodologies exploit differences or specific features in the spectral absorption and scattering properties of water constituents that imprint on the observed reflectance, for example larger chlorophyll-a absorption in the blue than in the green to infer chlorophyll-a concentration, or spectral slope of the backscattering coefficient to estimate particle size. The inversion schemes and empirical algorithms, including many variants, are described extensively in the literature; see the reviews of IOCCG (2006) and Werdell et al. (2018) for inherent optical properties and IOCCG (2014) for phytoplankton types.

Need to Observe Water Reflectance From Space

Due to the vastness and remoteness of the oceans, traditional observing platforms such as ships, moorings, free-drifting floats, and even aircraft, cannot collect marine reflectance data at the required spatial and temporal scales (local to global, hour to decade) to resolve the highly dynamic nature of biogeochemical phenomena. Turbulent diffusion, vertical mixing, advection, upwelling, and the life characteristics of marine organisms control these scales, resulting in complex patterns of ocean color variability (e.g., eddies, plumes, and fronts). A ship observing at a point in space and time, for example, cannot detect changes that may occur a short distance away from the station and before/after the measurements, and interpolating information from discrete stations may not capture actual variability. Only satellite instruments can provide, via water reflectance observations, a synoptic view of algal blooms, phytoplankton community structure, primary production, sediment plumes, oil spills, benthic habitats, and linkages between biology and the physical/chemical environment (e.g., Platt et al., 2008), although water reflectance is only sensitive to the surface layer (about one attenuation depth). Thanks to their global, repetitive, and long-term capability, satellite instruments constitute the only way to quantify and monitor the role of the ocean as a sink for carbon, to describe coherently inter-annual variability associated to large-scale phenomena (e.g., El Niño), to detect trends in carbon fixation, and to address how biological carbon uptake and aquatic ecosystems respond to climate change (National Research Council, 2008). Note, in this context, that marine reflectance may have a clearer signature of climate than derived quantities like chlorophyll concentration, because it integrates all the optically important water constituent alterations (Dutkiewicz et al., 2016). Depending on the applications, the satellite ocean color data requirements, in terms of spatial resolution, spectral resolution, frequency, and coverage, vary widely. For example, studies of phytoplankton phenology, carbon inventory, heat budget and ocean dynamics, and ecosystem management need global multi-spectral images at 1 km resolution every 2–3 days, but monitoring of coral reefs and sea grass beds requires multi- to hyper-spectral observations twice a year at a fine 10 m resolution over coastal and estuarine regions, and tracking harmful algal blooms necessitates frequent (hourly) hyper-spectral observations over specific areas (National Research Council, 2011). The applications are so diverse that the various, sometimes-conflicting data requirements, cannot be met with a single observing satellite (Muller-Karger et al., 2018).

Algorithms to Retrieve Water Reflectance From Space

Water reflectance observations from space are affected by a variety of interfering processes associated with the propagation of electromagnetic radiation in the atmosphere-surface system. In clear sky conditions, these processes are gaseous absorption, molecular scattering, aerosol scattering and absorption, and water surface (Fresnel) reflection. In cloudy conditions, scattering by cloud droplets makes it very difficult to sense the surface (the cloud signal largely dominates), except when clouds are optically thin or occupy a small fraction of the pixel, i.e., their effect on pixel reflectance is less than 0.2. The influence of the atmosphere and surface must be removed in the satellite imagery to give access to water reflectance, the signal of interest (containing information about water constituents). This is commonly referred to as atmospheric correction, even though the process includes removing surface effects. Gaseous absorption is easy to handle when the satellite sensors observe in atmospheric windows (the usual case), but complicated to correct when measurements are made in absorbing bands (e.g., hyper-spectral sensor observing in the entire visible spectrum), and molecular scattering can be computed accurately. The influence of scattering by aerosols, highly variable in space and time, and of reflection by a wind-ruffled surface, which may exhibit whitecaps, is especially difficult to correct. In coastal regions, absorbing aerosols, complex water optical properties, and bottom influence (non-null water reflectance in the near infrared), and the proximity of land (adjacency effects) introduce further difficulty. Fundamentally, accurate atmospheric correction is not easy to achieve since the contribution of the water body may only represent a small fraction of the measured signal, typically 10% in the blue over clear waters and a few percent over waters rich in phytoplankton and/or yellow substances. The accuracy requirements depend on the application, but based on the experience with the Coastal Zone Color Scanner (CZCS) proof-of-concept the announced goal is that the uncertainty in the water reflectance of clear (oligotrophic) waters at 443 nm should not exceed ±5% or ±0.002 (e.g., IOCCG, 2013). Atmospheric correction algorithms, therefore, aim at achieving this goal.

The standard approach for atmospheric correction, first suggested by Gordon (1978), consists of (1) estimating the aerosol/surface reflectance in the red and near infrared where the water body can be considered as totally absorbing (i.e., black), and (2) extrapolating the aerosol/surface reflectance to the shorter wavelengths. Algorithms based on this approach have been developed successfully and employed for the operational processing of data from most satellite ocean-color sensors. In the coastal zone where waters often contain inorganic material, the assumption of null water reflectance in the red and near infrared is not valid, and improvements to the standard algorithm have been proposed. The improvements in these regions consider spatial homogeneity for the spectral ratio of the aerosol and water reflectance in the red and near infrared (Ruddick et al., 2000) or for the aerosol type, defined in a nearby non-turbid area (Hu et al., 2000). They also use a bio-optical model (Moore et al., 1999; Siegel et al., 2000; Stumpf et al., 2003; Bailey et al., 2010), exploit differences in the spectral shape of the aerosol and marine reflectance (Lavender et al., 2005), or make use of observations in the short-wave infrared, where the ocean is black even in the most turbid situations (Gao et al., 2000; Wang and Shi, 2007; Oo et al., 2008; Wang et al., 2009).

Another approach to atmospheric correction is to determine simultaneously the key properties of aerosols and water constituents of the coupled system by minimizing an error criterion between the measured top-of-atmosphere (TOA) reflectance and the output of a radiation transfer (RT) model (e.g., Land and Haigh, 1997; Chomko and Gordon, 1998; Stamnes et al., 2003; Kuchinke et al., 2009; Shi et al., 2016). This belongs to the family of deterministic solutions to inverse problems. Through systematic variation of candidate aerosol models, aerosol optical thickness, hydrosol backscattering coefficient, yellow substance absorption, and chlorophyll-a concentration, or a subset of those parameters, a best fit to the spectral top-of-atmosphere reflectance (visible and near infrared) is obtained in an iterative manner. The advantage of this single-step approach, compared with the standard, two-step approach, resides in its ability to manage situations of both Case 1 and Case 2 waters. It also works in the presence of weakly and strongly absorbing aerosols, even if the vertical distribution of aerosols, an important variable (which governs the coupling between aerosol absorption and molecular scattering), is usually not varied in the optimization procedure. A main drawback is that the inversion relies on a water reflectance model that may not represent well bio-optical variability across diverse aquatic ecosystems. Another drawback is that convergence of the minimizing sequence may be slow in some algorithms, making it difficult to process large amounts of satellite data. To cope with this issue, a variant proposed in Brajard et al. (2006) and Jamet et al. (2005) consists of approximating the operator associated to the RT model by a function which is faster in execution than the RT code, e.g., by neural networks. It may also not be easy to differentiate absorption by aerosols and water constituents like yellow substances, processes that are indistinguishable in the observed TOA signal. As a result, the retrievals may not be robust to small perturbations on the TOA reflectance. This reflects the fact that atmospheric correction is an ill-posed inverse problem; in particular, different values of the atmospheric and oceanic parameter can correspond to close values of the TOA reflectance (Frouin and Pelletier, 2015). In the context of deterministic inverse problem, stability of the solution can be obtained by regularization, but regularization strategies are not implemented in the approaches described above.

Another route is to cast atmospheric correction as a statistical inverse problem and to define a solution in a Bayesian context. In this setting, some algorithms aim at estimating, based on simulations, a function performing a mapping from the TOA reflectance to the water reflectance. In Schroeder et al. (2007), a neural network model is fitted to simulated data. A similar approach is studied in Gross-Colzy et al. (2007a,b), where the (finite-dimensional) TOA signal, corrected for gaseous absorption and molecular scattering, is first represented in a basis such that the correlation between the ocean contribution and atmosphere contribution is, to some extent, minimized. This representation of the TOA reflectance makes the function approximation problem potentially easier to solve. In these studies, data are simulated for all the observation geometries. In Pelletier and Frouin (2004, 2006) and Frouin and Pelletier (2007), the angular information is decoupled from the spectral reflectance, and atmospheric correction is considered as a collection of similar inverse problems indexed by the observation geometry. In Frouin and Pelletier (2015), the solution of the inverse problem is expressed as a probability distribution that measures the likelihood of encountering values of water reflectance given the TOA reflectance (i.e., after it has been observed). This posterior distribution is a very rich object. Its complete reconstruction is computationally prohibitive, but one may extract (approximate) expectation and covariance, which gives an estimate of the water reflectance and a quantification of uncertainty in the water reflectance estimate. This is accomplished using partition-based models. In Saulquin et al. (2016), Gaussian mixture models represent the prior distributions of reference water and aerosol reflectance spectra, and maximum a posteriori estimation (based on optimization from random initializations) is used in the numerical inversion. Performance of the statistical algorithms depends critically on prior knowledge of aerosol properties and water reflectance and noise in the measurements.

Comparing the aforementioned schemes, the chief advantage of the standard scheme is that no assumption is made about water reflectance, the signal to retrieve, except to account for the non-black reflectance of Case 2 waters in the near infrared in some variants. However, such methods make significant assumptions about the atmospheric state, and often cannot actively account for multiple scattering interactions between the atmosphere and ocean. In all the other schemes, the solution is constrained by a reflectance model with (often empirical) bio-optical relations or picked in an (relatively small) ensemble of actual spectra. The reflectance model or the ensemble of possible solutions may not be representative of actual variability, especially if the objective is general applicability, i.e., a scheme that functions adequately for all types of waters. In fact, the number of parameters to vary in optimization schemes is usually limited, otherwise convergence may be too difficult to achieve, which restricts the use of the reconstructed water reflectance.

Atmospheric Correction Issues

The atmospheric correction algorithms so far proposed, whether empirical (standard approach, 2 steps), deterministic (spectral optimization, 1 step), or statistical (Bayesian inference, 1 step), rely on RT codes to generate look-up tables (e.g., Rayleigh scattering, aerosol optical properties) and/or simulate the TOA signal and its components. The codes have intrinsic errors depending on the way the RT equation is solved (scalar versus vector, matrix operator, doubling-adding, successive-orders-of-scattering, spherical harmonics, Monte Carlo, etc.) and how the atmosphere-surface-water system is modeled (e.g., number of layers). They employ parameterizations based on current knowledge to specify processes such as surface reflection by the agitated surface and diffuse reflection by whitecaps, but these parameterizations have uncertainties. The calculations are generally performed assuming a plane-parallel atmosphere, which yields significant errors with respect to calculations in a spherical-shell atmosphere, even at low Sun and view zenith angles. No horizontal changes in atmospheric properties are considered for slanted geometries. The "large target" formalism, in which surface reflectance is assumed homogeneous spatially, is used to express the RT equation, but this treatment is not appropriate near clouds, land, and sea ice, and in regions with high water reflectance contrast (adjacency or environment effects).

As already mentioned above, atmospheric correction is an ill-posed inverse problem, i.e., even without noise the different states of the atmosphere, surface, and water body may match well of the satellite signal. Determining the aerosol model from a somewhat arbitrary set of candidates according to the spectral dependence of the aerosol reflectance in the red, near infrared, and shortwave infrared, a key feature of the standard algorithm, does not guarantee that the selected model is the actual one. First, an aerosol model cannot be unambiguously identified from observations in the red and infrared alone, especially without polarized and multi-angular information. In this spectral range, sensitivity to small particles is limited (these particles scatter more light backward to space than large particles, i.e., they have a strong influence on the TOA signal), and it is not possible to distinguish absorbing aerosols from non-absorbing ones since the coupling between molecular scattering and aerosol absorption is ineffective. This inability to deal properly with absorbing aerosols constitutes a major drawback of the standard scheme. Second, the aerosol model selection strongly depends on the set of models to choose from. Defining the models conveniently so that they uniquely describe the range of observed spectral dependence of aerosol reflectance is not satisfactory, even though the models may be obtained from measurements (e.g., AERONET). One may argue that selecting the proper aerosol model is a secondary issue since the objective of the atmospheric correction is to retrieve water reflectance and not aerosol properties, but extrapolating aerosol reflectance to UV and visible wavelengths with an incorrect model may yield inaccurate estimates of the aerosol signal at those wavelengths (coupling terms may be quite different). Kahn et al. (2016) examined the sensitivity of ocean color retrievals to aerosol amount and type. They showed, from comparisons with AERONET observations, that aerosol optical thickness in the blue derived from the Sea-viewing Wide Field-of-view Sensor (SeaWiFS) was overestimated, leading to systematic differences in derived water reflectance.

Another issue with aerosols is their vertical distribution, which is fixed in the standard scheme and whose variability is often not accounted for in simulations of the TOA signal used in other schemes. This parameter, however, affects significantly the coupling between scattering by molecules and scattering and absorption by aerosols, especially in the UV and blue, where molecular scattering is effective, all the more as aerosols are absorbing (effect is still non-negligible when aerosols are non-absorbing). Absorbing aerosols tend to decrease the TOA reflectance, and the decrease is more pronounced when they are located higher in the atmosphere, exhibit higher loadings, are more absorbing, or as the surface is brighter. In the presence of such aerosols, using a fixed distribution may result in large, unacceptable errors on water reflectance retrievals. Depending on vertical structure, the estimates by the standard scheme may be lower (underestimation) by as much as 10 times the inaccuracy requirements for biological applications, or even be negative as revealed in many studies, theoretical and experimental. Neglecting the effect of aerosol absorption on atmospheric transmittance, which lowers its value, further contributes to underestimating water reflectance (when the retrieved water signal is positive). Most satellite ocean-color sensors, however, do not have the capability to provide information about aerosol altitude.

It is often assumed that the color of a water body can be observed from space only over areas not contaminated by Sun glint and free of clouds. The thinking, based on "common sense" visual observations, has been that the presence of even a small amount of glint or a thin cloud prevents utilization of the data. Standard atmospheric correction algorithms, therefore, apply strict glint and cloud filters, usually a radiance or reflectance threshold applied to measurements in the near infrared (typically 0.03 on the Rayleigh-corrected reflectance). Such threshold may also exclude regions with highly scattering hydrosols under clear conditions. In general, about 10–15% of the observed pixels pass through the glint and cloud filters. As a result, Level-2 daily products are very patchy, and weekly Level-3 products show many areas with no information. This limits considerably the utility of satellite water reflectance observations for operational oceanography. In the open ocean, global coverage every three to five days is necessary to resolve seasonal biological phenomena such as phytoplankton blooms. In coastal waters, wind forcing creates "events" (e.g., upwelling) that occur every two to ten days, and one-day coverage is the requirement for resolving the event time scale. These requirements are not achieved with the present satellite systems and state-of-the-art standard algorithms. Some techniques are promising, however, such as those proposed by Steinmetz et al. (2011) and Gross-Colzy et al. (2007a), which either exploit the fact that Sun glint and cloud signals are smooth spectrally and can be well represented by a simple polynomial or select the principal components of the TOA signal that are less influenced by atmospheric and surface effects. Accurate retrievals may be obtained by relaxing the reflectance threshold in the near infrared to 0.2, with the potential of increasing daily spatial coverage by over 50% in many areas.

The performance of one-step algorithms depends on the accuracy of the water reflectance model, i.e., its ability to describe expected conditions, and/or prior knowledge of the variables to retrieve. Many of these models are developed with simulated data sets that may not represent the diversity and complexity of the real ocean. The available field data sets to specify modes of variability and prior distributions, however, are too few. They do not sample adequately many regions (e.g., the Southern Oceans) and biogeochemical regimes, they are less frequent in winter, and they are often incomplete (e.g., limited spectral range, inherent optical properties not measured concomitantly). Hyper-spectral data that incorporates the large bio-optical variability in absorption and backscattering of different assemblages of phytoplankton, particularly in complex coastal and inland waters, is lacking. Most of the data are acquired in cloudy conditions, but satellite retrievals are generally obtained under clear skies. Depending on cloudiness, bio-optical relations may be different, as well as the quality (spectral, angular) of available sunlight. In other words, the domain of acceptable solutions may not be represented properly by existing data sets. Future measurement programs will contribute to a more complete and broader knowledge, but this will probably remain insufficient. Additional information about space and time variability of atmospheric and oceanic variables, possibly from coupled biogeochemical-physical dynamic models (regional, global), will improve retrieval accuracy.

Opportunities With PACE

The current generation of ocean color sensors, e.g., MODerate resolution Imaging Spectrometer (MODIS), Visible Infrared Imaging Radiometer Suite (VIIRS), and Ocean and Land Color Instrument (OLCI), Geostationary Ocean Color Imager (GOCI), and Second generation GLobal Imager (SGLI), provides limited spectral information on water reflectance, i.e., observations in a few spectral bands in the visible and near infrared. This makes it difficult to distinguish water constituents (e.g., phytoplankton species or groups), to quantify their relative abundance, and to infer ecosystem properties/processes. The retrieval of water reflectance, based on spectral information alone (visible to near infrared, sometimes including shortwave infrared), is good, but not sufficiently accurate in the coastal zone and over inland waters, where water and air properties are highly variable and intricate, aerosols are absorbing, and adjacency effects are substantial (see section Atmospheric Correction Issues). The PACE mission will carry a primary sensor, the Ocean Color Imager (OCI), and two multi-angle polarimeters, the Spectrometer for Planetary Exploration (SPEXone) and the Hyper-Angular Rainbow Polarimeter (HARP2). OCI is a hyper-spectral radiometer measuring at 5 nm resolution in the UV to NIR (350 to 885 nm) and possibly higher spectral sampling in selected spectral intervals, with additional lower resolution bands at 940, 1,038, 1,250, 1,378, 1,615, 2,130, and 2,260 nm. SPEXone will measure at 5 viewing angles from 385 to 770 nm in 2–5 nm steps, with reduced spectral resolution (10–40 nm) for polarization. HARP2 will measure polarization at 10 viewing angles in spectral bands centered on 441, 549, and 873 nm, and 60 angles for a band centered at 669 nm. Polarimetric accuracy, in terms of Degree of Linear Polarization (DoLP), is expected to be 0.003 for SPEXone and <0.01 for HARP2. Swath width (spatial coverage) is 1,500 km for both OCI and HARP2 and 100 km for SPEXone. This instrument package promises to advance our knowledge of water ecosystems and biogeochemistry to an unprecedented level, not only because the high spectral resolution allows one to retrieve more accurately multiple water-column and benthic constituents and separate a larger number of end members, or because polarization measurements can aid in the characterization of hydrosols, but also because of the great potential of combining spectral, directional, and polarized information to improve atmospheric correction, i.e., water reflectance estimates.

Extending the TOA observations to the UV, where aerosol absorption is effective, using the SWIR, where even the most turbid waters are black and sensitivity to the aerosol coarse mode is higher than at shorter wavelengths, and measuring at hyper-spectral resolution in the oxygen A-band to estimate aerosol altitude would allow, at least in principle, a more accurate atmospheric correction. Measuring in spectral intervals where solar irradiance exhibits sufficiently large variations and Raman scattering can be assumed constant, the Raman signal can be separated from the elastic signal. This would improve bio-optical algorithms in which Raman scattering effect is not taken into account and allow retrieval of information about absorbing material in clear waters. Multi-angle and polarized measurements, sensitive to aerosol properties (e.g., size distribution, index of refraction), would further help to specify the aerosol model. This may be accomplished by constraining the domain of possible aerosol types in a classic atmospheric correction scheme or, if the information is sufficiently accurate, by directly computing the aerosol scattering effect. The sensitivity of polarized reflectance to aerosol type has also the potential to improve inversion schemes that aim at retrieving simultaneously air and water properties. Using multi-angular information alone (i.e., without polarization), already possible with the Multi-angle Imaging SpectroRadiometer (MISR) and the Sea and Land Surface Temperature Radiometer (SLSTR), may also improve atmospheric correction in the presence of absorbing aerosols, and using the non-polarized or plane-parallel components of the TOA signal instead of the total signal may reduce the effect of Sun glint and boost the contribution of the water signal. Many of the ideas and approaches briefly exposed above have yet to be fully developed, tested, and evaluated, but they strongly suggest that most of the atmospheric correction issues associated with current ocean-color sensors (see section Atmospheric Correction Issues) will be solved during the PACE era. One important task, apart from technical studies, is to devise a strategy for atmospheric correction that ensures continuity and consistency with past and present missions while enabling full exploitation of the new PACE dimensions and capabilities.

Contents of the Study

In the following, the history and progress of atmospheric correction during the last two decades (i.e., since the beginning of the EOS era) is recounted, state-of-the-art approaches and algorithms are described, and possibilities/improvements in view of new knowledge and future missions, in particular PACE, are examined. In section Heritage Atmospheric Correction Algorithm, the standard 2-step heritage algorithm, from which operational ocean color products are currently generated, is described. Adjustments envisioned to deal with hyper-spectral measurements that extend to the UV (case of OCI) are proposed and challenges are discussed. In section Alternative Algorithms, alternative algorithms, deterministic or statistical, that utilize simultaneously all available information, are presented, and their ability to deal with situations that cannot be handled by the heritage algorithm (e.g., absorbing aerosols) is emphasized and illustrated. In section Enhancements using Multi-Angular and/or Polarimetric Information, the benefits of multi-angular and polarimetric observations to determine aerosol properties or enhance the contribution of the water body to the TOA signal, and of using these observations synergistically with multi- or hyper-spectral information, are identified. In section Improvements Using “Super-Sampling” in Selected Spectral Intervals, the super-sampling capability of the OCI in some spectral intervals is investigated to estimate ocean Raman scattering and improve retrievals of chlorophyll fluorescence and aerosol altitude. In section Significant Issues, issues that remained to be addressed satisfactorily, such as adjacency in a “large target" RT formalism, whitecaps and underwater bubbles, Earth's curvature, atmospheric horizontal/vertical heterogeneity, and observing in the UV where the atmosphere is optically thick and multiple scattering and coupling processes makes atmospheric correction especially difficult, are discussed and possible avenues considered. In section Strategy for Atmospheric Correction, a strategy for atmospheric correction is devised, that accounts for the accomplishments of the previous decades using the heritage algorithm and at the same time fully integrates the qualities of alternative schemes and the new PACE capabilities. In section Conclusions, finally, the recent developments in atmospheric correction are summarized, the expected improvements with the PACE instrumentation are highlighted, concerns and remaining gaps are reiterated, and research directions are suggested to address challenges and achieve a new level of accuracy in future satellite water reflectance products. All the figures of the study are provided separately online at: https://www.frontiersin.org/articles/10.3389/feart.2019.00145/full#supplementary-material.

HERITAGE ATMOSPHERIC CORRECTION ALGORITHM

Approach

The heritage approach to the retrieval of ocean bio-optical properties from satellite radiometric observations, as historically employed by all international space agencies and operational agencies, is a two-step process wherein the atmosphere (and surface contributions) are first removed using minimal assumptions about the water optical properties (Fukushima et al., 1998; Antoine and Morel, 1999; Ahn et al., 2012; Mobley et al., 2016), and the resulting spectral water-leaving radiances are then used to infer information on water column optical properties and constituent concentrations (e.g., O'Reilly et al., 1998; Morel and Maritorena, 2001; Hu et al., 2012; Werdell et al., 2013). Step one, the atmospheric correction process, is based on finding the solution to a set of deterministic models that enable the removal of atmospheric path and surface effects from the top of atmosphere (TOA) signal. The primary challenge is to determine the contribution of aerosols to the atmospheric path radiance, which is highly variable and thus must be inferred from the observations. The approach takes advantage of the very strong absorption property of water in the NIR/SWIR spectral range (longward of 750 nm) to separate the atmospheric and oceanic signal from the satellite observations (Gordon and Wang, 1994; Antoine and Morel, 1999).

This two-step approach assumes the additive property of light, where the spectral signal or radiance measured at the top of atmosphere (TOA) by a satellite sensor, L_{TOA}, is the summation of the radiance contribution from each component of the atmosphere-ocean (AO) system. Specifically,

$$L_{TOA}(\lambda) = L_{atm}(\lambda) + L_{surf}^{TOA}(\lambda) + L_w^{TOA}(\lambda) \qquad (1)$$

where $L_{atm}(\lambda)$ is the radiance contribution due to scattering and absorption of air molecules and aerosols, $L_{surf}^{TOA}(\lambda)$ is the contribution of light reflected from the ocean surface and propagated to the TOA, and $L_w^{TOA}(\lambda)$ is the subsurface ocean radiance that is transmitted through the ocean surface and propagated to the TOA. Note that the dependence on radiant path geometry from sun to surface and back to sensor (i.e., Sun and view zenith angles and relative azimuth angles (θ_s, θ, ϕ), is not shown here for brevity. Equation (1) can be further partitioned into multiple components of the atmosphere and ocean surface. The atmospheric path radiance, $L_{atm}(\lambda)$, for example, can be treated as the summation of the scattering by non-absorbing air molecules, $L_r(\lambda)$, which is well characterized as pure Rayleigh scattering, and the scattering by the aerosol particles and aerosol-molecule coupling processes, $L_a(\lambda)$, which depends on aerosol morphology, size distribution, concentration, and chemical composition. These atmospheric path radiance contributions are then modulated by losses due to transmittance through the absorbing atmospheric gases, $T_g(\lambda)$, such as ozone, oxygen, and water vapor to compute the TOA contribution. Similarly, the surface radiance term at TOA, $L_{surf}^{TOA}(\lambda)$, can be treated as the summation of the light diffused by whitecaps and foam on the ocean surface, $L_{wc}(\lambda)$, that propagates through the atmosphere and is therefore modulated by the atmospheric total (i.e., direct plus diffuse) transmittance along the surface-to-sensor path, $t_u(\lambda)$, and the ocean surface glint (specular reflection of the Sun), $L_g(\lambda)$, that is also propagated through the atmosphere and modulated by the direct atmospheric transmittance, $T_u(\lambda)$, along the specular direction, with both surface contributions also reduced by $T_g(\lambda)$ before reaching the TOA. The primary quantity of interest for ocean color is the water-leaving radiance, $L_w(\lambda)$, which is the subsurface radiance after transmission through the air-sea interface. $L_w(\lambda)$ is also modulated by $t_u(\lambda)$ and $T_g(\lambda)$ when measured at TOA. The total radiometric contribution of the AO system can thus be described as:

$$\begin{aligned} L_{TOA}(\lambda) = \big[& L_r(\lambda) + L_a(\lambda) + t_u(\lambda) L_{wc}(\lambda) \\ & + T_u(\lambda) L_g(\lambda) + t_u(\lambda) L_w(\lambda) \big] T_g(\lambda) \end{aligned} \qquad (2)$$

This formulation presumes that (1) the fraction of the sea covered by whitecaps is small and can be neglected, (2) the contribution of diffuse reflected skylight off the sea surface is accounted for in the $L_r(\lambda)$ and $L_a(\lambda)$ terms, (3) the surface is homogenous spatially, and (4) gaseous absorption and scattering processes are decoupled. The goal of the heritage atmospheric correction (AC) approach is to accurately estimate each radiance and transmittance term in Equation (2) so that the surface and atmospheric path radiance contribution can be subtracted from the observed TOA radiance to retrieve $L_w(\lambda)$. To remove the time variation of incident direct solar irradiance, Equation (2) can be written in terms of reflectance as:

$$\begin{aligned} \rho_{TOA}(\lambda) = \big[& \rho_r(\lambda) + \rho_a(\lambda) + t(\lambda)\rho_{wc}(\lambda) \\ & + T(\lambda)\rho_g(\lambda) + t(\lambda)\rho_w(\lambda) \big] T_g(\lambda) \end{aligned} \qquad (3)$$

In this expression, $t(\lambda) = t_u(\lambda) t_d(\lambda)$ and $T(\lambda) = T_u(\lambda) T_d(\lambda)$ where $t_d(\lambda)$ and $T_d(\lambda)$ are total and direct downward atmospheric transmittance along the Sun-to-surface path, respectively, $\rho_{TOA}(\lambda)$, $\rho_r(\lambda)$, and $\rho_a(\lambda)$ are $L_{TOA}(\lambda)$, $L_r(\lambda)$, and $L_a(\lambda)$ normalized by $E_s(\lambda)cos(\theta_s)/\pi$, $\rho_f(\lambda)$ and $\rho_w(\lambda)$ are $L_{wc}(\lambda)$ and $L_w(\lambda)$ normalized by $E_s(\lambda)cos(\theta_s)t_d(\lambda)/\pi$, and $\rho_g(\lambda)$ is $L_g(\lambda)$ normalized by $E_s(\lambda)cos(\theta_s)T_d(\lambda)/\pi$, where

$E_s(\lambda)$ is extraterrestrial spectral solar irradiance corrected for Earth-Sun distance. Thus in Equation (3) the signal to retrieve is $\rho_w(\lambda)$, the water reflectance just above the surface, hereafter referred to as water reflectance for short. Remote sensing reflectance, $R_{rs}(\lambda)$, often used instead of $\rho_w(\lambda)$, is defined as $R_{rs}(\lambda) = \rho_w(\lambda)/\pi$.

Procedures

Absorbing Gas Correction

Several gases in the atmosphere, including O_2 (Oxygen), O_3 (Ozone), NO_2 (Nitrogen Dioxide), H_2O (Water Vapor), CO (Carbon Monoxide), N_2O (Nitrous Oxide), CH_4 (Methane), and CO_2 (Carbon Dioxide), absorb the light along the path radiance. In heritage multispectral sensors such as MODIS or MERIS, the spectral bands used for ocean color are generally situated to avoid the strongest absorption features of O_2 and H_2O (i.e., the spectral bands are located in atmospheric transparency windows), however O_3 and NO_2 absorb light over a broad spectral range. For a given column concentration of gas measured in number density per unit area, equivalent to Dobson units (DU), and its vertical profile (pressure, temperature, and volume mixing ratio (VMR), the transmittance of gas can be calculated. Because ozone is concentrated very high in the atmosphere, the O_3 transmittance can be accurately estimated using the Beer-Lambert Law and the geometric air mass. The coupling between the absorption of gases and the scattering by non-absorbing gases and aerosols is not significant in this case. NO_2 absorption, however, occurs in the tropospheric layer of the atmosphere, and near a source region that is spatially limited, thus the coupling between the absorption and scattering can be significant and the Beer-Lambert Law treatment is not appropriate (Ahmad et al., 2007). Although multi-spectral sensor bands are typically selected to avoid the strong absorption features, the nominal spectral bands for sensors such as MODIS or SeaWiFS can still suffer from significant out-of-band (OOB) sensitivity to these gases, thus requiring sensor-specific corrections (Ding and Gordon, 1995).

Molecular Scattering Correction

Light scattering by air molecules in the atmosphere, mainly N_2 and O_2, can be accurately modeled following the principles of Rayleigh scattering. Typically, a vector radiative transfer (VRT) code is used to generate a set of Look-up-tables (LUTs) of spectral Rayleigh scattering as a function of radiant path geometry and wind-driven ocean surface roughness (e.g., Ahmad and Fraser, 1982 is used for all operational processing by NASA). The LUTs include the contribution of photons that are reflected by the wavy interface after being either scattered in the atmosphere and then transmitted (directly and diffusely) to the TOA or directly transmitted through the atmosphere and then diffusely transmitted to the TOA. Because this contribution, commonly referred to as skylight reflected radiance, is enhanced in violet and UV wavelengths (due to more effective Rayleigh scattering), its correction is particularly critical in retrieving accurate water reflectance moving from the visible into UV wavelengths. The VRT model generally assumes an atmosphere-ocean system with discrete wind-driven ocean surface roughness states described by the analytical, azimuthally symmetric Cox-Munk slope distribution model (Cox and Munk, 1954). A required input to the VRT code is the Rayleigh optical thickness of the atmosphere at each sensor spectral wavelength, which can be computed from existing models (e.g., Bodhaine et al., 1999) and convolved with the relative spectral response of each spectral band pass.

Sun Glint and Whitecap Correction

Sun glint is a strong signal that reflects off the flat ocean surface in the specular direction. With increasing wind speed, the surface roughness also increases, thus a glitter pattern appears. The glitter pattern is the reflected Sun glint in the off-principal plane of the Sun when a wave facet is tilted. The glitter pattern spreads off the principal plane proportionally to the increasing wind speed. Some ocean color sensors, such as SeaWiFS, have tilting capability that avoids the detection of light in the principal plane of the Sun, thus avoiding the specular reflection of the ocean surface. Even so, a significant residual Sun glint can reach the sensor, especially near the edges of the glint region in and near the principal plane. To estimate this glint reflectance contribution, $\rho_g(\lambda)$, the heritage AC algorithms typically rely on the Cox-Munk model (Cox and Munk, 1954).

The surface contribution from whitecaps and foam to the TOA radiance is typically estimated from whitecap reflectance and a wind speed dependent estimate of the fractional coverage of whitecaps on the ocean surface. The whitecap reflectance is assumed Lambertian and wavelength dependent (Koepke, 1984; Frouin et al., 1996; Stramska and Petelski, 2003). Opposite to the specular glint, the whitecap reflectance contribution at the TOA is diffuse in nature, and thus modulated by the total (direct + diffuse) transmittance of the atmosphere, $t(\lambda)$.

Aerosol Scattering Correction

Sources of the aerosol particles suspended in the atmosphere are natural, such as dust, sea-salt, mineral dust, or volcanic emissions, or anthropogenic in origin, such as sulfates, organics and smoke from biomass burning or urban/industrial output. Aerosols vary in morphology, size distribution, scattering properties, and concentration. Analogous to the Rayleigh correction, an aerosol LUT is typically used to remove the aerosol contribution to the TOA radiance. The LUT defines a set of aerosol models, where the aerosol correction algorithm determines the most appropriate aerosol type (aerosol model) for a given pixel, to perform the correction. Different aerosol types are defined based on a bimodal size distribution of fine and coarse particles of specified refractive index, each with a lognormal distribution. NASA's operational aerosol LUTs, for example, are based on aerosol modeling by Ahmad et al. (2010). In this case, the aerosol models were derived to match the observations from the Aerosol Robotic Network (AERONET), with aerosol radii, refractive index, and fine-mode fraction parameterized as an explicit function of the relative humidity (30, 50, 70, 75, 80, 85, 90, and 95%). In constructing the LUT, the microphysical properties of the aerosols are assumed to be homogenous spheres, and therefore follow the scattering by Mie theory. VRT simulations are performed to characterize the aerosol radiance contribution to the TOA signal for each aerosol type, assuming a standard aerosol vertical profile for marine aerosols [e.g., from Shettle and Fenn (1979)].

A primary assumption for the determination of aerosol type and concentration within the heritage atmospheric correction (AC) approaches is that water-leaving radiance contributions within the NIR/SWIR spectral regime can be considered negligible due to the strong water absorption (Gordon and Wang, 1994; Antoine and Morel, 1999). This is referred to as the dark pixel assumption and is valid for most of the global ocean, where the hydrosol scattering is insignificant in the NIR/SWIR part of the spectrum. For highly productive or turbid conditions, most common in coastal and inland waters, methods have been developed to estimate the water-leaving radiance in the NIR regime through iterative solutions and model extrapolation (e.g., Moore et al., 1999; Bailey et al., 2010), or switching algorithms are employed to restrict to the more strongly absorbing SWIR spectral range in the presence of turbid waters (Wang et al., 2009).

Advantages and Limitations

The primary advantage of the two-step heritage AC approaches is that they do not require strong assumptions about the magnitude or spectral distribution of the ocean radiance contribution. The approaches are limited, however, by strict reliance on the NIR-SWIR spectral regime to determine the aerosol contribution, which is then extrapolated to the visible spectral bands based on a pre-determined set of aerosol models. The heritage approaches fail in the presence of strongly absorbing aerosols, and they are challenged in complex or highly productive waters where the water-leaving signal in the NIR-SWIR spectral regime can be significant. A small uncertainty in the determination of the aerosol type in the NIR-SWIR spectral regime can be magnified when extrapolating that information to the blue spectral range.

Absorbing aerosols

The ability to account for the presence and impact of absorbing aerosols, such as terrigenous dust and black or biogenic carbon, is a long-standing challenge in ocean color AC (Li et al., 2003; Schollaert et al., 2003; Nobileau and Antoine, 2005; Antoine and Nobileau, 2006; Ransibrahmanakul and Stumpf, 2006). Absorbing aerosols are common in coastal waters, due in particular to air pollution, but they can be encountered over vast areas of the open oceans (Kaufman et al., 1997; Remer et al., 2008; Colarco et al., 2014). Large plumes of Saharan dust, for example, are routinely transported across the Atlantic and deposited in the Caribbean, and smoke plumes from biomass burning off the west of African can be found well into the equatorial Atlantic. Since the heritage AC algorithms rely exclusively on the NIR/SWIR spectral regime and thus cannot identify and account for the presence of strongly absorbing aerosol types, the water reflectance in such cases will typically be underestimated, which leads to an overestimation in the chlorophyll concentration (Gordon, 1997; Gordon et al., 1997; Chomko and Gordon, 1998; Schollaert et al., 2003; Nobileau and Antoine, 2005; Antoine and Nobileau, 2006; Shi and Wang, 2007).

Heritage OC sensors observe the ocean at a single viewing angle and at a limited set of spectral bands, and thus the AC algorithm is tasked with solving an underdetermined, ill-posed AO system. Additional constraints on the aerosol microphysical properties, such as the hygroscopic growth determined by relative humidity, helps in determining the type of aerosol for the AC, but absorbing aerosols have spectral absorbing signatures that are similar to other optically active components of the ocean such as colored dissolved organic matter (CDOM) and minerals. Additionally, most absorbing aerosol species absorb in the shorter (UV-visible) wavelengths, thus the NIR/SWIR heritage approach to aerosol determination is not sensitive to their optical variations (Kahn et al., 2016). Furthermore, there is no consensus on the range of microphysical properties that must be considered for absorbing aerosols, due to the variation in their morphology, chemical composition, etc., and knowledge of the aerosol vertical distribution, which is critical to properly quantify the impact of aerosol absorption, cannot be determined from heritage sensor systems.

Figure 1 shows the sensitivity of TOA radiance to changes in aerosol layer height (i.e., location in the vertical column) relative to a 3 km layer height. The analysis was performed using the Ahmad and Fraser (1982) VRT code, for a specific solar and viewing geometry at 412 nm and for varying single scattering albedo of an assumed dust aerosol model detailed in Ahmad and Franz (2014). Chlorophyll-a concentration, *Chl-a*, is 0.3 mgm^{-3}. From **Figure 1**, it can be seen that the TOA reflectance is overestimated for absorbing aerosol layers lower than 3 km, while it is underestimated when the aerosol is higher in the atmosphere. The relative magnitude of change depends on the amount of aerosol absorption and the optical thickness.

At higher optical thickness, the TOA reflectance shows more sensitivity to absorbing aerosol layer height on the order of $\sim$1 to 4%, while at small optical thickness, the sensitivity is $<$1%. It is important to note that unknown layer height of the absorbing aerosol can lead to a large error in the derived water reflectance from the AC process. Additionally, when absorbing aerosols are not detectable from satellite observations, their treatment as non-absorbing in the AC can lead to overestimation of the aerosol radiance, which is demonstrated in **Figure 2**. Based on VRT simulations, the heritage AC algorithm retrieves an overestimated aerosol reflectance (blue line) in the presence of absorbing aerosols, while the true reflectance is lower (red line), and thus an overestimated aerosol contribution leads to an underestimated remote sensing reflectance. These over/under estimation errors increase with decreasing wavelengths, thus compromising efforts to retrieve water reflectance into the UV spectral regime.

Plane-Parallel RT Limitation and Pseudo-Spherical RT Correction

Presently all atmospheric correction LUTs used for ocean color retrievals assume that the atmosphere consists of plane parallel layers, which are inhomogeneous vertically but homogeneous and infinite horizontally. This generally limits applicability to solar angles less than 70° and sensor view angles less than 50°. To extend the solar and view angle range, the sphericity of the Earth atmosphere must be accounted for in the RT simulations. Herman et al. (1995) have carried out a detailed comparison of TOA radiance for spherical and plane-parallel atmospheres and concluded that there is a strong agreement between the two methods except at highly oblique angles. For a spherical atmosphere, the RT calculations account for sphericity in both the incoming solar beam and the outgoing scattered beam. Vector RT calculations (with multiple scattering and polarization) are computationally expensive. If retrievals at very large solar zenith angles (>80°) and large view angles (>50°) are not required, then one can carry out the vector RT calculations for a spherical atmosphere in single scattering approximation, and use full multiple scattering for a plane parallel atmosphere (Caudill et al., 1997). Another simplification is to account for sphericity in the incident solar beam only, which is done by computing the air mass factor in a spherical model atmosphere, and perform the rest of the calculations in a plane parallel atmosphere. This is generally known as the pseudo-spherical correction (Deluisi and Mateer, 1971).

Figure 3 shows how the Sun zenith angle varies as the solar beam traverses through a spherical model atmosphere. It is θ'' at the top of layer 1 (TOA), θ' at the top of layer of layer 3 and θ at the Earth surface. For a plane-parallel model atmosphere, the Sun zenith angle for all the layers would be equal to θ. **Figure 4** shows the difference in TOA reflectance as simulated with both plane-parallel and pseudo-spherical assumptions, for a Rayleigh model atmosphere at 380 nm in the direction θ =30°, ϕ =144°. The figure shows that, for Sun zenith angle <50°, the difference is very small (<0.05%), but increases rapidly at higher Sun zenith angles. In the nadir direction, it is −0.12, −0.53, and −1.53% for Sun zenith angles of 60, 72, and 78°, respectively. For accurate water reflectance retrievals at solar zenith angles above 50, these results suggest that future AC algorithms should utilize spherical or, at a minimum, pseudo-spherical VRT simulations in the retrieval algorithm or in generating any required atmospheric LUTs.

From Multi-Spectral to Hyper-Spectral Remote Sensing

Challenges

The AC process must estimate and remove the atmospheric path radiance contribution due to the Rayleigh scattering by air molecules and scattering by aerosols from the measured TOA radiance, account for surface contributions, and correct for reflection and refraction of the air-sea interface. For a hyper-spectral sensor, the heritage AC approach can largely be employed as-is, by simply extending the Rayleigh and aerosol scattering tables and surface reflectance models to the hyper-spectral domain. A primary issue, however, is the influence of absorbing gases.

Heritage multispectral ocean color sensors such as SeaWiFS, MODIS, MEdium Resolution Imaging Spectrometer (MERIS), VIIRS, OLCI, and SGLI, detect the light at specific wavelengths or bands. These bands are strategically located to provide sufficient spectral information to enable estimation of the inherent optical properties and optically active constituent concentrations in the water column, while also being located in atmospheric window regions where the atmospheric transmittance is maximized. The window regions are selected primarily to avoid the absorption of water vapor in the atmosphere, which is highly variable and thus difficult to correct, and the narrow but strong spectral absorption features of oxygen. To fully utilize the greater spectral information available from a hyper-spectral ocean color sensor, as needed for emerging science such as the detection of phytoplankton types and phytoplankton community structure (a primary goal of the PACE mission), the observed signal must be corrected for these absorbing gases.

Figure 5 shows the atmospheric gas transmittance calculated at 5-nm spectral resolution from UV to SWIR. The transmittance includes ozone, oxygen, and water vapor (blue solid line), while the red circles are located at MODIS bands. As shown, the MODIS bands are located in the spectral window regions, where the impact of absorption by oxygen and water vapor is minimized. For a continuous 5-nm sampling, however, as expected from the PACE OCI sensor, several bands in the visible wavelengths will suffer absorption by strong spectral features of water vapor and oxygen. This is especially true in the red (600–720 nm), which is critical for distinguishing phytoplankton types and quantifying natural fluorescence of phytoplankton chlorophyll. Production of a continuous 5-nm sampling of visible remote sensing reflectance over the ocean is a primary goal to the PACE mission, thus proper compensation of absorbing gas features is needed.

To make full use of a hyper-spectral instrument for ocean color, the effect of water vapor must be estimated and corrected. This is challenging due to the complexity of the atmospheric water vapor profile, the spectrally variable nature of the absorption features, and the spatial heterogeneity of the water vapor concentration (Kaufman and Gao, 1992; Gao et al., 2000, 2009). Challenges also arise in the UV spectral range, where the AC is difficult due to the significant contribution of the atmospheric scattering, and the strong impact from absorbing aerosols.

Hyper-Spectral Atmospheric Correction

Similar to the heritage multispectral atmospheric correction, pre-computed hyper-spectral look-up tables (LUT) can be generated using VRT simulations to model the Rayleigh and aerosol contributions. The hyper-spectral optical properties used in the VRT simulations, such as the extraterrestrial solar irradiance, Rayleigh optical thickness, and the depolarization factors, would be optically weighted for each hyper-spectral band based on the measured spectral response functions. Hyper-spectral glint and whitecap radiance contributions can be modeled based on ancillary wind speed and observing geometry, as they are for the heritage multispectral AC approaches. The hyper-spectral aerosol type and concentration can also be estimated using heritage methods (Fukushima et al., 1998; Antoine and Morel, 1999; Ahn et al., 2012; Mobley et al., 2016), and similarly coupled with an iterative bio-optical model to separate the scattering contributions from aerosols and water-column constituents in turbid (high-scattering) waters (Moore et al., 1999; Bailey et al., 2010).

Since the heritage AC does not perform water vapor correction, except for out-of-band effects using the Gordon (1995) method, the algorithm must be enhanced to include such a correction, if spectral regions with modest to large water vapor features are to be used for ocean color science (i.e., 600–710 nm). Recently, the heritage AC algorithm maintained by NASA (Mobley et al., 2016) was extended to include the hyper-spectral algorithm of ATmospheric REMoval (ATREM) for the estimation and correction of water-vapor transmittance (Gao and Davis, 1997), as detailed in Ibrahim et al. (2018). ATREM calculates the transmittance using the HITRAN 2012 (Rothman et al., 2013) database at 0.05 cm^{-1} wavenumber spectral resolution, which is down-sampled to the sensor spectral resolution. ATREM has the capability to estimate the column water vapor amount (CWV) [given a water vapor volume mixing ratio (VMR) profile], and to correct for the water vapor absorption along the radiant path. It does so by using a 3-band ratio technique utilizing two atmospheric window channels around one strongly absorbing water vapor band as shown in **Figure 6**.

The trough in the TOA reflectance at the water vapor band (e.g., near 940 and 1,130 nm in **Figure 6**) relative to the two window bands is a direct measure of the water-vapor transmittance loss along the path that the light traveled, which can be correlated to the water-vapor amount. Strong water-vapor absorption features such as these are used to estimate the water-vapor transmittance, which is then extrapolated to the visible regime to correct for the weaker water-vapor absorption features in the 600–710 nm region. Note that the 3-band ratio technique assumes the surface reflectance is spectrally monotonic. Any surface spectral features within the spectral windows can lead to erroneous correction for water vapor transmittance losses, but ocean reflectance is generally monotonic in the red/NIR part of the spectrum, except in bloom conditions (Gower et al., 2008; Doron et al., 2011), very turbid (i.e., sediment-laden) waters (Doron et al., 2011; Knaeps et al., 2015), optically shallow waters (Fogarty et al., 2018), or when the sea is covered by floating vegetation (Dierssen et al., 2015a; Kudela et al., 2015) or whitecaps (Frouin et al., 1996).

For water vapor correction over oceans, the very strong water-vapor absorption features at 940-nm and at longer wavelengths can actually be too strong, as the small surface signal (typically 0.02 in reflectance) is completely absorbed before reaching the sensor. To demonstrate this, and identify alternative band selection for water vapor retrieval over oceans, a radiative transfer study was performed using the Monte Carlo-based VRT code MYSTIC (Mayer, 2009; Emde et al., 2016). The code was used to simulate the polarized TOA radiance for a simple Rayleigh atmosphere and absorbing flat ocean, at a very high wavenumber spectral resolution of 1 cm^{-1} ($\sim$0.01nm in VIS). Water vapor was assumed to be the only absorber in the atmosphere, and was coupled with the scattering in the VRT simulations. The simulation runs were calculated for 0.3, 0.5, 0.7, 1, 1.3, 1.5, 1.7, 2, 2.3, 2.5, 2.7, and 3 cm CWV at geometries permuted from 10° to 50° solar and viewing zenith angle with 10° step, while the relative azimuth was fixed to be 90° composing a total of 300 cases. The water vapor profile was assumed to be the US standard 1976 and the water vapor absorption coefficients were obtained from the HITRAN 2012 database (Anderson et al., 1986; Rothman et al., 2013).

Figure 7 shows the scatter plot between the assumed CWV in the VRT simulations and the retrieval of CWV by the AC algorithm. In this analysis, the water body was assumed black (not reflecting). We used three modes of retrieval. The first is using the average CWV retrieval using the strongly absorbing 940 nm band and the less sensitive 820 nm band shown in blue circles, with the error bar of 1 standard deviation due to changes in the simulated geometries. With this combination, the CWV retrieval shows a strong underestimation at higher water vapor concentrations. This is due to the combination of a weak ocean signal (in that case ocean surface reflectance) and a strongly absorbing 940-nm water vapor feature that leads to loss of sensitivity to further increases in CWV. The retrieval for CWV less than 1 cm, however, shows good performance suggesting that the 940-nm channel can be utilized to detect and retrieve small amounts of water vapor in the atmosphere, while its sensitivity saturates for larger than 1 cm CWV. The second mode of CWV retrieval shown in green circles, using an average of CWV retrievals at both 720 and 820 nm, shows very good performance along the whole dynamic range of CWV. Although the retrieval shows a slight bias at small CWV values, the impact of erroneous (biased) CWV at low values is less significant on the R_{rs} of the ocean, especially at weakly absorbing bands in the visible range of the spectrum. The third mode of CWV retrievals using 720 nm only, shows also a good retrieval along the whole dynamic range. Retrievals at low CWV values show less bias compared to the combination of 720 and 820 nm, while there is a stronger bias at high CWV values. The absolute average percent error is 19, 8.5, and 9% for retrievals using 820 and 940 nm, 720 and 820 nm, and 720 nm only, respectively. In Gao and Kaufman (2003), their CWV retrieval using MODIS showed a systematic bias relative to both a ground-based sunphotometers (AERONET) observations and a smaller bias to a ground-based, upward looking microwave radiometer (Gao and Kaufman, 2003). In the latter case, the error in CWV retrieval was less than 10%, which corroborates with the analysis shown here, except in the 820 and 940 nm combination, which is not ideal for a wide dynamic range of retrievals. Based on the analysis presented here, it is therefore recommended to use either 720 or 820 nm or both for the atmospheric correction of water vapor over oceans.

Application to HICO Imagery

To demonstrate the heritage AC extended to hyper-spectral, we present an application to Hyperspectral Imager for the Coastal Ocean (HICO) imagery, as detailed in Ibrahim et al. (2018). HICO (**Table 1**) is a hyper-spectral imaging radiometer that operated onboard the international space station (ISS) from 2009 to 2014, capturing over 10,000 scenes over the globe (Corson et al., 2008, 2010; Korwan et al., 2009; Lucke et al., 2011). HICO measured light with a spectral coverage from 353 nm to 1,080 nm with a 5.7 nm spectral resolution. It has a pointing capability in the cross-track direction. At the nadir looking direction, the spatial resolution is 90 m. HICO collected one scene per orbit of size 50 × 200 km that was scheduled weekly by the science team, with scenes mostly collected over coastal regions to derive products such as water clarity, benthic types, and bathymetry. HICO provided adequate radiometric performance to support

TABLE 1 | HICO sensor and data characteristics.

Platform	International Space Station (ISS)
Operation lifetime	2009–2014
Orbit repeat time/period	3 days/90 min
Scene size (km)	50 × 200
Pixel size (m)	∼100
Wavelength (nm)	353–1080 (128 bands)
Spectral resolution (nm)	5.7
Spectral FWHM (nm)	10 ($\leq$745 nm), 20 ($>$745 nm)
Sensor type	Offner Spectrometer
Signal-to-noise ratio (SNR)	$>$200:1 assuming 5% surface albedo
Polarization sensitivity	$<$5%

ocean color applications in these coastal regions, where high concentrations of phytoplankton and suspended sediments result in high water reflectance in the visible regime (e.g., Dierssen et al., 2015b), but scenes collected over darker, open ocean regions suffer from the relatively low signal to noise ratio (SNR), especially in the green to NIR regime (Korwan et al., 2009; Lucke et al., 2011).

For HICO, an operationally viable algorithm for hyper-spectral ocean color retrieval has been implemented and assessed (Ibrahim et al., 2018), which follows the heritage approach used by NASA for all global ocean color sensors (Mobley et al., 2016). Water vapor correction, using the 720-nm spectral window, was a significant addition to that heritage process. The AC for HICO is completely automated, requiring no scene-specific operator intervention. As such, this work demonstrates the first operationally viable algorithm for hyper-spectral water reflectance retrieval, and can serve as a baseline AC for OCI on PACE. To minimize biases in the water reflectance retrievals due to uncertainty in HICO's radiometric calibration or systematic algorithm errors, a system-level vicarious calibration was also developed and based on hyper-spectral *in-situ* measurements from MOBY (Franz et al., 2007).

The atmospheric correction algorithm and the gains derived from the vicarious calibration process were applied to the HICO observations to retrieve hyper-spectral remote sensing reflectance (R_{rs}). As a verification of system performance, the approach was applied to all HICO scenes available over the MOBY site. In **Figure 8**, R_{rs} derived from HICO after the atmospheric correction process with and without applying the vicarious gain factors are compared to MOBY's *in-situ* R_{rs} optically integrated to HICO's spectral response function. Also shown is co-incident R_{rs} from MODIS onboard Aqua (MODIS-A), when available. It is clear that the R_{rs} match-ups from HICO are improved after applying the vicarious calibrations, showing a good agreement with both *in-situ* MOBY and MODIS-A retrievals. HICO's R_{rs} also does not contain any features from the absorbing gases (i.e., negative reflectance at the 720-nm and 820-nm water vapor bands), including at the water vapor bands, emphasizing that the gaseous compensation process is performing well.

The hyper-spectral comparison of HICO and MOBY R_{rs} is very good. The improved NIR-band vicarious calibration, which determines the aerosol contribution for the atmospheric correction, reduces the bias in the visible spectrum. Overall, MODIS-A shows very good agreement in R_{rs} with MOBY, as expected, since the vicarious calibration was performed at the same site.

Figure 9 shows a true color image acquired by HICO in the Chesapeake Bay region at the east coast of the US, a highly complex and productive estuary with large anthropogenic influences on both the ocean and the atmosphere, and **Figure 10** shows the retrieved R_{rs} at selected bands in the visible spectrum.

The retrieval of R_{rs} captures the large dynamic range due to the changes in the bio-optical properties of the water body. The R_{rs} images of HICO in the blue part of the spectrum exhibit image artifacts, such as stripping and reduced sensitivity. This is resultant of degraded sensor performance due to electronic smear and strong polarization sensitivity detailed in (Lucke et al., 2011). A detailed comparison between MODIS and HICO R_{rs} estimates for that scene is described in Ibrahim et al. (2018).

Figure 11 shows the hyper-spectral R_{rs} retrieved from HICO and the multi-spectral MODIS-A retrievals at three stations (STs) in the image from Chesapeake Bay. As in **Figures 9**, **10**, Station 1 (ST1) is located in the York River, a highly turbid, highly productive region, Station 2 (ST2) is located at the mouth of the Chesapeake Bay, and Station 3 (ST3) is located just outside the bay in the Atlantic Ocean. The agreement between MODIS-A and HICO R_{rs} retrieval is very good for the three locations, indicating good consistency in algorithm performance regardless of the water type. **Figure 11** also demonstrates the spectral features that HICO can resolve as compared to the multi-spectral MODIS-A.

Recapitulation

The two-step heritage atmospheric correction algorithms have served the ocean community well, providing a reliable and efficient mechanism for the retrieval of water reflectance and derived marine bio-optical properties from multispectral satellite sensors. Within the framework of this heritage algorithm, and without employing deterministic or statistical methods, a prototype algorithm has been demonstrated for hyper-spectral atmospheric correction. This algorithm improves upon heritage by using measurements within and adjacent to water vapor absorption bands to derive column water vapor internally, without the need for ancillary inputs from reanalysis data. Exploration of this method points to the use of the 720 and 820 nm water vapor absorption bands to derive water vapor transmittance for use in the atmospheric correction algorithm, with the capability to produce column water-vapor concentration as a valuable additional product. Improvements will be required to accurately treat air-sea processes, such as wind-roughened and whitecap-prone seas, and conditions when the near infrared reflectance is enhanced due to surface blooms, vegetation or high turbidity.

ALTERNATIVE ALGORITHMS

In order to discuss different optimization methods, including Bayesian optimization schemes (Gelman et al., 2013), that may be of relevance to the analysis of PACE hyper-spectral data we will introduce the relationship between the Likelihood function $P\left(\boldsymbol{y}|\boldsymbol{x_w},\boldsymbol{x_{atm}}\right)$, the prior probabilities for the oceanic, $P(\boldsymbol{x_w})$, and atmospheric constituents, $P(\boldsymbol{x_{atm}})$, of interest and the posterior probability distribution, $P\left(\boldsymbol{x_w},\boldsymbol{x_{atm}}|\boldsymbol{y}\right)$, viz.,

$$P\left(\boldsymbol{x_w},\boldsymbol{x_{atm}}|\boldsymbol{y}\right)\sim P\left(\boldsymbol{y}|\boldsymbol{x_w},\boldsymbol{x_{atm}}\right)P(\boldsymbol{x_w})P(\boldsymbol{x_{atm}}), \tag{4}$$

where we are assuming that the prior probabilities for the atmospheric state and the oceanic state are independent. In this formalism $\boldsymbol{y}$ is the vector of reflectances observed at the top of the atmosphere, $\boldsymbol{x_w}$ is the vector of water reflectances and $\boldsymbol{x_{atm}}$ is the vector of atmospheric properties (if any) that are estimated as part of the atmospheric correction process. Rodgers (2000) provided a comprehensive description of this approach for the atmospheric sciences. While not all optimization schemes explicitly make the link to the posterior probability distribution and the benefits of its use in obtaining an optimal estimate, most in fact use cost functions that are closely related to this form. The prior distribution is in some cases used purely to stabilize the search for $\boldsymbol{x_w}$ and $\boldsymbol{x_{atm}}$ (section Statistical Algorithms), but in more sophisticated approaches it is derived from existing data bases or is related to known functions of $\boldsymbol{x_w}$ and $\boldsymbol{x_{atm}}$ (section Multi-term Statistical Algorithm, GRASP Retrieval).

Deterministic Algorithms

As noted above in section Algorithms to Retrieve Water Reflectance from Space, atmospheric correction is in principle an ill-posed problem since the range of possible atmospheric, surface and ocean states is not uniquely constrained even by hyperspectral measurements. Nonetheless, by suitably constraining the problem and fitting all the observed TOA reflectances simultaneously, stable solutions that are valid under a variety of conditions relevant to atmospheric correction for PACE can be obtained. Examples of this type of one step approach are provided by Stamnes et al. (2003) in which a simple iterative scheme is used to provide a least squares estimate of chlorophyll concentration and aerosol optical thickness and Li et al. (2008) where a maximum a posteriori estimate of chlorophyll concentration, absorption by colored dissolved organic material, backscattering by suspended particulate matter, aerosol optical thickness and aerosol fine mode fraction is obtained. Similar optimization schemes are described in Land and Haigh (1997), Chomko and Gordon (1998), Kuchinke et al. (2009), Steinmetz et al. (2011), Shi et al. (2016). By representing the ocean and atmosphere with simplified parametric forms the estimation problem becomes stable, since its dimensionality has been reduced. As the approach presented by Li et al. (2008) is an optimal estimate in the sense described by Rodgers (2000) its extension to include the types of measurement in the UV and O_2 A-band from a PACE OCI, that can be used to constrain aerosol absorption and vertical distribution, is natural. For example, in turbid coastal waters where absorbing aerosols are most likely to be an issue for atmospheric correction the ocean body reflectance in the deep blue and UV tends to be stable and low and can therefore be used primarily as a constraint on the atmosphere (Oo et al., 2008; He et al., 2012). The sensitivities of these radiances to aerosol absorption and vertical distribution, versus ocean body properties is incorporated into the retrieval scheme through its use of functional derivatives of the radiation field with respect to the parameters being retrieved (Jacobian matrices, see section Information Content Assessment) such that reflectances that are sensitive to a parameter play a greater role in its determination than those that are not sensitive to it.

More recently a particularly simple approach to representing the Rayleigh corrected atmosphere as a polynomial function of wavelength, referred to as POLYMER, was introduced (Steinmetz et al., 2011). Together with an ocean body reflectance parameterized with chlorophyll concentration and a non-covarying ocean body scattering term this representation was used to perform atmospheric correction in the presence of Sun glint. The application of this approach to PACE OCI data may be beneficial in terms of increased coverage by providing valid retrievals in the presence of Sun glint with a reflectance as bright as 20% and in the presence of semi-transparent clouds (Frouin et al., 2014). This is illustrated in **Figure 12**, which displays POLYMER-processed MERIS imagery acquired over the Northwest Atlantic (June 21, 2005). The satellite observation is contaminated by Sun glint and a variety of cloud systems, as evidenced in the RGB composite (**Figure 12**, left). Chlorophyll-a concentration is retrieved in the presence of the glint and thin clouds, and there is spatial continuity between cloud- or glint-contaminated areas and adjacent clear areas (**Figure 12**, right). A band of relatively high chlorophyll-a concentration, not detected in the RGB image, is revealed at the shelf break in the Bay of Biscay, a known phenomenon due to internal waves generated by the interaction of the surface tide with the steep topography (Pingree et al., 1986; Robinson, 2010).

However, it is important to recognize that all of the one-step methods described above have the same potential issue with regards to the atmospheric correction for PACE. While it is possible within this framework to provide water reflectance estimates that are relaxed from the assumed ocean body reflectance spectrum, e.g., Equation (10) of Steinmetz et al. (2011), it remains an open question as to how much and in what spectral domains the ocean body spectra assumed in the retrieval process will distort the estimated water reflectance spectra. Given the expected application of PACE OCI water reflectance to the identification of subtle absorption features (e.g., Gitelson et al., 2011) this clearly needs to be quantified as part of the use of any such algorithm. Tan et al. (2018) provide information about the representativeness of the 2-parameter water reflectance model now used in the POLYMER algorithm. The model, based on Park and Ruddick (2005), depends on chlorophyll concentration and a factor specifying the contribution of algal and non-algal particles to the backscattering coefficient. It was applied to 500 Case 1 and Case 2 water situations used in IOCCG (2006), and the parameter values giving the best fit against accurate Hydrolight simulations were determined following procedures described in Steinmetz et al. (2011). Agreement is generally good (about 10% RMS difference in the blue) between the two-parameter model results and Hydrolight values, i.e., much better than typical atmospheric correction errors), even in optically complex waters; many spectral details are correctly modeled in the 10-nm resolution reflectance spectrum. Significant differences exist in some cases, but having a more intricate model (i.e., using more parameters) might not guarantee convergence. The trade-off is between efficiency/robustness and accuracy.

Statistical Algorithms

Neural networks (NNs) and other machine-learning techniques have seen considerable and diverse use in addressing the atmospheric correction problem (Schiller and Doerffer, 1999; Jamet et al., 2004, 2005; Brajard et al., 2006, 2008, 2012; Gross-Colzy et al., 2007a; Schroeder et al., 2007; Fan et al., 2017). This is because NNs and in particular multilayer feedforward networks with non-linear transfer functions provide a universal method to approximate arbitrary non-linear functions (Hornik, 1989). They can therefore be used either to solve the atmospheric correction problem directly by having observed reflectance and viewing geometry as input and water reflectance as output (Schroeder et al., 2007), or to model the radiative transfer equation (RTE) itself, where they replace the time-consuming solution of the RTE in an optimal estimation scheme (e.g., Brajard and Jamet references). In Gross-Colzy et al. (2007a) the TOA reflectance, after correction for gaseous absorption and molecular scattering, is decomposed into principal components (PCs), and the PCs sensitive to the water reflectance are combined to retrieve the PCs of the water reflectance. This allows a reconstruction, therefore estimation, of the water reflectance. Neural network methodology is used to approximate the non-linear functions that relate the useful PCs of the satellite reflectance to those of the water reflectance. Keeping only the water-sensitive PCs of the measured signal reduces the influence of the atmosphere and surface, making the non-linear mapping easier and accurate. The speed inherent in neural networks, once trained, means that they are a valuable tool for global processing of ocean color imagery and can be readily extended to the atmospheric correction of the hyper-spectral ocean color observations that will be provided by PACE OCI.

Figure 13 displays an example of water reflectance retrieval obtained with the PC-based algorithm (Gross-Colzy et al., 2007a) applied to Sentinel-2 MultiSpectral Instrument (MSI) imagery. The MSI scene was acquired over the Gironde estuary on October 21, 2016. The PC-based algorithm uses TOA reflectance in 11 spectral bands to retrieve water reflectance at 15 wavelengths including 412, 510, and 620 nm (not observed with MSI). This is possible since the TOA PCs can be mapped to the water PCs defined on a different base. The consequence (advantage) for PACE, is that it might not be necessary to observe in spectral regions strongly affected by gaseous absorption to retrieve water reflectance in those regions. As expected, the offshore waters are characterized by relatively high reflectance at 443 nm and low reflectance at 620 nm, and almost null reflectance at 865 nm, in contrast with the more productive and turbid waters of the estuary, which exhibit high reflectance at 620 nm (>0.25) and 865 nm (>0.10). In the estuary, the water reflectance spectra are similar in shape and magnitude to those reported by Doxaran et al. (2002), even the feature around 750 nm. The high-resolution (30 m) images also reveal a sharp contrast between the turbid estuarine waters and the clearer offshore waters, i.e., relatively little mixing, which would not be observed in coarse resolution (e.g., 1 km) imagery.

In the case where the NNs are used to provide a direct solution of the atmospheric correction problem it is not clear that this is applicable to the PACE OCI hyper-spectral data. As there is no relaxation to the observations based on the estimate of the atmospheric state, in this approach the NN estimate of water reflectance can only reproduce something close to what is in its training data set. A procedure should be applied to check whether the observations are compatible with the training data set. One of the main reasons for obtaining the PACE OCI hyper-spectral observations is that there is currently no such data set available to train a NN. In the case where NNs are used to model the RTE something similar to the optimal estimation approach described by Rodgers (2000) can be implemented since the gradients of the RTE that are needed can be obtained in a straightforward way directly from the NN that provides the forward simulation of the RTE (Bishop, 1995). While the forward model in such an optimal estimation scheme may contain assumed water reflectance spectrum, that assumption can be relaxed in the last step of the correction process (e.g., Equation 8 of Brajard et al., 2012). We note that if the Likelihood (errors in the observations) and prior probabilities (uncertainties in the atmosphere and ocean state vectors) are both Gaussian then the cost function that is being minimized in the NN approach is remarkably similar to $-\log[P\left(\boldsymbol{x_w},\boldsymbol{x_{atm}}\middle|\boldsymbol{y}\right)]$, e.g., Equation (5) of (Brajard et al., 2012), and so the atmospheric correction will be similar to a Maximum A Posteriori estimate. However, the treatment of the priors is not based on data as one would expect in a completely Bayesian formulation, but is rather, a means to regularize the solution of the atmospheric correction problem. Nonetheless, based on their speed and applicability to cases where there are absorbing aerosols (Brajard et al., 2008) and to bright coastal waters (Brajard et al., 2012) NN atmospheric correction algorithms may well be appropriate for PACE OCI.

The identification of the cost function as akin to a Maximum A Posteriori estimate brings us to the subject of explicitly Bayesian AC approaches. While the use of a MAP estimate does not necessarily require detailed evaluation of the prior distributions, there are considerable benefits to doing so. As was noted above the priors can also be regarded as a way of regularizing the solution of the ill-posed atmospheric correction problem and ideally any such regularization should be based on independent observational, or theoretical evidence, rather than *ad hoc* estimates. Two recent papers introduce Bayesian methods for AC of ocean color (Frouin and Pelletier, 2015; Saulquin et al., 2016), although the solution approaches are completely different. Frouin and Pelletier (2015) construct a numerically efficient partitioning of the Rayleigh corrected, or "observed" spectral reflectance using a perfect binary tree. This partition is used in conjunction with inverse models estimated from simulated atmospheric and *in situ* ocean data to estimate the means and covariances of the water reflectance and the atmospheric state parameters. In addition a model probability is calculated, i.e., a quantitative measure of how well the TOA observations fit the forward model, allowing for the rejection of scenes for which the model is inappropriate. The method is numerically efficient and provides its own estimate of the mean and covariance of the water reflectance as an output. Since the atmospheric state is also estimated, a relaxation step similar to those identified above could be applied to the observed reflectance if that was required. However, the authors do point out that "using data instead of simulations for the water reflectance was deliberate, dictated by the fact that models do not take fully into account the natural correlations between the intervening optical parameters" and so the spectral variability of their water reflectance is not tied to a specific chlorophyll absorption spectrum. The numerical efficiency and fact that the spectral behavior is not tied to a specific absorption spectrum mean that this AC scheme should be applicable to PACE OCI. Saulquin et al. (2016) generate prior distributions that are Gaussian Mixture Models for the water reflectance and the atmospheric reflectance, using the MERMAID *in-situ* matchup database. They then use a gradient descent search to try and find a minimum of the Maximum A Posteriori cost function. Since the Maximum A Posteriori criterion may not be concave they use 25 random initializations to try and eliminate solutions that are captured in local minima. While this method has been successfully applied to AC in complex coastal waters, it is not clear that the existing method for finding the Maximum A Priori solution is sufficiently efficient for global applications.

Figure 14 presents an example of results obtained with the Bayesian methodology described in Frouin and Pelletier (2015). The scheme was applied to SeaWiFS imagery acquired over the Sea of Japan and northwest Pacific on April 7, 2001. In the Sea of Japan, the TOA reflectance at 865 nm (**Figure 14**, top left) is relatively high, due to dust from Northern China and pollution from the Korean Peninsula and Japan. This was confirmed by *in situ* aerosol measurements collected onboard R/V Brown during the ACE-Asia experiment and back trajectories (Kahn et al., 2004). In fact, most of the Sea of Japan was clear, but so hazy that, in the SeaWiFS Data Analysis System (SeaDAS) screening scheme applied here, many pixels were flagged as cloudy. The retrieved water reflectance at 555 and 412 nm, as well as associated uncertainties, and a quality index (p-value) are displayed in **Figure 14** (top left and right and bottom). This ability to provide uncertainties on a pixel-by-pixel basis, i.e., to quantify the quality of the retrievals, is characteristic of the statistical technique. The water reflectance at 555 and 412 nm corresponds to chlorophyll concentrations typical of those observed in the region (Yamada et al., 2004). The uncertainties are higher in the vicinity of clouds and the coast, reaching 0.01 at 412 nm and 0.002 at 555 nm. In general, however, the values are much lower, e.g., below 0.004 at 412 nm. The quality index indicates good retrievals everywhere (p-value > 0.05), but values are lower where aerosol loading is higher (e.g., Sea of Japan). The marine reflectance retrieved by the SeaDAS AC algorithm (Mobley et al., 2016; see also section Heritage Atmospheric Correction Algorithm), reprocessing version R2010.0, exhibits more spatial noise (**Figure 15**, top left and bottom left); values at 412 nm are unrealistic (e.g., sometimes negative) in the Sea of Japan. Histograms of valid data (**Figure 15**, top center and bottom center) show for the statistical technique a frequency maximum shifted toward higher values by about 0.006 at 412 nm, with a narrower spread. Such shift does not exist at 555 nm and 670 nm. Variograms of valid data in a selected sub-area (150 × 150 pixels) located in the Japan Sea confirm less noisy marine reflectance imagery derived by the statistical technique (**Figure 15**, top right and bottom right), i.e., values are closer to zero as distance becomes small, and they show a reduced spatial variability over a 60-pixel distance. The results suggest that absorbing aerosols can be handled adequately using spectral information at wavelengths influenced by aerosol absorption. Accuracy is expected to improve by using observations at wavelengths in the UV (case of PACE OCI, where molecular scattering and, therefore, the coupling between aerosol absorption and molecular scattering are effective. Independent information about aerosol altitude and aerosol type, for example from the PACE polarimeter or a transport model, may help to constrain the inversion by restricting the domain of possible solutions.

Multi-Term Statistical Algorithm, GRASP Retrieval

For more than a decade a multi-term statistical retrieval approach has been developed in Dubovik et al. (1995, 2006, 2011), Dubovik and King (2000), and Dubovik (2004). The approach is based on the maximum likelihood methodology and therefore it is fundamentally close to the Bayesian optimization schemes given by Equation (4). However, the Multi-Term emphasizes the use of multiple a priori constraints and the Likelihood function $P\left(\boldsymbol{y}|\boldsymbol{x}\right)$ is defined as follows:

$$P\left(\boldsymbol{x}|y, \boldsymbol{f_1}\left(\boldsymbol{x}\right), \ldots, \boldsymbol{f_N}(\boldsymbol{x})\right) = P\left(y|\boldsymbol{x}\right) \prod\nolimits_{i=1,\ldots,N} P(\boldsymbol{f_i}(\boldsymbol{x})|\boldsymbol{x}) \tag{5}$$

Here, $\boldsymbol{x}$ denotes $(\boldsymbol{x_w}, \boldsymbol{x_{atm}})$, $\boldsymbol{y}$ denotes measured multi-spectral, -angular, and -polarized reflectances, and $\boldsymbol{f_i}(\boldsymbol{x})$ denotes functions of $\boldsymbol{x}$ that are known a priori. If we have

$$\prod\nolimits_{i=1,\ldots,N} P(\boldsymbol{f_i}(\boldsymbol{x})|\boldsymbol{x}) = P\left(\boldsymbol{f_1}\left(\boldsymbol{x}\right)|\boldsymbol{x}\right) P\left(\boldsymbol{f_2}\left(\boldsymbol{x}\right)|\boldsymbol{x}\right) = P\left(\boldsymbol{x_w}|\boldsymbol{x}\right) P\left(\boldsymbol{x_{atm}}|\boldsymbol{x}\right) \tag{6}$$

then Equation (5) becomes equivalent to Equation (4). At the same time, Equation (5) is evidently more general than Equation (4) since in many situations Equation (5) cannot be reduced to Equation (4). This aspect is rather important in many practical situations. Indeed, using direct assumptions about $\boldsymbol{x_w}$ and $\boldsymbol{x_{atm}}$ may lead to significant biases since it is very difficult and nearly impossible to find correctly a direct estimate of unknown parameters. For example, aerosol optical thickness in some areas may change by an order of magnitude and a single a priori climatological value cannot be used. In these regards, using some other constraints may be more adequate for PACE retrieval. For example, in remote sensing smoothness constraints are known to be efficient (e.g., Twomey, 1977). Namely, if one retrieves aerosol size distribution $n(r)$, the limitation on the k-th derivative can be used as a priori constraint as $\partial^k(n(r))/\partial r^k \approx 0$. In principle such smoothness constraint is less restrictive, since it does not apply any direct limitation on the magnitude of the retrieved parameters, but it only eliminates the solution when the retrieved function has unrealistically strong oscillations (see illustration by Twomey, 1977; Dubovik and King, 2000). Once a multi-term approach is employed, multiple a priori constraints can be used. For example, the Dubovik and King (2000) AERONET retrieval uses a priori constraints on aerosol size distribution, and spectral dependencies of real and imaginary parts of complex refractive index simultaneously. Dubovik et al. (2011) in retrievals from Polarization and Directionality of the Earth's Reflectance (POLDER) onboard PARASOL derives simultaneously both aerosol and surface properties and for all spectrally dependent parameters of surface reflectance the smoothness constraints are also used. Moreover, Dubovik et al. (2011) proposed to define statistically optimized retrieval for a large group of POLDER/PARASOL observation pixels. For example, instead of Equation (5) for M pixels the Likelihood function can be defined as follows:

$$P(\boldsymbol{x_1},\ldots,\boldsymbol{x_M}|\boldsymbol{y_1},\ldots,\boldsymbol{y_M},\boldsymbol{f_1}(\boldsymbol{x_1},\ldots,\boldsymbol{x_M}),\ldots,\boldsymbol{f_N}(\boldsymbol{x_1},\ldots,\boldsymbol{x_M})) = P\left(\boldsymbol{y_1},\ldots,\boldsymbol{y_M}|x_1,\ldots,\boldsymbol{x_M}\right)\prod_{i=1,\ldots,N} P(\boldsymbol{f_i}\left(x_1,\ldots,\boldsymbol{x_M}\right)|x_1,\ldots,\boldsymbol{x_M}) \tag{7}$$

where a priori constraints can be applied not only on the magnitude of parameter variability within each pixel, but also on their variability between the pixels. This allows the use of priori inter-pixel constraints to further improve the overall accuracy of the retrieval. For example, it is well known that land surface reflectance changes slowly over time, while spatial variability of aerosol parameters is also limited. Dubovik et al. (2011) showed that using both these constraints helps to achieve stable retrieval of aerosol properties even in such difficult situations as over bright land surfaces. For ocean surface application of time constraint is less critical, though applying some very mild constraints on time and horizontal variability of ocean surface parameters is also useful. Overall advantage of multi-term statistical retrieval is the possibility of retrieving extended set of unknowns. For example, Dubovik et al. (2011) retrieves more than 40 parameters for each POLDER/PARASOL pixel that includes aerosol size distribution, complex refractive index, fraction of spherical particles, aerosol height and spectrally dependent parameters of surface bidirectional reflectance and polarization distribution functions. It is also important to note that all a priori assumptions are general, i.e., no location-specific assumptions with exception of water fraction (i.e., water or land) that is assumed a priori using the pixel geographic coordinates. Moreover, a single initial guess for aerosol and surface parameters is used. Therefore, the results retrieved from POLDER/PARASOL observations are fully driven by the measured total and polarized reflectances (6 wavelengths, 16 viewing directions, and 3 polarization states, i.e., 192 data points for each inversion). In the future, some solid climatological information (e.g., about land surface) can be included too. All radiative transfer calculations including calculation of Jacobians are performed during the retrieval and the solution is sought in continuous solution space. Therefore, the errors of the retrievals also can be estimated using statistical approach. Since full radiative transfer calculations are used, the retrieval is significantly slower compare to conventional look-up-table algorithms. Nonetheless, during the last few years the computing routine was significantly optimized and the retrieval speed is acceptable now for processing large volumes of data and even for near real time retrieval. For example, the entire POLDER/PARASOL archive of 9 years was processed by GRASP (Generalized Retrieval of Aerosol and Surface Properties, see Dubovik et al., 2014) code. **Figure 16** illustrates the global retrieval of aerosol optical thickness, angstrom exponent and single scattering albedo that allow identification of different aerosol types.

According to the Dubovik et al. (2011) concept, the surface reflectance for both land and ocean is retrieved together with the aerosol properties. Though, the retrieval of surface reflectance was not the focus of initial efforts, the robust results for aerosol retrieval may also generate accurate surface property retrievals. **Figures 17–19** illustrate the first results for ocean surface retrieval. The reflective properties of the ocean surface are modeled analogously to earlier POLDER algorithm developments (Deuzé et al., 2001; Herman et al., 2005; Tanré et al., 2011). The Fresnel's reflection on the agitated sea surface is taken into account using the Cox and Munk model (Cox and Munk, 1954). The above surface water reflectance is presumed to be nearly isotropic (Voss et al., 2007) and modeling shows that its polarization can be neglected (e.g., Chami et al., 2001; Chowdhary et al., 2006; Ota et al., 2010). This term and the whitecap reflection are taken into account by Lambertian unpolarized reflectances. The whitecap effective reflectance is driven by the wind speed at sea surface according to the Koepke (1984) model. The seawater reflectance at short wavelengths is not negligible and depends on the properties of oceanic waters. Thus, in the present model, the wind speed and the magnitude of seawater reflectance at each wavelength are retrieved together with aerosol properties. **Figures 17–20** illustrate the retrieval of chlorophyll concentration, remote sensing reflectance, and wind speed and their comparison with MODIS results and ECMWF reanalysis.

The ocean surface reflectance model used here did not explicitly separate the contribution from whitecap, foam, and possible cloud contamination. Therefore, as initial approach for deriving water reflectance $\rho_w(\lambda)$ and estimating chlorophyll concentrations, the PARASOL/GRASP retrieval was tuned to the best agreement of MODIS chlorophyll retrieval for year 2008. Specifically, the chlorophyll fraction was fitted by the power law between logarithm of chlorophyll concentration and logarithms of ratio of water reflectance (440/565 and 490/565). The coefficients were estimated from best fit of MODIS chlorophyll concentrations using 1-year (2008) comparisons. The contribution of whitecap, foam, and possible cloud contamination was subtracted from retrieved values of surface albedo at shorter wavelengths using values at 870 and 1,020 nm. The coefficients for this subtraction were also estimated using the same comparisons with MODIS. Using the obtained empirical relationships, the water reflectances and chlorophyll concentrations were obtained from PARASOL/GRASP retrievals. As one can see from **Figure 19**, the obtained values are in rather good agreement MODIS results for both the global distribution and for the magnitudes of obtained values. Finally, **Figure 20** displays the comparison of PARASOL/GRASP retrieved values of wind speed with the values provided by ECMWF ERA-Interim reanalysis data. Agreement is good between two data sets both for contour and location of specific geographical features and the correlation of the values. The agreement is especially encouraging taking into account that PARASOL/GRASP retrieval did not use any climatological or ancillary data. Thus the polarimetric multi-angular observations allow for robust retrieval of the wind speed. It should be noted that PARASOL/GRASP retrieval was performed for all non-cloudy ocean pixel including those in glint areas.

It should be noted that the above results shown for ocean surface properties are obtained from first version of PARASOL/GRASP processing without using quality control and any filtering. At present, dedicated efforts are planned for improving PARASOL/GRASP ocean surface retrieval. Specifically, it is planned detailed evaluation and refinement of the ocean surface model and other aspects of reflectance modeling and inversion. Also the core scientific code was realized in open source GRASP software (Dubovik et al., 2014, https://www.grasp-open.com/). This software benefits from the general flexibility of code concept and includes a number of convenient features for users. For example, different assumptions in forward model and inversion can be changed and tested. Also, the GRASP code is highly versatile. It can be applied to different types of satellite and ground-based observations. Therefore, there is high potential for different synergy retrievals using GRASP software or scientific approach.

Other Optimal Estimation Approaches

Other recent work in atmospheric correction (Thompson et al., 2018) employed the Rodgers (2000) inversion framework more directly, adapting the Optimal Estimation (OE) methodology used by prior remote sounding missions like OCO-2, AIRS, and TES (Cressie, 2018). OE is based on a maximum likelihood method similar to the Dubovik et al. (2011) GRASP algorithm (see above), while it uses direct a priori estimates of the state vector. OE begins with an initial heuristic guess of the surface and atmosphere state, and then performs an iterative gradient ascent of the probability density until converging to a local maximum. At each iteration it calculates the probability gradient based on a local linearization under which the density can be characterized exclusively using multivariate Gaussians.

One emphasis of OE literature that does not appear in GRASP is the explicit treatment of unknown parameters in the models, i.e. parameters which affect the measurement but which are not directly retrieved. Specifically, the observation likelihood $P(\boldsymbol{y}|\boldsymbol{x})$ incorporates an instrument measurement noise model with a signal-dependent covariance, $\boldsymbol{S}_y$, as well as any unknowns in the surface/atmosphere model which are not estimated directly. Such unknowns, represented by a covariance $\boldsymbol{S}_b$, are treated as random variables. Jacobian matrices $\boldsymbol{K}_b$ contain the partial derivatives of the measurement with respect to these unknowns, evaluated at the current estimated state. The total covariance of the observation system, $\boldsymbol{S}_\epsilon$, is therefore:

$$\boldsymbol{S}_\epsilon = \boldsymbol{S}_y + \boldsymbol{K}_b^T \boldsymbol{S}_b \boldsymbol{K}_b \tag{8}$$

Given a predictive forward model of the measurement $\boldsymbol{f}(\boldsymbol{x})$, and prior with mean $\boldsymbol{x}_a$ and covariance $\boldsymbol{S}_a$ the log probability density function leads naturally to a local cost function $\chi^2(\boldsymbol{x})$ defined as:

$$\chi^2(\boldsymbol{x}) = \left(\boldsymbol{y} - \boldsymbol{f}(\boldsymbol{x})\right)^T \boldsymbol{S}_\epsilon^{-1} \left(\boldsymbol{y} - \boldsymbol{f}(\boldsymbol{x})\right) + (\boldsymbol{x} - \boldsymbol{x}_a)^T \boldsymbol{S}_a^{-1} (\boldsymbol{x} - \boldsymbol{x}_a) \tag{9}$$

At convergence, a similar linearization provides the posterior predictive covariance $\hat{\boldsymbol{S}}$ of the estimated surface and atmosphere state.

$$\hat{\boldsymbol{S}} = \left(\boldsymbol{K}^T \boldsymbol{S}_\epsilon^{-1} \boldsymbol{K} + \boldsymbol{S}_a^{-1}\right)^{-1} \tag{10}$$

The Jacobian matrices $\boldsymbol{K}$ hold partial derivatives of the observation with respect to the state vector. These have conventionally been calculated at the solution state, though Cressie (2018) points out that this is inconsistent with the delta rule derivation of $\hat{\boldsymbol{S}}$. Consequently, it may be preferable to calculate $\boldsymbol{K}$ from a data-independent state such as the prior mean.

Posterior uncertainty distributions permit meaningful scientific hypothesis testing about surface properties by subsequent analyses. They can enable principled fusion of multiple measurements across space and time, under widely variable atmospheric conditions. This can help prevent regional bias—due, for example, to different water and atmospheric properties across latitudinal zones—from influencing global maps. More fundamentally, a full uncertainty accounting promotes a richer understanding of the observation system and its components. $\hat{\boldsymbol{S}}$ is a purely local estimate, but it has been used successfully to create closed uncertainty accounting for validation experiments that fully explains the discrepancies between remote and field data. Thompson et al. (2018) demonstrated a closed OE uncertainty budget for AVIRIS-NG, a grating spectrometer with hundreds of bands across the Visible/Shortwave Interval. That demonstration used terrestrial spectra, with *in-situ* measurements of surface reflectance on six diverse validation targets. The approach generalizes naturally to the aquatic domain.

The most significant difference between terrestrial and aquatic environments is of course the surface. Ideally, a parameterization would be general and flexible enough to capture both environments—this would serve for coastal investigations, which monitor challenging Case 2 waters, as well as wetlands and vegetation with partially-inundated pixels. The Thompson et al. (2018) study complemented the multi-band GRASP research with flexible surface reflectance priors modeling capable of representing hundreds of channels. It used a collection of multivariate Gaussians, fit using a "universal" library of diverse spectra and designed to envelope of possible spectra that might be encountered. At runtime, Euclidean or Mahalanobis distance identified the component that was closest to the current state estimate, and the result is used as the surface prior for that iteration. Considerable shrinkage regularization (Theiler, 2012) broadened these priors still further, ensuring that the system could retrieve spectral shapes that were outside the span of library spectra. A designer would be free to craft the appropriate spectral intervals and magnitudes of this regularization depending on the application, which is useful when generalizing GRASP examples to the spectroscopic case. In extreme cases, the designer could leave priors totally unconstrained outside key spectral windows containing atmospheric information, such as NIR bands for water vapor and aerosols, in order to preserve precise channel wise relationships for retrieval of very subtle absorption shapes with high-resolution spectra (Thompson et al., 2018). In general, the use of structured surface priors can capture many of the same information used heuristically by typical aerosol retrieval methods, such as a flat infrared profile, while providing additional statistical rigor.

Multi-component surface models are easy to augment with phenomena related to Fresnel surface effects to permit water retrievals. **Figure 21** shows the result of a transect across a scene imaged by NASA's PRISM airborne spectrometer. This shows Santa Monica bay during an algal bloom event (Trinh et al., 2017), imaged from an altitude of 20 km that is subject to 95% of the atmosphere column (making it a good analog to orbital measurements). Here an additional free parameter of the surface model represents the magnitude of surface glint, which is assumed to be completely specular to produce the spectral profile of the direct beam. Surface models are produced using a large library of synthetic water reflectance spectra generated using a range of semi-analytical parameterizations (IOCCG, 2006), with additional regularization applied. Panels A and B show two examples of dark water spectra, with error bars indicating 95% posterior predictive uncertainties. Panels C and D show two examples of more productive and turbid water. Remote sensing reflectance R_{rs} was retrieved using the optimal estimation approach of Thompson et al. (2018). The model incorporates uncertainties due to measurement noise as well as the retrieval process itself, though they are of course local linearized estimates and may not capture all probability density maxima. The spectra show characteristic phytoplankton absorption features as well as solar-induced fluorescence at 685 nm, even though such features did not appear in the initial reflectance library. The experiment demonstrates the ability of this methodology to retrieve novel reflectance profiles having a wide range of different water reflectance shapes.

ENHANCEMENTS USING MULTI-ANGULAR AND/OR POLARIMETRIC INFORMATION

For current instruments, the atmospheric correction, and subsequent retrieval of ocean properties, is a fundamentally underdetermined remote sensing problem. That is, the information contained in multi spectral observations cannot uniquely express the geophysical state. This leads to an inability, for example, to distinguish atmospheric from oceanic scattering, or to identify and account for aerosol absorption (IOCCG, 2010). While they can be mostly avoided in the open ocean, these issues are relevant in optically complex waters or in areas with non-maritime aerosols in the atmosphere.

One way to address underdetermined observations is to simply gather more information. The hyper-spectral capabilities of the OCI instrument on PACE are intended to better resolve in-water scattering and absorption. Aerosols, however, do not have strong spectral features, and their observation will remain underdetermined. The PACE science team has therefore investigated the capabilities provided by a Multi-Angle Polarimeter (MAP). MAP, as its name implies, is devoted to improving retrievals by also observing linear polarization at multiple viewing angles, in addition to multi-spectral or hyper-spectral radiometry.

The application of multi-angle polarimetry to satellite ocean color remote sensing is an emerging field of active research. In the previous section, the GRASP algorithm showed potential with POLDER data. In this section, we will describe theoretical studies exploring the information content of multi-angle polarimetry (section Information Content Assessment), followed by specific benefits of multi-angle observations (section Benefit of Multi-Angular Observations) and polarimetry (section Benefit of Polarimetric Observations) alone. Finally, we will discuss the benefits of combined multi-angle and polarimetric observations and provide examples of successful application of such instruments for ocean color remote sensing (section Benefit of Combining Multi-Angular and Polarimetric Observations). Background for the information content assessment described in section Information Content Assessment can also be found in **Appendix A**.

Information Content Assessment

Information content assessment tools are used to explore the capability of a measurement system, real or theoretical, in order to find the optimal algorithm or instrument design. Such tools rely on simulated observations, and are thus subject to the realism of such simulations. When designed properly, these information content assessments can provide valuable input to measurement system design. We have used information content assessment tools to make the case that a MAP is indeed valuable for ocean color remote sensing, specifically in the ability to accurately perform atmospheric correction of a scene and successfully determine the water reflectance vector $[\boldsymbol{\rho}_{\boldsymbol{w}}]$, from the reflectance observed at the sensor.

Our methodology is based upon the Bayesian approach using Gaussian distributions as described in Rodgers (2000), and implemented for aerosol remote sensing by Knobelspiesse et al. (2012) and references therein. Theoretical details can be found in **Appendix A**, while the specific implementation of our study is described here.

For this study, we used a Doubling and Adding radiative transfer model developed at the NASA Goddard Institute for Space Studies [see Knobelspiesse et al. (2012) for more details]. This model uses a single parameter (Chlorophyll-a concentration) to define the optical properties of the ocean body (Chowdhary et al., 2012). While this is overly simplistic for hyper-spectral systems such as OCI, it is appropriate for the multispectral MAP, which is intended for atmospheric correction. We simulated a maritime aerosol defined by (Smirnov et al., 2002) at five optical thicknesses over an ocean with three values of chlorophyll-a concentration, *Chl-a*, for total of fifteen simulated scenes. Simulation details are described in **Figure 22**.

TABLE 2 | Prototype MAP characteristics.

	# view angles	Radiometer	Polarimeter	Channels (nm)	Radiometric uncertainty	Polarimetric uncertainty
a	5: −50°, −25°,0°,25°,50°	Yes	No	Visible: 443, 555, 670, 865	3%	–
b	5: −50°, −25°,0°,25°,50°	Yes	No	Visible + NIR: 443, 555, 670, 865, 1640, 2250	3%	–
c	5: −50°, −25°,0°,25°,50°	Yes	Yes	Visible: 443, 555, 670, 865	3%	0.5%
d	5: −50°, −25°,0°,25°,50°	Yes	Yes	Visible + NIR: 443, 555, 670, 865, 1640, 2250	3%	0.5%
e	9: −70.5°, −60°, −45.6°, −26.1°, 0°, 26.1° 45.6°, 60°, 70.5°	Yes	No	Visible: 443, 555, 670, 865	3%	–
f	9: −70.5°, −60°, −45.6°, −26.1°, 0°, 26.1° 45.6°, 60°, 70.5°	Yes	No	Visible + NIR: 443, 555, 670, 865, 1640, 2250	3%	–
g	9: −70.5°, −60°, −45.6°, −26.1°, 0°, 26.1° 45.6°, 60°, 70.5°	Yes	Yes	Visible: 443, 555, 670, 865	3%	0.5%
h	9: −70.5°, −60°, −45.6°, −26.1°, 0°, 26.1° 45.6°, 60°, 70.5°	Yes	Yes	Visible + NIR: 443, 555, 670, 865, 1640, 2250	3%	0.5%

At the time this study was conducted, measurement characteristics for the MAP had yet to be finalized. We therefore chose to investigate a variety of prototypical MAP instrument described in **Table 2**. In each observed pixel, these instruments had either five or nine viewing angles, four visible channels or visible plus NIR spectral sensitivity, and were either radiometers or were sensitive to both the total and polarized radiometric state. All instruments had a combined (systematic and random) radiometric uncertainty of 3%, and polarimetric uncertainty of 0.005 (specified for the unitless DoLP). All instruments were compared to OCI as defined in the PACE Science Definition Team (SDT) report, containing 28 channels at UV, visible, NIR, and SWIR wavelengths (channels sensitive to gaseous absorption were omitted). Radiometric uncertainty was defined solely by threshold SNR requirements, implying perfect vicarious calibration and removal of systematic uncertainties. In our analysis, the MAP instrument is not vicariously calibrated, but OCI data are available to help the atmospheric correction (in other words, the theoretical measurement vector contains both MAP and OCI observations).

Figure 23 shows the Degrees of Freedom for Signal (DFS, see **Appendix A** for definition) for the cases with *Chl-a* specified at 0.3 mgm^{-3}. All MAP instruments have significantly higher DFS than OCI alone. As expected, MAP "h" (blue dashed line), which has the most channels and viewing angles, has the largest DFS, while even non-polarimetrically sensitive multi-angle radiometers (a, b, e, f, red and magenta lines) have 1–3 more DFS than OCI. Some instruments with different characteristics produce similar results, notably instrument "d" (blue solid line, a five angle polarimeter with visible and NIR channels) and instrument "g" (green dashed line, a nine angle polarimeter with visible channels only). Based on DFS alone, the capability of those designs appears equivalent, so other factors (such as cost or engineering difficulty) could drive the selection of the appropriate design. However, *DFS* does not necessarily indicate atmospheric correction capability, rather, the ability to determine all parameters in state space. This is also demonstrated by the increase in DFS with simulation aerosol optical thickness. Obviously, increasing the aerosol load above the ocean does not improve the ability to determine ocean properties, but it does improve the ability to determine aerosol optical properties, and this is shown in the increase in DFS. Finally, it should be noted that the corresponding results for *Chl-a* = 0.03 and 2.0 mgm^{-3} are nearly identical, so the DFS is largely insensitive to ocean color, at least as it is resolved in our simple ocean model.

The goal of atmospheric correction is not the retrieval of all parameters in the state space, but instead determination of water reflectance, $[\rho_w]$. For this reason, SDT report requirements are defined in terms of $[\rho_w]$ at the ocean surface. This is also why we have derived the byproduct error covariance matrix, $\hat{\mathbf{S}}_b$, for $[\rho_w]$. Diagonal elements of that matrix are the square of the expected retrieval uncertainty for each wavelength in $[\rho_w]$. **Figure 24** displays the ratio of this uncertainty to the predicted uncertainty of the OCI instrument alone. Thus a value of 1 indicates no improvement over OCI, while 0 is an infinite improvement. We chose this way of representing results in order to minimize the impact of imperfections in the radiative transfer model simulations, and because information content assessment is better at showing relative differences between measurement designs than absolute uncertainty values themselves.

Like in **Figure 23**, we find that MAP "h" (blue dashed line) offers the most improvement over OCI alone. Unlike in **Figure 23**, however, we find that "d" (blue solid line) and "g" (green dashled line) have different results. The nine angle visible wavelength MAP "g" is better than the five angle visible and NIR wavelength "d" at wavelengths less than 650 nm or so, and the reverse above 650 nm. However, $[\rho_w]$ wavelengths in the blue and green are most important for in water retrieval algorithms, so the "g" MAP is the preferable choice given this information.

Also unlike in **Figure 23**, we find that the ratio of MAP $\left[\boldsymbol{\rho_w}\right]$ uncertainty to that of OCI varies with *Chl-a* and aerosol optical depth. The relative improvement from one MAP prototype to another is, however, largely maintained.

To summarize, we have found that the addition of a MAP to PACE offers distinct atmospheric correction capability compared to OCI alone. This is even the case for a multi-angle radiometer without polarization sensitivity. As in all sensitivity studies, these results are subject to the realism of the study design and require careful interpretation. However, we now have the means to assess and guide the development of a MAP, in terms of SDT required values, should it be funded as part of PACE.

Benefit of Multi-Angular Observations

Multi-angle viewing provides information about aerosol properties in several ways, as discussed by Deschamps et al. (1994) in the context of POLDER and Diner et al. (1999, 2005) in the context of MISR, a multi-angle, non-polarimetrically sensitive radiometer that was launched into polar orbit in 1999 onboard NASA's Terra spacecraft. MISR observes the Earth at nine viewing angles in the along-track direction, and four spectral channels centered at 447, 558, 672, and 886 nm. Thus, each pixel has 36 different angle or spectral channel combinations, providing significant information about the aerosol state. First, the aerosol signal increases with increasing viewing zenith angle as the optical path through the atmosphere becomes longer. Second, several scattering angles are sampled in the observations, and the dependence with scattering angle is sensitive to aerosol type and size. This information may help to determine the proper aerosol type in atmospheric correction schemes, or at least to restrict the selection to a reduced set of possible (theoretical or statistical) models.

Diner et al. (1999) showed that sulfate (accumulation mode) and urban soot aerosols cannot be distinguished by observing at nadir in the red and infrared, while the multi-angle MISR data (9 geometries) in this spectral region are able to identify that an incorrect aerosol model has been assumed in the retrieval of optical depth. Gordon (1997), following Wang and Gordon (1994), had earlier indicated that it is possible to atmospherically correct MISR imagery over water bodies using a single spectral band (near infrared), by comparing the angular distribution of TOA radiance with predictions using aerosol models and selecting the model that best matches the measurements.

Kaufman et al. (1997) hypothesized that aerosol single scattering albedo could be estimated by observing in and out of the Sun glint. In their technique, the measurements not contaminated by Sun glint are used to estimate aerosol scattering properties, whereas the direct transmittance measurements at the center of the glint benefit the estimate of aerosol extinction. Ottaviani et al. (2013) confirmed that additional aerosol information exists in measurements containing Sun glint, not only for single scattering albedo retrieval, but also for optical thickness and refractive index retrieval.

Recently, Limbacher and Kahn (2017) used multi angle MISR data in a matching algorithm to retrieve simultaneously chlorophyll concentration and aerosol properties (model and optical thickness). The difference between observed TOA reflectance (not only multi angle, but also spectral) and simulated values stored in a look-up table is minimized. By accounting explicitly for the water body contribution to the TOA signal, aerosol type retrievals are expected to be more accurate. Chlorophyll concentration estimates were in agreement with *in situ* measurements, although the number of such measurements was limited. Because of this, results were also compared against MODIS observations, and a similar agreement was found. Chlorophyll concentration estimates were in agreement with *in situ* measurements and MODIS estimates over a wide range of geophysical conditions. This algorithm constitutes an extension, using directional information, of a spectral optimization scheme proposed by Gordon et al. (1997) and Chomko and Gordon (1998) to improve water reflectance retrievals from SeaWiFS and MODIS imagery in the presence of absorbing aerosols.

An alternative approach is to use multi-angle measurements to determine water reflectance using an approach analogous to the Langley extrapolation technique used in the sun photometer community (Shaw, 1983). The method, proposed by Thieuleux (2002), constrains the spectral extrapolation of scattering properties observed in the near infrared by a value of the aerosol absorption effect obtained in the short-wavelength bands using the multi-angular acquisitions. A separate estimation of the aerosol absorption optical thickness and vertical distribution, i.e., the variables that govern the aerosol absorption effect, is not necessary. This constitutes a great advantage, since these variables are difficult to retrieve. First, the TOA reflectance is corrected for molecular and aerosol scattering using spectral bands in the near infrared and/or shortwave infrared, as in the classic (heritage) atmospheric correction scheme. Second, the residual signal in all viewing directions, ρ_{abs}, composed of the aerosol absorption effect and the water signal (see section Improvements Using "Super-sampling" in Selected Spectral Intervals, Equation 14) is related to an absorption predictor, i.e., a function representing the directional effect of an absorbing aerosol, namely the product of molecular reflectance, ρ_r and air mass, m^*. By regressing ρ_{abs} vs. $m^*\rho_r$ (depends on geometry) one may get an estimate of the water reflectance ρ_w (the value at null m^* gives the water reflectance). Since the relation is non-linear, in practice one may normalize ρ_{abs} by molecular transmittance t_r. One may also use different absorption predictors, such as the absorption effect for a typical aerosol. **Figure 25** illustrates the method for fine and coarse aerosols. The water reflectance (fixed at 0.02 in this case) is obtained by "extrapolating" the relation between ρ_{abs}/t_r and $\rho_r m^*$ to zero air mass.

An example of application to POLDER imagery is given in **Figure 26**. The determination of the aerosol model, therefore the correction of aerosol scattering effects, was accomplished according to IOCCG (2010), using measurements at 670 and 865 nm in all the viewing directions not contaminated by Sun glint. The multi-angular information was only used to compute an average spectral dependence of the aerosol scattering. After removing the scattering effects, the residual signal at 443 and 565 nm normalized by molecular transmittance was regressed against the product of molecular scattering and air mass, yielding an estimate of the water reflectance. In the regression, water reflectance was assumed to be isotropic. The aerosol optical thickness imagery at 865 nm is displayed in **Figure 26** (top left). Relatively high values reaching 0.35 are obtained in the Eastern part of the Mediterranean basin. In this region, the standard atmospheric correction algorithm gives anomalously low marine reflectance at 443 nm (**Figure 26**, top right). The figure displays the average water reflectance over the viewing directions. After correction of the aerosol absorption effects, the water reflectance is higher in the dust-contaminated region (**Figure 26**, bottom left), which is consistent with the values in adjacent regions not affected by dust and with our knowledge of the bio-optical conditions in the Mediterranean Sea.

Some issues need to be examined to evaluate the feasibility of the multi-angular method and quantify its accuracy for the PACE mission in view of the capability of OCI and the multi-angle polarimeter. They include specifying the optimum set of viewing angles, investigating the influence of radiometric noise, defining requirements for relative multi-angle calibration, transferring the aerosol absorption information obtained by the polarimeter to OCI, and analyzing the influence of directionality in the water signal.

Benefit of Polarimetric Observations

Ocean Ocean color remote sensing is based on TOA measurements of total radiance or reflectance, i.e., the first component (I) of the Stokes vector. A major issue with this approach is that atmospheric and surface effects dominate the signal measured at the UV to visible wavelengths of interest (Gordon, 1997; Zhai et al., 2017). To reduce these effects, one may consider exploiting the polarization properties of reflected sunlight. Because molecules, hydrosols, aerosols, and the air-sea interface polarize incident sunlight differentially, there may exist viewing geometries (scattering angles) for which the contribution of the water body to the polarized or unpolarized component of the TOA reflectance may be enhanced. For those geometries, correction of the perturbing effects becomes easier, leading to a more accurate retrieval of the water signal. Additionally, in some systems the method of measuring polarization can inherently be more accurate than measuring direct reflectance (Tyo et al., 2006; Dubovik et al., 2019).

He et al. (2014) and Liu et al. (2017) provide evidence of the advantages of including polarimetry for atmospheric correction over water bodies. They describe a method for retrieving normalized water-leaving radiance using parallel polarization radiance ($PPR = I + Q$), where I and Q are the first two components of the Stokes vector. Their results, from both simulations and application to POLDER data, demonstrate that using *PPR* enhances the ocean color retrieval in two important ways. First, it reduces the Sun glint at moderate to large solar zenith angles. Second, it boosts the water signal relative to the total radiance received by satellite at large view angles. These advantages are explained by the compensating effect between the total radiance and the polarization. For example, as view zenith angles increase, because of the increasing long path length through the atmosphere, the total radiance received by the satellite increases, causing the relative ocean color signal reaching the satellite to decrease. Meanwhile, the magnitude of Q increases with path length, but in the negative sense, which offsets the increase in I, and damps the increase in *PPR* with path length through the atmosphere.

Instead of using total reflectance or *PPR*, one may consider working with the unpolarized component of the TOA reflectance, as early suggested by Frouin et al. (1994). The rationale behind this approach is that scattering by atmospheric constituents and reflection by the surface, i.e., the processes causing the perturbing effects, polarizes incident sunlight. One expects, therefore, that they will affect less the unpolarized TOA signal than the total TOA signal. Of course, scattering by water molecules and hydrosols also polarizes incident sunlight, but due to refraction at the air-water interface the scattering angle in water is generally large for typical viewing geometries, i.e., the polarization rate is usually small. In other words, the signal from the water body is mainly unpolarized (see Fougnie et al., 1999) and, in view of the above, the contribution of the water signal to the TOA signal may be enhanced. For the approach to be suitable, the unpolarized signal from the water body must not only be strong and contribute more to the TOA signal, but also sufficiently sensitive to water constituents (phytoplankton, dissolved matter, sediments).

Figure 27 displays the ratio of water bidirectional reflectance just below the surface to TOA reflectance at 443 nm for typical geophysical conditions, i.e., maritime aerosols of optical thickness 0.1 at 550 nm, chlorophyll-a concentration of 0.1 $\mathrm{mgm^{-3}}$, and wind speed of 5 $\mathrm{m\ s^{-1}}$, and solar zenith angles of 30° and 60°. The simulations were performed with the OSOAA radiation transfer code (Chami et al., 2001). For some combinations of viewing and solar angles, especially when viewing zenith angle is less than 60°, the unpolarized reflectance ratio is larger compared with the total reflectance ratio, and the enhancement is by a factor of 2-3 in some situations. The enhancement is relatively small in the center of the Sun glint region when solar zenith angle is 30°, because scattering angles are not favorable to reducing sufficiently the molecular contribution to the unpolarized atmospheric reflectance, and the most favorable viewing angles are around those corresponding to specular reflection. The maximum enhancement is confined to more vertical geometries (i.e., viewing zenith angles less than 45°) when solar zenith angle is 60°.

Since aerosols tend to polarize incident sunlight less than molecules, the enhancement obtained using unpolarized reflectance is reduced when aerosol optical thickness is increased, all the more as multiple scattering decreases polarization. When the aerosol optical thickness is 1 (**Figure 28**, top), there is only a marginal gain in the relative contribution of the water body for some viewing directions. Depending on the surface conditions (e.g., wind speed), the Sun glint pattern may include a wider range of viewing angles, displacing and extending the favorable geometries (not shown here). When the chlorophyll-a concentration is increased from 0.1 to 10 $\mathrm{mgm^{-3}}$ (**Figure 28**, bottom), aerosol optical thickness remaining 0.1 at 550 nm, the best viewing directions correspond to in air scattering angles of about 90° in the forward direction. The enhancement is also large in the Sun glint region. As scattering angle increases, and especially in the backscattering directions, the water signal becomes more unpolarized, resulting in a small or no enhancement with unpolarized observations.

Figure 29 displays the TOA unpolarized reflectance ratio versus the TOA total reflectance ratio at 443 nm for the situations of **Figures 27**, **28**. Reflectance ratio refers to the ratio of water reflectance just below the surface to TOA reflectance, expressed in percent. Only results for viewing zenith angles less than 60° (typical of satellite observations) are reported. As already mentioned, the unpolarized reflectance ratio is generally larger than the total reflectance ratio, for most viewing angles, except when aerosol optical thickness is large (i.e., 1 at 550 nm). In this case, the total reflectance ratio may be smaller by a few percent, which is practically not penalizing. Unpolarized observations in forward scattering directions, where polarization is effective, are most favorable to boost the contribution of the water signal. When chlorophyll concentration is high (i.e., 10 mgm^{-3}), the unpolarized reflectance ratio is up to three times larger than the total reflectance ratio. In such productive waters, for which the water signal is usually small, using unpolarized observations would greatly facilitate atmospheric correction, which may yield to more accurate estimates of water constituents/properties.

Now when working with unpolarized reflectance, the sensitivity of the unpolarized signal backscattered by the water body (obtained after atmospheric correction) to water composition may differ from that of the total reflectance, due to changes in the polarization rate (Chami et al., 2001; Chowdhary et al., 2006; Zhai et al., 2017). This sensitivity should remain sufficient for the methodology to be effective, since the ultimate objective is not an accurate retrieval of the water signal, but an accurate retrieval of the properties that affect the water signal. **Figure 30** displays, for typical solar and viewing angles, the sensitivity of the spectral ratio of water reflectance just below the surface at 443 and 550 nm, total or unpolarized, to chlorophyll-a concentration. This ratio is typically used in OC4x and OC3M algorithms. The atmospheric and surface conditions are those from **Figure 27**. Solar and viewing zenith angles are fixed at 30° and relative azimuth angle is 0°, 90°, or 180°. In the backscattering direction, as expected, the sensitivity to chlorophyll-a concentration remains unchanged whether using unpolarized or total water reflectance. In the forward scattering direction, the sensitivity is slightly higher at low chlorophyll-a concentration when using the unpolarized component (due to the decrease in polarization rate as chlorophyll concentration increases). This illustrates the potential of working with unpolarized reflectance, at least for chlorophyll-a concentration retrieval.

In summary, one may envision using the parallel polarization component (*PPR*) or the unpolarized component of TOA reflectance instead of the total reflectance (the usual way) to improve atmospheric correction of satellite optical imagery and retrieve properties (optical, biogeochemical) of the water body. The methodology only requires observations in a single direction, like with current ocean-color sensors. The advantages are that the water contribution to the measured signal may be substantially enhanced for a wide range of viewing angles and that Sun glint effects may be reduced. Also, in a classic atmospheric correction scheme, the polarization information in the near infrared (even in a single direction) would help to determine a proper aerosol model. A number of issues remain to be addressed; including radiometric calibration (polarization accuracy may degrade data quality) and bio-optical relations based on unpolarized component of water reflectance (need to be established, and experimental data are lacking). Furthermore, since molecular scattering strongly polarizes incident sunlight, one wonders whether the enhancement of the water signal would remain significant after removing the molecular signal (can be computed accurately, except in the presence of Sun glint) from the polarimetric measurements.

Benefit of Combining Multi-Angular and Polarimetric Observations

The shortcoming of conventional atmospheric correction methods in regions with complex marine and atmospheric compositions suggests an opportunity for a multi-angle polarimeter to supplement OCI remote sensing reflectance (R_{rs}) retrievals, particularly at short visible-UV wavelengths and in cases where the water surface in the NIR cannot be considered black, and will therefore provide significant risk reduction for meeting many PACE mission objectives. Indeed, measurements of the wavelength and angular dependence and polarization of the scattered radiance provide a determination of the aerosol physical properties, i.e., size distribution and refractive index (e.g., Hasekamp and Landgraf, 2005; Herman et al., 2005; Hasekamp et al., 2011). This information may be used to constrain the domain of possible aerosol types in a classic atmospheric correction scheme or, if sufficiently accurate, to directly compute the aerosol scattering effect. The sensitivity of polarized radiance to aerosol type has also the potential to improve inversion schemes that aim at retrieving simultaneously atmosphere and ocean properties.

Observational evidence is presented in **Figure 31** that shows retrievals of $\rho_w E_s/\pi$ (otherwise known as normalized water-leaving radiance, L_{wN}) obtained from AirMSPI measurements collected on February 6, 2013 over a SeaPRISM site off the coast of California. AirMSPI is a multi-angle polarimeter flying on the high altitude NASA ER-2 with 20 km of atmosphere between it and the ocean below. The SeaPRISM site on an offshore platform provides spectral L_{wn} measured just above the ocean surface. The retrieval was accomplished using an optimization-based multi-pixel retrieval algorithm (Dubovik et al., 2011). The forward radiative transfer calculations were performed using a Markov chain approach developed for a coupled atmosphere/surface system (Xu et al., 2011, 2012). The water reflectance was modeled as a depolarizing Lambertian surface reflection model, plus a polarizing part modeled by the Cox-Munk model (Cox and Munk, 1954; Mishchenko et al., 1997). Atmosphere and surface properties were retrieved simultaneously, and surface reflectance was retrieved independently at each wavelength.

The comparisons between the AirMSPI retrievals with the SeaPRISM ground truth (**Figure 31**) show that L_{wN} is retrieved much more accurately with multi-angle and polarization capability than when a more limited retrieval is made with just one angle and no polarization. Current satellite retrievals mitigate random and systematic errors over the open ocean by invoking standardized models for ocean surface spectral reflectance and aerosol scattering. However, in more complex waters, or when aerosol absorption is present at short wavelengths, traditional retrieval assumptions break down. The left-hand figure does not prescribe either an aerosol model or any surface spectral constraints, indicating that multi-angle and polarimetric imagery provides the necessary additional information in the more general scenario. The right hand panel does not invoke any of the enhanced capabilities, including expanded wavelength range, expected of the PACE OCI, and therefore suggests a worse retrieval than could actually be obtained by the radiometer alone.

Demonstrations that show the advantages of a MAP for atmospheric correction as applied to AirMSPI and POLDER are extremely promising, but still do not demonstrate how polarimeter data can be used to assist atmospheric correction of hyper-spectral radiometer measurements in complex coastal environments. These environments are located where traditional atmospheric correction assumptions do not apply, and where inherent optical properties (IOPs) can vary much more significantly and in more complex manners than in open ocean waters. In addition, OCI retrievals at UV and shortwave visible wavelengths present new challenges to atmospheric correction due to sensitivities to aerosol height in an atmospheric signal dominated by Rayleigh scattering and the interplay between scattering and gaseous absorption. For these optically complex regions and at these spectral ranges, adding information from MAP becomes most important for atmospheric correction. Efforts to acquire and make use of the appropriate demonstration data are highly recommended.

These constraints can enter the atmospheric correction procedures at a variety of levels. (1) At the simplest, they can improve our overall understanding of aerosol properties and distribution of aerosol type, which can be incorporated into heritage atmospheric correction lookup table and algorithm updates. (2) MAP based aerosol retrieval could be performed prior to OCI atmospheric correction, and direct that algorithm to a particular aerosol type and/or provide the aerosol optical depth. (3) An atmospheric correction algorithm may be performed directly with MAP observations, and after spectral and geometric interpolation, applied to OCI. (4) Both MAP and OCI observations are combined as inputs to a joint inversion. Implementation of any of these approaches would require that we overcome multi-sensor data fusion issues such as instrumental calibration, differing spatial resolution and varied geometry.

Clouds are ubiquitous in remote sensing of the ocean, so the ability to properly screen and remove "cloud contaminated" pixels is an important component of successful atmospheric correction. Such techniques must be conservative, but a "cloud free" pixel still may contain sub-pixel clouds, or be influenced by cloud adjacency effects such as shadows or other "3D" phenomena. Combined multi-angular and polarimetric observations are capable of identifying such effects, and in some cases, minimize their impact. Bréon and Goloub (1998) recognized that certain solar-view geometries observed by POLDER contained distinct cloud-bow features due to single scattering by liquid cloud drops, confirming earlier observations by Goloub et al. (1994) with airborne POLDER prototype observations. This was incorporated into POLDER cloud detection, cloud property retrieval, and cloud phase detection algorithms (Bréon and Colzy, 1999; Parol et al., 1999; Goloub et al., 2000). A later review of these capabilities by Parol et al. (2004) highlighted the utility of multi-angular polarimetric observations, but also found evidence of cloud contamination in an aggregate analysis of POLDER data. For these reasons, subsequent multi-angular polarimetric instruments were designed with the recognition that they would provide valuable data in both cloud and cloud free regions (e.g., Frouin et al., 2006; Mishchenko et al., 2007; Fougnie et al., 2018; Hasekamp et al., 2019). Additionally, polarimetric observations are recognized as being less sensitive to 3D effects (e.g., Davis and Marshak, 2010) but in certain geometries capable of detecting very optically thin cirrus clouds (Sun et al., 2014). The information contained in multi-angular polarimetric observations is highly sensitive to solar and observation geometry; it increases with additional measurements at angles containing the reflected cloud-bow. However, it can be large enough that simultaneous retrieval of cloud and aerosol property algorithms have been proposed for mixed cloud and cloud free pixels (Hasekamp, 2010), indicating the utility of such observations for properly cloud screened atmospheric correction.

IMPROVEMENTS USING "SUPER-SAMPLING" IN SELECTED SPECTRAL INTERVALS

The PACE OCI will have the capability to measure TOA radiance in spectral bands 5 nm wide with sampling at finer spectral steps (2.5, 1.25, or 0.625 nm). This fine spectral sampling provides the opportunity to estimate Raman scattering by water bodies and improve retrievals of phytoplankton chlorophyll fluorescence and aerosol vertical distribution. These applications involve the development of original techniques that exploit spectral fluctuations in solar irradiance, the filling by inelastic fluorescence of oxygen absorption lines in the B-band, and the coupling between aerosol scattering and oxygen absorption in the A-band. They require or will benefit from the high spectral sampling.

Estimation of Raman Scattering

Raman scattering occurs when an incident photon is scattered by water molecules excited into higher vibrational or rotational energy levels. The scattered photon has a frequency different from (usually lower than) that of the incident photon, i.e., the process is inelastic (kinetic energy of the incident photon is not conserved). This scattering by excitation is infrequent (1 in 10 million events), yet its contribution to diffuse water reflectance or "remote sensing" reflectance may reach 20% in the visible in clear oceanic areas (i.e., 40% of the world's oceans), as shown by Marshall and Smith (1990) and others and illustrated in **Figure 32**.

The Raman signal, therefore, needs to be known to improve the retrieval of oceanic variables (e.g., chlorophyll concentration) from "remote sensing" reflectance. The fact that Raman scattering at a given wavelength is influenced by the water optical properties at shorter wavelengths provides a second motivation to observe the Raman signal. Are the Raman scattering measurements interpretable in terms of water optical properties, and how can they complement other approaches? Measurements in the near UV, for example, should be strongly affected by CDOM absorption, while in the blue-green by chlorophyll absorption.

Raman scattering at a given wavelength is proportional to some integral of the solar irradiance at shorter wavelengths and, unlike elastic scattering by water and air constituents, its spectrum does not exhibit fluctuations in spectral solar irradiance (Fraunhofer lines and others). The approach to estimate the Raman scattering signal is thus to observe the TOA radiance at sufficiently high spectral resolution in a small wavelength interval, and to separate the part of the radiance that correlates with the solar irradiance spectrum (the elastic scattering) from the part that does not (the Raman scattering).

At the air-water interface, the spectral water-leaving radiance, $L_w(\lambda)$, is the addition of an elastic scattering contribution, $L_{w\_elastic}(\lambda)$ proportional to the solar spectral irradiance, $E_s(\lambda)$, and a Raman scattering contribution, $L_{w\_raman}(\lambda)$, i.e., the integral of the excitation by the Sun at shorter wavelengths. At the TOA, the observed spectral radiance, $L_{TOA}(\lambda)$, includes the signal due to atmospheric scattering and Fresnel reflection at the interface, $L_{atm}(\lambda)$, also proportional to $E_s(\lambda)$. Neglecting gaseous absorption and Sun glint effects for simplicity, $L_{TOA}(\lambda)$ can be written:

$$\begin{aligned} L_{TOA}(\lambda) &= L_{atm}(\lambda) + L_{w\_elastic}(\lambda)\ t_u(\lambda,\theta) \\ &\quad + L_{w\_raman}(\lambda)\ t_u(\lambda,\theta) \end{aligned} \tag{11}$$

The ability to de-correlate the elastic and inelastic scattering contributions does depend on the presence of some absorption bands in the extraterrestrial solar spectrum over the selected spectral interval. **Figure 33** shows the spectral solar irradiance, $E_s(\lambda)$, and the Raman "remote sensing" reflectance, $R_{rs\_raman}(\lambda)$ (defined as $L_{w\_raman}(\lambda)/E_d(\lambda)$ where E_d is the downward spectral solar irradiance at the surface, i.e., $E_s(\lambda)cos(\theta_s)t_d(\lambda)$, in the range 350–550 nm at a 5 nm resolution every 1.5 nm (approximating the spectral resolution and sampling expected from OCI). The Raman signal decreases with increasing chlorophyll-a concentration and CDOM absorption and exhibits fairly large spectral variations in some regions. For some intervals, namely 398.5–412.5 nm, 436.5–452.5, 473.5–484.5 nm, and 509.5–519.5 nm, however, the Raman signal is fairly constant with wavelength and the E_s variability with wavelength is sufficiently high to attempt a de-correlation of the Raman and elastic contributions to the TOA signal.

De-correlation of the two types of scattering can be accomplished by performing a linear fit of the observed spectral radiance (or equivalently reflectance) vs. the spectral solar irradiance in the intervals identified. In those relatively small spectral interval (10–15 nm wide), the spectral variation of the scattering properties, either elastic or Raman, can be assumed negligible, or, better, derived by a radiation transfer model with inputs of the optical aerosol and ocean properties as determined by the atmospheric correction algorithm. Note that the molecular atmospheric scattering contribution, which has a strong spectral dependence, can be subtracted from the TOA measurements. We have:

$$P(\lambda) = P_0(\lambda) + L_{w\_elastic}(\lambda) + \langle L_{w\_raman}\rangle + F(\lambda) \tag{12}$$

with $P_0(\lambda) = \left[L_{atm}(\lambda) - L_r(\lambda)\right]/t_u(\lambda,\theta)$ where $F(\lambda)$ is a spectral factor that depends on the water optical properties (since again they may not be constant over the spectral interval considered). The ordinate at the origin of the best linear fit P vs. E_s or downward irradiance at the surface, E_d, gives access to $\langle L_{w\_raman}\rangle$.

The approach and methodology are simple in principle, but to achieve useful accuracy a number of technical issues require attention: (1) Radiometric noise of the spectral measurements will result in an error on the water Raman scattering estimate that is amplified by the extrapolation of the linear fit to the ordinate axis; (2) Spectral resolution of the measurement will affect the variability of the spectral measurement as the solar spectrum is smoothed. A reduced variability of the solar spectrum will increase the error due to extrapolation; and (3) The sum of atmospheric and oceanic Raman scattering signals would be actually determined. Although the atmospheric Raman scattering is rather small (e.g., Vountas, 1998), it must be accounted for and subtracted from the water Raman scattering estimate; and (4) The Raman scattering signal can only be determined with good accuracy in some spectral intervals where the solar irradiance variability is large enough, namely around 390, 440, 475, and 515 nm, as indicated above. Interpolation/extrapolation to others wavelengths, definitively feasible, may not be straightforward since the Raman signal is not smooth spectrally.

Figure 34 illustrates the method feasibility. The various atmospheric functions were simulated in 5 nm bands shifted by 1.5 nm resolution for the 4 suitable spectral intervals using a successive-orders-of-scattering code. Aerosols were assumed of maritime type with an optical thickness of 0.2 at 550 nm, and wind speed was 5 m s^{-1}. Sun and view zenith angles were 30° and relative azimuth angle was 90°. The water-leaving radiance (elastic and inelastic components) was simulated using HYDROLIGHT for Case 1 waters with a chlorophyll-a concentration, *Chl-a*, of 0.03 mgm^{-3}. Typical CDOM absorption corresponding to biogenic particles was used. No noise was introduced on the TOA reflectance and atmospheric Raman scattering was neglected. Retrievals were obtained (1) assuming $F = 0$ (no spectral correction), and (2) assuming F was perfectly known.

When $F = 0$, large errors are obtained in the determination of $\langle L_{w\_raman}\rangle$, i.e., the methodology is not practically applicable. For example, in the 398.5–412.5 interval, the retrieved $\langle L_{w\_raman}\rangle$ value is 0.00028 instead of 0.00079 Wm^{-2}nm^{-1}sr^{-1} when *Chl-a* is 0.03 mgm^{-3}. In the 436.5–452.5 nm and 473.5–484.5 nm intervals, the retrieval is completely erroneous. When using F computed assuming that *Chl-a* is known, the $\langle L_{w\_raman}\rangle$ estimates are very close to the prescribed values. This indicates that knowledge of *Chl-a* is essential to retrieve $\langle L_{w\_raman} \rangle$ accurately.

Now *Chl-a* can be obtained from standard band-ratio algorithms with a typical uncertainty of ±30%. The impact of such uncertainty on the $\langle L_{w\_raman} \rangle$ retrieval is still too large. For the case mentioned above, the $\langle L_{w\_raman} \rangle$ estimate would range from 0.00058 to 0.00165 $\text{Wm}^{-2}\text{nm}^{-1}\text{sr}^{-1}$, which is not satisfactory. This means that *Chl-a* needs to be estimated more accurately for the methodology to work.

To estimate *Chl-a*, therefore *F*, more accurately, one may use the goodness of the linear fit (correlation coefficient). One expects that the linear regression will be more accurate when the spectral factor *F* corresponds to the actual *Chl-a* (see **Figure 34**). To increase sensitivity to *Chl-a*, especially in the presence of noise, the correlation coefficient may be computed for the 4 spectral intervals combined. This provides a practical way to determine the best *F* that corresponds to the observations. One could use a look-up table of *F(λ, Chl-a)* for each spectral interval to find the best *F* values that yield the best linear fit. As Raman scattering also depends on absorption by other variable constituents, the look-up table should include additional parameters (e.g., CDOM absorption coefficient). Additional theoretical and experimental work is needed, however, to demonstrate quantitatively the method's applicability to OCI imagery.

Estimation of Chlorophyll Fluorescence

Knowledge of the solar-induced chlorophyll fluorescence of natural waters is important to understanding the physiology of phytoplankton and investigating environmental influences on primary production and food web structure (e.g., Behrenfeld et al., 2009). Chlorophyll fluorescence can be remotely sensed from space, which has been routinely accomplished by instruments like MODIS and MERIS. The retrieval algorithms (Letelier and Abbott, 1996; Gower et al., 1999; Huot et al., 2005; Behrenfeld et al., 2009) involve the subtraction of a baseline representing the shape of the water reflectance spectrum without fluorescence. In waters containing sediments and yellow substances (Case 2 waters), determination of the baseline may not be accurate, yielding unacceptable uncertainties on the fluorescence height estimates, all the more as the chlorophyll concentration or the quantum yield of fluorescence are low. It is desirable to improve accuracy in these waters, for which fluorescence, unlike blue-to-green reflectance ratios, is a good measure of chlorophyll concentration.

To improve the estimate of chlorophyll fluorescence, one may use detailed spectral measurements in the oxygen B-band centered on 687 nm. The method exploits the fact that emitted fluorescence (observed at sea level) is excited at shorter wavelengths and is not affected by the oxygen absorption, contrary to the elastic water reflectance. As the absorption lines are partially filled due to inelastic fluorescence emission, the spectral change with respect to reflected solar radiance (i.e., to the elastic component) is sensitive to the fluorescence signal. By shifting the center wavelength in a spectral interval of 10–20 nm, one may be able to de-correlate the fluorescence signal from the elastic signal in the TOA measurements, therefore obtain a fluorescence estimate more independent from elastic scattering than the standard baseline technique. In other words, the fluorescence signal can be much more easily differentiated from the elastic signal when spectral measurements in the oxygen band are included.

Neglecting Sun glint, Raman scattering by water molecules, and assuming that in the spectral range of interest, i.e., 670–700 nm, gaseous absorption is only due to oxygen, the radiance L'_{TOA} measured from space, after correction for molecular scattering, can be expressed as:

$$
\begin{aligned}
L'_{TOA} = L_a T_{O2}\left(\theta_s, \theta, H_a\right) + L_{w\_elastic}\, t_u(\theta)\, T_{O2}\left(\theta_s, \theta, 0\right) \\
+ L_{w\_fluo}\, t_u(\theta)\, T_{O2}(\theta, 0) \quad (13)
\end{aligned}
$$

where $L_{w\_elastic}$ is the elastic water-leaving radiance, L_{w_fluo} is the radiance due to chlorophyll fluorescence, $T_{O2}\left(\theta_s, \theta, H_a\right)$ is the oxygen transmittance associated with the path radiance, $T_{O2}\left(\theta_s, \theta, 0\right)$ is the oxygen transmittance associated with the elastic water reflectance (affected by absorption along the Sun-to-surface path), and $T_{O2}(\theta, 0)$ is the oxygen transmittance associated with the fluorescence signal (only along the surface-to-satellite path). The transmittances $T_{O2}\left(\theta_s, \theta, H_a\right)$ and $T_{O2}\left(\theta_s, \theta, 0\right)$are different, the first one in particular depends significantly on the vertical distribution of the aerosols (average altitude or scale height H_a). In Equation (13), L_{w_fluo} can be expressed as the product of the radiance at the peak of fluorescence emission (i.e., 685 nm) and a known spectral function, *h* (see, e.g., Mobley, 1994), i.e., $L_{w\_fluo} = hL_{w\_fluo}(685)$.

The variable to retrieve is $L_{w\_fluo}(685)$, the fluorescence line height. This can be accomplished using a spectral optimization scheme, in which $L_{w\_fluo}(685)$ is varied to obtain the best fit between the modeled and actual (measured) TOA radiance L_{TOA}'. The aerosol radiance L_a and the aerosol optical thickness and model (affect transmittances) can be determined from measurements in the near infrared and/or shortwave infrared using standard algorithms. The oxygen transmittance $T_{O2}\left(\theta_s, \theta, H_a\right)$ can be computed from an estimate of H_a (e.g., from measurements in the oxygen absorption A-band centered on 763 nm, see Dubuisson et al., 2009 and section Estimation of Aerosol Vertical Profile) or assuming that the aerosols are located at an average aerosol altitude or at the surface. It is necessary to assume that the spectral shape of the elastic water-leaving radiance, $f(\lambda)$ is rather constant, or known from a model as a function of chlorophyll concentration, *Chl-a*, and particulate backscattering.

To demonstrate the method feasibility, Case 1 and Case 2 waters containing 0.1, 1, 5, and 30 mgm^{-3} of chlorophyll-a were considered. Absorption by yellow substances and sediment concentration were null for the Case 1 waters and fixed at 0.5 m^{-1} (440 nm) and 2 gm^{-3}, respectively, for the Case 2 waters. The fluorescence yield, which ranges from less than 0.01 to 0.10, was fixed at 0.05. Aerosols were of maritime type, with optical thickness of 0.2. The vertical profile of aerosol concentration was exponential with a scale height of 1 km. The TOA signal, including the coupling between oxygen absorption and aerosol scattering, was simulated with no noise using the quasi-single scattering approximation (a sufficient treatment to demonstrate feasibility). The HITRAN 2004 database was used to define spectroscopic parameters for oxygen absorption lines and compute oxygen transmittance. Absorption by water vapor was neglected. The simulations were performed for a single angular geometry, i.e., solar and viewing zenith angles of 45°, and a relative azimuth angle of 90°.

The spectral matching was accomplished on TOA reflectance, $\rho'_{TOA} = \pi' L_{OA}/[E_s \cos(\theta_s)]$ rather than radiance, using a function minimization scheme (Nelder and Mead, 1965) over the range 660–720 nm. (Similar results were obtained when restricting the range to 670–700 nm.) The aerosol optical properties (optical thickness and reflectance) were assumed perfectly known. The aerosol scale height H_a was assumed to be 0.5 km. The elastic water reflectance, $\rho_{w\_elastic} = \pi L_{w\_elastic}/[E_s \cos(\theta_s)\, t_d(\theta_s)]$, was parameterized as $\rho_{w\_elastic}(685) \langle f(\lambda) \rangle$ where $<f>$ is the average spectral function over all the water situations (*Chl-a* and water type). Thus the parameters used to adjust the modeled TOA reflectance, after correction for molecular scattering, were $\rho_{w\_elastic}(685)$ and $\rho_{w\_fluo}(685) = \pi L_{w\_fluo}/[E_s \cos(\theta_s)\, t_d(\theta_s)]$.

Figure 35 displays the results obtained for Case 1 and Case 2 waters containing 5 mgm^{-3} of chlorophyll-a. The retrieved and prescribed fluorescence signals agree well irrespective of water type, with differences <5% on $\rho_{w\_fluo}(685)$. The impact of a 0.5 km uncertainty on the 1 km aerosol scale height (i.e., 50%) is small, but increased errors may occur when the difference between actual and specified scale height is larger. Accuracy remains similar for all the chlorophyll-a values in Case 1 waters, but decreases substantially with decreasing *Chl-a* in Case 2 waters (**Figure 36**).

Compared with the standard baseline technique using bands centered on 665, 682, and 705 nm, the spectral optimization in the spectral range of the oxygen B-band provides much better results (**Figure 36**). For Case 1 waters, the errors on estimated $\rho_{w\_fluo}(685)$ are decreased from 15 to 20% to about 5%. For Case 2 waters, the improvement is even more dramatic: Errors are decreased from about 200% to 22% when *Chl-a* = 0.1 mgm^{-3}. The two techniques provide similar performance, however, in the presence of Case 2 when *Chl-a*> 5 mgm^{-3}, i.e., within about ±20%. Note that when *Chl-a* is high in Case 1 waters the influence of chlorophyll absorption at 670 nm on the elastic reflectance makes it more difficult to determine the baseline, which degrades the retrieval accuracy of the standard technique (**Figure 36**, left). These findings, based on simulations, were obtained in controlled conditions, and the documented advantages may not be as important in natural conditions, which needs to be examined in future work.

The above results, even though they demonstrate the potential of using the oxygen B-band to improve chlorophyll fluorescence estimates, were obtained without noise on the TOA signal. The acceptable level of radiometric noise needs to be evaluated to achieve useful accuracy. The wavelength range for spectral matching may be optimized for maximum sensitivity to fluorescence height and minimum sensitivity to elastic water reflectance. In this respect, one may consider differential absorption using narrow and wide spectral bands (e.g., 5 and 30 nm, respectively) centered on 687 nm. Centering the two bands on the same wavelength would reduce the impact of the elastic water signal on the estimates, but sensitivity to fluorescence height may be reduced (5 nm may be too wide for the narrow band). Errors in the retrieval of the aerosol optical thickness, reflectance, and scale height (supposed to be determined separately), need also to be included to determine realistically the expected error budget.

Estimation of Aerosol Vertical Profile

Information on the vertical aerosol profile is required for accurate atmospheric correction of satellite ocean-color imagery at short wavelengths (ultraviolet and blue) when absorbing aerosols are present (Gordon, 1997; Duforêt et al., 2007). This is due to the coupling between aerosol absorption and molecular scattering, which depends on the location of the aerosols in the vertical. Aerosol absorption reduces sun illumination and backscattering in the lower atmospheric layers, all the more as molecular scattering is large. Even if the standard atmospheric correction algorithm works well for "pure" scattering, an additional correction that depends on the aerosol vertical profile must be done at short wavelengths (see section Multiple Scattering).

The effect of aerosol absorption on the observed TOA reflectance, ρ_{TOA}, can be written as (e.g., Torres et al., 2002):

$$\rho_{abs} \approx -(1-\omega_{0a})\tau_a m^* [\rho_w t + \rho_r (P_s - P_a)/P_s] \tag{14}$$

where τ_a is the aerosol optical thickness, ω_{0a} is the aerosol single scattering albedo, $(1-\omega_{0a})\tau_a$ is the absorption optical thickness, and P_s and P_a are surface and aerosol layer pressure levels. The observed signal, ρ_{TOA}, is reduced due to aerosol absorption, all the more as aerosols are higher in the atmosphere, absorption optical thickness is larger, and air mass is larger. Note that marine reflectance exerts some influence on ρ_{abs}.

This is illustrated in **Figure 37**, which displays ρ_{abs} as a function of wavelength (350 to 1,000 nm) and aerosol pressure level (300 to 1,000 hP_a) for various aerosol models, i.e., continental (Con), urban (Urb), desert dust (DD), and biomass burning (BB). The calculations were made for a typical geometry, i.e., solar and viewing zenith angles of 30°, a relative azimuth angle of 90°, an aerosol optical thickness of 0.2 at 550 nm, and a null water reflectance. The absorption effect ρ_{abs} reaches −0.004 at 400 nm when aerosols are strongly absorbing (urban type) and located at 900 hP_a (**Figure 37**, left), but may be as large as 0.02 in magnitude at that wavelength when they are located higher in the vertical, i.e., at $P_a < 400$ hPa (**Figure 37**, right). For this relatively small aerosol optical thickness, ρ_{abs} remains significant in the presence of less absorbing aerosols (e.g., biomass burning and desert dust types), but would increase proportionally to optical thickness (see Equation 14). Neglecting ρ_{abs} in atmospheric correction algorithms, therefore, would yield unacceptable errors on water reflectance retrievals, well above the ±0.002 accuracy requirements for clear waters. Hence, taking into account aerosol vertical structure, a key variable controlling ρ_{abs}, is needed when dealing with absorbing aerosols.

As indicated above, the effect of aerosol absorption, when aerosols are concentrated in a layer of average pressure P_a, is proportional to the absorption optical thickness of the layer and to the molecular thickness below the layer, i.e., $P_s - P_a$. In the more general case of an aerosol profile, P_a is replaced, in first approximation, by an equivalent mean pressure $\langle P_a \rangle$, defined by the integral over pressure of the aerosol optical thickness (from top of atmosphere) normalized by the total aerosol optical thickness. Thus $\langle P_a \rangle$ is the vertical structure parameter to introduce for a more effective atmospheric correction in the ultraviolet and blue (details about the vertical structure do not need to be known). This equivalent pressure can be derived from spectral measurements in the oxygen A-band around 762 nm.

The envisioned methodology to retrieve $\langle P_a \rangle$ exploits the coupling between aerosol scattering and oxygen absorption. The TOA radiance measured in the oxygen A-band depends on the altitude of the atmospheric scatterers, especially aerosols. The higher the aerosols, the larger the reflectance, since a number of photons are backscattered to space instead of being absorbed by oxygen in the lower layers. In addition, the coupling between aerosol scattering and oxygen absorption, which enhances absorption, is less effective in this case because there are fewer molecules. Dubuisson et al. (2009) showed that the ratio of measurements in a band strongly attenuated by oxygen absorption (i.e., within the A-band) and in a band minimally attenuated (e.g., outside the A-band) is sensitive to aerosol altitude. Using a relatively large single band in the oxygen A-band (case of POLDER and MERIS), retrieval accuracy was only satisfactory when aerosol optical thickness was > 0.3.

The oxygen absorption band is a feature about 5 nm wide with two absorption maxima separated by about 3 nm. The oxygen transmission averaged at the spectral resolution of 5 nm, exhibits a larger absorption peak that at a larger spectral resolution, and some details of the spectrum are still present with a sampling every 1.25 nm, even 2.5 nm. Such sampling, possible with the PACE OCI, is expected to help retrieve more accurate information about the vertical profile of aerosol scattering. In juxtaposed 5 nm bands (or in larger spectral intervals) the spectral details would be missed, and the information about oxygen absorption would be too mixed with the out-of-band signal. An analysis of the effect of spectral resolution on the ability to use oxygen A-bands to retrieve aerosol layer height is given in Remer et al. (2019, this issue).

The inversion scheme is schematically the following. The objective is to retrieve the effective atmospheric pressure of the scattering aerosol profile, $\langle P_a \rangle$. Using a single scattering approximation, and neglecting surface reflectance, the TOA reflectance, ρ_{TOA}, can be written as:

$$\rho_{TOA}(\lambda) = \rho_{r,O2}(\lambda) + \rho_a(\lambda)\, T_{O2}(\lambda, \langle P_a \rangle) \tag{15}$$

Where $\rho_{r,O2}$ is the molecular scattering computed in the presence of oxygen absorption, ρ_a is the aerosol scattering reflectance interpolated from the close measurements at, for example, 748 and 865 nm, i.e., out of the absorption band, and T_{O2} is the oxygen transmittance at the equivalent pressure $\langle P_a \rangle$. The various terms of Equation 15 depend on angular geometry (not shown for simplification). A spectral fit algorithm is then applied to retrieve $\langle P_a \rangle$. The spectral fit, i.e., the retrieval accuracy, will definitively be better with measurements at 5 nm resolution every 1.5 nm in the oxygen A-band than with fewer measurements in consecutive 5 nm bands. The issues to investigate include the impact of spectral resolution and radiometric noise on the retrieval accuracy of $\langle P_a \rangle$, and the influence of aerosol type and amount, and surface reflectance, which may not be null in the oxygen A-band. Note, incidentally, that the derived apparent pressure would constitute an excellent test to detect and filter out semi-transparent or small broken clouds in the absence of measurements in the thermal infrared. Effort is already underway and reported in Remer et al. (2019, this issue) to confirm that aerosol layer top pressure can be retrieved using oxygen A-band spectroscopy at the 5 nm bands of OCI for aerosol optical thickness $\tau_a \geq 0.3$ for all surfaces and ≈ 0.1 for dark surfaces. In addition these studies show that τ_a may also be retrieved when angular information is added with a multi-angle polarimeter.

SIGNIFICANT ISSUES

In a seminal paper about atmospheric correction in the EOS era, Gordon (1997) discussed approximations and issues that remained to be addressed in developing and operating the 2-step multi-scattering standard algorithm. The issues at the time covered an extensive range of topics; they included whitecaps, aerosol vertical structure, appropriateness of aerosol models, absorbing aerosols, stratospheric aerosols, Earth's curvature, instrument polarization, surface roughness, in-water radiance distribution, diffuse transmittance, and radiometric calibration. Solutions (or approaches to solutions) were proposed to treat many of the issues, but some could not be handled properly, in particular those regarding aerosols. Alternative algorithms and the use of bi-directional and polarimetric information, however, have showed promise in difficult aerosol situations, either directly or indirectly (i.e., estimating aerosol optical properties separately), as demonstrated in sections Alternative Algorithms and Enhancements Using Multi-angular and/or Polarimetric Information. Some of the remaining issues are revisited here in view of new knowledge (whitecaps, Earth's sphericity), as well as others either not considered in Gordon (1997) (horizontal heterogeneity) or that came to the forefront with the new PACE capabilities (complex and large atmospheric interference in the UV).

Adjacency Effects

Evidence

Imagery of the Earth's surface (land and ocean) obtained from space at optical wavelengths is degraded due to the atmosphere (e.g., Tanré et al., 1979). One of these effects is the adjacency effect (also known as the environment or blurring effect), defined as the change in the digital number of a pixel caused by atmospheric scattering of radiance that originates outside of the sensor field-of-view. Tanré et al. (1987), among others, have provided evidence for the adjacency effect in satellite imagery of land and ocean/lakes. They showed that over water the spectral dependence of the aerosol scattering determined in the red and near infrared (where the ocean can be considered black) might differ substantially from the actual one when the environment reflectance is high (case of green vegetation). Building on previous work (Tanré et al., 1981), they proposed a theoretical formalism to describe, therefore correct the adjacency effect. Diner and Martonchik (1985) also investigated theoretically the influence of atmospheric scattering on blurring of surface details in imagery acquired from space. They predicted that blurring of a spatial boundary would be enhanced in the presence of large particles (increased forward scattering).

The adjacency effect is generally ignored in standard atmospheric correction schemes and operational processing of satellite ocean-color imagery. Yet its impact on water reflectance retrieval and derived products (e.g., chlorophyll-a concentration) may be important, especially near land, sea ice, and clouds, i.e., where the environment reflectance is much different from the target reflectance (e.g., Santer and Schmechtig, 2000). These authors reported from theoretical calculations that for a typical contrast between land and ocean reflectance of 0.3 at 865 nm and 0.07 at 670 nm, a chlorophyll-a concentration of 2 mgm^{-3} is underestimated by 25% at a distance of 10 km from a linear coastline when the atmospheric visibility is 23 km and by 50% when the visibility is 8 km. The underestimation becomes larger as chlorophyll-a concentration increases, with retrieved values 5 times smaller than actual values at 10 mgm^{-3} when the visibility is 8 km.

An example of adjacency effect is given in **Figure 38**, which displays MERIS Level 1 imagery at 865 nm over the Zuydersee in the Netherlands. Aerosol optical thickness is about 0.3. Higher reflectance is generally observed near the coast (**Figure 38**, left), which is attributed to scattering into the field-of-view of photons reflected by the contiguous vegetated land, highly reflective at 865 nm. The TOA reflectance change along a section across the Zuydersee (indicated by a black line in **Figure 38**, left) reaches about 0.02 toward the coast over a 5–10 km distance (**Figure 38**, right).

Figure 39 displays MERIS Level 2 imagery, i.e., water reflectance at 560 nm, after standard atmospheric correction. A band of smaller marine reflectance is observed all around Corsica and Northern Sardinia (**Figure 38**, left), whereas anomalously high reflectance is observed for the waters surrounded by ice in the Beaufort Sea (**Figure 25**, right). This is likely the complex result of adjacency effects at 560 nm and at the near-infrared wavelengths used for the atmospheric correction. Depending on the environment (vegetation or ice), the coupling between surface reflection and atmospheric scattering may either decrease (Corsica/Sardinia case) or increase (Beaufort Sea case) the apparent reflectance with increasing wavelength, but this spectral dependence is not captured by determining the atmospheric signal from measurements in the near infrared and extrapolating to shorter wavelengths. Other examples have been observed along the coast of the Baltic Sea, and in Norwegian fjords.

Formulation

Over a homogeneous water body of reflectance ρ_w, the TOA reflectance $\rho_{TOA}^{\mathrm{hom}}$ can be expressed approximately as [e.g., Tanré et al., 1979; see Equation 3)]:

$$\rho_{TOA}^{\mathrm{hom}} \approx T_g(\theta_s,\theta)[\rho_{atm} + \rho_w\, t_d(\theta_s)\, t_u(\theta)/(1-\rho_w S_{atm})] \quad (16)$$

where S_{atm} is the spherical albedo of the atmosphere and transmittance due to aerosol and molecule scattering and aerosol absorption. The term $(1-\rho_w S_{atm})$ accounts for multiple interactions between the atmosphere and the water body. Several approximations are used in Equation (16): (1) the surface is Lambertian; (2) Fresnel reflectance is neglected in the multiple interaction term, and (3) molecular absorption is decoupled from atmospheric scattering (i.e., T_g is simply a multiplicative factor).

Over a heterogeneous surface, one has to discriminate between the contribution of the target reflectance ρ_w viewed directly through the atmosphere and its background reflectance, ρ_e (Tanré et al., 1981, 1987; Santer and Schmechtig, 2000):

$$\begin{aligned}\rho_{TOA}^{het} \approx T_g(\theta_s,\theta)\left\{\rho_{atm} + t_d(\theta_s)\left[\rho_w exp(-\tau_{atm}/cos(\theta))\right.\right.\\ \left.\left.+\rho_e t_{u-dif}(\theta)\right]/(1-\rho_e S_{atm})\right\}\end{aligned} \quad (17)$$

where τ_a is the atmospheric optical thickness for scattering and $t_{u-dif}(\theta)$ is the diffuse component of total atmospheric transmittance due to atmospheric scattering, i.e., $t_u(\theta) = T_u(\theta) + t_{u-dif}(\theta)$. The approximation used in this second formulation is that the target background is homogeneous, which is of course an idealized case. Nevertheless, Equation 17 shows that the retrieval of ρ_w, using an atmospheric correction based on Equation 16 assuming a homogeneous scene, is affected by an error $\Delta\rho_{TOA}$ (i.e., the adjacency effect), which expression can be deduced from Equations 16 and 17:

$$\Delta\rho_{TOA} = \rho_{TOA}^{het} - \rho_{TOA}^{\mathrm{hom}} = (\rho_e - \rho_w)\, t_{u-dif}(\theta) T(\theta_s) \quad (18)$$

When the background is not uniform, which is the realistic case, the many individual contributions of every pixel that surrounds the target must be considered, and ρ_e becomes an average reflectance $\langle\rho_e\rangle$:

$$\langle\rho_e\rangle = \iint f\left(x,y\right)\rho_e\left(x,y\right)dxdy \quad (19)$$

where $f\left(x,y\right)$ is the atmospheric point spread function (PSF), which expresses the contribution to the measured reflectance of surface-leaving photons at horizontal coordinates $\left(x,y\right)$ scattered in the field of view, and $\rho_e\left(x,y\right)$ is the now spatially dependent environment reflectance. Given the properties of the atmospheric scattering, the PSF can be computed using a Monte Carlo code in backward mode, i.e., photons are injected in the direction of viewing and collected on the matrix of pixels at the surface (Reinersman and Carder, 1995). Eventually, the bi-directional reflectance of the pixel must be accounted for in Equation 19 (Sun glint, vegetation), which means an integration of the probability of viewing the given pixel from different altitudes.

For observations at nadir, $\langle\rho_e\rangle$ becomes (Tanré et al., 1981):

$$\langle\rho_e\rangle = \iint rg\left(r\right)\rho_e\left(r,\phi\right)drd\phi = \iint \left(\frac{dF}{dr}\right)\rho_e\left(r,\phi\right)drd\phi \quad (20)$$

r is the distance to the target, $rg\left(r\right)$ is equal to $f\left(r(x,y)\right)$, and $F\left(r\right)$ is the integral of $rg\left(r\right)$ between 0 and r, i.e., $F\left(r\right) = \int 2\pi r' g\left(r'\right)dr'$. The environment function $F\left(r\right)$ gives the relative contribution to $\langle\rho_e\rangle$ of surface points within a radius r of the target pixel, and normalization is obtained by integrating from $r = 0$ to infinity, i.e., $\int 2\pi F(r)\, dr = 1$.

Approximate analytical expressions of $F(r)$ are given in Tanré et al. (1981) for molecular and aerosol scattering (typical continental aerosol model, scale height of 2 km), i.e.,

$$F_m(r) \approx 1 - 0.93 exp(-0.08r) - 0.07 exp(-1.1r) \quad (21a)$$

$$F_a(r) \approx 1 - 0.037 exp(-0.2r) - 0.625 exp(-1.8r) \quad (21b)$$

where r is expressed in km. In the case of aerosols characterized by a scale height H_a different from 2 km, Equation 21b is simply modified by multiplying r in the two exponentials by the weighting factor $2/H_a$. For a mixture of molecules and aerosols, $F(r)$ becomes:

$$F(r) \approx [t_{ur-dif}\, F_m(r) + t_{ua-dif} F_a(r)]/(t_{ur-dif} + t_{ua-dif}) \quad (22)$$

where t_{ur-dif} and t_{ua-dif} are the diffuse transmittances for molecular and aerosol scattering, respectively. Equations (20) to (22) allow the computation of $\langle \rho_e \rangle$ and therefore $\Delta\rho_{TOA}$ for any pixel in a scene observed from space at nadir (or for nearly vertical sightings). They are helpful to understand the variability of the adjacency effect and to estimate its impact (i.e., expected errors) on the retrieval of the target reflectance. In the case of observations at slanted angles, the adjacency effect is more complicated to formulate analytically because of the lack of symmetry in azimuth [no simple insightful expression for $\langle \rho_e \rangle$].

Variability

The adjacency effect produced by molecular scattering and aerosol scattering is different and vary with $F(r)$ and the reflectance of the background/environment. These processes act over disparate scales, i.e., about 12 km for molecular scattering and less than 1 km for aerosol scattering (equations 21a and 21b). Pixels farther away have more influence, i.e., $F(r)$ has a larger spread, when aerosols are located higher in altitude ($1/H_a$ dependence in the exponentials of Equation 22). This also applies to cloudy situations. Furthermore, molecular scattering varies with wavelength and increases very rapidly in the blue, but F_m remains about the same with a good approximation. Aerosol scattering is less spectrally selective, but F_a given by Equation 21b is only typical. Changes in the aerosol physical properties, e.g., size distribution, would modify its single scattering phase function and the coefficients of the exponential decrease with distance r. Note that depending on solar and viewing geometry and Sun/sensor configuration with respect to the target and its environment, Fresnel reflection by the water surface (after scattering by the atmosphere) may contribute differently to the TOA signal (Santer and Schmechtig, 2000).

Figure 40 gives an example of adjacency effect when observing the ocean near the coast. The coastline is linear, the target is 5 km offshore, and the sensor is located above water or above land, viewing perpendicularly to the coastline at 30° zenith angle. The reflectance of land is 0.8 (typical value for snow) and isotropic, chlorophyll-a concentration is 1 mgm^{-3}, aerosols are of maritime type with scale height of 2 km and optical thickness of 0.3 at 550 nm, and wind speed is 5 m s^{-1}. The simulations are performed with a Monte Carlo Code operated in backward mode (Ramon et al., 2019). No assumptions are made regarding interactions between the surface and the atmosphere. TOA reflectance is higher due to the snow environment, especially at 380 nm, where atmospheric scattering is more effective (in first approximation the adjacency effect varies like $\tau_a \langle \rho_e \rangle$. For a Sun at zenith, the reflectance increase is 0.05 at 380 nm, 0.03 at 500 nm, and 0.01 at 800 nm. If not taken into account, these values, by acting directly and indirectly (via atmospheric correction), would yield unacceptable errors on water reflectance estimates. The effect is larger when the sensor is over land due to reduced Fresnel reflection. The degree of polarization, on the other hand, is smaller, especially when the sensor is above land.

Correction

The TOA imagery can be corrected systematically for the adjacency effect at the Level 1b and produce a Level 1c, so that the processing of Level 2 products can be done by assuming that the surface is homogeneous (i.e., using the "large target" formalism of standard atmospheric correction schemes). This can be accomplished using a classic de-convolution algorithm, in which the de-convolution matrix is determined iteratively, since the reflectance of neighboring Level 1b pixels is affected by the adjacency effect (Reinersman and Carder, 1995; Vermote et al., 1997; Santer and Zagolski, 2008). A single iteration should normally be sufficient. In Vermote et al. (1997), for example, $\langle \rho_e \rangle$ is obtained using the surface reflectance and aerosol properties determined assuming no adjacency effects. This allows one to estimate the adjacency effect, correct the TOA signal accordingly, and then iterate. One issue for operational application, however, is processing time, i.e., de-convolution schemes need to be optimized. The simplest option, easy to implement, is to correct only the adjacency effects associated with molecular scattering. A second option, more accurate, is to correct also the effects associated with aerosol scattering. This can be done by (1) assuming background aerosols or using aerosols with average properties (eventually seasonally and regionally dependent), or (2) estimating the aerosol properties (optical thickness, type, and altitude). In the case of clouds, one can assume that they are located at the surface, or one can estimate their altitude.

Another way to deal with the adjacency effect is to develop atmospheric correction algorithms that minimize its influence. In the scheme proposed by Gross-Colzy et al. (2007a), only the principal components of the TOA signal most sensitive to the water signal are used to estimate the water reflectance, which reduces the impact of ρ_{TOA} in many situations. In the POLYMER algorithm (Steinmetz et al., 2011) the atmospheric signal is modeled as a polynomial function of wavelength with three terms, i.e., $C_o + C_1\lambda^{-1} + C_2\lambda^{-4}$. The last term of the polynomial takes into account the coupling between molecular scattering and reflection by a gray surface (e.g., sea ice and clouds), which varies in λ^{-4}, but the polynomial may also account for other types of surface/atmosphere coupling.

Correcting systematically Level 1b imagery for the adjacency effect, either explicitly or implicitly via proper atmospheric correction schemes, is definitely recommended. For coarse resolution sensors, it may be sufficient to account for the effect due to molecular scattering (the spread function associated with aerosols is effective over a relatively small distance, typically 1–2 km). As a result, the accuracy, quality, and daily coverage of ocean-color products should be improved substantially over water surfaces contiguous to land surfaces, sea-ice, and clouds, and in the open ocean where spatial variability may be large (e.g., upwelling regions). Otherwise, non-negligible errors would affect the retrieval of water reflectance, with a significant change in spatial structure and correlation scales (may alter the interpretation of mesoscale variability patterns, see Doney et al., 2003).

Whitecaps

Importance

Whitecaps generated by breaking waves, generally composed of surface foam (large bubbles separated by a thin layer of water) and underwater bubbles, have a pronounced effect on the intensity and shape of visible light diffusively reflected by the ocean surface (e.g., Frouin et al., 1996; Moore et al., 2000; Stramski and Tegowski, 2001; Terrill et al., 2001; Zhang et al., 2002; Randolph et al., 2014). They may enhance dramatically water-leaving radiance on temporal scales of seconds to minutes (Frouin et al., 1996; Randolph et al., 2017) and affect large areas such as the windy Southern oceans. This is illustrated in **Figures 41**, **42**, which display, respectively, pictures of seas with whitecaps and a time series of surface reflectance affected by whitecaps. In the presence of whitecaps, the dark ocean appears much brighter (**Figure 41**). At a local scale, the water reflectance, about 0.08 in the blue in the absence of whitecaps, is increased to 0.4–0.7 (i.e., by a factor of 5–11) depending on the breaking event, and variability is large over time scales of 5 to 10 s (**Figure 42**). The frequency and intensity of such breaking wave features over a 1-km pixel would determine the enhanced reflectance observed by the PACE sensor.

When present, the enhanced reflectance from whitecaps needs to be removed in order to produce estimates of water reflectance suitable for standard ocean-optics applications. From space, since whitecap reflectivity is high, even a small fraction of whitecaps within the instrument's elementary field of view (i.e., within a pixel) may be problematic. The pixel reflectance is affected directly, but more importantly the spectral dependence of the whitecap reflectance skews the extrapolation to the visible of the aerosol signal determined in the near infrared, which may lead to water reflectance errors much larger (i.e., by an order of magnitude) than the requirements (Frouin et al., 1996).

Whitecap corrections are conducted as part of the overall "atmospheric correction" process, even though the signal does not originate in the atmosphere and can be considered a component of the water signal. The aim is to remove the signal due to actively breaking waves (Stage A), which includes surface foam (i.e., large bubbles separated by a thin layer of water) and underwater bubbles injected in the water column. It is not designed to remove enhancements due to the quiescent or mature phase of the whitecap (Stage B), when surface foam has dissipated, but bubbles are still present in the upper layer. In practice, much of the whitecap and the bubble plume signal is removed as part of the aerosol correction, since both foam and bubbles act to enhance near infrared reflectance and the current aerosol routines (heritage atmospheric correction) cannot distinguish between different sources of near infrared reflectance. However, some problems may arise due to the spectral dependence of whitecaps (mentioned above) and the coupling between molecular and aerosol scattering processes, which may differ significantly (since the amount of aerosols is artificially increased).

Current Approach to Whitecap Correction

The current approach is designed to remove the reflectance due to the actively breaking wave or bright white portion of the wave (Monahan, 1993) within each pixel. As part of that effort, an estimate of the fraction of the sea surface covered by whitecaps is generated for each pixel based on ancillary wind speed data. Whitecap fractions are commonly estimated using automated processing of digital photography of the sea surface (Brumer et al., 2017). However, comparisons of digital photography with radiometric approaches have shown that photographs capture primarily Stage A whitecaps and miss much of the Stage B bubble plumes that also enhance the surface reflectance. Many relations between whitecap fraction and wind speed have been developed over the last three decades for different ranges of wind speeds (Anguelova and Webster, 2006; Brumer et al., 2017). However, whitecap coverage can vary by several orders of magnitude at the same wind speed. At different locations in the world ocean, various environmental and meteorological factors act in concert but with different strengths and form a composite effect that either enhances or suppresses the effect of wind alone. These other factors include fetch and duration and the wind, water temperature, air temperature and stability of the lower atmosphere defined by the air/water temperature differential, salinity, current shear and long wave interaction, wave age, and the presence of surfactants such as organic films (reviewed in Scanlon and Ward, 2016). Hence, wind speed parameterizations should be viewed as "climatological" and cannot represent the instantaneous whitecap field required by remote sensing applications. In addition, other factors not related to wind speed could cause foam on water surfaces. High concentrations of the phytoplankton *Phaeocystis globos*a, for example, are associated with foam formation in coastal waters and on beaches (Armonies, 1989).

Satellite ocean color algorithms currently employ an expression for undeveloped seas based on wind speed at 10 m (U_{10}) where $f_{wc} = 8.75 \times 10^{-5}(U_{10} - 6.33)^{-3}$ (Stramska and Petelski, 2003), see **Figure 43**. This correction produces negative values below 6.33 m s^{-1} and is much higher than with other parameterizations at high wind speeds. To avoid overestimation, NASA implements a lower threshold of 6.33 m s^{-1} and an upper threshold equivalent to the whitecap fraction at 12 m s^{-1} in the operational code (**Figure 43**). Hence the highest fraction of the sea surface covered by whitecaps that is currently used is 1.6%. Although this range may cover the average conditions, whitecaps can occur at wind speeds as low as 3–4 m s^{-1} and the fractional whitecap coverage can approach 10% at wind speeds greater than 12 m s^{-1} (Brumer et al., 2017).

Measurement of the spectral reflectance of whitecaps is challenging due to the many types and stages of whitecaps, the rapid time scale on the order of seconds, determining the contribution of foam and background water, and potential contamination from reflectance of sun and skylight. Reflectance of whitecaps varies with the type of breaking wave (e.g., rolling breakers and plunging breakers) and the layers of foam produced. From historic data (Whitlock et al., 1982; Koepke, 1984), an age-averaged effective reflectance, ρ_{wc}, of 22% is used in the NASA standard whitecap algorithm for visible wavelengths up to 550 nm. Frouin et al. (1996) studied the visible and near infrared reflectance of sea foam found in the turbulent surf zone. Sea foam reflectance was found to monotonically decrease into the near infrared wavelengths due to enhanced water absorption in these wavelengths. The spectral dependence was confirmed from aircraft measurements of whitecaps in the open ocean (Nicolas et al., 2001). From this work, a reduction factor is applied for red and near infrared wavelengths such that whitecap reflectance is 0.889, 0.760, and 0.645 at 670, 765, and 865 nm respectively and interpolated between these values. Whitecap reflectance can be approximated for wavelengths between 555 and 865 nm as: $\rho_{wc}\,(\lambda > 555) = 0.22(-1.162 \times 10^{-3}\lambda + 1.653)$. For MODIS bands, this translates to whitecap reflectance of 22% from 412 to 555 nm and 19.3, 19.0, 17.2, and 14.1% at 667, 678, 748, and 869.5 nm, respectively.

Following the discussions above, the standard reflectance for actively breaking waves, ρ_{wc}, is multiplied by the estimated fraction of the sea surface covered by whitecaps, f_{wc}, to generate the within-pixel reflectance attributable to whitecaps. An important distinction must be made at this point. Whitecap reflectance is not treated as an "augmented" reflectance above the background reflectance, as is commonly interpreted. Because whitecaps are so bright, the signal is believed to dwarf the contributions from water reflectance and surface reflectance (skylight and glint). The estimate ρ_{wc} represents the total upwelling signal above the sea surface of a breaking wave, $E_u(0^+)$, normalized to the downwelling irradiance incident on the sea surface, $E_d(0^+)$. Hence, the ρ_{wc} used in this context is considered invariant of the water reflectance and sky conditions. However, the actual enhancements due to whitecap reflectance can be influenced by many other factors including the intensity of the wave breaking and the concentrations of optical constituents in the water.

This whitecap contribution to reflectance is propagated through the atmosphere to estimate the enhancement ρ_{wc}^{TOA} at the satellite. Assuming that whitecap reflectance is isotropic, we have:

$$\rho_{wc}^{TOA} = f_{wc}\ \rho_{wc} t_d(\theta_s) t_u(\theta) \tag{23}$$

The at-sensor signal due to whitecaps (ρ_{wc}^{TOA}) is then subtracted from the TOA reflectance measured at the satellite. This effectively accounts for the reflectance from the area of the sea surface that is covered by whitecaps. The whitecap-free area should also be weighted by (1-f_{wc}) following Gordon (1997). Ignoring this weighting term is generally not important in the currently implementation of the whitecap correction where whitecap fractions are <2%, but area-weighting the whitecap-free sea surface would be important if higher whitecap fractions were modeled like in the Southern Ocean or for applications to high spatial resolution satellites.

Future Possibilities

Several issues must be considered going forward into the PACE era. The algorithm discussed above is a very crude and inaccurate representation of the impact of foam and bubbles on water-leaving radiance. Data collected to date show that wind speed can only roughly approximate the whitecap coverage in a climatological sense and cannot provide accurate real-time estimates of fractional whitecap coverage. The current wind speed thresholds used in the whitecap approach provide a minimal and largely inaccurate estimate of whitecap fraction that can be an order of magnitude lower or higher in the environment. Furthermore, use of a single reflectance value for all whitecaps does not represent the large amount of variability in the types of breaking waves and foam that can occur on the sea surface. Reflectance of whitecaps is variable based on the strength of the wave breaking and is not necessarily invariant of water reflectance signal. The bubbles plume or Stage B also serves to enhance reflectance substantially above background reflectance and this component is not explicitly treated in the model. Finally, the PACE mission is proposed to be hyper-spectral from the ultraviolet (350 nm) to near-infrared (885 nm) and have shortwave infrared bands at 940, 1,038, 1,250, 1,378, 1,615, 2,130, 2,260 nm. The current simplified spectral model of whitecaps will need modification to account for the spectral variability of whitecap reflectance in the near and shortwave infrared (see below).

The PACE mission aims to provide a better separation of atmosphere and ocean processes. Currently, much of the whitecap and bubble correction, particularly during high wind conditions, is inaccurately modeled as an aerosol. Whitecaps and bubble serve to enhance reflectance across the near and short wave infrared and cannot be easily separated using the current aerosol routines. Aerosol modeling assumes that water-leaving radiance at two near infrared wavebands are zero or can be estimated with sufficient accuracy using a bio-optical model. The presence of foam and bubbles is not explicit to this formulation and can lead to errors in retrievals when incorrectly treated as spectrally dependent backscattering from waterborne hydrosols or from airborne aerosols.

With more spectral information, the contribution of whitecaps may be measurable in the hyper-spectral signal and removed as part of the data processing scheme without relying on wind speed measurements and single reflectance values (see Dierssen, 2019, this issue). Measured reflectances of whitecaps and generated foam reveal identifiable spectral features from visible to short wave infrared (**Figure 44**). These new values are largely consistent with the diminishing reflectance in NIR wavebands measured by Frouin et al. (1996), but also reveal many features in the signal that cannot be dealt with as a simple linear decrease into the near infrared. Reflectance dips occur particularly at 750, 980, and 1,150 nm that have enhanced liquid water absorption, a result of multiple scattering in and around the bubbles and foam.

A potential approach for PACE and other missions is to identify spectral features associated with whitecaps that are unique from atmospheric and oceanic spectral properties. Water absorbs differently based on whether it is in vapor, liquid or solid form. As discussed above, unique peaks and dips occur in the near infrared portion of the reflectance spectrum that are associated with weak absorbing features of liquid water. The measured spectrum of intense foam and bubbles at the sea surface associated with the wake of a ship with a peak reflectance of 40% in visible wavelengths, As derived in Dierssen (2019, this issue), the general shape of this reflectance can be modeled from the logarithm of water absorption.

The overall shape of whitecap reflectance is directly related to liquid water absorption from visible through shortwave infrared. Some divergence at ultraviolet and violet wavelengths is apparent and likely due to colored substances such as absorption due to colored dissolved organic matter in these coastal waters. However, the overall shape can be used to assess the contribution of whitecaps into the near infrared and shortwave infrared. Parameterizations based on other physical considerations (e.g., vertical structure) should be contemplated to allow a direct estimation of the whitecap effect on water reflectance.

One approach would be to measure the depth of a liquid water absorption feature (e.g., 980 nm) to estimate the "effective" contribution of whitecaps to the total pixel reflectance. If we presume that the water reflectance does not contain this liquid water feature, then the line-depth of the water-absorption feature at 980 nm, for example, can be related to a linear mixing of unaffected sea surface with different intensities and areas with foam and bubble plumes. If the background water is highly scattering due to sediments or floating vegetation, for example, then this water absorption feature may also be present in the background signal and such water types would need to be identified prior to assessing the whitecap contribution (Dierssen, 2019, this issue). Candidate algorithms to model the whitecap factor, A_{wc}, from the hyper-spectral radiance rather than the area-weighted whitecap fraction derived from wind speed are provided in Dierssen (2019, this issue). The whitecap factor is the fraction of a standard whitecap reflectance that accounts for enhancements in spectral reflectance of the sea surface above the background reflectance. Since A_{wc} is optically derived, it is better suited for atmospheric correction techniques because it specifically incorporates different levels of foam and bubbles associated with breaking waves and requires no implicit spatial scale.

In summary, decades of data have shown that wind speed models will not be able to predict the whitecap fraction with sufficient accuracy to use in daily remote sensing imagery. Use of other ancillary parameters such as fetch, air, and water temperature, and currents may have utility in further refining estimates of whitecap fraction. In the least, the Stramska and Petelski (2003) model should be replaced with a more recent parameterization that better fits both high and low wind speed conditions (e.g., Brumer et al., 2017). However, it is unlikely that the whitecap fraction and particularly the associated bubble plume will be predictable from wind speed data for any given image to within an order of magnitude (see scatter of data points in **Figure 43** above).

We should continue to refine spectral models of foam and bubbles to understand their impact on upwelling irradiance at the pixel level. As part of that effort, more hyper-spectral datasets are critical that provide a means to estimate reflectance of whitecaps over time and space under a wide variety of water types and whitecap conditions. New methods that seek to use the measured spectral information in near infrared wavelengths to estimate the contribution of whitecaps directly will provide a means to separate whitecaps from aerosols and other conditions where near infrared reflectance is non-negligible. Preliminary results have been conducted at the sea surface and more research is warranted to model the transmission of hyper-spectral reflectance from whitecaps through the atmosphere. Moreover, uncertainties need to be assessed when aerosol products are derived from at-sensor radiance that is "contaminated" by whitecaps and bubble plumes. Continuing to propagate such errors impacts the selection of spectral aerosol model and magnitude of aerosols, as well as impacts the spectral shape and magnitude of retrieved water-leaving radiance and associated ocean color products. Until correction methods with sufficient accuracy are found and tested widely across ocean provinces, we recommend that PACE images collected under high wind conditions, which may contain significant whitecap coverage, be flagged such that users will recognize higher uncertainty in the water reflectance and aerosol retrievals.

Finally, breaking waves on the ocean surface are areas of significant importance to air-sea interaction. Whitecaps foster climate-relevant physical and chemical processes in the ocean, including the production of sea salt aerosols, mixing processes, and the exchange of gas (e.g., CO_2, CH_4, DMS, water vapor) and heat with the atmosphere (Monahan and Spillane, 1984; Woolf, 1997; Asher and Wanninkhof, 1998; Woolf et al., 2007). Wave breaking generates turbulent kinetic energy in the surface ocean, driving upper ocean mixing, and transferring energy to currents and longer waves (Cavaleri et al., 2007). Visible manifestations of breaking waves (i.e., foam and bubbles) are related to the energy injected into the surface ocean. Using imagery to assess whitecaps directly will open up new science directions.

Earth's Curvature

It was mentioned in section From Multi-Spectral to Hyper-Spectral Remote Sensing that assuming a plane-parallel atmosphere might introduce significant atmospheric correction errors for Sun zenith angles $> 70°$. This was also the conclusion of Ding and Gordon (1995), who suggested that for those angles a sufficient treatment would be to compute the molecular reflectance with a spherical-shell atmosphere RT code. It is important to emphasize, however, that the effect of Earth's curvature is not only to increase intensity at grazing Sun zenith angles due to the smaller attenuation of the direct solar beam, but also to lower intensity at low Sun zenith angles due to a smaller illumination volume (e.g., Chowdhary et al., 2019, this issue;

Ramon et al., 2019). This second effect is generally understated, but critical for accurate atmospheric correction. **Figure 45** displays, as an example, Monte Carlo simulations of molecular reflectance, ρ_r, and aerosol reflectance, ρ_a, at 446, 558, 672, and 867 nm as a function of Sun zenith angle for a view zenith angle of 15° and a relative azimuth angle of 90°. Aerosols are of maritime type with optical thickness 0.1 at 550 nm. In the 0–75° Sun zenith angle range, differences between plane-parallel and spherical-shell calculations are relatively small (0.3–0.5%) for ρ_r, and reach 1.5% for ρ_a. However, since molecular scattering may be large and dominate the TOA signal, especially in the blue and UV, even a small fraction of 1% error in ρ_r would affect the water reflectance retrieval significantly (i.e., with resulting uncertainty above requirements). On the other hand, the impact of 1.5% differences in ρ_a is comparatively inconsequential for the aerosol loading considered (relatively small aerosol signal). But one expects non-negligible effects for higher view zenith angle and aerosol optical thickness. Thus Earth's curvature should be taken into account in generating at least Rayleigh LUTs (it is also recommended to use spherical-shell RT code for aerosol LUTs), and this for all solar and viewing geometries, not only large Sun zenith angles.

Multiple Scattering

Although the atmosphere is relatively thin optically compared with the water body, multiple scattering effects are not negligible in the atmosphere, especially at wavelengths for which scattering is effective (blue and UV). These effects are taken into account in atmospheric correction schemes, but their dependence on aerosol altitude is often neglected (case of the heritage algorithm in particular). It is generally assumed that aerosol altitude has a significant effect on the TOA signal only when aerosols are absorbing, which was discussed in section Estimation of Aerosol Vertical Profile. The coupling between scattering by molecules and aerosols, however, depends on their relative vertical distribution.

This is illustrated in **Figure 46**, which displays the coupling term of the aerosol reflectance at 443 nm for two very weakly absorbing models, i.e., Maritime with 98% humidity (M98) and Tropospheric with 70% humidity (T70). These models are part of the Shettle and Fenn (1979) suite used in early two-step atmospheric correction algorithms (e.g., Gordon and Wang, 1994; Gordon, 1997). Aerosol optical thickness is 0.1 at 865 nm, and aerosol concentration decreases exponentially with increasing altitude with scale height from 2 to 8 km. Sun zenith angle is 36.2°, and the results are presented as a function of viewing zenith angle (0 to 75°) in the principal plane of the Sun. Note that the coupling term can be negative since computed as the difference between the total atmospheric reflectance and the molecular component (i.e., with no aerosols) and the aerosol component (i.e., with no molecules) (Deschamps et al., 1983). It would always be positive if the molecular and aerosol components were computed for molecules only but in the presence of aerosols and for aerosols only but in the presence of molecules (Antoine and Morel, 1999). For some remote sensing geometries the effect of aerosol scale height reaches 0.002 (M98) and over 0.01 (T70) in amplitude, which in the case of T70 is one order of magnitude larger than the required accuracy on water reflectance. Thus it is important to include the effect of aerosol altitude when correcting the TOA signal for atmospheric effects, even when aerosols are little or not absorbing. This can be done using PACE observations at 5 nm resolution in the oxygen A-band, especially using the sub-5nm spectral sampling capabilities of the OCI, which allow an estimate of aerosol altitude or scale height (see section Estimation of Aerosol Vertical Profile).

UV Observations

Observing in the UV is important to separate absorption by CDOM and phytoplankton pigments, to distinguish hydrosol types (e.g., sediments from organic particles) in optically complex waters, to allow the discrimination of functional, taxonomic, and harmful algal groups, and to improve atmospheric correction in the presence of absorbing aerosols. Hence measurements in the UV (from 350 nm) constitute a key PACE mission requirement. Retrieving accurately the water signal in the UV, however, presents a number of specific challenges that originate chiefly from the large optical thickness of the atmosphere. These challenges are emphasized in the following; see also Chowdhary et al. (2019, this issue) for a discussion of the UV regime in the context of RT modeling for atmospheric correction.

(1) The water reflectance contribution to the TOA signal is small in the UV, often much smaller than in the visible, especially when CDOM absorption is strong. This can be exploited in some situations (i.e., when the water signal is negligible) to constrain the aerosol signal estimated from NIR to SWIR wavelengths in a classic atmospheric correction scheme, but in general the water reflectance retrieval is more difficult. In addition, errors in estimating the spectral shape and magnitude of reflected sky radiance off of wind-roughened seas are enhanced in the UV. Currently this component is modeled as part of the Rayleigh LUTs for wind-roughened surfaces and is not validated with field data. A further complication is that aerosol and CDOM absorption may act similarly, i.e., their effects on the TOA signal may not be easy to separate. Also the steep decrease of solar irradiance due to absorption bands in this spectral range makes radiometric calibration difficult.

(2) Multiple scattering and coupling processes between molecular scattering and aerosol absorption are effective, and the resulting effect strongly depends on the relative vertical distribution of molecules and aerosols. This significantly complicates the atmospheric correction problem, for which knowledge of aerosol altitude becomes necessary. This will be possible with OCI (see section Estimation of Aerosol Vertical Profile and Remer et al., 2019, this issue). In one-step deterministic and statistical schemes, however, aerosol altitude can be variable, i.e., taken into account in determining the best solution.

(3) The influence of the environment, and in general spatial heterogeneities in the atmosphere, surface, and water body properties, is substantial (since depending on atmospheric transmittance, which itself depends exponentially on optical thickness see section Adjacency Effects and **Figure 40**, left), and

the "large target" formalism may not yield acceptable water reflectance retrievals in coastal oceanic regions and water bodies surrounded by land (lakes, ponds, rivers).

(4) The spherical albedo of the atmosphere becomes large (e.g., 0.37 at 350 nm for a clear atmosphere) and neglecting the multiple interactions between the water body and the atmosphere may introduce errors of up to 2% (case of oligotrophic waters) on water reflectance estimates.

(5) Errors in the spectral dependence of aerosol scattering in the NIR and SWIR, by propagating through the standard algorithm, may translate into large errors in the UV (since further away than the visible). This and the complex RT processes in the UV make it difficult to achieve via "system" vicarious calibration (Franz et al., 2007) radiometric accuracy within a small fraction of 1%.

Figure 47 displays various components of the TOA signal and their relative importance for typical conditions, i.e., a WMO maritime atmosphere (aerosol optical thickness of 0.2 at 550 nm) over waters with chlorophyll-a concentration of 0.1 mgm^{-3} and CDOM absorption of 0.02 m^{-1} at 440 nm. Spectral range is 350–400 nm, Sun and view zenith angles are 30 and 15°, respectively, relative azimuth angle is 90°, aerosol scale height is 2 km, and wind speed is 7 $\mathrm{m\ s}^{-1}$. The water signal represents only 3 to 5% of the TOA signal and 34 to 42% of the TOA signal corrected for molecular scattering effects, with the lower values at 350 nm and the higher values at 400 nm. For waters with the same chlorophyll concentration but zero CDOM absorption, however, the contribution of the water signal would be larger, i.e., 8 to 12% and about 62%, respectively. For smaller aerosols, e.g., tropospheric type, the relative importance of the water signal would be reduced at shorter wavelengths. The small contribution of the water signal to the TOA signal stresses the importance of accurate radiometric calibration and modeling of molecular effects. In the case of **Figure 47**, an error as small as 0.1% on the TOA reflectance would already translate into a 3.3% error on the water reflectance at 350 nm.

Figure 48 displays the absorption effect of a continental aerosol with scale height of 2, 5, and 8 km on the TOA signal and the effect of CDOM absorption (0.01, 0.02, and 0.1 m^{-1} at 440 nm) on the water signal observed at TOA. The absorption effect is the difference between the atmospheric reflectance at TOA in the presence of aerosol absorption and without absorption (see section Estimation of Aerosol Vertical Profile and Equation 14). Chlorophyll-a concentration is 1 mgm^{-3}. Spectral range, angular geometry, wind speed, and aerosol optical thickness are the same as in **Figure 47**. For the CDOM absorption effect, i.e., the difference between the water signal with and without CDOM absorption, aerosol scale height (slightly affects the atmospheric transmittance) is 2 km. The spectral dependence of the aerosol and CDOM absorption effects is comparable, making distinction of the two signals difficult in some one-step atmospheric correction schemes (e.g., spectral-matching). For example, 0.01 m^{-1} of CDOM absorption has nearly the same effect as aerosol absorption when scale height is 2 km, i.e., about −0.002 over 50 nm.

STRATEGY FOR ATMOSPHERIC CORRECTION

The standard, 2-step approach to atmospheric correction of satellite ocean-color imagery has been used operationally by space agencies since the CZCS was launched in 1978 to process data from major large-scale ocean color missions into water reflectance. The approach has proved to be robust, sufficiently accurate, and useful for many applications, scientific and societal (IOCCG, 2008). Its chief advantage over a variety of alternatives, as pointed out in sections Heritage Atmospheric Correction Algorithm and Alternative Algorithms, is that essentially minimal assumptions about water reflectance, the signal to be retrieved, are made. Algorithms have evolved and improved to account for new capabilities (e.g., observations in the shortwave infrared to deal with turbid waters) and take advantage of new knowledge (e.g., aerosol optical properties, whitecap reflectance), but have followed the same principle of using a spectral region where the water body is not or little reflecting to isolate the perturbing influence of the atmosphere and surface. In view of the success of this heritage approach, and the fact that it has been selected and applied systematically to correct imagery from most ocean color sensors, it is highly desirable to continue its usage in current and future processing lines, in particular for the PACE OCI. The adaptation to hyper-spectral OCI would address the challenges associated with observing in the ultraviolet and dealing with strong gaseous absorption bands; see section From Multi-Spectral to Hyper-Spectral Remote Sensing. Observing in the UV, even with hyper-spectral capability, continues to be an open question and area of active research, but does not negate the overall benefit of proceeding with a heritage 2-step retrieval for OCI. This continuity would maintain a certain level of consistency across sensors from different missions, allowing for a long-term record of water reflectance relatively free of algorithm-related discrepancies and biases. Furthermore, new methodologies may not be applicable to some sensors, complicating the generation of accurate long-term time series.

The heritage algorithm, however, has important limitations, as discussed in section Procedures. In particular it cannot handle properly situations of absorbing aerosols (i.e., dust, biomass burning and pollution particles), which are encountered over large oceanic regions and the coastal zone, reducing the spatiotemporal coverage of ocean color products, therefore their utility for scientific investigations and operational oceanography. It also does not work in Sun glint regions and in the presence of clouds, resulting in a typical 10–15% daily spatial coverage. To resolve these issues, one needs to move to further explore and implement alternative algorithms, deterministic or statistical, such as those described in section Alternative Algorithms. These algorithms exploit observations in the entire set of available spectral bands and eventually include, depending on the sensor, bidirectional and polarization information, either directly or indirectly (e.g., to constrain the set of possible aerosol models). So far only a few new algorithms have been checked thoroughly and applied systematically (i.e., at the scale of a satellite mission), notably the Steinmetz et al. (2011) spectral matching POLYMER algorithm and the Schroeder et al. (2007) neural network algorithm. Neural network atmospheric correction including sun glint correction was part of MERIS standard processing for Case 2 waters during the whole lifetime of the mission. Most of the advanced algorithms have been only tested on a few images, and they need to be further evaluated theoretically and experimentally and examined for robustness, reliability, and general applicability in an operational context. Their potential, however, as demonstrated in the examples presented in section Alternative Algorithms, is undoubtedly great to improve atmospheric correction in difficult situations (i.e., absorbing aerosols, turbid waters, Sun glint, whitecaps, land proximity, sea ice, thin clouds), offering the opportunity to generate more accurate ocean color products with wider coverage (i.e., less gaps) that will allow a better description of ocean properties (IOPs, concentrations) and biogeochemical phenomena.

In view of the above, a suitable strategy for atmospheric correction during the PACE era would be to continue performing atmospheric correction with the standard, 2-step heritage algorithm, adapted/adjusted as necessary, but at the same time applying the best advanced algorithm that fits the characteristics and capabilities of a given sensor, or a suitable combination of sensors. In the case of PACE, it is expected (by mission design) that OCI and polarimeters will be used synergistically. The selected methodology may be different, indeed, for a sensor that only measures spectrally total TOA radiance and a sensor that also measures directionally polarized TOA radiance. Whenever possible satellite data from previous missions would be re-processed with the new algorithm. An elaborate flagging system, although not easy to define and validate, is necessary to warn the user about doubtful algorithm performance. The quality of the atmospheric correction processors, therefore selection of the best one, could be assessed following procedures developed by Müller et al. (2015a,b) for the ESA Ocean Color-Climate change Initiative (OC-CCI), which include in a straightforward fashion not only comparisons with *in situ* measurements, but also analysis of image quality and processor behavior along scan line (e.g., spatial and temporal homogeneity and consistency in water reflectance retrieval). Since individual advanced algorithms may lead to improved products (or may perform similarly) in some situations, or have advantageous features, their implementation in data analyzing systems such as SeaDAS would provide the user community with best options depending on the study or application. This strategy would generate two separate water reflectance products, which is not a problem as long as respective advantages and limitations are understood and uncertainties specified, preferentially on a pixel-by-pixel basis. Thus we would end up with a continuity product and an advanced product that fully exploits the mission capabilities, which for PACE will combine hyper-spectral radiometry and multi-angle polarimetry. The two products could be merged optimally, at the Level 3 highest resolution possible, i.e., native resolution, taking into account their uncertainties (bias and standard deviation). Various merging procedures exist (see IOCCG, 2007 for a review), and choosing the best procedure will depend critically on the representation of algorithm performance and uncertainties (expected to be better and smaller, respectively, for the advanced algorithm).

CONCLUSIONS

Substantial progress in atmospheric correction of ocean-color imagery has been made since the proof-of-concept CZCS mission that demonstrated the feasibility of retrieving water reflectance from space and led to the first generation of operational ocean-color sensors (SeaWiFS, MODIS, MERIS, VIIRS, etc). Compared with CZCS, the new sensors have higher radiometric sensitivity and they measure in more and better-defined spectral bands in the visible. They also have spectral bands in the near infrared and (for some sensors) shortwave infrared, facilitating the removal of atmosphere and surface effects. This has generated a flurry of activities aimed at developing efficient atmospheric correction algorithms that exploit the new capabilities, which has contributed to a better understanding of the problem and resulted in significant improvements and new avenues.

Since the first attempts, the approach to atmospheric correction has essentially remained a 2-step process, in which the perturbing effects of the atmosphere and surface are determined in spectral bands where the signal from the water body can be considered negligible (i.e., in the near infrared and/or shortwave infrared) and propagated or extrapolated to the shorter spectral bands. Definite improvements to algorithms based on this approach have been made, notably in the specification of the aerosol models (based on AERONET measurements), the correction of gaseous absorption (e.g., nitrous oxide influence in the blue), and the processing of imagery over optically complex waters, where the water-leaving signal in the near infrared (or even SWIR) is not negligible and must be estimated through iterative bio-optical modeling. A number of approximations and issues have been identified and studied, such as whitecaps, Sun glint, aerosol vertical structure, polarization, sea surface roughness, Earth curvature, in-water radiance angular distribution, diffuse transmittance, absorbing atmospheric gases, absorbing aerosols, stratospheric aerosols, optically thin clouds, highly turbid waters, and adjacency effects. For some of these issues, satisfactory solutions have been proposed and implemented operationally, but not for others (e.g., absorbing aerosols, whitecaps, adjacency effects). In the absence of satisfactory solutions for a given observing condition, the operational approach has been to allow the atmospheric correction to fail, or to flag the water reflectance retrievals as suspect quality. This has resulted in large data gaps in some regions, preventing the efficient utilization of ocean color products.

Alternative approaches, deterministic and statistical, which aim at inverting the top-of-atmosphere signal (i.e., retrieving the water reflectance) in a single step, have been developed with varied degrees of success. The information in all available spectral bands is generally used, which is advantageous in some situations (e.g., absorbing aerosols), but the main drawback is that water reflectance, i.e., the signal to retrieve, is often constrained by a model (which may not represent well the environmental conditions of a given observation). Some algorithms have been able to handle situations of Sun glint and thin clouds, increasing significantly the daily coverage of ocean color products. All the proposed methods, however, have been based on multi-spectral observations, the information generally available; few attempts have been made to exploit the polarized and/or directional properties of reflected sunlight (available for some sensors, e.g., POLDER and MISR), but the potential of these properties to improve atmospheric correction (e.g., to enhance the contribution of water reflectance, to deal effectively with Sun glint, and to determine absorption effects) has been recognized and, to some extent, demonstrated. The improvements revealed in the selected examples, however, need to be confirmed (e.g., by analyzing other situations) before drawing final conclusions.

The PACE mission, which will carry into space a spectrometer measuring at 5 nm resolution in the UV to NIR with additional spectral bands in the SWIR and two multi-angle polarimeters, has great potential for improving estimates of water reflectance in the post-EOS era. The improved instrument capabilities offer opportunities, but retrieving a continuous water reflectance spectrum at 5 nm resolution in the UV to NIR, a chief mission objective, poses new challenges. First, measurements in the UV, where molecular scattering is effective (and may dominate the signal), are strongly affected by the vertical structure of atmospheric scatterers, and adjacency effects are large. Second, correcting measurements in spectral regions where gaseous absorption is strong may be difficult when absorbers are located in lower atmospheric levels (e.g., water vapor) due to coupling between scattering and absorption. Observing in the UV to SWIR, however, is adapted to the problem since observations in the UV are sensitive to absorbing aerosols, those in the SWIR to coarse aerosols (and they allow a better separation of the atmospheric/surface signal), and those in the oxygen-A band (763 nm) to aerosol altitude, a parameter controlling aerosol absorption effects. This is especially useful for inversion schemes that incorporate all the available information to retrieve water reflectance. Polarized and multi-angular measurements, sensitive to aerosol type, increase the information content in the inversion process and, therefore, are expected to yield more accurate retrievals, but the possibilities and improvements have yet to be fully investigated.

During the PACE era one may envision an approach to atmospheric correction that is based primarily on the heritage 2-step algorithm, taking into account and extending past accomplishments, yet exploiting as much as possible new capabilities (observations in the UV and in oxygen-A band) and multi-angular polarimetry (e.g., to constrain the aerosol model ensemble or estimate directly aerosol absorption effects). It should be clear that polarized and directional measurements are essential here, due to the inherent limitations of the heritage algorithm, in particular its inability to handle absorbing aerosols, which may affect large oceanic areas. This strategy, aimed at ensuring continuity with previous ocean-color missions, should be complemented by the development and implementation of more sophisticated inversion schemes (deterministic, Bayesian) that, by the nature of their construction, their robustness, and their generalization capabilities, have the undeniable potential to become the new standard in the near future.

Despite the progress made and the major improvements in atmospheric correction expected during PACE, important gaps/issues still remain to be filled/tackled. They include (1) improving the accuracy of whitecap corrections, for which coverage and optical properties are highly variable and difficult to model, (2) accounting for Earth curvature effects in atmospheric radiative transfer, which may be significant even at small zenith angles, (3) correcting for adjacency effects (influential near land, sea ice, and clouds) and cloud shadows, (4) accounting for the coupling between scattering and absorption (especially important in the UV where the molecular scattering signal is large), (5) modeling accurately water reflectance, including polarization (too little is known about the polarization properties of hydrosols), and (6) acquiring a sufficiently representative data set of water reflectance in the UV to SWIR to describe the variety of water bodies (such prior information is needed in Bayesian approaches). Dedicated efforts, experimental as well as theoretical, are in order to gather the necessary information and resolve inadequacies. Ideas and solutions exist and have been put forward to address the unsolved issues, thanks especially to the new capabilities provided by PACE, which will mark the beginning of a new era of accurate ocean-color radiometry from space.

AUTHOR CONTRIBUTIONS

This work was a statement of findings by the Atmospheric Correction subgroup of the first NASA PACE Science Team (Principal Investigators and Associates). All the authors contributed to the conception and organization of the study, the analysis of the results, and the writing of the sections. They critically revised the manuscript and helped to bring about the final version. RF developed the overall structure of the manuscript and arranged the contents of the sections. He also led the writing of sections Introduction, Improvements Using Super-sampling in Selected Spectral Intervals, Significant Issues, Strategy for Atmospheric Correction, and Conclusions. LR, EB, OD, and AO contributed to the section Introduction and provided invaluable comments to the other sections. BF, AI, KK, ZA, and B-CG wrote the section Heritage Atmospheric Correction Algorithm. BC, JC, OD, XH, DT, OK, AD, RF, and P-WZ wrote the section Alternative Algorithms. LG, BP, FS, RF, and DR provided results for that section. KK, OK, LR, LG, OC, AO, and AD wrote or contributed to the section Enhancements Using Multi-Angular and/or Polarimetric Information. JT, P-YD, LR, OK, OC, AO, and AD provided useful insight for the section Improvements Using Super-sampling in Selected Spectral Intervals. HD, DR, P-YD, JT, and JC contributed to the section Significant Issues. BF, AI, and LR helped to work out the atmospheric correction strategy (section Strategy for Atmospheric Correction) and to form the conclusions of the study (section Conclusions).

FUNDING

The National Aeronautics and Space Administration's Ocean Biology and Biogeochemistry Program, managed by Dr. Paula Bontempi, provided funding for the study under solicitation NNH13ZDA001N-PACEST.

ACKNOWLEDGMENTS

The PRISM flight over Santa Monica Bay was enabled by a PRISM AITT grant from NASA ESTO. We thank other sponsors including: the NASA Earth Science Division for the AVIRIS-NG instrument and the data analysis program Utilization of Airborne Visible/Infrared Imaging Spectrometer Next Generation Data from an Airborne Campaign in India NNH16ZDA001N-AVRSNG, managed by Dr. Woody Turner; the Jet Propulsion Laboratory and California Institute of Technology President and Director's Fund; the Jet Propulsion Laboratory 20 Research and Technology Development Program; and the NASA Center Innovation Fund managed in conjunction with the Jet Propulsion Laboratory Office of the Chief Scientist and Technologist. RF acknowledges the technical support of Mr. John McPherson, Scripps Institution of Oceanography. A portion of this research took place at the Jet Propulsion Laboratory, California Institute of Technology.

SUPPLEMENTARY MATERIAL

The Supplementary Material for this article can be found online at: https://www.frontiersin.org/articles/10.3389/feart.2019.00145/full#supplementary-material

REFERENCES

Ahmad, Z., and Franz, B. (2014). *Effect of Mineral Dust On Ocean Color Retrievals From Space: A Radiative Transfer Simulation Study.* American Geophysical Union, Ocean Sciences Meeting 2016, abstract #ME54C-0950.

Ahmad, Z., Franz, B. A., McClain, C. R., Kwiatkowska, E. J., Werdell, J., Shettle, E. P., et al. (2010). New aerosol models for the retrieval of aerosol optical thickness and normalized water-leaving radiances from the SeaWiFS and MODIS sensors over coastal regions and open oceans. *Appl. Opt.* 49:5545. doi: 10.1364/AO.49.005545

Ahmad, Z., and Fraser, R. S. (1982). An iterative radiative transfer code for ocean-atmosphere Systems. *J. Atmos. Sci.* 39, 656–665. doi: 10.1175/1520-0469(1982)039<0656:AIRTCF>2.0.CO;2

Ahmad, Z., Mcclain, C. R., Herman, J. R., Franz, B. A., Kwiatkowska, E. J., Robinson, W. D., et al. (2007). Atmospheric correction for NO2 absorption in retrieving water-leaving reflectances from the SeaWiFS and MODIS measurements. *Appl. Opt.* 46, 6504–6512. doi: 10.1364/AO.46.006504

Ahn, J.-H., Park, Y.-J., Ryu, J.-H., Lee, B., and Oh, I. S. (2012). Development of atmospheric correction algorithm for Geostationary Ocean Color Imager (GOCI). *Ocean Sci. J.* 47, 247–259. doi: 10.1007/s12601-012-0026-2

Anderson, G., Clough, S., Kneizys, F., Chetwynd, J., and Shettle, E. (1986). *AFGL Atmospheric Constituent Profiles (0–120 km), Tech.* Rep. AFGL-TR-86-0110, Hanscom Air Force Base, MA: Air Force Geophysics Laboratory.

Anguelova, M. D., and Webster, F. (2006). Whitecap coverage from satellite measurements: A first step toward modeling the variability of oceanic whitecaps. *J. Geophys. Res.* 111:C03017. doi: 10.1029/2005JC003158

Antoine, D., and Morel, A. (1999). A multiple scattering algorithm for atmospheric correction of remotely sensed ocean colour (MERIS instrument): principle and implementation for atmospheres carrying various aerosols including absorbing ones. *Int. J. Remote Sens.* 20, 1875–1916. doi: 10.1080/014311699212533

Antoine, D., and Nobileau, D. (2006). Recent increase of Saharan dust transport over the Mediterranean Sea, as revealed from ocean color satellite (SeaWiFS) observations. *J. Geophys. Res.* 111:D12214. doi: 10.1029/2005JD006795

Armonies, W. (1989). Occurrence of meiofauna in Phaeocystis seafoam. *Mar. Ecol. Progr. Series* 53, 305–309. doi: 10.3354/meps053305

Asher, W. E., and Wanninkhof, R. (1998). The effect of bubble-mediated gas transfer on purposeful dual-gaseous tracer experiments. *J. Geophys. Res.* 103, 10555–10560. doi: 10.1029/98JC00245

Bailey, S. W., Franz, B. A., and Werdell, P. J. (2010). Estimation of near-infrared water-leaving reflectance for satellite ocean color data processing. *Opt. Express* 18:7521. doi: 10.1364/OE.18.007521

Behrenfeld, M. J., Westberry, T. K., Boss, E. S., O'Malley, R. T., Siegel, D. A., Wiggert, J. D., et al. (2009). Satellite-detected fluorescence reveals global physiology of ocean phytoplankton. *Biogeosciences* 6, 779–794. doi: 10.5194/bg-6-779-2009

Bishop, C. M. (1995). *Neural Networks for Pattern Recognition.* New York, NY: Oxford University Press.

Bodhaine, B. A., Wood, N. B., and Dutton, and, E. G., Slusser (1999). On Rayleigh optical depth calculations. *J. Atmos. Ocean. Technol.* 16, 1854–1861. doi: 10.1175/1520-0426(1999)016<1854:ORODC>2.0.CO;2

Brajard, J., Jamet, C., Moulin, C., and Thiria, S. (2006). Use of a neuro-variational inversion for retrieving oceanic and atmospheric constituents from satellite ocean colour sensor: application to absorbing aerosols. *Neural Netw.* 19, 178–185. doi: 10.1016/j.neunet.2006.01.015

Brajard, J., Moulin, C., and Thiria, S. (2008). Atmospheric correction of SeaWiFS ocean color imagery in the presence of absorbing aerosols off the Indian coast using a neuro-variational method. *Geophys. Res. Lett.* 35:L20604. doi: 10.1029/2008GL035179

Brajard, J., Santer, R., Crépon, M., and Thiria, S. (2012). Atmospheric correction of MERIS data for case-2 waters using a neuro-variational inversion. *Remote Sens. Environ.* 126, 51–61. doi: 10.1016/j.rse.2012.07.004

Bréon, F. M., and Colzy, S. (1999). Cloud detection from the spaceborne, POLDER instrument and validation against surface synoptic observations. *J. Appl. Meteorol.* 38, 777–785. doi: 10.1175/1520-0450(1999)038<0777:CDFTSP>2.0.CO;2

Bréon, F. M., and Goloub, P. (1998). Cloud droplet effective radius from spaceborne polarization measurements. *Geophys. Res. Lett.* 25, 1879–1882. doi: 10.1029/98GL01221

Brumer, S. E., Zappa, C. J., Brooks, I. M., Tamura, H., Brown, S. M., Blomquist, B. W., et al. (2017). Whitecap coverage dependence on wind and wave statistics as observed during SO GasEx and HiWinGS. *J. Phys. Oceanogr.* 47, 2211–2235. doi: 10.1175/JPO-D-17-0005.1

Caudill, T. R., Flittner, D. E., Herman, B. M., Torres, O., and McPeters, R. D. (1997). Evaluation of the pseudo-spherical approximation for backscattered ultraviolet radiances and ozone retrieval. *J. Geophys. Res. Atmos.* 102, 3881–3890. doi: 10.1029/96JD03266

Cavaleri, L., Alves, J.-H. G. M., Ardhuin, F., Babanin, A., Banner, M., Belibassakis, K., et al. (2007). Wave modelling – The state of the art. *Prog. Oceanogr.* 75, 603–674. doi: 10.1016/j.pocean.2007.05.005

Chami, M., Santer, R., and Dilligeard, E. (2001). Radiative transfer model for the computation of radiance and polarization in an ocean–atmosphere system: polarization properties of suspended matter for remote sensing. *Appl. Opt.* 40:2398. doi: 10.1364/AO.40.002398

Chomko, R. M., and Gordon, H. R. (1998). Atmospheric correction of ocean color imagery: use of the Junge power-law aerosol size distribution with variable refractive index to handle aerosol absorption. *Appl. Opt.* 37:5560. doi: 10.1364/AO.37.005560

Chowdhary, J., Cairns, B., and Travis, L. D. (2006). Contribution of water-leaving radiances to multiangle, multispectral polarimetric observations over the open ocean: bio-optical model results for case 1 waters. *Appl. Opt.* 45:5542. doi: 10.1364/AO.45.005542

Chowdhary, J., Cairns, B., Waquet, F., Knobelspiesse, K., Ottaviani, M., Redemann, J., et al. (2012). Sensitivity of multiangle, multispectral polarimetric remote sensing over open oceans to water-leaving radiance: analyses of RSP data acquired during the MILAGRO campaign. *Remote Sens. Environ.* 118, 284–308. doi: 10.1016/j.rse.2011.11.003

Chowdhary, J., Zhai, P., Boss, E., Dierssen, H., Frouin, R., Ibrahim, A., et al. (2019). Modeling atmosphere-ocean radiative transfer: A PACE mission perspective. *Front. Earth Sci.* 7:100. doi: 10.3389/feart.2019.00100

Colarco, P. R., Nowottnick, E. P., Randles, C. A., Yi, B., Yang, P., Kim, K.-M., et al. (2014). Impact of radiatively interactive dust aerosols in the NASA GEOS-5 climate model: Sensitivity to dust particle shape and refractive index. *J. Geophys. Res. Atmos.* 119, 753–786. doi: 10.1002/2013JD020046

Corson, M., Lucke, R. L., and Davis, C. O. (2010). "The Hyperspectral Imager for the Coastal Ocean (HICO) and environmental characterization of the coastal zone from the international space station," in *Imaging and Applied Optics Congress* (Washington, DC: OSA, OMA4).

Corson, M. R., Korwan, D. R., Lucke, R. L., Snyder, W. A., and Davis, C. O. (2008). "The Hyperspectral Imager for the Coastal Ocean (HICO) on the International Space Station," in *IGARSS 2008 - 2008 IEEE International Geoscience and Remote Sensing Symposium (IEEE)* (Boston, MA), IV-101-IV-104.

Cox, C., and Munk, W. (1954). Measurement of the roughness of the sea surface from photographs of the Sun's glitter. *J. Opt. Soc. Am.* 44:838. doi: 10.1364/JOSA.44.000838

Cressie, N. (2018). Mission CO_2ntrol: a statistical scientist's role in remote sensing of atmospheric carbon dioxide. *J. Am. Stat. Assoc.* 113, 152–168. doi: 10.1080/01621459.2017.1419136

Davis, A. B., and Marshak, A. (2010). Solar radiation transport in the cloudy atmosphere: a 3D perspective on observations and climate impacts. *Rep Progr Phys* 73:026801. doi: 10.1088/0034-4885/73/2/026801

Deluisi, J. J., and Mateer, C. L. (1971). On the application of the optimum statistical inversion technique to the evaluation of Umkehr observations. *J. Appl. Meteorol.* 10, 328–334. doi: 10.1175/1520-0450(1971)010<0328:OTAOTO>2.0.CO;2

Deschamps, P.-Y., Breon, F.-M., Leroy, M., Podaire, A., Bricaud, A., Buriez, J.-C., et al. (1994). The POLDER mission: instrument characteristics and scientific objectives. *IEEE Trans. Geosci. Remote Sens.* 32, 598–615. doi: 10.1109/36.297978

Deschamps, P. Y., Herman, M., and Tanre, D. (1983). Modeling of the atmospheric effects and its application to the remote sensing of ocean color. *Appl. Opt.* 22:3751. doi: 10.1364/AO.22.003751

Deuzé, J. L., Bréon, F. M., Devaux, C., Goloub, P., Herman, M., Lafrance, B., et al. (2001). Remote sensing of aerosols over land surfaces from POLDER-ADEOS-1 polarized measurements. *J. Geophys. Res. Atmos.* 106, 4913–4926. doi: 10.1029/2000JD900364

Dierssen, H., McManus, G. B., Chlus, A., Qiu, D., Gao, B.-C., and Lin, S. (2015b). Space station image captures a red tide ciliate bloom at high spectral and spatial resolution. *Proc. Natl. Acad. Sci. U.S.A.* 112, 14783–14787. doi: 10.1073/pnas.1512538112

Dierssen, H. M. (2019). Hyperspectral measurement, parameterizations, and atmospheric correction of whitecaps and foam from visible to shortwave infrared for ocean color remote sensing. *Front. Earth Sci.* 7:14. doi: 10.3389/feart.2019.00014

Dierssen, H. M., Chlus, A., and Russell, B. (2015a). Hyperspectral discrimination of floating mats of seagrass wrack and the macroalgae Sargassum in coastal waters of Greater Florida Bay using airborne remote sensing. *Remote Sens. Environ.* 167, 247–258. doi: 10.1016/j.rse.2015.01.027

Diner, D., and Martonchik, J. (1985). Influence of aerosol scattering on atmospheric blurring of surface features. *IEEE Trans. Geosci. Remote Sens.* GE-23, 618–624. doi: 10.1109/TGRS.1985.289379

Diner, D. J., Asner, G. P., Davies, R., Knyazikhin, Y., Muller, J.-P., Nolin, A. W., et al. (1999). New directions in earth observing: scientific applications of multiangle remote sensing. *Bull. Am. Meteorol. Soc.* 80, 2209–2228. doi: 10.1175/1520-0477(1999)080<2209:NDIEOS>2.0.CO;2

Diner, D. J., Braswell, B. H., Davies, R., Gobron, N., Hu, J., Jin, Y., et al. (2005). The value of multiangle measurements for retrieving structurally and radiatively consistent properties of clouds, aerosols, and surfaces. *Remote Sens. Environ.* 97, 495–518. doi: 10.1016/j.rse.2005.06.006

Ding, K., and Gordon, H. R. (1995). Analysis of the influence of O2 A-band absorption on atmospheric correction of ocean-color imagery. *Appl. Opt.* 34:2068. doi: 10.1364/AO.34.002068

Doney, S. C., Glover, D. M., McCue, S. J., and Fuentes, M. (2003). Mesoscale variability of Sea-viewing Wide Field-of-view Sensor (SeaWiFS) satellite ocean color: Global patterns and spatial scales. *J. Geophys. Res. Ocean.* 108:3024. doi: 10.1029/2001JC000843

Doron, M., Bélanger, S., Doxaran, D., and Babin, M. (2011). Spectral variations in the near-infrared ocean reflectance. *Remote Sens. Environ.* 115, 1617–1631. doi: 10.1016/j.rse.2011.01.015

Doxaran, D., Froidefond, J.-M., and Castaing, P. (2002). A reflectance band ratio used to estimate suspended matter concentrations in sediment-dominated coastal waters. *Int. J. Remote Sens.* 23, 5079–5085. doi: 10.1080/0143116021000009912

Dubovik, O. (2004). "Optimization of numerical inversion in photopolarimetric remote sensing, in: Photopolarimetry in Remote Sensing," in *Photopolarimetry in Remote Sensing,* eds G. Videen, Y. Yatskiv, M. Mishchenko (Dordrecht: Kluwer Academic Publishers), 65–106.

Dubovik, O., Herman, M., Holdak, A., Lapyonok, T., Tanré, D., Deuzé, J. L., et al. (2011). Statistically optimized inversion algorithm for enhanced retrieval of aerosol properties from spectral multi-angle polarimetric satellite observations. *Atmos. Meas. Tech.* 4, 975–1018. doi: 10.5194/amt-4-975-2011

Dubovik, O., and King, M. D. (2000). A flexible inversion algorithm for retrieval of aerosol optical properties from Sun and sky radiance measurements. *J. Geophys. Res. Atmos.* 105, 20673–20696. doi: 10.1029/2000JD900282

Dubovik, O., Lapyonok, T., Litvinov, P., Herman, M., Fuertes, D., Ducos, F., et al. (2014). *GRASP: A Versatile Algorithm for Characterizing the Atmosphere.* Warsaw: Newsroom. doi: 10.1117/2.1201408.005558

Dubovik, O., Li, Z., Mishchenko, M. I., Tanré, D., Karol, Y., and Yin, D. (2019). Polarimetric remote sensing of atmospheric aerosols: Instruments, methodologies, results, and perspectives. *J. Quant. Spectros. Radiat. Transf.* 224, 474–511. doi: 10.1016/j.jqsrt.2018.11.024

Dubovik, O., Sinyuk, A., Lapyonok, T., Holben, B. N., Mishchenko, M., Yang, P., et al. (2006). Application of spheroid models to account for aerosol particle nonsphericity in remote sensing of desert dust. *J. Geophys. Res.* 111:D11208. doi: 10.1029/2005JD006619

Dubovik, O. V., Lapyonok, T. V., and Oshchepkov, S. L. (1995). Improved technique for data inversion: optical sizing of multicomponent aerosols. *Appl. Opt.* 34:8422. doi: 10.1364/AO.34.008422

Dubuisson, P., Frouin, R., Dessailly, D., Duforêt, L., Léon, J.-F., Voss, K., et al. (2009). Estimating the altitude of aerosol plumes over the ocean from reflectance ratio measurements in the O2 A-band. *Remote Sens. Environ.* 113, 1899–1911. doi: 10.1016/j.rse.2009.04.018

Duforêt, L., Frouin, R., and Dubuisson, P. (2007). Importance and estimation of aerosol vertical structure in satellite ocean-color remote sensing. *Appl. Opt.* 46, 1107–1119. doi: 10.1364/AO.46.001107

Dutkiewicz, S., Hickman, A. E., Jahn, O., and Moneir, E. (2016). Optical signatures of climate change impacts on phytoplankton. *Am. Geophys. Union, Ocean Sci. Meet.* Abstr. #ME51A-08. Available online at: https://pace.oceansciences.org/docs/osm2016_dutkiewicz.pdf

Emde, C., Buras-Schnell, R., Kylling, A., Mayer, B., Gasteiger, J., Hamann, U., et al. (2016). The libRadtran software package for radiative transfer calculations (version 2.0.1). *Geosci. Model Dev.* 9, 1647–1672. doi: 10.5194/gmd-9-1647-2016

Fan, Y., Li, W., Gatebe, C. K., Jamet, C., Zibordi, G., Schroeder, T., et al. (2017). Atmospheric correction over coastal waters using multilayer neural networks. *Remote Sens. Environ.* 199, 218–240. doi: 10.1016/j.rse.2017.07.016

Fogarty, M. C., Fewings, M. R., Paget, A. C., and Dierssen, H. M. (2018). The influence of a sandy substrate, seagrass, or highly turbid water on albedo and surface heat flux. *J. Geophys. Res. Ocean.* 123, 53–73. doi: 10.1002/2017JC013378

Fougnie, B., Frouin, R., Lecomte, P., and Deschamps, P. Y. (1999). Reduction of skylight reflection effects in the above-water measurement of diffuse marine reflectance. *Appl. Opt.* 38:3844. doi: 10.1364/AO.38.003844

Fougnie, B., Marbach, T., Lacan, A., Lang, R., Schlüssel, P., Poli, G., et al. (2018). The multi-viewing multi-channel multi-polarisation imager–overview of the 3MI polarimetric mission for aerosol and cloud characterization. *J. Quant. Spectros. Radiat. Transf.* 219, 23–32. doi: 10.1016/j.jqsrt.2018.07.008

Franz, B. A., Bailey, S. W., Werdell, P. J., and McClain, C. R. (2007). Sensor-independent approach to the vicarious calibration of satellite ocean color radiometry. *Appl. Opt.* 46:5068. doi: 10.1364/AO.46.005068

Frouin, R., Deschamps, P.-Y., Rothschild, R., Stephan, E., Leblanc, P., Duttweiler, F., et al. (2006). "MAUVE/SWIPE: an imaging instrument concept with multi-angular, -spectral, and -polarized capability for remote sensing of aerosols, ocean color, clouds, and vegetation from space," in *Proceedings SPIE* (Goa), 64060E.

Frouin, R., Duforêt, L., and Steinmetz, F. (2014). "Atmospheric correction of satellite ocean-color imagery in the presence of semi-transparent clouds," in *Proceedings SPIE* (Beijing), 926108.

Frouin, R., and Pelletier, B. (2007). Fields of non-linear regression models for atmospheric correction of satellite ocean-color imagery. *Remote Sens. Environ.* 111, 450–465. doi: 10.1016/j.rse.2007.04.005

Frouin, R., and Pelletier, B. (2015). Bayesian methodology for inverting satellite ocean-color data. *Remote Sens. Environ.* 159, 332–360. doi: 10.1016/j.rse.2014.12.001

Frouin, R., Pouliquen, E., and Bréon, F.-M. (1994). "Ocean color remote sensing using polarization properties of reflected sunligh," in *Proceedings of 6th International Symposium on Physical Measurements and Signatures in Remote Sensing* (Val d'Isere), 665–674.

Frouin, R., Schwindling, M., and Deschamps, P.-Y. (1996). Spectral reflectance of sea foam in the visible and near-infrared: *In situ* measurements and remote sensing implications. *J. Geophys. Res. Ocean.* 101, 14361–14371. doi: 10.1029/96JC00629

Fukushima, H., Higurashi, A., Mitomi, Y., Nakajima, T., Noguchi, T., Tanaka, T., et al. (1998). Correction of atmospheric effect on ADEOS/OCTS ocean color data: Algorithm description and evaluation of its performance. *J. Oceanogr.* 54, 417–430. doi: 10.1007/BF02742444

Gao, B.-C., and Davis, C. O. (1997). "Development of a line-by-line-based atmosphere removal algorithm for airborne and spaceborne imaging spectrometers," in *Proceedings SPIE* (San Diego, CA), 3118.

Gao, B.-C., and Kaufman, Y. J. (2003). Water vapor retrievals using Moderate Resolution Imaging Spectroradiometer (MODIS) near-infrared channels. *J. Geophys. Res. Atmos.* 108:4389. doi: 10.1029/2002JD003023

Gao, B.-C., Montes, M. J., Davis, C. O., and Goetz, A. F. H. (2009). Atmospheric correction algorithms for hyperspectral remote sensing data of land and ocean. *Remote Sens. Environ.* 113, S17–S24. doi: 10.1016/j.rse.2007.12.015

Gao, B. C., Montes, M. J., Ahmad, Z., and Davis, C. O. (2000). Atmospheric correction algorithm for hyperspectral remote sensing of ocean color from space. *Appl. Opt.* 39:887. doi: 10.1364/AO.39.000887

Gelman, A., John, B., Carlin, J. B., Stern, H. L., Dunson, D. B., Vehtari, A., et al. (2013). *Bayesian Data Analysis*. New York, NY: Chapman and Hall/CRC.

Gitelson, A. A., Gao, B.-C., Li, R.-R., Berdnikov, S., and Saprygin, V. (2011). Estimation of chlorophyll-a concentration in productive turbid waters using a Hyperspectral Imager for the Coastal Ocean—the Azov Sea case study. *Environ. Res. Lett* 6, 24023–24029. doi: 10.1088/1748-9326/6/2/024023

Goloub, P., Deuze, J. L., Herman, M., and Fouquart, Y. (1994). Analysis of the POLDER polarization measurements performed over cloud covers. *IEEE Trans. Geosci. Rem. Sens.* 32, 78–88. doi: 10.1109/36.285191

Goloub, P., Herman, M., Chepfer, H., Riédi, J., Brogniez, G., Couvert, P., et al. (2000). Cloud thermodynamical phase classification from the POLDER spaceborne instrument. *J. Geophys. Res.* 105, 14747–14759. doi: 10.1029/1999JD901183

Gordon, H. R. (1978). Removal of atmospheric effects from satellite imagery of the oceans. *Appl. Opt.* 17:1631. doi: 10.1364/AO.17.001631

Gordon, H. R. (1995). Remote sensing of ocean color: a methodology for dealing with broad spectral bands and significant out-of-band response. *Remote Sens. Environ*. 34, 8245–8482. doi: 10.1364/AO.34.008363

Gordon, H. R. (1997). Atmospheric correction of ocean color imagery in the Earth Observing System era. *J. Geophys. Res. Atmos.* 102, 17081–17106. doi: 10.1029/96JD02443

Gordon, H. R., Du, T., and Zhang, T. (1997). Remote sensing of ocean color and aerosol properties: resolving the issue of aerosol absorption. *Appl. Opt.* 36:8670. doi: 10.1364/AO.36.008670

Gordon, H. R., and Wang, M. (1994). Retrieval of water-leaving radiance and aerosol optical thickness over the oceans with SeaWiFS: a preliminary algorithm. *Appl. Opt.* 33:443. doi: 10.1364/AO.33.000443

Gower, J., King, S., Borstad, G., and Brown, L. (2008). The importance of a band at 709 nm for interpreting water-leaving spectral radiance. *Can. J. Remote Sens.* 34, 287–297. doi: 10.5589/m08-022

Gower, J. F. R., Doerffer, R., and Borstad, G. A. (1999). Interpretation of the 685nm peak in water-leaving radiance spectra in terms of fluorescence, absorption and scattering, and its observation by MERIS. *Int. J. Remote Sens.* 20, 1771–1786. doi: 10.1080/014311699212470

Gross-Colzy, L., Colzy, S., Frouin, R., and Henry, P. (2007a). "A general ocean color atmospheric correction scheme based on principal components analysis: part I. performance on case 1 and case 2 water," in *Proceedings SPIE* (San Diego, CA), 668002.

Gross-Colzy, L., Colzy, S., Frouin, R., and Henry, P. (2007b). "A general ocean color atmospheric correction scheme based on principal components analysis: part II. Level 4 merging capabilities," in *Proceedings SPIE* (San Diego, CA), 668003.

Hasekamp, O. P. (2010). Capability of multi-viewing-angle photo-polarimetric measurements for the simultaneous retrieval of aerosol and cloud properties. *Atmos. Meas. Tech.* 3, 839–851. doi: 10.5194/amt-3-839-2010

Hasekamp, O. P., Fu, G., Rusli, S. P., Wu, L., Di Noia, A., aan de Brugh, J., et al. (2019). Aerosol measurements by SPEXone on the NASA PACE Mission: expected retrieval capabilities. *J. Quant. Spectros. Rad. Transf.* 227, 170–184. doi: 10.1016/j.jqsrt.2019.02.006

Hasekamp, O. P., and Landgraf, J. (2005). Retrieval of aerosol properties over the ocean from multispectral single-viewing-angle measurements of intensity and polarization: Retrieval approach, information content, and sensitivity study. *J. Geophys. Res.* 110:D20207. doi: 10.1029/2005JD006212

Hasekamp, O. P., Litvinov, P., and Butz, A. (2011). Aerosol properties over the ocean from PARASOL multiangle photopolarimetric measurements. *J. Geophys. Res.* 116:D14204. doi: 10.1029/2010JD015469

He, X., Bai, Y., Pan, D., Tang, J., and Wang, D. (2012). Atmospheric correction of satellite ocean color imagery using the ultraviolet wavelength for highly turbid waters. *Opt. Express* 20:20754. doi: 10.1364/OE.20.020754

He, X., Pan, D., Bai, Y., Wang, D., and Hao, Z. (2014). A new simple concept for ocean colour remote sensing using parallel polarisation radiance. *Sci. Rep.* 4:3748. doi: 10.1038/srep03748

Herman, B. M., Caudill, T. R., Flittner, D. E., Thome, K. J., and Ben-David, A. (1995). Comparison of the Gauss-Seidel spherical polarized radiative transfer code with other radiative transfer codes. *Appl. Opt.* 34:4563. doi: 10.1364/AO.34.004563

Herman, M., Deuzé, J.-L., Marchand, A., Roger, B., and Lallart, P. (2005). Aerosol remote sensing from POLDER/ADEOS over the ocean: improved retrieval using a nonspherical particle model. *J. Geophys. Res.* 110:D10SD02. doi: 10.1029/2004JD004798

Hornik, K. (1989). Multilayer feedforward networks are universal approximators. *Neural Netw.* 2, 359–366. doi: 10.1016/0893-6080(89)90020-8

Hu, C., Carder, K. L., and Muller-Karger, F. E. (2000). Atmospheric correction of SeaWiFS imagery over turbid coastal waters: a practical method. *Remote Sens. Environ.* 74, 195–206. doi: 10.1016/S0034-4257(00)00080-8

Hu, C., Lee, Z., and Franz, B. (2012). Chlorophyll *a* algorithms for oligotrophic oceans: a novel approach based on three-band reflectance difference. *J. Geophys. Res. Ocean.* 117:C01011. doi: 10.1029/2011JC007395

Huot, Y., Brown, C. A., and Cullen, J. J. (2005). New algorithms for MODIS sun-induced chlorophyll fluorescence and a comparison with present data products. *Limnol. Oceanogr. Methods* 3, 108–130. doi: 10.4319/lom.2005.3.108

Ibrahim, A., Franz, B., Ahmad, Z., Healy, R., Knobelspiesse, K., Gao, B.-C., et al. (2018). Atmospheric correction for hyperspectral ocean color retrieval with application to the Hyperspectral Imager for the Coastal Ocean (HICO). *Remote Sens. Environ.* 204, 60–75. doi: 10.1016/j.rse.2017.10.041

IOCCG (2006). "Remote sensing of inherent optical properties: fundamentals, tests of algorithms, and applications," in *Report No. 5 of the International Ocean-Colour Coordinating Group,* ed Z. Lee (Dartmouth, NS: IOCCG), 126.

IOCCG (2007). "Ocean-colour data merging," in *Report No. 6 of the International Ocean-Colour Coordinating Group,* ed W. W. Gregg (Dartmouth, NS: IOCCG), 68.

IOCCG (2008). "Why ocean colour? the societal benefits of ocean-colour technology," in *Report No. 7 of the International Ocean-Colour Coordinating Group,* eds T. Platt, N. Hoepffner, V. Stuart, and C. Brown (Dartmouth, NS: IOCCG), 141.

IOCCG (2010). "Atmospheric correction for remotely-sensed ocean-colour products," in *Reports No. 10 of the International Ocean-Colour Coordinating Group,* ed M. Wang (Dartmouth, NS: IOCCG), 78.

IOCCG (2012). "Mission requirements for future ocean-colour sensors," *Report No. 13 of the International Ocean-Colour Coordinating Group,* eds McClain and Meister (Dartmouth, NS: IOCCG), 106.

IOCCG (2013). "In-flight calibration of satellite ocean-colour sensors," *Report No. 14 of the International Ocean-Colour Coordinating Group,* ed R. Frouin (Dartmouth, NS: IOCCG), 106.

IOCCG (2014). "Phytoplankton functional types from space," *Report No. 15 of the International Ocean-Colour Coordinating Group,* ed S. Sathyendranath (Dartmouth, NS: IOCCG), 156.

Jamet, C., Moulin, C., and Thiria, S. (2004). Monitoring aerosol optical properties over the Mediterranean from SeaWiFS images using a neural network inversion. *Geophys. Res. Lett.* 31:L13107. doi: 10.1029/2004GL019951

Jamet, C., Thiria, S., Moulin, C., Crepon, M., Jamet, C., Thiria, S., et al. (2005). Use of a neurovariational inversion for retrieving oceanic and atmospheric constituents from ocean color imagery: A feasibility study. *J. Atmos. Ocean. Technol.* 22, 460–475. doi: 10.1175/JTECH1688.1

Kahn, R., Anderson, J., Anderson, T. L., Bates, T., Brechtel, F., Carrico, C. M., et al. (2004). Environmental snapshots from ACE-Asia. *J. Geophys. Res.* 109:D19SD14. doi: 10.1029/2003JD004339

Kahn, R. A., Sayer, A. M., Ahmad, Z., and Franz, B. A. (2016). The sensitivity of SeaWiFS ocean color retrievals to aerosol amount and type. *J. Atmos. Ocean. Technol.* 33, 1185–1209. doi: 10.1175/JTECH-D-15-0121.1

Kaufman, Y. J., and Gao, B.-C. (1992). Remote sensing of water vapor in the near IR from EOS/MODIS. *IEEE Trans. Geosci. Remote Sens.* 30, 871–884. doi: 10.1109/36.175321

Kaufman, Y. J., Tanré, D., Gordon, H. R., Nakajima, T., Lenoble, J., Frouin, R., et al. (1997). Passive remote sensing of tropospheric aerosol and atmospheric correction for the aerosol effect. *J. Geophys. Res. Atmos.* 102, 16815–16830. doi: 10.1029/97JD01496

Knaeps, E., Ruddick, K. G., Doxaran, D., Dogliotti, A. I., Nechad, B., Raymaekers, D., et al. (2015). A SWIR based algorithm to retrieve total suspended matter in extremely turbid waters. *Remote Sens. Environ.* 168, 66–79. doi: 10.1016/j.rse.2015.06.022

Knobelspiesse, K., Cairns, B., Mishchenko, M., Chowdhary, J., Tsigaridis, K., van Diedenhoven, B., et al. (2012). Analysis of fine-mode aerosol retrieval capabilities by different passive remote sensing instrument designs. *Opt. Express* 20:21457. doi: 10.1364/OE.20.021457

Koepke, P. (1984). Effective reflectance of oceanic whitecaps. *Appl. Opt.* 23:1816. doi: 10.1364/AO.23.001816

Korwan, D. R., Lucke, R. L., McGlothlin, N. R., Butcher, S. D., Wood, D. L., Bowles, J. H., et al. (2009). "Laboratory characterization of the Hyperspectral Imager for the Coastal Ocean (HICO)," in *2009 IEEE International Geoscience and Remote Sensing Symposium (IEEE)* (Biloxi, MS), II-69–II-72.

Kuchinke, C. P., Gordon, H. R., and Franz, B. A. (2009). Spectral optimization for constituent retrieval in Case 2 waters I: implementation and performance. *Remote Sens. Environ.* 113, 571–587. doi: 10.1016/j.rse.2008.11.001

Kudela, R. M., Palacios, S. L., Austerberry, D. C., Accorsi, E. K., Guild, L. S., and Torres-Perez, J. (2015). Application of hyperspectral remote sensing to cyanobacterial blooms in inland waters. *Remote Sens. Environ.* 167, 196–205. doi: 10.1016/j.rse.2015.01.025

Land, P. E., and Haigh, J. D. (1997). Atmospheric correction over Case 2 waters with an iterative fitting algorithm: relative humidity effects. *Appl. Opt.* 36:9448. doi: 10.1364/AO.36.009448

Lavender, S. J., Pinkerton, M. H., Moore, G. F., Aiken, J., and Blondeau-Patissier, D. (2005). Modification to the atmospheric correction of SeaWiFS ocean colour images over turbid waters. *Cont. Shelf Res.* 25, 539–555. doi: 10.1016/j.csr.2004.10.007

Letelier, R. M., and Abbott, M. R. (1996). An analysis of chlorophyll fluorescence algorithms for the moderate resolution imaging spectrometer (MODIS). *Remote Sens. Environ.* 58, 215–223. doi: 10.1016/S0034-4257(96)00073-9

Li, L., Fukushima, H., Frouin, R., Mitchell, B. G., He, M., Uno, I., et al. (2003). Influence of submicron absorptive aerosol on Sea-viewing Wide Field-of-view Sensor (SeaWiFS)-derived marine reflectance during Aerosol Characterization Experiment (ACE)-Asia. *J. Geophys. Res.* 108:4472. doi: 10.1029/2002JD002776

Li, W., Stamnes, K., Spurr, R., and Stamnes, J. (2008). Simultaneous retrieval of aerosol and ocean properties by optimal estimation: SeaWiFS case studies for the Santa Barbara Channel. *Int. J. Remote Sens.* 29, 5689–5698. doi: 10.1080/01431160802007632

Limbacher, J. A., and Kahn, R. A. (2017). Updated MISR dark water research aerosol retrieval algorithm-Part 1: Coupled 1.1 km ocean surface chlorophyll a retrievals with empirical calibration corrections. *Atmos. Meas. Tech.* 10, 1539–1555. doi: 10.5194/amt-10-1539-2017

Liu, J., He, X., Liu, J., Bai, Y., Wang, D., Chen, T., et al. (2017). Polarization-based enhancement of ocean color signal for estimating suspended particulate matter: radiative transfer simulations and laboratory measurements. *Opt. Express* 25:A323. doi: 10.1364/OE.25.00A323

Lucke, R. L., Corson, M., McGlothlin, N. R., Butcher, S. D., Wood, D. L., Korwan, D. R., et al. (2011). Hyperspectral imager for the coastal ocean: instrument description and first images. *Appl. Opt.* 50:1501. doi: 10.1364/AO.50.001501

Marshall, B. R., and Smith, R. C. (1990). Raman scattering and in-water ocean optical properties. *Appl. Opt.* 29:71. doi: 10.1364/AO.29.000071

Mayer, B. (2009). Radiative transfer in the cloudy atmosphere. *Eur. Phys. J. Conf.* 1, 75–99. doi: 10.1140/epjconf/e2009-00912-1

Mishchenko, M. I., Cairns, B., Kopp, G., Schueler, C. F., Fafaul, B. A., Hansen, J. E., et al. (2007). Accurate monitoring of terrestrial aerosols and total solar irradiance: introducing the Glory Mission. *Bull. Amer. Meteorol. Soc.* 88, 677–692. doi: 10.1175/BAMS-88-5-677

Mishchenko, M. I., Travis, L. D., Kahn, R. A., and West, R. A. (1997). Modeling phase functions for dustlike tropospheric aerosols using a shape mixture of randomly oriented polydisperse spheroids. *J. Geophys. Res. Atmos.* 102, 16831–16847. doi: 10.1029/96JD02110

Mobley, C. D. (1994). *Light and Water: Radiative Transfer in Natural Waters.* San Diego, CA: Academic Press.

Mobley, C. D., Werdell, J., Franz, B., Ahmad, Z., and Bailey, S. (2016). *Atmospheric Correction for Satellite Ocean Color Radiometry - A Tutorial and Documentation of the Algorithms used by the NASA Ocean Biology Processing Group*. Greenbelt, MD: NASA/TM-2016-217551, 73.

Monahan, E. C. (1993). "Occurrence and evolution of acoustically relevant sub-surface bubble plumes and their associated, remotely monitorable, surface whitecaps," in *Natural Physical Sources of Underwater Sound,* ed B.R. Kerman (Dordrecht: Springer Netherlands), 503–517. doi: 10.1007/978-94-011-1626-8_37

Monahan, E. C., and Spillane, M. C. (1984). "The role of oceanic whitecaps in air-sea gas exchange," In *Gas Transfer at Water Surfaces,* eds W. Brutsaert and G. H. Jirka (Dordrecht: Springer Netherlands), 495–503.

Moore, G. F., Aiken, J., and Lavender, S. J. (1999). The atmospheric correction of water colour and the quantitative retrieval of suspended particulate matter in Case II waters: Application to MERIS. *Int. J. Remote Sens.* 20, 1713–1733. doi: 10.1080/014311699212434

Moore, K. D., Voss, K. J., and Gordon, H. R. (2000). Spectral reflectance of whitecaps: Their contribution to water-leaving radiance. *J. Geophys. Res. Ocean.* 105, 6493–6499. doi: 10.1029/1999JC900334

Morel, A., and Maritorena, S. (2001). Bio-optical properties of oceanic waters: a reappraisal. *J. Geophys. Res. Ocean.* 106, 7163–7180. doi: 10.1029/2000JC000319

Müller, D., Krasemann, H., Brewin, R. J. W., Brockmann, C., Deschamps, P.-Y., Doerffer, R., et al. (2015a). The ocean colour climate change initiative: I. A methodology for assessing atmospheric correction processors based on *in-situ* measurements. *Remote Sens. Environ.* 162, 242–256. doi: 10.1016/j.rse.2013.11.026

Müller, D., Krasemann, H., Brewin, R. J. W., Brockmann, C., Deschamps, P.-Y., Doerffer, R., et al. (2015b). The ocean colour climate change initiative: II. Spatial and temporal homogeneity of satellite data retrieval due to systematic effects in atmospheric correction processors. *Remote Sens. Environ.* 162, 257–270. doi: 10.1016/j.rse.2015.01.033

Muller-Karger, F. E., Hestir, E., Ade, C., Turpie, K., Roberts, D. A., Siegel, D., et al. (2018). Satellite sensor requirements for monitoring essential biodiversity variables of coastal ecosystems. *Ecol. Appl.* 28, 749–760. doi: 10.1002/eap.1682

National Research Council (2008). *Ecological Impacts of Climate Change*. Washington, DC: The National Academies Press.

National Research Council (2011). *Assessing Requirements for Sustained Ocean Color Research and Operations*. Washington, DC: The National Academies Press.

Nelder, J. A., and Mead, R. (1965). A simplex method for function minimization. *Comput. J.* 7, 308–313. doi: 10.1093/comjnl/7.4.308

Nicolas, J.-M., Deschamps, P.-Y., and Frouin, R. (2001). Spectral reflectance of oceanic whitecaps in the visible and near infrared: Aircraft measurements over open ocean. *Geophys. Res. Lett.* 28, 4445–4448. doi: 10.1029/2001GL013556

Nobileau, D., and Antoine, D. (2005). Detection of blue-absorbing aerosols using near infrared and visible (ocean color) remote sensing observations. *Remote Sens. Environ.* 95, 368–387. doi: 10.1016/j.rse.2004.12.020

Oo, M., Vargas, M., Gilerson, A., Gross, B., Moshary, F., and Ahmed, S. (2008). Improving atmospheric correction for highly productive coastal waters using the short wave infrared retrieval algorithm with water-leaving reflectance constraints at 412 nm. *Appl. Opt.* 47:3846. doi: 10.1364/AO.47.003846

O'Reilly, J. E., Maritorena, S., Mitchell, B. G., Siegel, D. A., Carder, K. L., Garver, S. A., et al. (1998). Ocean color chlorophyll algorithms for SeaWiFS. *J. Geophys. Res. Ocean.* 103, 24937–24953. doi: 10.1029/98JC02160

Ota, Y., Higurashi, A., Nakajima, T., and Yokota, T. (2010). Matrix formulations of radiative transfer including the polarization effect in a coupled atmosphere–ocean system. *J. Quant. Spectrosc. Radiat. Transf.* 111, 878–894. doi: 10.1016/j.jqsrt.2009.11.021

Ottaviani, M., Knobelspiesse, K., Cairns, B., and Mishchenko, M. (2013). Information content of aerosol retrievals in the sunglint region. *Geophys. Res. Lett.* 40, 631–634. doi: 10.1002/grl.50148

Park, Y. J., and Ruddick, K. (2005). Model of remote-sensing reflectance including bidirectional effects for Case 1 and Case 2 waters. *Appl. Opt.* 44:1236. doi: 10.1364/AO.44.001236

Parol, F., Buriez, J. C., Vanbauce, C., Couvert, P., Sèze, G., Goloub, P., et al. (1999). First results of the POLDER "Earth Radiation Budget and Clouds" operational algorithm. *IEEE Trans. Geosci. Rem. Sens.* 37, 597–1612. doi: 10.1109/36.763273

Parol, F., Buriez, J. C., Vanbauce, C., Riédi, J., Doutriaux-Boucher, M., Vesperini, M., et al. (2004). Review of capabilities of multi-angle and polarization cloud measurements from POLDER. *Adv. Space Res.* 33, 1080–1088. doi: 10.1016/S0273-1177(03)00734-8

Pelletier, B., and Frouin, R. (2004). Fields of nonlinear regression models for inversion of satellite data. *Geophys. Res. Lett.* 31:L16304. doi: 10.1029/2004GL019840

Pelletier, B., and Frouin, R. (2006). Remote sensing of phytoplankton chlorophyll-a concentration by use of ridge function fields. *Appl. Opt.* 45:784. doi: 10.1364/AO.45.000784

Pingree, R. D., Mardell, G. T., and New, A. L. (1986). Propagation of internal tides from the upper slopes of the Bay of Biscay. *Nature* 321, 154–158. doi: 10.1038/321154a0

Platt, T., Forget, M.-H., White, G. N., Caverhill, C., Bouman, H., Devred, E., et al. (2008). Operational estimation of primary production at large geographical scales. *Remote Sens. Environ.* 112, 3437–3448. doi: 10.1016/j.rse.2007.11.018

Ramon, D., Steinmetz, F., Jolivet, D., Compiègne, M., and Frouin, R. (2019). Modeling polarized radiative transfer in the ocean-atmosphere system with the GPU-accelerated SMART-G Monte Carlo code. *J. Quant. Spectrosc. Radiat. Transf.* 222–223, 89–107. doi: 10.1016/j.jqsrt.2018.10.017

Randolph, K., Dierssen, H. M., Cifuentes-Lorenzen, A., Balch, W. M., Monahan, E. C., Zappa, C. J., et al. (2017). Novel methods for optically measuring whitecaps under natural wave-breaking conditions in the Southern Ocean. *J. Atmos. Ocean. Technol.* 34, 533–554. doi: 10.1175/JTECH-D-16-0086.1

Randolph, K., Dierssen, H. M., Twardowski, M., Cifuentes-Lorenzen, A., and Zappa, C. J. (2014). Optical measurements of small deeply penetrating bubble populations generated by breaking waves in the Southern Ocean. *J. Geophys. Res. Ocean.* 119, 757–776. doi: 10.1002/2013JC009227

Ransibrahmanakul, V., and Stumpf, R. P. (2006). Correcting ocean colour reflectance for absorbing aerosols. *Int. J. Remote Sens.* 27, 1759–1774. doi: 10.1080/01431160500380604

Reinersman, P. N., and Carder, K. L. (1995). Monte Carlo simulation of the atmospheric point-spread function with an application to correction for the adjacency effect. *Appl. Opt.* 34:4453. doi: 10.1364/AO.34.004453

Remer, L. A., Davis, A. B., Mattoo, S., Levy, R. C., Kalashnikova, O., Chowdhary, J., et al. (2019). Retrieving aerosol characteristics from the PACE mission, Part 1: Ocean Color Instrument. *Front. Earth Sci.* 7:152. doi: 10.3389/feart.2019.00152

Remer, L. A., Kleidman, R. G., Levy, R. C., Kaufman, Y. J., Tanré, D., Mattoo, S., et al. (2008). Global aerosol climatology from the MODIS satellite sensors. *J. Geophys. Res.* 113:D14SD07. doi: 10.1029/2007JD009661

Robinson, I. S. (2010). "Internal waves," in *Discovering the Ocean From Space,* ed I. S. Robinson (Berlin: Springer), 453–483.

Rodgers, C. D. (2000). *Inverse Methods for Atmospheric Sounding - Theory and Practice.* Singapore: World Scientific.

Rothman, L. S., Gordon, I. E., Babikov, Y., Barbe, A., Chris Benner, D., Bernath, P. F., et al. (2013). The HITRAN2012 molecular spectroscopic database. *J. Quant. Spectrosc. Radiat. Transf.* 130, 4–50. doi: 10.1016/j.jqsrt.2013.07.002

Ruddick, K. G., Ovidio, F., and Rijkeboer, M. (2000). Atmospheric correction of SeaWiFS imagery for turbid coastal and inland waters. *Appl. Opt.* 39:897. doi: 10.1364/AO.39.000897

Santer, R., and Schmechtig, C. (2000). Adjacency effects on water surfaces: primary scattering approximation and sensitivity study. *Appl. Opt.* 39:361. doi: 10.1364/AO.39.000361

Santer, R., and Zagolski, F. (2008). *ICOL Improve Contrast Between Ocean and Land ATBD – MERIS Level-1C*. Available online at: http://www.brockmann-consult.de/beam-wiki/download/attachments/13828113/ICOL_ATBD_1.1.pdf

Saulquin, B., Fablet, R., Bourg, L., Mercier, G., and d'Andon, O. F. (2016). MEETC2: Ocean color atmospheric corrections in coastal complex waters using a Bayesian latent class model and potential for the incoming sentinel 3 — OLCI mission. *Remote Sens. Environ.* 172, 39–49. doi: 10.1016/j.rse.2015.10.035

Scanlon, B., and Ward, B. (2016). The influence of environmental parameters on active and maturing oceanic whitecaps. *J. Geophys. Res. Ocean.* 121, 3325–3336. doi: 10.1002/2015JC011230

Schiller, H., and Doerffer, R. (1999). Neural network for emulation of an inverse model operational derivation of Case II water properties from MERIS data. *Int. J. Remote Sens.* 20, 1735–1746. doi: 10.1080/014311699212443

Schollaert, S. E., Yoder, J. A., O'reilly, J. E., Westphal, D. L., Yoder, J. E. A., O'reilly, J. E., et al. (2003). Influence of dust and sulfate aerosols on ocean color spectra and chlorophyll a concentrations derived from SeaWiFS off the U.S. east coast. *J. Geophys. Res.* 108:3191. doi: 10.1029/2000JC000555

Schroeder, T., Behnert, I., Schaale, M., Fischer, J., and Doerffer, R. (2007). Atmospheric correction algorithm for MERIS above Case-2 waters. *Int. J. Remote Sens.* 28, 1469–1486. doi: 10.1080/01431160600962574

Shaw, G. E. (1983). Sun photometry. *Bull. Am. Meteorol. Soc.* 64, 4–10. doi: 10.1175/1520-0477(1983)064andlt;0004:SPandgt;2.0.CO;2

Shettle, E. P., and Fenn, R. W. (1979). *Models for the Aerosols of the Lower Atmosphere and the Effects of Humidity Variations on their Optical Properties.* AFCRL Tech. Rep. 79 0214, Hanscom Air Force Base, MA: Air Force Cambridge Research Laboratory.

Shi, C., Nakajima, T., and Hashimoto, M. (2016). Simultaneous retrieval of aerosol optical thickness and chlorophyll concentration from multiwavelength measurement over East China Sea. *J. Geophys. Res. Atmos.* 121, 14,084-14,101. doi: 10.1002/2016JD025790

Shi, W., and Wang, M. (2007). Detection of turbid waters and absorbing aerosols for the MODIS ocean color data processing. *Remote Sens. Environ.* 110, 149–161. doi: 10.1016/j.rse.2007.02.013

Siegel, D. A., Wang, M., Maritorena, S., and Robinson, W. (2000). Atmospheric correction of satellite ocean color imagery: the black pixel assumption. *Appl. Opt.* 39:3582. doi: 10.1364/AO.39.003582

Smirnov, A., Holben, B. N., Dubovik, O., O'Neill, N. T., Eck, T. F., Westphal, D. L., et al. (2002). Atmospheric aerosol optical properties in the Persian gulf. *J. Atmos. Sci.* 59, 620–634. doi: 10.1175/1520-0469(2002)059<0620:AAOPIT>2.0.CO;2

Stamnes, K., Li, W., Yan, B., Eide, H., Barnard, A., Pegau, W. S., et al. (2003). Accurate and self-consistent ocean color algorithm: simultaneous retrieval of aerosol optical properties and chlorophyll concentrations. *Appl. Opt.* 42:939. doi: 10.1364/AO.42.000939

Steinmetz, F., Deschamps, P. Y., and Ramon, D. (2011). Atmospheric correction in presence of sun glint: application to MERIS. *Opt. Express* 19:9783. doi: 10.1364/OE.19.009783

Stramska, M., and Petelski, T. (2003). Observations of oceanic whitecaps in the north polar waters of the Atlantic. *J. Geophys. Res.* 108:3086. doi: 10.1029/2002JC001321

Stramski, D., and Tegowski, J. (2001). Effects of intermittent entrainment of air bubbles by breaking wind waves on ocean reflectance and underwater light field. *J. Geophys. Res. Ocean.* 106, 31345–31360. doi: 10.1029/2000JC000461

Stumpf, R. P., Arnone, R. A., Gould, R. W. Jr., Martinolich, P. M., and Ransibrahmanakul, V. (2003). "A partially coupled ocean-atmosphere model for retrieval of water-leaving radiance from SeaWiFS in coastal waters," in *SeaWiFS Postlaunch Technical Report Series, Vol. 22: Algorithm Updates for the Fourth SeaWiFS Data Processing*, eds S. B. Hooker and E. R. Firestone (Greenbelt, MD: NASA Goddard Space Flight Center), 51–59.

Sun, W., Videen, G., and Mishchenko, M. I. (2014). Detecting super-thin clouds with polarized sunlight. *Geophys. Res. Lett.* 41, 688–693. doi: 10.1002/2013GL058840

Tan, J., Frouin, R. J., Ramon, D., and Steinmetz, F. (2018). "Adequacy of semi-analytical water reflectance models in ocean-color remote sensing," in *Proceedings SPIE* (Honolulu, HI), 10778. doi: 10.1117/12.2501677

Tanré, D., Bréon, F. M., Deuzé, J. L., Dubovik, O., Ducos, F., François, P., et al. (2011). Remote sensing of aerosols by using polarized, directional and spectral measurements within the A-Train: the PARASOL mission. *Atmos. Meas. Tech* 4, 1383–1395. doi: 10.5194/amt-4-1383-2011

Tanré, D., Deschamps, P. Y., Duhaut, P., and Herman, M. (1987). Adjacency effect produced by the atmospheric scattering in thematic mapper data. *J. Geophys. Res.* 92:12000. doi: 10.1029/JD092iD10p12000

Tanré, D., Herman, M., and Deschamps, P. Y. (1981). Influence of the background contribution upon space measurements of ground reflectance. *Appl. Opt.* 20:3676. doi: 10.1364/AO.20.003676

Tanré, D., Herman, M., Deschamps, P. Y., and de Leffe, A. (1979). Atmospheric modeling for space measurements of ground reflectances, including bidirectional properties. *Appl. Opt.* 18:3587. doi: 10.1364/AO.18.003587

Terrill, E. J., Melville, W. K., and Stramski, D. (2001). Bubble entrainment by breaking waves and their influence on optical scattering in the upper ocean. *J. Geophys. Res. Ocean.* 106, 16815–16823. doi: 10.1029/2000JC000496

Theiler, J. (2012). "The incredible shrinking covariance estimator," in *Proceedings SPIE* 8391, *Automatic Target Recognition XXII,* 83910P. doi: 10.1117/12.918718

Thieuleux, F. (2002). *Contribution à l'amélioration de la correction atmosphérique pour l'observation spatiale de la couleur de l'océan.* [Ph.D. dissertation], No. *9567,* University of Lille, Villeneuve d'Asq, France, 190.

Thompson, D. R., Natraj, V., Green, R. O., Helmlinger, M. C., Gao, B.-C., and Eastwood, M. L. (2018). Optimal estimation for imaging spectrometer atmospheric correction. *Remote Sens. Environ.* 216, 355–373. doi: 10.1016/j.rse.2018.07.003

Torres, O., Bhartia, P. K., Herman, J. R., Sinyuk, A., Ginoux, P., Holben, B., et al. (2002). A long-term record of aerosol optical depth from TOMS observations and comparison to AERONET measurements. *J. Atmos. Sci.* 59, 398–413. doi: 10.1175/1520-0469(2002)059<0398:ALTROA>2.0.CO;2

Trinh, R. C., Fichot, C. G., Gierach, M. M., Holt, B., Malakar, N. K., Hulley, G., et al. (2017). Application of Landsat 8 for monitoring impacts of wastewater discharge on coastal water quality. *Front. Mar. Sci.* 4:329. doi: 10.3389/fmars.2017.00329

Twomey, S. (1977). *Introduction to the Mathematics of Inversion in Remote Sensing Inversion and Indirect Measurements.* Amsterdam: Elsevier.

Tyo, J. S., Goldstein, D. L., Chenault, D. B., and Shaw, J. A. (2006). Review of passive imaging polarimetry for remote sensing applications. *Appl. Opt.* 45:5453. doi: 10.1364/AO.45.005453

Vermote, E. F., El Saleous, N., Justice, C. O., Kaufman, Y. J., Privette, J. L., Remer, L., et al. (1997). Atmospheric correction of visible to middle-infrared EOS-MODIS data over land surfaces: Background, operational algorithm and validation. *J. Geophys. Res. Atmos.* 102, 17131–17141. doi: 10.1029/97JD00201

Voss, K. J., Morel, A., and Antoine, D. (2007). Detailed validation of the bidirectional effect in various Case 1 waters for application to ocean color imagery. *Biogeosciences* 4, 781–789. doi: 10.5194/bg-4-781-2007

Vountas, M. (1998). *Modeling and Parameterization of the Ring Effect: Impact on the Retrieval of Stratospheric Trace Gases*. [Ph.D. dissertation], University of Bremen, Bremen.

Wang, M., and Gordon, H. R. (1994). Estimating aerosol optical properties over the oceans with the multiangle imaging spectroadiometer: some preliminary studies. *Appl. Opt.* 33, 4042–4057. doi: 10.1364/AO.33.004042

Wang, M., and Shi, W. (2007). The NIR-SWIR combined atmospheric correction approach for MODIS ocean color data processing. *Opt. Express* 15:15722. doi: 10.1364/OE.15.015722

Wang, M., Son, S., and Shi, W. (2009). Evaluation of MODIS SWIR and NIR-SWIR atmospheric correction algorithms using SeaBASS data. *Remote Sens. Environ.* 113, 635–644. doi: 10.1016/j.rse.2008.11.005

Werdell, P. J., Franz, B. A., Bailey, S. W., Feldman, G. C., Boss, E., Brando, V. E., et al. (2013). Generalized ocean color inversion model for retrieving marine inherent optical properties. *Appl. Opt.* 52:2019. doi: 10.1364/AO.52.002019

Werdell, P. J., McKinna, L. I. W., Boss, E., Ackleson, S. G., Craig, S. E., Gregg, W. W., et al. (2018). An overview of approaches and challenges for retrieving marine inherent optical properties from ocean color remote sensing. *Prog. Oceanogr.* 160, 186–212. doi: 10.1016/j.pocean.2018.01.001

Whitlock, C. H., Bartlett, D. S., and Gurganus, E. A. (1982). Sea foam reflectance and influence on optimum wavelength for remote sensing of ocean aerosols. *Geophys. Res. Lett.* 9, 719–722. doi: 10.1029/GL009i006p00719

Woolf, D. K. (1997). "Bubbles and their role in gas exchange," in *The Sea Surface and Global Change*, eds P. S. Liss and R. A. Duce (Cambridge: Cambridge University Press), 173–206.

Woolf, D. K., Leifer, I. S., Nightingale, P. D., Rhee, T. S., Bowyer, P., Caulliez, G., et al. (2007). Modelling of bubble-mediated gas transfer: fundamental principles and a laboratory test. *J. Mar. Syst.* 66, 71–91. doi: 10.1016/j.jmarsys.2006.02.011

Xu, F., Davis, A. B., Sanghavi, S. V., Martonchik, J. V., and Diner, D. J. (2012). Linearization of Markov chain formalism for vector radiative transfer in a plane-parallel atmosphere/surface system. *Appl. Opt.* 51:3491. doi: 10.1364/AO.51.003491

Xu, F., Davis, A. B., West, R. A., Martonchik, J. V., and Diner, D. J. (2011). Markov chain formalism for vector radiative transfer in a plane-parallel atmosphere overlying a polarizing surface. *Opt. Lett.* 36:2083. doi: 10.1364/OL.36.002083

Yamada, K., Ishizaka, J., Yoo, S., Kim, H.-C., and Chiba, S. (2004). Seasonal and interannual variability of sea surface chlorophyll a concentration in the Japan/East Sea (JES). *Oceanogr. Prog. Oceanogr.* 61, 193–211. doi: 10.1016/j.pocean.2004.06.001

Zhai, P.-W., Knobelspiesse, K., Ibrahim, A., Franz, B. A., Hu, Y., Gao, M., et al. (2017). Water-leaving contribution to polarized radiation field over ocean. *Opt. Express* 25, A689–A708. doi: 10.1364/OE.25.00A689

Zhang, X., Lewis, M., Lee, M., Johnson, B., and Korotaev, G. (2002). The volume scattering function of natural bubble populations. *Limnol. Oceanogr.* 47, 1273–1282. doi: 10.4319/lo.2002.47.5.1273

Conflict of Interest Statement: LG is employed by company Pixstart, and DR and FS are employed by company HYGEOS.

The remaining authors declare that the research was conducted in the absence of any commercial or financial relationships that could be construed as a potential conflict of interest.

APPENDIX A: METHODOLOGY FOR INFORMATION CONTENT ASSESSMENT

The information content assessment described in section Information Content Assessment uses a Bayesian approach with Gaussian distributions as described in Rodgers (2000), and implemented for aerosol remote sensing by Knobelspiesse et al. (2012) and references therein. This method estimates retrieval uncertainty given an observational configuration and uncertainty with the Equation:

$$\hat{S}^{-1} = \boldsymbol{K}^{\boldsymbol{T}} \boldsymbol{S}_{\boldsymbol{\epsilon}} \boldsymbol{K} + S_a^{-1}$$

where $\hat{\boldsymbol{S}}$ is the retrieval error covariance matrix, $\boldsymbol{S}_{\boldsymbol{\epsilon}}$ is the observation error covariance matrix, $\boldsymbol{S}_{\boldsymbol{a}}$ is the *a priori* error covariance matrix, $\boldsymbol{K}$ is the Jacobian (forward model sensitivity) matrix, $^{\mathrm{T}}$ denotes the transpose, and $^{\boldsymbol{-1}}$ denotes the inverse. The observation error covariance matrix represents measurement uncertainty and is square, with the dimension of the number of measurements [m x m], made with each observation. The retrieval error covariance matrix, $\hat{\boldsymbol{S}}$, has a similar structure, but represents the uncertainty in parameters retrieved from the data and has the dimension of the number of retrieved parameters [n × n]. Essentially, it is the projection of observational uncertainties into state (parameter) space. The Jacobian matrix, $\boldsymbol{K}$, expresses the sensitivity of the atmosphere/ocean radiative transfer model to changes in the parameters to be retrieved, and has the dimension [m x n]. Radiative transfer simulations, indicated by the function $\boldsymbol{F}(\boldsymbol{x}) = \boldsymbol{y}$ (where $\boldsymbol{x}$ is a vector atmospheric and surface optical parameters, often called the state space, and $\boldsymbol{y}$ is the measurement vector), are used to estimate the Jacobian matrix

$$\boldsymbol{K_{i,j}(x)} = \frac{\boldsymbol{\partial F_i(x)}}{\boldsymbol{\partial x_j}} \approx \frac{\boldsymbol{F_i}\left(\boldsymbol{x}'\right) - \boldsymbol{F_i(x)}}{\boldsymbol{x'_j - x_j}}$$

where the partial derivative of the radiative transfer model for the simulated set of parameters, $\boldsymbol{x}$, is computed for each observation, $\boldsymbol{i}$, and each parameter, $\boldsymbol{j}$. We approximate the Jacobian using the forward difference technique, where the radiative transfer model is rerun with a perturbed parameter $\boldsymbol{x'_j}$, and the forward model is assumed linear over that perturbation.

This method provides the means to relate measurement characteristics to expected retrieval success. Instrument capability is defined by the contents of the measurement vector, $\boldsymbol{y}$, and the measurement uncertainty defined in $\boldsymbol{S}_{\boldsymbol{\epsilon}}$. The *a priori* error covariance matrix, $\boldsymbol{S}_{\boldsymbol{a}}$, describes what we know about state parameters $\boldsymbol{x}$ prior to a measurement. The Jacobian, $\boldsymbol{K}$, is the product of a radiative transfer model and thus computationally expensive to generate. It is, however, crucial since it links parameter to measurement space. In practice, we generate a Jacobian matrix for a very large measurement vector, encompassing all possible measurement spectral sensitivities, geometries, and polarimetric states, and then make a subset corresponding to the instrument system in question. Since the atmosphere/ocean system is highly nonlinear, we also need to repeat this analysis for a variety of states, and express the results as an aggregate of many states. For example, we might expect the ability to determine ocean properties decreases as the amount of aerosol loading increases, so we must test with a variety of aerosol amounts.

The averaging kernel matrix, $\boldsymbol{A}$ (also known as the model resolution matrix), is a useful reformulation that is an identity matrix for perfect retrieval ability. It is calculated as:

$$\boldsymbol{A} = \left[\boldsymbol{K}^{\boldsymbol{T}} \boldsymbol{S}_{\boldsymbol{\epsilon}} \boldsymbol{K} + S_a^{-1}\right]^{\boldsymbol{-1}} \boldsymbol{K}^{\boldsymbol{T}} \boldsymbol{S}_{\boldsymbol{\epsilon}} \boldsymbol{K}$$

where a null matrix indicates no ability to determine the state parameters beyond what is already known from the *a priori* matrix. The Degrees of Freedom for Signal is a scalar, representation of measurement system capability, calculated as *DFS=trace(***A***)*, and has the property $0 \leq DFS \leq n$. We use *DFS* to compactly show system capability for many simulated states.

We used a forward model that defines the measurement state with ocean and atmospheric physical and optical properties. However, PACE SDT requirements were expressed as the water reflectance [$\boldsymbol{\rho_w}$], which is instead a byproduct of the model. We must therefore project the results $\hat{\boldsymbol{S}}$ into this space. To do so, we first determine the Jacobian matrix, $\boldsymbol{J}$, for water reflectance in the same manner as $\boldsymbol{K}$*:*

$$\boldsymbol{J_{l,j}(x)} = \frac{\boldsymbol{\partial M_l(x)}}{\boldsymbol{\partial x_j}} \approx \frac{\boldsymbol{M_l}\left(\boldsymbol{x}'\right) - \boldsymbol{M_l(x)}}{\boldsymbol{x'_j - x_j}}$$

where λ corresponds to each wavelength in [$\boldsymbol{\rho_w}$], and $\boldsymbol{M}$ is the forward model component that produces the water reflectance. To project the retrieval error covariance matrix we therefore use

$$\hat{S}_{\boldsymbol{b}}^{\boldsymbol{-1}} = \boldsymbol{J}^{\boldsymbol{T}} \boldsymbol{K}^{\boldsymbol{T}} \boldsymbol{S}_{\epsilon} \boldsymbol{K} \boldsymbol{J} + \boldsymbol{J}^{\boldsymbol{T}} \boldsymbol{S}_{\boldsymbol{a}}^{\boldsymbol{-1}} \boldsymbol{J}$$

Where $\hat{\boldsymbol{S}}_b$ is the byproduct error covariance matrix. The indirect nature of this matrix may mean that it is has an implicit regularization. Comparison of $\hat{\boldsymbol{S}}_b$and the projection of the *a priori* error covariance matrix $\boldsymbol{J}^{\boldsymbol{T}} \boldsymbol{S}_a^{-1} \boldsymbol{J}$ can provide clues to the intermediate step constraints.

section Information Content Assessment contains an implementation of these techniques for several prototypical MAP designs for a variety of geophysical conditions. In practice, this means we construct Jacobian matrices to include all possible measurement spectral channels and geometries, and subset the Jacobian to represent the measurement system of interest. This is repeated for a variety of geophysical cases, and results presented in aggregate. In section Information Content Assessment we show the DFS as an overall metric of measurement capability, and $\hat{\boldsymbol{S}}_b$ for water reflectance to show atmospheric correction capability.

frontiers
in Earth Science

METHODS
published: 05 November 2019
doi: 10.3389/feart.2019.00283

Developing a Community of Practice for Applied Uses of Future PACE Data to Address Marine Food Security Challenges

Stephanie Schollaert Uz[1]*, Grace E. Kim[1,2], Antonio Mannino[1], P. Jeremy Werdell[1] and Maria Tzortziou[3]

[1] NASA Goddard Space Flight Center, Greenbelt, MD, United States, [2] Universities Space Research Association, Columbia, MD, United States, [3] The City College of New York, New York, NY, United States

The Plankton, Aerosol, Cloud, ocean Ecosystem (PACE) mission will include a hyperspectral imaging radiometer to advance ecosystem monitoring beyond heritage retrievals of the concentration of surface chlorophyll and other traditional ocean color variables, offering potential for novel science and applications. PACE is the first NASA ocean color mission to occur under the agency's new and evolving effort to directly engage practical end users prior to satellite launch to increase adoption of this freely available data toward societal challenges. Here we describe early efforts to engage a community of practice around marine food-related resource management, business decisions, and policy analysis. Obviously one satellite cannot meet diverse end user needs at all scales and locations, but understanding downstream needs helps in the assessment of information gaps and planning how to optimize the unique strengths of PACE data in combination with the strengths of other satellite retrievals, *in situ* measurements, and models. Higher spectral resolution data from PACE can be fused with information from satellites with higher spatial or temporal resolution, plus other information, to enable identification and tracking of new marine biological indicators to guide sustainable management. Accounting for the needs of applied researchers as well as non-traditional users of satellite data early in the PACE mission process will ultimately serve to broaden the base of informed users and facilitate faster adoption of the most advanced science and technology toward the challenge of mitigating food insecurity.

Keywords: satellite ocean color applications, PACE mission user community, phytoplankton, fisheries, aquaculture, societal impact

Edited by:
Irina Alexandrovna Mironova,
Saint Petersburg State University,
Russia

Reviewed by:
Yoav Lehahn,
University of Haifa, Israel
Tim J. Malthus,
CSIRO Oceans and Atmosphere
(O&A), Australia

***Correspondence:**
Stephanie Schollaert Uz
stephanie.uz@nasa.gov

Specialty section:
This article was submitted to
Atmospheric Science,
a section of the journal
Frontiers in Earth Science

***Received:** 09 December 2018*
***Accepted:** 17 October 2019*
***Published:** 05 November 2019*

Citation:
Schollaert Uz S, Kim GE, Mannino A, Werdell PJ and Tzortziou M (2019) Developing a Community of Practice for Applied Uses of Future PACE Data to Address Marine Food Security Challenges. Front. Earth Sci. 7:283. doi: 10.3389/feart.2019.00283

INTRODUCTION

Seafood is an important source of protein for much of the world's population. Wild catches cannot match growing demand and their sustainability is in question. Aquaculture is an increasingly important industry to feed the world's population. According to the Food and Agriculture Organization of the United Nations (FAO), as of 2017 more than 200 nations and $152 Billion per year are involved in the international trade of fish, shellfish, and fish products, as the most traded food product for developing countries at twice the value of the coffee trade (FAO, 2018).

However, fisheries face significant threats from environmental and human pressures. There is a need for sustainable and local seafood. Aquaculture has been increasing to supply this demand, yet coastal eutrophication and harmful algal blooms imperil the safety of this food source. Warming, acidification, deoxygenation, and pollution are a few of the environmental stressors that cause habitat shift or loss and undermine the sustainability of the fishing industry. Around the world, illegal, unreported, and unregulated fishing also jeopardizes food security, economic security, and human security. The latest global assessment by the Food and Agriculture Organization of the United Nations indicates that the percentage of fisheries that are unsustainably overfished has increased to one third (World Bank, 2017; FAO, 2018). Fragile states with limited capabilities to enforce their Exclusive Economic Zones need actionable information to evaluate their natural resources. Freely available remotely sensed data from satellites combined with *in situ* sensors provide environmental insights that can help resource managers and other operators respond to these challenges.

Global aquatic ecosystems have been regularly monitored from space during the past four decades by polar-orbiting, multispectral ocean color radiometers, transforming our understanding of processes that support life in the ocean (McClain, 2009). U.S. examples include the NASA Coastal Zone Color Scanner (CZCS; 1978–1986), Sea-viewing Wide Field-of-view Sensor (SeaWiFS; 1997–2010), Moderate Resolution Imaging Spectroradiometer (MODIS; 1999-present on Terra and 2002-present on Aqua), and Visible Infrared Imaging Radiometer System (VIIRS; 2012-present on Suomi NPP and 2018-present on NOAA-20). These satellite-borne sensors were designed to provide daily, global views of the open ocean where sampling opportunities are infrequent and expensive. In Europe, the Ocean and Land Color Imager (OLCI) was launched onboard Sentinel 3A and 3B in 2016 and 2018, respectively, with another two Sentinel 3 satellites planned to ensure continuity and consistency of services (Donlon et al., 2012; Groom et al., 2019). Additional ocean color sensors have been successfully launched into polar orbit by India, Japan, and China, and into geostationary orbit by South Korea (Groom et al., 2019).

NASA is currently developing the Plankton, Aerosol, Cloud, ocean Ecosystem (PACE) mission, with its launch scheduled for late 2022. PACE has several important technological advancements that will expand its use beyond the heritage instruments listed above, enabling it to enhance and extend current biological and water quality parameters measured from space with new spectral information (Werdell et al., 2019). The primary instrument on the observatory, the Ocean Color Instrument (OCI), consists of two spectrometers that continuously span the ultraviolet (UV) and orange and orange to near-infrared (NIR) spectral regions, as well as seven additional detectors to collect measurements at discrete NIR and shortwave infrared (SWIR) bands (**Figure 1**). Although not the focus of this manuscript, note that OCI is complemented on the observatory by two multi-angle polarimeters, the Spectropolarimeter for Planetary Exploration (SPEXone) (Hasekamp et al., 2019) and the Hyper Angular Rainbow Polarimeter (HARP2) (Martins et al., 2018). These instruments will provide additional aerosol and cloud data products relative to what is possible with OCI alone. **Table 1** provides additional details on characteristics of OCI and the PACE observatory. SPEXone and HARP2 are scheduled for delivery to NASA in the 3rd and 4th quarter of 2020 when integration and testing of the spacecraft begins. Testing and integration of the OCI flight unit will begin in 2020 and continue until delivery in the 3rd quarter of 2021 when integration and testing with the observatory begins. The PACE observatory has a scheduled launch window between November 2022 and March 2023. Public distribution of PACE science data products will begin immediately following official commissioning of the observatory, which is scheduled to occur 60 days after launch. As with most scientific satellites, delays in the delivery of the instruments or in the observatory integration and testing are possible and may result in postponement of the launch, which would in turn delay the availability of PACE science data.

The mission of NASA is to explore through a synthesis of science and technology. Traditionally, NASA Earth Science designs new Earth observing satellites based upon science research questions and then NOAA and the private sector adopt the results of the evolving technology and apply it to practical applications around fisheries and aquaculture. NOAA resource managers, researchers and private businesses have been using satellite data to assist with finding fish for decades, and especially since the launch of SeaWiFS in 1997 (e.g., Maul et al., 1984; Friedl et al., 2006; Wilson et al., 2008, 2009; Wall et al., 2009; Wilson, 2011). NASA is currently undergoing a paradigm shift to consider such practical applications of its satellite data in coordination with science research questions during the initial concept and pre-formulation of a mission before it becomes formalized (National Academies of Sciences Engineering and Medicine [NASEM], 2018). Although the international community has already been considering practical applications in their satellite design process (e.g., ESA's Copernicus Program), PACE is the first NASA ocean color mission that endeavors to engage operational stakeholders during the design-build phases of a mission prior to launch (**Figure 2**). Our objective is to prepare a community of practice that can immediately apply the advanced data from PACE as soon as it is available to maximize the nation's return on investments of this space-based asset. In this manuscript, we describe several early efforts to survey the fisheries and aquaculture communities, among others, about their current uses of ocean color data and how future PACE science data streams could help fill gaps. In addition to regularly attending international meetings to discuss capabilities and needs with scientists and users from around the world, we have undertaken a few targeted activities to foster the exchange of ideas and requirements between satellite data providers and stakeholders. The end goal is to increase access to satellite products that can guide more informed decisions by resource managers, the fishing industry, as well as artisanal and recreational fishers.

The activities and outcomes we describe in this manuscript are complementary to previous efforts to ensure the continuity of high quality ocean color satellite data for basic and applied research uses. For example, in 2011 an international committee of experts outlined minimum requirements to sustain

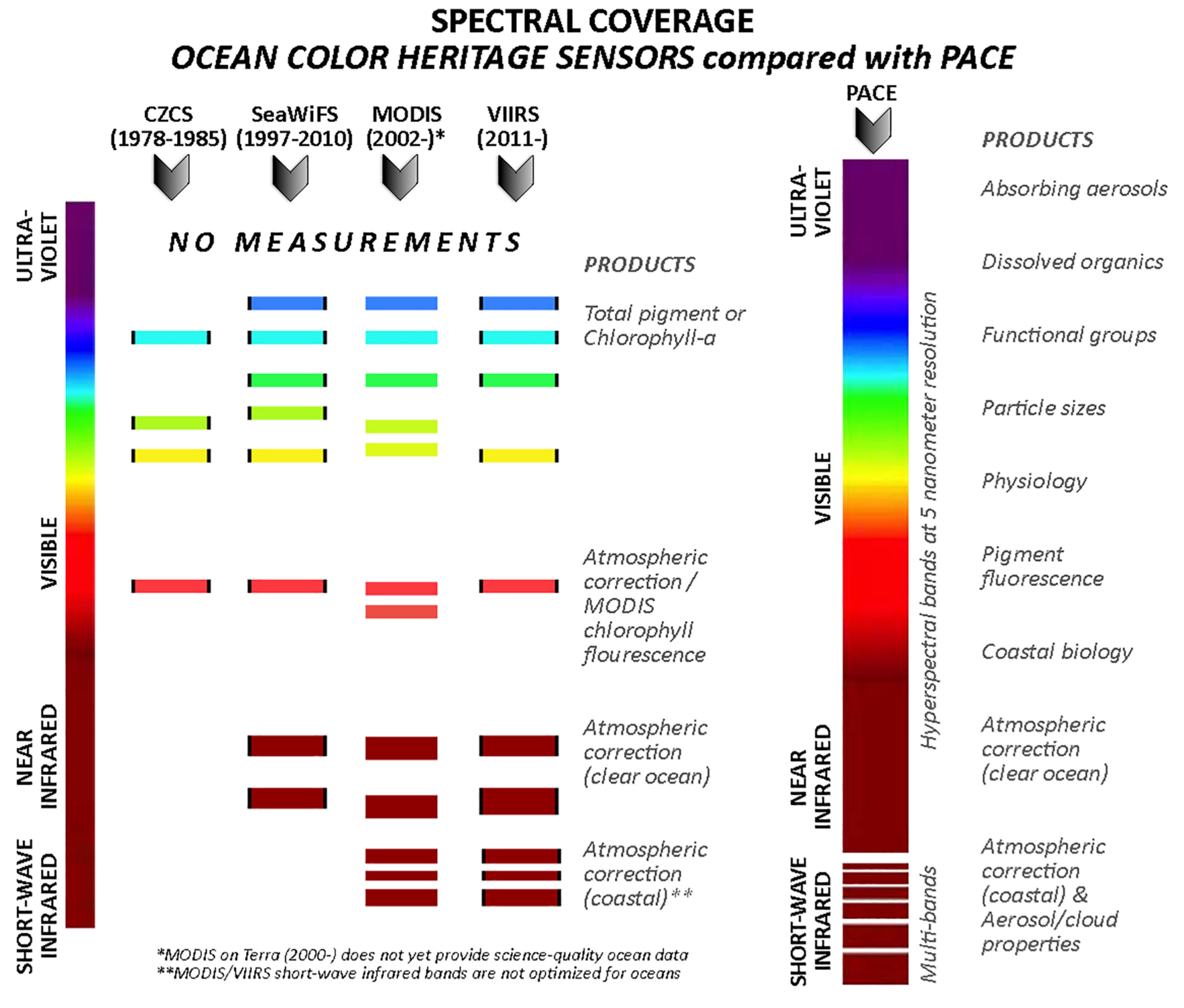

FIGURE 1 | The spectral coverage of ocean color heritage sensors compared to PACE. The hyperspectral capabilities of PACE OCI will provide new information about phytoplankton functional groups and metrics regarding the health of the ecosystem such as particle sizes and phytoplankton physiology. Source: https://pace.gsfc.nasa.gov.

global ocean color measurements for research and operational applications, and options to minimize the risk of a data gap (National Research Council [NRC], 2011). NOAA routinely conducts needs assessments targeted to various thematic and regional communities, including fisheries and water quality issues, and looks for ways to connect satellite data providers to practical end users. In 2007, the International Ocean Colour Coordinating Group (IOCCG) established a working group on the operational use of ocean color (IOCCG, 2008). In 2014, the IOCCG established a working group to develop a strategy for incorporating current and future satellite missions into global near-coastal and inland water quality monitoring efforts. Through breakout sessions at international conferences and their 2018 report (IOCCG, 2018), these working groups identified user needs and requirements in the context of existing observing capabilities, and offered suggestions for improving links between data providers and end users, as have other efforts (e.g., Nahorniak et al., 2013). We aim to accomplish similar objectives with an eye toward the role of new spectral capabilities by PACE through the activities described here.

SATELLITE OCEAN COLOR PROVIDES APPLICATIONS-RELEVANT DATA RECORDS

Heritage satellite OCIs observe the spectral radiance emanating from the top-of-the-atmosphere at discrete visible, NIR, and SWIR wavelengths. Atmospheric correction algorithms are applied to remove the contribution of the atmosphere and reflection off of the sea surface (e.g., foam and whitecaps) from the total signal to produce estimates of remote sensing

TABLE 1 | Key characteristics of OCI and the PACE observatory.

Characteristic	Description
OCI UV-NIR range (bandwidth)	Continuous from 340 to 890 nm in 5 nm steps (5 nm)
OCI SWIR range (bandwidth)	940 (45), 1038 (75), 1250 (30), 1378 (15), 1615 (75), 2130 (50), and 2260 (75) nm
OCI global coverage	2-day
OCI ground pixel	1 km at nadir
OCI instrument tilt	±20° to avoid Sun glint reflected off the ocean
OCI swath width	±56.5° (2663 km at 20° tilt)
Altitude	676.5 km
Orbit	Sun-synchronous, polar, 98° inclination
Equatorial crossing time	13:00 local
Data latency	Expected to be 6–12 h on average

reflectances [Rrs(λ); sr^{-1}], the light exiting the water normalized to the downwelling irradiance incident on the sea surface (Mobley et al., 2016). Bio-optical algorithms are then applied to the Rrs(λ) to derive geophysical properties of interest, such as surface concentrations of chlorophyll-a (Chl-a; mg m^{-3}) (O'Reilly et al., 1998). SeaWiFS, for example, collected data at six visible and two NIR wavelengths, where both NIR wavelengths were used for atmospheric correction and four of the six visible wavelengths were used to derive Chl-a. Other applications-relevant geophysical parameters derived from satellite ocean color include indicators of harmful algal blooms (HABs), water clarity, turbidity, sediments and detritus, shallow submerged and floating aquatic vegetation, surface oil slicks, and other variables estimated or inferred through regional correlations between field measurements and remotely sensed proxies (e.g., Stumpf et al., 2003; Hu et al., 2004; Stumpf and Tomlinson, 2005; Hu et al., 2009).

With respect to food security, the most relevant capability of a satellite OCI is its ability to monitor phytoplankton community structure (IOCCG, 2014). Understanding spatial and temporal changes in such structure provides insight into aquatic ecosystem health, water quality and related human health issues, as in the case of HABs, and ecological forecasting of aquatic resources including fisheries production. While ocean color methods for identifying different phytoplankton groups exist (e.g., Bracher et al., 2017; Mouw et al., 2017), most remain confounded by the limited number of wavelengths available on heritage instruments. Increased spectral resolution in the visible region offers improved characterization of spectral phytoplankton pigment absorption and particulate backscattering, both of which provide highly useful metrics for discriminating between phytoplankton groups and plankton size composition (Lubac et al., 2008; Bracher et al., 2009; Torrecilla et al., 2011; Catlett and Siegel, 2018). Several studies identify needs for hyperspectral measurements of at least 5 nm resolution to support classification of phytoplankton community structure (Lee et al., 2007; Vandermeulen et al., 2017). One promise of PACE is the utility of OCI's hyperspectral capability for the improved assessment of phytoplankton biomass, composition, and production (**Table 1**). Advances in such routine, global assessments will benefit ecosystem-based models, which aid in managing fisheries and coastal resources as well as policy-making related to monitoring of water clarity and detection and identification of the spatial extent and durations of HABs.

END USER ENGAGEMENT ACTIVITIES AROUND FISHERIES AND AQUACULTURE

In this section, we describe preliminary efforts to engage a diverse group of potential PACE data users from ocean color experts to novices and non-traditional user groups. The following sections explore these themes for attendees at our workshops, with a few specific case studies of current end users, the ways they utilize remote sensing technologies now, and their data needs related to remote sensing. All workshops were hosted in Washington, DC or Greenbelt, MD through the Applied Sciences activities of the Earth Science Division at NASA Goddard. The workshops

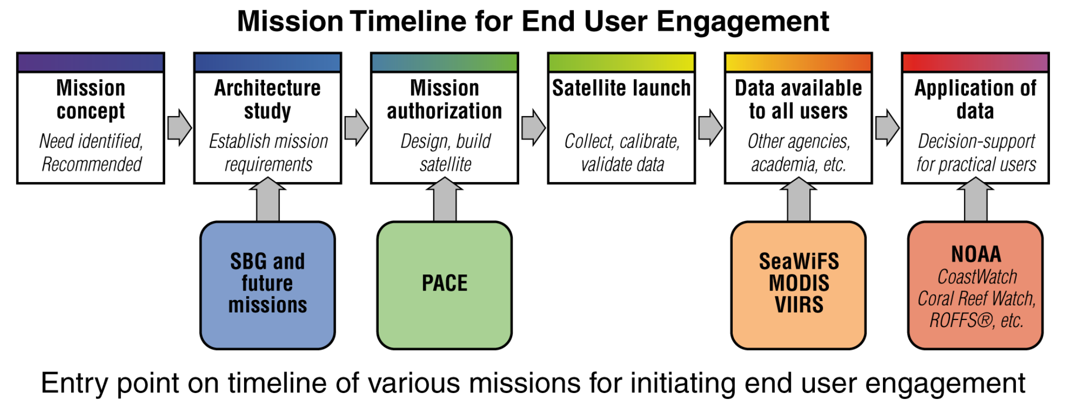

FIGURE 2 | A comparison of the entry point in the timeline for engaging end users in practical applications of satellite data by various NASA ocean color missions and operational activities by NOAA and the private sector. With PACE and future missions, such as Surface Biology and Geology (SBG), NASA now engages operational agencies and end users earlier in the satellite development process.

were promoted through routine communication channels (e.g., websites, monthly e-mailed newsletter, social media) with free and open registration by anyone interested in attending. The majority of participants in these activities and those who responded to our pre- and post-workshop surveys described their line of work as research, resource management, and public health. Other fields represented included policy/regulatory, remote sensing product development, commercial business, and applied remote sensing training and education. Casting a wide net of data users and potential users serves to deepen our awareness of broader needs beyond the traditional ocean color research community and also informs new groups about the possible applications of this freely available, public information resource.

A workshop on the societal applications of satellite data for ocean health and fisheries was co-hosted by NASA and World Resources Institute (WRI) with assistance from NOAA in November, 2017, garnering 152 registrants from multiple agencies from around the world, non-governmental organizations, and private businesses included research, education, resource management, policy, national security, public health and the fishing industry (Ward and Schollaert Uz, 2018). The meeting was live-streamed to enable remote participation, thus about 80 people participated in person with the rest online. The interactive program brought together multiple perspectives and diverse viewpoints (i.e., fishing businesses, resource managers, lawmakers). The format fostered dialogue between data providers, users, and potential users who could benefit from using satellite products. Four panels focused around the themes of ocean health in the context of climate change, fisheries and ecosystem health, links between fisheries and human security, and resources and tools for accessing ocean satellite data products. Agency managers and panelists shared science and products developed from publicly available ocean satellite data. A keynote presentation described how Global Fishing Watch monitors fishing activity from space to improve understanding, regulation, and protection. Notes taken during the workshop led to an extensive accounting of all presentations and discussions (Ward and Schollaert Uz, 2018).

Nearby NASA Goddard Space Flight Center, the Chesapeake Bay is the largest estuary in North America (**Figure 3**) and benefits the growing population of the region through its ecosystem services, fishing, and recreation. According to the Maryland Department of Natural Resources (DNR), the primary commercially harvested species in the Bay are oysters, blue crabs, and striped bass. Studies indicate the health of the Bay has seen some improvement in recent years, yet threats to its health persist (e.g., warming, oxygen minimum zones, pollution nutrient run-off). Increasing human presence in such a densely populated coastal region requires constant vigilance by agencies managing water quality, especially with a growing oyster aquaculture industry. In April, 2018 we began monthly meetings between NASA and NOAA satellite data providers with local resource managers around the Chesapeake Bay who routinely monitor shellfish beds and are interested in how remote sensing could help them improve the efficiency of their *in situ* sampling. In addition to meeting monthly, we held a day-long interagency workshop in August, 2018 attended by Chesapeake Bay science and applications stakeholders with the overall theme of monitoring water quality from space. The 95 participants included federal, state, and local agencies, non-governmental organizations, and universities. Future hyperspectral capabilities by PACE were highlighted, as they will provide the opportunity to measure additional indicators of ecological health and water quality. Workshop discussions focused on environmental variables needed by managers and whether and how remote sensing could address those needs through current or future capabilities, including water quality impacts to human health, shellfish poisoning, and quantifying the economic value of information needed to support decisions by resource managers and fishers (Schollaert Uz et al., 2018).

Discussions with these diverse international and regional groups drew increased attention to broader societal issues that could be informed by ocean color data and also identified applied research themes that need to be explored for development. Continuous engagement with these diverse groups informs NASA about their current challenges that satellite data could potentially address and keeps these groups informed about the status of PACE in its design cycle and the way its information will augment the international satellite fleet.

CURRENT USES OF REMOTE SENSING DATA FOR FISHERIES AND AQUACULTURE

Many examples of ocean color use toward marine food security have been previously described by efforts such as the Societal Applications in Fisheries and Aquaculture using Remotely Sensed Imagery (SAFARI) initiative (IOCCG, 2009). Here we provide updates on uses of remote sensing technologies through several examples, highlighting a few case studies shared during our workshops in which PACE data could help improve operations.

Oceanic management and conservation tools such as Coral Reef Watch and Ocean Health Index plus newer dynamic ecosystem models (e.g., Dynamic Seascapes within the Marine Biodiversity Observation Network) (Strong et al., 2006; Lewison et al., 2015; Hughes et al., 2017) rely on a combination of environmental and biological observations. These products merge *in situ* data, satellite sensors and big data techniques to quantify the effects of human impacts and natural variability on the marine ecosystem into useable indicators. The need for multiple data types is driven by the scientific understanding that there are multiple stressors acting on the marine ecosystem at the same time, which complicates the interpretation of trends in individual environmental variables.

Fisheries forecasting and management rely on multiple data streams to account for the dynamic nature of the aquatic environment. EcoCast, a fisheries sustainability tool, uses *in situ* and satellite data for environmental and species-specific information to maximize productive catch while minimizing bycatch (Hazen et al., 2018). This tool is one implementation of a new dynamic approach in fisheries management that accounts for

FIGURE 3 | Landsat 8 image of the Chesapeake Bay, tributaries, estuaries, sediment plumes and proximity to NASA Goddard. Measurements from space are used to guide *in situ* sampling by water quality resource managers, especially around oyster beds within the growing aquaculture industry. Credit: NASA/Michael Taylor and Ginger Butcher.

spatial and temporal variations in oceanic processes, as opposed to the traditional static approach with catch limits defined over a fixed area. From a commercial perspective, fisheries forecasting also utilizes a combination of remotely sensed physical (microwave SST) and biological (ocean color) indicators.

Aside from the technical challenges of fisheries management, regulatory agencies are tasked with the enforcement of lawful fishing. Global Fishing Watch tracks real-time commercial fishing activity to combat illegal, unreported and unregulated fishing and seafood fraud. This tool utilizes Automatic Identification System (AIS) data, a collison avoidance system for precise vessel location tracking. Combined with Sentinel-1 satellite radar data, Global Fishing Watch has been able to identify non-broadcasting vessels that attempt to go undetected in illegal fishing activities. In the year after its launch in 2016, this tool acquired over 5,000 core users from 189 countries, engaging a broad, international audience.

Harmful Algal Blooms

NOAA routinely monitors harmful algal blooms in coastal U.S. waters and the Great Lakes based on species' associations with environmental conditions (e.g., salinity fronts) and measured optical properties (Stumpf et al., 2003; Hu et al., 2004; Stumpf and Tomlinson, 2005). MERIS data is used to distinguish cyanobacteria blooms in U.S. inland waters (Wynne et al., 2008). During our Ocean Health and Fisheries workshop, a shellfish aquaculture farmer who has been operating in coastal ocean waters off Santa Barbara, California since 2002, Bernard Friedman described his business as intermittently plagued by harmful algal blooms. He provides ground-truth data to scientists developing the California-Harmful Algal Risk Mapping model to more precisely predict toxic algae events several days in advance (Anderson et al., 2016; Schollaert Uz, 2018), but the model's current resolution of 3 km^2 is too coarse to be reliable for him. Applying synoptic-scale satellite data to his 0.1 km^2 farm will require refining models in combination with additional observations, just as farmers on land use local weather forecasts from sophisticated models that assimilate many sources of observations.

Turbidity

For aquaculture planning, water clarity data products from MODIS at 250 m and Landsat-8 at 30 m are used in coastal waters (e.g., Snyder et al., 2017). The Shellfish Monitoring unit of the Maryland Department of the Environment (MDE) routinely patrols the Chesapeake Bay looking for signs of failing septic systems. MDE collects and analyzes water samples near oyster beds and closes the beds to harvesting whenever fecal coliform levels exceed a safe threshold. Scouting for failing septic systems is labor-intensive and time-consuming. DNR and MDE use available satellite products, e.g., water clarity (**Figure 4**), but see an opportunity to increase the efficiency of field sampling through a combination of more advanced remote sensing and other assets (e.g., models, autonomous observations).

Economic Valuation of Ecosystem Services

Economic benefits of improved water quality on commercial fisheries in the Chesapeake Bay have been evaluated by incorporating the effect of water quality changes on production and growth of the stock and producer and consumer surplus. Benefit assessments are complicated by environmental, regulatory, and business factors, such as new firms entering a commercial fishery once water quality improves and stocks grow. An estimate of the benefit of improved water quality in the Chesapeake Bay to striped bass sport fishing alone was valued at $15M in 1996 dollars (Morgan and Owens, 2001; Moore and Griffiths, 2017). Efforts to specifically address the benefit of incorporating Earth observations into decisions is currently being undertaken by the NASA-funded Consortium for the Valuation of Applications Benefits Linked with Earth Science (VALUABLES). This consortium has begun conducting rigorous, quantitative studies about how people use improved information to make decisions and quantify how these decisions improve socioeconomically meaningful outcomes such as lives saved or resources conserved. Within the next few years, they plan to evaluate the use of satellite data applied to water quality decisions, hopefully including PACE data.

ASPIRATIONAL USES OF SATELLITE DATA AND BARRIERS TO USE

In this section, we present survey results from the two workshops described in Section "End User Engagement Activities Around Fisheries and Aquaculture." Links to the surveys are provided below, along with links to other material about each workshop. The post-workshop surveys were completed by 45 respondents, with an additional 37 responses collected during the second workshop around specific water quality needs of resource managers around the Chesapeake Bay. Common survey results are graphed in **Figure 5**. Respondents expressed an overall need for satellite data to support decision making in fisheries management and water quality generally (**Figure 5A**), with smaller percentages of responses for more specific aims such as management of a specific water body or species (under "other management"). Attendees expressed a need for both physical and biological remotely sensed parameters, such as sea surface temperature and salinity, along with ocean color products such as chlorophyll-a concentration and water clarity parameters. Attendees at the Ocean Health workshop uniquely indicated sea surface height as a data need, while Chesapeake Bay workshop attendees require bottom characteristics, submerged aquatic vegetation, precipitation, and terrestrial products for their work. The most desired derived products are harmful algal bloom detection and water safety indices, such as potability and specific bacterial indices (**Figure 5B**).

The main barriers to using satellite and Earth Observation products in their work by most attendees (77%) is a lack of data processing and analysis skills, data access issues and the need for training (**Figure 5C**). Filling this need is an on-going challenge

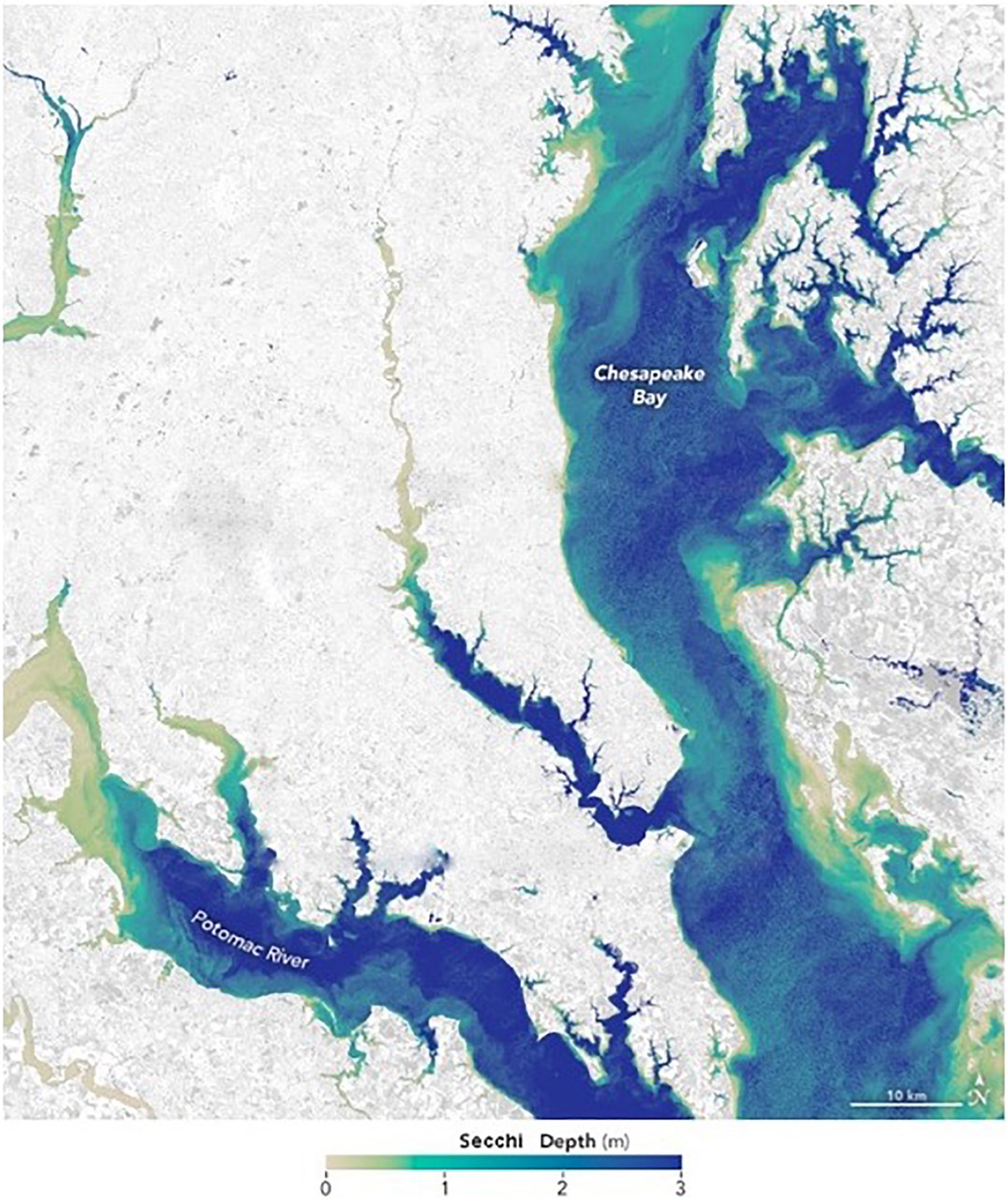

FIGURE 4 | Secchi depth indicates water clarity of the upper Chesapeake Bay and several tributaries derived from the Landsat OLI April 13, 2016 scene. Credit: NASA Earth Observatory and Lachlan McKinna.

for data providers and end users alike. IOCCG (2018) discusses a new efforts in Earth Observation data delivery, shifting from the old model of downloading and processing data locally to a new model of moving the processing software to the data source. This is motivated by the ever-increasing volume of data available and the challenges it presents to users for data processing. For example, with Platform as a Service cloud computing services, the provider hosts the data, hardware and/or software on its own infrastructure (e.g., Google Earth Engine, international Open Data Cube, ESA's Thematic Exploitation Platform and Copernicus Data and Information Access Service, DIAS). Cloud computing services will be even more important for PACE data, as the volume of its hyperspectral data will greatly exceed those of existing polar-orbiting multi-spectral ocean color satellites.

Spectral, spatial, frequency, and latency needs vary widely by community. Attendees primarily seek high spatial resolution for their applications, with 58% stating their ideal spatial scale for data products is finer than 100 m, and a further 21% indicating multiple scales of measurement are important depending on the application. The need for data at <10 m resolution was unique to responses from the Chesapeake Bay workshop, which include users who require this fine scale for land and/or aquatic products. Temporally, 54% indicated their ideal scale for data products is monthly to seasonal, while 35% seek weekly or

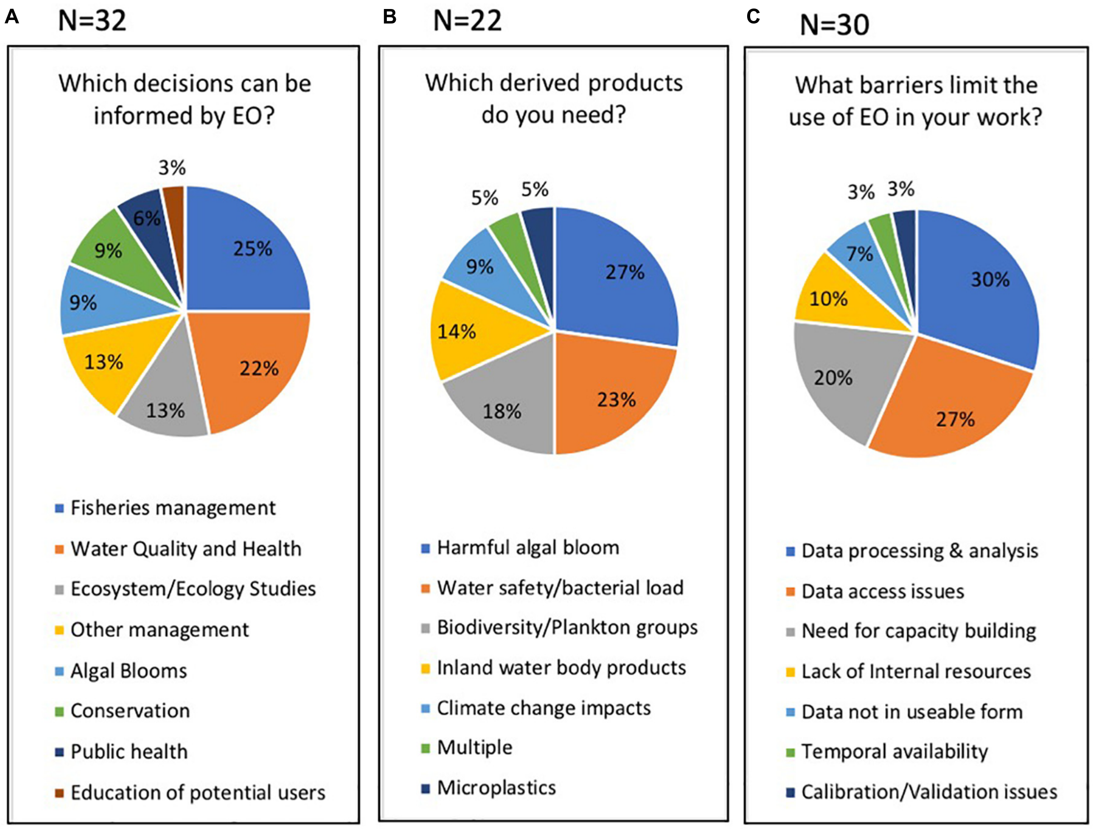

FIGURE 5 | Survey responses from the workshops quantifying **(A)** end user decision categories, **(B)** product needs and **(C)** barriers to the use of Earth Observations (EO).

more frequent temporal resolution. Needs for near real-time data were expressed by the commercial sector and fisheries management applications.

NEXT STEPS

Trade-offs in coverage, resolution, or frequency present barriers for practical use and have limited the local application of existing resources. With global coverage, polar-orbiting satellites capture slow-moving, mesoscale and larger biological features as often as daily, but cannot resolve transient, features on the order of 1km or less. Ocean ecosystems move and change - more similar to weather systems in the atmosphere than vegetation on land. Higher resolution Landsat 8 and Sentinel-2a&b data (10–30 m) are now used to intermittently monitor inland and coastal water quality albeit with a 5–16 days repeat cycle (Franz et al., 2015; Claverie et al., 2018; Keith et al., 2018). PACE will provide higher spectral resolution more frequently with which to distinguish phytoplankton communities (**Figure 6**), but still not as frequently as a geostationary platform such as GOCI that can capture diurnal changes (Ryu et al., 2012). Biogeochemical-ecosystem models integrated with radiative transfer models yield the absorption and scattering of light by optical constituents and spectrally resolved irradiance and been verified against *in situ* observations and satellite-derived products (e.g., Dutkiewicz et al., 2015). Models that further combine optical satellite data with fisheries demographic information have recently been developed to predict the location of an endangered species in order to guide resource manager in protection efforts (Breece et al., 2018). Future models that integrate the benefits of each satellite platform (e.g., high spectral resolution from PACE, high temporal frequency from geostationary, and higher spatial resolution from commercial or international sensors) with *in situ* observations at depth will enable the routine derivation of locally actionable three-dimensional information that a single satellite alone cannot provide.

Assessing the needs of the fisheries and aquaculture community around the Chesapeake Bay through collaboration and regular meetings with resource managers informs applied science priorities for PACE. Many variables that factor into resource manager decisions cannot currently be retrieved from satellite measurements (e.g., toxins, fecal coliform, pH, O_2). We need a multi-faceted monitoring system that exploits ecological associations with satellite-derived products. Aquatic features move and change faster than polar-orbiting satellites can observe. Clouds and the intervening atmosphere obstruct a satellite view of the water at visible and infrared wavelengths. Despite challenges, a synoptic view of key variables (e.g., SST, Chl-a, salinity) improves the efficiency of *in situ* sampling

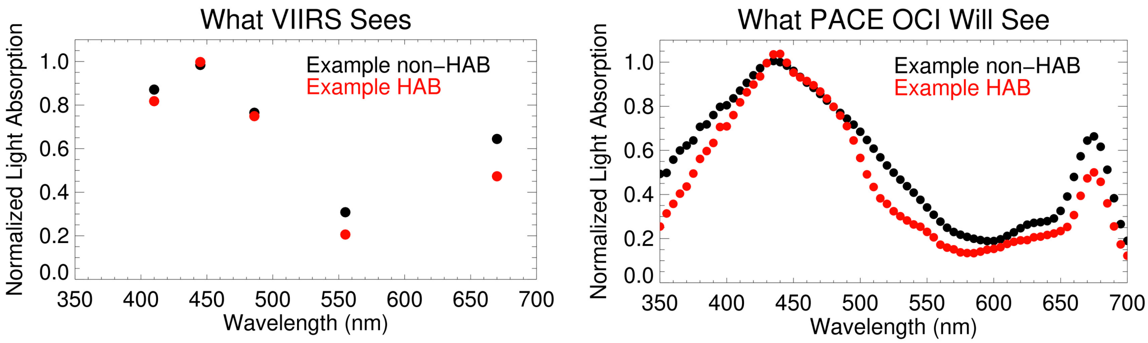

FIGURE 6 | A comparison of the spectral absorption signature of an algal bloom that's not harmful (non-HAB, black dots) compared to a harmful algal bloom (HAB, red dots) as detected at VIIRS wavelengths (left) compared to future retrievals at PACE OCI wavelengths. In this example, the non-HAB and HAB refer to the background diatom signature and that of *Noctiluca scintillans*, respectively. A phytoplankton community dominated by one versus the other has significant consequences for the marine food web and fisheries, as has been observed in the Arabian Sea (Gomes et al., 2014).

around aquaculture sites. Sustained satellite measurements also provide a long-term average from which anomalies may be detected. Through our regional effort in the Chesapeake Bay, we collaborate with MDE, NOAA, UMD and others to sample the optical, biological, physical, and chemical properties of water flowing into the Bay from land with a goal of finding unique hyperspectral signatures associated with various water quality indicators. Any progress to apply space-based assets through this and other such campaigns will assist NASA to prioritize PACE satellite data products and data distribution in support of fisheries and aquaculture. No single observing system will meet all needs by resource managers and others, but assimilation could exploit the strengths of each asset (i.e., high spectral resolution by PACE, high spatial resolution by harmonized Landsat/Sentinel, high temporal resolution by GOES). We are planning future interagency workshops around integrating satellite and *in situ* observations with modeling efforts to increase the utility of satellite data products.

The NASA Applied Sciences Program works together with NASA satellite missions prior to launch to engage user communities, solicit data and accuracy requirements for their operations and prepare them for the upcoming mission (Brown and Escobar, 2014). Now referred to as the Early Adopter program, this was discussed at both workshops as one way to engage end users early in the mission development process and have them test their applications with synthetic data. The European Space Agency conducted user needs assessments to make engineering choices prior to the Copernicus mission. By the time a NASA mission becomes official, it has historically been too late to make substantial hardware trade-offs but taking into account input from Early Adopters is still feasible for setting software priorities. As a cost-capped mission, the PACE Project did not receive funding to formally establish an Early Adopter program until recently. Initial efforts to recruit future early adopters have begun and the PACE Mission expects to begin executing a dedicated effort in 2020 to foster a community of practice specifically around the data that will be collected by OCI and the two multi-angle polarimeters and work directly with those implementing these observing systems.

PROFESSIONAL REVIEW OF THE PACE USER COMMUNITY

One of the main objectives of the PACE Applied Science Program is to engage potential data users during the early stages of mission development to ensure the PACE product suite and delivery mechanisms meet the most urgent demands of users and have the broadest impact. As part of these outreach activities, we have recently designed a professional review of Earth science data end users and experts who have been using, or are interested in using, observations relevant to PACE data products to address a broad range of applied science questions, from food and water security to fisheries, water quality assessments, air quality monitoring and improved pollution forecasts (PACE Mission Survey, 2019). Conducted via an online questionnaire of 17 questions, the professional review will be used to characterize the PACE mission user community in terms of its composition, activities, remote sensing needs, and research interests. The review questions are structured around three themes: user information, data use and requirements, and data access and outreach. We used experiences from satellite data user community evaluations conducted previously for other NASA missions, including SMAP (Soil Moisture Active Passive) and ICESat-2 (Ice, Cloud and land Elevation Satellite-2) (Brown and Escobar, 2014). The main goal of the PACE survey is to solicit data product, data accuracy and access needs, and apply results to plan outreach and applications before PACE launches in order to tailor them to user needs and enhance the societal value of the mission.

The target audience for the professional review is users from a wide range of sectors from around the world, including non-government organizations, non-profit organizations, private industry, universities, local, state and federal agencies. The subject community includes over 1,000 members, representing multiple disciplines including ocean biogeochemistry, oceanography, ecological forecasting, hazards, water resources and quality, terrestrial resources, weather, climate, air quality and human health. To characterize the community in terms of its composition, the survey includes questions on experience and training, and whether the responder is involved in policy making that involves hazard mitigation, increasing public awareness of emergencies, planning for environmental contingencies such as air quality, water quality, and marine resources, monitoring of environmental parameters, or conducts environmental research.

The need to bridge the gap between the increasing amount of satellite data available and end user requirements for data products, tools, and user training, has been widely highlighted by the international Earth Observations community (World Meteorological Organization [WMO], 2017). The Earth Science Division Directive on Project Applications Program presents guidance to all future directed NASA missions, emphasizing the need to characterize potential satellite data application uses and user needs during the early stages of a satellite mission development to increase the relevance and usefulness of their data products (i.e., latency, direct downloads, spatial resolution, data format, repeat frequency). Information from community surveys and professional reviews can help improve understanding on the use of satellite data for environmental applications by users globally, and to identify current gaps in data products, limitations in data access, and areas for improvement (Brown and Escobar, 2014). For example, a professional review conducted for the Famine EarlyWarning System Network (FEWS NET) created by the United States Agency for International Development (USAID) to improve their emergency response capabilities in Africa, had a significant influence on FEWS NET operations, including increased investment in higher resolution and better quality rainfall and vegetation data (Ross et al., 2009).

CONCLUSION

The recent Decadal Survey serves as a guiding document for NASA programs of Earth observations from space, placing a new emphasis on use-inspired science, whereby end-user needs explicitly inspire research scientists with the hope of improved outcomes for those applications. This is complementary to the curiosity-inspired science that has historically guided work in this field, in which societal benefits are considered after the scientific research has been completed. In response to this new direction, NASA is initiating direct interaction with the satellite data user community. The early efforts described here have begun to engage a community that could use future PACE data in support of fisheries and aquaculture. Through these activities, we are increasing access to satellite products that can give resource managers, lawmakers, fishing and aquaculture businesses the best available remotely sensed information. This ensures that satellite data providers and program managers understand the impact of various choices they make about PACE (e.g., data processing, latency, product development, and applied research efforts) and it will prepare future users of PACE data and engage them around the potential strengths, limitations, and uncertainties. Data gaps and barriers and a need for more training and dialogue have been identified, particularly around preparing the operational community to assimilate OCI data into early warning systems and dynamic ecosystem models.

Technical limitations aside, there are also practical limits to the satellite data products that PACE will be able to provide. The needs of end-users are as diverse as the data requirements and delivery mechanisms to address those needs. While the role of NASA is to explore new frontiers and foster innovative uses of its satellite data for societal benefit, massaging the data into just the right product and format for each user is not. Likewise, NOAA provides operational products, but has to balance the government's interest in providing timely, open access to global environmental data to promote and protect the safety and security of the American public while not competing with private businesses. Other organizations have developed the ability to take NASA and NOAA satellite data products and get them into the hands of new users. For example, in its Aquaduct water risk platform WRI provides satellite products to the business and investment community via Bloomberg's mapping tool where it is accessed by more than 400K users around the world. Regularly exchanging ideas with diverse end-user groups informs the PACE Mission about potential downstream uses of its data while preparing user communities for the advancements that are coming so that they can align resources to be ready to take full advantage of the data as soon as it flows. Engaging stakeholders on these and future follow-up activities with NOAA and other federal and state agencies and businesses (e.g., fishing, tourism, big data), we will be able to increase the return on investment of PACE data by providing useful satellite products that give managers, fishers, and aquaculture businesses the best available information. Synergy with operational partners and end-users of satellite data products is essential to realizing the full potential of this and future NASA missions. Interagency collaboration on stakeholder engagement through working groups, workshops, and applied research projects will help us understand how current and future satellite data can be optimized in new ways to solve societal problems around marine food security.

NOTES

Workshop agendas and presentations are available at the following sites: NASA/WRI Ocean Health and Fisheries workshop, 2017, Washington, DC: https://www.wri.org/events/2017/11/nasa-wri-ocean-health-and-fisheries-applications-workshop. Post-workshop-Survey: https://www.surveymonkey.com/r/MF2VSHJ. Interagency Chesapeake Bay workshop, 2018, Greenbelt, MD: https://science.gsfc.nasa.gov/610/applied-sciences/chesapeake_bay_workshop.html. Post-workshop Survey: https://docs.google.com/forms/d/1y4hA7JA-eDrKwZbjKUkgEtwakyxrcR0v-_oVhBeil7E/viewform?edit_requested=true.

AUTHOR CONTRIBUTIONS

SS led the workshops, surveys, and working group, and wrote and revised the manuscript. GK analyzed the survey data and helped to revise the manuscript. AM presented at the workshops, participated in the working group, and provided project content to the manuscript. PW presented at the workshop, attended the working group, and edited the manuscript. MT attended the working group and provided content on the PACE Mission Applications survey.

FUNDING

This study was supported by the NASA funding at NASA Goddard through the PACE Project and Applied Sciences Ecological Forecasting Program.

ACKNOWLEDGMENTS

Workshop planning and hosting assistance from Woody Turner of the NASA Applied Sciences Program on Ecological Forecasting, Cara Wilson of NOAA, and Janet Ranganathan of WRI, respectively, as well as meaningful discussions with all panelists and participants of both workshops are gratefully recognized. Motivation to form the interagency Chesapeake Bay working group began with Mark Trice of Maryland DNR and has sustained through collaboration with Rusty McKay of MDE, Shelly Tomlinson and Mike Ondrusek of NOAA, Rossana Del Vecchio of UMD, and many others. NASA Goddard Applied Sciences team members Brendan McAndrew and Jamie Dulaney assist with the monthly meetings and workshops. Encouragement from Jim Irons, Earth Sciences Division Director at NASA Goddard, fosters these activities. Finally, we are grateful to Jim Yoder, Professor Emeritus at URI, and the reviewers for helpful comments on earlier versions of this manuscript.

REFERENCES

Anderson, C. R., Kudela, R. M., Kahru, M., Chao, Y., Rosenfeld, L. K., Bahr, F. L., et al. (2016). Initial skill assessment of the california - harmful algae risk mapping (C-HARM) system. *Harmful Algae* 59, 1–18. doi: 10.1016/j.hal.2016.08.006

Bracher, A., Bouman, H. A., Brewin, R. J. W., Bricaud, A., Brotas, V., Ciotti, A. M., et al. (2017). Obtaining phytoplankton diversity from ocean color: a 697 scientific roadmap for future development. *Front. Mar. Sci.* 4:698. doi: 10.3389/fmars.2017.00055

Bracher, A., Vountas, M., Dinter, T., Burrows, J. P., Röttgers, R., and Peeken, I. (2009). Quantitative observation of cyanobacteria and diatoms from space using PhytoDOAS on SCIAMACHY data. *Biogeosciences* 6, 751–764. doi: 10.5194/bg-6-751-2009

Breece, M. W., Fox, D. A., Haulsee, D. E., Wirgin, I. I., and Oliver, M. J. (2018). Satellite driven distribution models of endangered atlantic sturgeon occurrence in the mid-atlantic bight. *ICES J. Mar. Sci.* 75, 562–571. doi: 10.1093/icesjms/fsx187

Brown, M. E., and Escobar, V. M. (2014). Assessment of soil moisture data requirements by the potential smap data user community: review of smap mission user community. *IEEE J. Sel. Top. Appl. Earth Obs. Remote Sens.* 7, 277–283. doi: 10.1109/JSTARS.2013.2261473

Catlett, D., and Siegel, D. A. (2018). Phytoplankton pigment communities can be modeled using unique relationships with spectral absorption signatures in a dynamic coastal environment. *J. Geophys. Res.* 123, 246–264. doi: 10.1002/2017jc013195

Claverie, M., Ju, J., Masek, J. G., Dungan, J. L., Vermote, E. F., Roger, J.-C., et al. (2018). The harmonized landsat and sentinel-2 surface reflectance data set. *Remote Sens. Environ.* 219, 145–161. doi: 10.1016/j.rse.2018.09.002

Donlon, C., Berruti, B., Buongiorno, A., Ferreira, M. H., Femenias, P., Frerick, J., et al. (2012). The global monitoring for environment and security (GMES) Sentinel-3 mission. *Remote Sens. Environ.* 120, 37–57.

Dutkiewicz, S., Hickman, A. E., Jahn, O., Gregg, W. W., Mouw, C. B., and Follows, M. J. (2015). Capturing optically important consituents and propoerites in a marine biogeochemical and ecosystem model. *Biogeosciences* 12, 4447–4481. doi: 10.5194/bg-12-4447-2015

FAO (2018). *The State of World Fisheries and Aquaculture 2018 - Meeting the Sustainable Development Goals*. Rome: FAO.

Franz, B. A., Bailey, S. W., Kuring, N., and Werdell, P. J. (2015). Ocean color measurements with the operational land imager on landsat-8: implementation and evaluation in Seadas. *Appl. Remote Sens.* 2:096070. doi: 10.1117/I.JRS.9.096070

Friedl, L., Wilson, C., Chao, Y., Bograd, S., and Turner, W. (2006). Using satellite data products to manage living marine resources. *EOS* 87:437. doi: 10.1111/brv.12359

Gomes, H. D. R., Goes, J. I., Matondkar, S. G. P., Buskey, E. J., Basu, S., Parab, S., et al. (2014). Massive outbreaks of *Noctiluca scintillans* blooms in the Arabian Sea due to spread of hypoxia. *Nat. Commun.* 5:4862. doi: 10.1038/ncomms5862

Groom, S., Sathyendranath, S., Ban, Y., Bernard, S., Brewin, R., Brotas, V., et al. (2019). Satellite ocean colour: current status and future perspective. *Front. Mar. Sci.* 6:485. doi: 10.3389/fmars.2019.00485

Hasekamp, O. P., Fu, G., Rusli, S. P., Wu, L., Di Noia, A., Brugh, J. A. D., et al. (2019). Aerosol measurements by SPEXone on the NASA PACE mission: expected retrieval capabilities. *J. Quant. Spectrosc. Radiat. Transf.* 227, 170–184. doi: 10.1016/j.jqsrt.2019.02.006

Hazen, E. L., Scales, K. L., Maxwell, S. M., Briscoe, D. K., Welch, H., Bograd, S. J., et al. (2018). A dynamic ocean management tool to reduce bycatch and support sustainable fisheries. *Sci. Adv.* 4:eaar3001. doi: 10.1126/sciadv.aar3001

Hu, C., Chen, Z., Clayton, T. D., Swarzenski, P., Brock, J. C., and Muller-Karger, F. E. (2004). Assessment of estuarine water-quality indicators using MODIS medium-resolution bands: initial results from Tampa Bay, FL. *Remote Sens. Environ.* 93, 423–441. doi: 10.1016/j.rse.2004.08.007

Hu, C., Li, X., Pichel, W. G., and Muller-Karger, F. E. (2009). Detection of natural oil slicks in the NW Gulf of Mexico using MODIS imagery. *Geophys. Res. Lett.* 36:1. doi: 10.1029/2008GL036119

Hughes, T. P., Kerry, J. T., Álvarez-Noriega, M., Álvarez-Romero, J. G., Anderson, K. D., Baird, A. H., et al. (2017). Global warming and recurrent mass bleaching of corals. *Nature* 543, 373–377. doi: 10.1038/nature21707

IOCCG, (2008). "Why ocean colour? the societal benefits of ocean-colour technology," in *Reports of the International Ocean-Colour Coordinating Group*, eds T. Platt, N. Hoepffner, V. Stuart, and C. Brown, (Dartmouth: IOCCG).

IOCCG, (2009). "Remote sensing in fisheries and aquaculture," in *Reports of the International Ocean-Colour Coordinating Group, No. 8*, eds M.-H. Forget, V. Stuart, and T. Platt, (Dartmouth: IOCCG).

IOCCG, (2014). *Phytoplankton Functional Types from Space*. Dartmouth: IOCCG.

IOCCG, (2018). "earth observations in support of global water quality monitoring," in *IOCCG Report Series, No. 17, International Ocean Colour Coordinating Group*, eds S. Greb, A. Dekker, and C. Binding, (Dartmouth: IOCCG).

Keith, D., Rover, J., Green, J., Zalewsky, B., Carpenter, M., Thursby, G., et al. (2018). Monitoring algal blooms in drinking water reservoirs using the landsat-8 operational land imager. *Int. J. Remote Sens.* 39, 2818–2846. doi: 10.1080/01431161.2018.1430912

Lee, Z. P., Carder, K., Arnone, R., and He, M. X. (2007). Determination of primary spectral bands for remote sensing of aquatic environments. *Sensors* 7, 3428–3441. doi: 10.3390/s7123428

Lewison, R. L., Hobday, A. J., Maxwell, S. M., Hazen, E. L., Hartog, J. R., Dunn, D. C., et al. (2015). Dynamic ocean management: identifying the critical ingredients of dynamic approaches to ocean resource management. *Bioscience* 65, 486–498. doi: 10.1093/biosci/biv018

Lubac, B., Loisel, H., Guiselin, N., Astoreca, R., Artigas, L. F., and Mériaux, X. (2008). Hyperspectral and multispectral ocean color inversions to detect *Phaeocystis globosa* blooms in coastal waters. *J. Geophys. Res.* 113:C06026. doi: 10.1029/2007JC004451

Martins, J. V., Fernandez-Borda, R., McBride, B., Remer, L. A., and Barbosa, H. M. J. (2018). "The HARP hyperangular imaging polarimeter and the need for small satellite payloads with high science payoff for earth science remote sensing," in *Proceedings of IEEE International Geoscience and Remote Sensing Symposium, IGARSS 2018*, Valencia.

Maul, G. A., Williams, F., Roffer, M., and Sousa, F. M. (1984). Remotely sensed oceanographic patterns and variability of blue fin tuna catch in the Gulf of Mexico. *Oceanol. Acta* 7, 469–479.

McClain, C. R. (2009). A decade of satellite ocean color observations. *Annu. Rev. Mar. Sci.* 1, 19–42. doi: 10.1146/annurev.marine.010908.163650

Mobley, C. D., Werdell, J., Franz, B., Ahmad, Z., and Bailey, S. (2016). *Atmospheric Correction for Satellite Ocean Color Radiometry*. Washington, D.C: NASA.

Moore, C., and Griffiths, C. (2017). Welfare analysis in a two-stage inverse demand model: an application to harvest changes in the chesapeake Bay. *Empir. Econ.* 55, 1181–1206. doi: 10.1007/s00181-017-1309-3

Morgan, C., and Owens, N. (2001). Benefits of water quality policies: the Chesapeake Bay. *Ecol. Econ.* 39, 271–284. doi: 10.1016/s0921-8009(01)00212-9

Mouw, C. B., Hardman-Mountford, N. J., Alvain, S., Bracher, A., Brewin, R. J. W., Bricaud, A., et al. (2017). A consumer's guide to satellite remote sensing of multiple phytoplankton groups in the global ocean. *Front. Mar. Sci.* 4:862. doi: 10.3389/fmars.2017.00041

Nahorniak, J., Letelier, R., Asanuma, I., Muller-Karger, F., King, E., and Colazo, M. (2013). *Ocean Satellite Data: Requests from the Fishery and Aquaculture Community, Report from the OSU/NASA Dream Ocean Satellite Image Workshop*. Newort, OR: NASA.

National Academies of Sciences Engineering and Medicine [NASEM], (2018). *Thriving on Our Changing Planet: A Decadal Strategy for Earth Observation from Space*. Washington, DC: The National Academies Press.

National Research Council [NRC], (2011). *Assessing the Requirements for Sustained Ocean Color Research and Operations*. Washington, DC: The National Academies Press.

O'Reilly, J. E., Maritorena, S., Mitchell, B. G., Siegel, D. A., Carder, K. L., Garver, S. A., et al. (1998). Ocean color chlorophyll algorithms for SeaWiFS. *J. Geophys. Res.* 103, 24937–24953. doi: 10.1029/98jc02160

PACE Mission Survey (2019). *PACE Mission Survey*. Available at: https://www.surveymonkey.com/r/7S2B7NF (accessed May 2, 2019).

Ross, K. W., Brown, M. E., Verdin, J. P., and Underwood, L. W. (2009). Review of FEWS NET biophysical monitoring requirements. *Environ. Res. Lett.* 4:024009. doi: 10.1088/1748-9326/4/2/024009

Ryu, J. H., Han, H. J., Cho, S., Park, Y. J., and Ahn, Y. H. (2012). Overview of geostationary ocean color imager (GOCI) and GOCI data processing system (GDPS). *Ocean Sci. J.* 47, 223–233. doi: 10.1007/s12601-012-0024-4

Schollaert Uz, S. (2018). *Using Scientific Muscle to Grow Safer Mussels. NASA Earth Observatory*. Available at: https://earthobservatory.nasa.gov/IOTD/view.php?id=91595 (accessed January 18, 2018).

Schollaert Uz, S., Turpie, K., Tomlinson, M., and Brown, C. W. (2018). *Prioritizing Aquatic Science And Applications Needs in the Cheseapeake Bay for a Space-Borne Hyperspectral Mission, Abstract GC13F-1092 Presented at the 2018 Fall Meeting, AGU, Washington, DC.* Available at: https://ntrs.nasa.gov/archive/nasa/casi.ntrs.nasa.gov/20190000495.pdf (accessed December 10, 2018).

Snyder, J., Boss, E., Weatherbee, R., Thomas, A. C., Brady, D., and Newell, C. (2017). Oyster aquaculture site selection using landsat 8-derived sea surface temperature, turbidity, and chlorophyll *a*. *Front. Mar. Sci.* 4. doi: 10.3389/fmars.2017.00190

Strong, A. E., Arzayus, F., Skirving, W., and Heron, S. F. (2006). "identifying coral bleaching remotely via coral reef watch - improved integration and implications for changing climate," in *Coral Reefs and Climate Change: Science and Management. Coastal and Estuarine Studies*, eds J. T. Phinney, et al. (Washington, DC: American Geophysical Union), 163–180.

Stumpf, R. P., Culver, M. E., Tester, P. A., Tomlinson, M., Kirkpatrick, G. J., Pederson, B. A., et al., (2003). Monitoring *Karenia brevis* blooms in the Gulf of Mexico using satellite ocean color imagery and other data. *Harmful Algae* 2, 147–160. doi: 10.1016/S1568-9883(02)00083-5

Stumpf, R. P., and Tomlinson, M. C. (2005). "Remote sensing of harmful algal blooms," in *Remote Sensing of Coastal Aquatic Environments*, eds R. L. Miller, C. E. DelCastillo, and B. A. McKee (Dordrecht: Springer), 277–296. doi: 10.1007/1-4020-3100-9_12

Torrecilla, E., Stramski, D., Reynolds, R. A., Millan-Nunez, E., and Piera, J. (2011). Cluster analysis 938 of hyperspectral optical data for discriminating phytoplankton pigment assemblages in the open 939 ocean. *Remote Sens. Environ.* 115, 2578–2593. doi: 10.1016/j.rse.2011.05.014

Vandermeulen, R. A., Mannino, A., Neeley, A., Werdell, J., and Arnone, R. (2017). Determining the optimal spectral sampling frequency and uncertainty thresholds for hyperspectral remote sensing of ocean color. *Opt. Express* 25:A785. doi: 10.1364/OE.25.00A785

Wall, C., Muller-Karger, F. E., and Roffer, M. (2009). Linkages between environmental conditions and recreational king mackerel (*Scomberomorus cavalla*) catch off west-central Florida. *Fish. Oceanogr.* 18, 185–199. doi: 10.1111/j.1365-2419.2009.00507.x

Ward, A., and Schollaert Uz, S. (2018). Interagency workshop on societal applications of satellite data for ocean health and fisheries. *Earth Obs.* 30, 9–20.

Werdell, P. J., Behrenfeld, M. J., Bontempi, P. S., Boss, E., Cairns, B., Davis, G. T., et al. (2019). The plankton, aerosol, cloud, ocean ecosystem (pace) mission: status, science, advances. *Bull. Amer. Meteor. Soc.* 100, 1775–1794. doi: 10.1175/BAMS-D-18-0056.1

Wilson, C. (2011). The rocky road from research to operations for satellite ocean-colour data in fishery management. *ICES J. Mar. Sci.* 68, 677–686. doi: 10.1093/icesjms/fsq168

Wilson, C., Chen, C., Clark, C., Fanning, P., Forget, M.-H., Friedland, K., et al. (2009). "Remote sensing applications to fisheries management," in *Remote Sensing in Fisheries and Aquaculture, IOCCG Report 8*, eds M.-H. Forget, V. Stuart, and T. Platt, (Dartmouth, NS: IOCCG), 43–56.

Wilson, C., Morales, J., Nayak, S., Asanuma, I., and Feldman, G. (2008). "Ocean colour radiometry and fisheries. in why ocean colour?," in *The Societal Benefits of Ocean-Colour Technology*, eds T. Platt, N. Hoepffner, V. Stuart, and C. Brown, (Dartmouth, NS: IOCCG), 47–58.

World Bank (2017). *The Sunken Billions Revisited: Progress and Challenges in Global Marine Fisheries. Environment and Development*. Washington, DC: World Bank.

World Meteorological Organization [WMO] (2017). *Survey on the Use of Satellite Data. 2017. WMO Space Programme SP-13, World Meteorological Organization*. Available at: http://www.wmo.int/pages/prog/sat/meetings/documents/IPET-SUP-3_Doc_09-01_WMOUserSurvey2016.pdf (accessed May 2, 2019).

Wynne, T. T., Stumpf, R. P., Tomlinson, M. C., Warner, R. A., Tester, P. A., Dyble, J., et al. (2008). Relating spectral shape to cyanobacterial blooms in the laurentian great lakes. *Int. J. Remote Sens.* 29, 3665–3672. doi: 10.1080/01431160802007640

Conflict of Interest: The authors declare that the research was conducted in the absence of any commercial or financial relationships that could be construed as a potential conflict of interest.

Advantages of publishing in Frontiers

Frontiers
Avenue du Tribunal-Fédéral 34
1005 Lausanne | Switzerland

Visit us: www.frontiersin.org
Contact us: info@frontiersin.org | +41 21 510 17 00